Vol. 65 ▪ No. 4 ▪ April 2024

JNM

The Journal of Nuclear Medicine

JNM Podcasts
jnm.snmjournals.org/podcasts

The debut episode discussing FAP is online now!

FEATURED ARTICLE

First-in-Human ^{212}Pb-PSMA–Targeted α-Therapy SPECT/CT Imaging in a Patient with Metastatic Castration-Resistant Prostate Cancer. Matthew R. Griffiths et al. See page 664.

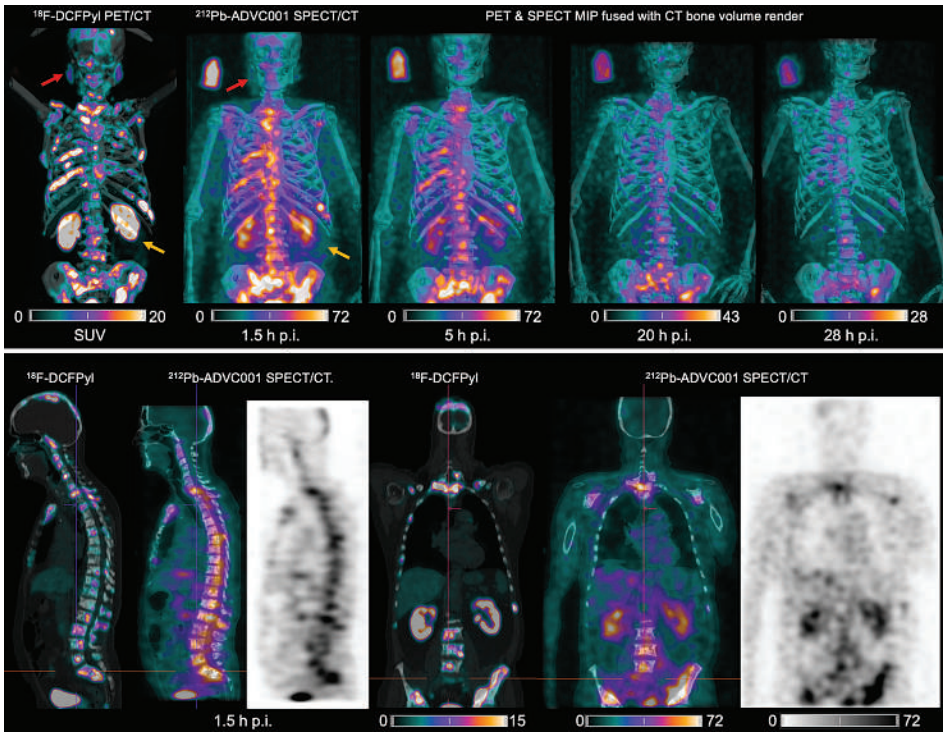

Theranostics in ovarian cancer: The potential for targeting with ^{89}Zr- and ^{177}Lu-labeled humanized antibodies. Kyeara N. Mack et al. See page 580.

SNMMI SOCIETY OF NUCLEAR MEDICINE & MOLECULAR IMAGING

SNMMI would like to thank our Value Initiative Industry Alliance member companies for their support. Together we have made incredible progress advancing patient care and precision medicine.

Leadership Circle

BLUE EARTH DIAGNOSTICS
A Bracco Company

SIEMENS Healthineers

CardinalHealth
Essential to care™

CURIUM™
LIFE FORWARD

Eisai

GE HealthCare

itm
PASSION FOR PRECISION

LANTHEUS

Lilly

NOVARTIS

UNITED IMAGING

Visionary Member

MIM SOFTWARE

Principal Member

BAYER

BRACCO
LIFE FROM INSIDE

CAPINTEC
A MIRION MEDICAL COMPANY

CELLECTAR BIOSCIENCES

cyclomedica

DAXOR
THE BLOOD VOLUME COMPANY

EVERGREEN THERAGNOSTICS

isotopia
Nuclear Medicine

JUBILANT RADIOPHARMA

Life Molecular Imaging

monrol

SHINE

SPECTRUM
DYNAMICS MEDICAL

Telix

Corporate Member

HERMES MEDICAL SOLUTIONS

MEDTRACE

NorthStar
MEDICAL RADIOISOTOPES, LLC

RayzeBio

Voximetry

032024-44

SNMMI SOCIETY OF NUCLEAR MEDICINE & MOLECULAR IMAGING
VALUE INITIATIVE

Learn more about becoming a Value Initiative Member Company:
valueinitiative.snmmi.org

SCAN QR CODE FOR
MORE INFORMATION

Innovate. Illuminate.

June 8-11
2024

SNMMI ANNUAL MEETING

CANADA
TORONTO

The premier educational, scientific, research, and networking event in nuclear medicine and molecular imaging, the SNMMI Annual Meeting provides physicians, technologists, pharmacists, laboratory professionals, and scientists with an indepth view of the latest research and development in the field as well as providing insights into practical applications for the clinic.

Mark your calendars to join us in **Toronto, June 8-11, 2024**, for a front-row seat to explore the most important nuclear medicine and molecular imaging science and research happening throughout the world.

www.snmmi.org/am

Early Bird Deadline: April 11, 2024

SNMMI SOCIETY OF NUCLEAR MEDICINE & MOLECULAR IMAGING
ANNUAL MEETING

03202440

SNMMI MARS SHOT

Funding Innovation for the Future of Nuclear Medicine

The SNMMI Mars Shot initiative ignites the focus, determination, and resources needed to unlock long-sought answers to using nuclear medicine to combat human illnesses. Be a part of this transformative journey, turning groundbreaking nuclear medicine research into the treatments of tomorrow, and redefining healing on a global scale.

DONATE TODAY

JNM
Volume 65 • Number 4 • April 2024

DISCUSSIONS WITH LEADERS

STATE OF THE ART

IS IT REALLY HAPPENING?

ONCOLOGY

Clinical

Basic

THERANOSTICS

Clinical

Basic

JNM The Journal of NUCLEAR MEDICINE

The Official Publication of **SNMMI**

MISSION STATEMENT: *The Journal of Nuclear Medicine* advances the knowledge and practice of molecular imaging and therapy and nuclear medicine to improve patient care through publication of original basic science and clinical research.

JNM (ISSN 0161-5505 [print]; ISSN 2159-662X [online]) is published monthly by SNMMI, 1850 Samuel Morse Drive, Reston, VA 20190-5316. Periodicals postage is paid at Herndon, VA, and additional mailing offices. Postmaster, send address changes to *The Journal of Nuclear Medicine,* 1850 Samuel Morse Drive, Reston, VA 20190-5316. The costs of publication of all nonsolicited articles in *JNM* were defrayed in part by the payment of page charges. Therefore, and solely to indicate this fact, these articles are hereby designated "advertisements" in accordance with 18 USC section 1734.

DISCLOSURE OF COMMERCIAL INTEREST: Johannes Czernin, MD, editor-in-chief of *The Journal of Nuclear Medicine,* has indicated that he is a founder of Sofie Biosciences and holds equity in the company and in intellectual property invented by him, patented by the University of California, and licensed to Sofie Biosciences. He is also a founder and board member of Trethera Therapeutics and holds equity in the company and in intellectual property invented by him, patented by the University of California, and licensed to Trethera Therapeutics. He also serves on the scientific advisory boards of RayzeBio and Aktis Oncology. No other potential conflicts of interest were reported. Manuscripts submitted to *JNM* with potential conflicts are handled by a guest editor.

EDITORIAL COMMUNICATIONS should be sent to: Editor-in-Chief, Johannes Czernin, MD, *JNM* Office, SNMMI, 1850 Samuel Morse Drive, Reston, VA 20190-5316. Phone: (703) 326-1185; Fax: (703) 708-9018. To submit a manuscript, go to https://submit-jnm.snmjournals.org.

BUSINESS COMMUNICATIONS concerning permission requests should be sent to the publisher, SNMMI, 1850 Samuel Morse Drive, Reston, VA 20190-5316; (703) 708-9000; home page address: jnm.snmjournals.org. Subscription requests and address changes should be sent to Membership Department, SNMMI at the address above. Notify the Society of change of address and telephone number at least 30 days before date of issue by sending both the old and new addresses. Claims for copies lost in the mail are allowed within 90 days of the date of issue. Claims are not allowed for issues lost as a result of insufficient notice of change of address. For information on advertising, contact Team SNMMI (Kevin Dunn, Rich Devanna, and Charlie Meitner; (201) 767-4170; fax: (201) 767-8065; TeamSNMMI@cunnasso.com). Advertisements are subject to editorial approval and are restricted to products or services pertinent to nuclear medicine. Closing date is the first of the month preceding the date of issue.

INDIVIDUAL SUBSCRIPTION RATES for the 2024 calendar year are $665 within the United States and Canada; $714 elsewhere. Make checks payable to the SNMMI. CPC IPM Sales Agreement No. 1415158. Sales of individual back copies from 1999 through the current issue are available for $60 at http://www.snmmi.org/subscribe (subscriptions@snmmi.org; fax: (703) 667-5134). Individual articles are available for sale online at http://jnm.snmjournals.org.

Discussions with leaders: Henryk Barthel talks with Julie Price about her career in advancing neuroimaging to enhance understanding of the brain and neurodegeneration. . . . . ***Page 499***

Theranostics and SBRT in oligometastasis: Kishan and colleagues address the current promise and potential contributions of metastasis-directed therapy in oligometastatic prostate cancer, including radiopharmaceutical and stereotactic body radiation therapies in managing disease. . . . ***Page 502***

^{18}F-FDG MTV in lymphoma: Barrington and colleagues look at current evidence and promising datasets supporting the use of PET-derived metabolic tumor volume for clinical risk stratification in lymphoma. . . . . ***Page 510***

^{68}Ga-FAPI in invasive lobular cancer: Sahin and colleagues assess the utility of ^{68}Ga-fibroblast activation protein inhibitor PET/CT as an alternative to ^{18}F-FDG PET/CT for staging invasive lobular breast cancer. . . . . ***Page 512***

Early radiation pneumonitis model for NSCLC: Thor and colleagues explore whether published models and pretreatment ^{18}F-FDG PET/CT–derived features can predict radiation pneumonitis within 3 mo after completion of chemoradiation/immunotherapy in stage III non–small cell lung cancer. . . . . ***Page 520***

NSCLC diagnosis and FAP expression: Li and colleagues report on the diagnostic accuracy of ^{68}Ga-labeled fibroblast activation protein inhibitor–04 PET/CT for lymph node metastases in non–small cell lung cancer and identify tumor ^{68}Ga-FAPI-04 uptake correlations with FAP expression. . . . . ***Page 527***

[^{67}Cu]Cu-EB-TATE theranostic and NETs: Njotu and colleagues detail preclinical evaluation of this long-lived somatostatin analog against somatostatin receptor subtype 2–positive neuroendocrine tumors. . . . . ***Page 533***

PSMA PET AUC updates: Hope and Jadvar review current indications for the use of PSMA PET imaging and note additional appropriate use criteria occasioned by the approval of ^{18}F-rh-PSMA-7.3. . . . . ***Page 540***

Pretreatment PSMA PET/CT and ^{223}Ra outcomes: Bosch and colleagues compare outcomes in patients with bone-only metastatic castration-resistant prostate cancer selected for ^{223}Ra-dichloride therapy by baseline imaging with PSMA PET/CT or CT. . . . . ***Page 541***

SUV_{max} on PSMA PET and γ-probe signal: Berrens and colleagues study correlations between the SUV_{max} of recurrent prostate cancer lesions on preoperative PSMA PET/CT and their intraoperative counts measured using the Drop-In γ-probe. . . . . ***Page 548***

^{68}Ga-PSMA PET/MRI and PI-RADS 3 classification: Shi and colleagues explore the added value of ^{68}Ga-labeled PSMA-11 PET/MRI in classifying Prostate Imaging Reporting and Data System category 3 lesions to avoid unnecessary biopsies. . . . . ***Page 555***

RECIP 1.0 and [^{18}F]PSMA-1007 PET: Hartrampf and colleagues evaluate the performance of these recently proposed response criteria in predicting overall survival in patients undergoing PSMA-targeted radioligand therapy and imaged with [^{18}F]PSMA-1007 PET/CT. . . . . ***Page 560***

STP with NLME and model selection: Hardiansyah and colleagues investigate the accuracy of single-time-point renal dosimetry imaging using SPECT/CT data, a nonlinear mixed-effects model, and a population-based model selection for ^{177}Lu-labeled PSMA therapy. . . . . ***Page 566***

[^{177}Lu]Lu-DOTA-JR11 and treatment-resistant meningioma: Eigler and colleagues compare the therapeutic index of this new radiolabeled somatostatin receptor antagonist with that of the established receptor agonist [^{177}Lu]Lu-DOTA-TOC in progressive, standard therapy–refractory meningioma. . . . . ***Page 573***

Theranostic potential in ovarian cancer: Mack and colleagues research the preclinical theranostic promise of a radiolabeled humanized antibody, huAR9.6, in targeting fully glycosylated and hypoglycosylated MUC16 isoforms in ovarian cancer. . . . . ***Page 580***

GPC-3 targeting in liver cancer: Lin and colleagues detail preclinical studies demonstrating the potential of a novel compound containing a macrocyclic peptide binder that can be complexed with different radioisotopes as a theranostic agent for GPC3-positive hepatocellular carcinoma. . . . . ***Page 586***

PSMA-targeted α-radiotherapy: El Fakiri and colleagues report on the design, development, and preclinical evaluation of ^{211}At-based radiopharmaceuticals that use clinically approved PSMA-617 as part of a theranostic strategy in prostate cancer. . . . . ***Page 593***

Internal carotids for PET quantification: Providência and colleagues assess the use of the internal carotids for quantifying brain glucose metabolism before and after partial-volume correction in ^{18}F-FDG PET imaging. . . . . ***Page 600***

Total-body PET/CT applications: Slart and members of the SNMMI Cardiovascular Council provide perspective on potential applications, challenges, opportunities, and remaining challenges of applying PET/CT with a long-axial field of view in cardiovascular disease. . . . . ***Page 607***

PET/CT and angiogenesis in ILD: Porter and colleagues investigate correlations between [^{18}F]FDG uptake and lung biopsy histologic markers in patients with fibrotic interstitial lung disease, highlighting the potential role of vasculature and angiogenesis in fibrosis. . . . . ***Page 617***

Automated PET/CT H&N tumor delineation: Kovacs and colleagues identify and evaluate promising state-of-the-art deep learning methods for ^{18}F-FDG PET gross tumor volume delineation in head and neck cancer. . . . . ***Page 623***

Mutations, RT, and NSCLC: Bourbonne introduce a model enabling prediction of KEAP1/NFE2L2 mutational status using PET/CT-extracted radiomics features to classify patients with non–small cell lung cancer at risk of local relapse after radiotherapy. . . . . ***Page 630***

NSCLC PET biomarkers: Hovhannisyan-Baghdasarian and colleagues assess imaging parameters characterizing the shift of SUV_{max} toward the lesion edge during tumor progression, their complementarity to conventional PET features, and prognostic value in advanced non–small cell lung cancer. . . . . ***Page 635***

Automated PET/CT tumor quantification: Leung and colleagues report on development of a deep semisupervised transfer learning approach for fully automated, whole-body tumor segmentation and prognosis on PET/CT. . . . . ***Page 643***

uMI Panorama PET/CT: Li and colleagues provide an assessment of the physical performance of this novel PET/CT system using silicon photomultiplier and application-specific integrated circuit technologies, per the National Electrical Manufacturers Association NU 2-2018 standard. . . . . ***Page 652***

Accomplishments of Saul Hertz: Greenspan and colleagues review the professional milestones of this nuclear medical pioneer in radioactive iodine therapy, including personal and historical context relevant to his legacy in the field. . . . . ***Page 659***

^{212}Pb SPECT/CT in pCa: Griffiths and colleagues present first-in-humans ^{212}Pb SPECT/CT images in a 73-y-old man with metastatic castration-resistant prostate cancer, highlighting potential for postinfusion radiopharmaceutical biodistribution imaging and patient-specific dosimetry for ^{212}Pb-targeted α-therapy. . . . . ***Page 664***

^{123}I-PARPi in neuroendocrine carcinoma: Ndlovu and colleagues describe [^{123}I]-PARP-inhibitor SPECT/CT as a noninvasive tool for whole-body assessment of PARP upregulation in lung small-cell neuroendocrine carcinoma, with implications for patient selection and response prediction in PARPi therapy. . . . . ***Page 665***

Advancing Neuroimaging

Julie Price Talks with Henryk Barthel About Enhanced Understanding of the Brain and Neurodegeneration

Julie C. Price[1] and Henryk Barthel[2]

[1]*Harvard Medical School, Massachusetts General Hospital A.A. Martinos Center for Biomedical Imaging, Boston, Massachusetts; and*
[2]*Leipzig University Medical Center, Leipzig, Germany*

Henryk Barthel, MD, PhD, a professor in the Klinik und Poliklinik für Nuklearmedizin at the University of Leipzig (Germany), talked with Julie C. Price, PhD, a professor of radiology at the Harvard Medical School and director of PET Pharmacokinetic Modeling in the Athinoula A. Martinos Center for Biomedical Imaging at the Massachusetts General Hospital (MGH; Boston). She is also faculty codirector for research at the MGH Center for Diversity and Inclusion (CDI). She specializes in PET imaging methodology with a focus on kinetic modeling of ligand–protein binding interactions in studies of aging, neuropsychiatric disorders, and neurodegeneration.

Dr. Price received her PhD from Johns Hopkins University in the Radiation Health Sciences Program led by Henry N. Wagner, MD. She completed postdoctoral training in quantitative PET in the National Institutes of Health (NIH) PET/Nuclear Medicine Department. From 1994 to 2016, she was a faculty member in radiology at the University of Pittsburgh, where she led PET methodology and worked with the group that established amyloid PET using Pittsburgh Compound-B (PiB). At MGH, she continues multidisciplinary PET research, with a primary focus on methods to improve early detection and longitudinal assessments of tau protein deposition with Harvard Aging Brain Study colleagues. She is a fellow of the Society of Nuclear Medicine and Molecular Imaging and the American Institute for Medical and Biologic Engineering. She has served as chair of the NIH Clinical Neuroscience and Neurodegeneration Study section and on the advisory council to the director of the NIH Center for Scientific Review.

Dr. Barthel: *Julie, thanks so much for this interview. From your CV I learned that in 2016 you moved to Boston to the Martinos Center. Can you elaborate on your role there?*

Dr. Price: I lead a PET methodology and data analysis group and am a research principal investigator. We're very collaborative and support various neuroimaging efforts. Much of my effort is also spent supporting research development for early-career researchers and helping to support the development of NIH-funded research applications in various areas, such as pain, addiction, and neurodegeneration, often involving PET/MR imaging. I've also helped to develop 2 NIH training grants at the Martinos Center. One is an AD-oriented T32 postdoctoral training program that aims to build a more diverse AD workforce across a range of clinical and technical research areas, in response to a targeted NIH funding announcement. Another NIH training grant with Bruce Fischl, PhD, is a summer internship program in neuroimaging that targets talented high school students from low income and ethnic or racial minority groups who are interested in STEM fields.

Julie C. Price, PhD

Dr. Barthel: *Wonderful to hear that training is part of the focus of your Martinos activities. This is so important and much appreciated. What makes the Martinos Center such a special place to work?*

Dr. Price: It's special because of the good people, impressive imaging resources, rich history of innovative imaging developments and applications, and international diversity. The center has about 120 faculty, 100 fellows, 8 tomograph bays for human research (3-T, 7-T, PET/MR), and many other resources (e.g., small-bore MR and PET/MR, hyperpolarizer, and spectroscopy systems). People are encouraged to work independently but collaboratively. You can walk down the hallway and have interesting conversations with 2 or 3 people who might help to solve a problem or stimulate a new idea. The trainees and even research assistants or coordinators who come in for a couple of years before going to medical or graduate school are very interested in research. This makes it a dynamic environment for mentoring. I give a lot of credit to Bruce Rosen, MD, PhD, the director of the Martinos Center, who works with faculty to promote excellence and provide a supportive environment during challenging academic times. He is a great mentor and colleague.

Dr. Barthel: *Harvard is also the home of the famous Harvard Aging Brain Study. In which way are you involved in this?*

Dr. Price: Among other tasks, I am involved in the PET methodology and support decision making related to PET methodology. This is a remarkable study. The findings have contributed to the framework of understanding of early AD. From its beginning as a program project in 2010, it had a specific focus on older individuals who were not clinically impaired. This study has really helped set the stage for therapeutic trial enrollments, contributing to a better understanding of AD and in vivo mapping of neuropathology during this preclinical phase. This was done by imaging amyloid burden and, when tau PET tracers became available, tau burden. At that time, it also became possible to investigate the in vivo synergy between amyloid and tau during the disease course. It became evident that the time point when neuropathologic tau deposition kicks

Published online Mar. 7, 2024.

DOI: 10.2967/jnumed.124.267651

in is not clearly driven by a single level of amyloid load and that further understanding of this complex process might be crucial. Keith Johnson, MD, and Reisa Sperling, MD, are doing a great job as principal investigators leading this effort and stimulating new investigations, such as those studying resilience and resistance to AD pathology.

Dr. Barthel: *These results are now moving into the clinical arena as drugs are developed that can potentially be applied at exactly the time point when the tau kicks in. It's fantastic to see how research translates into clinical use.*

Before you moved to Boston, you worked at the University of Pittsburgh, famous as the place where amyloid imaging was invented. The first human amyloid PET data were published by the Pitt group together with the Uppsala (Sweden) group in 2004. These are exciting times for amyloid imaging because now, nearly 20 years later, we have a chance to see amyloid imaging truly entering the clinical arena and making a difference to our patients. How were you involved in the development and testing of PiB, the first successful amyloid tracer?

Dr. Price: I was more involved with PiB in an operational and validation sense, particularly when they were moving to human imaging. I was less involved in the preclinical studies that Chester A. Mathis, PhD, William E. Klunk, MD, PhD, and others were performing. When they started to translate research into humans, then I became very involved. I remember when Chet and Bill asked me to go to Uppsala with them to review the initial human data; we were really excited. It was a great opportunity for me. The proof-of-concept human imaging study performed in Uppsala provided critical evidence that cortical PiB SUV measures were about 2-fold greater in AD patients than in control subjects. The next step was to apply for NIH funding, which provided the opportunity to perform a quantitative in vivo evaluation and analysis of human PiB PET data, including subjects with mild cognitive impairment, incorporating structural MRI data and full kinetic modeling. We also compared PiB retention against ^{18}F-FDG metabolism and ^{15}O-water blood flow measures. We also performed PiB PET test/retest studies.

Dr. Barthel: *This was groundbreaking work. It quickly became apparent that kinetic modeling can be done in amyloid imaging quite easily without arterial sampling. This brings me to another topic. I would also like to talk a bit about the AD Neuroimaging Initiative (ADNI). For our readers, the ADNI provides a very large database of imaging and nonimaging data in subjects at different AD stages and in controls, which can be used for various research purposes. How important do you consider the ADNI for our research?*

Dr. Price: The ADNI is immensely important to our research field. It began in 2004, and its data have been used to generate thousands of publications, about 1,400 just from 2021 and 2022. The ADNI has had a significant impact. It was one of the largest NIH public–private partnership studies in our field. It changed the landscape for those in the United States who were focused on federal funding for AD research. This framework has been extended internationally. It helped to standardize methods for AD biomarkers testing by standardizing protocols. Altogether, the great success of this data-sharing project stimulated other public–private partnerships. It has had a profound additional effect on the field by laying the groundwork for therapeutic trial considerations.

Dr. Barthel: *I agree. ADNI is a role model of a data-sharing platform that can serve as a paradigm for other imaging fields. Another question: I have observed over the years that for many brain PET tracers, static imaging is chosen over dynamic imaging, mainly to save time. By doing so, we lose the capability for absolute quantification. This is true even for the use of brain PET to test drug effects over time. Why do you think that we are struggling to use dynamic imaging and kinetic modeling more often?*

Dr. Price: There is a conception (in some cases correct) that dynamic imaging is too expensive, too labor-intensive, and associated with significant patient burden. However, dynamic imaging can be uniquely beneficial. Kinetic modeling of dynamic scan data acquired over a 60-min period or even a split acquisition of early- and late-postinjection imaging (such as the Amsterdam coffee-break approach) is feasible and can provide more quantitative outcome measures. As we move earlier and earlier in the disease process, which is likely in some future drug testing trials, as dynamic imaging is more and more feasible in terms of participant burden. But what is really important is the notion of the tissue uptake ratio. In the case of amyloid PET imaging, for example, the amount of amyloid load can affect the degree to which the tissue ratio is biased and the appropriate time interval for making the assessment. Dynamic studies are needed to carefully map these issues and to understand what is lost or gained by late scan ratio simplification, because bias will arise in ratio uptake measures (relative to quantitative measures) as a result of radioligand clearance effects (lack of equilibrium). Our field often accepts this bias, because the late scan uptake ratio measure is feasible. The ratio is also generally less biased when working in that preclinical space with lower amyloid or tau load when trying to detect earlier stages of deposition within the brain. With some of these amyloid or tau tracers we can assess more than just the pathology load from a dynamic study, such as surrogate measures of relative blood flow from the early postinjection PET data that are reflective of radioligand delivery from the vasculature into the brain. This is exciting and potentially relevant for studies of vascular factors that might cause someone to be more vulnerable to the deleterious effects of therapies—in addition to providing more in vivo information on patient status. So, certainly for the Harvard Aging Brain Study, amyloid PET information is still collected dynamically over 60 min, and I think this has been a positive approach.

> " … it would be beneficial to have a new generation of brain PET scanners that are both improved and more affordable. This would allow greater public access to advanced brain imaging technology across various settings. Both expense and expertise are required to achieve this—that's why it is so important to mentor new generations of dedicated scientists who can improve technology translation."

Dr. Barthel: *This might be even more relevant for the tau tracers.*

Dr. Price: This is true. For at least some of these tracers, static tissue uptake ratios do not reach a plateau during the late-scan PET acquisition interval, particularly for high binders, making the imaging outcome susceptible to variations in the scan start time

(i.e., higher uptake ratio values when postinjection imaging start times are delayed).

Dr. Barthel: *This brings me to the exciting ongoing development of new-generation tau tracers. One tau tracer, flortaucipir, is already approved by the U.S. Food and Drug Administration. What is your impression of these emerging new-generation tracers? Do we need better tau tracers?*

Dr. Price: It's important to reduce off-target signal in tau PET and to use a radiotracer with the best signal-to-noise and dynamic range. I haven't worked with all of the tau radiotracers, but those that allow robust assessment of uptake in brain areas where neuropathologic protein deposition occurs early in AD, such as the mesial temporal areas, would be good tracers of choice.

Apart from amyloid and tau tracers and in terms of emerging new-generation radiotracers, it would be of great significance to have new radioligands that enable robust imaging of α-synuclein and TAR DNA-binding protein 43 neuropathology. These capabilities would expand our primary pathology imaging approach to Parkinson disease, frontotemporal dementia, and other disorders.

Dr. Barthel: *Let's talk about an interesting technology development we are currently seeing. Different groups worldwide are working on dedicated brain PET scanners. What is your opinion? Does this make sense to you?*

Dr. Price: In my opinion, technological advances for dedicated brain scanners are important in terms of targeting very early disease. Just within the AD realm, it would be important for us to accurately image emergent tau pathology in the small locus coeruleus to further our in vivo understanding of the aging process and AD. But these imaging systems can be quite expensive and require top-level expertise. So, in addition, it would be beneficial to have a new generation of brain PET scanners that are both improved and more affordable. This would allow greater public access to advanced brain imaging technology across various settings. Both expense and expertise are required to achieve this—that's why it is so important to mentor new generations of dedicated scientists who can improve technology translation.

Dr. Barthel: *This aim of broadening access to imaging technology brings me to my last point: diversity. Diversity is increasingly considered to be important in science, as well as in everyday life. You are working at the CDI at MGH. Can you tell us a bit more about your efforts in this regard?*

Dr. Price: The MGH CDI has been clinically focused since it began almost 30 years ago. The goals included working to improve recruitment and retention of diverse individuals who are underrepresented in medicine (UiM) and to increase opportunities for these individuals to advance to senior positions in academic medicine at MGH. In October 2021, an initiative was launched to further expand CDI efforts into the research realm. Cesar Castro, MD, and I were chosen to be faculty codirectors for research at that center. There we have a strong focus on supporting individuals and networking. My efforts focus more on PhD researchers within the medical school environment. We try to understand an individual's aspirations and resources and provide support through one-on-one meetings on funding opportunities, the processes of grant development and review, CVs, and career development opportunities. Sometimes more difficult issues are addressed, such as challenges with mentors. On a more general level, we also support larger initiatives within MGH research training programs, ranging from undergraduates, medical students, graduate students, and postdocs to residents and early career faculty, for whom internal career development awards are available. My efforts involve a range of research initiatives targeting UiM recruitment and retention and building a diverse research community.

Dr. Barthel: *This sounds like very important work. Diversity is becoming a huge topic in clinical trials, with the Imaging Dementia—Evidence for Amyloid Scanning (IDEAS) study representing just 1 example in our field. We are living in a diverse world, and clinical studies need to reflect the diversity in the population.*

Dr. Price: We know that for some of the AD therapeutics currently being tested, differences in efficacy could depend on side effects, comorbidities, and genetic factors. Also, the impact of a diagnosis or of a positive amyloid scan may lead in specific cases to consideration of therapeutic options requiring frequent treatment visits. An individual's ability to take part might depend on access to a nearby health center that can provide the treatment.

Dr. Barthel: *Thanks so much, Julie, for these great insights and for your time.*

The Potential Contribution of Radiopharmaceutical Therapies in Managing Oligometastatic Disease

Amar U. Kishan[1,2], Shankar Siva[3], Michael S. Hofman[4], James Nagarajah[5], Ana P. Kiess[6], Phuoc Tran[7], and Jeremie Calais[8]

[1]Department of Radiation Oncology, UCLA, Los Angeles, California; [2]Department of Urology, UCLA, Los Angeles, California; [3]Peter MacCallum Cancer Centre and Sir Peter MacCallum Department of Oncology, University of Melbourne, Melbourne, Victoria, Australia; [4]Prostate Cancer Theranostics and Imaging Centre of Excellence, Molecular Imaging and Therapeutic Nuclear Medicine, Peter MacCallum Cancer Centre, Melbourne, Victoria, Australia; Sir Peter MacCallum Department of Oncology, University of Melbourne, Melbourne, Victoria, Australia; [5]Roentgeninstitut Duesseldorf, Duesseldorf, Germany; [6]Department of Radiation Oncology and Molecular Radiation Sciences, School of Medicine, Johns Hopkins University, Baltimore, Maryland; [7]Department of Radiation Oncology, University of Maryland School of Medicine, Baltimore, Maryland; and [8]Ahmanson Translational Theranostics Division, Department of Molecular and Medical Pharmacology, David Geffen School of Medicine, UCLA, Los Angeles, California

There is a growing understanding of the oligometastatic disease state, characterized by the presence of 5 or fewer lesions. Advanced molecular imaging techniques, such as prostate-specific membrane antigen PET, refines the ability to detect oligometastatic recurrences (oligorecurrences) early. These developments have led to the exploration of metastasis-directed therapy (MDT) in oligorecurrent disease as an alternative to or as a means of delaying systemic therapy. Unfortunately, MDT often does not provide a durable cure, and progression—particularly progression in multiple new areas—remains a concern. Simultaneously, developments in radioligand therapy (RLT) have led to studies showing overall survival benefits with α-emitting and β-emitting RLT in advanced, high-volume, metastatic castration-resistant prostate cancer. The success of RLT in late-stage disease suggests that earlier use in the disease spectrum may be impactful. Specifically, integration of RLT with MDT might reduce progression, including polymetastatic progression, in the setting of oligorecurrent disease.

Key Words: stereotactic body radiotherapy; radioligand therapy; oligometastatic prostate cancer

J Nucl Med 2024; 65:502–509
DOI: 10.2967/jnumed.123.266772

As our understanding of the natural history and biology of prostate cancer evolves, we have gained appreciation for the fact that metastatic prostate cancer is a heterogeneous disease entity composed of multiple subgroups with distinct prognoses (*1*,*2*). The most intuitive method of subclassifying metastatic disease—based on the burden or volume of disease—is also the most evidence-based, as a lower burden of disease has consistently been associated with improved overall survival (OS) (*3*–*7*). At the extreme end of this spectrum of disease would be the oligometastatic disease state, formally postulated in 1995 and now considered to be a distinct disease stage characterized by the presence of a limited number of clinically detectable metastases, typically 5 or fewer (*8*,*9*). Oligometastatic disease can be further dichotomized on the basis of the temporal sequence of presentation: de novo oligometastatic disease refers to oligometastatic spread detected at the time of initial diagnosis, and recurrent oligometastatic disease (or oligorecurrent disease) refers to oligometastatic disease detected after prior definitive-intent local therapy. Conceptually alongside increasing evidence, the oligometastatic disease state could be considered a combination of truly indolent disease biology with limited polymetastatic potential, truly aggressive disease biology identified early in the course, or traditionally subclinical disease that has been identified by increasingly sensitive imaging (*10*,*11*).

The recognition of the oligometastatic disease state occurred in synchrony with years of diligent basic, translational, and clinical research that have identified substantial survival benefits with androgen deprivation therapy (ADT) and second-generation androgen receptor signaling inhibitors in metastatic hormone-sensitive prostate cancer (mHSPC) (*12*). Although the improvement in efficacy has been undeniable, ADT alone, let alone with second-generation agents, is associated with significant detriments in quality of life (*13*).

Furthermore, significant imaging advances have led to a substantial improvement in detection of metastatic spread, allowing diagnosis of metastatic disease far earlier—and thus at a substantially lower burden—than previously possible. Chief among these advancements is the development of prostate-specific membrane antigen (PSMA)–based PET/CT. PSMA PET/CT offers substantially improved sensitivity and specificity for the identification of extraprostatic disease in both the de novo and the recurrent settings (*14*). A reasonable conclusion would be that molecular imaging–defined oligometastatic disease represents the lowest potential burden of disease along the metastatic spectrum, and therefore alternative therapeutic strategies to those typically used for conventionally defined mHSPC can and should be pursued.

OVERVIEW OF METASTASIS-DIRECTED THERAPY (MDT) IN PROSTATE CANCER

To this end, MDT has emerged as an attractive option for the growing population of patients diagnosed with molecularly defined mHSPC. The premise for why MDT might significantly impact

Received Oct. 21, 2023; revision accepted Jan. 23, 2024.
For correspondence or reprints, contact Amar U. Kishan (aukishan@mednet.ucla.edu).
Published online Feb. 15, 2024.

natural history, rather than simply provide local control for treated lesions, stems from the discovery that metastasis-to-metastasis spread in the same patient is common, either through de novo monoclonal seeding of daughter metastases or through the transfer of multiple tumor clones between metastatic sites (*15*). Indeed, in contrast to the traditional belief in solid oncology that the cancer is no longer curable once it becomes metastatic, aggressive MDT to eliminate all sites of macroscopic disease in a patient with oligometastatic disease has been shown to lead to long-term disease control and possibly even a cure in certain cases (*16–25*).

The development of stereotactic body radiation therapy (SBRT), which involves the delivery of an ablative dose of radiation precisely to the lesions in 5 or fewer treatment sessions, is a critical tool for MDT. Given its biologic advantage of a higher dose per fraction, increased convenience with a shorter treatment course, a high local control rate, and a modest toxicity profile, SBRT has become the radiation modality of choice when delivering MDT. The randomized SABR-COMET trial is one of the earlier trials that tested whether MDT delivered via SBRT could improve outcomes in patients with oligometastatic disease. In this trial, 99 patients with controlled primary malignancies of various histologies who had 5 or fewer metastatic lesions were randomized 2:1 to SBRT to all sites of disease or the palliative standard of care (which included non-SBRT palliative radiation). The most common primary tumor types were breast ($n = 18$), lung ($n = 18$), colorectal ($n = 18$), and prostate ($n = 16$). At a median follow-up of 25 mo, median OS was 41 mo among patients receiving SBRT versus 28 mo in patients receiving the standard of care ($P = 0.09$) (*26*). With longer-term follow-up (median, 51 mo), SBRT was still associated with an increased OS (5-y OS, 42.3% vs. 17.7%; $P = 0.006$) and progression-free survival (PFS) (5-y PFS, not reached vs. 17.3%; $P = 0.001$) (*17*). However, an increased risk of grade 2 toxicity or higher was seen (29% vs. 9%, $P = 0.026$).

For prostate cancer specifically, MDT for oligorecurrent disease has been evaluated in 4 prospective studies, including 2 randomized phase II trials (Table 1). The STOMP trial enrolled 62 men with oligorecurrent disease after prior surgery or radiation who had no more than 3 metastases visible on ^{11}C-choline PET and randomized them to observation versus MDT (*18*). The primary endpoint was ADT-free survival, with ADT starting at the time of polymetastatic progression, local progression, or symptoms. PFS was a composite secondary endpoint, defined by biochemical progression (as per PCWG2 (*27*)), RECIST-based local progression

NOTEWORTHY

- MDT, particularly in the form of SBRT, has been shown to improve PFS and systemic treatment-free survival in men with oligorecurrent prostate cancer in multiple prospective studies.
- Long-term cures after MDT are rare, and a substantial proportion of patients experience polyprogression within 2 y of MDT.
- ^{223}Ra and ^{177}Lu-PSMA RLT have been shown to improve OS in patients with mCRPC, but responses in advanced disease are not durable because of the aggressive natural history and high burden of disease that can become nonresponsive.
- Integrating theranostic therapy with metastasis-directed SBRT may limit polyprogression and improve durable response rates and intervals.

TABLE 1
Summary of Prospective Trials of MDT for Oligorecurrent Hormone-Sensitive Prostate Cancer

Trial	Design	Imaging	Patients (*n*)	Lesion distribution	Median follow-up	Result
STOMP (*18*)	Phase II RCT MDT vs. surveillance (80% MDT was SBRT)	Choline PET/CT (1–3 lesions)	62	Bone, 39%; node, 55%; viscera, 2%	36	PFS, 10 vs. 6 mo; ADT-FS, 21 vs. 13 mo
ORIOLE (*19*)	Phase II RCT SBRT vs. surveillance	Conventional imaging (1–3 lesions)	54	Bone, 39%; node, 61%	19	6-mo progression rate: 19% vs. 61%
POPSTAR (*20*)	Phase I SBRT (33% had ADT)	NaF PET/CT (1–3 lesions)	33	Bone, 61%; node, 36%; bone and node, 3%	24	2-y distant PFS, 58%; 2-y ADT-FS, 48%
MRgRT (*23*)	Phase II single MDT (73% SBRT)	Negative conventional and positive PSMA PET/MRI/CT (1–5 lesions)	37	Node, 92%; bone, 8%	16	22% had complete response with PSA < 0.05; ADT-FS, 17.7 mo

RCT = randomized controlled trial; ADT-FS = ADT-free survival.

(*28*), distant progression, and death from any cause. Among patients who received MDT, 81% received SBRT. Initial results at a median follow-up of 36 mo showed that MDT improved ADT-free survival from 13 to 21 mo and improved the median time to biochemical progression from 6 to 10 mo. In an update with longer follow-up, the PFS benefit of MDT was maintained (hazard ratio [HR], 0.48; $P = 0.01$) (*29*).

The ORIOLE trial enrolled 54 patients with oligorecurrent disease after prior surgery or radiation who had no more than 3 metastases visible on conventional imaging (*19*). The primary endpoint was the proportion of men with disease progression at 6 mo, defined as a composite endpoint of a PSA rise of at least 2 ng/dL and 25% above nadir; concern for radiologic progression by either CT, MRI, or bone scanning; symptomatic progression of disease; initiation of ADT for any reason; or death. All patients underwent ^{18}F-DCFPyL PSMA PET/CT as well, though patients and investigators were masked to the results. Overall, SBRT reduced the proportion of men with disease progression from 61% to 19% at 5 mo ($P = 0.005$). With a median follow-up of 18.8 mo, the median PFS with SBRT was not reached, whereas it was 5.8 mo with observation (HR, 0.3; $P = 0.002$). Among the 36 men who underwent PSMA PET/CT, 16 (44.4%) had lesions not seen on conventional imaging. The proportion of progression at 6 mo was only 5% for men with no untreated PSMA-positive lesions, versus 38% for those with any untreated PSMA-positive lesions ($P = 0.03$). Median distant metastasis-free survival was 29.0 mo in men with no untreated lesions, versus 6.0 mo in men with any untreated lesion ($P < 0.001$).

In an update with a median follow-up of 5.3 y, the PFS benefit of MDT was maintained (HR, 0.48; $P = 0.01$) (*29*). In a per-protocol analysis, MDT improved castration-resistant prostate cancer–free survival (HR, 0.51; $P = 0.12$) (*30*).

A pooled analysis of both trials with a median follow-up of 52.5 mo found that MDT significantly improved PFS from 5.9 to 11.9 mo, with a pooled HR of 0.44 ($P < 0.001$) (*29*). However, radiographic PFS, time to castration-resistant prostate cancer, and OS were not improved. Patients whose tumors harbored a high-risk mutational signature (defined by pathogenic somatic mutations within *ATM, BRCA1/2, Rb1,* and *TP53*) had a shorter PFS, though these patients had a significantly larger PFS benefit from MDT as well.

Two additional single-arm phase II trials have used advanced molecular imaging to investigate MDT in patients with oligorecurrent disease. The POPSTAR trial enrolled 33 men who had up to 3 bony or lymph node lesions seen on a screening ^{18}F-NaF-PET/CT scan (*20*). The primary endpoints were feasibility and tolerability; secondary outcomes included local and distant PFS, with the former scored by RECIST (*28*). Local PFS was 93% at 2 y, whereas 2-y distant metastasis-free survival was 39%. Twenty-two of the patients had hormone-sensitive disease, and among these patients, the freedom from ADT was 48% at 24 mo. The PSMA MRgRT trial enrolled patients with negative results on conventional imaging and 5 or fewer lesions on ^{18}F-DCFPyL PSMA PET/MRI/CT who had a rising PSA of 0.4–3.0 ng/mL (*23*). Ultimately, 37 patients received MDT. At a median follow-up of 15.9 mo, 22% of patients had a complete biochemical response (PSA reduced to <0.05 ng/mL) and 60% of patients had a PSA decline of at least 50%. The median time to PSA progression was 17.7 mo. An update of the initial PSMA MRgRT cohort found that, with an extended follow-up to 40.7 mo, the biochemical response rate was maintained at 59.4%, with a complete biochemical response in 27% (*31*). In a validation cohort of 37 patients with identical enrollment criteria and a median follow-up of 14.3 mo, a biochemical response was seen in 43% of patients, with a complete response in 13.5%.

Taken together, studies confirm that MDT (predominantly delivered with SBRT) for patients with oligorecurrent prostate cancer significantly delays PSA-based progression. Importantly, MDT is safe: across these trials, of the 165 patients who received MDT, only 2 grade 3 toxicities attributable to MDT were seen. This contrasts with SABR-COMET, in which 3 treatment-related deaths were seen. The difference may be explainable by the fact that patients on the 4 prostate trials rarely had visceral metastases, which can be more challenging to irradiate.

Despite the favorable safety profile and overall initial efficacy, however, there are clearly patients who progress after MDT and may benefit from further treatment intensification (*32*,*33*). In a retrospective study of 258 patients with oligorecurrent mHSPC who had a median follow-up time of 25.2 mo, the median time to PSA recurrence after MDT was 15.7 mo and the median distant metastasis-free survival was 19.1 mo. Among patients who did not receive ADT, the median time to PSA recurrence was 10.9 mo and distant metastasis-free survival was 12.4 mo. Another 20 men were treated with a defined course of ADT; after stopping ADT, the median biochemical PFS was 17.6 mo. Overall, bone-only recurrence was the most common form of failure (44.2% of patients with recurrences), with another 24.8% of recurrences involving osseous disease in addition to another site. Node-only recurrences accounted for 26.5% of recurrences. Interestingly, the original site of recurrence was associated with subsequent sites of recurrence. Among patients treated for a bone lesion, most recurrences (86.5%) involved at least 1 osseous structure. For patients treated for a node-only lesion, most recurrences were also node-only (64.5%), though an osseous component was seen in 32.3% of recurrences. Three modes of progression were defined. Class I progressors, accounting for 40.9% of patients overall and 27.6% treated without ADT, had long-term control with no recurrences after 18 mo. Class II progressors, or oligoprogressors, had no more than 3 lesions at recurrence and accounted for 36% of patients overall and 44.8% of those treated without ADT. Class III progressors, or polyprogressors, had more than 3 lesions at recurrence and accounted for 23.1% of patients overall and 27.6% of those treated without ADT. Among patients who had advanced molecular imaging for follow-up, rather than conventional imaging, a lower percentage had long-term control (36.3%) and a higher percentage had polyprogression (26%). Overall, these data suggest that systemic therapy intensification is warranted in some patients with oligorecurrent mHSPC. Given that most men with early oligometastatic disease defined by molecular imaging may be seeking to avoid ADT—which may be primarily cytostatic in this context—alternative forms of systemic intensification warrant investigation.

OVERVIEW OF RADIOLIGAND THERAPY (RLT) AND THERANOSTIC THERAPIES IN PROSTATE CANCER

RLT, also known as radionuclide therapy, refers to the systemic administration of radiolabeled drugs targeting proteins that are specific to abnormal cells, allowing the delivery of localized radiation at the cellular level (*34*). Radioligands can be broadly classified into α-emitting radioligands and β-emitting radioligands. α-particles have short pathlengths of 50–80 μm, possess a linear energy transfer of 100 keV/μm, and can cause significant direct

DNA damage (*35*,*36*). β-particles have a longer pathlength of 0.05–12 mm as well as lower linear energy transfer of 0.2 keV/μm (*37*). β-particles may thus be less directly efficacious, particularly against smaller lesions, and may have more toxicity against nontarget tissues (*38*). Overall, only 1 α-emitter is approved for clinical use, whereas multiple β-emitters are approved across different cancers. Specifically in the context of prostate cancer, 2 older β-emitters were approved for palliative use, but 1 α-emitter, ^{223}Ra-dichloride (^{223}Ra), and 1 β-emitter, ^{177}Lu vipivotide tetraxetan (^{177}Lu-PSMA-617), have been shown to improve OS (*39*). Studies with these agents are summarized below and in Table 2.

^{223}Ra is a targeted α-emitter that, as a calcium mimetic, is preferentially incorporated into the bony matrix in areas of high bone turnover such as osteoblastic or sclerotic metastases (*40–42*).^{223}Ra is thus an attractive RLT for metastatic castration-resistant prostate cancer (mCRPC), a lethal, end-stage form of prostate cancer in which bone-related complications are a leading cause of death (*43*). The benefit of ^{223}Ra was shown in the ALSYMPCA trial (*44*). In this trial, 921 men with progressive mCRPC and 2 or more symptomatic bone metastases with no known visceral metastases were randomized in a 2:1 fashion to receive either 6 doses of ^{223}Ra (dosed at 50 kBq/kg of body weight every 4 wk) or placebo, in addition to the standard of care. The primary endpoint was OS, and this was improved by the addition of ^{223}Ra (median OS, 14.9 vs 11.3 mo; $P < 0.001$). The time to the first symptomatic skeletal event was significantly prolonged as well (median, 15.6 vs. 9.8 mo; $P < 0.001$). No significant differences in adverse events of grade 3 or higher were noted between arms. At the median follow-up of 13 mo, no acute myeloid leukemia, myelodysplastic syndrome, or new primary bone cancers were seen (*45*). Quality of life was also assessed; using an estimation of pain-related symptoms based on the Functional Assessment of Cancer Therapy–Prostate questionnaire, patients receiving ^{223}Ra were found to be more likely to experience meaningful improvements in pain (30.2% vs. 20.1%; $P = 0.010$) (*46*). An earlier randomized phase II trial using a similar dosing regimen, but with only 4 doses total, identified a benefit in terms of time to first bone-related event as well (*47*). A trial-level metaanalysis that included both studies found a pooled HR of 0.70 (95% CI, 0.58–0.83) for improving OS (*48*). Unfortunately, the addition of ^{223}Ra to abiraterone acetate with prednisone failed to improve symptomatic skeletal event–free survival or OS in the evaluation of ^{223}Ra in combination with abiraterone in castration-resistant prostate cancer (ERA 223) trial (*49*). Significantly more fractures were seen in patients receiving ^{223}Ra (9% vs. 3%), particularly in patients not receiving bone protection agents.

Theranostics is a precision medicine approach that uses targeted radioactive compounds to image specific cell surface markers and subsequently uses RLTs to irradiate tissues expressing these markers (*50*). ^{177}Lu-PSMA-617 is a chemically modified DOTA-conjugated PSMA binder that has allowed the first theranostic therapy in prostate cancer. In the VISION trial, 831 patients with mCRPC and at least 1 PSMA-positive lesion were randomized in a 2:1 ratio to either 4 or 6 cycles of 7.4 GBq of ^{177}Lu-PSMA-617 every 6 weeks with standard of care versus standard of care alone (*51*). Specific eligibility criteria were at least 1 PSMA-positive lesion with uptake greater than liver parenchyma and no large PSMA-negative lesions, disease progression after treatment with at least 1 second-generation androgen receptor signaling inhibitor and 1 or 2 taxanes, and life expectance of more than 6 mo. Treatment with ^{177}Lu-PSMA-617 improved OS (median, 15.3 vs.

TABLE 2
Summary of Selected Phase II–III Randomized Trials of ^{223}Ra and ^{177}Lu-Based RLTs in Prostate Cancer

Trial	Design	Dosage	Inclusion criteria	Patients (*n*)	Result
ALSYMPCA (*44*)	Phase III RCT; standard of care + 6 doses of ^{223}Ra vs. standard of care	50 kBq per kilogram of body weight every 4 wk	Progressive mCRPC and ≥2 symptomatic bone metastases with no known visceral metastases	921	OS, 14.9 vs. 11.3 mo; time to first symptomatic skeletal event, 15.6 vs. 9.8 mo; meaningful improvements in pain (30.2% vs. 20.1%)
VISION (*51*)	Phase III RCT; 4–6 cycles of ^{177}Lu-PSMA-617 vs. standard of care	7.4 GBq every 6 wk	Progressive mCRPC ≥1 PSMA-positive lesion with uptake greater than liver parenchyma and no PSMA-negative lesions	831	Improved OS, median 15.3 mo vs. 11.3 mo; radiographic PFS, median 8.7 vs. 3.4 mo; time to first symptomatic skeletal event or death, median of 11.5 vs. 6.8 mo
TheraP (*53*)	Phase II RCT; op to 6 cycles of ^{177}Lu-PSMA-617 vs. cabazitaxel	8.5 GBq for first cycle, with 0.5-GBq decrease per subsequent cycle (6 wk between cycles)	Progressive mCRPC ≥1 PSMA-positive lesion with SUV_{max} ≤20 (with all other PSMA-avid sites having SUV_{max} of ≥10) and nondiscordant findings between PSMA and ^{18}F-FDG PET/CT	200	PSA response rate (50% reduction or more), 66% vs. 37%; progression was delayed with ^{177}Lu-PSMA-617 (HR, 0.63)

RCT = randomized controlled trial.

TABLE 3
Summary of Prospective Studies Integrating RLT with External-Beam Radiotherapy in Oligorecurrent Disease

Trial	Inclusion	*n*	RLT and dosage	Timing of RLT	Primary endpoint
Randomized evaluating addition of RLT to SBRT					
LUNAR (NCT05496959)	≤5 lesions outside prostate/prostate bed on PSMA PET/CT	90	^{177}Lu-PNT2002 (6.8 GBq per cycle, 2 cycles given 6–8 wk apart)	Neoadjuvant	PFS: progression defined on basis of PSMA PET/CT scans obtained at 12 mo or at time of PSA-based biochemical progression; initiation of salvage therapy
POPSTAR II (NCT05560659)	≤5 sites of nodal or bony metastases, with at least 1 site with SUV_{max} 2× SUV_{max} liver	92	^{177}Lu-PNT2002 (6 GBq (±10%) per cycle, 2 cycles 6–8 wk apart)	SABR between cycles 1 and 2	PFS: progression defined as biochemical or clinical
RAVENS (NCT04037358)	≤3 metastases with at least 1 bone (on CT or bone scan) or ≤5 metastases with at 1 least 1 bone (on PET/CT); PSADT < 15 mo; PSA ≥ 0.5	64	^{223}Ra (55 kBq per cycle, 6 cycles 4 wk apart)	SABR concurrent with cycle 1	PFS: progression defined as biochemical (PSA increased by ≥2 ng/mL from nadir) or clinical (based on conventional imaging or initiation of ADT)
PSMA-DC (NCT05939414)	≤5 metastases by PSMA PET only with none on CT or bone scan	450	^{177}Lu-PSMA-617 (6.8 GBq per cycle, 4 cycles given 6 wk apart)	Neoadjuvant	Metastasis-free survival: defined as lack of metastasis identifiable on bone scan, CT, or MRI
Phase II single arm evaluating adding radiotherapy to RLT					
ProstACT target (NCT05146973)	Recurrent after prostatectomy; ≤5 nodal lesions, all at or below aortic bifurcation with SUV_{max} > 5; radiotherapy here is conventionally fractionated salvage radiotherapy	50	^{177}Lu-DOTA-TLX591-CHO (2.8 GBq per cycle, 2 cycles given 2 wk apart)	Adjuvant	PSA-based PFS: time from enrollment to time of PSA increase > 25%
NCT03361735	≤4 metastases with at least 1 bone lesion and ≤1 visceral or nodal lesions	24	^{223}Ra 5 (55 kBq per cycle, 6 cycles 4 wk apart)	9 mo of ADT, with SBRT starting on day 1 of ADT and radium starting on day 31 of ADT	Time to treatment failure: time from initiation of ADT for metastatic disease until PSA increase to >pre-ADT level or PSA > 10 (whichever is smaller) or radiographic or clinical progression or resumption of ADT by physician's choice

PSADT = PSA doubling time; RCT = randomized controlled trial.

11.3 mo; $P < 0.0001$) and radiographic PFS (median, 8.7 vs. 3.4 mo; $P < 0.001$). Grade 3 or higher adverse events were higher in the experimental group (52.7% vs. 38.0%), but overall quality of life was not impacted. The most common adverse events included fatigue, dry mouth, anemia, and back pain. Time to first symptomatic skeletal event or death was also prolonged (median, 11.5 vs. 6.8 mo; $P < 0.001$). A subsequent quality-of-life analysis found that time to worsening of quality of life by the Functional Assessment of Cancer Therapy–Prostate metric was prolonged with ^{177}Lu-PSMA-617 (*52*). Hematologic adverse events of grade 3 or higher included decreased hemoglobin (15% vs. 6%), lymphocyte concentrations (51% vs. 19%), and platelet counts (9% vs 2%).

The phase II TheraP trial randomized 200 patients with mCRPC and prior docetaxel treatment to ^{177}Lu-PSMA-617 or cabazitaxel (*53*). Patients were required to have at least 1 ^{68}Ga-PSMA–positive lesion with an SUV_{max} of at least 20 (with all other PSMA-avid sites having an SUV_{max} of $\geq$10) and nondiscordant findings between PSMA and ^{18}F-FDG PET/CT. The dosage schedule for ^{177}Lu-PSMA-617 was 8.5 GBq for the first cycle with a 0.5-GBq decrease per each subsequent cycle (maximum of 6 cycles with 6 wk between cycles). The primary endpoint was the PSA response rate ($\geq$50% reduction), and treatment with ^{177}Lu-PSMA-617 did significantly improve this (66% vs. 37%, $P < 0.0001$). The effect of treatment on PFS was not constant with time, and the impact appeared to be more pronounced after 6 mo. However, when a Cox model was used, progression was delayed with ^{177}Lu-PSMA-617 (HR, 0.63; $P = 0.0028$). ^{177}Lu-PSMA-617 did not increase the rate of overall toxicities of grade 3 or higher (33% vs. 53%), though thrombocytopenia was more common with ^{177}Lu-PSMA-617 (11% vs. 0%). Improvements in quality of life and symptoms were seen with ^{177}Lu-PSMA-617 with respect to diarrhea, fatigue, social functioning, and insomnia, and deterioration-free survival for global health status was better for men receiving ^{177}Lu-PSMA-617 at 6 mo (9% vs. 13%, $P = 0.0002$). A post hoc analysis found that ^{68}Ga-PSMA-PET SUV_{mean} was predictive of a higher likelihood of a favorable response and a high ^{18}F-FDG PET metabolic tumor volume associated with a lower response regardless of randomly assigned treatment (*54*).

^{177}Lu-PSMA-I&T (also known as ^{177}Lu-PNT2002) is the second PSMA-targeting RLT that has been studied in large clinical trials. It has more kidney uptake, but less lacrimal uptake, than ^{177}Lu-PSMA-617 (*55–57*) and has shown anticancer activity in the compassionate-use setting for patients with heavily pretreated mCRPC (*58*). It is being studied in 2 phase III randomized trials in the mCRPC space: SPLASH (NCT04647526) and ECLIPSE (NCT05204927). Preliminary results from both were expected in late 2023.

COMBINING RLT WITH MDT

Overall, the data suggest that although MDT for mHSPC is effective at controlling individual lesions, its potential as a curative option is limited because of the existence of occult disease at the time of treatment. The use of advanced molecular imaging for patient selection may increase the percentage of patients with a long-term response, but ultimately most patients will still experience progression. RLT possesses significant antineoplastic activity even in the most advanced setting of mCRPC but ultimately is not a curative option given the natural history of CRPC and a limit to the number of cycles that can safely be administered (*59*). The ultimate limitation after RLT may also depend on the emergence of PSMA-negative, ^{18}F-FDG–positive disease that is no longer effectively targeted. Earlier administration of RLT therapy before such clones can emerge and when the burden of disease is lower may increase the effectiveness of RLT in durably controlling disease. A logical synergy between MDT and the theranostic approach might be achieved using both MDT and RLT in patients with oligorecurrent mHSPC. The disease setting would by definition include a low burden of disease, and we would not expect the presence of PSMA-negative ^{18}F-FDG–positive occult disease, which would improve the efficacy of the RLT. Similarly, the addition of RLT and the use of imaging to select patients with lower-volume disease would improve the efficacy of MDT by reducing the rates of oligo- and polyprogression.

The potential benefit of this synergy also rests on the hypothesis that RLT would be effective, without combination with ADT, in mHSPC. This was tested in the randomized multicenter phase II BULLSEYE trial (*60*). In this trial, men with mHSPC and 5 or fewer lesions, with an SUV_{max} of more than 15 for all lesions and a PSA doubling time of no more than 6 mo were randomized in a 1:1 fashion to 2–4 cycles of 7.4 GBq of ^{177}Lu-PSMA-617 versus deferred ADT. The primary endpoint is progression within 24 wk of cycle 2, with progression defined as a 100% increase in PSA or radiographic or clinical progression. Early results based on the first 42 patients enrolled on the study indicated a promising effect from the treatment (*34*). The median PSA was 4.5 ng/dL at inclusion. At 6 mo of follow-up, 10% of patients on the treatment arm versus 77% of patients on the control arm had experienced progression. The median PFS was not reached in the treatment arm, versus 4 mo in the control arm ($P < 0.001$). Overall, 24% of patients had a complete biochemical and imaging response. Only 3 grade 3 adverse events were seen. Though early, these interim results support the concept that RLT agents are active in the setting of mHSPC as well.

The direct question of whether the integration of RLTs with MDT will improve outcomes in mHSPC is being tested in 3 randomized phase II trials and 2 single-arm phase 2 studies. These are summarized in Table 3. The RAVENS and LUNAR trials will be fully accrued by the end of 2023. The phase III PSMA-DC study (NCT05939414) is also planned to open to accrual in late 2023 for patients with only molecular oligometastatic disease. As data supporting RLT in earlier disease states matures, more studies integrating RLT with MDT are likely on the horizon.

CONCLUSION

An increased appreciation of the oligometastatic state in prostate cancer has led to a paradigmatic shift in approaches to managing selected patients with low-volume or oligorecurrent mHSPC. Among the most promising is the use of MDT, particularly via SBRT, to significantly prolong progression and the initiation of ADT. In tandem, clinical trials have shown survival benefits to the use of α-emitting ^{223}Ra and β-emitting ^{177}Lu-PSMA agents in more advanced mCRPC. Given that progression, particularly polyprogression, remains a common pattern of progression after MDT for oligorecurrent disease, the integration of RLTs with MDT seems a rational approach. Several clinical trials, including 3 randomized phase II trials, have already been launched evaluating this concept. The results of these studies are eagerly anticipated, and further clinical studies will be necessary to define the optimal integration and sequencing of these agents.

DISCLOSURE

Amar Kishan received personal fees from ViewRay, Inc., Varian Medical Systems, Inc., and Janssen Pharmaceuticals outside the submitted work, as well as research funding from ViewRay, Janssen Pharmaceuticals, PointBiopharma, and Lantheus. He reports research funding from grant PC210066 from the Department of Defense. Michael Hofman reports financial support from Novartis (including AAA and Endocyte), AstraZeneca, Bayer Corp., Isotopia, and MIM Software Inc.; a consulting or advisory relationship with Astellas Pharma Inc.; and consulting fees for lectures or advisory boards from Astellas and AstraZeneca in the last 2 y and from Janssen, Merck/MSD, and Mundipharma in the last five years. Ana Kiess has institutional clinical research funding from Bayer, Novartis/AAA, and Merck and has participated in an unpaid consulting and advisory board for Novartis. Phuoc Tran received a research grant from Bayer; consulted for Bayer, RefleXion, Myovant, Natsar Pharmaceuticals, Regeneron, Lantheus, and Janssen; and has a patent licensed to Natsar Pharmaceuticals. Jeremie Calais reports prior consulting services for Advanced Accelerator Applications, Astellas, Blue Earth Diagnostics, Curium Pharma, DS Pharma, EXINI, GE Healthcare, Isoray, IBA RadioPharma, Janssen Pharmaceuticals, Lightpoint Medical, Lantheus, Monrol, Novartis, Progenics, POINT Biopharma, Radiomedix, Sanofi, and Telix Pharmaceuticals outside the submitted work. No other potential conflict of interest relevant to this article was reported.

REFERENCES

1. Deek MP, Van der Eecken K, Phillips R, et al. The mutational landscape of metastatic castration-sensitive prostate cancer: the spectrum theory revisited. *Eur Urol.* 2021;80:632–640.
2. Sutera P, Van Der Eecken K, Kishan AU, et al. Definitions of disease burden across the spectrum of metastatic castration-sensitive prostate cancer: comparison by disease outcomes and genomics. *Prostate Cancer Prostatic Dis.* 2022;25:713–719.
3. Kyriakopoulos CE, Chen YH, Carducci MA, et al. Chemohormonal therapy in metastatic hormone-sensitive prostate cancer: long-term survival analysis of the randomized phase III E3805 CHAARTED trial. *J Clin Oncol.* 2018;36:1080–1087.
4. Fizazi K, Tran N, Fein L, et al. Abiraterone plus prednisone in metastatic, castration-sensitive prostate cancer. *N Engl J Med.* 2017;377:352–360.
5. Hoyle AP, Ali A, James ND, et al. Abiraterone in "high-" and "low-risk" metastatic hormone-sensitive prostate cancer. *Eur Urol.* 2019;76:719–728.
6. Kawahara T, Yoneyama S, Ohno Y, et al. Prognostic value of the LATITUDE and CHAARTED risk criteria for predicting the survival of men with bone metastatic hormone-naïve prostate cancer treated with combined androgen blockade therapy: real-world data from a Japanese multi-institutional study. *BioMed Res Int.* 2020;2020:7804932.
7. Sutera P, Van Der Eecken K, Kishan AU, et al. Definitions of disease burden across the spectrum of metastatic castration-sensitive prostate cancer: comparison by disease outcomes and genomics. *Prostate Cancer Prostatic Dis.* 2022;25:713–719.
8. Hellman S, Weichselbaum RR. Oligometastases. *J Clin Oncol.* 1995;13:8–10.
9. Huynh MA, Tang C, Siva S, et al. Review of prospective trials assessing the role of stereotactic body radiation therapy for metastasis-directed treatment in oligometastatic genitourinary cancers. *Eur Urol Oncol.* 2023;6:28–38.
10. Rao A, Vapiwala N, Schaeffer EM, Ryan CJ. Oligometastatic prostate cancer: a shrinking subset or an opportunity for cure? *Am Soc Clin Oncol Educ Book.* 2019;39:309–320.
11. Sutera PA, Shetty AC, Hakansson A, et al. Transcriptomic and clinical heterogeneity of metastatic disease timing within metastatic castration-sensitive prostate cancer. *Ann Oncol.* 2023;34:605–614.
12. Sartor O, de Bono JS. Metastatic prostate cancer. *N Engl J Med.* 2018;378:645–657.
13. Nguyen PL, Alibhai SM, Basaria S, et al. Adverse effects of androgen deprivation therapy and strategies to mitigate them. *Eur Urol.* 2015;67:825–836.
14. Roberts MJ, Maurer T, Perera M, et al. Using PSMA imaging for prognostication in localized and advanced prostate cancer. *Nat Rev Urol.* 2023;20:23–47.
15. Gundem G, Van Loo P, Kremeyer B, et al. The evolutionary history of lethal metastatic prostate cancer. *Nature.* 2015;520:353–357.
16. Gomez DR, Blumenschein GR Jr, Lee JJ, et al. Local consolidative therapy versus maintenance therapy or observation for patients with oligometastatic non-small-cell lung cancer without progression after first-line systemic therapy: a multicentre, randomised, controlled, phase 2 study. *Lancet Oncol.* 2016;17:1672–1682.
17. Palma DA, Olson R, Harrow S, et al. Stereotactic ablative radiotherapy for the comprehensive treatment of oligometastatic cancers: long-term results of the SABR-COMET phase II randomized trial. *J Clin Oncol.* 2020;38:2830–2838.
18. Ost P, Reynders D, Decaestecker K, et al. Surveillance or metastasis-directed therapy for oligometastatic prostate cancer recurrence: a prospective, randomized, multicenter phase II trial. *J Clin Oncol.* 2018;36:446–453.
19. Phillips R, Shi WY, Deek M, et al. Outcomes of observation vs stereotactic ablative radiation for oligometastatic prostate cancer: the ORIOLE phase 2 randomized clinical trial. *JAMA Oncol.* 2020;6:650–659.
20. Siva S, Bressel M, Murphy DG, et al. Stereotactic ablative body radiotherapy (SABR) for oligometastatic prostate cancer: a prospective clinical trial. *Eur Urol.* 2018;74:455–462.
21. Kneebone A, Hruby G, Ainsworth H, et al. Stereotactic body radiotherapy for oligometastatic prostate cancer detected via prostate-specific membrane antigen positron emission tomography. *Eur Urol Oncol.* 2018;1:531–537.
22. Supiot S, Vaugier L, Pasquier D, et al. OLIGOPELVIS GETUG P07, a multicenter phase II trial of combined high-dose salvage radiotherapy and hormone therapy in oligorecurrent pelvic node relapses in prostate cancer. *Eur Urol.* 2021;80:405–414.
23. Glicksman RM, Metser U, Vines D, et al. Curative-intent metastasis-directed therapies for molecularly-defined oligorecurrent prostate cancer: a prospective phase II trial testing the oligometastasis hypothesis. *Eur Urol.* 2021;80:374–382.
24. Bowden P, See AW, Frydenberg M, et al. Fractionated stereotactic body radiotherapy for up to five prostate cancer oligometastases: interim outcomes of a prospective clinical trial. *Int J Cancer.* 2020;146:161–168.
25. Pasqualetti F, Panichi M, Sainato A, et al. [^{18}F]choline PET/CT and stereotactic body radiotherapy on treatment decision making of oligometastatic prostate cancer patients: preliminary results. *Radiat Oncol.* 2016;11:9.
26. Palma DA, Olson R, Harrow S, et al. Stereotactic ablative radiotherapy versus standard of care palliative treatment in patients with oligometastatic cancers (SABR-COMET): a randomised, phase 2, open-label trial. *Lancet.* 2019;393:2051–2058.
27. Scher HI, Halabi S, Tannock I, et al. Design and end points of clinical trials for patients with progressive prostate cancer and castrate levels of testosterone: recommendations of the Prostate Cancer Clinical Trials Working Group. *J Clin Oncol.* 2008;26:1148–1159.
28. Eisenhauer EA, Therasse P, Bogaerts J, et al. New response evaluation criteria in solid tumours: revised RECIST guideline (version 1.1). *Eur J Cancer.* 2009;45:228–247.
29. Deek MP, Van der Eecken K, Sutera P, et al. Long-term outcomes and genetic predictors of response to metastasis-directed therapy versus observation in oligometastatic prostate cancer: analysis of STOMP and ORIOLE trials. *J Clin Oncol.* 2022;40:3377–3382.
30. Ost P, Reynders D, Decaestecker K, et al. Surveillance or metastasis-directed therapy for oligometastatic prostate cancer recurrence (STOMP): five-year results of a randomized phase II trial [abstract]. *J Clin Oncol.* 2020;38(suppl):10.
31. Glicksman RM, Ramotar M, Metser U, et al. Extended results and independent validation of a phase 2 trial of metastasis-directed therapy for molecularly defined oligometastatic prostate cancer. *Int J Radiat Oncol Biol Phys.* 2022;114:693–704.
32. Deek MP, Taparra K, Dao D, et al. Patterns of recurrence and modes of progression after metastasis-directed therapy in oligometastatic castration-sensitive prostate cancer. *Int J Radiat Oncol Biol Phys.* 2021;109:387–395.
33. Soldatov A, von Klot CAJ, Walacides D, et al. Patterns of progression after ^{68}Ga-PSMA-ligand PET/CT-guided radiation therapy for recurrent prostate cancer. *Int J Radiat Oncol Biol Phys.* 2019;103:95–104.
34. EANM'23 abstract book congress Sep 9-13, 2023. *Eur J Nucl Med Mol Imaging.* 2023;50:1–898.
35. Mulford DA, Scheinberg DA, Jurcic JG. The promise of targeted α-particle therapy. *J Nucl Med.* 2005;46(suppl 1):199S–204S.
36. Pouget JP, Constanzo J. Revisiting the radiobiology of targeted alpha therapy. *Front Med (Lausanne).* 2021;8:692436.
37. Tranel J, Feng FY, James SS, Hope TA. Effect of microdistribution of alpha and beta-emitters in targeted radionuclide therapies on delivered absorbed dose in a GATE model of bone marrow. *Phys Med Biol.* 2021;66:035016.
38. Fendler WP, Cutler C. More α than β for prostate cancer? *J Nucl Med.* 2017;58:1709–1710.
39. Ramnaraign B, Sartor O. PSMA-targeted radiopharmaceuticals in prostate cancer: current data and new trials. *Oncologist.* 2023;28:392–401.
40. Sindhu KK, Nehlsen AD, Stock RG. Radium-223 for metastatic castrate-resistant prostate cancer. *Pract Radiat Oncol.* 2022;12:312–316.

41. Bruland ØS, Nilsson S, Fisher DR, Larsen RH. High-linear energy transfer irradiation targeted to skeletal metastases by the alpha-emitter ^{223}Ra: adjuvant or alternative to conventional modalities? *Clin Cancer Res.* 2006;12:6250s–6257s.
42. Henriksen G, Fisher DR, Roeske JC, Bruland ØS, Larsen RH. Targeting of osseous sites with alpha-emitting ^{223}Ra: comparison with the beta-emitter ^{89}Sr in mice. *J Nucl Med.* 2003;44:252–259.
43. Lange PH, Vessella RL. Mechanisms, hypotheses and questions regarding prostate cancer micrometastases to bone. *Cancer Metastasis Rev.* 1998;17:331–336.
44. Parker C, Nilsson S, Heinrich D, et al. Alpha emitter radium-223 and survival in metastatic prostate cancer. *N Engl J Med.* 2013;369:213–223.
45. Parker CC, Coleman RE, Sartor O, et al. Three-year safety of radium-223 dichloride in patients with castration-resistant prostate cancer and symptomatic bone metastases from phase 3 randomized alpharadin in symptomatic prostate cancer trial. *Eur Urol.* 2018;73:427–435.
46. Nilsson S, Cislo P, Sartor O, et al. Patient-reported quality-of-life analysis of radium-223 dichloride from the phase III ALSYMPCA study. *Ann Oncol.* 2016; 27:868–874.
47. Nilsson S, Franzén L, Parker C, et al. Bone-targeted radium-223 in symptomatic, hormone-refractory prostate cancer: a randomised, multicentre, placebo-controlled phase II study. *Lancet Oncol.* 2007;8:587–594.
48. Terrisse S, Karamouza E, Parker CC, et al. Overall survival in men with bone metastases from castration-resistant prostate cancer treated with bone-targeting radioisotopes: a meta-analysis of individual patient data from randomized clinical trials. *JAMA Oncol.* 2020;6:206–216.
49. Smith M, Parker C, Saad F, et al. Addition of radium-223 to abiraterone acetate and prednisone or prednisolone in patients with castration-resistant prostate cancer and bone metastases (ERA 223): a randomised, double-blind, placebo-controlled, phase 3 trial. *Lancet Oncol.* 2019;20:408–419.
50. Jia AY, Kiess AP, Li Q, Antonarakis ES. Radiotheranostics in advanced prostate cancer: current and future directions. *Prostate Cancer Prostatic Dis.* April 14, 2023 [Epub ahead of print].
51. Sartor O, de Bono J, Chi KN, et al. Lutetium-177-PSMA-617 for metastatic castration-resistant prostate cancer. *N Engl J Med.* 2021;385:1091–1103.
52. Fizazi K, Herrmann K, Krause BJ, et al. Health-related quality of life and pain outcomes with [^{177}Lu]Lu-PSMA-617 plus standard of care versus standard of care in patients with metastatic castration-resistant prostate cancer (VISION): a multicentre, open-label, randomised, phase 3 trial. *Lancet Oncol.* 2023;24:597–610.
53. Hofman MS, Emmett L, Sandhu S, et al. [^{177}Lu]Lu-PSMA-617 versus cabazitaxel in patients with metastatic castration-resistant prostate cancer (TheraP): a randomised, open-label, phase 2 trial. *Lancet.* 2021;397:797–804.
54. Buteau JP, Martin AJ, Emmett L, et al. PSMA and FDG-PET as predictive and prognostic biomarkers in patients given [^{177}Lu]Lu-PSMA-617 versus cabazitaxel for metastatic castration-resistant prostate cancer (TheraP): a biomarker analysis from a randomised, open-label, phase 2 trial. *Lancet Oncol.* 2022;23:1389–1397.
55. Ruigrok EAM, van Vliet N, Dalm SU, et al. Extensive preclinical evaluation of lutetium-177-labeled PSMA-specific tracers for prostate cancer radionuclide therapy. *Eur J Nucl Med Mol Imaging.* 2021;48:1339–1350.
56. Schuchardt C, Zhang J, Kulkarni HR, Chen X, Müller D, Baum RP. Prostate-specific membrane antigen radioligand therapy using ^{177}Lu-PSMA I&T and ^{177}Lu-PSMA-617 in patients with metastatic castration-resistant prostate cancer: comparison of safety, biodistribution, and dosimetry. *J Nucl Med.* 2022;63:1199–1207.
57. Wester HJ, Schottelius M. PSMA-targeted radiopharmaceuticals for imaging and therapy. *Semin Nucl Med.* 2019;49:302–312.
58. Heck MM, Tauber R, Schwaiger S, et al. Treatment outcome, toxicity, and predictive factors for radioligand therapy with ^{177}Lu-PSMA-I&T in metastatic castration-resistant prostate cancer. *Eur Urol.* 2019;75:920–926.
59. Schäfer H, Mayr S, Büttner-Herold M, et al. Extensive ^{177}Lu-PSMA radioligand therapy can lead to radiation nephropathy with a renal thrombotic microangiopathy-like picture. *Eur Urol.* 2023;83:385–390.
60. Privé BM, Janssen MJR, van Oort IM, et al. Lutetium-177-PSMA-I&T as metastases directed therapy in oligometastatic hormone sensitive prostate cancer, a randomized controlled trial. *BMC Cancer.* 2020;20:884.

Is ^{18}F-FDG Metabolic Tumor Volume in Lymphoma Really Happening?

Sally F. Barrington[1], Anne-Ségolène Cottereau[2], and Josée M. Zijlstra[3]

[1]King's College London and Guy's and St. Thomas' PET Centre, School of Biomedical Engineering and Imaging Sciences, King's College London, United Kingdom; [2]Department of Nuclear Medicine, Cochin Hospital, APHP, Paris Cité University, Paris, France; and [3]Department of Hematology and Cancer Center Amsterdam, Amsterdam UMC, Vrije Universiteit Amsterdam, The Netherlands

Tumor burden influences prognosis in lymphoma, with unidimensional bulk used for risk assessment and decisions about radiotherapy consolidation (*1*). Total metabolic tumor volume (TMTV) using ^{18}F-FDG PET emerged 10 y ago as a promising biomarker (*2*) that was superior to bulk (*3*). However, until now, metabolic tumor volume (MTV) has not been used in clinical practice or trial design. We attribute this to lack of common methodology, the perception that measurement is difficult, and the unavailability of software tools. Consensus is also required about which tumor areas to include (*4*). Furthermore, MTV has been evaluated in datasets providing binary cutoffs to divide patients into prognostic groups, which are data-driven and population-dependent (*5*).

WHAT IS CHANGING?

A New Benchmark Method Has Been Established

Because prognostication and interobserver agreement are equally good irrespective of the measurement method (*6*), choice should reflect ease of use. One method has emerged as simple, quick to perform using academic and commercial software, and closely matching the visual perception of nuclear medicine reads from 6 published methods in diffuse large B-cell lymphoma (DLBCL) (*7*) and Hodgkin lymphoma (*8*). The delineation method uses an SUV of at least 4.0 and a minimum individual lesion volume of 3 cm^3. The SUV of 4.0 limits physiologic uptake that requires editing compared with lower thresholds and reduces underestimation of heterogeneous lesions compared with percentage SUV thresholds. The 41% SUV_{max} threshold, although frequently studied, has increased variability across software depending on whether SUV_{max} is defined as the maximum in the TMTV or as lesional. If lesional, the clustering algorithm can influence how lesions are outlined. The minimum volume reduces measurement complexity without significantly influencing TMTV. The method using an SUV of 4.0 is insensitive to uptake time and to the presence or absence of later progression in patients (*7*) and is the least sensitive to reconstruction method, including ultra-high-sensitivity reconstructions (*9*) used in advanced technologies such as total-body PET/CT. In approximately 80% of DLBCL cases, minimal reader interaction was required—for example, removing physiologic uptake with single clicks, achievable in 2–3 min (*7*) with additional manual editing in 20% of cases.

The vision for standardization of MTV measurement was outlined in this journal (*4*) with a proposal for a benchmark dataset using a common method with consensus MTV values and segmentations as outputs. Data from the MTV road map have been presented involving 12 readers from 9 countries using 3 academic software programs. Readers analyzed 60 cases from 3 lymphoma subtypes (*10*). TMTV measurement was unaffected by the software used, with close reader agreement in 52 of 60 cases. Disagreement was mainly due to interpretation of diffuse splenic uptake with smaller, less clinically relevant differences due to manual editing of physiologic uptake.

The benchmark will soon be made publicly available so readers can check the reliability of MTV measurements using local software and their clinical interpretation. New measurement methods, including artificial intelligence approaches, can be evaluated against the benchmark, with both being tested in the same dataset provided patient outcomes are known, to determine whether newer methods improve prognostication, reduce reader time, or improve agreement. The benchmark can also be used to explore questions such as the prognostic relevance of the spleen.

A concern about the transition to one method could be whether research using other methods might be wasted and that the method using an SUV of 4.0 has not been widely tested in indolent, albeit less common, subtypes. A statistical method for combining batches (ComBat) of data using different methods (*11*) has been successfully applied in retrospective trial datasets (*12*). Nonetheless, having a standardized approach for prospective study in aggressive lymphoma is a critical step for universal adoption of MTV as a biomarker.

New Prognostic Indices Have Been Incorporated

Other major developments are testing of TMTV in large datasets, expression as a continuous variable, and incorporation with established risk factors.

The method using an SUV of 4.0 was explored in 1,214 patients with newly diagnosed DLBCL (*13*) by the Positron Emission Tomography Reanalysis (PETRA) consortium in 5 international trials. First, the best statistical relationship was derived to associate MTV with progression-free and overall survival. The relationship was a linear spline with 2 coefficients, such that the same incremental change had different impacts on survival above and below the median. MTV performed better than the International Prognostic Index (comprising binary cutoffs for age, lactate dehydrogenase, stage, performance status, and more than one extranodal site) (*14*). Most International Prognostic Index factors proved redundant when combined with MTV. The optimal "International Metabolic Prognostic Index" included 3 factors: MTV and age (as continuous variables) and stage (I–IV). Its continuous nature means progression-free

Received Dec. 15, 2023; revision accepted Jan. 29, 2024.
For correspondence or reprints, contact Sally Barrington (sally.barrington@kcl.ac.uk).
Published online Feb. 22, 2024.

DOI: 10.2967/jnumed.123.267022

survival can be predicted for individual patients by entering MTV, age, and stage in a simple Excel (Microsoft) spreadsheet (https://petralymphoma.org/impi). The International Metabolic Prognostic Index allows for intelligent trial design, selecting a progression-free survival cutoff at which the benefit of a novel treatment will likely outweigh the risk of standard treatment in high-risk patients. The integration of MTV with patient factors has also been explored in 2,174 patients from trial and real-world datasets, with performance status being identified as an independent risk factor and MTV plus performance status outperforming the International Prognostic Index (*12*). Optimal selection of high-risk patients is relevant because new treatments such as CAR T-cell therapy and bispecific monoclonal antibodies are being tested in phase III trials in first- and second-line DLBCL.

HOW SHOULD WE BUILD ON THE SUCCESS OF MTV?

The success of MTV has generated interest in other radiomic features, which can be measured once TMTV is delineated. The independent prognostic value of disease dissemination—for example, the maximum distance between lesions—was first reported by Cottereau et al. (*15*). Biologic explanations for this phenomenon were recently explored in Hodgkin lymphoma (*16*). The PETRA consortium suggested the potential to replace "stage" in the International Metabolic Prognostic Index by "Dmaxbulk," the maximum distance between the bulkiest and the furthest lesion, with a small incremental benefit for a radiomics score that also included performance status and SUV_{peak} (*17*). Preliminary reports that integrate PET with emerging molecular markers in circulating tumor DNA (*18*) may further improve baseline and dynamic risk. Methods to establish reliable dynamic MTV measurement are also being explored (*19*).

Confidence in TMTV is growing with agreement about standardization. A similar pragmatic approach of a simple, albeit not perfect, method led to widespread adoption of the Deauville score for lymphoma (*20*).

Now MTV needs to feature in trial design, either alone or within prognostic indices such as the International Metabolic Prognostic Index for risk stratification. To develop clinical decision tools, MTV (with or without other radiomic features) should be prospectively evaluated at baseline and interim with liquid biomarkers for minimal residual disease.

The first trial using MTV, Deauville score, and circulating tumor DNA to risk-adapt treatment is already under way in Hodgkin lymphoma (www.clinicaltrials.gov/study/NCT04866654).

In conclusion, MTV for risk stratification in DLBCL is feasible now in the clinic and being evaluated in a clinical trial on Hodgkin lymphoma. A benchmark dataset will be available soon for standardization of measurement by PET centers, software developers, and vendors. "The time to prepare for risk adaptation in lymphoma by standardizing measurement of metabolic tumor burden is over" (*4*): it is time to get on board.

DISCLOSURE

Sally Barrington acknowledges support from the National Institute for Health and Care Research (NIHR) (RP-2016-07-001). This work was also supported by core funding from the Wellcome/EPSRC Centre for Medical Engineering at King's College London (WT203148/Z/16/Z). The views expressed are those of the authors and not necessarily those of the NHS, the NIHR, or the Department of Health and Social Care. Josée Zijlstra acknowledges support from KWF Dutch Cancer Society. No other potential conflict of interest relevant to this article was reported.

ACKNOWLEDGMENT

We acknowledge the vision of our late colleague, Prof. Michel Meignan, founder of the international workshops on PET in lymphoma and myeloma (https://www.lymphomapet.com/), whose leadership inspired the development of MTV as a biomarker.

REFERENCES

1. Specht L, Nordentoft AM, Cold S, Clausen NT, Nissen NI. Tumor burden as the most important prognostic factor in early stage Hodgkin's disease. Relations to other prognostic factors and implications for choice of treatment. *Cancer.* 1988;61:1719–1727.
2. Meignan M, Sasanelli M, Casasnovas RO, et al. Metabolic tumour volumes measured at staging in lymphoma: methodological evaluation on phantom experiments and patients. *Eur J Nucl Med Mol Imaging.* 2014;41:1113–1122.
3. Mikhaeel NG, Smith D, Dunn JT, et al. Combination of baseline metabolic tumour volume and early response on PET/CT improves progression-free survival prediction in DLBCL. *Eur J Nucl Med Mol Imaging.* 2016;43:1209–1219.
4. Barrington SF, Meignan M. Time to prepare for risk adaptation in lymphoma by standardizing measurement of metabolic tumor burden. *J Nucl Med.* 2019;60:1096–1102.
5. El-Galaly TC, Villa D, Cheah CY, Gormsen LC. Pre-treatment total metabolic tumour volumes in lymphoma: does quantity matter? *Br J Haematol.* 2022;197:139–155.
6. Ilyas H, Mikhaeel NG, Dunn JT, et al. Defining the optimal method for measuring baseline metabolic tumour volume in diffuse large B cell lymphoma. *Eur J Nucl Med Mol Imaging.* 2018;45:1142–1154.
7. Barrington SF, Zwezerijnen BGJC, de Vet HCW, et al. Automated segmentation of baseline metabolic total tumor burden in diffuse large B-cell lymphoma: which method is most successful? A study on behalf of the PETRA consortium; 32680929. *J Nucl Med.* 2021;62:332–337.
8. Driessen J, Zwezerijnen GJC, Schöder H, et al. The impact of semiautomatic segmentation methods on metabolic tumor volume, intensity, and dissemination radiomics in ^{18}F-FDG PET scans of patients with classical Hodgkin lymphoma. *J Nucl Med.* 2022;63:1424–1430.
9. Ferrández MC, Eertink JJ, Golla SSV, et al. Combatting the effect of image reconstruction settings on lymphoma [^{18}F]FDG PET metabolic tumor volume assessment using various segmentation methods. *EJNMMI Res.* 2022;12:44–49.
10. Boellaard R, Buvat I, Ceriani L, et al. International benchmark for total metabolic tumor volume assessment in baseline FDG PET/CT of lymphoma patients [abstract]. *J Nucl Med.* 2023;64(suppl 1):83.
11. Orlhac F, Eertink JJ, Cottereau A, et al. A guide to ComBat harmonization of imaging biomarkers in multicenter studies. *J Nucl Med.* 2022;63:172–179.
12. Thieblemont C, Chartier L, Dührsen U, et al. A tumor volume and performance status model to predict outcome before treatment in diffuse large B-cell lymphoma. *Blood Adv.* 2022;6:5995–6004.
13. Mikhaeel NG, Heymans MW, Eertink JJ, et al. Proposed new dynamic prognostic index for diffuse large B-cell lymphoma: international metabolic prognostic index. *J Clin Oncol.* 2022;40:2352–2360.
14. International Non-Hodgkin's Lymphoma Prognostic Factors Project. A predictive model for aggressive non-Hodgkin's lymphoma. *N Engl J Med.* 1993;329:987–994.
15. Cottereau AS, Meignan M, Nioche C, et al. Risk stratification in diffuse large B-cell lymphoma using lesion dissemination and metabolic tumor burden calculated from baseline PET/CT. *Ann Oncol.* 2021;32:404–411.
16. Durmo R, Donati B, Rebaud L, et al. Prognostic value of lesion dissemination in doxorubicin, bleomycin, vinblastine, and dacarbazine-treated, interimPET-negative classical Hodgkin lymphoma patients: a radio-genomic study. *Hematol Oncol.* 2022;40:645–657.
17. Eertink JJ, Zwezerijnen GJC, Heymans MW, et al. Baseline PET radiomics outperforms the IPI risk score for prediction of outcome in diffuse large B-cell lymphoma. *Blood.* 2023;141:3055–3064.
18. Kurtz DM, Scherer F, Jin MC, et al. Circulating tumor DNA measurements as early outcome predictors in diffuse large B-cell lymphoma. *J Clin Oncol.* 2018;36:2845–2853.
19. Zwezerijnen GJC, Eertink JJ, Burggraaff CN, et al. Interobserver agreement on automated metabolic tumor volume measurements of Deauville score 4 and 5 lesions at interim ^{18}F-FDG PET in diffuse large B-cell lymphoma. *J Nucl Med.* 2021;62:1531–1536.
20. Barrington SF, Mikhaeel NG, Kostakoglu L, et al. Role of imaging in the staging and response assessment of lymphoma: consensus of the International Conference on Malignant Lymphomas Imaging Working Group. *J Clin Oncol.* 2014;32:3048–3058.

^{68}Ga-FAPI PET/CT as an Alternative to ^{18}F-FDG PET/CT in the Imaging of Invasive Lobular Breast Carcinoma

Ertan Sahin[1], Tulay Kus[2], Alper Aytekin[3], Evren Uzun[4], Umut Elboga[1], Latif Yilmaz[3], Yusuf B. Cayirli[1], Merve Okuyan[1], Vuslat Cimen[1], and Ufuk Cimen[1]

[1]Department of Nuclear Medicine, Gaziantep University, Gaziantep, Turkey; [2]Department of Medical Oncology, Gaziantep University, Gaziantep, Turkey; [3]Department of General Surgery, Gaziantep University, Gaziantep, Turkey; and [4]Department of Pathology, Gaziantep University, Gaziantep, Turkey

Accurate staging of invasive lobular carcinoma (ILC), a subtype of breast cancer, is vital for effective clinical management. Although ^{18}F-FDG PET/CT is a commonly used tool, its efficacy varies across different histologic subtypes. To mitigate this challenge, our investigation delves into the potential utility of ^{68}Ga-fibroblast activation protein inhibitor (FAPI) PET/CT as an alternative for staging ILC, aiming to address a significant research gap using a more expansive patient cohort than the smaller samples commonly found in the existing literature. **Methods:** In this retrospective analysis, women diagnosed with primary ILC of the breast underwent both ^{18}F-FDG PET/CT and ^{68}Ga-FAPI PET/CT. Both modalities were compared across all lesion locations with the used reference standard. The interval between scans was 1 wk, without any intervening treatments. Lesions were categorized visually, and tracer activity was analyzed using SUV_{max}, tumor-to-background uptake ratio, and uptake ratios. Both modalities were compared across various parameters, and statistical analysis was performed using SPSS 22.0. A P value of less than 0.05 was chosen to determine statistical significance. **Results:** The study included 23 female ILC patients (mean age, 51 y) with hormone-positive, human epidermal growth factor receptor type 2–negative tumors. Most (65%) had the luminal A subtype. ^{68}Ga-FAPI PET/CT outperformed ^{18}F-FDG PET/CT, with higher tumoral activity and tumor-to-background uptake ratios ($P < 0.001$). Primary tumors showed significantly increased uptake with ^{68}Ga-FAPI PET/CT ($P < 0.001$), detecting additional foci, including multicentric cancer. Axillary lymph node metastases were more frequent and had higher uptake values with ^{68}Ga-FAPI PET/CT ($P = 0.012$). Moreover, ^{68}Ga-FAPI PET/CT identified more lesions, including bone and liver metastases. Pathologic features did not significantly correlate with imaging modalities, but a positive correlation was observed between peritumoral lymphocyte ratio and ^{68}Ga-FAPI PET/CT–to–^{18}F-FDG PET/CT uptake ratios ($P = 0.026$). **Conclusion:** This study underscores ^{68}Ga-FAPI PET/CT's superiority over ^{18}F-FDG PET/CT for ILC. ^{68}Ga-FAPI PET/CT excels in detecting primary breast masses, axillary lymph nodes, and distant metastases; can complement ^{18}F-FDG PET/CT in ILC; and holds potential as an alternative imaging method in future studies.

Key Words: ^{68}Ga-FAPI-PET/CT; ^{18}F-FDG PET/CT; lobular breast carcinoma

J Nucl Med 2024; 65:512–519
DOI: 10.2967/jnumed.123.266798

Breast cancer is the most common cancer in women worldwide, comprising 25% of female cancer cases (*1*). Invasive lobular carcinoma (ILC) accounts for about 10% of all invasive breast cancer cases (*2*,*3*). Precise clinical staging is crucial for treatment decisions and prognosis (*4*,*5*).

Staging methods combine systemic and local assessments. Systemic staging uses various diagnostic tools such as bone scans, abdominal CT/MRI, thoracic CT, and ^{18}F-FDG PET. Local disease extent is determined with mammography, ultrasound, and breast MRI (*6*). ^{18}F-FDG PET/CT, crucial for breast cancer management, aids in initial staging, restaging, treatment response evaluation, and recurrence detection (*7*).

The utility of ^{18}F-FDG PET/CT, however, exhibits variability among histologic subtypes, particularly in the case of ductal and lobular breast cancers. The inherent challenges of identifying ILC with ^{18}F-FDG PET/CT stem from distinct molecular and pathologic features, including lower cellular density, receptor expression, and metastatic patterns (*2*,*3*); furthermore, primary and metastatic ILC is less ^{18}F-FDG–avid than invasive ductal cancer (IDC), leading to the weakness of ^{18}F-FDG PET for ILC (*8*,*9*). Additionally, factors such as small tumor size (<1 cm), in situ carcinomas, micrometastases, low-grade tumors, and benign pathologies can compromise the sensitivity and specificity of ^{18}F-FDG PET/CT in breast cancer (*10*–*12*).

To address limitations, prior research explored alternatives such as ^{18}F-fluoroestradiol, especially for ILC (*13*,*14*). Recently, a new radiopharmaceutical targeting fibroblast activation protein (FAP) has gained attention for tumor diagnosis and staging. FAP, highly expressed in cancer-associated fibroblasts (CAFs) (*15*–*18*), shows promise in PET studies, especially in combination with ^{68}Ga, due to favorable pharmacokinetics and high tumor background activity (*19*–*22*).

The unique role of the tumor stroma and the abundant stromal expression of FAP in primary breast cancer suggest a potential for high accuracy in FAPI-directed imaging (*23*,*24*). Recent studies have emerged comparing ^{18}F-FDG PET/CT and ^{68}Ga-FAPI PET/CT in breast cancer (*25*–*27*). Recent studies, including one by Eshet et al., compare ^{18}F-FDG PET/CT and ^{68}Ga-FAPI PET/CT in breast cancer, specifically in patients with ILC, albeit within a limited cohort (*25*–*27*).

Motivated by the paucity of literature on this subject, this study aimed to evaluate whether ^{68}Ga-FAPI PET/CT outperforms ^{18}F-FDG PET/CT in the context of ILC, with a focus on a larger patient cohort.

Received Oct. 4, 2023; revision accepted Jan. 11, 2024.
For correspondence or reprints, contact Ertan Sahin (er_ahin@yahoo.com).
Published online Mar. 14, 2024.

MATERIALS AND METHODS

Patient Selection and Evaluation

This study, approved by the Institutional Clinical Research Ethics Committee, included 23 women with ILC. They underwent ^{18}F-FDG PET/CT and ^{68}Ga-FAPI PET/CT for staging before systemic chemotherapy or surgery (Fig. 1). Secondary confirmation methods, such as bone scintigraphy–radiologic imaging or repeat ^{68}Ga-FAPI PET/CT, were routinely used because of potential limitations in ^{18}F-FDG PET/CT for the ILC subtype. The interval between scans was limited to 1 wk, with no intervening treatments. Eligible patients were 18 y old or older, with no recent systemic treatment or radiotherapy and a confirmed diagnosis of ILC. All provided written informed consent. Exclusions comprised men, individuals under 18 y old, secondary malignancy, severe hepatic–renal impairment, pregnancy, and breastfeeding.

Patient Preparation and PET/CT Imaging Protocols

^{18}F-FDG PET/CT. The patients underwent a standardized preparation regimen before the ^{18}F-FDG PET/CT imaging session, including a 12-h fast. Blood glucose levels had to be below 150 mg/dL. A 5 MBq/kg dose of ^{18}F-FDG was administered intravenously. Sixty minutes later, imaging was conducted using a Discovery IQ PET/CT device (GE Healthcare), scanning from the vertex to the mid femur.

^{68}Ga-FAPI PET/CT. ^{68}Ga-FAPI was synthesized and labeled using the Modular Lab-Easy system (Eckert & Ziegler) in a modular laboratory at our center, following a procedure akin to prior studies (*18*,*19*). Quality control assessments using thin-layer chromatography and high-performance liquid chromatography affirmed a radiochemical purity exceeding 98%. Subsequently, a 2–3 MBq/kg dose of synthesized ^{68}Ga-FAPI was intravenously injected into patients. Forty-five minutes later, PET/CT imaging was conducted using the Discovery IQ PET/CT device, covering the vertex to the mid femur.

Pathologic Evaluation

In the pathologic assessment, specimens obtained through Tru-Cut (Merit Medical) biopsy and excision were confirmed as malignant on the basis of criteria such as anaplasia, absence of myoepithelial cells, and the presence of mitosis or necrosis. Cases were evaluated for histologic tumor type, presence of ductal or lobular carcinoma in situ, nuclear grade, tumor-to-stroma ratio, and lymphocyte density and were graded using the Nottingham histologic scoring system.

Immunohistochemistry on tissue sections assessed estrogen receptor, progesterone receptor, Ki-67, and human epidermal growth factor receptor 2/neu expression. Estrogen receptor and progesterone receptor were evaluated in decimal percentiles, with staining intensity graded as weak, moderate, or strong. Invasive carcinomas with estrogen receptor and progesterone receptor between 1% and 10% were considered low positive, less than 10% staining was negative (score 1), and intense staining in more than 10% was positive (score 3). Human epidermal growth factor receptor 2/neu–equivocal cases were verified with human epidermal growth factor receptor 2 silver in situ hybridization, categorizing tumors into 5 molecular subtypes based on immunohistochemical results.

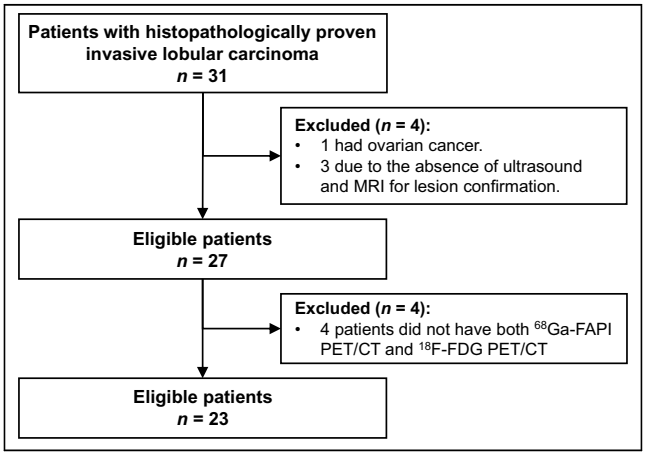

FIGURE 1. Descriptive flowchart of study.

Evaluation of Images and Patient-Lesion Analysis

Two experienced nuclear medicine physicians meticulously reviewed the PET/CT images, categorizing lesions as positive if detected by at least 1 specialist and negative if not detected. Classification of lesions without histopathologic confirmation was based on imaging methods (ultrasound, mammography, CT, MRI) and clinical findings. Histopathologic examination was conducted for 5 axillary lymph nodes in metastatic lesions, whereas decisions for other sites relied on imaging methods and clinical data.

For both PET/CT methods, areas with higher uptake than background were assessed as positive; findings from other modalities were also considered in the assessment. Images in axial, coronal, and sagittal planes were available for review. Semiquantitative analysis used SUV_{max}, with volumes of interest around primary breast lesions in 3 planes for both scans. SUV_{max} for primary lesions and metastases was determined, and radiopharmaceutical uptake exceeding background was quantified using SUV_{max} and tumor-to-background uptake ratio. The obtained imaging findings from both PET/CT methods were compared on both a patient basis and a lesion basis for further analysis and interpretation. Staging was done according to the method of the American Joint Committee on Cancer (*28*).

Reference Standard

All patients who were evaluated had been discussed in the multidisciplinary council for breast cancer before the data were scanned retrospectively. This council includes departments such as medical oncology, radiation oncology, general surgery, medical pathology, radiology, and nuclear medicine. Additional foci observed in PET/CT imaging for multifocal or multicentric primary malignancies, which had not undergone histopathologic testing, were further assessed using previous mammography and MRI results to determine malignancy. If there was no histopathologic evidence, regional lymph nodes observed in PET/CT imaging were correlated with previous ultrasonographic and MRI results, taking into account their molecular and morphologic characteristics depicted in the PET/CT imaging.

Moreover, the molecular and morphologic properties of distant lymph node, visceral, and bone involvement reported through PET/CT imaging were evaluated alongside routinely performed conventional imaging, as for breast lesions and regional lymph nodes. Finally, alignment of the latest decisions with the conclusions documented by the multidisciplinary council was ensured through consensus, also considering treatment response evaluations across all lesion sites during follow-up periods. The median follow-up was 4 mo (range, 3–6 mo). Consequently, the integration of multiple diagnostic modalities and multidisciplinary discussions formed a robustly constructed reference standard.

Statistical Analysis

The study data underwent descriptive statistical analysis, presenting numeric variables as mean and SD and categoric variables through frequency and percentage analysis. The normality and homogeneity of variance were tested using the Shapiro–Wilk and Levene tests, respectively. For nonnormally distributed dependent variables, the Wilcoxon signed-rank test was used, whereas the Mann–Whitney *U* test compared nonnormally distributed independent variables. Continuous variables were evaluated with the Pearson correlation test, and categoric

variables with the Spearman correlation test. SPSS 22.0 software was used for statistical analyses, with the significance level set at a P value of less than 0.05.

RESULTS

Patient Demographics and Tumor Characteristics

In total, 23 women with ILC were enrolled in this study. Their mean age was 51 y (range, 37–79 y), with 8 being premenopausal. Before undergoing PET/CT, 4 patients had undergone breast surgery. Additionally, 2 patients had bilateral breast cancer involvement (Fig. 2). The pathologic and clinical characteristics of the patients are summarized in Table 1.

Comparative PET/CT Analysis

The study revealed that ^{68}Ga-FAPI PET/CT exhibited increased tumoral activity retention, along with elevated tumor-to-background uptake ratios, in comparison to ^{18}F-FDG PET/CT, across all lesion locations (13.22 ± 8.1 vs 3.43 ± 2.12; $P < 0.001$; $z = -3.621$). Furthermore, significantly increased ^{68}Ga-FAPI uptake (mean, 13.8 ± 5.1) was detected in primary tumoral lesions compared with ^{18}F-FDG uptake (mean, 3.9 ± 3.0; $P < 0.001$; $z = 3.621$) (Table 2; Figs. 3 and 4).

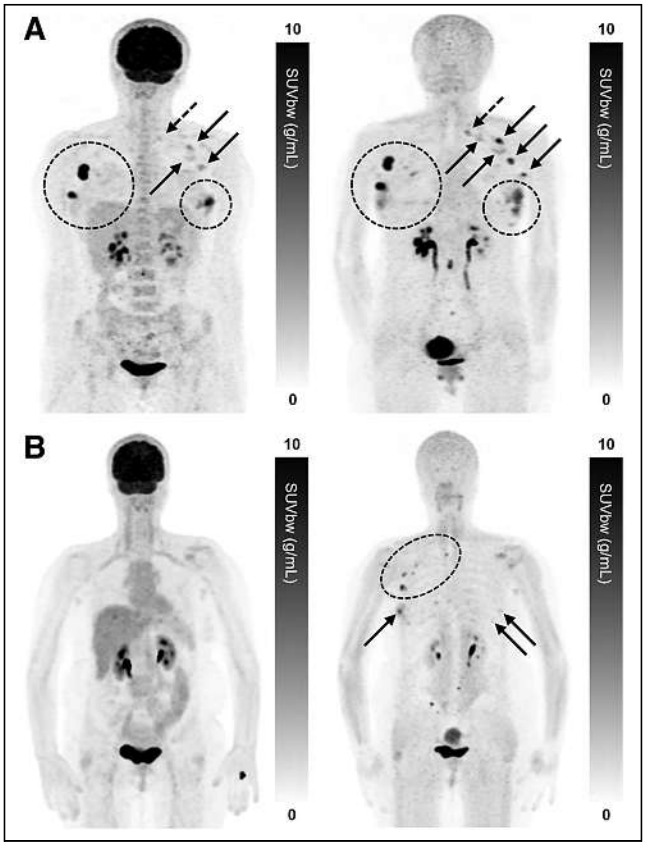

FIGURE 2. Maximum-intensity projection ^{18}F-FDG PET (left) and ^{68}Ga-FAPI PET (right) images of synchronous ILC. (A) 42-y-old patient with multicentric primary lesions (encircled), regional (solid arrows), and distant inferior jugular lymph node (dashed arrows) seen on ^{18}F-FDG PET and subsequently confirmed on ^{68}Ga-FAPI PET, which also revealed additional malignant foci aligned with MRI. Some lesions exhibited high activity retention on ^{68}Ga-FAPI PET. (B) 53-y-old patient showing no significant uptake on ^{18}F-FDG PET but synchronous bilateral lesions (arrows) on ^{68}Ga-FAPI PET, which also identified pathologic lymph nodes (encircled), resulting in upstaging. SUVbw = body-weight SUV.

TABLE 1
Clinical and Pathologic Features of Patients

Feature	Data
Mean age (y)	51 (range, 37–79)
Pathologic score	
5	2 (8.7)
6	6 (26.1)
7	7 (30.4)
8	3 (13,1)
9	5 (21.7)
Grade	
1	2 (8.7)
2	13 (56.5)
3	8 (34.8)
Mean ratio of tumor to stroma	0.91 (SD, 1.92)
Peritumoral lymphocyte infiltration	
Evident	6 (26.1)
Not evident	17 (73.9)
Molecular subtypes	
Luminal A	15 (65)
Luminal B/human epidermal growth factor receptor 2–negative	8 (35)
Primary surgery before scanning	
Yes	4 (17)
No	19 (83)
Premenopausal	8 (35)
Postmenopausal	15 (65)
Bilateral breast cancer	
Yes	2 (9)
No	21 (91)
Metastatic disease	
Yes	11 (47.8)
No	12 (52.2)

Qualitative data are number followed by percentage in parentheses.

Among the 23 patients, 19 had a primary breast lesion, whereas 4 had previously undergone mastectomy. Among those with a primary breast lesion, 6 had a solitary breast lesion, and 13 had multicentric breast cancer. The median size of primary breast lesions was 20.5 mm (range, 3–80 mm). In total, 44 breast lesions were analyzed, with only 2 lesions in the breast measuring less than 8 mm, indicating that all lesions were likely to be ^{18}F-FDG PET/CT–avid. Although the number of primary breast lesions detected was identical for both ^{18}F-FDG PET/CT and ^{68}Ga-FAPI PET/CT (25 lesions), ^{68}Ga-FAPI PET/CT identified an additional 19 foci (Table 3). Notably, among the 7 patients initially assessed as having solitary breast cancer based on ^{18}F-FDG PET/CT, ^{68}Ga-FAPI PET/CT revealed them to have multicentric breast cancer. Moreover, ^{68}Ga-FAPI PET/CT detected a higher number of multicentric foci in 3 patients. Additionally, 4 patients exhibited nonavid lesions in the contralateral breast on ^{18}F-FDG PET/CT that

TABLE 2
SUV_{max} of ^{18}F-FDG PET/CT and ^{68}Ga-FAPI PET/CT According to Lesion Location

Lesion location	SUV_{max}		*P**
	^{18}F-FDG PET/CT	^{68}Ga-FAPI PET/CT	
Primary breast	3.9 ± 3.0	13.8 ± 5.1	0.001
Local/distant lymph node metastasis	1.15 ± 0.8	11.5 ± 5.9	0.012
Liver metastasis†	1.73 ± 1.27	6,37 ± 3,5	None
Bone metastasis	5.3 ± 4.1	19.1 ± 6.0	0.017

*Wilcoxon signed-rank test.
†Number of lesions (n = 3) was found to be insufficient for meaningful statistical analysis.
Data are mean ± SD.

were detectable on ^{68}Ga-FAPI PET/CT. No correlation was observed between the size of primary breast lesions and either ^{18}F-FDG PET/CT uptake (P = 0.33; r = 0.151) or ^{68}Ga-FAPI PET/CT uptake (P = 0.19; r = 0.201), possibly because most lesions were 1 cm or larger, where ^{18}F-FDG sensitivity is already higher.

Axillary lymph node metastasis was detected in 1 patient with ^{18}F-FDG PET/CT and in 8 patients with ^{68}Ga-FAPI PET/CT. The mean uptake value of ^{68}Ga-FAPI PET/CT (11.5 ± 5.9) was significantly higher than that of ^{18}F-FDG PET/CT (1.15 ± 0.8; P = 0.012; z = 2.521) (Table 2; Figs. 2 and 3). In total, 134 lymph nodes were measured, with short diameters ranging from 5 to 18 mm. Among them, 89.5% had a short diameter of 8 mm or less. Both ^{18}F-FDG PET/CT and ^{68}Ga-FAPI PET/CT showed involvement in 6 lymph nodes (4.5%). ^{18}F-FDG PET/CT demonstrated no uptake in 34 lymph nodes, whereas ^{68}Ga-FAPI PET/CT exhibited uptake in 25.4% of these nodes. Ninety-four lymph nodes were classified as benign by both imaging modalities (70.1%). Of the 40 metastatic lymph nodes, 30 were at level 1, and the rest were at level 2. There was a strong positive correlation between lymph node short diameter and ^{18}F-FDG PET/CT uptake values (P < 0.001; r = 0.625), whereas higher accumulation on ^{68}Ga-FAPI PET/CT resulted in higher sensitivity, and these lesions suffered less from the partial-volume effect (P < 0.001; r = 0.319).

Regarding metastatic sites, in 18 of 23 (78.2%) patients ^{68}Ga-FAPI PET/CT identified new lesions not seen on ^{18}F-FDG PET/CT, including multifocal primary lesions within the breast, local or distant lymph nodes, bone, and liver (Table 3; Figs. 4 and 5). Although 1 distant lymph node metastasis was detected on ^{18}F-FDG PET/CT, ^{68}Ga-FAPI PET/CT revealed an additional 3 patients with distant lymph node metastasis (mean, 3.0 and 8.5 ± 2.8, respectively). Bone metastases were detected in 7 of 8 patients on ^{18}F-FDG PET/CT, and an additional patient with bone metastasis was identified using ^{68}Ga-FAPI PET/CT. The total number of bone metastases detected on ^{18}F-FDG PET/CT was 264, compared with 473 on ^{68}Ga-FAPI PET/CT (Table 3; Fig. 5). In 87.5% of patients, the number of bone metastases detected by ^{68}Ga-FAPI PET/CT was higher than that detected by ^{18}F-FDG PET/CT. The mean uptake of ^{68}Ga-FAPI PET/CT was 19.1 ± 6.0, whereas it was 5.3 ± 4.1 for ^{18}F-FDG PET/CT (P = 0.017; z = 2.380) (Table 2). Furthermore, 3 new solitary liver metastases, undetectable on ^{18}F-FDG PET/CT, were visualized using ^{68}Ga-FAPI PET/CT (mean, 6.37 ± 3.5) (Table 3; Fig. 4).

The TNM classification and staging of 23 patients were compared between 2 imaging modalities. T categories were assessed in 19 patients, with operated cases classified as Tx. Both modalities showed a similar distribution among T category groups (Tx, T1, T2, T3, and T4). N category variations were observed: ^{18}F-FDG PET/CT showed 88% N0, 8% N1, and 4% N3, whereas ^{68}Ga-FAPI PET/CT showed 52%, 44%, and 4%, respectively, with 36% upstaging in N0 cases. Both modalities had comparable results for the M category, but ^{68}Ga-FAPI PET/CT revealed a 13% upstaging rate, indicating its ability to detect additional metastatic lesions. Lastly, the anatomic stage group analysis revealed 1 case (4.4%) as stage IA, 11 cases (47.8%) as IIA, 1 case (4.4%) as IIB, 1 case (4.4%) as IIIB, and 9 cases (39.1%) as IV. The single case identified as IA on ^{18}F-FDG PET/CT was later identified as IIA on ^{68}Ga-FAPI PET/CT, also in line with the reference standard. Similarly, 3 of the cases identified as IIA, 1 case identified as IIB, and 2 cases identified as IIA were later upstaged by ^{68}Ga-FAPI PET/CT to IIB, IV, and IV, respectively (Table 4).

Correlation Analysis of Imaging Uptake Ratios and Pathologic Features

The mean uptake value in patients with luminal A disease was 4.42 ± 3.66 by ^{18}F-FDG PET/CT, whereas it was 2.44 ± 0.23 in the luminal B subgroup (P = 0.092). Correspondingly, these values were 13.6 ± 5.4 and 14.6 ± 5.7 by ^{68}Ga-FAPI PET/CT (P = 0.706). There was no correlation between the luminal A or B subgroup and the ratio of ^{18}F-FDG PET/CT to ^{68}Ga-FAPI PET/CT SUV_{max} (P = 0.102; r = −0.42).

Moreover, no significant correlation was found between the other pathologic features of tumor and the uptake ratio of ^{18}F-FDG to ^{68}Ga-FAPI PET/CT (glandular differentiation [r = 0.32; P = 0.17], nuclear polymorphism [r = 0.23; P = 0.34], mitosis count [r = 0.31; P = 0.18], grade score [r = 0.38; P = 0.099], grade [r = 0.19; P = 0.43], or tumor-to-stroma ratio [r = 0.29; P = 0.21]). In contrast, a moderately significant positive correlation was observed between the peritumoral lymphocyte ratio and the ^{68}Ga-FAPI PET/CT–to–^{18}F-FDG PET/CT SUV_{max} ratio (r = 0.498; P = 0.026). This suggests that a higher peritumoral lymphocyte ratio was associated with a higher uptake ratio of ^{68}Ga-FAPI PET/CT to ^{18}F-FDG PET/CT.

DISCUSSION

False-negative rates are higher for ILCs than for ductal breast cancers. Although MRI demonstrates high sensitivity in detecting

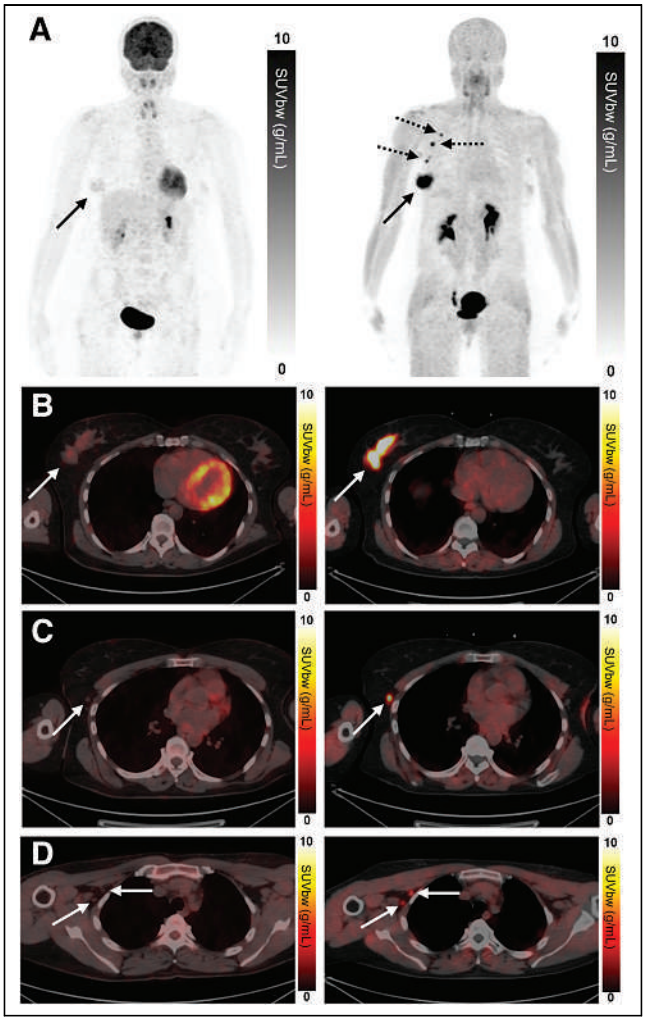

FIGURE 3. Maximum-intensity projection ^{18}F-FDG PET (left) and ^{68}Ga-FAPI PET (right) images (A) and axial hybrid ^{18}F-FDG PET/CT (left) and ^{68}Ga-FAPI PET/CT (right) images (B–D) of 50-y-old patient with right bifocal ILC. (A and B) Two adjacent breast lesions with low ^{18}F-FDG PET/CT uptake showed significantly higher uptake on ^{68}Ga-FAPI PET/CT (solid arrows). Dashed arrows in right panel indicate regional lymph nodes detected by FAPI PET/CT. (C and D) Axillary lymph nodes (arrows) without activity on ^{18}F-FDG PET/CT exhibited significant uptake on ^{68}Ga-FAPI PET/CT, leading to upstaging in N category. SUVbw = body-weight SUV.

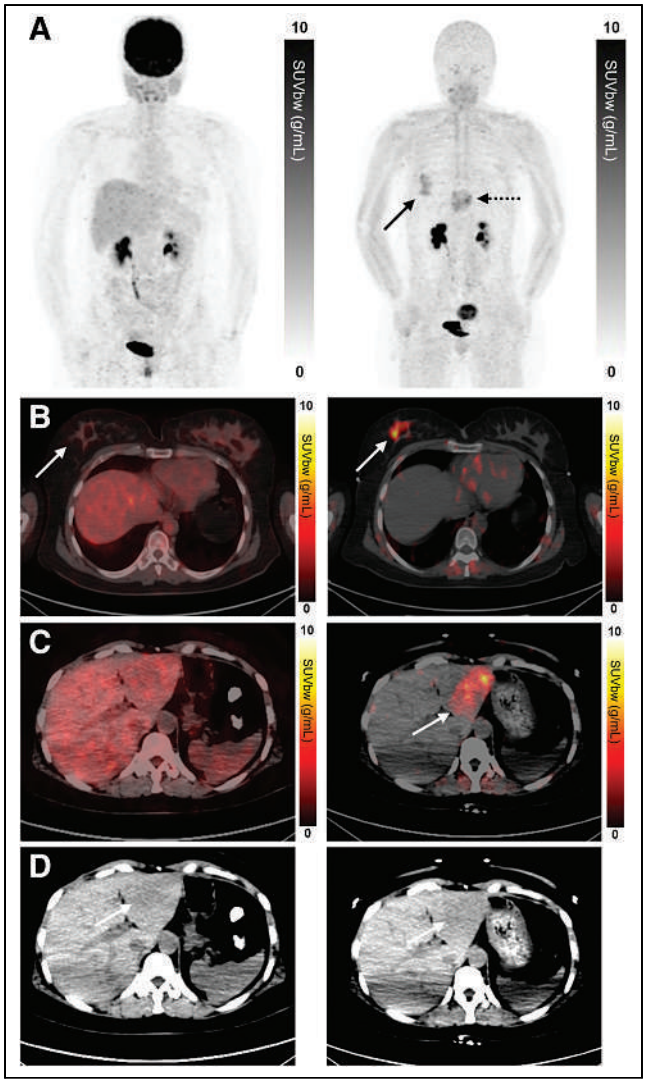

FIGURE 4. Maximum-intensity projection ^{18}F-FDG PET (left) and ^{68}Ga-FAPI PET (right) images (A), axial hybrid ^{18}F-FDG PET/CT (left) and ^{68}Ga-FAPI PET/CT (right) images (B and C), and axial CT images (D) of 42-y-old patient with right ILC. (A and B) Although ^{18}F-FDG PET/CT showed no significant activity in right breast lesion (white arrows), ^{68}Ga-FAPI PET/CT revealed substantial uptake. Dashed arrow in right panel A indicates liver lesion, whereas solid arrow indicates primary lesion. (C and D) In addition, liver lesion with vague borders on CT images (arrows) had no significant ^{18}F-FDG uptake but exhibited high ^{68}Ga-FAPI uptake, confirmed as breast cancer metastasis through MRI, indicating stage IV disease. SUVbw = body-weight SUV.

primary breast masses and axillary lymph nodes, ^{18}F-FDG PET serves as the most valuable tool for identifying distant metastases. In the presence of ILC, a secondary imaging method becomes necessary. Given that the stroma volume can surpass that of neoplastic cells, ^{68}Ga FAPI PET/CT appears to offer greater sensitivity than ^{18}F-FDG PET/CT, especially for detecting small lesions or those with low or heterogeneous glucose metabolism.

The limited sensitivity of ^{18}F-FDG PET/CT may be attributed not only to the low-grade nature of ILC but also to its pathogenetic characteristics. E-cadherin, a calcium-dependent transmembrane protein responsible for maintaining tissue integrity and cell-to-cell adhesion while preventing tissue invasion (*29*), is absent in approximately 85% of cases of ILC. This absence leads to a loss of adhesion proteins and disrupts the morphologic pattern, resulting in tumor cells that are individually dispersed or arranged in a single-file pattern, loosely distributed throughout a fibrous matrix with minimal desmoplastic response (*30*). Additionally, the tumor-infiltrating lymphocyte rate is typically low. Theoretically, the unique nature of ILC may reduce the sensitivity of ^{18}F-FDG PET/CT because of the dispersion of glucose-intensive tumor tissue; however, this may not affect the effectiveness of ^{68}Ga-FAPI PET/CT.

Although the benefits of ^{68}Ga-FAPI PET/CT have been demonstrated in numerous studies involving small patient cohorts (*31*), it is not yet routinely recommended by national guidelines because of the lack of high-level evidence. Initially, Kömek et al. conducted a prospective study on 20 patients with breast cancer, demonstrating that the sensitivity and specificity of ^{68}Ga-FAPI PET/CT in detecting primary breast lesions were 100% and 95.6%, respectively. In comparison, the sensitivity and specificity of ^{18}F-FDG PET/CT were 78.2% and 100%, respectively (*25*).

TABLE 3
Comparison of Lesion Number on ^{18}F-FDG PET/CT and ^{68}Ga-FAPI PET/CT According to Location

Lesion location	New malignant lesions*	Coherent malignant lesions†	Benign lesions‡	Total lesions	
				^{18}F-FDG PET/CT	^{68}Ga-FAPI PET/CT
Primary breast	19	25	0	25	34
Local/distant lymph node metastasis	34	6	94	100	134
Liver metastasis	3	0	0	0	3
Bone metastasis	209	264	0	264	473
Total	265	295	94	389	644

*Number of new malignant lesions detected on ^{68}Ga-FAPI PET/CT in line with reference standard.
†Number of malignant lesions detected on both PET/CT modalities in line with reference standard.
‡Number of lesions detected on both PET/CT modalities and concluded to be benign according to reference standard.

Subsequently, Elboga et al. conducted a retrospective study on 48 invasive breast cancer patients, revealing that ^{68}Ga-FAPI PET/CT detected a higher number of primary breast lesions and new metastatic lesions with higher uptake values than did ^{18}F-FDG PET/CT (*26*). The effectiveness of ^{18}F-FDG PET/CT was decreasing, especially in the ILC subtype, highlighting the need for a more effective imaging method, particularly in this patient group. In a prospective study by Alçın et al., which included 11 cases of ILC (*32*), patients with low avidity as determined by ^{18}F-FDG PET/CT scans were examined. The study found that ^{68}Ga-FAPI PET/CT yielded higher sensitivity and higher SUV_{max} than did ^{18}F-FDG PET/CT in breast cancer patients with low ^{18}F-FDG affinity. Additionally, ^{68}Ga-FAPI PET/CT identified additional lesions in the primary region, lymph nodes, and 1 lung metastatic nodule. Another prospective pilot trial involving 7 ILC patients with disease that was not ^{18}F-FDG–avid indicated that ^{68}Ga-FAPI PET/CT detected an increased number of lesions compared with CT alone ($P = 0.022$) (*27*).

Examining these studies reveals a lack of specificity and limited patient numbers within the ILC subgroup. Therefore, our retrospective study comparing ^{68}Ga-FAPI PET/CT with ^{18}F-FDG PET/CT in ILC patients holds significance for data accumulation and knowledge expansion. With a larger patient cohort than other studies, our findings show that ^{68}Ga-FAPI PET/CT detected more lesions and exhibited high tumor-to-background uptake ratios. Regardless of pathologic features, new lesions in the primary breast, local or distant lymph nodes, bone, and liver were found in 73.9% of patients using ^{68}Ga-FAPI PET/CT compared with ^{18}F-FDG PET/CT.

We studied 44 breast lesions, with only 2 having a size less than 8 mm. Although all lesions likely showed ^{18}F-FDG PET/CT uptake

TABLE 4
Comparison of TNM Classifications and Anatomic Stage Groups Between 2 Modalities

Category	Stage	^{18}F-FDG PET/CT	^{68}Ga-FAPI PET/CT	Upstaging
T ($n = 25$)	T1	4 (16.0)	4 (16.0)	0
	T2	15 (60.0)	15 (60.0)	
	T3	1 (4.0)	1 (4.0)	
	T4	1 (4.0)	1 (4.0)	
	Tx	4(16.0)	4 (16.0)	
N ($n = 25$)	N0	22 (88.0)	13 (52.0)	9 (36.0)
	N1	2 (8.0)	11 (44.0)	
	N3	1 (4.0)	1 (4.0)	
M ($n = 23$)	M0	14 (60.9)	11 (47.8)	3 (13.0)
	M1	9 (39.1)	12 (52.2)	
Anatomic stage group ($n = 23$)	IA	1 (4.4)	0	7 (30.4)
	IIA	11 (47.8)	7 (30.4)	
	IIB	1 (4.4)	3 (13.0)	
	IIIB	1 (4.4)	1 (4.4)	
	IV	9 (39.1)	12 (52.2)	

Data are number followed by percentage in parentheses.

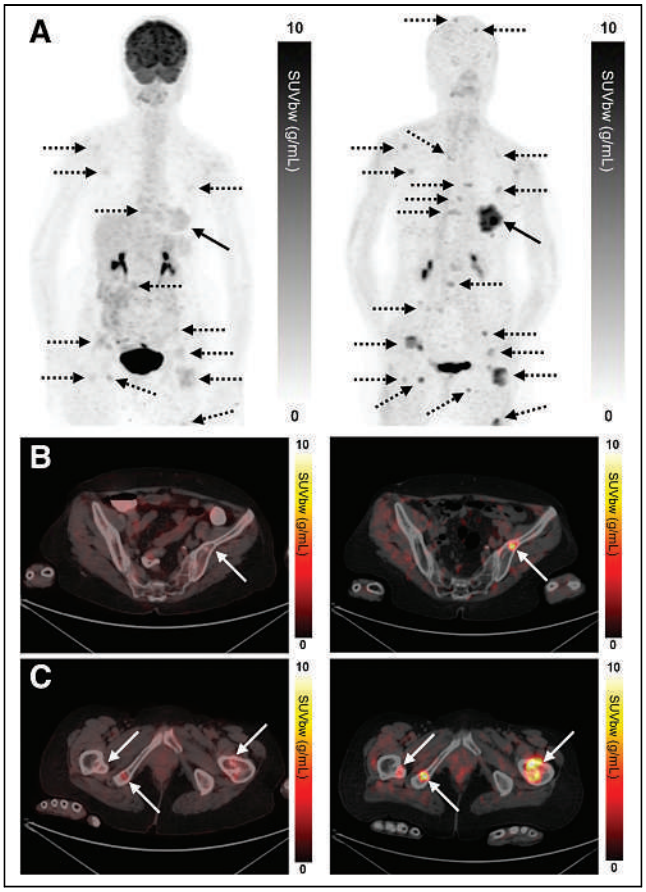

FIGURE 5. Maximum-intensity projection ^{18}F-FDG PET (left) and ^{68}Ga-FAPI PET (right) images (A) and axial hybrid ^{18}F-FDG PET/CT (left) and ^{68}Ga-FAPI PET/CT (right) images (B and C) of 68-y-old patient with left ILC. (A and B) Notable difference in uptake between ^{18}F-FDG PET/CT and ^{68}Ga-FAPI PET/CT was observed in left breast lesion (solid arrow). Multiple disseminated focal uptakes (dashed arrows) corresponding to predominantly ^{68}Ga-FAPI–avid bone lesions were detected, including in calvarium and vertebral column. (B and C) Most bone lesions (arrows) showed osteolytic features in both ^{18}F-FDG PET/CT and ^{68}Ga-FAPI PET/CT, with high ^{68}Ga-FAPI avidity. SUVbw = body-weight SUV.

regardless of size, ^{68}Ga-FAPI PET/CT identified 19 additional foci. MRI is more specific for primary breast lesions; however, ^{68}Ga-FAPI PET/CT, though not a replacement, has demonstrated superiority over ^{18}F-FDG PET/CT in previous studies.

Both ^{18}F-FDG PET/CT and ^{68}Ga-FAPI PET/CT consistently assessed tumor sizes in various T categories, showing agreement in primary tumor evaluation. Despite differences in N category analysis, ^{68}Ga-FAPI PET/CT exhibited higher sensitivity, leading to a 36% upstaging from N0 cases initially identified by ^{18}F-FDG PET/CT. Although overall M category results were comparable, ^{68}Ga-FAPI PET/CT revealed a 13% upstaging rate, detecting additional metastatic lesions. This has significant implications for treatment planning and prognosis assessment. Anatomic stage group analysis highlighted nuanced diagnostic capabilities, especially reclassifying regional diseases from stage III to IV in ^{68}Ga-FAPI PET/CT compared with ^{18}F-FDG PET/CT.

In our study a moderately significant positive correlation was identified between the peritumoral lymphocyte ratio and the ratio of ^{68}Ga-FAPI PET/CT to ^{18}F-FDG PET/CT ($r = 0.498$; $P = 0.026$). In a translational study conducted by Costa et al. (*33*), distinct subsets of CAFs within breast cancer were identified and labeled as CAF-S1 through CAF-S4, and CAF-S1 fibroblasts were associated with the infiltration of FOXP3+ T lymphocytes in breast cancer cases. In line with these findings, the observed correlation between peritumoral lymphocyte infiltration and FAPI involvement suggests that this connection could potentially serve as an indicative measure of FAP's function within immune modulation.

In addition to its success in detecting primary lesions, ^{68}Ga-FAPI PET/CT also excelled in detecting lymph node uptake. Our study showed that ^{68}Ga-FAPI PET/CT identifies axillary lymph node metastases more effectively than ^{18}F-FDG PET/CT does. Despite morphologic suspicions in ^{18}F-FDG PET/CT, 89.5% of nodes with a short diameter of 8 mm or less did not exhibit ^{18}F-FDG uptake. Unlike ^{18}F-FDG, ^{68}Ga-FAPI uptake displayed a weak correlation with lymph node size, suggesting size-independent uptake.

Consistent with the studies mentioned previously, ^{68}Ga-FAPI PET/CT appeared to be superior to ^{18}F-FDG PET/CT in detecting distant metastases in our study (*25–27*,*32*).

Eshet et al. conducted a prospective pilot trial that indicated that ^{68}Ga-FAPI PET/CT detected more lesions than CT alone ($P = 0.022$) in 7 ILC patients whose disease was not ^{18}F-FDG–avid (*27*). A notable aspect of this study is that metastatic or progressing sites were poorly demonstrated not only by ^{18}F-FDG PET/CT but also by conventional CT and bone scans. This suggests that secondary imaging methods may be inadequate for recognizing the ILC subtype. Furthermore, in this case series, ^{68}Ga-FAPI PET/CT revealed more extensive skeletal disease, aligning with our findings.

In the present study, the number of bone metastases was increased on ^{68}Ga-FAPI PET/CT compared with ^{18}F-FDG PET/CT in 7 of 8 patients (87.5%). The mean ^{68}Ga-FAPI uptake for bone metastasis was significantly higher than the mean ^{18}F-FDG uptake ($P = 0.017$; $z = 2.380$).

We found 3 liver metastases missed by ^{18}F-FDG PET/CT but detectable with ^{68}Ga-FAPI PET/CT. Building on our previous research (*26*), we argue that ^{68}Ga-FAPI PET/CT, with its low liver background activity, enhances liver metastasis detection, evident in the high tumor-to-background uptake ratios.

Despite ^{68}Ga-FAPI PET/CT's capability to reveal new breast lesions, their significance should be confirmed histopathologically or considered primary on the basis of MRI results. The primary value of ^{68}Ga-FAPI PET/CT lies in detecting regional lymph node and distant metastases, especially when other imaging modalities such as ultrasound, CT, and bone scintigraphy may be insufficient for primary breast lesions.

There are limited studies, as mentioned earlier, comparing ^{68}Ga-FAPI PET/CT and ^{18}F-FDG PET/CT head to head, and these studies include only a low number of ILC patients (*27*,*32*). Our study, with the highest number of ILC cases to our knowledge, offers a comprehensive comparison between ^{18}F-FDG and ^{68}Ga-FAPI PET/CT, making a unique contribution to the literature. It highlights the ability of ^{68}Ga-FAPI PET/CT to lower false-negative rates compared with ^{18}F-FDG PET/CT.

Although our case number was relatively high compared with the limited studies on this subject in the literature, our main limitation is the relatively low case count. Other important limitations include the lack of a prospective randomized study design and the absence of histopathologic confirmation for all metastatic lesions, excluding primary breast lesions and target lesions.

CONCLUSION

Our study contributes to the evidence supporting ^{68}Ga-FAPI PET/CT's utility in ILC, including staging. Nuanced differences, especially in lymph node involvement and metastatic lesion detection, underscore its complementary role with ^{18}F-FDG PET/CT. These insights can inform clinical decisions, providing a more comprehensive understanding of disease extent and refining treatment strategies for breast cancer patients. Larger-cohort studies are needed to validate and build on these initial findings.

DISCLOSURE

No potential conflict of interest relevant to this article was reported.

KEY POINTS

QUESTION: Is ^{68}Ga-FAPI PET/CT a more useful imaging method than ^{18}F-FDG PET/CT in ILC?

PERTINENT FINDINGS: In this cohort study examining 23 women with ILC, ^{68}Ga-FAPI PET/CT appeared to be superior to ^{18}F-FDG PET/CT in showing the primary lesion and metastases of the lymph nodes and other organs.

IMPLICATIONS FOR PATIENT CARE: ^{68}Ga-FAPI PET/CT might become a viable alternative to ^{18}F-FDG PET/CT based on the outcomes of future studies involving larger patient cohorts.

REFERENCES

1. Ferlay J, Soerjomataram I, Dikshit R, et al. Cancer incidence and mortality worldwide: sources, methods and major patterns in GLOBOCAN 2012. *Int J Cancer.* 2015;136:E359–E386.
2. Li CI, Anderson BO, Daling JR, et al. Trends in incidence rates of invasive lobular and ductal breast carcinoma. *JAMA.* 2003;289:1421–1424.
3. Li CI, Daling JR. Changes in breast cancer incidence rates in the United States by histologic subtype and race/ethnicity, 1995 to 2004. *Cancer Epidemiol Biomarkers Prev.* 2007;16:2773–2780.
4. Siegel RL, Miller KD, Jemal A. Cancer statistics, 2018. *CA Cancer J Clin.* 2018; 68:7–30.
5. Goetz MP, Gradishar WJ, Anderson BO, et al. NCCN guidelines insights: breast cancer version, 3.2018. *J Natl Compr Canc Netw.* 2019;17:118–126.
6. Lebron-Zapata L, Jochelson MS. Overview of breast cancer screening and diagnosis. *PET Clin.* 2018;13:301–323.
7. Kitajima K, Miyoshi Y. Present and future role of FDG-PET/CT imaging in the management of breast cancer. *Jpn J Radiol.* 2016;34:167–180.
8. Hogan MP, Goldman DA, Dashevsky B, et al. Comparison of ^{18}F-FDG PET/CT for systemic staging of newly diagnosed invasive lobular carcinoma versus invasive ductal carcinoma. *J Nucl Med.* 2015;56:1674–1680.
9. Borst MJ, Ingold JA. Metastatic patterns of invasive lobular versus invasive ductal carcinoma of the breast. *Surgery.* 1993;114:637–641.
10. Kumar R, Chauhan A, Zhuang H, et al. Clinicopathologic factors associated with false negative FDG-PET in primary breast cancer. *Breast Cancer Res Treat.* 2006; 98:267–274.
11. Avril N, Rose CA, Schelling M, et al. Breast imaging with positron emission tomography and fluorine-18 fluorodeoxyglucose: use and limitations. *J Clin Oncol.* 2000;18:3495–3502.
12. McCart Reed AE, Kutasovic JR, Lakhani SR, Simpson PT. Invasive lobular carcinoma of the breast: morphology, biomarkers and 'omics. *Breast Cancer Res.* 2015;17:12.
13. Ulaner GA, Jhaveri K, Chandarlapaty S, et al. Head-to-head evaluation of ^{18}F-FES and ^{18}F-FDG PET/CT in metastatic invasive lobular breast cancer. *J Nucl Med.* 2021;62:326–331.
14. Kurland BF, Peterson LM, Lee JH, et al. Estrogen receptor binding (^{18}F-FES PET) and glycolytic activity (^{18}F-FDG PET) predict progression-free survival on endocrine therapy in patients with ER+ breast cancer. *Clin Cancer Res.* 2017;23:407–415.
15. Siveke JT. Fibroblast-activating protein: targeting the roots of the tumor microenvironment. *J Nucl Med.* 2018;59:1412–1414.
16. Garin-Chesa P, Old LJ, Rettig WJ. Cell surface glycoprotein of reactive stromal fibroblasts as a potential antibody target in human epithelial cancers. *Proc Natl Acad Sci USA.* 1990;87:7235–7239.
17. Hamson EJ, Keane FM, Tholen S, Schilling O, Gorrell MD. Understanding fibroblast activation protein (FAP): substrates, activities, expression and targeting for cancer therapy. *Proteomics Clin Appl.* 2014;8:454–463.
18. Jansen K, Heirbaut L, Cheng JD, et al. Selective inhibitors of fibroblast activation protein (FAP) with a (4-quinolinoyl)-glycyl-2-cyanopyrrolidine scaffold. *ACS Med Chem Lett.* 2013;4:491–496.
19. Loktev A, Lindner T, Mier W, et al. A tumor-imaging method targeting cancer associated fibroblasts. *J Nucl Med.* 2018;59:1423–1429.
20. Lindner T, Loktev A, Altmann A, et al. Development of quinoline-based theranostic ligands for the targeting of fibroblast activation protein. *J Nucl Med.* 2018;59: 1415–1422.
21. Giesel FL, Kratochwil C, Lindner T, et al. ^{68}Ga-FAPI PET/CT: biodistribution and preliminary dosimetry estimate of 2 DOTA-containing FAP-targeting agents in patients with various cancers. *J Nucl Med.* 2019;60:386–392.
22. Kratochwil C, Flechsig P, Lindner T, et al. ^{68}Ga-FAPI PET/CT: tracer uptake in 28 different kinds of cancer. *J Nucl Med.* 2019;60:801–805.
23. Scanlan MJ, Raj BK, Calvo B, et al. Molecular cloning of fibroblast activation protein alpha, a member of the serine protease family selectively expressed in stromal fibroblasts of epithelial cancers. *Proc Natl Acad Sci USA.* 1994;91:5657–5661.
24. Šimková A, Busek P, Sedo A, Konvalinka J. Molecular recognition of fibroblast activation protein for diagnostic and therapeutic applications. *Biochim Biophys Acta Proteins Proteomics.* 2020;1868:140409.
25. Kömek H, Can C, Güzel Y, et al. ^{68}Ga-FAPI-04 PET/CT, a new step in breast cancer imaging: a comparative pilot study with the ^{18}F-FDG PET/CT. *Ann Nucl Med.* 2021;35:744–752.
26. Elboga U, Sahin E, Kus T, et al. Superiority of ^{68}Ga-FAPI PET/CT scan in detecting additional lesions compared to ^{18}FDG PET/CT scan in breast cancer. *Ann Nucl Med.* 2021;35:1321–1331.
27. Eshet Y, Tau N, Apter S, et al. The role of ^{68}Ga-FAPI PET/CT in detection of metastatic lobular breast cancer. *Clin Nucl Med.* 2023;48:228–232.
28. *AJCC Cancer Staging Manual.* Springer International Publishing; 2017:589–636.
29. Vleminckx K, Vakaet L Jr, Mareel M, Fiers W, Van Roy F. Genetic manipulation of E-cadherin expression by epithelial tumor cells reveals an invasion suppressor role. *Cell.* 1991;66:107–119.
30. Thomas M, Kelly ED, Abraham J, Kruse M. Invasive lobular breast cancer: a review of pathogenesis, diagnosis, management, and future directions of early stage disease. *Semin Oncol.* 2019;46:121–132.
31. Wass G, Clifford K, Subramaniam RM. Evaluation of the diagnostic accuracy of FAPI PET/CT in oncologic studies: systematic review and metaanalysis. *J Nucl Med.* 2023;64:1218–1224.
32. Alçın G, Arslan E, Aksoy T. ^{68}Ga-FAPI-04 PET/CT in selected breast cancer patients with low FDG affinity a head-to-head comparative study. *Clin Nucl Med.* 2023;48:e420–e430.
33. Costa A, Kieffer Y, Scholer-Dahirel A, et al. Fibroblast heterogeneity and immunosuppressive environment in human breast cancer. *Cancer Cell.* 2018;33:463–479.e10.

An ^{18}F-FDG PET/CT and Mean Lung Dose Model to Predict Early Radiation Pneumonitis in Stage III Non–Small Cell Lung Cancer Patients Treated with Chemoradiation and Immunotherapy

Maria Thor[1], Chen Lee[1], Lian Sun[1], Purvi Patel[1], Aditya Apte[1], Milan Grkovski[1], Annemarie F. Shepherd[2], Daphna Y. Gelblum[2], Abraham J. Wu[2], Charles B. Simone II[2], Jamie E. Chaft[3], Andreas Rimner[2], Daniel R. Gomez[2], Joseph O. Deasy[1], and Narek Shaverdian[2]

[1]*Department of Medical Physics, Memorial Sloan Kettering Cancer Center, New York, New York;* [2]*Department of Radiation Oncology, Memorial Sloan Kettering Cancer Center, New York, New York; and* [3]*Thoracic Oncology Service, Memorial Sloan Kettering Cancer Center, New York, New York*

Radiation pneumonitis (RP) that develops early (i.e., within 3 mo) (RP_{Early}) after completion of concurrent chemoradiation (cCRT) leads to treatment discontinuation and poorer survival for patients with stage III non–small cell lung cancer. Since no RP_{Early} risk model exists, we explored whether published RP models and pretreatment ^{18}F-FDG PET/CT–derived features predict RP_{Early}. **Methods:** One hundred sixty patients with stage III non–small cell lung cancer treated with cCRT and consolidative immunotherapy were analyzed for RP_{Early}. Three published RP models that included the mean lung dose (MLD) and patient characteristics were examined. Pretreatment ^{18}F-FDG PET/CT normal-lung SUV featured included the following: 10th percentile of SUV (SUV_{P10}), 90th percentile of SUV (SUV_{P90}), SUV_{max}, SUV_{mean}, minimum SUV, and SD. Associations between models/features and RP_{Early} were assessed using area under the receiver-operating characteristic curve (AUC), *P* values, and the Hosmer–Lemeshow test (pHL). The cohort was randomly split, with similar RP_{Early} rates, into a 70%/30% derivation/internal validation subset. **Results:** Twenty (13%) patients developed RP_{Early}. Predictors for RP_{Early} were MLD alone (AUC, 0.72; $P = 0.02$; pHL, 0.87), SUV_{P10}, SUV_{P90}, and SUV_{mean} (AUC, 0.70–0.74; $P = 0.003$–0.006; pHL, 0.67–0.70). The combined MLD and SUV_{P90} model generalized in the validation subset and was deemed the final RP_{Early} model (RP_{Early} risk $= 1/[1+e^{(-x)}]$; $x = -6.08 + [0.17 \times MLD] + [1.63 \times SUV_{P90}]$). The final model refitted in the 160 patients indicated improvement over the published MLD-alone model (AUC, 0.77 vs. 0.72; $P = 0.0001$ vs. 0.02; pHL, 0.65 vs. 0.87). **Conclusion:** Patients at risk for RP_{Early} can be detected with high certainty by combining the normal lung's MLD and pretreatment ^{18}F-FDG PET/CT SUV_{P90}. This refined model can be used to identify patients at an elevated risk for premature immunotherapy discontinuation due to RP_{Early} and could allow for interventions to improve treatment outcomes.

Key Words: immunotherapy; non–small cell lung cancer; PET/CT; pneumonitis; radiation

J Nucl Med 2024; 65:520–526
DOI: 10.2967/jnumed.123.266965

The addition of immune checkpoint blockade (ICB) consolidation therapy after concurrent chemoradiation (cCRT) in patients with locally advanced non–small cell lung cancer (NSCLC) has significantly improved survival and represents the current standard of care (*1–3*). The ICB consolidation therapy is administered intravenously over 1 y and has led to a 3-fold increase in the median progression-free survival and a 10% absolute increase in the 5-y overall survival compared with the prior cCRT alone standard of care (*4*). However, ICB consolidation therapy has also been found to increase the incidence of symptomatic pneumonitis (*1*,*5*,*6*). Before the use of ICB consolidation, radiation pneumonitis (RP) would result in morbidity but was rarely associated with poor survival. However, the development of RP is increasingly important since it can now lead to the premature discontinuation of ICB consolidation therapy before the planned 1 y and is thereby associated with poorer survival (*5*,*7*). Furthermore, early RP (i.e., developing $\leq$3 mo after completion of cCRT; RP_{Early}) has recently been suggested as the most critical toxicity, as it can lead to a markedly insufficient duration of ICB therapy (*7*,*8*).

Models to predict the risk of RP have been developed to guide radiation therapy (RT) planning and inform patient counseling, but these models have been derived from patients treated with cCRT alone, and the models further underestimate the rate of RP in patients treated with cCRT and ICB (*6*). This is largely due to the higher rate of RP with the addition of ICB consolidation (*6*) but is also due to the limited ability of these models to accurately predict patients with RP even after cCRT alone (*9*). Given the increased use of ICB consolidation therapy and a growing number of strategies to use immunotherapy agents with cCRT (*10*), models that accurately estimate the risk of RP in the era of ICB therapy are warranted. In cohorts treated with cCRT alone, pretreatment ^{18}F-FDG PET/CT imaging features are associated with increased RP risk (*11*). In noncancerous patients, such features have been indicative of pulmonary inflammation and hypothesized to be related to the density and activation of inflammatory immune cells in the lung (*12*,*13*).

There are currently no RP risk models specifically developed for RP_{Early}. In this study, we hypothesized that incorporating pretreatment ^{18}F-FDG PET/CT features with RT dose would yield risk models able to successfully identify patients with an exacerbated risk of this new critical toxicity, RP_{Early}.

Received Oct. 29, 2023; revision accepted Jan. 11, 2024.
For correspondence or reprints, contact Maria Thor (thorm@mskcc.org).
Published online Mar. 14, 2024.

MATERIALS AND METHODS

Cohort

In total, 178 patients who had locally advanced NSCLC and were consecutively treated with cCRT and durvalumab between May 2017 and December 2021 at a multisite tertiary cancer center were reviewed, and the 160 patients with pretreatment ^{18}F-FDG PET/CT scans available were included in this study. Patients avoided strenuous exercise for more than 24 h—and fasted for 6 h—before ^{18}F-FDG injection. The required blood sugar level was less than 200 mg/dL. After ^{18}F-FDG administration, the patients were instructed to rest quietly in the injection room. Before the study, the patients were asked to void the urinary bladder. ^{18}F-FDG PET/CT was performed according to institutional guidelines, which are based on the joint European Association of Nuclear Medicine/Society of Nuclear Medicine and Molecular Imaging/European Society for Radiotherapy and Oncology practice recommendations for the use of ^{18}F-FDG PET/CT for external-beam treatment planning in lung cancer (*14*). The PET/CT scans were acquired in 3 dimensions on a Discovery 690 or 710 PET/CT (GE Healthcare Inc.) (*15*). Patients were positioned on a flat RT tabletop. Whole-body PET acquisitions commenced about 60 min after administration of approximately 480 MBq of ^{18}F-FDG, at 3 min/bed position. All PET emission data were corrected for attenuation, scatter, and random events and were iteratively reconstructed into a $128 \times 128 \times 47$ matrix (voxel dimensions, $5.47 \times 5.47 \times 3.27$ mm) using an ordered-subset expectation maximization algorithm (2 iterations, 16 subsets) incorporating time-of-flight and point-spread function modeling. A gaussian postprocessing filter of 6.4 mm in full width at half maximum was also applied. Respiratory motion correction was not performed.

Patients were prescribed 60 Gy in 2-Gy fractions concurrent with platinum doublet chemotherapy (*6*,*16*). Durvalumab consolidation was initiated at a median of 1.4 mo after cCRT completion (Table 1). All patients had standard follow-ups after treatment, with a history, physical examination, and chest CT scan being obtained every 3 mo for the first 2 y. RP of grade 2 or higher was defined as a patient's having worsening pulmonary symptoms, including dyspnea or cough not attributable to other causes, within 12 mo from the completion of cCRT and having CT-based imaging changes within the irradiated field (*5*,*17*). Three RP endpoints were studied: 3 mo after completion of cCRT (RP_{Early}), more than 3 mo after completion of cCRT (RP_{Late}) (Table 2), and the combination thereof ($RP_{Early+Late}$), which is the definition that has traditionally been used. Patients with clinical and imaging characteristics consistent with RP were retrospectively assessed for their clinical course of RP, and RP grading was based on the Common Terminology Criteria for Adverse Events, version 5.0. This retrospective study was completed under an institutional review board–approved protocol.

Modeling

Applying Published Risk Models to RP_{Early}. In our previous work (*17*), which focused on RP in the thorax after any type of ICB, 3 published RP models were identified and explored: QUANTEC mean lung dose (MLD) alone (*18*); MLD, age, obstructive lung disease, smoking status, and tumor location (*19*); and MLD, age, and obstructive lung disease (*9*). The MLD was extracted for the total normal lung (excluding the tumor) and converted to an equivalent dose in 2-Gy fractions, assuming 3 Gy for the fractionation sensitivity parameter α/β ($EQD2_3$) (*18*); the other model parameters were extracted from the medical records. Each published model's coefficients were applied to the corresponding parameters (with no refitting). Model suitability was assessed both as calibration via the Hosmer–Lemeshow test (pHL; ideal value, 0.50) and as discrimination via the area under the receiver-operating characteristic curve (AUC; ideal value, 1.00) and P value (ideal value, 0). Each of the 3 published models was also studied for association with RP_{Late} in addition to $RP_{Early+Late}$.

Integrating ^{18}F-FDG PET/CT Features with Published Risk Models for RP_{Early}. To obtain ^{18}F-FDG PET/CT features, the normal lung in the planning CT scan was propagated onto the low-dose CT scan using Plastimatch routines for b-spline–based deformable image registration within the computational environment for RT research (*20*). All propagated normal-lung contours were quality-controlled to limit the influence of registration uncertainties. The SUV was normalized with respect to the body mass. Since most second-order histogram lung ^{18}F-FDG PET/CT features have previously been found to be nonreproducible across reconstruction algorithms (*21*–*24*), only first-order histogram features of the SUV were extracted: 10th percentile of SUV (SUV_{P10}), 90th percentile of SUV (SUV_{P90}), SUV_{max}, SUV_{mean}, minimum SUV, and SD. These features adhered to the Image Biomarker Standardization Initiative (*25*) and were automatically extracted using the radiomics toolbox of the computational environment for RT research (*26*).

A TRIPOD type 2b model (*27*) was generated in which the 160-patient cohort was randomly split, but with similar RP_{Early} and RP_{Late} rates, into a 112-patient subset (70%) used to build the model. The remaining 48-patient subset (30%) was used for internal validation of the built model. During model building, each feature was univariately associated with RP_{Early} using logistic regression with bootstrap resampling (repeated over 1,000 samples), and a candidate predictor was indicated by a P value of less than 0.05. The model parameters in the published models that were found to significantly predict RP_{Early} were refitted to the training data, and a new multivariate model was built with the published model parameters and the ^{18}F-FDG PET/CT predictors. Again, the pHL, AUC, and P values were used to assess model suitability but now of the new combined ^{18}F-FDG PET/CT and published model parameters.

RESULTS

Patient Treatment and RP Characteristics

In total, 38 (24%) of the 160 evaluated patients developed RP at a median of 3 mo (range, 1–9 mo) from cCRT completion (Table 1), initiated durvalumab significantly earlier than patients without RP (median, 41 vs. 45 d; $P = 0.03$; Table 1), and were initiated on steroid therapy. Twenty-four (63%) of the 38 patients with RP had resolution or near resolution of RP symptoms 3 mo from onset (Table 2), and of these, 6 (16%) patients were rechallenged with durvalumab, whereas the remaining patients permanently discontinued durvalumab.

Of the 38 patients who experienced RP, 20 (53%) patients did so as RP_{Early} and the remaining 18 (47%) as RP_{Late} (Supplemental Table 1). Among patients with RP_{Early}, 10 (50%) remained on steroids 3 mo from symptom onset and the remaining 10 (50%) had resolution or near resolution of RP symptoms. Additionally, 4 (20%) patients with RP_{Early} were rechallenged with durvalumab (Table 2). The appearance of RP on the diagnostic CT scan along with the corresponding treatment planning CT scan to illustrate the RT field is given in Supplemental Figure 1 (supplemental materials are available at http://jnm.snmjournals.org) for 1 representative patient who developed RP_{Early} and 1 representative patient who developed RP_{Late}.

Assessment of Published RP Models in Predicting RP_{Early}

Among the 3 published models tested, only the QUANTEC MLD-alone model (*18*) significantly predicted RP_{Early} (AUC, 0.72; $P = 0.02$; pHL, 0.87; Fig. 1A); the other 2 models (*9*,*19*) did not (AUC, 0.62, 0.62; $P = 0.10$, 0.57). Refitting the MLD model

TABLE 1
Patient Characteristics

Characteristic	No RP (n = 122)	RP (n = 38)	P*
Age (y)	67 (49–84)	73 (45–86)	0.10
Sex			
Female	48 (39)	17 (45)	0.56
Male	74 (61)	21 (55)	
Smoking history			
Ever	119 (98)	35 (92)	0.13
During RT	13 (11)	0 (0)	0.04
Performance status			
ECOG 0	65 (53)	19 (50)	
ECOG 1	57 (47)	19 (50)	0.73
AJCC eighth overall stage			
IIIA	31 (25)	10 (26)	0.20
IIIB	74 (61)	16 (42)	
IIIC	17 (14)	12 (32)	
Diagnosed lung disease			
Yes	34 (28)	33 (87)	0.18
COPD	33 (27)	15 (39)	
Asthma	1 (1)	2 (5)	
Diabetes mellitus	27 (22)	9 (24)	0.84
Histology			
Adenocarcinoma	68 (56)	26 (68)	0.14
Squamous cell	41 (34)	11 (29)	
Other	13 (11)	1 (3)	
PDL1 expression			
<1%	39 (32)	13 (34)	0.83
≥1%-49	26 (21)	8 (21)	
≥50%	31 (25)	11 (29)	
Unknown	26 (21)	6 (16)	
Chemotherapy regimen			
Carboplatin/paclitaxel	56 (46)	15 (39)	0.61
Carboplatin/pemetrexed	32 (26)	12 (32)	
Cisplatin/pemetrexed	22 (18)	7 (18)	
Cisplatin/etoposide	10 (8)	4 (11)	
Other	2 (2)	—	
Days from cCRT end to Durvalumab start	45 (10–234)	41 (13–82)	0.03

*Wilcoxon rank-sum test comparing characteristics between patients with and without RP.

ECOG = Eastern Cooperative Oncology Group; AJCC = American Joint Committee on Cancer; COPD = chronic obstructive pulmonary disease; PDL1 = programmed cell death ligand 1.

Qualitative data are number and percentage; continuous data are median and range.

improved calibration (pHL, 0.65 vs. 0.87). At the National Comprehensive Cancer Network, MLD of 20 Gy or less (MLD $EQD2_3 \leq 15$ Gy), the predicted risk of RP_{Early} was 20%. To explore the feasibility of reducing MLD beyond this guideline, 9 of 20 patients with RP_{Early} were randomly selected for replanning of their RTs. Three treatment planners specializing in thoracic cancers each replanned 3 patients intending to maximally reduce MLD without compromising any other clinical treatment planning criteria. The MLD could be further reduced in all patients and to a median of 12 $EQD2_3$ Gy (range, 8–15 Gy in $EQD2_3$), compared with the original 13 $EQD2_3$ Gy (range, 9–16 $EQD2_3$ Gy), with individual differences ranging from 0.2 to 2.8 $EQD2_3$ Gy. This MLD reduction resulted in a 1%–6% decrease in predicted RP_{Early} (Fig. 2).

TABLE 2
Data for 38 Patients in Whom RP Developed

cCRT end (mo)	Durvalumab start (mo)	CTCAE grade	RP treatment course	Persistent RP symptoms at 3 mo	Rechallenged with durvalumab
1.3	0.8	3	Hospitalized, oxygen, steroid taper	No	No
1.4	0.1	2	Steroid taper and antibiotics	No	Yes
1.5	0.1	3	Hospitalized, oxygen, steroid taper	Yes, remains on steroids	No
1.6	0.4	2	Steroid taper	Yes, remains on steroids	No
1.7	1.0	3	Hospitalized, oxygen, steroid taper	No	No
2.0	0.3	2	Steroid taper and antibiotics	Yes, remains on steroids	No
2.2	1.1	3	Hospitalized, oxygen, steroid taper	Yes, remains on steroids	No
2.2	1.8	2	Steroid taper and antibiotics	No	Yes
2.3	0.5	2	Steroid taper	No	No
2.3	0.9	2	Steroid taper	No	No
2.5	0.9	2	Steroid taper and antibiotics	No	No
2.5	1.0	2	Steroid taper	Yes, remains on steroids	No
2.7	1.3	3	Hospitalized, oxygen, steroid taper	Yes, remains on steroids	No
3.0	2.1	3	Hospitalized, steroid taper	Yes, remain on steroids	No
3.2	2.5	3	Steroid taper and antibiotics	Yes, remains on steroids, in pulmonary rehab	No
3.3	1.6	2	Steroid taper and antibiotics	Yes, remains on steroids	No
3.3	2.4	2	Steroid taper and antibiotics	No	No
3.3	2.6	2	Steroid taper and antibiotics	Yes, remains on steroids	Yes
3.4	2.8	2	Steroid taper and antibiotics	No	No
3.5	2.8	3	Steroid taper, supplemental oxygen	No	No
3.7	1.9	2	Steroid taper	No	No
3.8	2.3	2	Steroid taper	No	Yes
3.8	2.5	3	Hospitalized, oxygen, steroid taper	Yes, remains on steroids	No
3.9	1.5	3	Hospitalized, oxygen, steroid taper	No	No
3.9	2.3	3	Hospitalized, oxygen, steroid taper	No	No
4.5	3.0	2	Steroid taper	Yes, remains on steroids	No
4.5	3.9	3	Hospitalized, oxygen, steroid taper	Yes, remains on steroids and oxygen	No
4.8	3.0	2	Steroid taper	No	Yes
5.7	4.8	2	Steroid taper	No	No
5.9	4.5	2	Steroid taper and antibiotics	No	No
5.9	4.6	2	Steroid taper	No	No
6.5	5.3	3	Hospitalized, oxygen, steroid taper	Yes, remains on steroids	No
6.8	4.9	2	Steroid taper	No	No
8.0	6.4	2	Steroid taper and antibiotics	No	No
8.4	7.8	2	Steroid taper	No	No
8.7	6.0	2	Steroid taper	No	No
9.0	8.1	2	Steroid taper	No	No

CTCAE = Common Terminology Criteria for Adverse Events.

Improved Ability to Correctly Identify RP_{Early} by Integrating ^{18}F-FDG PET/CT with MLD

Among all patients, the median SUV_{mean} and SUV_{max} were 0.65 (range, 0.03–1.9) and 10 (range, 0.09–27), respectively. With similar magnitudes of association, SUV_{mean}, SUV_{P10}, and SUV_{P90} significantly predicted RP_{Early} (AUC, 0.65–0.66; P = 0.003–0.006; pHL, 0.67–0.70). These 3 ^{18}F-FDG PET/CT features were all strongly intercorrelated (Spearman's rho = 0.95). Therefore, bivariate models between MLD and each of these features were built. All bivariate models significantly predicted RP_{Early} in the

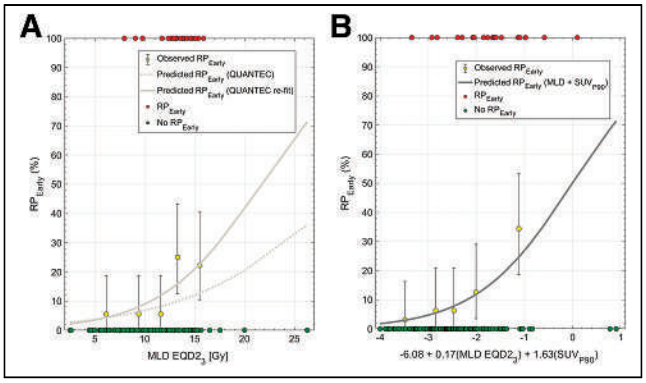

FIGURE 1. (A) Dose–response curve for QUANTEC's MLD model (*18*) (dotted line) applied to RP_{Early} and refitted MLD model for RP_{Early} (solid line) in 160-patient cohort. Observed data are aggregated in quintiles (yellow; error bars: 95% binomial CIs), in addition to each observation stratified by RP_{Early} status. (B) Predicted dose–response curve combining MLD with SUV_{P90} in 160-patient cohort; observed data are aggregated as quintiles (yellow; error bars: 95% binomial CIs), in addition to each observation stratified by RP_{Early} status.

derivation subset (AUC, 0.79–0.80; $P = 0.0005$–0.0008; pHL, 0.61–0.64), whereas only the model including MLD and SUV_{P90} generalized in the internal validation subset (AUC, 0.65, $P = 0.03$, pHL, 0.96). This model was, therefore, considered final. Thereafter and only to obtain model coefficients, the final model was refitted to the entire cohort (AUC, 0.77, $P = 0.0001$, pHL, 0.65; Fig. 2); the risk of RP_{Early} is given by the following logistic function equation: RP_{Early} risk $= 1/[1+e^{(-x)}]$; $x = -6.08 + [0.17 \times \text{MLD}] + [1.63 \times SUV_{P90}]$. In the riskiest model quintile, MLD and SUV_{P90} were 15 Gy and 1.51 (Fig. 1B: the rightmost bin), whereas in the least risky quintile, they were 6.7 Gy and 0.89 (Fig. 1B: the leftmost bin). The median SUV_{P90} among patients with RP_{Early} was 1.2 (range, 0.8–2.4), compared with 1.0 (range, 0.05–2.8) for patients without RP_{Early}. According to the bivariate MLD and SUV_{P90} model, the risk of RP_{Early} varies for MLDs of similar magnitude. For example, an MLD of 13 Gy is associated with a risk of RP_{Early} varying from 8% to 17% depending on a patient's distribution of SUV_{P90} (Fig. 3).

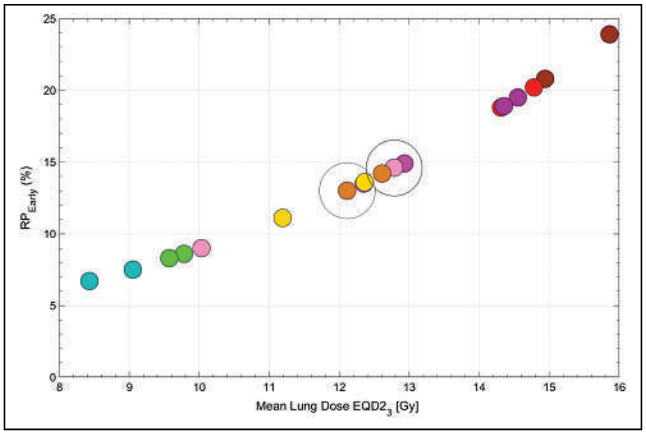

FIGURE 2. Predicted RP_{Early} based on refitted MLD model alone for random 9-patient subset with RP_{Early} in which replanning was performed. Each color represents each patient, and rightmost circle is MLD from original treatment plan; leftmost circle is MLD from replanning procedure. Population median MLD before and after replanning is denoted by larger circles (right: MLD from original plan; left: MLD after replanning).

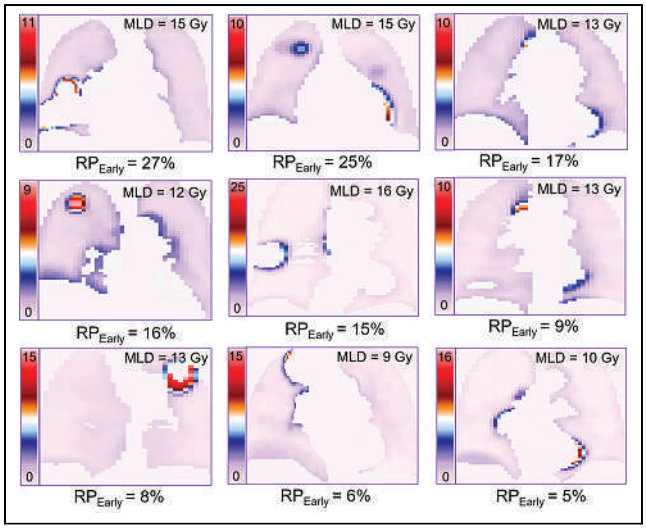

FIGURE 3. Midcoronal slices of highest SUV_{P90} voxelwise distribution maps for 9-patient subset that developed RP_{Early} and were randomly selected for MLD-sparing replanning. MLD $EQD2_3$ is inserted for each patient in upper right corner.

No Risk Model Established for RP_{Late}

None of the 3 published models (AUC, 0.44–0.52; $P = 0.50$–0.69; pHL, 0.85–0.99) or any of the 6 ^{18}F-FDG PET/CT features (AUC, 0.55–0.60; $P = 0.14$–0.58; pHL, 0.71–0.73) predicted RP_{Late}. Similarly, no published model significantly predicted $RP_{Early+Late}$ (AUC, 0.55–0.60; $P = 0.07$–0.98; pHL, 0.99–1.00), but all SUV parameterizations except SUV_{max} were significantly associated with $RP_{Early+Late}$ (AUC, 0.64–0.67; $P = 0.006$–0.01; pHL, 0.64–0.66), which was likely driven by the stronger association between SUV features and RP_{Early}.

DISCUSSION

RP_{Early} in patients with locally advanced NSCLC can lead to the premature discontinuation of life-prolonging ICB consolidation therapy. To date, no risk prediction models have been tested for, or specifically tailored to, RP_{Early}. Herein, we present a novel model that combines the MLD with SUV_{P90} of the normal lung from pretreatment ^{18}F-FDG PET/CT, which leads to an improved ability to identify the risk of RP_{Early} over using MLD alone (AUC, 0.72 vs. 0.77). Thus, these results suggest that patients at high risk of RP_{Early} could be identified by assessing the pretreatment SUV_{P90}, which could thereby inform patient-specific treatments lowering the MLD to further mitigate RP_{Early}. Importantly, the MLD was found to predict RP_{Early} but not RP_{Late}, suggesting that the risk of RP_{Early}, the most consequential RP in the setting of cCRT and ICB, can be directly mitigated and modified by limiting the MLD of the normal lung.

There is an increased risk of RP in patients who have locally advanced NSCLC treated with cCRT and ICB consolidation therapy compared with cCRT alone (*5*,*28*,*29*), with about 25% of patients treated with cCRT and ICB consolidation therapy expected to develop RP. However, only recently have data emerged that early discontinuation of ICB consolidation because of RP is associated with poorer survival and disease control (*6*–*8*). We have shown that RP models derived from patients treated with cCRT alone widely underestimate the rate of RP in patients treated with cCRT and ICB consolidation (*5*). Although there have been

reports of specific RT dose–volume histogram metrics being associated with the risk of RP in patients treated with ICB consolidation (*30*,*31*), these studies have been limited by a small number of patients, leading to inconclusive, conflicting results. Without dose–volume histogram guidelines derived for patients receiving cCRT and ICB consolidation therapy, RT planning and delivery to limit the risk of RP, particularly RP_{Early}, are suboptimal. All 3 published RP models explored here focused on RP prior to the introduction of ICB consolidation (*9*,*18*,*19*). Interestingly, the QUANTEC MLD model (*18*) was found to be associated with RP_{Early} (AUC, 0.72; $P = 0.04$). The model (*19*) that in addition to MLD included age, chemotherapy, obstructive lung disease, smoking status, and tumor location did not predict RP_{Early} (AUC, 0.62; $P = 0.57$), and neither did the model (*9*) that included MLD, age, and obstructive lung disease (AUC, 0.62; $P = 0.10$). Taken together, the inability of published models that include patient characteristics to predict RP_{Early} in patients treated with cCRT and ICB consolidation therapy motivates the need to identify other relevant characteristics to improve the ability to accurately capture RP_{Early}. After thorough model building, the final model generated here that combined SUV_{P90} with MLD had an improved ability to predict RP_{Early} over using MLD alone.

The normal-lung SUV from ^{18}F-FDG PET/CT has previously been found to be elevated among patients with chronic obstructive pulmonary disorder (*32*) and to be associated with inflammation in acute lung injury (*13*). The underlying mechanisms of a high SUV in the normal lung have been hypothesized to be attributed to increased density and baseline activation of inflammatory immune cells, as their activation is characterized by increased glucose utilization leading to an increased SUV. Since RP is a consequence of radiation injury and is characterized by increased infiltration of inflammatory cells (*33*), baseline SUV_{P90} could be an estimate of the degree of pretreatment lung inflammation and, therefore, possibly associated with increased susceptibility toward RP. In this study, we demonstrated that our RP_{Early} model can allow for patient-specific thoracic RT planning to minimize RP_{Early} and ICB discontinuation. Depending on the patient-specific pretreatment SUV_{P90}, the same MLD is associated with a wide risk range of RP_{Early}. In addition, this study indicated that MLD can be further optimized by replanning the RT, which we did for a random 9-patient subset: We demonstrated that the original MLD could be reduced in all patients by 0.2–2.8 $EQD2_3$ Gy and from a median of 13 $EQD2_3$ Gy (range, 9–16 $EQD2_3$ Gy) to a median of 12 $EQD2_3$ Gy (range, 8–15 $EQD2_3$ Gy). This resulted in an RP_{Early} predicted risk reduction of 1%–6% and from a median of 15% (range, 8%–24%) based on the original MLD to 13% (range, 7%–21%) based on the replanned MLD. Reducing the rate of RP_{Early} beyond this would likely require more conformal treatment modalities including particle therapy.

This study provided critical information to guide RT planning and potential risk stratification for patients treated with cCRT and ICB consolidation and further highlighted ideal multidisciplinary expertise and management to optimize lung cancer care (*34*). Although this was a large study including 160 patients across a multiple-site center, the study had limitations such as a retrospective design based on patients with stage IIIA–IIIC locally advanced NSCLC, and no external validation was performed. These aspects encourage the need for rigorous validation (*9*) to assess model generalizability and thereby model applicability in other thoracic cohorts presenting with different disease, imaging, patient, and treatment characteristics.

CONCLUSION

Our findings demonstrate that in patients treated with cCRT and ICB consolidation, the RT dose to the normal lungs is strongly associated with the risk of RP_{Early}, the most consequential RP that is associated with poorer survival. Furthermore, we generated a risk model for RP_{Early} based on the upper end of SUV (SUV_{P90}) of the normal lung from pretreatment ^{18}F-FDG PET/CT together with the associated MLD. This model identifies the risk of RP_{Early} with higher accuracy than using MLD alone and could be used to enable patient-specific thoracic RTs specifically tailored to identify and mitigate the risk of RP_{Early} in the context of cCRT and ICB therapies. Such an approach would be anticipated to improve treatment tolerability and, thereby, decrease the likelihood of discontinuing ICB therapies and ultimately prolong survival.

DISCLOSURE

This research was funded in part through NIH/NCI Cancer Center support grant P30 CA008748. No other potential conflict of interest relevant to this article was reported.

KEY POINTS

QUESTION: Does incorporating pretreatment ^{18}F-FDG PET/CT features with RT dose yield models that would successfully identify patients with an exacerbated risk of RP_{Early}?

PERTINENT FINDINGS: A model was derived that combines the MLD of the normal lung with the SUV_{P90} of the normal lung. The model provided an improved ability to identify RP_{Early} risk over MLD alone.

IMPLICATIONS FOR PATIENT CARE: Incorporating pretreatment SUV_{P90} into clinical practice would enable the delivery of patient-specific RP_{Early} respecting RTs.

REFERENCES

1. Antonia SJ, Villegas A, Daniel D, et al. Durvalumab after chemoradiotherapy in stage III non–small-cell lung cancer. *N Engl J Med.* 2017;377:1919–1929.
2. Antonia SJ, Villegas A, Daniel D, et al. Overall survival with durvalumab after chemoradiotherapy in stage III NSCLC. *N Engl J Med.* 2018;379:2342–2350.
3. Faivre-Finn C, Vicente D, Kurata T, et al. Four-year survival with durvalumab after chemoradiotherapy in stage III NSCLC: an update from the PACIFIC trial. *J Thorac Oncol.* 2021;16:860–867.
4. Spigel DR, Faivre-Finn C, Gray JE, et al. Five-year survival outcomes from the PACIFIC trial: durvalumab after chemoradiotherapy in stage III non-small cell lung cancer. *J Clin Oncol.* 2022;40:1301–1311.
5. Shaverdian N, Thor M, Shepherd AF, et al. Radiation pneumonitis in lung cancer patients treated with chemoradiation plus durvalumab. *Cancer Med.* 2020;9:4622–4631.
6. Shaverdian N, Offin M, Shepherd AF, et al. Association between the early discontinuation of durvalumab and poor survival in patients with stage III NSCLC. *JTO Clin Res Rep.* 2021;2:100197.
7. Xu T, Wu L, Gandhi S, et al. Treatment-related pulmonary events induced by chemoradiation and durvalumab affect survival in locally advanced non-small cell lung cancer. *Radiother Oncol.* 2022;176:149–156.
8. Alessi JV, Ricciuti B, Wang X, et al. Impact of TMB/PD-L1 expression and pneumonitis on chemoradiation and durvalumab response in stage III NSCLC. *Nat Commun.* 2023;14:4238.
9. Thor M, Deasy J, Iyer A, et al. Toward personalized dose-prescription in locally advanced non-small cell lung cancer: validation of published normal tissue complication probability models. *Radiother Oncol.* 2019;138:45–51.
10. Remon J, Levy A, Singh P, Hendriks LEL, Aldea M, Arrieta O. Current challenges of unresectable stage III NSCLC: are we ready to break the glass ceiling of the PACIFIC trial? *Ther Adv Med Oncol.* 2022;14:17588359221113268.

11. Castillo R, Pham N, Ansari S, et al. Pre-radiotherapy PDG PRT predicts radiation pneumonitis in lung cancer. *Radiat Oncol.* 2014;9:74.
12. Vass L, Fisk M, Cheriyan J, et al. Quantitative ^{18}F-fluorodeoxyglucose positron emission tomography/computed tomography to assess pulmonary inflammation in COPD. *ERJ Open Res.* 2021;7:00699–02020.
13. Jones HA, Marsino PS, Shakur BH, Morrell NW. In vivo assessment of lung inflammatory cell activity in patients with COPD and asthma. *Eur Respir J.* 2003; 21:567–573.
14. Vaz SC, Adam JA, Delgado Bolton RC, et al. Joint EANM/SNMMI/ESTRO practice recommendations for the use of 2-[^{18}F]FDG PET/CT external beam radiation planning in lung cancer V1.0. *Eur J Nucl Med Mol Imaging.* 2022;49: 1386–1406.
15. Grkovski M, Schwartz J, Rimner A, et al. Reproducibility of ^{18}F-fluoromisonidazole intratumor distribution in non-small cell lung cancer. *EJNMMI Res.* 2016;6:79.
16. Thor M, Shepherd AF, Preeshagul I, et al. Pre-treatment immune status predicts disease control in NSCLCs treated with chemoradiation and durvalumab. *Radiother Oncol.* 2022;167:158–164.
17. Shaverdian N, Beattie J, Thor M, et al. Safety of thoracic radiotherapy in patients with prior immune-related adverse events from immune checkpoint inhibitors. *Ann Oncol.* 2020;31:1719–1724.
18. Marks LB, Bentzen SM, Deasy JO, et al. Radiation dose–volume effects in the lung. *Int J Radiat Oncol Biol Phys.* 2010;76(suppl):S70–S76.
19. Appelt AL, Vogelius IR, Farr KP, Khalil AA, Bentzen SM. Towards individualized dose constraints: adjusting the QUANTEC radiation pneumonitis model for clinical risk factors. *Acta Oncol.* 2014;53:605–612.
20. Deasy JO, Blanco AI, Clark VH. CERR: a computational environment for radiotherapy research. *Med Phys.* 2003;30:979–985.
21. Orlhac F, Soussan M, Maisonobe JA, Garcia CA, Vanderlinden B, Buvat I. Tumor texture analysis in ^{18}F-FDG PET: relationships between texture parameters, histogram indices, standardized uptake values, metabolic volumes, and total lesion glycolysis. *J Nucl Med.* 2014;55:414–422.
22. van Velden FHP, Kramer GM, Frings V, et al. Repeatability of radiomic features in non-small-cell lung cancer [^{18}F]FDG-PET/CT studies: impact of reconstruction and delineation. *Mol Imaging Biol.* 2016;18:788–795.
23. Yan J, Chu-Shern JL, Loi HY, et al. Impact of image reconstruction settings on texture features in ^{18}F-FDG PET. *J Nucl Med.* 2015;56:1667–1673.
24. Lasnon C, Majdoub M, Lavigne B, et al. ^{18}F-FDG PET/CT heterogeneity quantification through textural features in the era of harmonization programs: a focus on lung cancer. *Eur J Nucl Med Mol Imaging.* 2016;43:2324–2335.
25. Zwanenburg A, Vallières M, Abdalah MA, et al. The Image Biomarker Standardization Initiative: standardized quantitative radiomics for high-throughput image-based phenotyping. *Radiology.* 2020;295:328–338.
26. Apte AP, Iyer A, Crispin-Ortuzar M, et al. Technical note: extension of CERR for computational radiomics: a comprehensive MATLAB platform for reproducible radiomics research. *Med Phys.* 2018;45:3713–3720.
27. Moons KGM, Altman DG, Reitsma JB, et al. Transparent reporting of a multivariable prediction model for individual prognosis or diagnosis (TRIPOD): explanation and elaboration. *Ann Intern Med.* 2015;162:W1-73.
28. Gao RW, Day CN, Yu NY, et al. Dosimetric predictors of pneumonitis in locally advanced non-small cell lung cancer patients treated with chemoradiation followed by durvalumab. *Lung Cancer.* 2022;170:58–64.
29. Hassanzadeh C, Sita T, Savoor R, et al. Implications of pneumonitis after chemoradiation and durvalumab for locally advanced non-small cell lung cancer. *J Thorac Dis.* 2020;12:6690–6700.
30. Mayahara H, Uehara K, Harada A, et al. Predicting factors of symptomatic radiation pneumonitis induced by durvalumab following concurrent chemoradiotherapy in locally advanced non-small cell lung cancer. *Radiat Oncol.* 2022; 17:7.
31. Diamond BH, Belani N, Masel R, et al. Predictors of pneumonitis in patients with locally advanced non-small cell lung cancer treated with definitive chemoradiation followed by consolidative durvalumab. *Adv Radiat Oncol.* 2022;8:101130.
32. de Prost N, Tucci MR, Vidal Melo MF. Assessment of lung inflammation with ^{18}F-FDG PET during acute lung injury. *AJR.* 2010;195:292–300.
33. Kainthola A, Haritwal T, Tiwari M, et al. Immunological aspect of radiation-induced pneumonitis, current treatment strategies, and future prospects. *Front Immunol.* 2017;8:506.
34. Berghmans T, Lievens Y, Aapro M, et al. European Cancer Organisation Essential Requirements for Quality Cancer Care (ERQCC): lung cancer. *Lung Cancer.* 2020;150:221–239.

^{68}Ga-FAPI-04 PET/CT in Non–Small Cell Lung Cancer: Accurate Evaluation of Lymph Node Metastasis and Correlation with Fibroblast Activation Protein Expression

Chongjiao Li*[1], Qiongrong Chen*[2], Yueli Tian[1], Jie Chen[1], Kui Xu[1], Zhiwei Xiao[1], Juan Zhong[1], Jianyuan Wu[3], Bing Wen[1], and Yong He[1]

[1]Department of Nuclear Medicine, Zhongnan Hospital of Wuhan University, Wuhan, China; [2]Department of Pathology, Zhongnan Hospital of Wuhan University, Wuhan, China; and [3]Clinical Trial Centre, Zhongnan Hospital of Wuhan University, Wuhan, China

Fibroblast activation protein (FAP) is a promising diagnostic and therapeutic target in various solid tumors. This study aimed to assess the diagnostic efficiency of ^{68}Ga-labeled FAP inhibitor (FAPI)–04 PET/CT for detecting lymph node metastasis in non–small cell lung cancer (NSCLC) and to investigate the correlation between tumor ^{68}Ga-FAPI-04 uptake and FAP expression. **Methods:** We retrospectively enrolled 136 participants with suspected or biopsy-confirmed NSCLC who underwent ^{68}Ga-FAPI-04 PET/CT for initial staging. The diagnostic performance of ^{68}Ga-FAPI-04 for the detection of NSCLC was evaluated. The final histopathology or typical imaging features were used as the reference standard. The SUV_{max} and SUV_{mean}, ^{68}Ga-FAPI–avid tumor volume (FTV), and total lesion FAP expression (TLF) were measured and calculated. FAP immunostaining of tissue specimens was performed. The correlation between ^{68}Ga-FAPI-04 uptake and FAP expression was assessed using the Spearman correlation coefficient. **Results:** Ninety-one participants (median age, 65 y [interquartile range, 58–70 y]; 69 men) with NSCLC were finally analyzed. In lesion-based analysis, the diagnostic sensitivity and positive predictive value of ^{68}Ga-FAPI-04 PET/CT for detection of the primary tumor were 96.70% (88/91) and 100% (88/88), respectively. In station-based analysis, the diagnostic sensitivity, specificity, and accuracy for the detection of lymph node metastasis were 72.00% (18/25), 93.10% (108/116), and 89.36% (126/141), respectively. Tumor ^{68}Ga-FAPI-04 uptake (SUV_{max}, SUV_{mean}, FTV, and TLF) correlated positively with FAP expression (r = 0.470, 0.477, 0.582, and 0.608, respectively; all $P \leq 0.001$). The volume parameters FTV and TLF correlated strongly with FAP expression in 31 surgical specimens (r = 0.700 and 0.770, respectively; both $P < 0.001$). **Conclusion:** ^{68}Ga-FAPI-04 PET/CT had excellent diagnostic efficiency for detecting lymph node metastasis, and ^{68}Ga-FAPI-04 uptake showed a close association with FAP expression in participants with NSCLC.

Key Words: non–small cell lung cancer; lymph node metastasis; FAP expression; ^{68}Ga-FAPI; PET/CT

J Nucl Med 2024; 65:527–532
DOI: 10.2967/jnumed.123.266806

Lung cancer is the leading cause of cancer-related mortality in men and the second-leading cause in women worldwide, with a 5-y survival rate of only 10%–33% (*1*). Non–small cell lung cancer (NSCLC) is the most common histologic type and accounts for more than 80% of all lung cancers (*2*). An accurate definition of disease extent at initial diagnosis is important for informing the choice of treatment strategy and patient management in NSCLC.

PET/CT combining anatomic and functional imaging capabilities can improve the staging accuracy of lung cancer compared with conventional imaging (*3*); however, ^{18}F-FDG, as the most commonly used imaging agent, has some limitations. Some factors (e.g., lesion diameter < 8–10 mm, mucinous adenocarcinoma, ground-glass nodule) may lead to false-negative findings, whereas reactive lymphoid hyperplasia, lymphadenitis, granulomatous inflammation, and tuberculosis can lead to false-positive findings, resulting in the misdiagnosis of lymph node metastasis (*4*,*5*). The identification of novel molecular targets and development of new imaging agents are thus critical for lung cancer evaluation (*6*,*7*).

Cancer-associated fibroblasts are an important component of the tumor microenvironment, contributing to epithelial cell growth and tumorigenicity and promoting tumor invasion and metastasis (*8*). Fibroblast activation protein (FAP) is a marker expressed specifically on the surface of cancer-associated fibroblasts. FAP inhibitors (FAPIs), which specifically target FAP, have attracted increasing interest, and various radiopharmaceuticals based on quinoline have recently been developed as pan-cancer tracers with favorable characteristics and good clinical application prospects (*9*).

Several recent studies investigating the diagnostic efficiency of ^{68}Ga-FAPI and ^{18}F-FAPI PET/CT in lung cancer have achieved initial encouraging results (*10*–*15*). ^{68}Ga-FAPI demonstrated good staging efficiency, particularly for the detection of primary tumors and distant metastasis (bone and pleura) (*11*,*12*,*14*); however, the diagnostic efficacy of ^{68}Ga-FAPI for the detection of lymph node metastasis remains uncertain because of limited histologic evidence provided by only 2 studies (*12*,*14*). In addition, despite the high detection rate of lung cancer by ^{68}Ga-FAPI PET/CT, its usefulness in NSCLC is also currently limited by a lack of histopathologic evidence regarding tumor FAP expression level, which is crucial for the future routine application of ^{68}Ga-FAPI in clinical practice. We therefore aimed to evaluate the diagnostic performance of ^{68}Ga-FAPI-04 PET/CT for the diagnosis of lymph node metastasis and to investigate the correlation between ^{68}Ga-FAPI-04 uptake by the primary tumor and FAP immunostaining in NSCLC.

MATERIALS AND METHODS

Participants

This was a secondary analysis of an ongoing clinical trial at our hospital. The study was approved by the Medical Ethics Committee of

Received Oct. 5, 2023; revision accepted Feb. 13, 2024.
For correspondence or reprints, contact Yong He (vincentheyong@163.com).
*Contributed equally to this work.
Published online Mar. 7, 2024.

Zhongnan Hospital of Wuhan University and registered in ClinicalTrails.gov (NCT05034146), and each participant signed an informed consent form. Participants with suspected or biopsy-proven NSCLC were enrolled for initial clinical staging from March 2021 to June 2023. The inclusion criteria were suspected or newly diagnosed NSCLC and no antitumor treatment before PET/CT. The exclusion criteria were no definite pathologic diagnosis, 2 or more concurrent primary tumors, small cell lung cancer, and benign lung disease.

Details of image acquisition (*16*,*17*), imaging analysis (*18*), and diagnosis reference standards (*19*–*21*) are provided in the supplemental materials (available at http://jnm.snmjournals.org).

Immunostaining of FAP and Glucose Transporter-1 (GLUT-1)

FAP expression levels in all available tissues were confirmed by immunostaining. Paraffin-embedded tissues were cut into 4-μm sections for hematoxylin–eosin, FAP, and GLUT-1 staining. The senior pathologist observed all stained sections under a light microscope (Olympus BX-53). The immunostaining results for FAP and GLUT-1 were scored semiquantitatively on the basis of the intensity and proportion of positive signal in the cytoplasm of stromal fibroblasts and cancer cells, respectively. The final immunostaining scores were 0 (negative), 1 (mild), 2 (intermediate), and 3 (intense) (supplemental materials).

Statistical Analysis

Statistical analysis was performed using SPSS (version 19.0) and GraphPad Prism (version 8). Categoric variables were presented as numbers with percentages, and continuous variables were presented as mean ± SD or as median with interquartile range, according to whether the data were normally distributed. The diagnostic efficiency of ^{68}Ga-FAPI-04 for NSCLC was calculated. Independent sample *t* tests were used to compare 2 continuous variables with normal distributions; otherwise, the Mann–Whitney *U* test was used. Diagnostic accuracy was compared using McNemar test. The correlation between FAP expression and ^{68}Ga-FAPI-04 uptake was analyzed using the Spearman correlation coefficient. Multiple groups of data were compared using 1-way ANOVA. The area under the receiver operating characteristic curve was calculated. A 2-tailed *P* value of less than 0.05 represented statistical significance.

RESULTS

Participant Characteristics

We retrospectively enrolled 136 participants, of whom 91 with NSCLC with a surgery- or biopsy-proven pathologic diagnosis were analyzed. The clinicopathologic characteristics of the participants are summarized in Table 1 and Supplemental Table 1. The participant selection process is shown in Figure 1.

TABLE 1
Clinicopathologic Features of Participants with NSCLC

Feature	Value
No. of participants	91
Age (y)	
Median	65
Interquartile range	58–70
Range	35–83
Sex	
Men	69 (75.82)
Women	22 (24.18)
Smoking	
Yes	51 (56.04)
No	40 (43.96)
Largest diameter of primary tumor (mm)	
Median	36
Interquartile range	22–54
Density of tumor	
Partial solid nodule	8 (8.79)
Solid nodule or mass	83 (91.21)
Location of primary tumor	
Left upper lobe	25 (27.47)
Left lower lobe	21 (23.08)
Right upper lobe	24 (26.37)
Right middle lobe	7 (7.69)
Right lower lobe	14 (15.38)
Pathologic type	
SCC	27 (29.67)
Adenocarcinoma	55 (60.44)
Adenosquamous carcinoma	1 (1.10)
Sarcomatoid carcinoma	2 (2.20)
Large cell neuroendocrine carcinoma	3 (3.30)
Large cell carcinoma	1 (1.10)
Undefined type	2 (2.20)
TNM stage	
I	22 (24.18)
II	6 (6.59)
III	22 (24.18)
IV	41 (45.05)

IQR = interquartile range.
Unless otherwise indicated, values are number and percentage; percentages may not total 100 because of rounding.

Primary Tumor Detection

We evaluated 91 primary tumors in 91 participants with NSCLC. The diagnostic sensitivity and positive predictive value of ^{68}Ga-FAPI-04 PET/CT for the detection of primary tumor based on visual evaluation were 96.70% (88/91) and 100% (88/88), respectively. Representative true-positive and false-negative cases are shown in Figure 2.

The ^{68}Ga-FAPI–avid tumor volume (FTV) and total lesion FAP expression (TLF) of the primary tumor were higher in men and in participants with a smoking history, larger tumor size (>3 cm), higher clinical stage (III–IV), and nonadenocarcinoma. The SUV_{max} of the primary tumor was higher in participants with larger tumors (>3 cm) (15.10 vs. 8.53, $P < 0.001$), higher clinical stage (III–IV) (14.86 ± 5.78 vs. 10.06 ± 4.80, $P < 0.001$), and nonadenocarcinoma (15.15 ± 5.95 vs. 12.23 ± 5.64, $P = 0.02$). Participants with larger tumors and higher clinical stage also had higher tumor-to-background and tumor-to-liver ratios. The time interval between injection and acquisition had no effect on ^{68}Ga-FAPI-04 uptake in the primary tumor (Supplemental Table 2). The median SUV_{max} (14.93 vs. 12.75, $P = 0.031$), FTV (26.88 vs. 4.52, $P < 0.001$), and TLF (222.77 vs. 30.14, $P < 0.001$) were higher in squamous cell carcinomas (SCCs) than in adenocarcinomas.

Lymph Node Metastasis Detection

Thirty-one participants underwent surgical lymph node dissection, and 7 received endobronchial ultrasound–guided transbronchial

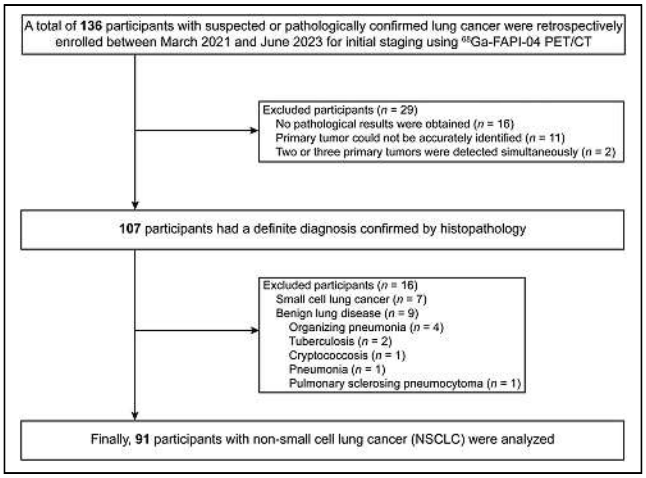

FIGURE 1. Detailed selection process of participants included in this study.

needle aspiration puncture biopsy of the mediastinal lymph nodes. In total, 141 stations comprising 357 lymph nodes were assessed. The diagnostic sensitivity, specificity, and accuracy of ^{68}Ga-FAPI-04 in station-based analysis were 72.00% (18/25), 93.10% (108/116), and 89.36% (126/141), respectively (Table 2), and the equivalent values in lesion-based analysis were 58.06% (18/31), 94.79% (309/326), and 91.60% (327/357), respectively, for the detection of lymph node involvement by ^{68}Ga-FAPI-04 (Supplemental Table 3). The pathologic results demonstrated that false-positive lymph nodes were reactive lymphoid hyperplasia. Representative cases of true-positive and false-positive lymph nodes are shown in Figure 3.

Metastatic lymph nodes had a larger median short diameter (1.06 vs. 0.56 cm), SUV_{max} (7.46 vs. 1.82), SUV_{mean} (4.23 vs. 1.23), tumor-to-background ratio (4.01 vs. 0.87), and tumor-to-liver ratio (6.00 vs. 1.44) than nonmetastatic lymph nodes (all $P < 0.001$) (Supplemental Table 4). ^{68}Ga-FAPI-04 showed excellent predictive efficiency for lymph node involvement, with a diagnostic sensitivity and specificity for differentiating lymph node metastasis of 62.96% (17/27) and 96.70% (176/182), respectively, using an SUV_{max} of 4.815 as the optimal cutoff (Supplemental Table 5).

Changes in N-Stage, TNM Stage, and Therapeutic Management

Thirty-one participants underwent lymph node dissection, including 23 N0, 4 N1, and 4 N2. ^{68}Ga-FAPI-04 accurately predicted N-stage in 21 participants (67.74%, 21/31), overestimated it in 6, and underestimated it in 4. Compared with ^{68}Ga-FAPI-04, conventional imaging (chest contrast-enhanced CT) accurately determined N-stage in 19 (61.29%, 19/31) participants, overestimated it in 7, and underestimated it in 5 (Supplemental Table 6). The diagnostic accuracy of ^{68}Ga-FAPI-04 was higher than that of conventional imaging, but the difference was not significant ($P = 0.727$).

The diagnostic accuracies of ^{68}Ga-FAPI-04 and conventional imaging for TNM stage were 82.42% (75/91) and 68.13% (62/91), respectively ($P = 0.029$). ^{68}Ga-FAPI-04 PET/CT overestimated the stage in 6 participants and underestimated it in 7, and the primary tumor could not be identified because of negative ^{68}Ga-FAPI-04 uptake in 3 participants. TNM stage was misdiagnosed on conventional imaging in 29 participants, including 7 overestimated, 17 underestimated, and 5 primary tumors missed. Compared with conventional imaging, ^{68}Ga-FAPI-04 PET/CT caused a change in treatment management for 21 (23.08%, 21/91) participants; primary tumors were found in 4 participants and the therapeutic regimens were changed in 17 participants (Supplemental Table 7).

Correlation of Tumor Uptake with FAP and GLUT-1 Expression

Forty-eight primary tumor samples (31 surgical and 17 biopsy specimens) were evaluated with an FAP-positive staining rate of 100%. FAP staining was found not only in cancer-associated fibroblasts in the tumor stroma but also in a few tumor cells in 12 cases. ^{68}Ga-FAPI–derived SUV_{max}, SUV_{mean}, FTV, and TLF correlated positively with FAP expression level in the primary tumor (r = 0.470, 0.477, 0.582, and 0.608, respectively; all $P \leq 0.001$) (Fig. 4; Supplemental Fig. 1). For 31 surgical specimens, SUV_{max} and SUV_{mean} showed moderate positive correlations with tumor FAP expression level (r = 0.614 and 0.624, respectively; both $P < 0.001$), and FTV and TLF showed strong correlations with tumor FAP expression (r = 0.700 and 0.770, respectively; both $P < 0.001$). The other 17 biopsy specimens showed no correlation between tumor ^{68}Ga-FAPI-04 uptake and FAP expression. ^{68}Ga-FAPI–derived parameters also showed moderate positive correlations (r = 0.610, 0.623, 0.561, and 0.684, respectively; all $P \leq 0.002$) with FAP expression in adenocarcinomas (n = 29). FAP expression levels were generally higher in SCCs (n = 15), with no relationship between tumor ^{68}Ga-FAPI-04 uptake and FAP expression.

Six NSCLC tumor tissues also underwent FAP and GLUT-1 double staining (Fig. 5). FAP was expressed predominantly in the tumor stroma and a small proportion of tumor cells, whereas GLUT-1 was expressed mainly in tumor cells. The median immunostaining scores were 2.50 (interquartile range, 1–3) for FAP and 2 (interquartile range, 0.75–3) for GLUT-1. The ^{18}F-FDG-derived SUV_{mean} correlated significantly with GLUT-1 expression (r = 0.926, $P = 0.008$) (Supplemental Table 8).

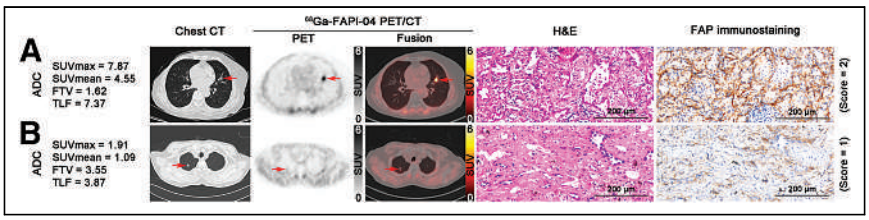

FIGURE 2. Represent true-positive (A) and false-negative (B) mixed ground glass nodules on chest CT, ^{68}Ga-FAPI-04 PET/CT, and corresponding hematoxylin–eosin (H&E) and FAP immunostaining (magnification ×100). (A) 76-y-old woman with history of postoperative right-sided breast cancer 1 y previously with ^{68}Ga-FAPI–avid adenocarcinoma (ADC; arrows) measuring 18 × 12 × 15 mm in left upper lobe with moderate FAP expression (pT1bN0M0, IA2). (B) 76-y-old man with ADC (arrows) measuring 13 × 10 × 20 mm in right upper lobe with visually negative ^{68}Ga-FAPI-04 uptake and weak FAP expression (pT1bN0M0, IA2).

Comparison of Tumor ^{68}Ga-FAPI-04 Uptake Between Different FAP-Immunostaining Scores

According to the integrated FAP expression scores, 48 participants were finally classified as scores 1 (n = 12), 2 (n = 13), or 3 (n = 23) (Fig. 6). The ^{68}Ga-FAPI–derived SUV_{max}, SUV_{mean}, FTV, and TLF increased gradually with increasing score (all $P < 0.003$). Participants with a score of 3 had higher ^{68}Ga-FAPI-04 uptake than those with a score of 1 in terms of mean

TABLE 2
Diagnostic Performance of ^{68}Ga-FAPI-04 PET/CT for Detection of Lymph Node Metastasis in NSCLC (Station-Based Analysis)

Stations of LN	TP	FP	FN	TN	Total	Sensitivity (%)	Specificity (%)	PPV (%)	NPV (%)	Accuracy (%)
2R	0	0	0	4	4	NA	100	NA	100	100
3	0	0	0	2	2	NA	100	NA	100	100
4 L	2	0	1	2	5	66.67	100	100	66.67	80
4R	5	0	0	11	16	100	100	100	100	100
5	1	1	1	11	14	50	91.67	50	91.67	85.71
6	0	0	0	1	1	NA	100	NA	100	100
7	3	2	2	22	29	60	91.67	60	91.67	86.21
8	0	0	0	2	2	NA	100	NA	100	100
9 L	0	0	0	7	7	NA	100	NA	100	100
9R	0	0	0	3	3	NA	100	NA	100	100
10 L	2	1	2	9	14	50	90	66.67	81.82	78.57
10R	3	4	0	5	12	100	55.56	42.86	100	66.67
11 L	1	0	1	12	14	50	100	100	92.31	92.86
11R	0	0	0	11	11	NA	100	NA	100	100
12 L	1	0	0	4	5	100	100	100	100	100
12R	0	0	0	2	2	NA	100	NA	100	100
Total	18	8	7	108	141	72.00	93.10	69.23	93.91	89.36

TP = true positive; FP = false positive; FN = false negative; TN = true negative; PPV = positive predictive value; NPV = negative predictive value; NA = not applicable.

SUV_{max} (15.33 ± 5.84 vs. 7.94 ± 5.24), SUV_{mean} (8.70 ± 3.48 vs. 4.50 ± 2.94), median FTV (20.12 vs. 2.57 cm^3), and TLF (155.70 vs. 10.69) (all $P < 0.002$). Among 29 participants with lung adenocarcinoma, a higher FAP-immunostaining score indicated intense tumor ^{68}Ga-FAPI-04 uptake, but there was no significant difference between the groups with scores of 2 ($n = 3$) and 3 ($n = 12$) in participants with SCC.

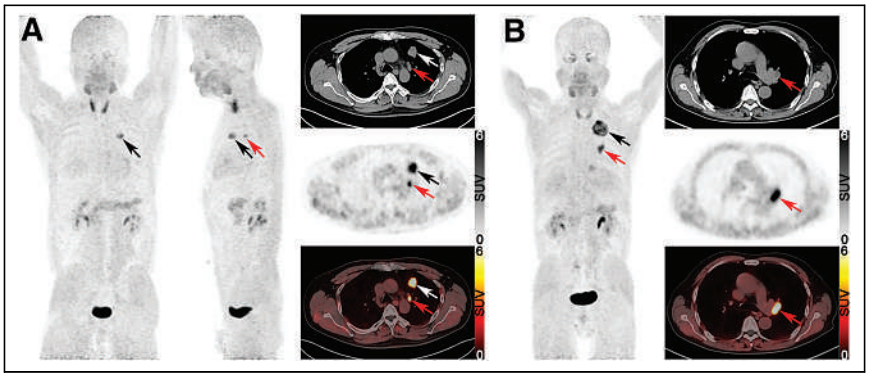

FIGURE 3. Representative cases of true-positive and false-positive lymph nodes on ^{68}Ga-FAPI-04 PET/CT. (A) PET/CT images showed ^{68}Ga-FAPI–avid soft-tissue mass (black and white arrows) and enlarged lymph node (red arrows) in ipsilateral mediastinum (station 5) with intense ^{68}Ga-FAPI-04 accumulation (SUV_{max}, 7.46) in 54-y-old man. Histopathology demonstrated adenocarcinoma with lymph node metastasis (pT2aN2M0, IIIA). (B) PET/CT images revealed well-defined solid ^{68}Ga-FAPI–avid mass (black arrow) and enlarged lymph nodes in left hilum with intense ^{68}Ga-FAPI-04 uptake (SUV_{max}, 10.33; red arrows) in 62-y-old man. Histopathology confirmed adenocarcinoma with reactive hyperplasia of left hilar lymph node (pT2bN0M0, IIA).

DISCUSSION

In the present study, we aimed to assess the nodal stage performance of ^{68}Ga-FAPI-04 PET/CT in NSCLC and to determine whether ^{68}Ga-FAPI-04 tumor uptake could accurately reflect FAP expression. Our results indicated that ^{68}Ga-FAPI-04 had excellent performance for identifying mediastinal and hilar lymph node metastases, and volume-based PET parameters showed a significant correlation with FAP expression in primary NSCLC tumors.

It is important to make an accurate diagnosis of pulmonary lesions, to inform subsequent treatment options and clinical prognosis. ^{68}Ga-FAPI-04 recently demonstrated high accuracy for the detection of primary tumors in lung cancer, ranging from 90% to 100% (*11*,*12*,*14*). Moreover, ^{68}Ga-FAPI uptake may be related to the pathologic type of tumor, and the current study accordingly found that SUV_{max}, FTV, and TLF were all higher in SCCs and other rare tumor types than in adenocarcinomas. Both ^{68}Ga-FAPI and ^{18}F-FDG revealed similar detection efficiencies for most solid lesions. Nonsolid nodules were a major cause of false-negative findings, with a detection rate of 75% (6/8) in our study; however, compared with ^{18}F-FDG, ^{68}Ga-FAPI-04 had better detection efficiency (77.8% [21/27] vs. 40.7% [11/27]) and a higher SUV_{max} (4.1 vs. 2.8) for

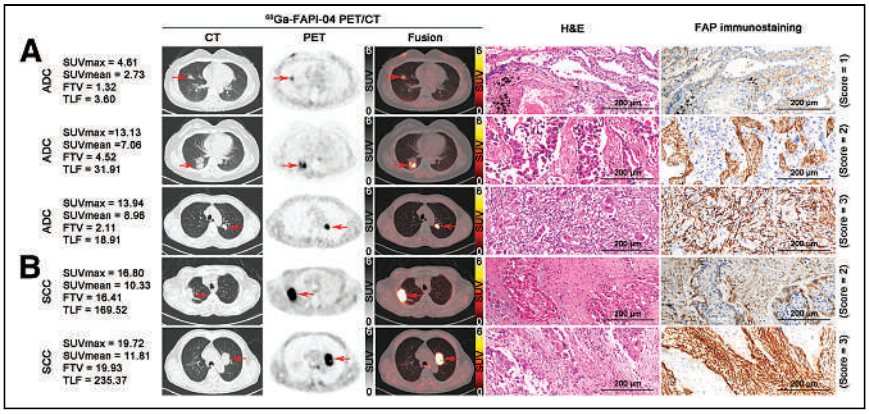

FIGURE 4. Representative ^{68}Ga-FAPI-04 PET/CT, hematoxylin-eosin (H&E), and FAP immunostaining (magnification ×100) images of pulmonary adenocarcinoma (ADC, A) and SCC (B). (A) Top row: 48-y-old woman with ADC (arrows) in right middle lobe with mild ^{68}Ga-FAPI-04 uptake and weak FAP expression (pT1bN0M0, IA2). Middle row: 49-y-old woman with ^{68}Ga-FAPI–avid ADC (arrows) in right inferior lobe with moderate FAP expression (pT2aN0M0, IB). Bottom row: 66-y-old man with ADC (arrows) in left superior lobe with intense ^{68}Ga-FAPI-04 uptake and strong FAP expression (pT1bN0M0, IA2). (B) Top row: 78-y-old man with SCC (arrows) in right superior lobe with intense ^{68}Ga-FAPI-04 uptake and moderate FAP expression (cT3N0M1c, IVB). Bottom row: 66-y-old man with ^{68}Ga-FAPI-04–avid SCC (arrows) in left superior lobe with strong FAP expression (pT2aN1M0, IIB).

detecting nonsolid nodules (<3 cm) (*12*). ^{68}Ga-FAPI-04 may thus be a good alternative tracer for the diagnosis of NSCLC.

Accurate evaluation of lymph node involvement is crucial in choosing the treatment strategy for patients with early-stage or resectable NSCLC. ^{18}F-FDG PET/CT has significantly improved the accuracy of lymph node staging of NSCLC compared with contrast-enhanced CT; however, false-positive (inflammatory diseases of lymph nodes) and false-negative (microscopic lymph node metastases) findings limit the diagnostic effectiveness of ^{18}F-FDG for the N-stage of NSCLC, leading to relatively low sensitivity (49.6%–72.2%) and specificity (81.5%–95%) in per-station analysis (*22*,*23*). Compared with ^{18}F-FDG, ^{68}Ga-FAPI showed better diagnostic efficiency for detecting lymph node metastasis, especially in terms of diagnostic specificity (97.6%–99% vs. 6%–88.8%) in NSCLC, whereas metastatic lymph nodes also had a higher SUV_{max} than nonmetastatic ones for ^{68}Ga-FAPI (10.3 vs. 2.9), but not ^{18}F-FDG (*12*,*14*). Similar to previous studies, we also demonstrated a high specificity of 93.10% indicating the value of ^{68}Ga-FAPI-04 for diagnosing true-negative lymph nodes. The false-negative lymph nodes detected by ^{68}Ga-FAPI-04 are mainly due to small nodules (short diameter < 0.5 cm), necrosis, and micrometastases. The present study identified some false-positive nodes, and the pathologic results showed many accumulated macrophages and phagocytosed carbon particles in the lymph node, suggesting that it may be related to FAP expression in macrophages and the individual's working environment. Our results showed that ^{68}Ga-FAPI-04 had an accuracy of 67.74% (21/31) for N-staging in surgical NSCLC, which was slightly lower than in a previous study (80% [8/10]) (*14*). Overall, these findings suggest that ^{68}Ga-FAPI-04 has good potential for detecting lymph node involvement, thus guiding the surgical strategy for lymph node dissection in patients with early-stage or resectable NSCLC.

FAP is closely associated with tumor progression and a worse clinical outcome (*24*,*25*). FAP expression levels are important in terms of FAP targeting PET imaging and radionuclide therapy in patients with lung cancer. The reported FAP-positivity rate in NSCLC is 76.2%–97.3%, with variations in expression levels among histopathologic types (*24*,*26*). Wei et al. demonstrated a moderate correlation between ^{18}F-FAPI–derived SUV_{max} and FAP expression in 6 surgical and 26 biopsy lung cancer specimens (r = 0.439) (*15*). However, our results confirmed that volume-based PET parameters (FTV and TLF) were strongly associated with FAP expression, suggesting that tumor uptake burden can reflect FAP expression more accurately than SUV in NSCLC. We also found that most SCCs (12/15) showed intense FAP expression, higher ^{68}Ga-FAPI-04 uptake, and a sharp outline, partially consistent with the results of Moreno-Ruiz et al. (*25*). FAP expression in adenocarcinomas varied greatly, with weak expression in highly differentiated adenocarcinomas. Additionally, adenosquamous and sarcomatoid carcinomas showed strong FAP expression, whereas FAP expression was weak in most large cell neuroendocrine carcinomas and small cell lung cancers. The strong FAP expression and high ^{68}Ga-FAPI-04 uptake (SUV_{max}, 12.85 ± 6.69) in benign lung disease (e.g., organizing pneumonia, tuberculosis, and cryptococcosis) revealed by our study suggest that we should pay more attention to these in routine clinical practice. Overall, ^{68}Ga-FAPI–derived FTV and TLF may thus accurately reflect the expression level of FAP, which could serve as a predictive indicator for FAP-targeted radionuclide therapy in patients with advanced NSCLC.

Our study had some limitations. First, the diagnosis of some distant metastatic lesions was based mainly on the typical imaging performance and lacked supporting histopathologic evidence. Second, the subgroup analysis sample (SCC) for FAP immunostaining was relatively small, which may affect the accuracy of the results. Third, the sample size for FAP and GLUT-1 double staining was also small, and the data may

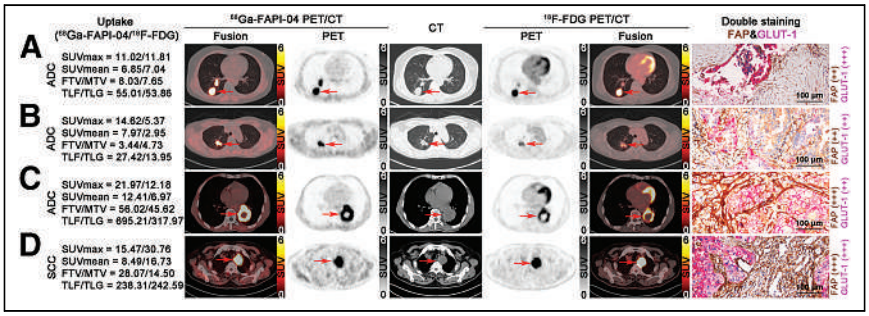

FIGURE 5. Representative ^{68}Ga-FAPI-04, ^{18}F-FDG PET/CT, and double immunostaining (magnification ×100) images of participants with NSCLC. (A) 67-y-old woman with adenocarcinoma (ADC; arrows) in right lower lobe (cT2N2M0, IIIA). (B) 65-y-old woman with ADC (arrows) in right upper lobe (pT1cN0M0, IA3). (C) 75-y-old man with ADC (arrows) in left lower lobe (ypT1aN0M0). (D) 68-y-old man with SCC (arrows) in left upper lobe (cT4N0M0, IIIA). Brown and rose-red in double immunostaining images represent FAP and GLUT-1 immunostaining, respectively. MTV = metabolic tumor volume; TLG = total lesion glycolysis.

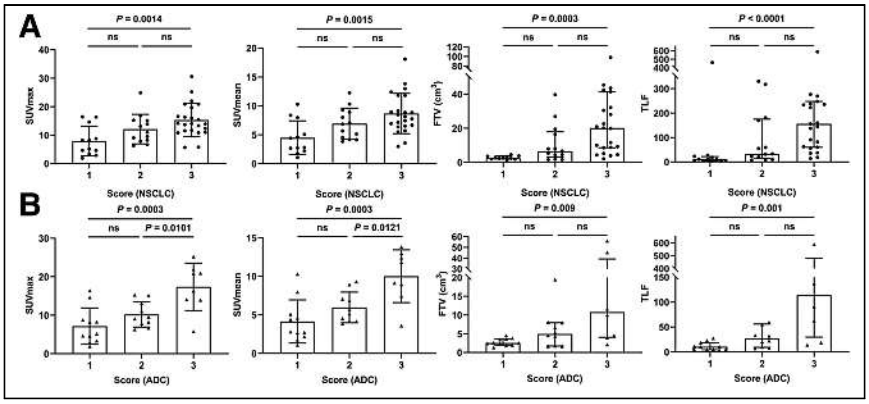

FIGURE 6. Comparison of ^{68}Ga-FAPI-04 uptake in primary tumor in relation to FAP-immunostaining score in participants with NSCLC (A) and lung adenocarcinoma (ADC, B). Lines in SUV_{max} and SUV_{mean} groups represent mean and SD; lines in FTV and TLF groups represent median and interquartile range. $P < 0.05$ indicates significant difference. ns = not statistically significant.

not be representative. Further large-scale multicenter prospective clinical trials are therefore required to validate the current findings regarding ^{68}Ga-FAPI-04 in NSCLC.

CONCLUSION

^{68}Ga-FAPI-04 PET/CT can accurately identify lymph node involvement, which is important for informing the choice of surgery in participants with resectable NSCLC. Tumor ^{68}Ga-FAPI-04 uptake correlated with FAP expression in NSCLC, especially in terms of the volume parameters (FTV and TLF). ^{68}Ga-FAPI-04 may become a valuable alternative tracer agent for imaging NSCLC, and ^{68}Ga-FAPI-derived volume parameters may be potential predictors of FAP-targeted radioligand therapy in patients with advanced NSCLC.

DISCLOSURE

This study received funding from the Improvement Project for Theranostic Ability on Difficulty Miscellaneous Disease (Tumor) (ZLYNXM202007), the Medical Sci-Tech Innovation Platform of Zhongnan Hospital of Wuhan University (PTXM2022013), the National Natural Science Foundation of China (82372005 and 82171986), Hubei Provincial Natural Science Foundation (2022CFB169), and Hubei Province Health and Family Planning Scientific Research Project (WJ2023M051). No other potential conflict of interest relevant to this article was reported.

KEY POINTS

QUESTION: Does ^{68}Ga-FAPI-04 PET accumulation correlate with FAP expression in NSCLC?

PERTINENT FINDINGS: ^{68}Ga-FAPI-04 PET/CT revealed excellent diagnostic efficiency, and ^{68}Ga-FAPI–derived volumetric parameters showed strong correlations with FAP expression in NSCLC.

IMPLICATIONS FOR PATIENT CARE: Our findings may accelerate the clinical translation of FAP-targeted radioligand therapy in patients with advanced NSCLC.

REFERENCES

1. Sung H, Ferlay J, Siegel RL, et al. Global cancer statistics 2020: GLOBOCAN estimates of incidence and mortality worldwide for 36 cancers in 185 countries. *CA Cancer J Clin.* 2021;71:209–249.
2. Vaz SC, Adam JA, Delgado Bolton RC, et al. Joint EANM/SNMMI/ESTRO practice recommendations for the use of 2-[^{18}F]FDG PET/CT external beam radiation treatment planning in lung cancer V1.0. *Eur J Nucl Med Mol Imaging.* 2022;49:1386–1406.
3. Kandathil A, Subramaniam RM. FDG PET/CT for primary staging of lung cancer and mesothelioma. *Semin Nucl Med.* 2022;52:650–661.
4. Lopci E, Kobe C, Gnanasegaran G, Adam JA, de Geus-Oei LF. PET/CT variants and pitfalls in lung cancer and mesothelioma. *Semin Nucl Med.* 2021;51:458–473.
5. Kandathil A, Kay FU, Butt YM, Wachsmann JW, Subramaniam RM. Role of FDG PET/CT in the eighth ed. of TNM staging of non-small cell lung cancer. *Radiographics.* 2018;38:2134–2149.
6. Telo S, Calderoni L, Vichi S, Zagni F, Castellucci P, Fanti S. Alternative and new radiopharmaceutical agents for lung cancer. *Curr Radiopharm.* 2020;13:185–194.
7. Novruzov E, Mori Y, Antke C, et al. A role of non-FDG tracers in lung cancer? *Semin Nucl Med.* 2022; 52:720–733.
8. Sahai E, Astsaturov I, Cukierman E, et al. A framework for advancing our understanding of cancer-associated fibroblasts. *Nat Rev Cancer.* 2020;20:174–186.
9. Kratochwil C, Flechsig P, Lindner T, et al. ^{68}Ga-FAPI PET/CT: tracer uptake in 28 different kinds of cancer. *J Nucl Med.* 2019;60:801–805.
10. Giesel FL, Adeberg S, Syed M, et al. FAPI-74 PET/CT using either ^{18}F-AlF or cold-kit ^{68}Ga labeling: biodistribution, radiation dosimetry, and tumor delineation in lung cancer patients. *J Nucl Med.* 2021;62:201–207.
11. Wang L, Tang G, Hu K, et al. Comparison of ^{68}Ga-FAPI and ^{18}F-FDG PET/CT in the evaluation of advanced lung cancer. *Radiology.* 2022;303:191–199.
12. Zhou X, Wang S, Xu X, et al. Higher accuracy of [^{68}Ga]Ga-DOTA-FAPI-04 PET/CT comparing with 2-[^{18}F]FDG PET/CT in clinical staging of NSCLC. *Eur J Nucl Med Mol Imaging.* 2022;49:2983–2993.
13. Wei Y, Ma L, Li P, et al. FAPI compared with FDG PET/CT for diagnosis of primary and metastatic lung cancer. *Radiology.* 2023;308:e222785.
14. Wu J, Deng H, Zhong H, et al. Comparison of ^{68}Ga-FAPI and ^{18}F-FDG PET/CT in the evaluation of patients with newly diagnosed non-small cell lung cancer. *Front Oncol.* 2022;12:924223.
15. Wei Y, Cheng K, Fu Z, et al. [^{18}F]AlF-NOTA-FAPI-04 PET/CT uptake in metastatic lesions on PET/CT imaging might distinguish different pathological types of lung cancer. *Eur J Nucl Med Mol Imaging.* 2022;49:1671–1681.
16. Li C, Tian Y, Chen J, et al. Usefulness of [^{68}Ga]FAPI-04 and [^{18}F]FDG PET/CT for the detection of primary tumour and metastatic lesions in gastrointestinal carcinoma: a comparative study. *Eur Radiol.* 2023;33:2779–2791.
17. Li C, Tian Y, Shen Y, Wen B, He Y. Utility of volumetric metabolic parameters on preoperative FDG PET/CT for predicting tumor lymphovascular invasion in non-small cell lung cancer. *AJR.* 2021;217:1433–1443.
18. El-Sherief AH, Lau CT, Wu CC, Drake RL, Abbott GF, Rice TW. International Association for the Study of Lung Cancer (IASLC) lymph node map: radiologic review with CT illustration. *Radiographics.* 2014;34:1680–1691.
19. Macedo F, Ladeira K, Pinho F, et al. Bone metastases: an overview. *Oncol Rev.* 2017;11:321.
20. Heindel W, Gübitz R, Vieth V, Weckesser M, Schober O, Schäfers M. The diagnostic imaging of bone metastases. *Dtsch Arztebl Int.* 2014;111:741–747.
21. Jena A, Taneja S, Talwar V, Sharma JB. Magnetic resonance (MR) patterns of brain metastasis in lung cancer patients: correlation of imaging findings with symptom. *J Thorac Oncol.* 2008;3:140–144.
22. Li X, Zhang H, Xing L, et al. Mediastinal lymph nodes staging by ^{18}F-FDG PET/CT for early stage non-small cell lung cancer: a multicenter study. *Radiother Oncol.* 2012;102:246–250.
23. Lu P, Sun Y, Sun Y, Yu L. The role of ^{18}F-FDG PET/CT for evaluation of metastatic mediastinal lymph nodes in patients with lung squamous-cell carcinoma or adenocarcinoma. *Lung Cancer.* 2014;85:53–58.
24. Liao Y, Ni Y, He R, Liu W, Du J. Clinical implications of fibroblast activation protein-α in non-small cell lung cancer after curative resection: a new predictor for prognosis. *J Cancer Res Clin Oncol.* 2013;139:1523–1528.
25. Moreno-Ruiz P, Corvigno S, Te Grootenhuis NC, et al. Stromal FAP is an independent poor prognosis marker in non-small cell lung adenocarcinoma and associated with p53 mutation. *Lung Cancer.* 2021;155:10–19.
26. Chen X, Liu X, Wang L, et al. Expression of fibroblast activation protein in lung cancer and its correlation with tumor glucose metabolism and histopathology. *Eur J Nucl Med Mol Imaging.* 2022;49:2938–2948.

Efficacy of [^{67}Cu]Cu-EB-TATE Theranostic Against Somatostatin Receptor Subtype-2–Positive Neuroendocrine Tumors

Fabrice Ngoh Njotu[1,2], Jessica Pougoue Ketchemen[1], Anjong Florence Tikum[1], Hanan Babeker[1,2], Brian D. Gray[3], Koon Y. Pak[3], Maruti Uppalapati[2], and Humphrey Fonge[1,4]

[1]Department of Medical Imaging, College of Medicine, University of Saskatchewan, Saskatoon, Saskatchewan, Canada; [2]Department of Pathology and Laboratory Medicine, College of Medicine, University of Saskatchewan, Saskatoon, Saskatchewan, Canada; [3]Molecular Targeting Technologies, Inc., West Chester, Pennsylvania; and [4]Department of Medical Imaging, Royal University Hospital Saskatoon, Saskatoon, Saskatchewan, Canada

β^--emitting ^{177}Lu-octreotate is an approved somatostatin receptor subtype 2 (SSTR2)–directed peptide receptor radionuclide therapy for the treatment of gastroenteropancreatic neuroendocrine tumors (NETs). However,^{177}Lu-octreotate has fast pharmacokinetics, requiring up to 4 treatment doses. Moreover, ^{177}Lu is less than ideal for theranostics because of the low branching ratio of its γ-emissions, which limits its SPECT imaging capability. Compared with ^{177}Lu, ^{67}Cu has better decay properties for use as a theranostic. Here, we report the preclinical evaluation of a long-lived somatostatin analog, [^{67}Cu]Cu-DOTA-Evans blue-TATE (EB-TATE), against SSTR2-positive NETs. **Methods:** The in vitro cytotoxicity of [^{67}Cu]Cu-EB-TATE was investigated on 2-dimensional cells and 3-dimensional spheroids. In vivo pharmacokinetics and dosimetry were studied in healthy BALB/c mice, whereas ex vivo biodistribution, micro-SPECT/CT imaging, and therapy studies were done on athymic nude mice bearing QGP1.SSTR2 and BON1.SSTR2 xenografts. Therapeutic efficacy was compared with [^{177}Lu]Lu-EB-TATE. **Results:** Projected human effective doses of [^{67}Cu]Cu-EB-TATE for male (0.066 mSv/MBq) and female (0.085 mSv/MBq) patients are tolerable. In vivo micro-SPECT/CT imaging of SSTR2-positive xenografts with [^{67}Cu]Cu-EB-TATE showed tumor-specific uptake and prolonged accumulation. Biodistribution showed tumor accumulation, with concurrent clearance from major organs over a period of 72 h. [^{67}Cu]Cu-EB-TATE was more effective (60%) at eliminating tumors that were smaller than 50 mm^3 within the first 15 d of therapy than was [^{177}Lu]Lu-EB-TATE (20%) after treatment with 2 doses of 15 MBq administered 10 d apart. Mean survival of [^{67}Cu]Cu-EB-TATE–treated groups was 90 d and more than 90 d, whereas that of [^{177}Lu]Lu-EB-TATE was more than 90 d and 89 d against vehicle control groups (26 d and 53 d), for QGP1.SSTR2 and BON1.SSTR2 xenografts, respectively. **Conclusion:** [^{67}Cu]Cu-EB-TATE exhibited high SSTR2-positive NET uptake and retention, with favorable dosimetry and SPECT/CT imaging capabilities. The antitumor efficacy of [^{67}Cu]Cu-EB-TATE is comparable to that of [^{177}Lu]Lu-EB-TATE, with [^{67}Cu]Cu-EB-TATE being slightly more effective than [^{177}Lu]Lu-EB-TATE for complete remission of small tumors. [^{67}Cu]Cu-EB-TATE therefore warrants clinical development.

Key Words: [^{67}Cu]Cu-EB-TATE; PRRT; SPECT/CT imaging; SSTR2; dosimetry

J Nucl Med 2024; 65:533–539
DOI: 10.2967/jnumed.123.265997

Received May 12, 2023; revision accepted Jan. 29, 2024.
For correspondence or reprints, contact Humphrey Fonge (humphrey.fonge@usask.ca) or Maruti Uppalapati (maruti.uppalapati@usask.ca).
Published online Mar. 14, 2024.

Neuroendocrine tumors (NETs) are a large group of diverse cancers of neuroendocrine origin that develop mostly within the gastrointestinal (66%) and pulmonary (31%) systems and account for 0.46% of malignancies of these systems (*1*). About 80% of NETs overexpress somatostatin receptor subtype 2 (SSTR2; 1 of 5 SSTRs [SSTR1–SSTR5]) (*2*). Using this receptor as bait has improved the diagnosis and treatment of NETs, primarily through the peptide receptor radionuclide therapy approach, which uses somatostatin analogs such as octreotate and octreotide labeled with radionuclides (*3*). So far, Health Canada, the Food and Drug Administration, and the European Medicines Agency have approved the use of β^--emitting ^{177}Lu-DOTA-Tyr^3-octreotate complex ([^{177}Lu]Lu-DOTATATE) for the treatment of metastatic or inoperable progressive gastroenteropancreatic NETs after PET image diagnosis with the short-lived [^{68}Ga]Ga-DOTATATE (^{68}Ga half-life [$t_{1/2}$], 67.71 min) (*4,5*).

The therapeutic effectiveness of [^{177}Lu]Lu-DOTATATE is attributed to the decay characteristics of its long-lived ^{177}Lu isotope ($t_{1/2}$, 6.65 d; β^-, 100%; mean β^--energy, 134 keV; maximum β^--energy, 497 keV), which gives its ionizing β^--emissions a tumor penetration depth of 2 mm, and the tumor specificity and high binding affinity of octreotate. Similarly, the short-lived ^{68}Ga is optimal for PET imaging, thus making it a theranostics pair with ^{177}Lu (*5*). However, a limitation in differential clearance exists with a short-lived radionuclide (^{68}Ga) to estimate dosimetry for a long-lived radionuclide (^{177}Lu), an important consideration as it allows for accurate prospective determination of peptide receptor radionuclide therapy dose at an optimal therapeutic index. Additionally, the short $t_{1/2}$ of ^{68}Ga could limit the sensitivity of the diagnostic, especially for lesions in organs with a high blood pool. This thus poses the need for a matched theranostics pair or, extraordinarily, a theranostic single.

Copper has 2 medical radionuclides, long-lived ^{67}Cu ($t_{1/2}$, 2.58 d; β^-, 100%; mean β^--energy, 141 keV; maximum β^--energy, 562 keV) and ^{64}Cu ($t_{1/2}$, 12.7 h), which are increasingly being exploited for their theranostics potentials. This surge is marked by recent advancements in the production of clinical-grade ^{67}Cu and its potential to be used as a theranostic single (*6,7*). The β^--emissions of ^{67}Cu have higher mean and maximal energies than those of ^{177}Lu and therefore are expected to have therapeutic effects similar to or better than those of ^{177}Lu. For SPECT imaging, ^{177}Lu (γ-energy, 208 keV [11.1%], 113 keV [6.6%]) has a less than ideal branching ratio of its γ-rays compared with ^{67}Cu (γ-energy, 93 keV [16%];

185 keV [48%]), making ^{67}Cu a better SPECT isotope and, more desirably, a theranostics single.

To improve the pharmacokinetics of octreotate, a truncated Evans blue was attached to DOTA-octreotate as a reversible albumin binder (*8*). The resulting peptide DOTA-Evans blue-TATE (EB-TATE) has improved pharmacokinetics and tumor uptake after radiolabeling with ^{177}Lu ([^{177}Lu]Lu-EB-TATE and ^{86}Y ([^{86}Y]Y-EB-TATE (*8*). Given the theranostics potential of ^{67}Cu, it was therefore of foremost importance to investigate the diagnostic and therapeutic potential of [^{67}Cu]Cu-EB-TATE (Supplemental Fig. 1; supplemental materials are available at http://jnm.snmjournals.org (*9,10*)) in SSTR2-positive NET models in vitro and in vivo. The in vivo effectiveness of [^{67}Cu]Cu-EB-TATE was compared with that of [^{177}Lu]Lu-EB-TATE, which is currently in phase I and II clinical trials (*8,11*).

MATERIALS AND METHODS

Materials

EB-TATE was obtained from Molecular Targeting Technologies Inc. through a research collaboration agreement, ^{67}Cu was purchased as electron linear accelerator–produced $^{67}CuCl_2$ [^{68}Zn(γ,p)^{67}Cu] from Canadian Isotope Innovations Corp., and ^{177}Lu was purchased as $LuCl_3$ from the McMaster Nuclear Reactor at McMaster University. The AR42J cell line was purchased from ATCC Inc., whereas the SSTR2-transfected cell lines BON1.SSTR2 and QGP1.SSTR2 were a kind donation from Carsten Grötzinger (Department of Hepatology and Gastroenterology, Charité–Universitätsmedizin Berlin) (*12*).

Ethics Statement

All animal procedures were performed in accordance with the guidelines on laboratory animal care and use of the Canadian Council on Animal Care and were approved by the Saskatchewan University Animal Care Committee (protocol 20220021).

Cell Culture, Flow Cytometry, and Xenografts

Cell culture conditions and xenograft establishment information are provided in the supplemental materials. BON1.SSTR2 and QGP1.SSTR2 cell lines were authenticated using short tandem repeat profiling (Centre for Applied Genomics, Hospital for SickKids) and had no detectable *Mycoplasma* before their use. To determine the relative overexpression of SSTR-2 in AR42J, BON1.SSTR2, and QGP1.SSTR2, flow cytometric analysis was performed (supplemental methods).

Radiolabeling of [^{67}Cu]$CuCl_2$ and [^{177}Lu]$LuCl_3$

To radiolabel EB-TATE with ^{67}Cu or ^{177}Lu, 50 μL of a 1 mg/mL solution of EB-TATE (dissolved in 150 mM ammonium acetate, pH 5.8) were added to a 1.5-mL Eppendorf tube containing [^{67}Cu]$CuCl_2$ or [^{177}Lu]$LuCl_3$ pH-adjusted with 150 mM ammonium acetate (250 MBq in 200 μL, pH 5.8). The tube was heated at 90°C for 40 min in a thermomixer. The extent of chelation of either ^{67}Cu or ^{177}Lu to EB-TATE was determined by spotting, developing 0.5 μL of the reaction volume (^{68}Ga-peptide thin-layer chromatography eluent pack; Trasis) for 5 min, and visualizing the peak using a Scan-RAM radio–thin-layer chromatography detector (LabLogic).

Radio–thin-layer chromatography yields of less than 95% led to purification using a Sep-Pak C18 1-cm^3 vac cartridge (catalog no. WAT054960; Waters), after which the Sep-Pak–purified sample was analyzed using reverse-phase C18 high-performance liquid chromatography (2796 bioseparations module, 2487 dual l absorbance detector, and XBridge C18 5-μm, 4.6 × 150 mm column; Waters).

The in vitro stability of [^{67}Cu]Cu-EB-TATE (n = 3) was determined after incubation in phosphate-buffered saline or human serum at 4°C and 37°C for 7 d, and the results were plotted using Prism (version 9; GraphPad).

Internalization

Using ^{177}Lu-DOTATATE, Tamborino et al. showed that the extent of DNA double-strand break is proportional to the proximity of the emission to the DNA (*13*). The extent of internalization of [^{67}Cu]Cu-EB-TATE into NET cell lines AR42J, BON1.SSTR2, and QGP1.SSTR2 was determined after treating the cells at 37°C (3 per concentration per temperature of incubation and per cell line) using the Nuclei EZ Prep isolation kit (catalog no. NUC201; Sigma-Aldrich) and counted on a γ-counter (Wallac Wizard 1480; PerkinElmer) as reported previously (*14*). A 4°C incubation assay was performed as a control. The extent of internalization was obtained by presenting the difference in internalization at 37°C and 4°C as a percentage of the total count rate on cells before acid wash (Supplemental Eq. 1).

In Vitro Cytotoxicity (2- and 3-Dimensional)

The in vitro cytotoxicity of [^{67}Cu]Cu-EB-TATE on monolayer (2-dimensional) and 3-dimensional spheroids using AR42J, BON1.SSTR2, and QGP1.SSTR2 cells was determined using IncuCyte S3 live-cell imaging (Sartorius Essen Bioscience) as previously described (*15*) (details in the supplemental materials).

Pharmacokinetics, Biodistribution, Dosimetry, and Micro-SPECT/CT Imaging

Pharmacokinetics was studied by injecting healthy female BALB/c mice (n = 3) with 3.9 ± 0.2 MBq (0.32 ± 0.013 nmol) of [^{67}Cu]Cu-EB-TATE through a tail vein following laboratory standard operating procedures (*14*).

Biodistribution was studied after injecting female athymic BALB/c nude mice bearing BON1.SSTR2 and QGP1.SSTR2 xenografts on either flank with 6.9 ± 1.2 MBq (0.57 ± 0.10 nmol) of [^{67}Cu]Cu-EB-TATE via a tail vein. Mice were euthanized at 1, 72, and 120 h (3 per time point) after injection, and activity in all organs was counted using a γ-counter and expressed as percentage injected activity per gram of organ (%IA/g) and %IA.

To estimate radiation dosimetry, healthy BALB/c mice (20 female and 24 male) were injected with 5.2 ± 1.1 MBq (0.43 ± 0.09 nmol) of [^{67}Cu]Cu-EB-TATE through the tail vein and euthanized at 25 min, 1 h, 6 h, 24 h, 48 h, and 72 h (3–4 per time point) after injection. The carcasses were collected and analyzed using a γ-counter, and activity was expressed as %IA/g and %IA. The mouse biodistribution (%IA/g) data were extrapolated to human data (%IA) using the formula %IA (human) = [%IA/g (mouse) × total body weight of mouse (in kg) × mass of human organ (in g)]/total body weight of human (in kg). For each organ, this was plotted against sampling time and used to estimate the residence time of the agent in the organ in MBq-h/MBq, represented by the area under the time–activity function integrated to infinity (complete decay) of the ^{67}Cu. The residence time was fitted into the OLINDA kinetics model (OLINDA/EXM, version 2.2; Hermes Medical Solutions) to generate absorbed doses in units of cGy/mCi of ^{67}Cu administered.

SPECT/CT imaging of female athymic BALB/c nude mice bearing BON1.SSTR2 and GQP1.SSTR2 xenografts was performed at 1, 6, 24, 48, and 72 h after a tail vein injection of 8.0 ± 1.4 MBq of [^{67}Cu]Cu-EB-TATE (n = 3), using a Vector4CT scanner (MILabs). The SPECT images were acquired over 35 min, whereas the CT images were acquired over 5 min. Generated CT and SPECT images were analyzed on the PMOD 3.7 software package (PMOD).

Radiotherapy

Female athymic BALB/c nude mice bearing subcutaneous BON1.SSTR2 (n = 15) and QGP1.SSTR2 (n = 16) xenografts (84.2 ± 63.3 mm^3) were allocated to 3 groups (5 or 6/group) per

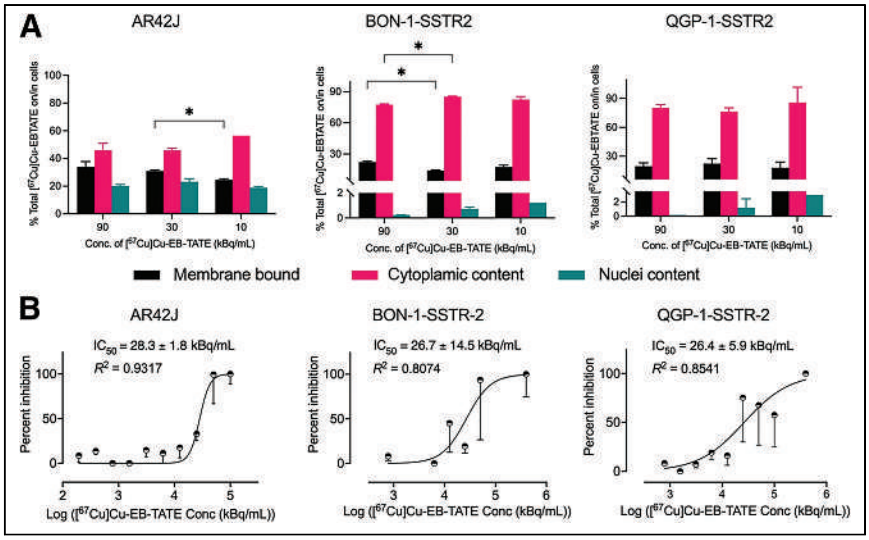

FIGURE 1. Internalization and in vitro cytotoxicity of [^{67}Cu]Cu-EB-TATE in NET cell lines with different SSTR2 densities. (A) Internalization after 2.5 h of incubation at different concentrations of [^{67}Cu]Cu-EB-TATE. (B) In vitro cytotoxicity in 2-dimensional monolayer of NET cell lines using live cell imaging. IC_{50} = 50% inhibitory concentration. *$P < 0.0332$.

xenograft model, each receiving the vehicle (saline), 2 doses of 15 MBq (10 d apart) of [^{67}Cu]Cu-EB-TATE in saline, or 2 doses of 15 MBq (10 d apart) of [^{177}Lu]Lu-EB-TATE in saline, via a tail vein in a final volume of 100 μL. The mice were monitored daily for general health status, and tumor and body weight were measured 3 times a week. The tumor size endpoint for euthanasia was 1,500 mm^3. Tumor size was measured using a digital caliper, and volume was determined using the formula [length × $width^2$]/2.

Statistical Analysis

All results are presented as mean ± SD, except when otherwise stated as the mean ± SEM of at least 3 replicated experiments. Percentage tumor growth inhibition of test groups was determined relative to control groups using the formula $[1 - \Delta T/\Delta C] \times 100$, where ΔT and ΔC are the differences between the final and initial tumor volumes of the test and control groups, respectively. Statistical analysis was performed using GraphPad Prism 9. ANOVA was performed on the slope parameters of spheroid growth, followed by the Dunnett post hoc test to compare treatment groups.

RESULTS

Radiolabeling and In Vitro Stability

The best specific activity of [^{67}Cu]Cu-EB-TATE was found to be 5 MBq/μg of peptide, with a resulting radiochemical yield of 95% by instant thin-layer chromatography, whereas radiolabeling of [^{177}Lu]Lu-EB-TATE at this specific activity resulted in a radiochemical yield of 90% (Supplemental Figs. 2A and 2B). Radiochemical purity as shown by reverse-phase C18 high-performance liquid chromatography was at least 98% (Supplemental Fig. 3). The in vitro stability of [^{67}Cu]Cu-EB-TATE was determined in phosphate-buffered saline at 4°C and in human serum at 37°C for 7 d. Average daily yields of intact [^{67}Cu]Cu-EB-TATE, normalized to the initial yield on day 0 as 100%, showed that [^{67}Cu]Cu-EB-TATE was more than 91% stable on day 6 in both human serum and phosphate-buffered saline (Supplemental Fig. 4).

Overexpression of SSTR-2 in NET Cell Lines

Flow cytometry using phycoerythrin-conjugated anti-SSTR2 showed that QGP1.SSTR2 has an increased expression of SSTR2 compared with standard high-expressing AR42J, which has similar expression levels to BON1.SSTR2 (Supplemental Figs. 5 and 6).

Internalization of [^{67}Cu]Cu-EB-TATE and Cytotoxicity Against NET Cell Lines In Vitro

The internalization of [^{67}Cu]Cu-EB-TATE was studied in AR42J, BON1.SSTR2, and QGP1.SSTR2 cell lines. After 2.5 h of incubation followed by compartmental internalization analyses, the total internalization fraction (nuclei plus cytoplasmic) at 90 kBq/mL was observed to increase slightly, though not significantly, from 66.1% ± 5.4% (AR42J) to 78.6 ± 1.2 (BON1.SSTR22, $P = 0.0834$) and to 80.4 ± 3.5 (QGP1.SSTR2, $P = 0.0898$). Moreover, no differences were seen in total internalization for a given cell line across the 3 tested concentrations except for AR42J (at 30 kBq/mL and 10 kBq/mL) and BON1.SSTR2 (90 kBq/mL and 30 kBq/mL) (Fig. 1A).

The concentration of [^{67}Cu]Cu-EB-TATE that inhibited 50% of NET cells AR42J, BON1.SSTR2, and QGP1.SSTR2 in vitro after 72 h of treatment was determined and presented as mean ± SEM. There were no significant differences in the 50% inhibitory concentrations for AR42J (28.3 ± 1.8 kBq/mL), BON1.SSTR2 (26.7 ± 14.5 kBq/mL), or QGP1.SSTR2 (26.4 ± 5.9 kBq/mL) (Fig. 1B).

To further evaluate the cytotoxicity of [^{67}Cu]Cu-EB-TATE in vitro, spheroid models of BON1.SSTR2 and QGP1.SSTR2 were developed. [^{67}Cu]Cu-EB-TATE at activity concentrations of at least 8 kBq/mL inhibited the growth of QGP1.SSTR2 spheroids but not the growth of BON1.SSTR2 spheroids (Supplemental Figs. 7A and 7B). At 150 h after treatment, QGP1.SSTR2 spheroids' size decreased from 0.57 ± 0.04 mm^2 to 0.54 ± 0.02 mm^2 ($P = 0.0002$)

TABLE 1
Pharmacokinetics of [^{67}Cu]Cu-EB-TATE in Healthy Female BALB/c Mice

Pharmacokinetic parameter	Data
Area under curve (%IA·h/mL)	634.9 ± 6.9
Distribution $t_{1/2}$ (h)	0.6 ± 0.1
Clearance $t_{1/2}$ (h)	33.5 ± 5.2
Elimination constant (h^{-1})	0.13 ± 0.01
Volume at steady-state (mL)	6.9 ± 1.1
Clearance rate (mL/h)	0.16 ± 0.00

Data are mean ± SD. Mice were injected with 3.86 ± 0.16 MBq (0.32 ± 0.013 nmol) of [^{67}Cu]Cu-EB-TATE, and values were obtained from %IA/mL and time (h).

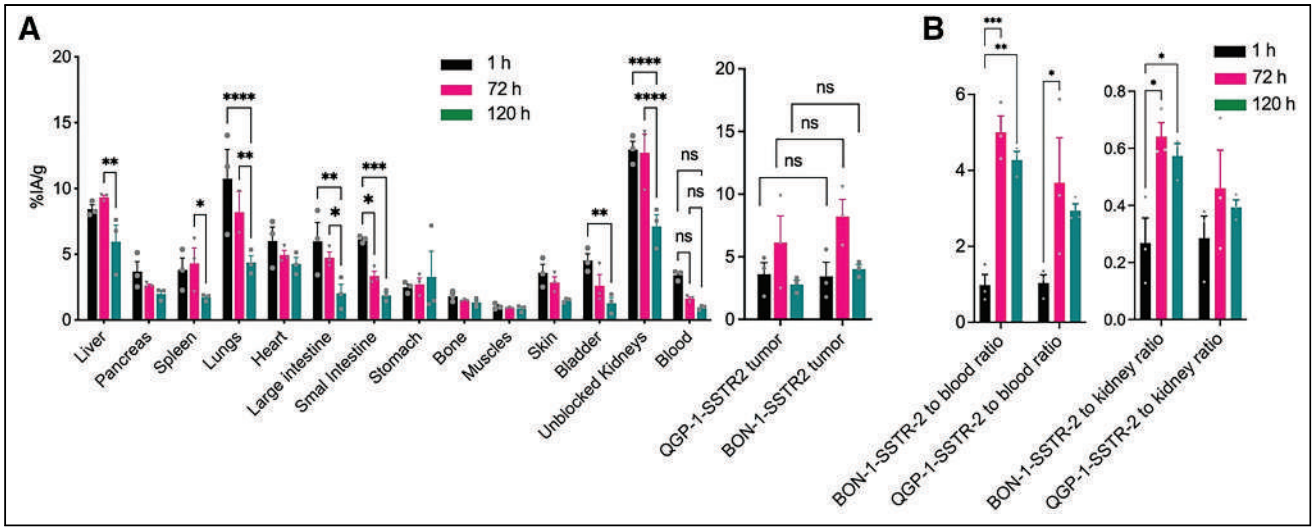

FIGURE 2. Ex vivo biodistribution of [^{67}Cu]Cu-EB-TATE in athymic nude mice bearing QGP1.SSTR2 and BON1.SSTR2 xenografts. (A) Retention of [^{67}Cu]Cu-EB-TATE in tumors and blood, accompanied by clearance from major organs. (B) Increase in tumor-to-blood and tumor-to-kidney ratios over time. ns = no significance. *$P \leq 0.0332$. **$P \leq 0.0021$. ***$P \leq 0.00002$. ****$P \leq 0.0001$.

and $0.48 \pm 0.0.03$ mm^2 ($P < 0.0001$) at 200 kBq/mL, and 1,000 kBq/mL, respectively, against 0.62 ± 0.04 mm^2 for control spheroids. For BON1.SSTR2, spheroid growth changed from 0.74 ± 0.04 mm^2 to 0.94 ± 0.06 mm^2 ($P = 0.1766$) and 0.89 ± 0.03 mm^2 ($P = 0.0953$) at 200 kBq/mL and 1,000 kBq/mL, respectively, against 1.01 ± 0.09 mm^2 for control.

Similarly, spheroid death as indicated by red object count (per image) increased with time and with activity concentration of [^{67}Cu]Cu-EB-TATE in both spheroid models (Supplemental Fig. 7C).

Pharmacokinetics, Biodistribution, Micro-SPECT/CT Imaging, and Dosimetry

In healthy female BALB/c mice, [^{67}Cu]Cu-EB-TATE exhibited a biphasic $t_{1/2}$ with a fast distribution and slow clearance phase (Table 1; Supplemental Fig. 8). Athymic BALB/c nude mice bearing a QGP1.SSTR2 xenograft on the right flank and a BON1.SSTR2 xenograft on the left flank were injected with [^{67}Cu]Cu-EB-TATE through a tail vein. Ex vivo biodistribution, reported as %IA/g at 1, 72, and 120 h after injection, showed a clear trend in clearance from major tissues except the tumor, where retention was well evident (Fig. 2A). Uptake of [^{67}Cu]Cu-EB-TATE in QGP1.SSTR2 and BON1.SSTR2 xenografts was similar (P values for 1, 72, and 120 h being 0.9910, 0.7148, and 0.1347, respectively) (Fig. 2A). Analyses of tumor-to-blood and tumor-to-kidney ratios are also shown (Fig. 2B).

Micro-SPECT/CT images showed high bladder uptake at 1 h after injection (4.5 ± 0.1%IA/g) but not at later times. The kinetics of distribution of [^{67}Cu]Cu-EB-TATE in organs and tumors clearly showed clearance from all organs except the tumors, where there was accumulation (Fig. 3). Images acquired from another mouse with a bigger QGP1.SSTR2 xenograft showed little uptake in the kidneys and livers, compared with the tumor at 72 h after injection (Supplemental Fig. 9).

Organ dose estimation after an intravenous injection of 5.22 ± 1.11 MBq of [^{67}Cu]Cu-EB-TATE in healthy BALB/c male and female mice (3–4 per sex per time point) was performed using %IA/g data for 5 time points between 1 and 72 h (Supplemental Table 1). Projected human absorbed doses (mSv/MBq) for organs, and effective and total-body dose, are presented (Table 2). In female mice, the organs with the highest dose (in decreasing order) were kidneys > lungs > liver > heart > pancreas > spleen, whereas for males, the order was liver > lungs > spleen > pancreas.

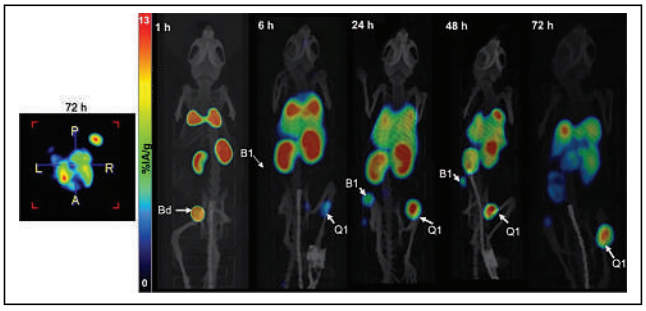

FIGURE 3. Kinetics of [^{67}Cu]Cu-EB-TATE uptake using micro-SPECT/CT. Maximum-intensity projection micro-SPECT/CT image of mouse injected with 6.45 MBq (0.53 nmol) of [^{67}Cu]Cu-EB-TATE shows accumulation and retention of theranostic in tumors and clearance from healthy organs. A = anterior; B1 = BON1.SSTR2 xenograft; Bd = bladder; P = posterior; Q1 = QGP1.SSTR2 xenograft.

Efficacy of [^{67}Cu]Cu-EB-TATE in Mouse Xenografts

Athymic BALB/c nude mice bearing either BON1.SSTR2 or QGP1.SSTR2 xenografts were treated using 2 doses of either [^{67}Cu]Cu-EB-TATE or [^{177}Lu]Lu-EB-TATE (administered 10 d apart) or vehicle (saline) as control. Tumor volumes between groups at the start of treatment were statistically similar except for QGP1.SST2 saline-treated versus QGP1.SSTR2 [^{177}Lu]Lu-EB-TATE–treated ($P = 0.0428$) (Supplemental Tables 2A and 2B). [^{67}Cu]Cu-EB-TATE was effective against BON1.SSTR2 and QGP1.SSTR2 xenografts, with results comparable to [^{177}Lu]Lu-EB-TATE. Moreover, treatment with 15 MBq of [^{67}Cu]Cu-EB-TATE or [^{177}Lu]Lu-EB-TATE, administered 10 d apart, was tolerated by athymic BALB/c nude mice as indicated by body weight (Figs. 4 and 5).

For QGP1.SSTR2 therapy (Fig. 4A), the [^{67}Cu]Cu-EB-TATE treatment group had 90.3% tumor inhibition by day 15 compared

TABLE 2
Projected Human Absorbed Doses of [^{67}Cu]Cu-EB-TATE

Organ	Absorbed dose (mSv/MBq)	
	Female	Male
Adrenals	3.54E−02	2.10E−02
Brain	1.69E−02	1.90E−02
Breast	5.28E−03	
Esophagus	2.09E−02	1.62E−02
Eyes	9.28E−04	7.67E−04
Gallbladder	2.29E−02	2.81E−02
Left colon	1.59E−01	1.52E−01
Small intestine	6.93E−03	9.56E−02
Stomach	1.40E−02	3.40E−02
Right colon	7.30E−03	8.86E−03
Rectum	1.27E−03	1.86E−03
Heart wall	1.93E−01	1.27E−01
Kidneys	6.02E−01	1.03E−02
Liver	3.42E−01	3.09E−01
Lungs	3.91E−01	2.88E−01
Ovaries	1.81E−03	
Pancreas	1.61E−01	1.07E−01
Prostate		1.60E−03
Salivary glands	1.47E−03	1.20E−03
Red marrow	8.54E−03	6.08E−03
Osteogenic cells	1.35E−02	9.26E−03
Spleen	1.41E−01	1.19E−01
Testes		1.53E−04
Thymus	1.81E−02	1.10E−02
Thyroid	7.37E−03	6.41E−03
Bladder	1.21E−02	1.47E−02
Uterus	1.73E−03	
Total body	2.34E−02	1.59E−02
Effective dose	8.50E−02	6.61E−02

with the [^{177}Lu]Lu-EB-TATE treatment group, which had 70.2% tumor inhibition. By day 90, 2 of 5 mice in the [^{67}Cu]Cu-EB-TATE treatment group had complete remission, compared with 1 of 5 mice with complete remission in the [^{177}Lu]Lu-EB-TATE treatment group. The median survival (1,500 mm^3 study endpoint) of the saline group was 26 d, compared with 90 d for the [^{67}Cu]Cu-EB-TATE group. At 90 d after treatment, median survival for the [^{177}Lu]Lu-EB-TATE–treated mice had not been reached (Fig. 4B). Interestingly, [^{67}Cu]Cu-EB-TATE was better tolerated than [^{177}Lu]Lu-EB-TATE as shown by the slope of body weights ($P < 0.0001$) (Fig. 4C).

For BON1.SSTR2, both [^{67}Cu]Cu-EB-TATE and [^{177}Lu]Lu-EB-TATE treatments showed similar effectiveness (Fig. 5A). By day 26 after the start of treatment, the [^{67}Cu]Cu-EB-TATE treatment group had a tumor inhibition of 95.4%, which was similar to that of the [^{177}Lu]Lu-EB-TATE treatment group, at 92.7% inhibition. By day 90, 1 of 5 mice in both the [^{67}Cu]Cu-EB-TATE treatment group and the [^{177}Lu]Lu-EB-TATE treatment group had complete remission. The median survival (1,500 mm^3 study endpoint) of the saline group was 53 d, whereas that for the [^{67}Cu]Cu-EB-TATE treatment group was not reached by day 90. In comparison, median survival for the [^{177}Lu]Lu-EB-TATE–treated group was 89 d (Fig. 5B). Tolerance to treatments as indicated by body weight was similar (slopes, $P = 0.1368$) (Fig. 5C).

DISCUSSION

Given the unique theranostic properties of ^{67}Cu as a single agent or in combination with ^{64}Cu (*16,17*), and considering the recent advances in ^{67}Cu production (*6*), this study was aimed to investigate the theranostic properties of [^{67}Cu]Cu-EB-TATE against SSTR2-positive NETs. Previous preclinical NET studies on peptide receptor radionuclide therapy have used SSTR2 transduced or transfected cell lines such as the human non–small lung cancer cell line A-427 (*18*), the human primary pancreatic tumor cell line QGP, and the human metastatic peripancreatic cell line BON1 (*19,20*) or endogenous SSTR2-expressing cell lines such as the rat pancreatic neuroendocrine cell line AR42J (*7,11*). Here, SSTR2-transfected BON1 (BON1.SSTR2) and QGP1 (QGP1.SSTR2) with clinically relevant levels of receptor expression were used. In vitro internalization and cytotoxicity studies were performed to prevalidate these NET cell lines for therapy studies using [^{67}Cu]Cu-EB-TATE (Fig. 1; Supplemental Figs. 5–7).

Initially, we looked to show that [^{67}Cu]Cu-EB-TATE had similar pharmacologic properties to [^{177}Lu]Lu-EB-TATE. To this end,

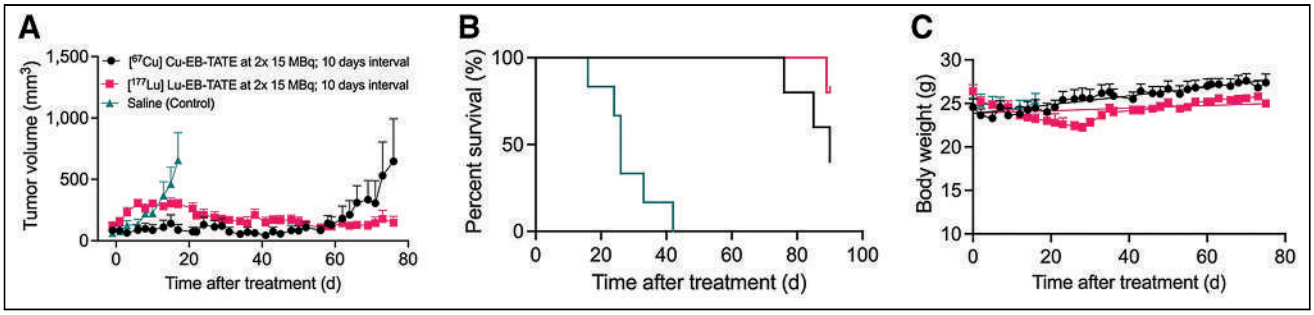

FIGURE 4. Efficacy of [^{67}Cu]Cu-EB-TATE against SSTR2-positive QGP1.SSTR2 xenograft. QGP1.SSTR2 tumor–bearing athymic BALB/c nude mice (5 or 6/group) were injected with 15 MBq of either [^{67}Cu]Cu-EB-TATE or [^{177}Lu]Lu-EB-TATE on days 0 and 10. Control mice were injected with vehicle (saline) on day 0. Tumors were measured 3 times per week and plotted against days after treatment (A). Percentage survival was also plotted (B), and body weight was monitored for entire duration of study (90 d) (C). Plots were discontinued when tumor volume of mouse in particular group reached 1,500 mm^3. Survival was defined as time to reach tumor volume ≥ 1,500 mm^3 or time of 90 d.

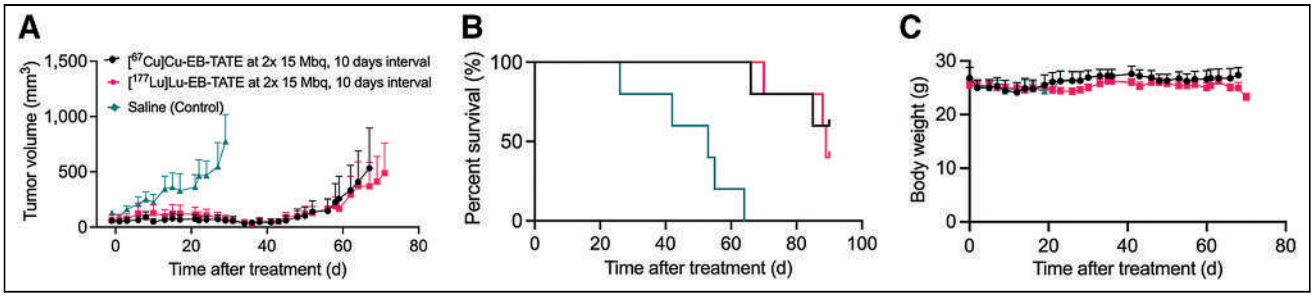

FIGURE 5. Efficacy of [^{67}Cu]Cu-EB-TATE against BON1.SSTR2 xenograft. BON1.SSTR2 tumor–bearing athymic BALB/c nude mice (n = 5/group) were injected with 15 MBq of either [^{67}Cu]Cu-EB-TATE or [^{177}Lu]Lu-EB-TATE on days 0 and 10. Control mice were injected with vehicle (saline) on day 0. Tumors were measured 3 times per week and plotted against days after treatment (A). Percentage survival was also plotted (B), and body weight was monitored for entire duration of study (90 d) (C). Plots were discontinued when tumor volume of mouse in particular group reached 1,500 mm^3. Survival was defined as time to reach tumor volume ≥ 1,500 mm^3 or time of 90 d.

we studied the pharmacokinetics and dosimetry of [^{67}Cu]Cu-EB-TATE in healthy BALB/c mice and confirmed that [^{67}Cu]Cu-EB-TATE had prolonged circulation (distribution $t_{1/2}$, 0.6 ± 0.1 h; clearance $t_{1/2}$, 33.5 ± 5.2 h) (Table 1). Blood distribution of [^{177}Lu]Lu-EB-TATE in human NET patients has been similarly reported, with prolonged clearance (distribution $t_{1/2}$, 9.47 h; clearance $t_{1/2}$, 236 h) (*21*). The projected human dose of [^{67}Cu]Cu-EB-TATE in the kidneys (unblocked) as obtained in this study (female, 0.60 mSv/MBq; male, 0.01 mSv/MBq) (Table 2) is less than the actual kidney dose in NET patients for [^{177}Lu]Lu-EB-TATE (1.15 mSv/MBq) but similar to [^{177}Lu]Lu-DOTATATE (0.36 mSv/MBq) (*21*). Interestingly, the projected human effective dose for [^{67}Cu]Cu-EB-TATE in male patients (0.066 mSv/MBq) is less than that in female patients (0.085 mSv/MBq) and that for [^{177}Lu]Lu-EB-TATE (0.080 mSv/MBq) but similar to that for [^{177}Lu]Lu-DOTATATE (0.069 mSv/MBq) (*21*). The reported kidney dose for [^{64}Cu]Cu-SarTATE has been similar (0.20 mSv/MBq), with an effective dose of 0.045 mSv/MBq (*22*).

The ex vivo biodistribution of [^{67}Cu]Cu-EB-TATE was studied in athymic nude mice bearing both QGP1.SSTR2 and BON1.SSTR2 xenografts. Prolonged accumulation was observed in tumors (Fig. 2A), peaking at 72 h after injection [QGP1.SSTR2, 8.2 ± 2.4%IA/g [P = 0.4206, not statistically significant]; BON1.SSTR2, 6.1 ± 3.7%IA/g [P = 0.0474]) from 1 h. Tian et al. earlier reported a similar tumor accumulation of ^{86}Y-EB-TATE at 48 h after injection (*8*) in a HCT116.SSTR2 xenograft model. Therefore, tumor uptake in this study was similar to what was observed with other radiometals. Confirmatively, acquired micro-SPECT/CT images of [^{67}Cu]Cu-EB-TATE (Fig. 3) showed specific binding and high retention in NET tumors, with clearance from healthy organs. Conversely, [^{177}Lu]Lu-DOTATATE tumor uptake peaked at 1 h because of fast blood clearance (*23*). This translates to a higher-activity injection of DOTATATE to attain dose levels similar to EB-TATE peptide.

QGP1.SSTR2 tumor–bearing mice and BON1.SSTR2 tumor–bearing mice were treated using [^{67}Cu]Cu-EB-TATE, [^{177}Lu]Lu-EB-TATE, or saline. [^{67}Cu]Cu-EB-TATE and [^{177}Lu]Lu-EB-TATE were both efficacious against the 2 tumor models. Interesting, [^{67}Cu]Cu-EB-TATE appeared (not statistically significantly) to be more efficacious at eliminating QGP1.SSTR2 tumors (complete remission in 2/5) than was [^{177}Lu]Lu-EB-TATE (complete remission in 1/5), though with a shorter average tumor growth delay (Figs. 4A and 5A). The 90-d median survival was prolonged, against saline control, for [^{67}Cu]Cu-EB-TATE–treated mice (QGP1.SSTR2, 90 d; BON1.SSTR2, not reached) (log-rank P < 0.0001) and [^{177}Lu]Lu-EB-TATE–treated mice (QGP1.SSTR2, not reached; BON1.SSTR2, 89 d) (Figs. 4B and 5B). This survival is better than that in a 100-d study whose median survival for [^{225}Ac]Ac-MACROPATATE (an octreotide derivative labeled with ^{225}Ac via an 18-membered macrocyclic chelator macropa) was 55 d, versus 26 d for saline control, in an H68 NET xenograft model. Similarly, [^{225}Ac]Ac-MACROPATATE was not as effective as [^{225}Ac]Ac-DOTATATE, with 80% (8/10) survival at 100 d (*24*). The efficacies and tolerance displayed by [^{67}Cu]Cu-EB-TATE and [^{177}Lu]Lu-EB-TATE were similar. Given its superior image quality, [^{67}Cu]Cu-EB-TATE can be used to estimate organ dosimetry and to treat and monitor treatment of SSTR2-positive tumors. In a PET/CT setting, [^{64}Cu]Cu-EB-TATE diagnostic PET images could be of added value given the inherent resolution of the modality. Given the recent increased availability of high-specific-activity [^{67}Cu]Cu and [^{64}Cu]Cu, these theranostics have tremendous potential for the management of NETs.

CONCLUSION

As rationalized, the therapeutic potential of [^{67}Cu]Cu-EB-TATE was similar to that of [^{177}Lu]Lu-EB-TATE. In addition, [^{67}Cu]Cu-EB-TATE exhibited excellent SPECT/CT imaging capabilities even at 96 h after injection, which would in theory allow for better sensitivity and tumor delineation, particularly for lesions in organs that have a high blood pool and cannot be delineated using ^{68}Ga tracers. It would also allow for increased accuracy in dosimetry estimation compared with situations in which other surrogate radionuclides are used. [^{67}Cu]Cu-EB-TATE therefore warrants clinical investigation as a theranostic.

DISCLOSURE

This work was realized with funding from the Sylvia Fedoruk Centre for Nuclear Innovation (grant J2018-0042). Koon Pak and Brian Gray are employees and shareholders of Molecular Targeting Technologies Inc., which has an exclusive license from the National Institutes of Health for EB-TATE. No other potential conflict of interest relevant to this article was reported.

ACKNOWLEDGMENTS

We appreciate Dr. Carsten Grötzinger for providing us with SSTR2-transfected QGP1.SSTR2 and BON1.SSTR2 cell lines. We thank Dr. Vijay Gaja of the Canadian Isotope Innovations Corp. for providing us with ^{67}Cu.

KEY POINTS

QUESTION: Is [^{67}Cu]Cu-EB-TATE an effective theranostic for the management of SSTR2-expressing NETs, and what possible edge does it present over [^{177}Lu]Lu-EB-TATE peptide receptor radionuclide therapy?

PERTINENT FINDINGS: In vivo tumor uptake and retention of [^{67}Cu]Cu-EB-TATE was excellent, giving it great dosimetry estimation and SPECT imaging capabilities. [^{67}Cu]Cu-EB-TATE was effective against SSTR2-positive neuroendocrine xenografts. Moreover, it appeared to be very effective in eliminating small-volume tumors.

IMPLICATIONS FOR PATIENT CARE: [^{67}Cu]Cu-EB-TATE has the potential for SPECT imaging, dosimetry, and treatment of NET tumors, particularly for the elimination of small-volume metastasis.

REFERENCES

1. Barakat MT, Meeran K, Bloom SR. Neuroendocrine tumours. *Endocr Relat Cancer.* 2004;11:1–18.
2. Patel P, Galoian K. Molecular challenges of neuroendocrine tumors. *Oncol Lett.* 2018;15:2715–2725.
3. Tsoli M, Chatzellis E, Koumarianou A, Kolomodi D, Kaltsas G. Current best practice in the management of neuroendocrine tumors. *Ther Adv Endocrinol Metab.* 2019;10:2042018818804698.
4. Hennrich U, Kopka K. Lutathera®: the first FDA- and EMA-approved radiopharmaceutical for peptide receptor radionuclide therapy. *Pharmaceuticals (Basel).* 2019;12:114.
5. Deppen SA, Liu E, Blume JD, et al. Safety and efficacy of ^{68}Ga-DOTATATE PET/CT for diagnosis, staging, and treatment management of neuroendocrine tumors. *J Nucl Med.* 2016;57:708–714.
6. Mou L, Martini P, Pupillo G, Cieszykowska I, Cutler CS, Mikolajczak R. ^{67}Cu production capabilities: a mini review. *Molecules.* 2022;27:1501.
7. Cullinane C, Jeffery CM, Roselt PD, et al. Peptide receptor radionuclide therapy with ^{67}Cu-CuSarTATE is highly efficacious against a somatostatin-positive neuroendocrine tumor model. *J Nucl Med.* 2020;61:1800–1805.
8. Tian R, Jacobson O, Niu G, et al. Evans blue attachment enhances somatostatin receptor subtype-2 imaging and radiotherapy. *Theranostics.* 2018;8:735–745.
9. Luley KB, Biedermann SB, Kunstner A, et al. A comprehensive molecular characterization of the pancreatic neuroendocrine tumor cell lines BON-1 and QGP-1. *Cancers (Basel).* 2020;12:691.
10. Vandamme T, Peeters M, Dogan F, et al. Whole-exome characterization of pancreatic neuroendocrine tumor cell lines BON-1 and QGP-1. *J Mol Endocrinol.* 2015;54:137–147.
11. Thakur S, Daley B, Millo C, et al. ^{177}Lu-DOTA-EB-TATE, a radiolabeled analogue of somatostatin receptor type 2, for the imaging and treatment of thyroid cancer. *Clin Cancer Res.* 2021;27:1399–1409.
12. Exner S, Prasad V, Wiedenmann B, Grotzinger C. Octreotide does not inhibit proliferation in five neuroendocrine tumor cell lines. *Front Endocrinol (Lausanne).* 2018;9:146.
13. Tamborino G, Perrot Y, De Saint-Hubert M, et al. Modeling early radiation DNA damage occurring during ^{177}Lu-DOTATATE radionuclide therapy. *J Nucl Med.* 2022;63:761–769.
14. Hartimath SV, Alizadeh E, Solomon VR, et al. Preclinical evaluation of ^{111}In-labeled PEGylated maytansine nimotuzumab drug conjugates in EGFR-positive cancer models. *J Nucl Med.* 2019;60:1103–1110.
15. Tikum AF, Nambisan AK, Ketchemen JP, et al. Simultaneous imaging and therapy using epitope-specific anti-epidermal growth factor receptor (EGFR) antibody conjugates. *Pharmaceutics.* 2022;14:1917.
16. Loft M, Carlsen EA, Johnbeck CB, et al. ^{64}Cu-DOTATATE PET in patients with neuroendocrine neoplasms: prospective, head-to-head comparison of imaging at 1 hour and 3 hours after injection. *J Nucl Med.* 2021;62:73–80.
17. Hao G, Mastren T, Silvers W, Hassan G, Oz OK, Sun X. Copper-67 radioimmunotheranostics for simultaneous immunotherapy and immuno-SPECT. *Sci Rep.* 2021;11:3622.
18. Parry JJ, Eiblmaier M, Andrews R, et al. Characterization of somatostatin receptor subtype 2 expression in stably transfected A-427 human cancer cells. *Mol Imaging.* 2007;6:56–67.
19. Guenter R, Aweda T, Carmona Matos DM, et al. Overexpression of somatostatin receptor type 2 in neuroendocrine tumors for improved Ga68-DOTATATE imaging and treatment. *Surgery.* 2020;167:189–196.
20. Jin XF, Auernhammer CJ, Ilhan H, et al. Combination of 5-fluorouracil with epigenetic modifiers induces radiosensitization, somatostatin receptor 2 expression, and radioligand binding in neuroendocrine tumor cells in vitro. *J Nucl Med.* 2019;60:1240–1246.
21. Zhang J, Wang H, Jacobson O, et al. Safety, pharmacokinetics, and dosimetry of a long-acting radiolabeled somatostatin analog ^{177}Lu-DOTA-EB-TATE in patients with advanced metastatic neuroendocrine tumors. *J Nucl Med.* 2018;59:1699–1705.
22. Hicks RJ, Jackson P, Kong G, et al. ^{64}Cu-SARTATE PET imaging of patients with neuroendocrine tumors demonstrates high tumor uptake and retention, potentially allowing prospective dosimetry for peptide receptor radionuclide therapy. *J Nucl Med.* 2019;60:777–785.
23. Liu F, Zhu H, Yu J, et al. ^{68}Ga/^{177}Lu-labeled DOTA-TATE shows similar imaging and biodistribution in neuroendocrine tumor model. *Tumour Biol.* 2017;39:1010428317705519.
24. King AP, Gutsche NT, Raju N, et al. ^{225}Ac-MACROPATATE: a novel alpha-particle peptide receptor radionuclide therapy for neuroendocrine tumors. *J Nucl Med.* 2023;64:549–554.

PSMA PET AUC Updates: Inclusion of rh-PSMA-7.3

Thomas A. Hope[1] and Hossein Jadvar[2]

[1]*Department of Radiology and Biomedical Imaging, University of California, San Francisco, San Francisco, California; and*
[2]*Department of Radiology, University of Southern California, Los Angeles, California*

With the approval of ^{18}F-rh-PSMA-7.3 (^{18}F-flotufolastat [Posluma; BlueEarth]), the appropriate use criteria for prostate-specific membrane antigen (PSMA) PET needs to be updated a second time (*1,2*). The approval for ^{18}F-rh-PSMA-7.3 was based on 2 prospective phase 3 clinical trials, the LIGHTHOUSE and SPOTLIGHT trials (*3,4*). The LIGHTHOUSE trial evaluated the sensitivity and specificity of ^{18}F-rh-PSMA-7.3 in men with unfavorable intermediate- to very high–risk prostate cancer and demonstrated a sensitivity ranging between 23% and 30% across the 3 readers and a specificity of 93%–97% (*4*). The sensitivity was slightly lower than that reported with ^{18}F-DCFPyL and ^{68}Ga-PSMA-11 (*5,6*), which might be explained by the higher percentage of men with unfavorable intermediate-risk prostate cancer in the LIGHTHOUSE trial. The SPOTLIGHT trial evaluated the verified detection rate (ranged from 51% to 54% across readers) and positive predictive value (ranged from 46% to 60%) in patients with biochemically recurrent prostate cancer (*3*). Given the differences in methodology, it is difficult to compare these rates with the comparable trials performed with ^{18}F-DCFPyL and ^{68}Ga-PSMA-11, in which correct localization rate and positive predictive value were used, respectively (*7,8*). Overall, all 3 agents should be considered equivalent for the staging of disease initially and at the time of biochemical recurrence.

The third main indication for PSMA PET is the selection of patients for PSMA radioligand therapy. In the most recent update to the PSMA appropriate use criteria document, ^{18}F-DCFPyL and ^{68}Ga-PSMA-11 were considered equivalent for the selection of patients with PSMA radioligand therapy (*2*). There are no data evaluating the role of ^{18}F-rh-PSMA-7.3 for selecting patients for PSMA radioligand therapy, although admittedly the same is true for ^{18}F-DCFPyL. The appropriate use committee agreed that ^{18}F-rh-PSMA-7.3 can also be used to select patients for PSMA radioligand therapy. Because of the higher physiologic uptake in the liver, patients who meet the VISION criteria using rh-PSMA-7.3 are candidates for treatment. Currently, there are limited data on the biodistribution of ^{18}F-rh-PSMA-7.3 and how that compares with ^{18}F-DCFPyL and ^{68}Ga-PSMA-11, and therefore it is unclear what the lower limit of uptake with ^{18}F-rh-PSMA-7.3 should be for patient selection, and it is possible that there are a small minority of patients who would meet criteria for treatment with ^{68}Ga-PSMA-11 and ^{18}F-DCFPyL but would not meet criteria for ^{18}F-rh-PSMA-7.3.

The approval of ^{18}F-rh-PSMA-7.3 provides another PSMA-targeted radiopharmaceutical that will help increase patient access to PSMA PET imaging. Overall, ^{18}F-rh-PSMA-7.3 should be considered equivalent to ^{68}Ga-PSMA-11 and ^{18}F-DCFPyL, with the caveat that the higher uptake in the liver with ^{18}F-rh-PSMA-7.3 may impact the selection of a small number of patients for PSMA radioligand therapy compared with patients screened using the other 2 agents.

DISCLOSURE

Thomas Hope has grant funding to the institution from Clovis Oncology, GE Healthcare, Lantheus, Janssen, Novartis, the Prostate Cancer Foundation, Telix Pharmaceuticals, and the National Cancer Institute (R01CA235741 and R01CA212148). He received personal fees from Bayer, Cardinal Health, BlueEarth Diagnostics, and Lantheus and received fees from and has an equity interest in RayzeBio and Curium. No other potential conflict of interest relevant to this article was reported.

REFERENCES

1. Jadvar H, Calais J, Fanti S, et al. Appropriate use criteria for prostate-specific membrane antigen PET imaging. *J Nucl Med.* 2022;63:59–68.
2. Hope TA, Jadvar H. Updates to appropriate use criteria for PSMA PET. *J Nucl Med.* 2022;63(5):14N.
3. Jani AB, Ravizzini GC, Gartrell BA, et al. Diagnostic performance and safety of ^{18}F-rhPSMA-7.3 positron emission tomography in men with suspected prostate cancer recurrence: results from a phase 3, prospective, multicenter study (SPOTLIGHT). *J Urol.* 2023;210:299–311.
4. Surasi DS, Eiber M, Maurer T, et al. Diagnostic performance and safety of positron emission tomography with ^{18}F-rhPSMA-7.3 in patients with newly diagnosed unfavourable intermediate- to very-high-risk prostate cancer: results from a phase 3, prospective, multicentre study (LIGHTHOUSE). *Eur Urol.* 2023;84:361–370.
5. Hope TA, Eiber M, Armstrong WR, et al. Diagnostic accuracy of ^{68}Ga-PSMA-11 PET for pelvic nodal metastasis detection prior to radical prostatectomy and pelvic lymph node dissection: a multicenter prospective phase 3 imaging trial. *JAMA Oncol.* 2021;7:1635–1642.
6. Pienta KJ, Gorin MA, Rowe SP, et al. A phase 2/3 prospective multicenter study of the diagnostic accuracy of prostate specific membrane antigen PET/CT with ^{18}F-DCFPyL in prostate cancer patients (OSPREY). *J Urol.* 2021;206:52–61.
7. Fendler WP, Calais J, Eiber M, et al. Assessment of ^{68}Ga-PSMA-11 PET accuracy in localizing recurrent prostate cancer: a prospective single-arm clinical trial. *JAMA Oncol.* 2019;5:856–863.
8. Morris MJ, Rowe SP, Gorin MA, et al. Diagnostic performance of ^{18}F-DCFPyL-PET/CT in men with biochemically recurrent prostate cancer: results from the CONDOR phase III, multicenter Study. *Clin Cancer Res.* 2021;27:3674–3682.

Received Nov. 9, 2023; accepted Nov. 9, 2023.
For correspondence or reprints, contact Thomas A. Hope (thomas.hope@ucsf.edu).
Published online Jan. 4, 2024.

DOI: 10.2967/jnumed.123.267042

The Impact of Baseline PSMA PET/CT Versus CT on Outcomes of ^{223}Ra Therapy in Metastatic Castration-Resistant Prostate Cancer Patients

Dianne Bosch*[1], Kim J.M. van der Velden*[1], Irma M. Oving[2], Dirk N.J. Wyndaele[3], Leo E. Weijs[4], W. Dick van Schelven[5], Wim J.G. Oyen[6–8], Erik T. te Beek[9], Addy C.M. van de Luijtgaarden[10], Diederik M. Somford[11], James Nagarajah[12], Rick Hermsen[13], Niven Mehra[14], Winald R. Gerritsen[14], Maarten J. van der Doelen[1], and Inge M. van Oort[1]

[1]Department of Urology, Radboud University Medical Center, Nijmegen, The Netherlands; [2]Department of Medical Oncology, Ziekenhuisgroep Twente, Almelo, The Netherlands; [3]Department of Nuclear Medicine, Catharina Hospital, Eindhoven, The Netherlands; [4]Department of Radiology and Nuclear Medicine, Ziekenhuisgroep Twente, Almelo, Netherlands; [5]Department of Nuclear Medicine, Medical Center Leeuwarden, Leeuwarden, The Netherlands; [6]Department of Radiology and Nuclear Medicine, Rijnstate Hospital, Arnhem, The Netherlands; [7]Department of Biomedical Sciences, Humanitas University, Milan, Italy; [8]Department of Nuclear Medicine, Humanitas Clinical and Research Center, Milan, Italy; [9]Department of Nuclear Medicine, Reinier de Graaf Gasthuis, Delft, The Netherlands; [10]Department of Medical Oncology, Reinier de G raaf Gasthuis and Reinier Haga Prostate Cancer Center, Delft, The Netherlands; [11]Department of Urology, Canisius-Wilhelmina Hospital, Nijmegen, The Netherlands; [12]Department of Radiology and Nuclear Medicine, Radboud University Medical Center, Nijmegen, The Netherlands; [13]Department of Nuclear Medicine, Canisius-Wilhelmina Hospital, Nijmegen, The Netherlands; and [14]Department of Medical Oncology, Radboud University Medical Center, Nijmegen, The Netherlands

Imaging before ^{223}Ra-dichloride (^{223}Ra) therapy is crucial for selecting metastatic castration-resistant prostate cancer (mCRPC) patients with bone-only disease. The purpose of this study was to evaluate if baseline prostate-specific membrane antigen (PSMA) PET/CT (bPSMA) versus CT is associated with outcomes of ^{223}Ra therapy. **Methods:** A secondary analysis of the data of a prospective observational study (NCT04995614) was performed. Patients received a maximum of 6 ^{223}Ra cycles and were retrospectively divided into the bPSMA or baseline CT (bCT) groups. All patients received baseline bone scintigraphy. Primary endpoints were alkaline phosphatase and prostate-specific antigen response. Secondary endpoints were overall survival (OS) and radiologic response. **Results:** Between 2017 and 2020, 122 mCRPC patients were included: 18 (14.8%) in the bPSMA group and 104 (85.2%) in the bCT group. All baseline characteristics were comparable. No significant differences in alkaline phosphatase or prostate-specific antigen response were found. The bCT group showed an OS significantly shorter than that of the bPSMA group (12.4 vs. 19.9 mo, $P = 0.038$). In 31 of 76 patients (40.1%) in the bCT group who also received posttherapy CT, lymph node or visceral metastases (soft-tissue involvement [STI]) were detected after ^{223}Ra therapy, compared with 0 of 15 patients in the bPSMA group who received posttherapy PSMA PET/CT or CT. No significant difference in OS was found between patients in the bCT or posttherapy CT subgroup without STI (46/76) and the bPSMA group. **Conclusion:** bPSMA versus CT does not seem to impact biochemical response during ^{223}Ra therapy in mCRPC patients. Nevertheless, patients in the bCT group had a significantly shorter OS, most likely due to underdetection of STI in this group. Therefore, replacing bCT with PSMA PET/CT appears to be a valuable screening method for identifying patients who will benefit most from ^{223}Ra therapy.

Key Words: ^{223}Ra; computer tomography; castration-resistant prostate cancer; overall survival; PSMA PET/CT

J Nucl Med 2024; 65:541–547
DOI: 10.2967/jnumed.123.266654

Metastatic castration-resistant prostate cancer (mCRPC) is characterized as prostate cancer progression despite adequate androgen-deprivation therapy (*1*). Bone metastases are prevalent in over 90% of end-stage mCRPC (*2,3*) and a leading factor in skeleton-related events (SREs), morbidity, and mortality (*4,5*). Symptomatic bone metastases can be treated with ^{223}Ra-dichloride (^{223}Ra), a radionuclide that actively incorporates into metastatic lesions, where it emits α-particles that induce tumor cell death (*6,7*). The phase 3 ALSYMPCA trial demonstrated that treatment with ^{223}Ra compared with placebo significantly prolonged overall survival (OS), led to a more frequent decline in alkaline phosphatase (ALP), enhanced quality of life, and presented fewer SREs (*8–11*). ^{223}Ra therapy should be withheld in patients with extensive malignant lymphadenopathy or visceral metastases (*12,13*), of which the latter is observed in up to 32% of mCRPC patients (*3*). Therefore, baseline imaging plays a crucial role in assessing eligibility for ^{223}Ra therapy and currently consists of either baseline CT (bCT) or prostate-specific membrane antigen (PSMA) PET/CT, in addition to bone scintigraphy (*12,14*). PSMA PET/CT has a higher diagnostic sensitivity and specificity for detecting pelvic nodal or distant metastases than CT (*15–17*) and has been shown to be able to detect previously unknown visceral metastases in a small cohort of mCRPC patients who underwent screening for ^{223}Ra therapy (*18*). To our knowledge, there is only one retrospective study available evaluating the impact

Received Sep. 10, 2023; revision accepted Jan. 5, 2024.
For correspondence or reprints, contact Maarten J. van der Doelen (maarten.vanderdoelen@radboudumc.nl).
*Contributed equally to this work.
Published online Feb. 29, 2024.

of baseline PSMA PET/CT (bPSMA) compared with CT on outcomes of ^{223}Ra therapy, and this study suggested that staging with PSMA PET/CT results in better therapeutic responses with greater declines in ALP and prostate-specific antigen (PSA) because of better patient selection (*19*). On the basis of the hypothesis that the higher diagnostic accuracy of PSMA PET/CT will lead to better patient selection and therefore outcomes of the proposed treatment, we studied the impact of bPSMA versus CT on outcomes of ^{223}Ra therapy in mCRPC patients.

MATERIALS AND METHODS

Study Design and Patient Population

We performed a secondary analysis of a prospective observational multicenter cohort study that evaluated mCRPC patients treated with ^{223}Ra at 11 institutions throughout The Netherlands between April 2017 and July 2020 (NCT04995614) (*20*). Eligible patients had histologically proven mCRPC with symptomatic bone metastases and no visceral metastases. The study protocol was approved by the medical ethics committee (CMO 2017-3220) and the institutional review boards of all participating centers. Informed consent was obtained from all individual patients.

Study Procedures and Follow-up

Patients were treated with ^{223}Ra according to the standard of care at a dose of 55 kBq/kg of body weight injected intravenously every 4 wk, with a maximum of 6 injections. Every patient received a baseline bone scintigraphy to determine the extent and localization of bone metastases. Additionally, every patient received a contrast-enhanced high-dose CT of the thorax and abdomen or a low-dose ^{68}Ga-PSMA-11 or ^{18}F-PSMA-1007 PET/CT from the top of the skull down to the mid thigh to detect soft-tissue involvement (STI), defined as lymph or visceral node metastases. The choice for baseline imaging modality was made according to local standard clinical care in the respective hospitals. Baseline imaging was performed no more than 12 wk before the start of therapy. At least 1 wk before every ^{223}Ra injection, laboratory evaluation was performed. Laboratory evaluation and posttherapy imaging (bone scintigraphy combined with either CT or PSMA PET/CT) were performed 4–8 wk after the last injection. All patients were followed until death or March 3, 2023.

Subgroup Categorization

Patients were retrospectively allocated to the bPSMA or bCT group on the basis of imaging modality before ^{223}Ra therapy. Additionally, patients were retrospectively allocated to the posttherapy PSMA PET/CT (pPSMA) or posttherapy CT (pCT) subgroups.

Study Outcomes

The primary endpoint was biochemical response, defined as at least a 30% decline in ALP or PSA level from baseline during ^{223}Ra therapy, as described in the ALSYMPCA trial (*9*). Any decline in PSA level from baseline during treatment was determined. ALP and PSA superresponders were defined as patients with at least a 50% decline from baseline during treatment.

Secondary endpoints were the best percentage change in ALP or PSA response from baseline during treatment, radiologic response, occurrence of SREs, and OS. Radiologic response after ^{223}Ra therapy was evaluated by monitoring the presence of newly detected STI. Only patients who received identical baseline and posttherapy imaging techniques were eligible for radiologic response evaluation. RECIST version 1.1, the Prostate Cancer Working Group 3 criteria, and the PSMA PET progression criteria were used (*21–23*). SREs were defined as surgery or radiotherapy to the bone, spinal cord compression, and symptomatic pathologic fractures (*22*). OS was defined as the time from the start of ^{223}Ra therapy to the date of death from any cause or the date of the last follow-up.

Data Analysis

Statistical analysis was performed for the total cohort and the subgroups. Subgroups were compared using χ^2 and Mann–Whitney U tests for categoric and continuous variables, respectively. OS was analyzed for subgroups using Kaplan–Meier curves and the log-rank test. A 2-sided P value of less than 0.05 was considered statistically significant. Statistical analyses were performed using SPSS 27.0 (IBM Corp.), and figures were created using GraphPad Prism 9.0 (GraphPad Software Inc.).

RESULTS

Patient Characteristics

Of the 122 included patients, 18 patients (14.8%) underwent bPSMA and 104 patients (85.2%) underwent bCT imaging (Table 1). All patients received a baseline bone scintigraphy. Seventy-seven patients (63.1%) completed the full course of 6 ^{223}Ra cycles. No significant differences in any of the baseline characteristics were found between the 2 groups.

Biochemical Response

No significant differences in biochemical responses were found between the bPSMA and bCT groups (Table 2). ALP responses were found in 55.6% of bPSMA patients versus 62.5% of bCT patients ($P = 0.576$). More ALP superresponders were found in the bPSMA group than in the bCT group (50.0% vs. 28.8%, respectively; $P = 0.076$). In the bPSMA group, more patients had some PSA response than in the bCT group (44.4% vs. 29.8%, respectively; $P = 0.219$).

Radiologic Response

Eleven of 18 bPSMA patients (61.1%) also received a pPSMA (bPSMA/pPSMA subgroup) (Fig. 1). Seventy-six of 104 bCT patients (73.1%) also received a pCT (bCT/pCT subgroup). Patients switched from bPSMA to pCT in 4 of 18 cases (22.2%) and from bCT to pPSMA in 7 of 104 cases (6.7%).

No significant differences were found in any of the baseline characteristics between the bPSMA/pPSMA and bCT/pCT subgroups (Supplemental Table 1; supplemental materials are available at http://jnm.snmjournals.org). None of the 15 bPSMA patients who received posttherapy imaging were found to have newly detected STI. In 31 of 76 (40.1%) bCT/pCT patients, STI was newly detected after therapy (Table 3), with visceral metastases being detected in 16 patients (51.6%) and lymph node metastases in 20 patients (64.5%). In retrospect, small visceral metastases were already visible on bCT imaging in 2 patients. Among the bCT/pPSMA patients, newly detected STI was found in 6 of 7 patients (85.7%), with visceral metastases being detected in 4 patients (66.7%) and lymph node metastases in 6 patients (100%).

SREs

SREs occurred during and after ^{223}Ra therapy in 6 of 18 (36.4%) and 30 of 104 (28.8%) patients of the bPSMA and bCT groups, respectively ($P = 0.700$). External-beam radiotherapy to relieve skeletal symptoms was the most common SRE (61.5%) (Supplemental Table 2).

OS

Median OS for the total cohort was 12.8 mo (95% CI, 3.3–46.4 mo). Patients in the bPSMA group had a significantly longer median OS of 19.9 mo (95% CI, 3.1 mo to not reached) than

TABLE 1
Baseline Patient Demographics and Clinical Characteristics

Parameter	Total cohort (n = 122)	bPSMA group (n = 18)	bCT group (n = 104)	P
Age (y)	73.1 (65.2–78.3)	70.8 (63.7–76.2)	73.2 (65.7–78.6)	0.392
Gleason score ≥ 8	80 (65.6)	12 (66.7)	68 (65.4)	0.957
Gleason score missing	1 (0.8)	0 (0)	1 (1.0)	
ECOG performance score				
ECOG 0	51 (41.8)	8 (44.4)	43 (41.3)	0.161
ECOG 1	53 (43.4)	5 (27.8)	48 (46.2)	
ECOG 2 and 3	18 (14.8)	5 (27.8)	13 (12.5)	
Prior SRE	55 (45.1)	11 (61.1)	44 (42.3)	0.139
Prior life-prolonging drugs				
Enzalutamide or abiraterone	97 (79.5)	15 (83.3)	82 (78.8)	0.663
Docetaxel	74 (60.7)	6 (33.3)	40 (38.50	0.679
Cabazitaxel	18 (14.8)	11 (61.1)	63 (60.6)	0.966
^{177}Lu-PSMA radioligand therapy	1 (0.8)	0 (0)	1 (1.0)	0.676
None	12 (9.8)	2 (11.1)	10 (9.6)	0.844
Time mCRPC to ^{223}Ra (mo)	21.4 (10.4–41.6)	20.2 (7.4–46.2)	21.8 (10.5–41.6)	0.724
Time since start last treatment to ^{223}Ra (mo)	10.5 (6.9–16.0)	11.5 (5.6–16.7)	10.4 (6.9–15.9)	0.910
Time since start last treatment to ^{223}Ra missing (mo)	20 (16.4)	3 (16.7)	17 (16.3)	
Time baseline imaging to ^{223}Ra (mo)	0.89 (0.66–1.58)	1.02 (0.74–1.77)	0.84 (0.67–1.57)	0.154
Hemoglobin (mmol/L)	7.8 (7.3–8.3)	7.9 (7.4–8.3)	7.8 (7.3–8.3)	0.908
Lactate dehydrogenase (U/L)	233.5 (204.0–280.0)	222.5 (202.8–259.8)	236.0 (206.0–287.3)	0.494
ALP (U/L)	142 (102.0–233.5)	136.0 (91.0–179.3)	143.5 (102.8–241.8)	0.495
PSA (ng/mL)	87.9 (29.4–256.3)	99.5 (31.8–206.3)	85.4 (27.4–257.5)	0.718
Lymph node metastases (≥15 mm)	17 (13.9)	3 (16.7)	14 (13.5)	0.717
Extent of bone metastases				
Low volume (<6 metastases)	15 (12.3)	4 (22.2)	11 (10.6)	0.655
Intermediate volume (6–20 metastases)	33 (27.0)	2 (11.1)	31 (29.8)	
High volume (>20 metastases)	62 (50.8)	12 (66.7)	50 (48.1)	
Superscan	12 (9.8)	0 (0)	12 (11.5)	
No. administered ^{223}Ra injections				
1 − 3	22 (18.0)	2 (11.1)	20 (19.2)	0.694
4 and 5	23 (18.9)	4 (22.2)	19 (18.3)	
6	77 (63.1)	12 (66.7)	65 (62.5)	
Cause of discontinuation*				
End of therapy	77 (63.1)	12 (66.7)	65 (62.5)	0.649
Progression of disease	28 (23.0)	3 (16.7)	25 (24.0)	
Myelotoxicity	10 (8.2)	2 (11.1)	5 (4.8)	
Other	7 (5.7)	1 (5.6)	9 (8.7)	
Death	0 (0)	0 (0)	0 (0)	
Opioid use	55 (45.1)	7 (38.9)	48 (46.2)	0.567
Bone health agent use	82 (67.2)	11 (61.1)	71 (68.3)	0.550
Denosumab†	57/82 (69.5)	7/11 (63.6)	50/71 (70.4)	
Bisphosphonates†	25/82 (30.5)	4/11 (36.4)	21/71 (29.6)	

*Data summarized according to most important reason for discontinuation, with progression of disease being most important followed by myelotoxicity. Other causes of discontinuation included pain, SRE, adverse events, and patient wish.

†Data are number and valid percentage. Valid percentage is calculated percentage in case of subgroup analyses.

ECOG = Eastern Cooperative Oncology Group.

Qualitative data are number and percentage. Continuous data are median and interquartile ranges.

TABLE 2
Biochemical Response During ^{223}Ra Therapy for Total Cohort and bPSMA and bCT Groups

Parameter	Total cohort (n = 122)	bPSMA group (n = 18)	bCT group (n = 104)	P
ALP				
Best response* (%)	−36.4 (−53.5 to −19.1)	−47.9 (−56.4 to −0.8)	−35.8 (−53.1 to −23.7)	0.963
Response*, decline ≥ 30%	75 (61.5)	10 (55.6)	65 (62.5)	0.576
Superresponse*, decline ≥ 50%	39 (32.0)	9 (50.0)	30 (28.8)	0.076
PSA				
Best response* (%)	19.8 (−10.5 to 69.7)	1.1 (−15.3 to 52.6)	21.5 (−6.1 to 73.6)	0.486
Any response*, any decline	39 (32.0)	8 (44.4)	31 (29.8)	0.219
Response*, decline ≥ 30%	18 (14.8)	2 (11.1)	16 (15.4)	0.637
Superresponse*, decline ≥ 50%	10 (8.2)	0 (0)	10 (9.6)	0.170

*ALP and PSA responses are compared with baseline. Negative value indicates decline in ALP or PSA values during or after ^{223}Ra therapy.

Qualitative data are number and percentage. Continuous data are median and interquartile ranges in IU/L for ALP and ng/mL for PSA.

did those in the bCT group (12.4 mo, 95% CI, 3.3–37.2 mo; P = 0.038) (Fig 2A).

In an exploratory analysis, OS was compared for patients in the bCT/pCT subgroup with and without newly detected STI after therapy. The patients in the bCT/pCT subgroup with newly detected STI had a significantly shorter OS than that in those without newly detected STI (median OS, 10.6 vs. 14.9 mo, respectively; $P < 0.01$) (Table 3; Fig. 2B). No significant OS difference was found between the bCT/pCT subgroup without newly detected metastases and the overall bPSMA group (P = 0.456).

DISCUSSION

In this prospective cohort study, we investigated the impact of bPSMA versus bCT on the outcomes of ^{223}Ra therapy in mCRPC patients. Patients who received bCT had a significantly shorter OS than those who underwent bPSMA. We did not observe significant differences in biochemical response rates.

Our study found ALP and PSA responses similar to those in the ALSYMPCA trial and previous retrospective studies on ^{223}Ra therapy in mCRPC patients (*8,24–26*). To date, only Ahmadzadehfar et al. reported outcomes on biochemical response during ^{223}Ra therapy based on different baseline imaging modalities (*26*). In this study, both ALP and PSA response rates were significantly higher when using bPSMA than when using bCT. Although we did not observe significant differences, the bPSMA group showed more ALP superresponders and PSA responses (any decline) than did the bCT group.

Overall, the OS of 12.8 mo found in our study is in line with other real-world studies evaluating ^{223}Ra therapy (*20,27*). We found a remarkably longer median OS for patients in the bPSMA

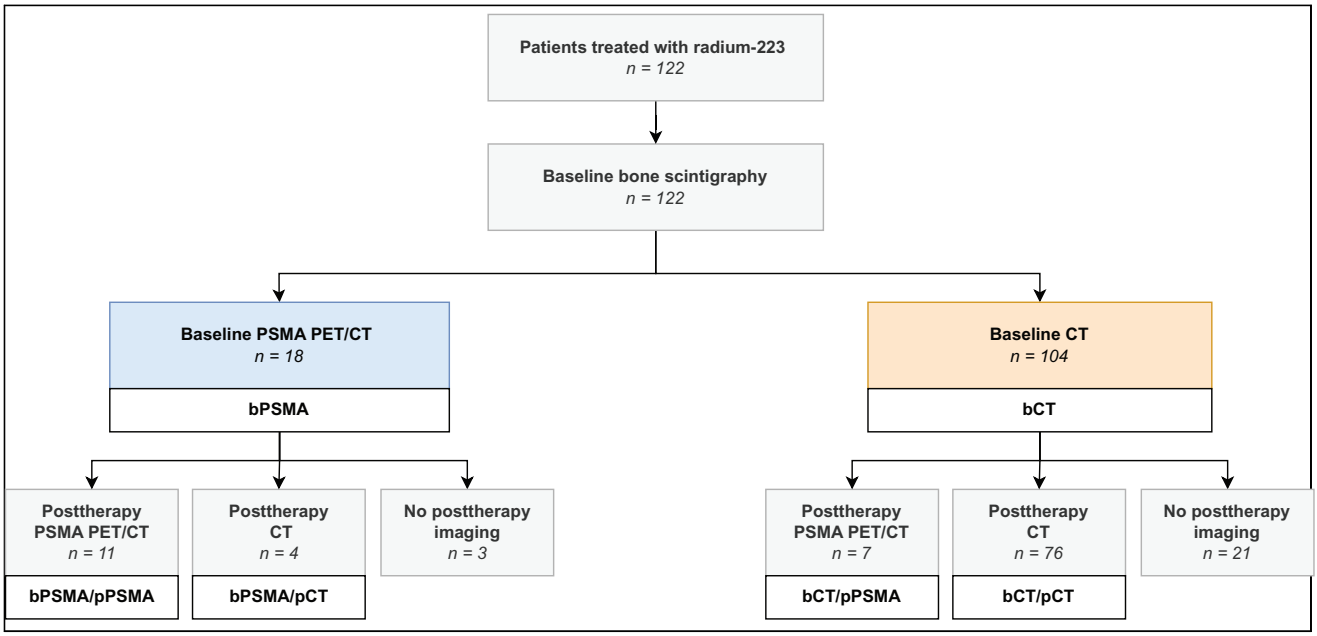

FIGURE 1. CONSORT (Consolidated Standards of Reporting Trials) diagram. Stratification of study population was based on baseline and posttherapy imaging methods used for radiologic response evaluation.

TABLE 3
OS Among Subgroups

Baseline imaging	Posttherapy imaging	*n*	OS (mo)	*P*
bPSMA	Total	18	19.9 (12.7–29.0)	0.038 vs. bCT
	pPSMA	11/18		
	STI	0/11		
	No STI	11/11	21.2 (6.7–NR)	
	pCT	4/18		
	STI	0/4		
	No STI	4/4	20.3 (13.8–NR)	
	No imaging	3/18	4.9 (3.1–NR)	
bCT	Total	104	12.4 (7.9–18.2)	0.038 vs. bPSMA
	pPSMA	7/104	16.0 (12.4–23.2)	
	STI	6/7	14.6 (8.9–NR)	
	No STI	1/7	21.5 (NR)	
	pCT	76/104	12.7 (8.4–20.4)	
	STI	31/76	10.6 (2.9–35.0)	<0.01 vs. bCT/pCT no STI
	No STI	45/76	14.9 (5.9–54.8)	0.456 vs. bPSMA
	No imaging	21/104	9.2 (1.6–45.7)	

NR = not reached.
OS data are median and 95% CI.

group than for patients in the bCT group (19.9 vs. 12.4 mo, respectively), whereas all baseline characteristics were comparable. The most probable explanation for this finding is the absence of newly detected STI in any of the 15 patients in the bPSMA/pPSMA and bPSMA/pCT subgroups, whereas STI was frequently detected after therapy in the bCT/pCT and bCT/pPSMA subgroups (40.1% and 85.7%, respectively). Our exploratory analysis confirmed a significant difference in OS between bCT/pCT patients with and without newly detected STI after therapy. Conversely, the OS of patients in the bCT/pCT subgroup without newly detected STI did not significantly differ from the OS of the bPSMA group. These findings are supported by data in the literature that suggest mCRPC patients with visceral metastases have a significantly shorter OS than patients without visceral metastases (*28,29*).

It seems unlikely that the newly detected STI after treatment in the bCT group was not already present at the start of ^{223}Ra therapy, since development of visceral disease takes approximately 1.6 y from CRPC diagnosis (*3*). In retrospect, the posttherapy-detected STI was already visible at the bCT in 2 patients. We encountered a lower proportion of patients with a PSA decline in the bCT group than in the bPSMA group, possibly due to the presence of STI (*3*). The presumed underdetection of STI at the start of ^{223}Ra therapy in the bCT group might have caused the treatment to be less effective. However, as there was no control group, our results may still be explained by the natural history of the disease and unrelated to ^{223}Ra therapy itself.

Our study has several limitations that should be considered when interpreting the results. The retrospective allocation of patients into the bPSMA and bCT groups might have led to selection bias. However, the groups did not significantly differ in any of the baseline characteristics, and the baseline imaging modality choice was made according to local standards of care in the respective hospitals. To the best of our knowledge, patient characteristics did not influence the imaging modality of choice. In addition, none of the patients received both imaging modalities at baseline. Furthermore, the small sample size of the subgroups may have contributed to the lack of statistical significance in biochemical response analyses. Because of these limitations, conclusions should be drawn with caution.

Our study fills a gap of knowledge as little research has been done on the impact of using PSMA PET/CT instead of CT when selecting mCRPC patients for ^{223}Ra therapy. To our knowledge, our population is the largest cohort of patients addressing this research question. It is probable that the OS benefit associated with PSMA PET/CT as a therapeutic eligibility assessment modality can be extrapolated to other therapies for metastatic prostate cancer. Patients who might benefit less from ^{223}Ra monotherapy because of the presence of STI may be redirected to other treatments, such as the combination of docetaxel plus ^{223}Ra therapy (DORA trial, NCT03574571). Additionally, the outcomes of this study raise the question whether existing evidence-based guidelines are still valid for current daily practice, as PSMA PET/CT appears to become a potential replacement of CT in the management of mCRPC. For instance, a recently published article on the use of ^{68}Ga-PSMA PET/CT for response evaluation of ^{223}Ra therapy demonstrated that total tumor volume within the bone at baseline ^{68}Ga-PSMA PET/CT was associated with treatment response and development of extraosseous disease during treatment (*30*). This emphasizes the need for prospective randomized clinical trials, preferably incorporating masking of the practitioner, to assess the impact of PSMA PET/CT compared with CT on therapeutic choices and outcomes (*31*).

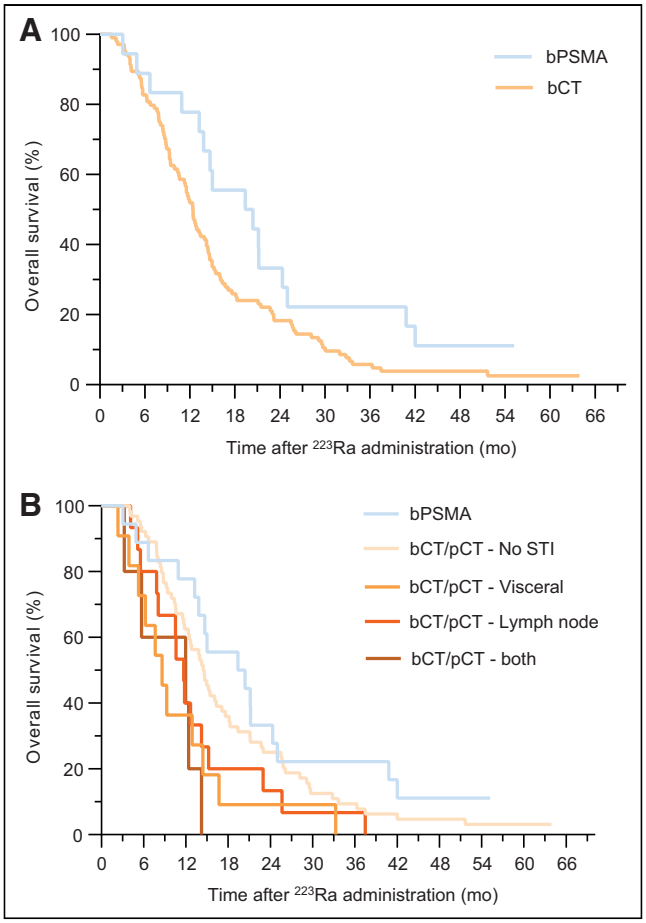

FIGURE 2. OS among subgroups: OS of bPSMA and bCT groups (A) and OS of bPSMA and bCT/pCT subgroups (B). Latter are divided into further subgroups: without STI, with lymph node metastases, with visceral metastases, and with both lymph node and visceral metastases.

CONCLUSION

bPSMA does not appear to be a strong predictor of biochemical response during ^{223}Ra therapy when compared with CT. However, patients who underwent bCT had a significantly shorter OS, most likely due to underdetection of STI before the start of ^{223}Ra therapy. Therefore, replacing bCT with bPSMA appears to be a valuable screening method to identify the patients who will benefit most from ^{223}Ra therapy.

DISCLOSURE

This work was supported by Bayer Healthcare The Netherlands. The funding organization had no role in the design or conduct of the study; collection, management, analysis, or interpretation of the data; or preparation, review, or approval of the article. Dianne Bosch received speaker honoraria from MSD. Wim Oyen received consultancy and speaker fees from Bayer and AAA Novartis. Addy van der Luijtgaarden is a member of the advisory board of the Dutch prostate cancer foundation, received speaker and advisory honoraria from Janssen Pharmaceuticals, and received financial support for an educational program from Astellas. Diederik Somford is a member of the advisory boards of Janssen Pharmaceuticals, Astellas, and Bayer and received research grants from Astellas outside the submitted work. Rick Hermsen was a member of the advisory board of Bayer, received personal fees and travel expenses from Bayer outside the submitted work, and received personal fees from ABX and Blue Earth Diagnostics for image review. Niven Mehra received personal fees from Bayer outside the submitted work, Sanofi, and MSD; received research grants from BMS; and received research grants and personal fees from Pfizer outside the submitted work, AstraZeneca, Astellas, Janssen Pharmaceuticals, MSD, and Roche. Winald Gerritsen is a member of the advisory boards for Bristol-Myers Squibb, Astellas, Janssen Pharmaceuticals, Bayer, Sanofi Genzyme, Amgen, Morphosys, and CureVac; received speaker fees from Bayer and MSD; and received research funding from Astellas, Bayer, and Janssen Pharmaceuticals. Maarten van der Doelen received research grants from Bayer and Janssen Pharmaceuticals and received speaker fees from Astellas. Irma Oving is a member of the advisory boards for MSD, Pfizer, and AstraZeneca and received research grants and personal fees from Astellas, Bayer, Janssen Pharmaceuticals, MSD/AstraZeneca, and Pfizer. No other potential conflict of interest relevant to this article was reported.

KEY POINTS

QUESTION: How does using PSMA PET/CT instead of CT to select patients for ^{223}Ra therapy impact the outcome?

PERTINENT FINDINGS: In this prospective cohort study, we found a significantly longer median OS for patients who received bPSMA compared than for those who received bCT, most likely due to underdetection of STI at the start of ^{223}Ra therapy.

IMPLICATIONS FOR PATIENT CARE: PSMA PET/CT appears to be a valuable screening method to identify the patients who will benefit most from ^{223}Ra therapy.

REFERENCES

1. Sartor O, de Bono JS. Metastatic prostate cancer. *N Engl J Med.* 2018;378:645–657.
2. Bubendorf L, Schöpfer A, Wagner U, et al. Metastatic patterns of prostate cancer: an autopsy study of 1,589 patients. *Hum Pathol.* 2000;31:578–583.
3. Pezaro C, Omlin A, Lorente D, et al. Visceral disease in castration-resistant prostate cancer. *Eur Urol.* 2014;65:270–273.
4. Coleman RE. Metastatic bone disease: clinical features, pathophysiology and treatment strategies. *Cancer Treat Rev.* 2001;27:165–176.
5. Saad F, Lipton A, Cook R, Chen YM, Smith M, Coleman R. Pathologic fractures correlate with reduced survival in patients with malignant bone disease. *Cancer.* 2007;110:1860–1867.
6. Henriksen G, Breistøl K, Bruland ØS, Fodstad Ø, Larsen RH. Significant antitumor effect from bone-seeking, alpha-particle-emitting ^{223}Ra demonstrated in an experimental skeletal metastases model. *Cancer Res.* 2002;62:3120–3125.
7. Suominen MI, Fagerlund KM, Rissanen JP, et al. Radium-223 inhibits osseous prostate cancer growth by dual targeting of cancer cells and bone microenvironment in mouse models. *Clin Cancer Res.* 2017;23:4335–4346.
8. Sartor O, Coleman RE, Nilsson S, et al. An exploratory analysis of alkaline phosphatase, lactate dehydrogenase, and prostate-specific antigen dynamics in the phase 3 ALSYMPCA trial with radium-223. *Ann Oncol.* 2017;28:1090–1097.
9. Parker C, Nilsson S, Heinrich D, et al. Alpha emitter radium-223 and survival in metastatic prostate cancer. *N Engl J Med.* 2013;369:213–223.
10. Sartor O, Coleman R, Nilsson S, et al. Effect of radium-223 dichloride on symptomatic skeletal events in patients with castration-resistant prostate cancer and bone metastases: results from a phase 3, double-blind, randomised trial. *Lancet Oncol.* 2014;15:738–746.
11. Nilsson S, Cislo P, Sartor O, et al. Patient-reported quality-of-life analysis of radium-223 dichloride from the phase III ALSYMPCA study. *Ann Oncol.* 2016; 27:868–874.
12. Poeppel TD, Handkiewicz-Junak D, Andreeff M, et al. EANM guideline for radionuclide therapy with radium-223 of metastatic castration-resistant prostate cancer. *Eur J Nucl Med Mol Imaging.* 2018;45:824–845.

13. Summary of product characteristics: Xofigo. European Medicines Agency website. https://www.ema.europa.eu/en/documents/product-information/xofigo-epar-product-information_en.pdf. Published November 28, 2013. Updated October 30, 2023. Accessed February 5, 2024.
14. Parker C, Heidenreich A, Nilsson S, Shore N. Current approaches to incorporation of radium-223 in clinical practice. *Prostate Cancer Prostatic Dis.* 2018;21:37–47.
15. Hofman MS, Lawrentschuk N, Francis RJ, et al. Prostate-specific membrane antigen PET-CT in patients with high-risk prostate cancer before curative-intent surgery or radiotherapy (proPSMA): a prospective, randomised, multicentre study. *Lancet.* 2020;395:1208–1216.
16. Hope TA, Goodman JZ, Allen IE, Calais J, Fendler WP, Carroll PR. Metaanalysis of ^{68}Ga-PSMA-11 PET accuracy for the detection of prostate cancer validated by histopathology. *J Nucl Med.* 2019;60:786–793.
17. Heinzel A, Boghos D, Mottaghy FM, et al. ^{68}Ga-PSMA PET/CT for monitoring response to ^{177}Lu-PSMA-617 radioligand therapy in patients with metastatic castration-resistant prostate cancer. *Eur J Nucl Med Mol Imaging.* 2019;46:1054–1062.
18. Bräuer A, Rahbar K, Konnert J, Bögemann M, Stegger L. Diagnostic value of additional ^{68}Ga-PSMA-PET before ^{223}Ra-dichloride therapy in patients with metastatic prostate carcinoma. *Nucl Med (Stuttg).* 2017;56:14–22.
19. Ahmadzadehfar H, Azgomi K, Hauser S, et al. ^{68}Ga-PSMA-11 PET as a gatekeeper for the treatment of metastatic prostate cancer with ^{223}Ra: proof of concept. *J Nucl Med.* 2017;58:438–444.
20. van der Doelen MJ, Oving IM, Wyndaele DNJ, et al. Health-related quality of life, psychological distress, and fatigue in metastatic castration-resistant prostate cancer patients treated with radium-223 therapy. *Prostate Cancer Prostatic Dis.* 2023;26:142–150.
21. Eisenhauer EA, Therasse P, Bogaerts J, et al. New response evaluation criteria in solid tumours: revised RECIST guideline (version 1.1). *Eur J Cancer.* 2009;45:228–247.
22. Scher HI, Morris MJ, Stadler WM, et al. Trial design and objectives for castration-resistant prostate cancer: updated recommendations from the Prostate Cancer Clinical Trials Working Group 3. *J Clin Oncol.* 2016;34:1402–1418.
23. Fanti S, Hadaschik B, Herrmann K. Proposal for systemic-therapy response-assessment criteria at the time of PSMA PET/CT imaging: the PSMA PET progression criteria. *J Nucl Med.* 2020;61:678–682.
24. van der Doelen MJ, Stockhaus A, Ma Y, et al. Early alkaline phosphatase dynamics as biomarker of survival in metastatic castration-resistant prostate cancer patients treated with radium-223. *Eur J Nucl Med Mol Imaging.* 2021;48:3325–3334.
25. Badrising SK, Louhanepessy RD, van der Noort V, et al. A prospective observational registry evaluating clinical outcomes of radium-223 treatment in a nonstudy population. *Int J Cancer.* 2020;147:1143–1151.
26. Kuppen MC, Westgeest HM, van der Doelen MJ, et al. Real-world outcomes of radium-223 dichloride for metastatic castration resistant prostate cancer. *Future Oncol.* 2020;16:1371–1384.
27. Frantellizzi V, Monari F, Mascia M, et al. Validation of the 3-variable prognostic score (3-PS) in mCRPC patients treated with ^{223}radium-dichloride: a national multicenter study. *Ann Nucl Med.* 2020;34:772–780.
28. Armstrong AJ, Garrett-Mayer E, de Wit R, Tannock I, Eisenberger M. Prediction of survival following first-line chemotherapy in men with castration-resistant metastatic prostate cancer. *Clin Cancer Res.* 2010;16:203–211.
29. Halabi S, Lin CY, Kelly WK, et al. Updated prognostic model for predicting overall survival in first-line chemotherapy for patients with metastatic castration-resistant prostate cancer. *J Clin Oncol.* 2014;32:671–677.
30. de Jong AC, Segbers M, Ling SW, et al. ^{68}Ga-PSMA PET/CT for response evaluation of ^{223}Ra treatment in metastatic prostate cancer. *J Nucl Med.* 2023;64:1556–1562
31. Kelly R, Jensen A, Karunaratna N, et al. Prostate-specific membrane antigen positron emission tomography-computed tomography use prior to systemic therapy in metastatic castration-resistant prostate cancer. *BJU Int.* 2023;131:179–182.

Strong Correlation Between SUV_{max} on PSMA PET/CT and Numeric Drop-In γ-Probe Signal for Intraoperative Identification of Prostate Cancer Lesions

Anne-Claire Berrens*[1,2], Malou A. Sorbi*[1], Maarten L. Donswijk[3], Hilda A. de Barros[1], Samaneh Azargoshasb[1,2], Matthias N. van Oosterom[1,2], Daphne D.D. Rietbergen[1,2,4], Elise M. Bekers[5], Henk G. van der Poel[1,6], Fijs W.B. van Leeuwen[1,2], and Pim J. van Leeuwen[1]

[1]*Department of Urology, Netherlands Cancer Institute–Antoni van Leeuwenhoek Hospital, Amsterdam, The Netherlands;* [2]*Interventional Molecular Imaging Laboratory, Department of Radiology, Leiden University Medical Centre, Leiden, The Netherlands;* [3]*Department of Nuclear Medicine, Netherlands Cancer Institute–Antoni van Leeuwenhoek Hospital, Amsterdam, The Netherlands;* [4]*Department of Nuclear Medicine, Leiden University Medical Centre, Leiden, The Netherlands;* [5]*Department of Pathology, Netherlands Cancer Institute–Antoni van Leeuwenhoek Hospital, Amsterdam, The Netherlands; and* [6]*Department of Urology, Amsterdam University Medical Centre, Location VUmc, Amsterdam, The Netherlands*

Prostate-specific membrane antigen (PSMA) PET is used to select patients with recurrent prostate cancer for metastasis-directed therapy. A surgical approach can be achieved through radioguided surgery (RGS), using a Drop-In γ-probe that traces lesions that accumulate the radioactive signal. With the aim of guiding patient selection for salvage surgery, we studied the correlation between the SUV_{max} of lesions on preoperative PSMA PET/CT and their intraoperative counts/s measured using the Drop-In γ-probe. **Methods:** A secondary analysis based on the prospective, single-arm, and single-center feasibility study was conducted (NCT03857113). Patients (n = 29) with biochemical recurrence after previous curative-intent therapy and a maximum of 3 suggestive lesions within the pelvis on preoperative PSMA PET/CT were included. Patients treated with androgen deprivation therapy within 6 mo before surgery were excluded. All patients received an intravenous injection of ^{99m}Tc-PSMA-I&S 1 d before surgery. Radioguidance was achieved using a Drop-In γ-probe. Correlation was determined using the Spearman rank correlation coefficient (ρs). Subgroup analysis was based on the median SUV_{max}. **Results:** In total, 33 lesions were visible on the PSMA PET/CT images, with a median overall SUV_{max} of 6.2 (interquartile range [IQR], 4.2–9.7). RGS facilitated removal of 31 lesions. The median Drop-In counts/s were 134 (IQR, 81–220) in vivo and 109 (IQR, 72–219) ex vivo. The intensity of the values correlated with SUV_{max} (ρs = 0.728 and 0.763, respectively; $P < 0.001$). Subgroup analysis based on median SUV_{max} in the group with an SUV_{max} of less than 6 showed no statistically significant correlation with the numeric signal in vivo (ρs = 0.382; $P = 0.221$) or the signal-to-background-ratio (ρs = 0.245; $P = 0.442$), whereas the group with an SUV_{max} of 6 or more showed respective statistically significant positive correlations (ρs = 0.774 [$P < 0.001$] and ρs = 0.647 [$P = 0.007$]). **Conclusion:** Our findings indicate that there is a direct relation between SUV_{max} on PSMA PET/CT and the readout recorded by the surgical Drop-In probe, thereby indicating that SUV_{max} can be used to select patients for PSMA RGS. For more definitive subgroup definitions for treatment recommendations, further studies are necessary to validate the present findings.

Key Words: SUV_{max}; radioguided surgery; prostate specific membrane antigen; PSMA PET/CT; prostate cancer; γ-probe

J Nucl Med 2024; 65:548–554
DOI: 10.2967/jnumed.123.267075

Despite curative-intent treatment in primary prostate cancer, recurrences occur in 20%–40% of patients (*1*,*2*). Targeting the prostate-specific membrane antigen (PSMA), a protein that is highly overexpressed on the surface of most prostate cancer cells, supports PET imaging. A technology that has substantially enhanced the diagnosis of prostate cancer metastases in intermediate- and high-risk primary patients (*3*), PSMA PET/CT can detect metastatic lesions in patients with biochemical recurrence at prostate-specific antigen (PSA) values of less than 0.5 ng/mL (*4*,*5*), thereby enabling curative metastasis-directed treatment options such as salvage radiotherapy and salvage lymph node dissection.

To accommodate PSMA-targeted surgery, γ-emitting PSMA ligands have been developed that facilitate image-guided surgery (*6*,*7*). In a PSMA-guided workflow, PSMA PET/CT provides the surgical road map, and a secondary PSMA ligand is used to provide intraoperative guidance. Signal intensities of primary tumors on PSMA PET/CT (SUV_{max}) have been reported to vary substantially (*8*).

For guidance during surgery, the γ-emitting ^{99m}Tc-based tracer [^{99m}Tc]Tc-PSMA-I&S has been most frequently used (*9*). This agent not only facilitates PSMA ligand SPECT/CT, albeit with an inferior performance compared with PSMA PET/CT (*10*,*11*), but also facilitates intraoperative lesion localization via γ-tracing (counts/s) (*12*), so-called radioguided surgery (RGS) (Fig. 1). Expanding from traditional γ-probes in open surgery (*12–15*), the introduction of the miniaturized Drop-In γ-probe (Eurorad S.A.) facilitated dissemination of these procedures to robotic surgery (*16–19*). Limited research has been conducted on the SUV_{max} in relation to intraoperative numeric signal. Although the intraoperative counts/s vary substantially (*18*,*19*), there are indications that these values relate to the SUV_{max} (*20*).

The aim of this study was to further corroborate the relation between the SUV_{max} on PSMA PET/CT and the surgical signal

Received Nov. 16, 2023; revision accepted Jan. 11, 2024.
For correspondence or reprints, contact Anne-Claire Berrens (a.berrens@nki.nl).
*Contributed equally to this work.
Published online Mar. 14, 2024.

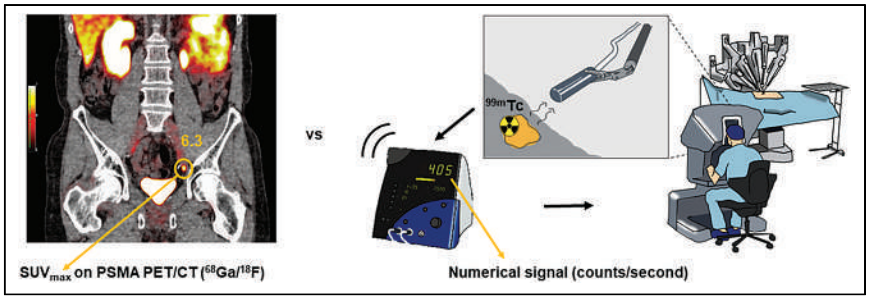

FIGURE 1. Illustration of PSMA PET/CT vs. numeric signal (counts/s) as seen by operating surgeon during robot-assisted surgery.

detected using [^{99m}Tc]Tc-PSMA-I&S. Ultimately, the goal is to identify cutoffs that can be used to refine the selection criteria for PSMA-targeted RGS.

MATERIALS AND METHODS

Study Design and Patient Population

A secondary analysis was performed on data from a prospective, single-center feasibility study that was approved by the local ethics committee at The Netherlands Cancer Institute (ClinicalTrials.gov identifier NCT03857113). All subjects gave written informed consent. The institutional review board approved this retrospective study (IRBdm21-106). Patients were included if they had biochemical recurrence (PSA between 0.2 and 4 ng/mL at 2 consecutive measurements) after previous curative-intent treatment and a maximum of 3 soft-tissue lesions (local or nodal recurrences) on PSMA PET/CT. Patients were excluded if they were receiving androgen deprivation therapy within 6 mo prior to surgery. Patients were treated with robot-assisted ^{99m}Tc-PSMA–targeted salvage RGS between June 2020 and November 2022 (*19*).

Preoperative Imaging and Analysis

All patients underwent PSMA PET/CT within the Prostate Cancer Network Netherlands (*Prostaatkankernetwerk Nederland*). Patients were scanned using [^{68}Ga]Ga-PSMA-11, [^{18}F]DCFPyl, or [^{18}F]JK-PSMA-7 within 125 d before RGS, according to local protocols. Two experienced nuclear medicine physicians reevaluated the preoperative imaging using Osirix MD (Pixmeo SARL). On preoperative PSMA PET/CT, the SUV_{max} of lesions noted in the clinical report was determined by drawing a volume of interest over the lesions. The short-axis diameter of the morphologic substrate, if visible on concurrent CT, was measured.

One day before surgery, a single dose of [^{99m}Tc]Tc-PSMA-I&S (median, 541 MBq; interquartile range [IQR], 482–559 MBq) was injected intravenously and assessed by performing SPECT/CT on the morning of surgery, a median of 17 h (IQR, 17.3–17.8 h) after the injection. The preoperative scintigraphy was reevaluated after the evaluators had been masked to clinical or study-related data, including the preoperative PSMA PET/CT and intraoperative findings. The number and location of suggestive lesions were noted.

Intraoperative Measurements

Within a median of 21 h after injection, RGS was performed. All surgical procedures were done using a da Vinci Xi robot (Intuitive Surgical). Radioguidance was achieved using a Drop-In γ-probe translating the radiosignal to the numeric signal. First, radiotracer activity measurements of anatomic landmarks near target prostate cancer lesions (i.e., iliac artery, iliac vein, and psoas muscle) were performed to determine the background signal. Second, the locations of the suspected prostate cancer lesions were scanned in vivo with the Drop-In probe to assess the signal-to-background ratio (SBR). To confirm successful removal of radioactive tissue, ex vivo validations were performed using the Drop-In γ-probe. A detailed description of the surgical procedures was provided by de Barros et al. (*19*).

Histopathologic Evaluation and Immunohistochemistry

All dissected specimens were sent for histopathologic examination with hematoxylin and eosin staining and, if needed, immunohistochemical pan cytokeratin AE13 (cytokeratin AE1 and AE3) staining. On prostate cancer–positive tissues, additional immunohistochemical PSMA staining was performed (clone 3E6; Dako) to assess the PSMA intensity. The total immunostaining score (TIS) was calculated using:

$$\text{TIS} = \text{proportion score} \times \text{corresponding intensity scores}.$$

The proportion score represented the percentage of cells that stained positively with a particular intensity and could range between 0% and 100%. The intensity score represented the intensity of the stained cells and could range between 0 and 3 (0, no staining; 1, weak; 2, moderate; 3, strong). One pathologist analyzed all intraoperative obtained tissues. The size of the node was measured along the long axis. The TIS of each tumor-positive region was correlated with the SUV_{max} and the numeric signal of the in vivo and ex vivo measurements.

Statistical Analysis

Data were summarized by frequency and percentage for categoric variables and mean and median with ranges for continuous variables. The numeric signal was normalized to account for differences in injected activity of ^{99m}Tc, using the average injected dose as the standard (550 MBq). For continuous variables, normality of distribution was verified with Kolmogorov–Smirnov testing. The primary outcome of interest was the correlation of the SUV_{max} of the prostate cancer lesions on preoperative PSMA PET/CT and the in vivo numeric signal of the PSMA-positive prostate cancer lesions recorded with the Drop-In γ-probe. A secondary outcome was the ex vivo signal and the PSMA intensity on histopathology's correlation with SUV_{max}. All were analyzed using the Spearman rank correlation coefficient (ρs) to determine the correlation. To evaluate the visual perception of a potential correlation, a scatterplot was produced. The different PSMA PET tracers were compared using a Kruskal–Wallis statistical test, and the SPECT/CT subgroups were compared using a Mann–Whitney *U* statistical test. To identify meaningful subgroups for clinical applicability, median regression with concave fusion penalizations was used (*21*). A *P* value of less than 0.05 was considered statistically significant. Statistical analysis was performed with SPSS Statistics, version 29.0 (IBM).

RESULTS

Patient Characteristics

After staging on PSMA PET/CT, 29 patients who had suspected nodal disease ($n = 25$) or locally recurrent prostate cancer ($n = 4$) were included (Fig. 2). As primary treatment, 21 patients (72%) underwent radical prostatectomy and 8 (28%) underwent radiotherapy. Subsequently, 13 patients (45%) underwent salvage therapy before [^{99m}Tc]Tc-PSMA RGS (Table 1).

Preoperative Imaging and Analysis

In total, 33 PSMA-avid lesions were identified on the preoperative PSMA PET/CT. The overall median SUV_{max} on preoperative PSMA PET/CT was 6.2 (IQR, 4.2–9.7) and did not differ between

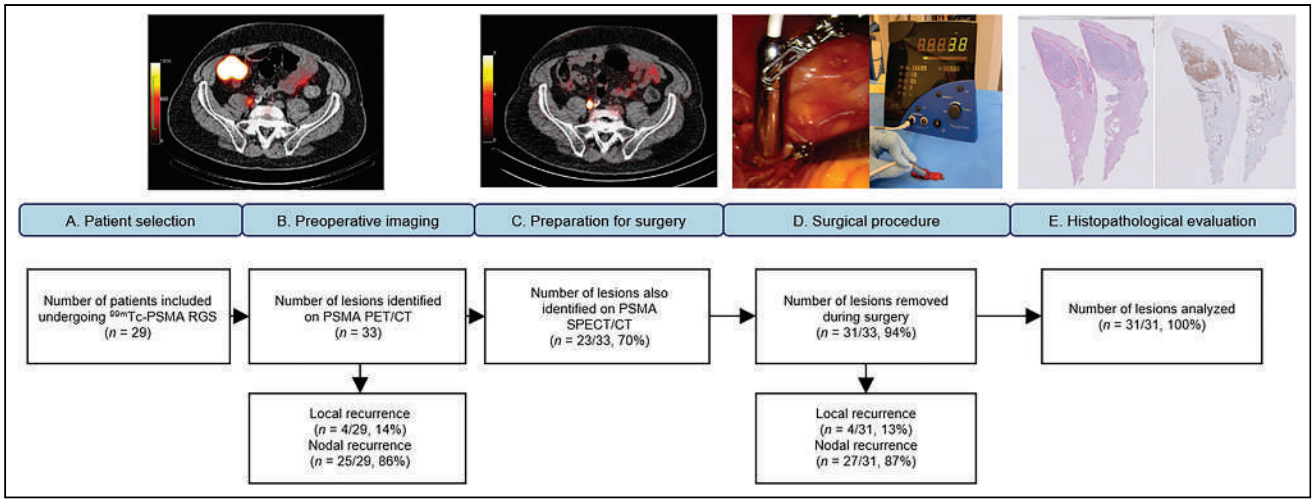

FIGURE 2. Workflow and inclusions. (A–C) Patient selection for salvage [^{99m}Tc]Tc-PSMA RGS (A), preoperative PSMA PET/CT (B), and [^{99m}Tc]Tc-PSMA-I&S imaging (C) demonstrate parailiac lesion in patient with biochemical recurrence. (D) Intraoperative activity measurements with Drop-In γ-probe. (E) Immunohistochemistry (PSMA staining) at histopathologic examination.

TABLE 1
Patient Characteristics

Parameter	Result
Age at [^{99m}Tc]Tc-PSMA RGS (y)	68 (66–72)
Previous primary treatment	
RALP	4 (14)
RALP + ePLND	17 (59)
EBRT	2 (7)
EBRT + HT	5 (17)
Brachytherapy	1 (3)
Previous salvage treatment	
Radiotherapy fossa	5 (17)
Radiotherapy prostate + pelvis	3 (10)
Salvage prostatectomy + LND	1 (3)
Radiotherapy pelvis	1 (3)
Radiotherapy fossa + SLND	1 (3)
Radiotherapy fossa + lutetium PSMA	1 (3)
Radiotherapy prostate + pelvis + previous SLND	1 (3)
No previous salvage treatment	16 (55)
Type of recurrence	
Nodal	25 (86)
Local	4 (14)
PSA before [^{99m}Tc]Tc-PSMA RGS	0.91 (0.5–2.4)
Number of positive lesions on PSMA PET/CT	
1 lesion	25 (86)
2 lesions	4 (14)

RALP = robot-assisted laparoscopic prostatectomy; ePLND = extended pelvic lymph node dissection; EBRT = external-beam radiation therapy; HT = hormone therapy; (S)LND = (salvage) lymph node dissection.

Qualitative data are number and percentage; continuous data are median and IQR.

the different tracers ($P = 0.559$) (Table 2). Ninety-seven percent of the PSMA PET/CT scans were conducted on a European Association of Nuclear Medicine Research Ltd.–accredited system (*22*,*23*). Twenty-seven of the 33 (82%) identified lesions were smaller than 1 cm, with a median size of 4 mm (IQR, 3.8–6 mm). The size of the PSMA PET/CT–avid lesion correlated significantly with the SUV_{max} ($\rho s = 0.728$; $P < 0.001$). The PSA before RGS showed a weak, nonsignificant correlation with the SUV_{max} ($\rho s = 0.2041$; $P = 0.289$), as did the PSA density (defined as PSA before surgery multiplied by the size of the lesion or lesions on PSMA PET/CT) ($\rho s = 0.390$; $P = 0.073$).

Of the 33 lesions found on PSMA PET/CT, 23 (70%) were observed on PSMA-I&S SPECT/CT and 10 (30%) were not. Within the group of lesions that were not visible on SPECT/CT, the median SUV_{max} was 4.9 (IQR, 3.3–6.4), whereas the group of lesions visible on SPECT/CT had a median SUV_{max} of 7.4 (IQR, 5.3–14.3) ($P = 0.028$). Visibility on SPECT/CT was not associated with a higher numeric signal in vivo ($P = 0.237$) or a higher SBR ($P = 0.453$)

Intraoperative

In total, 31 of 33 (94%) lesions were successfully removed during robot-assisted RGS. One suggestive LN could not be localized because of extensive intestinal adhesions (3 mm on PSMA PET/CT; SUV_{max}, 5.3), and 1 LN (3 mm on PSMA PET/CT; SUV_{max}, 1.8) located in the pararectal fat could not be detected because of high

TABLE 2
Characteristics of Diagnostic Preoperative Imaging and Preparation for Surgery

Parameter	Result
Diagnostic preoperative imaging	
Type of PSMA PET/CT	
[^{68}Ga]Ga-PSMA	6 (21)
[^{18}F]DCFPyL	13 (45)
[^{18}F]JK-PSMA-7	10 (34)
Median incubation time (min)	58 (50–61)
[^{68}Ga]Ga-PSMA	49 (44–52)
[^{18}F]DCFPyL	58 (56–61)
[^{18}F]JK-PSMA-7	61 (58–74)
Dose of PSMA PET/CT tracer (MBq)	197 (161–201)
[^{68}Ga]Ga-PSMA	146 (134–159)
[^{18}F]DCFPyL	180 (164–203)
[^{18}F]JK-PSMA-7	201 (200–202)
SUV_{max} of suspected lesion on PSMA PET/CT overall	6.2 (4.2–9.7)
[^{68}Ga]Ga-PSMA	7.7 (3.0–11.6)
[^{18}F]DCFPyL	5.5 (4.2–9.1)
[^{18}F]JK-PSMA-7	6.4 (4.8–16.2)
Time from PSMA PET/CT to operation (d)	33 (15–50)
Size of suspected lesion on PSMA PET/CT (mm)	4 (3.8–6)
Size of suspected lesion on PSMA PET/CT	
<1 cm	27 (82)
≥1 cm	4 (12)
Not measurable	2 (6)
EARL accreditation for PSMA PET/CT	
Yes	28 (97)
No	1 (3)
Preparation for surgery	
Dose of ^{99m}Tc-tracer (MBq)	541 (482–559)
Time from injection of ^{99m}Tc-tracer to SPECT/CT (h)	17.25 (17.25–17.75)
Lesion visible on PSMA PET/CT also visible on SPECT/CT	
Yes	23 (70)
No	10 (30)

EARL = European Association of Nuclear Medicine Research Ltd.
Qualitative data are number and percentage; continuous data are median and IQR.

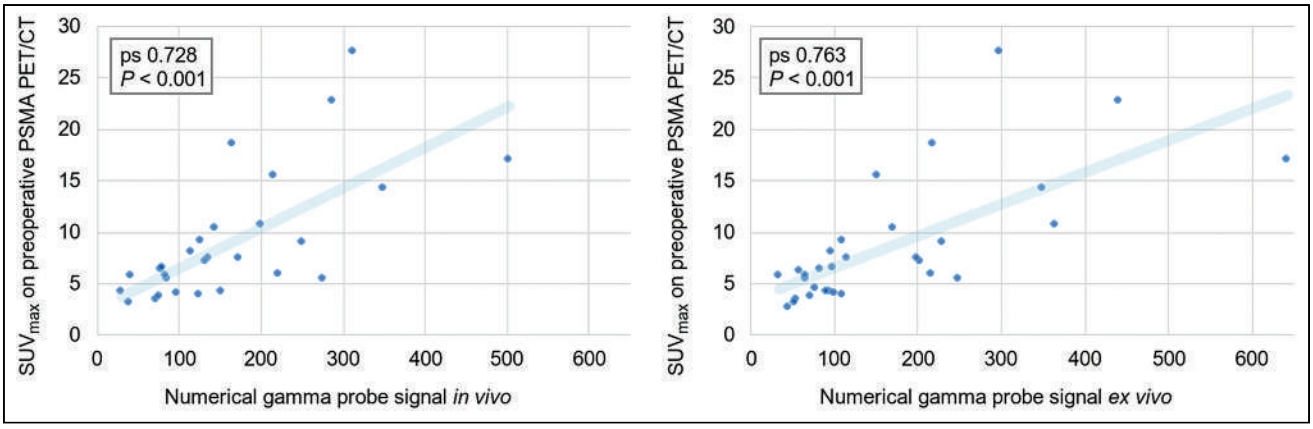

FIGURE 3. Scatterplot illustrating correlation between SUV_{max} on preoperative PSMA PET/CT and in vivo and ex vivo numeric signal of Drop-In γ-probe.

background signal in the rectum as a result of hepatobiliary tracer clearance. The numeric signal of the lesion was recorded both in vivo and ex vivo (median, 134 counts/s [IQR, 81–220] and 109 counts/s [IQR, 72–219], respectively). The median SBR in vivo was 2.3 (IQR, 1.7–3.9). No correlation was seen between the duration of the surgery (median, 136 min; IQR, 101–155) and the SUV_{max} (ρs = −1.44; $P = 0.457$) or the counts in vivo (ρs = −1.38; $P = 0.492$).

Correlation Between SUV_{max} and Intraoperative Numeric Signal

A significant and strong positive correlation was found between the overall SUV_{max} and the intraoperative measures (ρs = 0.728 and 0.763 for in vivo and ex vivo, respectively; $P < 0.001$) (Fig. 3). Median regression analysis identified 2 SUV_{max} subgroups (<6 and ≥6). The former subgroup showed no statistically significant correlation with the numeric signal in vivo (ρs = 0.382; $P = 0.221$), whereas the latter did (ρs = 0.774; $P < 0.001$). Ex vivo results were similar ($SUV_{max} < 6$, ρs = 0.308 [$P = 0.284$]; $SUV_{max} \geq 6$, ρs = 0.752 [$P < 0.001$]). A very moderate, nonsignificant, correlation was observed between the size of the lesion on preoperative PSMA PET/CT and numeric signal in vivo (ρs = 0.421; $P = 0.057$) and ex vivo (ρs = 0.492; $P = 0.015$).

Overall, a moderate correlation was found for the SUV_{max} of the prostate cancer lesions on preoperative PSMA PET/CT and the SBR in vivo (ρs = 0.524; $P = 0.004$). Subgroup analysis showed no correlation between an SUV_{max} of less than 6 (ρs = 0.245; $P = 0.442$) and the SBR, whereas a strong correlation was observed for lesions with an SUV_{max} of 6 or higher (ρs = 0.647; $P = 0.007$).

Correlation Between SUV_{max} and PSMA Intensity Staining

Among the removed lesions, the median TIS was 2.3 (IQR, 2.0–3.0) (Table 3). The distribution of PSMA intensity was homogeneous in 46% of the lesions and heterogeneous in 54%. The type of distribution had no significant impact on SUV_{max} ($P = 0.602$). No positive correlation was found between SUV_{max} and TIS (ρs = −0.433; $P = 0.015$). Multiplying TIS by the size of the lesion at pathology did not show a correlation with SUV_{max} on preoperative PSMA PET/CT (ρs = 0.190; $P = 0.353$).

DISCUSSION

By directly comparing pre- and intraoperative PSMA-targeting strategies, we could identify a significant, positive correlation between SUV_{max} and Drop-In γ-probe measurements. The higher the SUV_{max} is, the greater is the distinction between the tumor and surrounding structures in vivo, suggesting a more reliable road map. Lesion identification may seem less straightforward with a lower SUV_{max} but was not impossible since nearly all lesions in the present study were identified and removed. Our results are in line with the findings of Gondoputro et al., who performed successful RGS on lesions with a median SUV_{max} of 4.4 (*18*). SUV_{max} should therefore be considered among various parameters in the case assessment. Not all removed lesions were seen on the preoperative SPECT/CT, possibly because of timing and background interference (*11*). Although one might assume that the greater the distinction the shorter the duration of the surgery, the current results are inconclusive in this regard. A possible explanation might be the other factors that influence duration, such as adhesions, the type of tissue surrounding the lesion, and the learning curve of the operating surgeon.

On the basis of median regression, we defined 2 SUV_{max} subgroups (<6 and ≥6) that showed clear differences in sensitivity and specificity. However, external validation of these findings is needed in larger series since subgroups were not defined a priori. Nevertheless, with an increasing population subjected to

TABLE 3
Intraoperative and Histopathologic Outcomes

Parameter	Result
Intraoperative outcome	
Time from injection of ^{99m}Tc-tracer to operation (h)	21 (19.75–21.1)
Lesions removed during operation	31 (94)
Counts/s Drop-In γ-probe in vivo	134 (81–220)
Counts/s Drop-In γ-probe ex vivo	109 (72–219)
Counts/s in suspected lesion to activity in PAV ratio (SBR)	2.3 (1.7–3.9)
Histopathologic outcome, TIS	2.3 (2.0–3.0)

PAV = psoas, artery, and vein; TIS = total immunostaining score; SBR = signal-to-background ratio.

Qualitative data are number and percentage; continuous data are median and IQR.

oligometastatic treatment by PSMA RGS (*9*), definitions of optimal subgroups for RGS are desired.

For clinical applicability it would be less time-consuming to base the preoperative assessment on the size of the lesion. This study showed, however, that lesion size was not a significant predictor for the number of intraoperative numeric signal, whereas SUV_{max} appeared to be a strong and significant predictor and should therefore be preferred when selecting patients.

No positive correlation was observed between SUV_{max} and PSMA intensity staining defined as the TIS, possibly because of the wide variation in SUV_{max} and the fact that TIS ranged mostly from moderate to strong. Another influential factor could be the reporting of lymph node size solely as diameter, and the evaluation of TIS per slide, which omits consideration of its 3 dimensions. Little is known regarding the TIS and SUV_{max} of prostate cancer–positive lymph nodes. Looking at radical prostatectomy specimens, Rüschoff et al. also found no significant correlation between SUV_{max} on PSMA PET/CT and immunohistochemical PSMA intensity expression (*24*), whereas Jiao et al. and Vetrone et al. did find a correlation (*25*,*26*), possibly explained by different tumor characteristics or growth patterns (*8*).

Limitations include the high variability in a relatively small number of included patients and the retrospective nature of the secondary analysis. For the scope of this article, only PSMA PET/CT–positive nodes were included. The inclusion criteria of the prospective study introduce a possible selection bias (*19*). The nature of the surrounding tissue is always a consideration when measuring activity in vivo. To minimize the effect of background signal, in the prospective study the values were documented in real time after careful positioning of the Drop-In γ-probe. A limitation remains, however, in that the surrounding tissue type was not considered in this secondary analysis. In addition, applicability in open surgery was not studied.

Subgroup analysis was performed although subgroups were not specified a priori; inferential issues might therefore emerge. Subgroups based on the median are dependent on the cohort and may alter slightly after validation in larger cohorts. Furthermore, there were differences in the median SUV_{max} used for different PSMA PET/CT tracers and systems—although an accurate representation of daily clinical practice. Although our groups were much smaller, the differences were similar to those seen by de Bie et al., who found recurrent prostate cancer to have a nonsignificantly higher SUV_{max} in the [^{68}Ga]Ga-PSMA-11 group (*27*). In addition, all surgical procedures were performed in a single tertiary center experienced in the use of ^{99m}Tc-tracers and the Drop-In γ-probe.

With the growing implementation of PSMA RGS and minimally invasive robotic surgery, it is expected that PSMA PET/CT will assume a fundamental role in the selection of patients, thereby helping to optimize the treatment of patients with oligometastatic prostate cancer recurrence and perhaps also during primary treatment.

CONCLUSION

This study showed a significant positive correlation between the SUV_{max} on preoperative PSMA PET/CT and the intraoperative numeric signal measured by the Drop-In γ-probe, thereby indicating that SUV_{max} can be considered a parameter to select patients for PSMA RGS. Further studies are needed to validate the present subgroup definitions before treatment recommendations can be made.

DISCLOSURE

Fijs W.B van Leeuwen is supported by an NWO-TTW-VICI grant (TTW 16141). No other potential conflict of interest relevant to this article was reported.

KEY POINTS

QUESTION: Does the SUV_{max} on preoperative PSMA PET/CT correlate with the intraoperative γ-probe signal during radioguided prostate cancer surgery?

PERTINENT FINDINGS: A secondary analysis based on the prospective, single-arm, and single-center feasibility study was conducted. Results showed a strong and statistically significant correlation between the SUV_{max} on preoperative PSMA PET/CT and the intraoperative numeric γ-probe signal

IMPLICATIONS FOR PATIENT CARE: Our findings of a direct relation between the SUV_{max} on PSMA PET/CT and the intraoperative signal indicates that SUV_{max} can be considered among other parameters to select patients for PSMA RGS.

ACKNOWLEDGMENTS

We thank the nuclear medicine, pathologic, and surgical staff of the Netherlands Cancer Institute.

REFERENCES

1. Boorjian SA, Houston Thompson R, Tollefson MK, Rangel LJ, Bergstralh EJ, Blute ML. Long-term risk of clinical progression after biochemical recurrence following radical prostatectomy: the impact of time from surgery to recurrence. *Eur Urol.* 2011;59:893–899.
2. Suardi N, Porter CR, Reuther AM, et al. A nomogram predicting long-term biochemical recurrence after radical prostatectomy. *Cancer.* 2008;112:1254–1263.
3. Hofman MS, Lawrentschuk N, Francis RJ, et al. Prostate-specific membrane antigen PET-CT in patients with high-risk prostate cancer before curative-intent surgery or radiotherapy (proPSMA): a prospective, randomised, multicentre study. *Lancet.* 2020;395:1208–1216.
4. Morigi JJ, Stricker PD, van Leeuwen PJ, et al. Prospective comparison of ^{18}F-fluoromethylcholine versus ^{68}Ga-PSMA PET/CT in prostate cancer patients who have rising PSA after curative treatment and are being considered for targeted therapy. *J Nucl Med.* 2015;56:1185–1190.
5. Perera M, Papa N, Roberts M, et al. Gallium-68 prostate-specific membrane antigen positron emission tomography in advanced prostate cancer: updated diagnostic utility, sensitivity, specificity, and distribution of prostate-specific membrane antigen-avid lesions—a systematic review and meta-analysis. *Eur Urol.* 2020;77:403–417.
6. Hensbergen AW, van Willigen DM, van Beurden F, et al. Image-guided surgery: are we getting the most out of small-molecule prostate-specific-membrane-antigen-targeted tracers? *Bioconjug Chem.* 2020;31:375–395.
7. Derks YHW, van Lith SAM, Amatdjais-Groenen HIV, et al. Theranostic PSMA ligands with optimized backbones for intraoperative multimodal imaging and photodynamic therapy of prostate cancer. *Eur J Nucl Med Mol Imaging.* 2022;49:2425–2435.
8. Demirci E, Kabasakal L, Sahin OE, et al. Can SUVmax values of Ga-68-PSMA PET/CT scan predict the clinically significant prostate cancer? *Nucl Med Commun.* 2019;40:86–91.
9. Berrens AC, Knipper S, Marra G, et al. State-of-the-art in prostate specific membrane antigen (PSMA)-targeted surgery: a systematic review *Eur Urol Open Science.* 2023;54:43–55.
10. Koehler D, Sauer M, Klutmann S, et al. Feasibility of ^{99m}Tc-MIP-1404 for SPECT/CT imaging and subsequent PSMA-radioguided surgery in early biochemically recurrent prostate cancer: a case series of 9 patients. *J Nucl Med.* 2023;64:59–62.
11. Berliner C, Steinhelfer L, Chantadisai M, et al. Delayed imaging improves lesion detectability in [^{99m}Tc]Tc-PSMA-I&S SPECT/CT in recurrent prostate cancer. *J Nucl Med.* 2023;64:1036–1042.

12. Maurer T, Weirich G, Schottelius M, et al. Prostate-specific membrane antigen-radioguided surgery for metastatic lymph nodes in prostate cancer. *Eur Urol.* 2015; 68:530–534.
13. Robu S, Schottelius M, Eiber M, et al. Preclinical evaluation and first patient application of ^{99m}Tc-PSMA-I&S for SPECT imaging and radioguided surgery in prostate cancer. *J Nucl Med.* 2017;58:235–242.
14. Rauscher I, Duwel C, Wirtz M, et al. Value of ^{111}In-prostate-specific membrane antigen (PSMA)-radioguided surgery for salvage lymphadenectomy in recurrent prostate cancer: correlation with histopathology and clinical follow-up. *BJU Int.* 2017;120:40–47.
15. Kratzik C, Dorudi S, Schatzl M, Sinzinger H. Tc-99m-PSMA imaging allows successful radioguided surgery in recurrent prostate cancer. *Hell J Nucl Med.* 2018;21: 202–204.
16. van Leeuwen FWB, van Oosterom MN, Meershoek P, et al. Minimal-invasive robot-assisted image-guided resection of prostate-specific membrane antigen-positive lymph nodes in recurrent prostate cancer. *Clin Nucl Med.* 2019;44:580–581.
17. Erfani S, Sadeghi R, Aghaee A, Ghorbani H, Roshanravan V. Prostate-specific membrane antigen radioguided surgery for salvage pelvic lymph node dissection in a man with prostate cancer. *Clin Nucl Med.* 2022;47:e174–e176.
18. Gondoputro W, Scheltema MJ, Blazevski A, et al. Robot-assisted prostate-specific membrane antigen-radioguided surgery in primary diagnosed prostate cancer. *J Nucl Med.* 2022;63:1659–1664.
19. de Barros HA, van Oosterom MN, Donswijk ML, et al. Robot-assisted prostate-specific membrane antigen-radioguided salvage surgery in recurrent prostate cancer using a DROP-IN gamma probe: the first prospective feasibility study. *Eur Urol.* 2022;82:97–105.
20. Azargoshasb S, de Barros HA, Rietbergen DDD, et al. Artificial intelligence-supported video analysis as a means to assess the impact of DROP-IN image guidance on robotic surgeons: radioguided sentinel lymph node versus PSMA-targeted prostate cancer surgery. *Adv Intell Syst.* 2023;5:2300192.
21. Zhang Y, Wang HJ, Zh Z. Robust subgroup identification. *Stat Sin.* 2019;29:1873–1889.
22. Werner RA, Hartrampf PE, Fendler WP, et al. Prostate-specific membrane antigen reporting and data system version 2.0. *Eur Urol.* 2023;84:491–502.
23. Aide N, Lasnon C, Veit-Haibach P, Sera T, Sattler B, Boellaard R. EANM/EARL harmonization strategies in PET quantification: from daily practice to multicentre oncological studies. *Eur J Nucl Med Mol Imaging.* 2017;44:17–31.
24. Rüschoff JH, Ferraro DA, Muehlematter UJ, et al. What's behind ^{68}Ga-PSMA-11 uptake in primary prostate cancer PET? Investigation of histopathological parameters and immunohistochemical PSMA expression patterns. *Eur J Nucl Med Mol Imaging.* 2021;48:4042–4053.
25. Jiao J, Kang F, Zhang J, et al. Establishment and prospective validation of an SUV_{max} cutoff value to discriminate clinically significant prostate cancer from benign prostate diseases in patients with suspected prostate cancer by ^{68}Ga-PSMA PET/CT: a real-world study. *Theranostics.* 2021;11:8396–8411.
26. Vetrone L, Mei R, Bianchi L, et al. Histology and PSMA expression on immunohistochemistry in high-risk prostate cancer patients: comparison with ^{68}Ga-PSMA PET/CT features in primary staging. *Cancers (Basel).* 2023;15:1716.
27. de Bie KCC, Veerman H, Bodar YJL, et al. Higher preoperative maximum standardised uptake values (SUV_{max}) are associated with higher biochemical recurrence rates after robot-assisted radical prostatectomy for [^{68}Ga]Ga-PSMA-11 and [^{18}F]DCFPyL positron emission tomography/computed tomography. *Diagnostics (Basel).* 2023;13:2343.

The Value of ^{68}Ga-PSMA PET/MRI for Classifying Patients with PI-RADS 3 Lesions on Multiparametric MRI: A Prospective Single-Center Study

Jingyan Shi*[1], Danyan Li*[2], Mengxia Chen*[1], Yao Fu[3], Shan Peng[3], Qing Zhang[1], Jing Liang[1], Qun Lu[1], Jiaming Lu[2], Shuyue Ai[4], Feng Wang[4], Xuefeng Qiu[1], and Hongqian Guo[1]

[1]*Department of Urology, Nanjing Drum Tower Hospital, Affiliated Hospital of Medical School, Nanjing University, Nanjing, China;* [2]*Department of Radiology, Nanjing Drum Tower Hospital, Affiliated Hospital of Nanjing University Medical School, Nanjing, China;* [3]*Department of Pathology, Nanjing Drum Tower Hospital, Affiliated Hospital of Nanjing University Medical School, Nanjing, China; and* [4]*Department of Nuclear Medicine, Nanjing First Hospital, Nanjing Medical University, Nanjing, China*

Prostate Imaging Reporting and Data System (PI-RADS) category 3 lesions remain a diagnostic challenge for detecting clinically significant prostate cancer (csPCa). This article evaluates the added value of ^{68}Ga-labeled prostate-specific membrane antigen-11 (^{68}Ga-PSMA) PET/MRI in classifying PI-RADS 3 lesions to avoid unnecessary biopsies. **Methods:** Sixty biopsy-naïve men with PI-RADS 3 lesions on multiparametric MRI were prospectively enrolled between February 2020 and October 2022. In all, 56 participants underwent ^{68}Ga-PSMA PET/MRI and prostate systematic biopsy. ^{68}Ga-PSMA PET/MRI was independently evaluated and reported by the 5-level PRIMARY score developed within the PRIMARY trial. Receiver-operating-characteristic curve analysis was used to estimate the diagnostic performance. **Results:** csPCa was detected in 8 of 56 patients (14.3%). The proportion of patients with csPCa and a PRIMARY score of 1, 2, 3, 4, and 5 was 0% (0/12), 0% (0/13), 6.3% (1/16), 38.5% (5/13), and 100% (2/2), respectively. The estimated area under the curve of the PRIMARY score was 0.91 (95% CI, 0.817–0.999). For a PRIMARY score of 4–5 versus a PRIMARY score of 1–3, the sensitivity, specificity, positive predictive value, and negative predictive value were 87.5%, 83.3%, 46.7%, and 97.5%, respectively. With a PRIMARY score of at least 4 to make a biopsy decision in men with PI-RADS 3 lesions, 40 of 48 patients (83.3%) could avoid unnecessary biopsies, at the expense of missing 1 of 8 (12.5%) csPCa cases. **Conclusion:** ^{68}Ga-PSMA PET/MRI has great potential to classify patients with PI-RADS 3 lesions and help avoid unnecessary biopsies.

Key Words: ^{68}Ga-PSMA PET/MRI; PRIMARY score; PI-RADS; unnecessary biopsy

J Nucl Med 2024; 65:555–559
DOI: 10.2967/jnumed.123.266742

Prostate multiparametric MRI (mpMRI) is currently recommended before prostate biopsy because of its promising value in the detection and localization of clinically significant prostate cancer (csPCa) (*1*,*2*). Over the last decade, mpMRI has been increasingly used as a biopsy-triage tool and has been used in guiding targeted biopsy (*2*–*4*). The Prostate Imaging Reporting and Data System (PI-RADS) is a 5-point scale based on imaging features and is designed to standardize radiology reporting (*5*). PI-RADS category 3, which presents an equivocal suggestion of csPCa, remains a significant diagnostic challenge. Although biopsy is recommended under the current guidelines, less than 20% of PI-RADS 3 lesions contain csPCa (*6*,*7*). PI-RADS 3 lesions present a dilemma to both urologists and patients because immediate biopsy could be unnecessary; however, a monitoring strategy could lead to some missed diagnoses of csPCa. Hence, specifically identifying csPCa among PI-RADS 3 patients will have significant implications for clinical diagnosis.

^{68}Ga-labeled prostate-specific membrane antigen (^{68}Ga-PSMA) PET/CT has exhibited increasing value in assessing the presence of primary intraprostatic tumors (*8*,*9*). Studies indicate that ^{68}Ga-PSMA PET/CT has some superiority over mpMRI in detecting primary tumors (*10*–*12*). Our previous study found that the combination of mpMRI and ^{68}Ga-PSMA PET/CT improved the diagnostic accuracy of csPCa compared with mpMRI alone, with significant improvement in accurate diagnosis in PI-RADS 3 lesions (*13*). Recently, ^{68}Ga-PSMA PET/CT showed some value in stratifying PI-RADS 3 lesions in a retrospective study (*14*). However, to the best of our knowledge, the value of ^{68}Ga-PSMA PET/MRI, which provides anatomic localization and radiologic information simultaneously, in classifying PI-RADS 3 lesions has never been investigated.

To assess whether ^{68}Ga-PSMA PET/MRI can classify patients with PI-RADS 3 lesions on mpMRI and avoid unnecessary biopsies, this study prospectively included men with PI-RADS 3 lesions and assigned the patients for ^{68}Ga-PSMA PET/MRI scanning before prostate biopsy was performed. The 5-level PRIMARY system developed within the PRIMARY trial was applied to report ^{68}Ga-PSMA PET/MRI findings. Using the pathologic results of the biopsies as the reference, we analyzed the diagnostic utility of ^{68}Ga-PSMA PET/MRI to verify our hypothesis.

MATERIALS AND METHODS

Patients

Between February 2020 and October 2022, consecutive men were assessed for eligibility in the study. Inclusion criteria included biopsy-naïve men with solitary or multiple PI-RADS 3 lesions on mpMRI within 3 mo. Patients with concurrent PI-RADS 4–5 lesions were

Received Sep. 24, 2023; revision accepted Jan. 23, 2024.
For correspondence or reprints, contact Hongqian Guo (dr.ghq@nju.edu.cn), Xuefeng Qiu (xuefeng_qiu@nju.edu.cn), or Feng Wang (fengwangcn@hotmail.com).
*Contributed equally to this work.
Published online Mar. 14, 2024.

excluded. This prospective study was approved by the Ethics Committee of Nanjing Drum Tower Hospital (approval 2020-173-02) and registered on Clinicaltrials.gov (NCT 04573179). Written informed consent from the patients was obtained.

mpMRI Imaging Acquisition and Analysis

All candidates underwent pelvic mpMRI using an Achieva 3.0-T TX scanner (Philips) with a 16-channel phased-array coil as described previously (*15*). Image sequences of the prostate included T1-weighted images, T2-weighted images, and diffusion-weighted images at *b* values of 50, 800, and 1500, respectively, and dynamic-contrast enhanced images after gadolinium injection. The apparent diffusion coefficient was generated using Philips WorkStation software. For participant selection, images with full technical quality were reevaluated independently by 2 dual-trained board-certified radiologists who had over 10 y of experience with a subspecialty in urologic radiology. The images were then scored according to PI-RADS version 2. Concordant conclusions regarding the location of mpMRI findings and whether they were benign or malignant (i.e., PI-RADS 3 vs. PI-RADS 4–5) were required of the 2 readers.

^{68}Ga-PSMA PET/MRI Acquisition

^{68}Ga-PSMA-11 was synthesized as described previously (*16*) and intravenously injected at a median activity of 142 MBq (range, 111–185 MBq). Patients were required to void their bladders the moment before the scan. After a median of 60 min (range, 50–80 min), simultaneous PET/MRI was performed on a uPMR 790 PET/MRI system (United Imaging Healthcare).

The PET/MRI acquisition consisted of 2 parts: a whole-body PET/MRI following the workflow of the protocol reported previously (*17*) and a dedicated MRI examination of the pelvis for prostate access (*18*). This required 5 bed positions with 6 min per bed position with free breathing and 4 min per bed position during breath-hold. MR-based attenuation correction started simultaneously with the PET scan, thus ensuring optimal temporal and regional correspondence between MRI and PET data. Whole-body PET/MRI acquisition was performed from the thigh to the brain, including 3-dimensional gradient-echo T1-weighted imaging sequences, transverse fast spin-echo T2-weighted image sequences with fat suppression, diffusion-weighted images, cranial 3-dimensional T1-weighted imaging sequences, and cranial 3-dimensional T2 fluid-attenuated inversion recovery sequences. Dedicated PET/MRI acquisition in the pelvis with a 12-channel phased-array coil was subsequently started, and sagittal and transverse high-resolution T2-weighted images, transverse and coronal T2-weighted images with fat suppression, transverse high-resolution T1-weighted images, and diffusion-weighted image sequences (4,452/78-ms repetition time/echo time; 3 mm thick with an intersection gap of 10 mm; 340 × 220 field of view; 600 × 800 matrix; 0/800/1,500 s/mm^2 *b*-factor) were acquired. Image reconstruction was performed with time of flight and an iterative ordered-subset expectation maximization algorithm.

^{68}Ga-PSMA PET/MRI Analysis

All ^{68}Ga-PSMA PET/MR images were independently reviewed by 2 experienced nuclear medicine specialists masked to the previous mpMRI and clinical outcomes. The 5-level PRIMARY system, which is based on a combination of ^{68}Ga-PSMA pattern information and intensity, was used to report prostate ^{68}Ga-PSMA PET/MRI findings according to a previous study (*19*). In contrast, the prostate zones were delineated on MRI, which provided more accurate zonal anatomy than did the CT images.

In brief, lesions of concern were identified on PET (higher uptake than background) and analyzed on the fused PET/MR images. Readers interrogated the PET/MR images for specific patterns: diffuse transition zone (TZ) activity (pattern A), symmetric central zone activity (pattern B), focal TZ activity (pattern C), and focal peripheral zone activity (pattern D) (Fig. 1). All patterns were documented, and the most clinically significant pattern was used in cases of multiple patterns. Uptake (SUV_{max}) was measured in each prostate quadrant, with the single highest value used for analysis. Afterward, a PRIMARY score using a combination of pattern information and SUV_{max} was assigned to each participant. Descriptions and examples of different PRIMARY scores are shown in Figure 1.

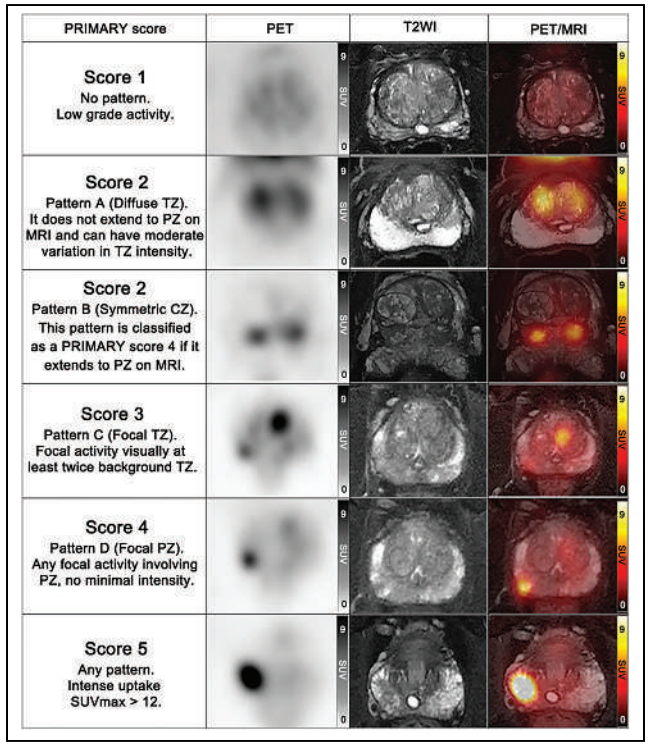

FIGURE 1. ^{68}Ga-PSMA PET/MRI examples of PRIMARY scores. T2WI = T2-weighted image; PZ = peripheral zone; CZ = central zone.

Prostate Biopsy and Histopathology Examination

All patients underwent transperineal 12-core systematic biopsy and mpMRI/ultrasound fusion-guided targeted biopsy (*20*). Lesions of concern from mpMRI and ^{68}Ga-PSMA PET were both targeted if all treating physicians agreed on the abnormalities on the basis of the key images. All biopsies were performed by the same urologist who had over 5 y of experience with prostate biopsy. Tumor grade was assigned according to the 2014 grade group guidelines of the International Society of Urological Pathology (*21*). csPCa was defined as an International Society of Urological Pathology grade group of greater than 1, whereas clinically insignificant PCa (International Society of Urological Pathology group 1) and benign conditions were defined as non-csPCa (*22*).

Statistical Analysis

In addition to basic descriptive statistics, receiver-operating-characteristic curve analysis was performed to evaluate the diagnostic performance of the PRIMARY score, and a 95% CI was calculated as proposed by Obuchowski (*23*). The optimal cutoff value was chosen using the Youden method. The area under the curve (AUC) was compared using the DeLong test. Statistical analysis was performed using IBM SPSS statistics software, version 26.0. A *P* value of less than 0.05 was considered to indicate a significant difference.

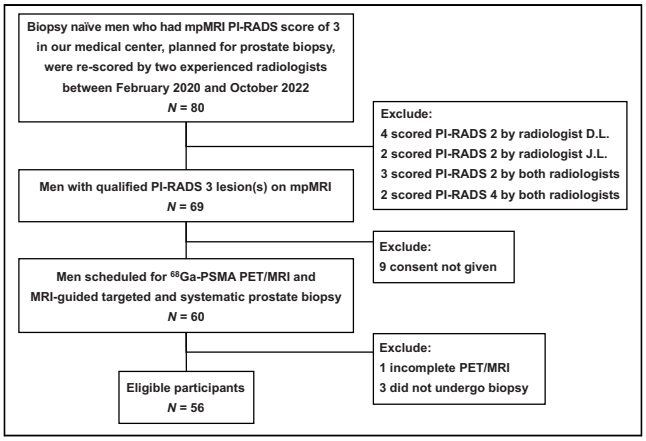

FIGURE 2. Flowchart showing final eligible participants.

RESULTS

Participant Characteristics

Of 80 potential candidates, 56 men were qualified for analysis (Fig. 2). ^{68}Ga-PSMA PET/MRI was performed with a median interval of 2.4 wk (interquartile range, 0.7–6.0 wk) from mpMRI scanning and with a median interval of 1 wk (interquartile range, 0.5–1.0 wk) from biopsy. Baseline characteristics are shown in Table 1. Twelve participants (16.2%) had no pattern on ^{68}Ga-PSMA PET/MRI, 15 (20.3%) exhibited pattern A, 3 (4.1%) exhibited pattern B, 25 (33.8%) had pattern C, and 19 (25.7%) had pattern D. Among the 56 participants, csPCa was detected in 8 patients (14.3%) by biopsy, whereas insignificant PCa was detected in 6 (10.7%) patients. Of the patients with csPCa, 2 of 8 cases (25%) were missed by systematic biopsy, whereas no csPCa was missed by targeted biopsy.

TABLE 1
Baseline Features of Included Cases (n = 56)

Characteristic	Finding
Age (y)	67 (63–71)
BMI (kg/m^2)	24.5 (23.3–26.2)
PSA (ng/mL)	6.9 (5.5–9.5)
PSMA pattern*	
No pattern	12 (16.2)
Pattern A (diffuse TZ)	15 (20.3)
Pattern B (symmetric CZ)	3 (4.1)
Pattern C (focal TZ)	25 (33.8)
Pattern D (focal PZ)	19 (25.7)
Grade group of biopsy	
Benign	42 (75)
ISUP 1	6 (10.7)
ISUP 2	3 (5.4)
ISUP ≥3	5 (8.9)

*Number exceeds sample size because patients may exhibit more than 1 pattern simultaneously.

BMI = body mass index; PSA = prostate-specific antigen; CZ = central zone; PZ = peripheral zone; ISUP = the International Society of Urological Pathology.

Continuous data are median and interquartile range. Qualitative data are number and percentage.

TABLE 2
Results of Tumor Detection with PRIMARY Scores

PRIMARY score	Histology (n = 48) Negative	Positive	csPCa (%)
1	12	0	0
2	13	0	0
3	15	1	6.3
4	8	5	38.5
5	0	2	100
Total	48	8	14.3

Diagnostic Performance of ^{68}Ga-PSMA PET/MRI

The rates of detection of csPCa by the PRIMARY score is shown in Table 2. The proportion of men with csPCa and a PRIMARY score of 1, 2, 3, 4, or 5 was 0% (0/12), 0% (0/13), 6.3% (1/16), 38.5% (5/13), and 100% (2/2), respectively. The estimated AUC of the PRIMARY score was 0.91 (95% CI, 0.817–0.999) (Fig. 3). The Youden-selected threshold was 4. For a PRIMARY score of 4–5 versus a PRIMARY score of 1–3, the sensitivity, specificity, positive predictive value, and negative predictive value were 87.5%, 83.3%, 46.7%, and 97.5%, respectively (Table 3).

When a PRIMARY score of at least 4 was used to make a biopsy decision in men with PI-RADS 3 lesions, 40 of 48 (83.3%) participants could avoid unnecessary biopsies, including 4 of 6 (66.7%) men with insignificant cancer and 36 of 42 (85.7%) men with benign conditions, at the expense of missing 12.5% (1/8) of csPCa cases.

DISCUSSION

Diagnosis of PI-RADS category 3 lesions remains a significant clinical challenge. In this study, 56 biopsy-naïve men with

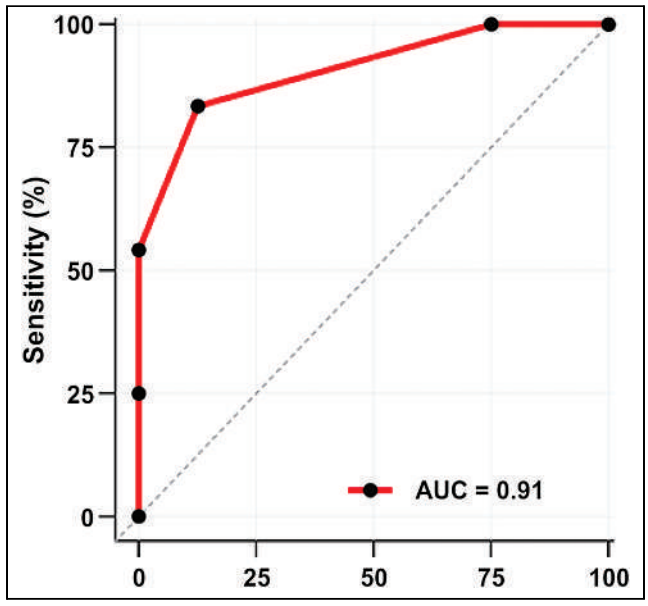

FIGURE 3. Receiver-operating-characteristic curve for PRIMARY score.

TABLE 3
Performance Characteristics of PRIMARY Score at Cutoff Points of 3 and 4 for Patients with PI-RADS 3 Lesions

AUC	Threshold	Sensitivity	Specificity	PPV	NPV
0.91 (0.80–0.97)	4*	87.5% (47.3%–99.7%)	83.3% (69.8%–92.5%)	46.7% (30.6%–63.4%)	97.5% (86.4%–99.6%)
	3	100% (63.1%–100.0%)	54.2% (39.2%–68.6%)	26.7% (21.1%–33.1%)	100% (—)

*Youden-selected threshold.
PPV = positive predictive value; NPV = negative predictive value.
Data in parentheses are 95% CI.

PI-RADS 3 lesions on mpMRI were prospectively included, and ^{68}Ga-PSMA PET/MR scanning was performed before prostate biopsy. ^{68}Ga-PSMA PET/MRI was independently reviewed, and a PRIMARY score was assigned to each participant. As a result, 14.3% of the patients harbored csPCa, in line with the 13%–21% reported in previous articles (*24*,*25*). The estimated AUC of the PRIMARY score in predicting csPCa was 0.91. With a threshold of a PRIMARY score of 4, sensitivity and specificity for csPCa were both high (87.5% and 83.3%, respectively). Adding a PRIMARY score of at least 4 into the biopsy decision could avoid 83.3% (40/48) unnecessary biopsies, at the expense of missing 12.5% (1/8) of csPCa cases. Further validation is warranted before clinical implementation. To the best of our knowledge, this is the first prospective study to show the value of ^{68}Ga-PSMA PET/MRI in classifying PI-RADS 3 lesions and to avoid unnecessary biopsy.

Several studies have assessed the added value of traditional clinical parameters (e.g., age (*26*), previous biopsy status (*26*), prostate-specific antigen density (*26*,*27*)) and imaging parameters (e.g., prostate volume (*28*,*29*), lesion location (*30*), apparent diffusion coefficient value (*28*,*29*) on mpMRI) in classifying PI-RADS 3 lesions. Despite the variety of parameters presented, prostate-specific antigen density is most commonly used to assist with biopsy decision for PI-RADS 3 lesions, with AUC ranging from 0.62 to 0.67 (*26*,*31*) and being 0.72 in our cohort (Supplemental Table 1; supplemental materials are available at http://jnm.snmjournals.org). In a recently retrospective high-volume multicenter study, prostate-specific antigen density with a cutoff of 0.15 was used to predict csPCa in patients with PI-RADS 3 lesions, and 58.4% of biopsies would have been avoided, at the cost of missing 6.5% of csPCa cases (*26*). Several prediction models have been developed combining clinical and imaging parameters for the same purpose. Recently, a risk model based on clinical and MRI-derived parameters was developed in a multiinstitutional study, with an AUC of 0.78; the most desirable outcome of this model was avoiding 25% unnecessary biopsies at the expense of missing only 5% of csPCa cases (*30*). Nevertheless, the added values of the aforementioned parameters or models seem to be limited, varied in cohorts, and lacking validation in prospective settings.

As is well known, mpMRI shows high sensitivity (0.91; 95% CI, 0.83–0.95) but low specificity (0.37; 95% CI, 0.29–0.46) for csPCa detection (*32*). ^{68}Ga-PSMA PET may bridge the gap because of its superb specificity in identifying 84.6%–95.0% of csPCa cases (*10*,*12*). The improved specificity in detecting csPCa was reported when mpMRI was combined with ^{68}Ga-PSMA PET (*11*,*33*). The recently introduced PRIMARY score may further improve the specificity because the classification relies mainly on pattern rather than intensity. The 2 low-risk patterns including the diffuse TZ activity and symmetric central zone activity, both occurring centrally in the prostate, are shown to be potential causes of false positives (*34*,*35*). It is reported that increasing SUV_{max} did not raise the probability of csPCa in these 2 patterns (*19*).

The present study performed ^{68}Ga-PSMA PET/MRI, and the 5-level PRIMARY score was applied. Using the MRI phase to demarcate prostatic zones, improved tumor location was offered and better specificity of ^{68}Ga-PSMA patterns could be expected indisputably. In our cohort, no csPCa was found in low-risk patterns including no pattern, pattern A, and pattern B. The good performance could be attributed to the combination of the improved tumor localization offered by MRI and the improved specificity offered by PET imaging and ^{68}Ga-PSMA patterns. In addition, the top score with an SUV_{max} greater than 12 remains at 100% specificity, as reported in the PRIMARY study (*36*). In all, the AUC of the PRIMARY score was estimated to be 0.91, which significantly outperformed the clinical prostate-specific antigen density parameter (Supplemental Table 1).

In this study, a PRIMARY score of 3 was rated to be negative as determined by the Youden index, which was different from that of the PRIMARY study. For one reason, the presence of csPCa in the TZ is not common and is even rarer among PI-RADS 3 patients. As shown in our cohort, only 12.5% (1/8) of csPCa cases were detected from the TZ. For another reason, compared with a threshold of 3 and a cutoff of 4, specificity was improved significantly from 52.08% to 83.33%, while preserving a high level of sensitivity (decreasing from 100% to 87.5%). As a result, as much as 83.3% (40/48) of PI-RADS category 3 patients could avoid unnecessary biopsies.

Our study still has some limitations. First, this was a single-center study with a relatively small sample size. Although all patients were enrolled and tested prospectively, more large-volume studies are needed to confirm the conclusions of the current study. Second, the subjectivity in scoring the PI-RADS system may impose difficulty in applying our findings to other medical centers. To compensate for this and to make sure the PI-RADS 3 participants in this study adhered to the PI-RADS version 2.0 standardization, participants with PI-RADS 3 lesions were reevaluated independently by 2 senior radiologists, and concordant conclusions were required for inclusion. Third, our work supported the benefits of performing ^{68}Ga-PSMA PET/MRI for the mpMRI PI-RADS 3 population, but further work is required to determine whether this potential reduction in biopsy by adding an imaging modality is cost-effective.

CONCLUSION

^{68}Ga-PSMA PET/MRI showed a promising performance in classifying patients with PI-RADS 3 lesions on mpMRI. Using a PRIMARY score of 4–5 versus a PRIMARY score of 1–3, the sensitivity and specificity for csPCa were 87.5% and 83.3%,

respectively. Unnecessary biopsies could be avoided in 83.3% of cases with the sacrifice of missing 12.5% (1/8) of csPCa cases, which needs to be further investigated in larger-cohort studies.

DISCLOSURE

This study was supported by grants from the Sino-German Mobility Programme (M-0670), the National Natural Science Foundation of China (82172639), and the Natural Science Foundation of Jiangsu Province (BE2020622). No other potential conflict of interest relevant to this article was reported.

KEY POINTS

QUESTION: Could ^{68}Ga-PSMA PET/MRI classify patients with PI-RADS 3 lesions on mpMRI and help with biopsy decisions?

PERTINENT FINDINGS: A PRIMARY score derived from ^{68}Ga-PSMA PET/MRI exhibited high diagnostic accuracy among PI-RADS 3 patients, with an AUC of 0.91. Using the threshold of 4, the sensitivity (87.5%) and specificity (83.3%) for csPCa were both high. As much as 83.3% of unnecessary biopsies could be avoided but at the sacrifice of missing 12.5% of csPCa cases.

IMPLICATIONS FOR PATIENT CARE: PI-RADS 3 patients could be referred for ^{68}Ga-PSMA PET/MRI before prostate biopsy.

REFERENCES

1. Mottet N, van den Bergh RCN, Briers E, et al. EAU-EANM-ESTRO-ESUR-SIOG guidelines on prostate cancer: 2020 update. Part 1: screening, diagnosis, and local treatment with curative intent. *Eur Urol.* 2021;79:243–262.
2. Ahmed HU, El-Shater Bosaily A, Brown LC, et al. Diagnostic accuracy of multiparametric MRI and TRUS biopsy in prostate cancer (PROMIS): a paired validating confirmatory study. *Lancet.* 2017;389:815–822.
3. Schoots IG, Roobol MJ, Nieboer D, Bangma CH, Steyerberg EW, Hunink MG. Magnetic resonance imaging-targeted biopsy may enhance the diagnostic accuracy of significant prostate cancer detection compared to standard transrectal ultrasound-guided biopsy: a systematic review and meta-analysis. *Eur Urol.* 2015;68:438–450.
4. van der Leest M, Cornel E, Israël B, et al. Head-to-head comparison of transrectal ultrasound-guided prostate biopsy versus multiparametric prostate resonance imaging with subsequent magnetic resonance-guided biopsy in biopsy-naïve men with elevated prostate-specific antigen: a large prospective multicenter clinical study. *Eur Urol.* 2019;75:570–578.
5. Weinreb JC, Barentsz JO, Choyke PL, et al. PI-RADS Prostate Imaging–Reporting and Data System: 2015, version 2. *Eur Urol.* 2016;69:16–40.
6. Maggi M, Panebianco V, Mosca A, et al. Prostate Imaging Reporting and Data System 3 category cases at multiparametric magnetic resonance for prostate cancer: a systematic review and meta-analysis. *Eur Urol Focus.* 2020;6:463–478.
7. Venderink W, van Luijtelaar A, Bomers JGR, et al. Results of targeted biopsy in men with magnetic resonance imaging lesions classified equivocal, likely or highly likely to be clinically significant prostate cancer. *Eur Urol.* 2018;73:353–360.
8. Hope TA, Goodman JZ, Allen IE, Calais J, Fendler WP, Carroll PR. Metaanalysis of ^{68}Ga-PSMA-11 PET accuracy for the detection of prostate cancer validated by histopathology. *J Nucl Med.* 2019;60:786–793.
9. Fendler WP, Schmidt DF, Wenter V, et al. ^{68}Ga-PSMA PET/CT detects the location and extent of primary prostate cancer. *J Nucl Med.* 2016;57:1720–1725.
10. Berger I, Annabattula C, Lewis J, et al. ^{68}Ga-PSMA PET/CT vs. mpMRI for locoregional prostate cancer staging: correlation with final histopathology. *Prostate Cancer Prostatic Dis.* 2018;21:204–211.
11. Donato P, Roberts MJ, Morton A, et al. Improved specificity with ^{68}Ga PSMA PET/CT to detect clinically significant lesions "invisible" on multiparametric MRI of the prostate: a single institution comparative analysis with radical prostatectomy histology. *Eur J Nucl Med Mol Imaging.* 2019;46:20–30.
12. Rhee H, Thomas P, Shepherd B, et al. Prostate specific membrane antigen positron emission tomography may improve the diagnostic accuracy of multiparametric magnetic resonance imaging in localized prostate cancer. *J Urol.* 2016;196:1261–1267.
13. Chen M, Zhang Q, Zhang C, et al. Combination of ^{68}Ga-PSMA PET/CT and multiparametric MRI improves the detection of clinically significant prostate cancer: a lesion-by-lesion analysis. *J Nucl Med.* 2019;60:944–949.
14. Yang J, Tang Y, Zhou C, Zhou M, Li J, Hu S. The use of ^{68}Ga-PSMA PET/CT to stratify patients with PI-RADS 3 lesions according to clinically significant prostate cancer risk. *Prostate.* 2023;83:430–439.
15. Zhang Q, Wang W, Zhang B, et al. Comparison of free-hand transperineal mpMRI/TRUS fusion-guided biopsy with transperineal 12-core systematic biopsy for the diagnosis of prostate cancer: a single-center prospective study in China. *Int Urol Nephrol.* 2017;49:439–448.
16. Zhang Q, Zang S, Zhang C, et al. Comparison of ^{68}Ga-PSMA-11 PET-CT with mpMRI for preoperative lymph node staging in patients with intermediate to high-risk prostate cancer. *J Transl Med.* 2017;15:230.
17. Drzezga A, Souvatzoglou M, Eiber M, et al. First clinical experience with integrated whole-body PET/MR: comparison to PET/CT in patients with oncologic diagnoses. *J Nucl Med.* 2012;53:845–855.
18. Souvatzoglou M, Eiber M, Martinez-Moeller A, et al. PET/MR in prostate cancer: technical aspects and potential diagnostic value. *Eur J Nucl Med Mol Imaging.* 2013;40(suppl 1):S79–S88.
19. Emmett L, Papa N, Buteau J, et al. The PRIMARY score: using intraprostatic ^{68}Ga-PSMA PET/CT patterns to optimize prostate cancer diagnosis. *J Nucl Med.* 2022;63:1644–1650.
20. Marra G, Zhuang J, Beltrami M, et al. Transperineal freehand multiparametric MRI fusion targeted biopsies under local anaesthesia for prostate cancer diagnosis: a multicentre prospective study of 1014 cases. *BJU Int.* 2021;127:122–130.
21. Epstein JI, Egevad L, Amin MB, Delahunt B, Srigley JR, Humphrey PA. The 2014 International Society of Urological Pathology (ISUP) consensus conference on Gleason grading of prostatic carcinoma: definition of grading patterns and proposal for a new grading system. *Am J Surg Pathol.* 2016;40:244–252.
22. Fütterer JJ, Briganti A, De Visschere P, et al. Can clinically significant prostate cancer be detected with multiparametric magnetic resonance imaging? A systematic review of the literature. *Eur Urol.* 2015;68:1045–1053.
23. Obuchowski NA. Nonparametric analysis of clustered ROC curve data. *Biometrics.* 1997;53:567–578.
24. Borkowetz A, Hadaschik B, Platzek I, et al. Prospective comparison of transperineal magnetic resonance imaging/ultrasonography fusion biopsy and transrectal systematic biopsy in biopsy-naïve patients. *BJU Int.* 2018;121:53–60.
25. Oerther B, Engel H, Bamberg F, Sigle A, Gratzke C, Benndorf M. Cancer detection rates of the PI-RADSv2.1 assessment categories: systematic review and meta-analysis on lesion level and patient level. *Prostate Cancer Prostatic Dis.* 2022;25:256–263.
26. Sigle A, Borkowetz A, von Hardenberg J, et al. Prediction of significant prostate cancer in equivocal magnetic resonance imaging lesions: a high-volume international multicenter study. *Eur Urol Focus.* 2023;9:606–613.
27. Görtz M, Radtke JP, Hatiboglu G, et al. The value of prostate-specific antigen density for Prostate Imaging-Reporting and Data System 3 lesions on multiparametric magnetic resonance imaging: a strategy to avoid unnecessary prostate biopsies. *Eur Urol Focus.* 2021;7:325–331.
28. Al Hussein Al Awamlh B, Marks LS, Sonn GA, et al. Multicenter analysis of clinical and MRI characteristics associated with detecting clinically significant prostate cancer in PI-RADS (v2.0) category 3 lesions. *Urol Oncol.* 2020;38:637.e9–637.e15.
29. Hermie I, Van Besien J, De Visschere P, Lumen N, Decaestecker K. Which clinical and radiological characteristics can predict clinically significant prostate cancer in PI-RADS 3 lesions? A retrospective study in a high-volume academic center. *Eur J Radiol.* 2019;114:92–98.
30. Fang AM, Shumaker LA, Martin KD, et al. Multi-institutional analysis of clinical and imaging risk factors for detecting clinically significant prostate cancer in men with PI-RADS 3 lesions. *Cancer.* 2022;128:3287–3296.
31. Tosoian JJ, Singhal U, Davenport MS, et al. Urinary MyProstateScore (MPS) to rule out clinically-significant cancer in men with equivocal (PI-RADS 3) multiparametric MRI: addressing an unmet clinical need. *Urology.* 2022;164:184–190.
32. Drost FH, Osses DF, Nieboer D, et al. Prostate MRI, with or without MRI-targeted biopsy, and systematic biopsy for detecting prostate cancer. *Cochrane Database Syst Rev.* 2019;4:CD012663.
33. Eiber M, Weirich G, Holzapfel K, et al. Simultaneous ^{68}Ga-PSMA HBED-CC PET/MRI improves the localization of primary prostate cancer. *Eur Urol.* 2016;70:829–836.
34. Pizzuto DA, Müller J, Mühlematter U, et al. The central zone has increased ^{68}Ga-PSMA-11 uptake: "Mickey Mouse ears" can be hot on ^{68}Ga-PSMA-11 PET. *Eur J Nucl Med Mol Imaging.* 2018;45:1335–1343.
35. Ganeshalingam R, Hsiao E. Compressed central zone uptake on PSMA PET/CT: a potential pitfall in interpretation. *Clin Nucl Med.* 2019;44:570–571.
36. Emmett L, Buteau J, Papa N, et al. The additive diagnostic value of prostate-specific membrane antigen positron emission tomography computed tomography to multiparametric magnetic resonance imaging triage in the diagnosis of prostate cancer (PRIMARY): a prospective multicentre study. *Eur Urol.* 2021;80:682–689.

Prognostic Performance of RECIP 1.0 Based on [^{18}F]PSMA-1007 PET in Prostate Cancer Patients Treated with [^{177}Lu]Lu-PSMA I&T

Philipp E. Hartrampf[1], Thomas Hüttmann[1], Anna Katharina Seitz[2], Hubert Kübler[2], Sebastian E. Serfling[1], Takahiro Higuchi[1], Wiebke Schlötelburg[1], Kerstin Michalski[1], Andrei Gafita[3], Steven P. Rowe[4], Martin G. Pomper[3], Andreas K. Buck[1], and Rudolf A. Werner[1,3,5]

[1]Department of Nuclear Medicine, University Hospital Würzburg, Würzburg, Germany; [2]Department of Urology and Pediatric Urology, University Hospital Würzburg, Würzburg, Germany; [3]Russell H. Morgan Department of Radiology and Radiological Science, Johns Hopkins School of Medicine, Baltimore, Maryland; [4]Division of Molecular Imaging and Therapeutics, Department of Radiology, University of North Carolina, Chapel Hill, North Carolina; and [5]Division of Nuclear Medicine, Department of Diagnostic and Interventional Radiology and Nuclear Medicine, University Hospital, Goethe University Frankfurt, Frankfurt, Germany

In metastatic castration-resistant prostate cancer (mCRPC) patients treated with prostate-specific membrane antigen (PSMA)–targeted radioligand therapy (RLT), the recently proposed criteria for evaluating response to PSMA PET (RECIP 1.0) based on ^{68}Ga- and ^{18}F-labeled PET agents provided prognostic information in addition to changes in prostate-specific antigen (PSA) levels. Our aim was to evaluate the prognostic performance of this framework for overall survival (OS) in patients undergoing RLT and imaged with [^{18}F]PSMA-1007 PET/CT and compare the prognostic performance with the PSA-based response assessment. **Methods:** In total, 73 patients with mCRPC who were scanned with [^{18}F]PSMA-1007 PET/CT before and after 2 cycles of RLT were retrospectively analyzed. We calculated the changes in serum PSA levels (ΔPSA) and quantitative PET parameters for the whole-body tumor burden (SUV_{mean}, SUV_{max}, PSMA tumor volume, and total lesion PSMA). Men were also classified following the Prostate Cancer Working Group 3 (PCWG3) criteria for ΔPSA and RECIP 1.0 for PET imaging response. We performed univariable Cox regression analysis, followed by multivariable and Kaplan–Meier analyses. **Results:** Median OS was 15 mo with a median follow-up time of 14 mo. Univariable Cox regression analysis provided significant associations with OS for ΔPSA (per percentage, hazard ratio [HR], 1.004; 95% CI, 1.002–1.007; $P < 0.001$) and PSMA tumor volume (per unit, HR, 1.003; 95% CI, 1.000–1.005; $P = 0.03$). Multivariable Cox regression analysis confirmed ΔPSA (per percentage, HR, 1.004; 95% CI, 1.001–1.006; $P = 0.006$) as an independent prognosticator for OS. Kaplan–Meier analyses provided significant segregation between individuals with versus those without any PSA response (19 mo vs. 14 mo; HR, 2.00; 95% CI, 0.95–4.18; $P = 0.04$). Differentiation between patients with or without progressive disease (PD) was also feasible when applying PSA-based PCWG3 (19 mo vs. 9 mo for non-PD and PD, respectively; HR, 2.29; 95% CI, 1.03–5.09; $P = 0.01$) but slightly failed when applying RECIP 1.0 ($P = 0.08$). A combination of both response systems (PCWG3 and RECIP 1.0), however, yielded the best discrimination between individuals without versus those with PD (19 mo vs. 8 mo; HR, 2.78; 95% CI, 1.32–5.86; $P = 0.002$). **Conclusion:** In patients with mCRPC treated with RLT and imaged with [^{18}F]PSMA-1007, frameworks integrating both the biochemical (PCWG3) and PET-based response (RECIP 1.0) may best assist in identifying subjects prone to disease progression.

Key Words: PSMA; RECIP; PET/CT; [^{18}F]PSMA-1007; [^{177}Lu]Lu-PSMA I&T; PCWG3

J Nucl Med 2024; 65:560–565
DOI: 10.2967/jnumed.123.266702

In patients with prostate cancer, treatment monitoring is essential but may be complex in individuals with high disease burden who are scheduled for varying therapies, including the recently approved lutetium vipivotide tetraxetan (Pluvicto; Novartis) (*1,2*). Despite favorable results in a randomized trial (*3*), a substantial portion of men will not benefit from treatment with [^{177}Lu]Lu-labeled prostate-specific membrane antigen (PSMA) ligands (*3,4*). Thus, refined outcome assessment by an early identification of patients experiencing progressive disease (PD) is intensively sought. In this regard, monitoring the prostate-specific antigen (PSA) levels of patients undergoing treatment may allow the determination of high-risk individuals when applying a framework system such as criteria suggested by the Prostate Cancer Working Group 3 (PCWG3) (*5*). Changes in PSA levels, however, may have limited value in a castration-resistant setting for segregating between PD and true responses (*6*). Beyond biochemical evaluations, quantification of PSMA expression (as measured by SUVs) or PSMA-avid whole-body tumor volume may also assist in identifying patients experiencing PD under radioligand therapy (RLT) (*7*). Such conventional assessments exclusively focusing on quantified radiotracer accumulation, however, may ignore new lesions appearing on interim scans. To overcome this dilemma, the recently proposed response evaluation criteria in PSMA PET/CT (RECIP 1.0) were introduced, which were validated in a bicentric cohort of 124 patients staged with [^{68}Ga]Ga-PSMA-11 and [^{18}F]rhPSMA-7/7.3 (*8*). Interestingly, the authors concluded that a composite endpoint of PSA response and RECIP 1.0 was superior to PSA measurement only (*8*). A comparison among PSMA PET/CT-based frameworks for monitoring response to treatment, for example, PSMA PET progression criteria (*9*), adapted PERCIST (*10,11*), RECIST 1.1 (*12*), or RECIP 1.0 (*8*), has shown that the

Received Sep. 19, 2023; revision accepted Jan. 5, 2024.
For correspondence or reprints, contact Philipp E. Hartrampf (hartrampf_p@ukw.de).
Published online Mar. 7, 2024.

latter system appears to be the most promising (*11*). Whether RECIP 1.0 shows comparable results in patients exclusively imaged with [^{18}F]PSMA-1007 PSMA PET has not yet been validated. Such findings, however, would be of relevance, as the latter radiotracer is increasingly used in the clinic because of a longer half-life and higher image resolution than for ^{68}Ga-labeled PET agents (*13,14*).

Thus, in the present study, we aimed to evaluate the prognostic performance of RECIP 1.0 for overall survival (OS) in patients scheduled for RLT and imaged with [^{18}F]PSMA-1007 PET/CT. Moreover, we also determined the associations of changes in PSA values, quantitative changes derived from [^{18}F]PSMA-1007 PET, and biochemical and imaging response systems (PCWG3 and RECIP 1.0) with OS.

MATERIALS AND METHODS

Patient Cohort

In this single-center study, 172 patients with metastatic castration-resistant prostate cancer (mCRPC) who were treated with [^{177}Lu]Lu-PSMA I&T at the University Hospital of Würzburg were retrospectively evaluated. Of these, 73 (42%) were eligible for inclusion in this study because they had previously undergone [^{18}F]PSMA-1007 PET/CT and had an interim scan after 2 cycles of RLT, and survival data were also available. Eligibility criteria for RLT were as follows: prior therapy with enzalutamide/abiraterone and chemotherapy or refusal of or deemed unfit for chemotherapy, an Eastern Cooperative Oncology Group performance status no greater than 2, and PSMA-positive disease as confirmed on PSMA PET. Written informed consent was obtained from all subjects. The local ethics committee waived the requirement for further approval because of the retrospective nature of the study (waiver number 20220502 01). Parts of this cohort have already been reported previously (*15–20*). However, the analysis of PSMA PET/CT imaging before and after 2 cycles of RLT for association with OS in the context of RECIP 1.0 was not previously included.

Therapy Work-up

Before the initiation of RLT and 6 wk after the second cycle of RLT, all patients underwent a whole-body [^{18}F]PSMA-1007 PET scan with CT for attenuation correction and anatomic coregistration. A detailed description of radiotracer synthesis and imaging procedures can be found in a previously published work (*21*).

PSA levels were measured at baseline and at follow-up. In addition, blood samples were collected at each cycle for serum chemistry (PSA level, creatinine, lactate dehydrogenase, aspartate aminotransferase, alkaline phosphatase, and C-reactive protein) and routine hematology (leukocytes, hemoglobin, and platelets). Samples were analyzed using an automated hematology analyzer (XN-9000; Sysmex) and a fully automated serum chemistry analyzer (Cobas; Roche Diagnostics) (*19*). Patient histories were reviewed retrospectively from medical records. For biochemical response, modified PCWG3 criteria were applied as provided in Table 1 (*5*).

Image Analysis

PET/CT images were analyzed with Syngo.via software (VB60 datasheet; Siemens Healthineers) for visual interpretation and the Beth Israel plug-in for FIJI (ImageJ) for segmentation (*22*). SUV_{max}, SUV_{peak}, and SUV_{mean} of all lesions, as well as the total-body PSMA-avid tumor volume (PSMA-TV, in mL), were determined using a semiautomatic algorithm with a fixed threshold SUV of 3. All lesions were then reviewed by 1 expert reader, with inconclusive cases undergoing a second review by another expert reader. PSMA-TV was multiplied by SUV_{mean} to calculate the total-lesion PSMA (TL-PSMA) (*7*). Differences between baseline and follow-up were calculated as the percentage increase or decrease for all quantitative PET parameters and PSA levels. The RECIP 1.0 classification was used to define the treatment response (Table 1) (*8*).

Treatment Protocol

[^{177}Lu]Lu-PSMA I&T was synthesized as described previously (*16*). Every 6–8 wk, for a maximum of 8 cycles, patients received approximately 6.0 GBq of [^{177}Lu]Lu-PSMA I&T. Patients with renal impairment had an approximately 20% reduction in activity (*20*).

Statistical Analysis

GraphPad Prism 9.3.0 was used for statistical analysis. Data are presented as median and range. OS was defined as the time from interim PSMA PET/CT to death (presented as median). Patients were considered to have PD in the combined assessment if they had PD according to either RECIP 1.0 or PCWG3 criteria or both. Univariable and multivariable Cox regression analyses were used to test for association with OS. Kaplan–Meier curves and log-rank tests were also performed. The

TABLE 1
RECIP 1.0 Classification (*8,30*) and Modified PSA Response According to PCWG3 (*5*)

Disease stage	Description
RECIP 1.0*	
PD	>20% increase of tumor volume with appearance of new lesions
StD	<30% decrease in tumor volume with or without appearance of new lesions, or ≥30% decrease in tumor volume with appearance of new lesions, or <20% increase in tumor volume with or without appearance of new lesions, or ≥20% increase in tumor volume without appearance of new lesions
Partial response	>30% decrease in tumor volume without appearance of new lesions
Complete response	Absence of any PSMA uptake on follow-up PET scan
PCWG3	
PD	≥25% increase in PSA levels at interim PET
Response	≥50% decrease in PSA levels at interim PET

*New lesions were defined as tumor uptake of PSMA ligand higher than that of surrounding background, with SUV_{max} higher than blood-pool SUV_{max}, which was not present at baseline PET.

hazard ratio (HR) and 95% CI are presented. The Harrell C statistic was used to compare Cox regression models for OS with higher Harrell C values, indicating a better model fit (*23*). Statistical significance was defined as a P value of less than 0.05.

RESULTS

Patient Characteristics

We included 73 patients with a median initial Gleason score of 9 (range, 6–10) and a median age of 72 y (range, 46–88 y). Subjects were treated with a median of 4 cycles of [^{177}Lu]Lu-PSMA I&T (cumulative activity, 19.1 GBq; range, 11.2–50.9 GBq). Median OS was 15 mo, and 31 patients had died at follow-up. The median follow-up was 14 mo.

The median baseline PSA value was 107 ng/mL (range, 2.9–3,590 ng/mL). Before initiation of RLT, nearly all patients (72/73, 98.6%) presented with bone metastases, 49 of 73 patients (67.1%) showed lymph node metastases, and 28 of 73 patients (38.4%) showed visceral metastases (21.9% liver and 15.1% lung). Prior systemic treatments included antihormonal agents (73/73, 100%), enzalutamide (58/73, 79.5%), abiraterone (50/73, 68.5%), and chemotherapy (58/73, 79.5%).

PET quantification yielded the following median baseline values: PSMA-TV, 730.7 cm^3 (range, 5.0–3,301 cm^3); TL-PSMA, 5,135 cm^3 (range, 20.2–33,441 cm^3); SUV_{max}, 39.7 (range, 6.6–190.9); SUV_{peak}, 19.3 (range, 4.3–94.1), and SUV_{mean}, 7.6 (range, 4.0–16.3) (Table 2).

Changes of PET-Based Parameters and PSA After 2 Treatment Cycles

After 2 cycles of RLT with [^{177}Lu]Lu-PSMA I&T, 30 of 73 (41.1%), 37 of 73 (50.7%), 61 of 73 (83.6%), 58 of 73 (79.5%), and 62 of 73 (84.9%) patients showed a reduction of PSMA-TV, TL-PSMA, SUV_{max}, SUV_{peak}, and SUV_{mean}, respectively. Any reduction of PSA levels was found in 49.3% of patients. Table 3 provides an overview of respective changes.

According to RECIP 1.0, 8 of 73 patients (11%) were classified as partial response, 36 of 73 patients (49.3%) were classified as stable disease (StD), and 29 of 73 patients (39.7%) were classified as PD. According to the PCWG3 criteria, 22 of 73 patients (30.1%) were classified as partial response, 18 of 73 patients (24.7%) were classified as StD, and 33 of 73 patients (45.2%) were classified as PD.

Changes in Tumor Volume Are Associated with OS

Univariable Cox regression analysis provided significant associations with OS only for changes in serum PSA values (per percentage, HR, 1.004; 95% CI, 1.002–1.007; $P = 0.001$) and changes in PSMA-TV (per unit, HR, 1.003; 95% CI, 1.000–1.005; $P = 0.03$). Any PSA decrease (HR, 0.50; 95% CI, 0.23–1.09; $P = 0.08$) and a PSA decrease of greater than 50% (HR, 0.43; 95% CI, 0.17–0.97; $P = 0.05$) slightly failed to reach significance. The change in TL-PSMA showed no relevant link to OS, and the appearance of new lesions ($P \geq 0.24$) was also not significantly associated with shorter survival ($P \geq 0.10$).

In a multivariable Cox regression analysis with an adjustment for a change in PSMA-TV and the appearance of new lesions, the change in serum PSA levels (per percentage, HR, 1.004; 95% CI, 1.000–1.006; $P = 0.03$) remained an independent variable for OS (Table 4).

TABLE 2
Patient Characteristics

Parameter	Data
Clinical variables	
Age at first cycle of PSMA RLT (y)	72 (46–88)
$Interval_{Diagnosis\text{-}RLT}$ (mo)	77 (9–274)
Treatment cycles per patient	4 (2–8)
Cumulative activity (GBq)	19.1 (11.2–50.9)
Gleason score	9 (6–10)
Baseline laboratory values	
PSA (ng/mL)	107.0 (2.9–3,590)
CRP (mg/dL)	0.42 (0.1–12.7)
LDH (U/L)	245.0 (152–593)
Hemoglobin (g/dL)	12.0 (7.7–14.8)
AP (U/L)	127.0 (39.0–3,330)
PSMA-TV (cm^3)	730.7 (5.0–3,301)
TL-PSMA (cm^3)	5135 (20.2–33,441)
SUV_{max}	39.7 (6.6–190.9)
SUV_{peak}	19.3 (4.3–94.1)
SUV_{mean}	7.6 (4.0–16.3)
Sites of metastases (*n*) (total $n = 73$)	
Bone	72 (98.6%)
Lymph node	49 (67.1%)
Visceral	28 (38.4%)
Liver	16 (21.9%)
Lung	11 (15.1%)
Prior treatments (%)	
Radical prostatectomy	41.1
Primary radiation therapy to prostate	13.7
Antihormonal treatment	100
Enzalutamide	79.5
Abiraterone	68.5
Chemotherapy	79.5
^{223}Ra	2.7

$Interval_{Diagnosis\text{-}RLT}$ = time between initial diagnosis and first RLT; CRP = C-reactive protein; LDH = lactate dehydrogenase; AP = alkaline phosphatase.
Continuous data are median and range

RECIP 1.0 and PCWG3 Can Identify Patients Experiencing Treatment Failure

Using RECIP 1.0 and PCWG3 classification in a Cox regression analysis, framework-defined PD was also associated with shorter OS for PCWG3 PD (HR, 2.3; 95% CI, 1.02–5.1; $P = 0.04$) or PD on the basis of PCWG3 and RECIP 1.0 (HR, 3.3; 95% CI, 1.5–7.8; $P = 0.004$). RECIP 1.0 PD (HR, 2.1; 95% CI, 0.96–4.6; $P = 0.06$), however, failed to reach significance. The combination of PCWG3 and RECIP 1.0 also showed the highest C-index of 0.69 (0.60 for RECIP 1.0 and 0.63 for PCWG3; Table 4).

TABLE 3
Change After 2 Cycles of RLT

Variables	Data	Reduction
Change in PSMA-TV (cm^3)	+27.2 (−66.9–8,934)	30 (41.1%)
Bone	+28.1 (−71.4–1,699)	
Lymph node	−21.8 (−100–5,835)	
Change in TL-PSMA (cm^3)	−0.8 (−86.6–5,627)	37 (50.7%)
Change in SUV_{max}	−30.1 (−83.7–43.7)	61 (83.6%)
Change in SUV_{peak}	−31.6 (−86.7–60.3)	58 (79.5%)
Change in SUV_{mean}	−25.5 (−71.3–38.1)	62 (84.9%)
Change in PSA	+1.9 (−99.1–870)	36 (49.3%)

Continuous data are median and range. Quantitative data are number of patients and percentage.

Kaplan–Meier analyses confirmed those findings by providing significant segregation between individuals without versus those with PCWG3 PD (19 mo vs. 9 mo; HR, 2.29; 95% CI, 1.03–5.09; $P = 0.01$) and between individuals without versus those with combined (RECIP 1.0 and PCWG3) PD (19 mo vs. 8 mo; HR, 2.78; 95% CI, 1.32–5.86; $P = 0.002$; Fig. 1). RECIP 1.0 alone, however, could not significantly differentiate between individuals without versus those with PD ($P = 0.08$). Moreover, we observed significant survival differences in patients with versus those without a PSA response of greater than 50% (17 mo vs. 14 mo; HR, 2.17; 95% CI, 1.07–4.43; $P = 0.04$) and in patients with versus those without any PSA response (19 mo vs. 14 mo; HR, 2.00; 95% CI, 0.95–4.18; $P = 0.04$). The appearance of new lesions on PET failed to reach significance ($P = 0.11$; Supplemental Fig. 1; supplemental materials are available at http://jnm.snmjournals.org).

In 40 patients, who were classified as non-PD according to the PCWG3 criteria, RECIP 1.0 PD was recorded in 5 individuals (12.5%). These 5 subjects showed an OS that was significantly shorter than that of RECIP 1.0 non-PD patients (7 mo vs. 19 mo; HR, 3.06; 95% CI, 0.59–15.9; $P < 0.02$). In contrast, 44 subjects were classified as non-PD according to RECIP 1.0, but 9 patients (20.5%) would have been classified with PD following the PCWG3 criteria. The survival difference was even more pronounced using the PCWG3 criteria (3 mo vs. 19 mo for PD and non-PD, respectively; HR, 6.09; 95% CI, 0.86–43.0; $P < 0.001$; Supplemental Fig. 2).

DISCUSSION

When the frameworks for PSA (PCWG3) and PSMA PET response (RECIP 1.0) were applied, patients with PCWG3 PD had an OS that was significantly shorter than that of non-PD patients, whereas this was not significant for RECIP 1.0. The combination of both classifications, however, provided the most accurate evaluation of identifying patients not responding to RLT.

Comparable to previous findings in a mixed cohort imaged with ^{68}Ga- and ^{18}F-labeled PSMA PET (*8*), the present study indicates that established biochemical and PET response systems are also applicable to a cohort of men imaged exclusively with ^{18}F-labeled agent PSMA-1007.

In approximately 50% of our patients, we observed a PSA reduction after 2 cycles of PSMA RLT, which was significantly associated with improved OS. This confirms the results of a previous metaanalysis (*24*) and highlights the overall importance of PSA response in patients undergoing PSMA RLT. Furthermore, blood collection was performed after 2 cycles (i.e., 13–14 wk after initiation of RLT), which is in line with the recommended timing of the PCWG3 criteria (*5*). Interestingly, any PSA response and a PSA reduction of at least 50% (indicative for response according to the PCWG3 criteria (*5*)) yielded comparable results for survival.

Beyond biochemical investigations, we also analyzed the percentage changes of TL-PSMA and PSMA-TV, and only the latter

TABLE 4
Univariable and Multivariable Cox Regression

	Univariable				Multivariable		
Parameter	HR	95% CI	C-index	*P*	HR	95% CI	*P*
Change in PSMA-TV (%)	1.003	1.000–1.005	0.68	0.03	1.001	0.9972–1.004	0.62
Change in TL-PSMA (%)	1.002	1.000–1.004	0.65	0.13			
Change in SUV_{mean} (%)	1.000	0.9800–1.018	0.51	0.90			
Change in SUV_{peak} (%)	1.005	0.9945–1.015	0.54	0.34			
Change in SUV_{max} (%)	1.005	0.9923–1.017	0.54	0.46			
Change in PSA (%)	1.004	1.002–1.007	0.69	0.001	1.004	1.000–1.006	0.03
New metastases	1.902	0.8780–4.249	0.60	0.10	1.023	0.4469–2.536	0.96
RECIP 1.0 PD*	2.100	0.9611–4.590	0.60	0.06			
PCWG3 PD*	2.288	1.018–5.100	0.63	0.04			
RECIP+PCWG3 PD*	3.297	1.493–7.791	0.69	0.004			
Any PSA response	0.5026	0.2278–1.092	0.61	0.08			
PSA response >50%	0.4339	0.1720–0.9728	0.63	0.05			

*Tested vs. all non-PD patients in entire cohort.

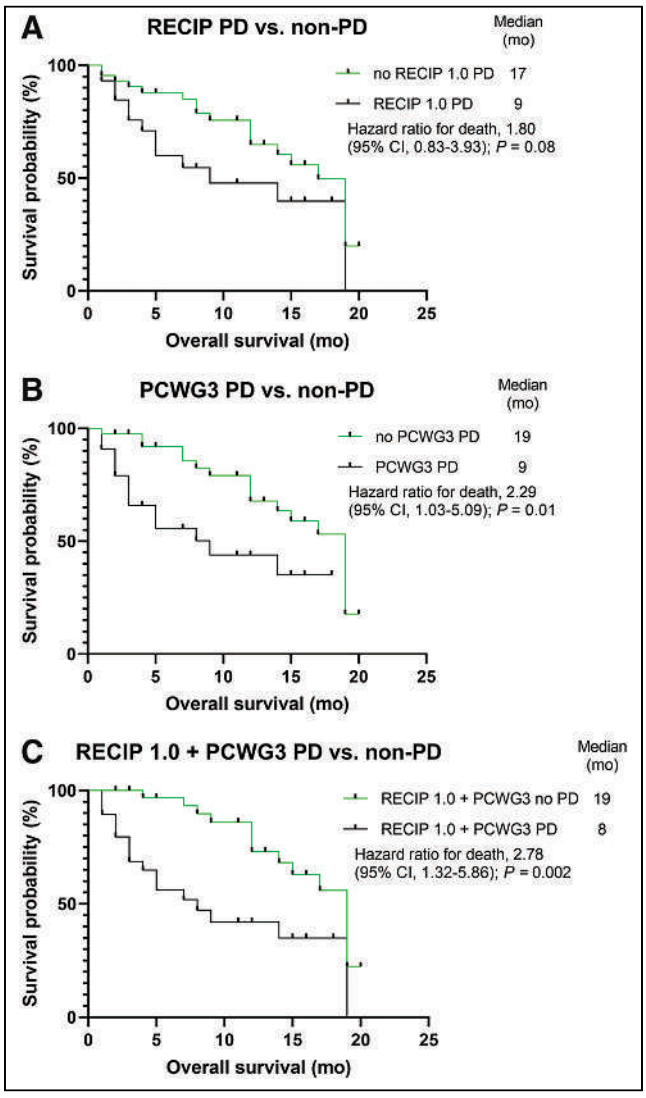

FIGURE 1. Kaplan–Meier analyses of patients grouped according to RECIP 1.0, PCWG3 PSA, and combined assessment for PD or non-PD. Patients with PD according to RECIP 1.0 (OS, 9 mo vs. 17 mo) (A), PCWG3 PSA (OS, 9 mo vs. 19 mo) (B), and combined PD (OS, 8 mo vs. 19 mo) (C) showed shorter OS. However, only segregations based on PCWG3 and PCWG3 with RECIP 1.0 reached significance.

metric showed a significant association with OS in a univariable analysis but missed significance in a multivariable model. This is in contrast to findings published by Grubmüller et al., whose evaluation was not conducted after 2 cycles of RLT (as in the present study) but at the end of therapy (*25*). Rosar et al. used a classification with a cutoff of +30% and −30% for PSMA-TV or TL-PSMA to define PD and partial response, whereas StD was defined as changes between those cutoffs. Using that classification, they reported that patients with StD or PD based on TL-PSMA had a higher risk of death (HR, 2.76), whereas PSA response according to the PCWG3 criteria did not reach significance (*26*). Those discrepant findings relative to our results, however, may be partially explained by the different radiotracers used for imaging ([^{68}Ga]Ga-PSMA-11) and treatment ([^{177}Lu]Lu-PSMA-617) when compared with the current study ([^{18}F]PSMA-1007 and [^{177}Lu]Lu-PSMA I&T). As such, future investigations may also determine the prognostic value of PET-based quantification under RLT but focusing on other also clinically relevant theranostic pairs, for example, ^{18}F-piflufolastat (Pylarify; Lantheus) combined with [^{177}Lu]Lu-PSMA-617. Moreover, the intensity of PSMA expression may also be crucial in the context of OS prognostication (*27*). For instance, in [^{177}Lu]Lu-PSMA-617–treated individuals, only PSMA PET with a certain level of target expression may be suited for outcome prediction when PSMA-TV reduction is considered (*28*). Of note, in our study, respective quantitative parameters such as SUV_{mean} or SUV_{peak} were still substantially elevated.

In the cohort used to establish RECIP 1.0 response, the best cutoff for progression was defined as a 20% increase of PSMA-TV, whereas the most appropriate threshold for response was set by a 30% reduction (using [^{68}Ga]Ga-PSMA-11 and [^{18}F]rhPSMA-7/7.3). OS was improved in patients with RECIP 1.0 partial response and StD compared with OS in patients with RECIP 1.0 PD (*8*). Those results were confirmed in a mixed cohort of [^{68}Ga]Ga-PSMA-11 and [^{18}F]PSMA-1007, with patients with PD having a significantly shorter OS than patients without PD (HR, 2.69) (*29*). In our cohort only including patients imaged with [^{18}F]PSMA-1007 PET, we cannot fully confirm the prognostic ability of RECIP 1.0 as survival was prolonged in patients with non-PD but without reaching significance relative to that with RECIP 1.0 PD. Hence, ours and previous findings (*8,29*) indicate that this framework may be useful for identifying subjects prone to PD, but reevaluation may be required, for example, if PSMA PET radiotracers other than those discussed herein are used.

In patients with PCWG3-based non-PD, almost 13% of the patients had RECIP 1.0 PD with an OS inferior to that of patients without PD, which is virtually identical to the 14% reported by Gafita et al. (*8*). Interestingly, in our cohort, 4 of these 5 patients showed reduction in PSA values but not by 50% or greater. In contrast, approximately 20% of patients with RECIP 1.0–classified non-PD were classified with PCWG3 PD and also showed inferior OS. As such, those discordant assignments to the PD versus non-PD groups based on PCWG3 and RECIP 1.0 along with outcome differences emphasize that one system alone may not be sufficient to identify high-risk patients prone to therapeutic failure. In this regard, a previous study has also shown that the prognostic ability for PD as defined by PSA is slightly inferior to that by RECIP 1.0 or the combination of PSA and RECIP 1.0 (*8*). In our cohort, the prognostic ability for PD as defined by RECIP 1.0 was inferior to that with PCWG3 criteria and, in particular, with a combination of PCWG3 and RECIP 1.0, which achieved the best prognostic value (C-index, 0.69). Thus, our results may favor a more widespread adoption of combined PSA and PSMA evaluations (PCWG3 and RECIP 1.0) in the clinic or in future trials.

It is noteworthy that the RECIP 1.0 definitions use the appearance of new lesions to define progression. Occurrence of new metastases, however, does not necessarily indicate PD if tumor volume is stable, and this criterion has been incorporated in this framework to avoid overstaging (*8*). Of note, this approach is also supported by our findings, as new metastases on PET alone were not associated with shorter OS.

Limitations include the retrospective character of this study and the small number of patients in certain subcategories, for example, between patients with new lesions versus no new lesions or between PSA-based responders and nonresponders. However, our findings indicate that for [^{18}F]PSMA-1007, RECIP 1.0 response alone should be used with caution. In this regard, a combination of PSA and molecular imaging response classifications is most suitable to identify subjects prone to treatment failure. Nonetheless,

quantitative assessments are time-consuming, and thus, our investigation may be repeated using the recently proposed visual RECIP 1.0 (*30*).

CONCLUSION

In men undergoing PSMA RLT and imaged with [^{18}F]PSMA-1007 PET, changes in PSA levels, but not PSMA-TV, emerged as an independent prognosticator for OS. In the context of [^{18}F]PSMA-1007, treatment evaluation may rather not be conducted based only on RECIP 1.0. A dual-response assessment using criteria from PCWG3 and RECIP 1.0, however, provided the best prognostic ability to identify patients with mCRPC at risk of PD. Taken together, ours and previous findings highlight the clinical relevance of structured biochemical and imaging response assessments in patients scheduled for RLT.

DISCLOSURE

Andreas Buck and Kerstin Michalski have received speaker honoraria from Novartis. Rudolf Werner has received speaker honoraria from Novartis and reports advisory board work for Novartis/AAA and Bayer. This work was supported by the IZKF Wuerzburg (grant Z-2/91 to Wiebke Schlötelburg) and the Bavarian Cancer Research Center (personal grant to Kerstin Michalski). No other potential conflict of interest relevant to this article was reported.

KEY POINTS

QUESTION: Can biochemical (changes in PSA levels according to PCWG3) and image-based response criteria (applying RECIP 1.0) predict OS in prostate cancer patients treated with [^{177}Lu]Lu-PSMA I&T and imaged with [^{18}F]PSMA-1007 PET?

PERTINENT FINDINGS: PCWG3 criteria were able to distinguish PD versus non-PD individuals, but the combination of PCWG3 and RECIP provided the strongest prognostic value.

IMPLICATIONS FOR PATIENT CARE: In patients with prostate cancer treated with [^{177}Lu]Lu-PSMA I&T, the combination of PCWG3 and RECIP 1.0 (from [^{18}F]PSMA-1007 PET) can identify subjects prone to PD, thereby emphasizing the importance of biochemical and image-based standardized response assessment.

REFERENCES

1. FDA approves Pluvicto/Locametz for metastatic castration-resistant prostate cancer. *J Nucl Med.* 2022;63(5):13N.
2. Novartis receives European Commission approval for Pluvicto® as the first targeted radioligand therapy for treatment of progressive PSMA–positive metastatic castration-resistant prostate cancer. Novartis website. https://www.novartis.com/news/media-releases/novartis-receives-european-commission-approval-pluvicto-first-targeted-radioligand-therapy-treatment-progressive-psma-positive-metastatic-castration-resistant-prostate-cancer. Published December 13, 2022. Accessed February 15, 2024.
3. Sartor O, de Bono J, Chi KN, et al. Lutetium-177-PSMA-617 for metastatic castration-resistant prostate cancer. *N Engl J Med.* 2021;385:1091–1103.
4. Hofman MS, Emmett L, Sandhu S, et al. [^{177}Lu]Lu-PSMA-617 versus cabazitaxel in patients with metastatic castration-resistant prostate cancer (TheraP): a randomised, open-label, phase 2 trial. *Lancet.* 2021;397:797–804.
5. Scher HI, Morris MJ, Stadler WM, et al. Trial design and objectives for castration-resistant prostate cancer: updated recommendations from the Prostate Cancer Clinical Trials Working Group 3. *J Clin Oncol.* 2016;34:1402–1418.
6. Emmenegger U, Ko YJ. PSA-based treatment response criteria in castration-resistant prostate cancer: promises and limitations. *Can Urol Assoc J.* 2009;3:375–376.
7. Schmuck S, von Klot CA, Henkenberens C, et al. Initial experience with volumetric ^{68}Ga-PSMA I&T PET/CT for assessment of whole-body tumor burden as a quantitative imaging biomarker in patients with prostate cancer. *J Nucl Med.* 2017; 58:1962–1968.
8. Gafita A, Rauscher I, Weber M, et al. Novel framework for treatment response evaluation using PSMA PET/CT in patients with metastatic castration-resistant prostate cancer (RECIP 1.0): an international multicenter study. *J Nucl Med.* 2022; 63:1651–1658.
9. Fanti S, Hadaschik B, Herrmann K. Proposal for systemic-therapy response-assessment criteria at the time of PSMA PET/CT imaging: the PSMA PET progression criteria. *J Nucl Med.* 2020;61:678–682.
10. Wahl RL, Jacene H, Kasamon Y, Lodge MA. From RECIST to PERCIST: evolving considerations for PET response criteria in solid tumors. *J Nucl Med.* 2009;50(suppl 1): 122S–150S.
11. Gafita A, Rauscher I, Fendler WP, et al. Measuring response in metastatic castration-resistant prostate cancer using PSMA PET/CT: comparison of RECIST 1.1, aPCWG3, aPERCIST, PPP, and RECIP 1.0 criteria. *Eur J Nucl Med Mol Imaging.* 2022;49:4271–4281.
12. Eisenhauer EA, Therasse P, Bogaerts J, et al. New response evaluation criteria in solid tumours: revised RECIST guideline (version 1.1). *Eur J Cancer.* 2009;45: 228–247.
13. Piron S, Verhoeven J, Vanhove C, De Vos F. Recent advancements in ^{18}F-labeled PSMA targeting PET radiopharmaceuticals. *Nucl Med Biol.* 2022;106–107:29–51.
14. Werner RA, Derlin T, Lapa C, et al. ^{18}F-labeled, PSMA-targeted radiotracers: leveraging the advantages of radiofluorination for prostate cancer molecular imaging. *Theranostics.* 2020;10:1–16.
15. Hartrampf PE, Seitz AK, Weinzierl FX, et al. Baseline clinical characteristics predict overall survival in patients undergoing radioligand therapy with [^{177}Lu]Lu-PSMA I&T during long-term follow-up. *Eur J Nucl Med Mol Imaging.* 2022;49: 4262–4270.
16. Hartrampf PE, Bundschuh RA, Weinzierl FX, et al. mCRPC patients with PSA fluctuations under radioligand therapy have comparable survival benefits relative to patients with sustained PSA decrease. *Eur J Nucl Med Mol Imaging.* 2022;49: 4727–4735.
17. Hartrampf PE, Weinzierl FX, Buck AK, et al. Matched-pair analysis of [^{177}Lu]Lu-PSMA I&T and [^{177}Lu]Lu-PSMA-617 in patients with metastatic castration-resistant prostate cancer. *Eur J Nucl Med Mol Imaging.* 2022;49:3269–3276.
18. Hartrampf PE, Weinzierl FX, Seitz AK, et al. Any decline in prostate-specific antigen levels identifies survivors scheduled for prostate-specific membrane antigen-directed radioligand therapy. *Prostate.* 2022;82:1406–1412.
19. Hartrampf PE, Weinzierl FX, Serfling SE, et al. Hematotoxicity and nephrotoxicity in prostate cancer patients undergoing radioligand therapy with [^{177}Lu]Lu-PSMA I&T. *Cancers (Basel).* 2022;14:647.
20. Hartrampf PE, Hüttmann T, Seitz AK, et al. SUV_{mean} on baseline [^{18}F]PSMA-1007 PET and clinical parameters are associated with survival in prostate cancer patients scheduled for [^{177}Lu]Lu-PSMA I&T. *Eur J Nucl Med Mol Imaging.* 2023; 50:3465–3474.
21. Michalski K, Ruf J, Goetz C, et al. Prognostic implications of dual tracer PET/CT: PSMA ligand and [^{18}F]FDG PET/CT in patients undergoing [^{177}Lu]PSMA radioligand therapy. *Eur J Nucl Med Mol Imaging.* 2021;48:2024–2030.
22. Schindelin J, Arganda-Carreras I, Frise E, et al. Fiji: an open-source platform for biological-image analysis. *Nat Methods.* 2012;9:676–682.
23. Longato E, Vettoretti M, Di Camillo B. A practical perspective on the concordance index for the evaluation and selection of prognostic time-to-event models. *J Biomed Inform.* 2020;108:103496.
24. Sadaghiani MS, Sheikhbahaei S, Werner RA, et al. ^{177}Lu-PSMA radioligand therapy effectiveness in metastatic castration-resistant prostate cancer: an updated systematic review and meta-analysis. *Prostate.* 2022;82:826–835.
25. Grubmüller B, Senn D, Kramer G, et al. Response assessment using ^{68}Ga-PSMA ligand PET in patients undergoing ^{177}Lu-PSMA radioligand therapy for metastatic castration-resistant prostate cancer. *Eur J Nucl Med Mol Imaging.* 2019;46:1063–1072.
26. Rosar F, Wenner F, Khreish F, et al. Early molecular imaging response assessment based on determination of total viable tumor burden in [^{68}Ga]Ga-PSMA-11 PET/CT independently predicts overall survival in [^{177}Lu]Lu-PSMA-617 radioligand therapy. *Eur J Nucl Med Mol Imaging.* 2022;49:1584–1594.
27. Shagera QA, Artigas C, Karfis I, et al. ^{68}Ga-PSMA PET/CT for response assessment and outcome prediction in metastatic prostate cancer patients treated with taxane-based chemotherapy. *J Nucl Med.* 2022;63:1191–1198.
28. Seifert R, Kessel K, Schlack K, et al. Total tumor volume reduction and low PSMA expression in patients receiving Lu-PSMA therapy. *Theranostics.* 2021;11:8143–8151.
29. Kind F, Eder AC, Jilg CA, et al. Prognostic value of tumor volume assessment on PSMA PET after ^{177}Lu-PSMA radioligand therapy evaluated by PSMA PET/CT consensus statement and RECIP 1.0. *J Nucl Med.* 2023;64:605–610.
30. Gafita A, Djaileb L, Rauscher I, et al. Response evaluation criteria in PSMA PET/CT (RECIP 1.0) in metastatic castration-resistant prostate cancer. *Radiology.* 2023;308:e222148.

Single-Time-Point Renal Dosimetry Using Nonlinear Mixed-Effects Modeling and Population-Based Model Selection in [^{177}Lu]Lu-PSMA-617 Therapy

Deni Hardiansyah[1,2], Elham Yousefzadeh-Nowshahr[2,3], Felix Kind[4], Ambros J. Beer[3], Juri Ruf[4], Gerhard Glatting*[2,3], and Michael Mix*[4,5]

[1]*Medical Physics and Biophysics, Physics Department, Faculty of Mathematics and Natural Sciences, Universitas Indonesia, Depok, Indonesia;* [2]*Medical Radiation Physics, Department of Nuclear Medicine, Ulm University, Ulm, Germany;* [3]*Department of Nuclear Medicine, Ulm University, Ulm, Germany;* [4]*Department of Nuclear Medicine, Medical Center – University of Freiburg, Faculty of Medicine, University of Freiburg, Freiburg, Germany; and* [5]*Nuclear Medicine Division, Department of Medical Imaging and Clinical Oncology, Faculty of Medicine and Health Science, Stellenbosch University, Cape Town, South Africa*

The aim of this study was to investigate the accuracy of single-time-point (STP) renal dosimetry imaging using SPECT/CT data, a nonlinear mixed-effects (NLME) model, and a population-based model selection (PBMS) in a large population for ^{177}Lu-labeled prostate-specific membrane antigen therapy. **Methods:** Biokinetic data (mean ± SD) of [^{177}Lu]Lu-PSMA-617 in kidneys at time points 1 (1.8 ± 0.8 h), 2 (18.7 ± 0.9 h), 3 (42.6 ± 1.0 h), 4 (66.3 ± 0.9 h), and 5 (160.3 ± 24.2 h) after injection were obtained from 63 patients with metastatic castration-resistant prostate cancer using SPECT/CT. Thirteen functions were derived from various parameterizations of 1- to 5-exponential functions. The function's parameters were fitted in the NLME framework to the all-time-point (ATP) data. The PBMS NLME method was performed using the goodness-of-fit test and Akaike weight to select the best function fitting the data. The best function from ATP fitting was used to calculate the reference time-integrated activity and absorbed doses. In STP dosimetry, the parameters of a particular patient with STP data were fitted simultaneously to the STP data at different time points of that patient with ATP data of all other patients. The parameters from STP fitting were used to calculate the STP time-integrated activity and absorbed doses. Relative deviations (RDs) and root-mean-square errors (RMSEs) were used to analyze the accuracy of the calculated STP absorbed dose compared with the reference absorbed dose obtained from the best-fit ATP function. The performance of STP dosimetry using PBMS NLME modeling was compared with the Hänscheid and Madsen methods. **Results:** The function $A_1\,e^{-(\lambda_1+\lambda_{phys})t}+A_2\,e^{-(\lambda_2+\lambda_{phys})t}-A_3\,e^{-(\lambda_3+\lambda_{phys})t}-(A_1+A_2-A_3)\,e^{-(\lambda_{bc}+\lambda_{phys})t}$ was selected as the best-fit ATP function, with an Akaike weight of 100%. For STP dosimetry, the STP measurement by SPECT/CT at time point 3 (42.6 ± 1.0 h) showed a relatively low mean RD of −4.4% ± 9.4% and median RD of −0.7%. Time point 3 had the lowest RMSE value compared with those at the other 4 time points. The RMSEs of the absorbed dose RDs for time points 1–5 were 23%, 16%, 10%, 20%, and 53%, respectively. The STP dosimetry using the PBMS NLME method outperformed the Hänscheid and Madsen methods for all investigated time points. **Conclusion:** Our results show that a single measurement of SPECT/CT at 2 d after injection might be used to calculate accurate kidney-absorbed doses using the NLME method and PBMS.

Key Words: STP dosimetry; Akaike weight; model selection; NLME modeling; PSMA

J Nucl Med 2024; 65:566–572
DOI: 10.2967/jnumed.123.266268

Molecular radiotherapy targeting the prostate-specific membrane antigen (PSMA) is a promising palliative treatment option in patients with metastatic castration-resistant prostate cancer (*1*), using the overexpression of the PSMA in prostate cancer cells (*2*). [^{177}Lu]Lu-PSMA-617 has shown high treatment efficacy and tolerability in both phase II (*3–5*) and phase III (*6*) trials. Although [^{177}Lu]Lu-PSMA-617 therapy is generally well tolerated, several organs, such as kidneys, salivary glands, and bone marrow, are considered organs at risk (*7*). It has been reported that renal and hematopoietic toxicity are the main side effects of [^{177}Lu]Lu-PSMA therapy and peptide receptor radionuclide therapy (*8*). Furthermore, the established kidney tolerance dose of 23 Gy based on data from external radiation therapy (*5*) constitutes the main dose-limiting factor for repeated treatment over multiple cycles. Thus, various protocols for kidney protection using amino acids (*9*) and dosimetry during [^{177}Lu]Lu-PSMA therapy have been developed.

Calculation of the absorbed dose in molecular radiotherapy dosimetry is based on the time-integrated activity (TIA) and the dose factor (*10*). Estimating individual absorbed doses in molecular radiotherapy is desirable for therapy optimization and kidney protection. However, the individual absorbed dose is often not calculated in routine clinical practice, as it needs repeated imaging to determine the TIA (*11,12*). This repeated imaging corresponds to a high workload and additional patient burden, requiring several patient visits. Therefore, a method with fewer imaging sessions is highly desirable.

The feasibility of using a reduced number of imaging data per patient for TIA determination has been investigated for [^{177}Lu]Lu-PSMA therapy (*13,14*), peptide receptor radionuclide therapy (*15–24*), radioiodine therapy (*25,26*), and radioimmunotherapy (*27*). One of the favorable approaches for dosimetry based on single-time-point (STP) imaging data is the nonlinear mixed-effects (NLME) method (*28*). For STP dosimetry, it has been shown (*17*) that the application of NLME modeling resulted in a low number of TIAs with an error exceeding

Received Jul. 5, 2023; revision accepted Jan. 23, 2024.
For correspondence or reprints, contact Deni Hardiansyah (denihardiansyah@ui.ac.id).
*Contributed equally to this work.
Published online Feb. 29, 2024.

10% compared with the all-time-point (ATP) TIAs. The percentage of TIAs with a 10% error was approximately 3 times lower than that using the dose mapping methods introduced by Hänscheid et al. (*18*) and the curve-fitting methods introduced by Madsen et al. (*23*). Recently, the implementation of NLME and a physiologically based pharmacokinetic model in STP dosimetry could lead to an accurate determination of TIAs in various organs, including kidneys and tumors (*11*).

Although NLME modeling in STP dosimetry has shown promising results, it has thus far been implemented only in populations with relatively few patients (i.e., 10 (*17*) or fewer (*11*) patients). Implementation of the technique in larger patient populations is needed to validate the concept and increase the statistical significance of the accuracy of STP dosimetry with NLME modeling. In addition, identifying the optimal fit function through a population-based model selection (PBMS) (*29*) with large patient populations is highly desirable for increasing reproducibility. Therefore, in this study, we implemented a PBMS method in the NLME framework to identify the best model describing the [^{177}Lu]Lu-PSMA-617 biokinetic data in kidneys and performed STP dosimetry using NLME modeling in a larger population of 63 patients.

MATERIALS AND METHODS

Biokinetic Data

In brief, biokinetic data of [^{177}Lu]Lu-PSMA-617 in kidneys from 63 patients with metastasized castration-resistant prostate cancer in the first treatment cycle were used in this study (*8,30*). A [^{177}Lu]Lu-PSMA-617 activity with a median of 6 GBq/cycle was administered intravenously to the patients, followed by SPECT/CT imaging measurements (mean ± SD) at time points 1 (1.8 ± 0.8 h), 2 (18.7 ± 0.9 h), 3 (42.6 ± 1.0 h), 4 (66.2 ± 0.9 h), and 5 (160.3 ± 24.2 h) after injection. Acquisitions were performed on a SPECT/CT scanner (BrightView XCT; Philips Healthcare) using a medium-energy general-purpose collimator. An energy window of ±10% around the 208-keV peak was used for the measurements. Cone-beam CT scans with 30 mAs at 120 kV were used for attenuation correction. Scatter was corrected during reconstruction with the vendor implementation of the effective-scatter source estimation method (*31*). SPECT was reconstructed using the ordered-subsets expectation maximization algorithm without resolution recovery (*8*). The calibration factor for ^{177}Lu was measured using the National Electrical Manufacturers Association image-quality phantom. The calculated calibration factor for the imaging protocol used was 9.9 ± 0.4 cps/MBq. Kidney segmentation and analysis were done using the software package Rover ABX (ABX Advanced Biochemical Compounds GmbH) (*32*). The kidneys were delineated on CT images. At each time point, the activity was measured in both the left and the right kidneys. To compensate for spill-out effects caused by the limited resolution of the SPECT system, all segmented kidney volumes of interest were extended by 2 SPECT voxels in all directions. The enlargement factor was determined by a phantom study. Finally, the fraction of injected activity in both kidneys was used in this study. The institutional review board (vote no. 326/18) approved the retrospective study, and all subjects gave written informed consent.

Fit Function Set: Sums-of-Exponential (SOE) Functions

The following SOE functions were used to describe the biokinetics of [^{177}Lu]Lu-PSMA-617 in kidneys (Eqs. 1–13).

$$f_2(t) = A_1 e^{-(\lambda_1 + \lambda_{phys})t} \quad \text{Eq. 1}$$

$$f_3(t) = A_1 e^{-(\lambda_1 + \lambda_{phys})t} - A_1 e^{-(\lambda_2 + \lambda_{phys})t} \quad \text{Eq. 2}$$

$$f_{4a}(t) = A_1 e^{-(\lambda_1 + \lambda_{phys})t} + A_2 e^{-(\lambda_2 + \lambda_{phys})t} \quad \text{Eq. 3}$$

$$f_{4b}(t) = A_1 e^{-(\lambda_1 + \lambda_{phys})t} - A_2 e^{-(\lambda_2 + \lambda_{phys})t} - (A_1 - A_2) e^{-(\lambda_{bc} + \lambda_{phys})t} \quad \text{Eq. 4}$$

$$f_{4c}(t) = A_1 e^{-(\lambda_1 + \lambda_{phys})t} + A_2 e^{-(\lambda_2 + \lambda_{phys})t} - (A_1 + A_2) e^{-(\lambda_{bc} + \lambda_{phys})t} \quad \text{Eq. 5}$$

$$f_{5a}(t) = A_1 e^{-(\lambda_1 + \lambda_{phys})t} + A_2 e^{-(\lambda_2 + \lambda_{phys})t} - (A_1 + A_2) e^{-(\lambda_3 + \lambda_{phys})t} \quad \text{Eq. 6}$$

$$f_{5b}(t) = A_1 e^{-(\lambda_1 + \lambda_{phys})t} + A_2 e^{-(\lambda_{phys})t} - A_3 e^{-(\lambda_3 + \lambda_{phys})t} - (A_1 + A_2 - A_3) e^{-(\lambda_{bc} + \lambda_{phys})t} \quad \text{Eq. 7}$$

$$f_{6a}(t) = A_1 e^{-(\lambda_1 + \lambda_{phys})t} + A_2 e^{-(\lambda_2 + \lambda_{phys})t} - A_3 e^{-(\lambda_3 + \lambda_{phys})t} - (A_1 + A_2 - A_3) e^{-(\lambda_{bc} + \lambda_{phys})t} \quad \text{Eq. 8}$$

$$f_{6b}(t) = A_1 e^{-(\lambda_1 + \lambda_{phys})t} + A_2 e^{-(\lambda_2 + \lambda_{phys})t} + A_3 e^{-(\lambda_{phys})t} - (A_1 + A_2 + A_3) e^{-(\lambda_3 + \lambda_{phys})t} \quad \text{Eq. 9}$$

$$f_{6c}(t) = A_1 e^{-(\lambda_1 + \lambda_{phys})t} + \mathrm{A}_2 e^{-(\lambda_{phys})t} - A_3 e^{-(\lambda_2 + \lambda_{phys})t} - (A_1 + A_2 - A_3) e^{-(\lambda_3 + \lambda_{phys})t} \quad \text{Eq. 10}$$

$$f_{6d}(t) = A_1 e^{-(\lambda_1 + \lambda_{phys})t} + A_2 e^{-(\lambda_2 + \lambda_{phys})t} + A_3 e^{-(\lambda_3 + \lambda_{phys})t} - (A_1 + A_2 + A_3) e^{-(\lambda_{bc} + \lambda_{phys})t} \quad \text{Eq. 11}$$

$$f_{7a}(t) = A_1 e^{-(\lambda_1 + \lambda_{phys})t} + A_2 e^{-(\lambda_2 + \lambda_{phys})t} + A_3 e^{-(\lambda_{phys})t} - A_4 e^{-(\lambda_3 + \lambda_{phys})t} - (A_1 + A_2 + A_3 - A_4) e^{-(\lambda_{bc} + \lambda_{phys})t} \quad \text{Eq. 12}$$

$$f_{7b}(t) = A_1 e^{-(\lambda_1 + \lambda_{phys})t} + A_2 e^{-(\lambda_2 + \lambda_{phys})t} - A_3 e^{-(\lambda_3 + \lambda_{phys})t} - (A_1 + A_2 - A_3) e^{-(\lambda_4 + \lambda_{phys})t} \quad \text{Eq. 13}$$

where f_i is a fit function, with i being the total number of estimated parameters; $A_j (j = 1,2,3,4)$ are the coefficients of the respective exponential terms; $\lambda_j (j = 1,2,3)$ are the biologic clearance or uptake rates of the radiopharmaceutical in the kidneys; λ_{bc} is the rate of blood circulation set to $\lambda_{bc} = \frac{\ln(2)}{1\ \text{min}}$; and λ_{phys} is the physical decay constant of ^{177}Lu ($\lambda_{phys} = \ln(2)/\text{half-life}$, with the ^{177}Lu half-life of 6.6443 d (*33*)). The A_j and λ_j parameters were constrained to have values greater than 0.

Prior knowledge of radiopharmaceutical kinetics was used as the foundation of the chosen functions and constraints in this study, as suggested by Burnham et al. (*34*). Therefore, the following were implemented: only SOE functions were considered (*35,36*); a constraint of $f_i(t = 0) = 0$ was used, except for f_2 and f_{4a}; a rapid increase in activity in the kidneys with a half-life of 1 min ($\ln(2)/\lambda_{bc}$) was added, which is caused by the blood circulation time in humans (*29,37*); and the radioactive decay was considered as an exponential factor (*38–40*). The functions f_2 and f_3 were added for comparison, as these mono- and biexponential functions, respectively, are often used in the literature (*18,23,35*).

Study Workflow

Figure 1 shows the workflow of the study. The parameters of the SOE functions (Eqs. 1–13) were fitted to the ATP biokinetic data of [^{177}Lu]Lu-PSMA-617 in kidneys (Biokinetic Data section) using the NLME method (Supplemental Eqs. 1–3) (*41,42*). In this study, parameters of the SOE functions in Equations 1–13 were modeled as a combination of fixed and random effects. NLME model fittings and simulations were performed in MATLAB software, version R2020a (https://www.mathworks.com/help/stats/nlmefitsa.html). The PBMS NLME approach was used to select the best-fit SOE function describing the data (*43*). The fittings were randomly repeated 1,000 times to find the best-fit starting values. The SOE function passing the goodness-of-fit test (Supplemental Eqs. 4–6) (*35,44,45,47*) with the highest Akaike weight was selected as the fit function most supported by the data (*35,43,48*).

The best-fit SOE function from the model selection and ATP fitting was then used to calculate the reference TIA (Fig. 1). Calculation of

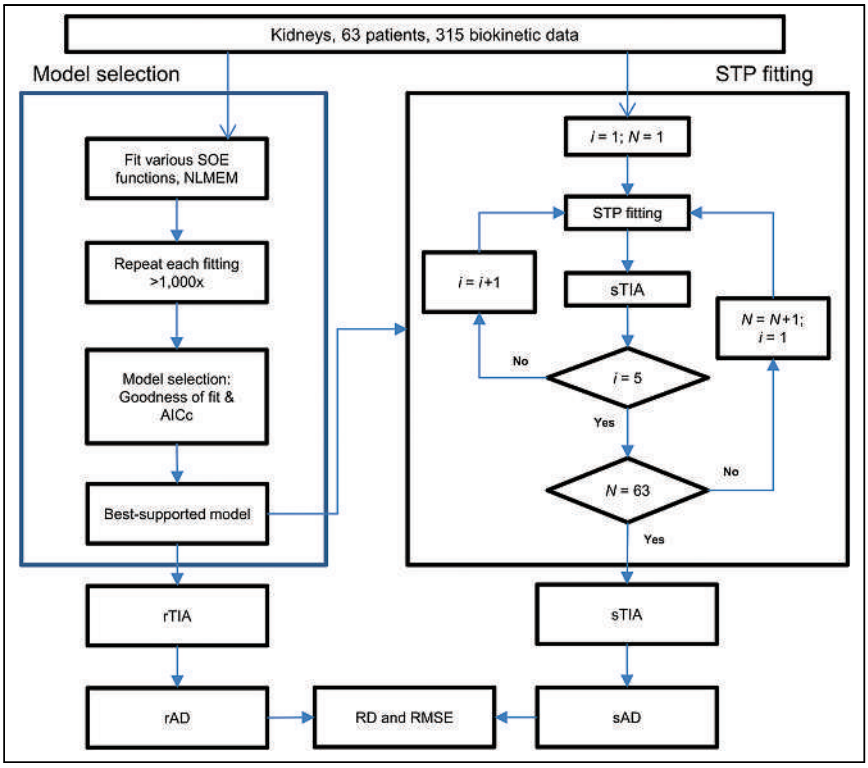

FIGURE 1. Workflow of study. PBMS NLME approach was used to select best fit function based on goodness of fit and Akaike weight. Reference absorbed doses were based on ATP fittings using best-fit function. STP absorbed doses were calculated analogously using only STP data for investigated patient. RDs and RMSEs were used to analyze accuracy of STP absorbed doses against reference absorbed doses. AIC_c = corrected Akaike information criterion; i = time point; N = total number of patients; NLMEM = PBMS NLME; rAD = reference absorbed dose; rTIA = reference TIA; sAD = STP absorbed dose; sTIA = STP TIA.

the TIAs was based on the analytic solution of the SOE functions. In STP dosimetry, the parameters of a specific patient with STP data were fitted simultaneously to the STP data at different time points of that patient with all data points of all other patients.

The STP dosimetry methods introduced by Hänscheid et al. and Madsen et al., which have been widely adopted in STP studies (*20,22,49–51*), were implemented in this study for comparison. The methods were initially used to describe the biokinetics of [^{177}Lu]Lu-DOTATATE/TOC and [^{90}Y]Y-DOTATOC (*18,23*). In this study, the methods were assumed to be applicable for [^{177}Lu]Lu-PSMA-617. The corresponding TIAs for the Hänscheid and Madsen methods were calculated using the following equations:

$$\text{Hänscheid TIA}_i = A(t_i) \times \frac{2 \times t_i}{\ln(2)}, \quad \text{Eq. 14}$$

$$\text{Madsen TIA}_i = A(t_i) \times \frac{e^{\hat{k} t_i}}{\hat{k}}, \quad \text{Eq. 15}$$

where $A(t_i)$ is the activity measured at time point i, t_i is the time of measurement i, and $\hat{k}$ is the population effective clearance rate constant calculated using the leave-one-out method.

The S value of 2.93×10^{-5} Gy $\times$ min^{-1} $\times$ MBq^{-1} (*46,52*) for male patients was used to calculate the absorbed dose using NLME ATP fitting (reference absorbed doses), NLME STP fitting (STP absorbed doses), and the STP Hänscheid and Madsen methods.

Relative deviations (RDs) and root-mean-square errors (RMSEs) were used to analyze the accuracy of the calculated STP absorbed doses, STP Hänscheid method, and STP Madsen method with the reference absorbed doses as the reference. The RDs and the RMSEs were calculated according to

$$RD_k = \frac{sAD_k - rAD}{rAD}, \quad \text{Eq. 16}$$

$$RMSE_k = \sqrt{(SDRD_k)^2 + (\text{mean } RD_k)^2}, \quad \text{Eq. 17}$$

where sAD is STP absorbed dose, rAD is reference absorbed dose, RD_k is the RD of the STP method at time point k, $RMSE_k$ is the root-mean square of RD_k over all patients, and $SDRD_k$ is the SD of RD_k. The reference TIA was computed through population fitting, using a notably high parameter-to-data ratio within our dataset, specifically 315 data points and 13 parameters (Table 1). In contrast, individual patient fitting using a monoexponential function as in the Hänscheid and Madsen methods uses a significantly lower ratio, such as 3 data points and 2 parameters. This results in a higher uncertainty of the resulting TIA.

RESULTS

The NLME fittings for functions f_{4b}, f_{5a}, f_{5b}, f_{6b}, f_{6c}, f_{6d}, f_{7a}, and f_{7b} did not pass the goodness-of-fit test. On the basis of the PBMS NLME method, the function f_{6a} was selected as the best-fit function, with an Akaike weight of 100% (Table 1; Supplemental Fig. 1; supplemental materials are available at http://jnm.snmjournals.org). The estimated fixed-effect values are presented in Table 2. The estimated random-effect values ranged from 0.08 to 0.52. The intraindividual variability (a in Supplemental Eq. 3) was 0.079. Figure 2 shows the percentage RD of the TIAs from ATP fitting with functions f_2, f_3, f_{4a}, and f_{4c} to the TIAs from ATP fitting with function f_{6a}. The mean percentage RDs in Figure 2 are 1.3% ± 14.4%, 1.1% ± 14.2%, 0.1% ± 1.9%, and 0.2% ± 2.0% for functions f_2, f_3, f_{4a}, and f_{4c}, respectively.

Figure 3 shows the population RD of the absorbed dose for STP dosimetry at different time points. The mean of the population RD for STP dosimetry is shown in Supplemental Table 1. The medians of the population RD for STP dosimetry at time points 1–5 were −2% (range, −55% to 59%), −4% (range, −53% to 10%), −0.7% (range, −39% to 20%), −0.1% (range, −32% to 106%), and 0.4% (range, −40% to 348%), respectively. The RMSE values of the absorbed dose RDs for time points 1–5 were 23%, 16%, 10%, 20%, and 53%, respectively. Thus, the STP dosimetry at time point 3 has the lowest mean RD and RMSE values.

Use of STP dosimetry with the PBMS NLME method outperformed the Hänscheid and Madsen methods for all time points (Fig. 3; Supplemental Table 1). The STP NLME model at time point 3 could not accurately calculate the TIA in a few outlier patients (outside the mean ± 2 SDs of the RD), that is, patients 12, 36, 41, and 44, with absorbed dose RDs of 26%, 39%, 23% and 29%, respectively (Fig. 4).

DISCUSSION

In this study, 315 biokinetic data were used and the SOE function $f_{6a}(t) = A_1\, e^{-(\lambda_1 + \lambda_{phys})t} + A_2\, e^{-(\lambda_2 + \lambda_{phys})t} - A_3\, e^{-(\lambda_3 + \lambda_{phys})t} - (A_1 + A_2 - A_3)\, e^{-(\lambda_{bc} + \lambda_{phys})t}$ was selected from the PBMS NLME

TABLE 1
PBMS with NLME Model Results for ATP fitting

Equation no.	Function name	K*	Maximum percentage CV†	Maximum absolute off-diagonal correlation matrix element	Akaike weight (%)‡
1	f_2	5	25	0.21	4.5×10^{-62}
2	f_3	7	—§	—§	—
3	f_{4a}	9	41	0.43	1.3×10^{-15}
4	f_{4b}	9	—§	—§	—
5	f_{4c}	9	41	0.43	2.3×10^{-13}
6	f_{5a}	11	156	0.37	—
7	f_{5b}	11	120	0.73	—
8	f_{6a}	13	44	0.03	100
9	f_{6b}	13	107	0.66	—
10	f_{6c}	13	59	0.85	—
11	f_{6d}	13	11,836	0.47	—
12	f_{7a}	15	54	0.75	—
13	f_{7b}	15	2×10^{30}	0.59	—

*Number of parameters of NLME model for corresponding SOE function.
†Maximum percentage CV of fitted parameters for corresponding SOE function (percentage CV was calculated as $\sqrt{\exp(\omega^2)-1} \times 100\%$ (*42*), with ω^2 being variance of fixed effect).
‡Akaike weight indicates probability with which this function best describes data from analyzed set of functions. Only those SOE functions with percentage CV $<$ 50 and a maximum absolute off-diagonal correlation matrix element $<$ 0.8 were considered.
§Random-effect value ω^2 of parameter λ_2 was not identifiable.
Total number of kidney biokinetic data used in this analysis is 315.

method based on the goodness-of-fit test and Akaike weight of 100% (Table 1). The SOE function f_{6a} shows 2 uptake and clearance phases of the radiopharmaceutical in kidneys. This function shows a higher parameter-to-data ratio in our patient population than the frequently used monoexponential function in the literature (Fig. 2) (*18,23*). The total number of exponential terms and parameters in this study for [^{177}Lu]Lu-PSMA-617 (4 exponentials and 6 parameters) is higher than found in our recent study for [^{177}Lu]Lu-PSMA-I&T ($A_1\, e^{-(\lambda_1 + \lambda_{phys})t} + A_2\, e^{-(\lambda_{phys})t}$ [2 exponentials and 3 parameters]) (*43*). These differences can be attributed to the total number of data and the schedule and range of the measurements between the studies, that is, 315 biokinetic data of [^{177}Lu]Lu-PSMA-617 measured between 0.7 h after injection and 236 h after injection (this study) versus 46 biokinetic data of [^{177}Lu]Lu-PSMA-I&T measured between 0.5 h after injection and 168 h after injection (*43*). This shows that adding more data covering a broader time range is beneficial as it allows the identification of a function with a larger number of parameters. This function should in turn be able to better reflect the biokinetics of the radiopharmaceutical.

TABLE 2
Parameters Estimated from ATP Fitting Obtained from Best Function Derived Using PBMS with NLME Modeling (i.e., f_{6a})

Model parameters (unit)	Fixed effect (percentage CV)	Random effect (variance, interpatient variability)
A_1 (percentage IA)	1.64 (29.8)	0.22
A_2 (percentage IA)	0.84 (27.2)	0.16
A_3 (percentage IA)	0.49 (43.6)	0.38
λ_1* (1/h)	6.03×10^{-2} (31.3)	0.30
λ_2† (1/h)	9.07×10^{-3} (22.6)	0.08
λ_3‡ (1/h)	7.19×10^{-2} (42.5)	0.52
Intrapatient variability (*a* in Supplemental Eq. 3)	0	0.079

*Biologic clearance rate λ_1 corresponds to half-life of 11.5 h.
†Biologic clearance rate λ_2 corresponds to half-life of 76.4 h.
‡Biologic uptake rate λ_3 corresponds to half-life of 9.63 h.

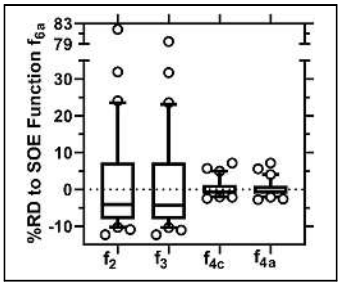

FIGURE 2. RD values of TIAs obtained from ATP fitting using functions f_2, f_3, f_{4a}, and f_{4c} to TIAs obtained from ATP fitting using best function according to PBMS NLME method, that is, f_{6a}. Box plots show median, 25th and 75th percentiles, whiskers at 5th and 95th percentiles, and outliers. Percentage RDs for functions f_{4a} or f_{4c} are relatively small because of marginal contribution of uptake phase. Function f_3 was added for comparison in Figure 2, as this function is often used in the literature (*17,35,39*). For broad range of covered sampling times after injection in population investigated here, single biologic elimination phase (as is also case for f_2) is insufficient.

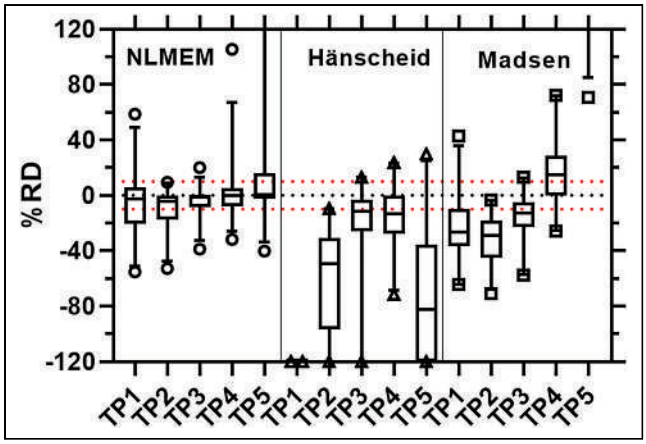

FIGURE 3. RD values of TIAs obtained using PBMS NLME (NLMEM) function f_{6a} (Eq. 8), Hänscheid method (Eq. 14), and Madsen method (Eq. 15) for STP dosimetry at time points 1–5. TIAs from ATP fittings calculated using PBMS NLME function f_{6a} were used as reference values. Box plots show median, 25th and 75th percentiles, whiskers at 2.5th and 97.5th percentiles, and outliers. TP = time point.

It has been shown that STP data at 48 h after injection would lead to a relatively accurate prediction of kidney TIAs for [^{177}Lu]Lu-PSMA (*20*). For [^{177}Lu]Lu-PSMA-I&T therapy, simulation results by Rinscheid et al. showed STP data at around 52 h after injection as the optimal time point for calculating kidney TIAs (*14*). This work identified time points 2 and 3, having a relatively low mean and median RD of absorbed doses (Fig. 3) in our [^{177}Lu]Lu-PSMA-617 dataset. Time point 3 (42.6 ± 1.0 h) was identified as having the lowest RMSE value. Time point 3 in our study for kidneys is consistent with the optimal time point for STP dosimetry reported in the literature (*14,20*).

The percentages of the total number of patients with absolute RDs higher than 10% for STP dosimetry using time points 1–5 were 59% (n = 37), 40% (n = 25), 24% (n = 15), 35% (n = 22), and 38% (n = 24), respectively (Supplemental Table 1). Time point 3 was selected as optimal for STP dosimetry as it has the lowest RMSE and mean RD value. Therefore, PBMS NLME and STP imaging of [^{177}Lu]Lu-PSMA-617 kinetics might be used to determine absorbed doses in kidneys accurately, with only 4 outliers (RDs outside the threshold of mean ± 2 SDs) at time point 3 (Fig. 4).

The fractions of percentage RDs lower than 10% for STP dosimetry at time point 3 using the methods of Hänscheid et al. and Madsen et al. were 0.44 and 0.41, respectively, whereas the best model according to the PBMS NLME approach demonstrated that the fraction of percentage RDs lower than 10% for STP dosimetry at time point 3 was 0.76. This finding aligns with the literature, suggesting that NLME modeling can reduce the number of patients with a percentage RD lower than 10% calculated using the Hänscheid and Madsen methods (*17*). One contributing factor to these results is the use of monoexponential functions (f_2) (*18,23*). The monoexponential function had a lower quality in describing the biokinetic data in our patient population than the best model f_{6a} derived from PBMS NLME (Fig. 2; Supplemental Table 1). The superiority of our method in this study may also be attributed to the different radiopharmaceuticals (including the different functions used) and the different study populations.

In this study, calculation of the absorbed dose was based on the self-dose. The kidney non–self-dose has been reported to contribute up to 10% to the kidney dose for [^{177}Lu]Lu-DOTATATE (*53*). Therefore, further study is needed to investigate how to add the non–self-dose using STP dosimetry with the PBMS NLME method.

NLME modeling uses a population pharmacokinetic approach, wherein instead of individually fitting the data from each individual, all data within the population are simultaneously fitted. The benefit of using NLME models is that they do not require the data to be comprehensive or densely sampled, as is often the case in nonlinear

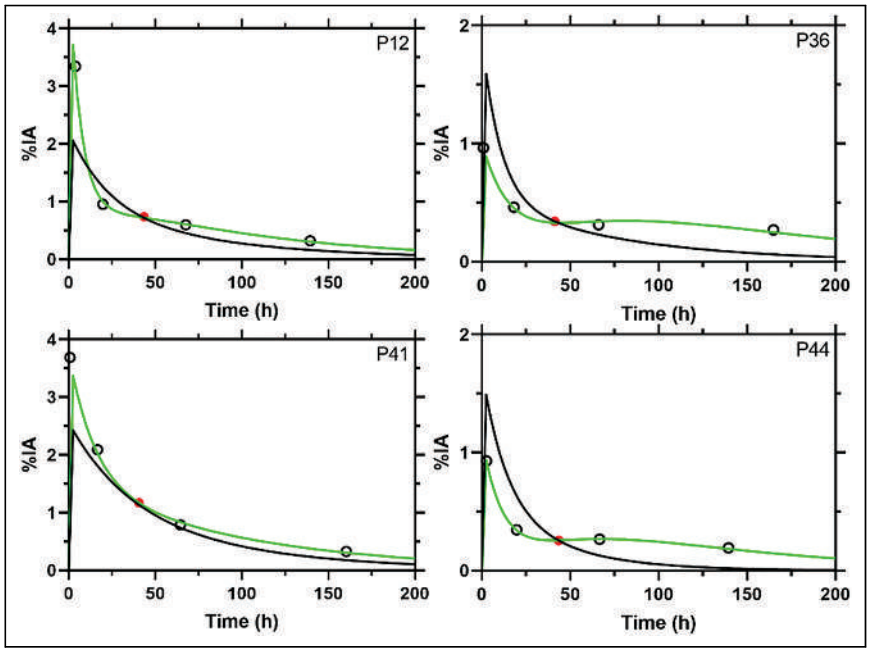

FIGURE 4. Time–activity curves from ATP (green lines) and STP (black lines) fittings at time point 3 simulated with function f_{6a} for 4 outlier patients. Estimated individual parameters indicate that these outliers had lowest biologic clearance λ_2 (4.8×10^{-3}/h to 6.7×10^{-3}/h) in population and were relatively lower than fixed effect (9.1×10^{-3}/h) (Table 2), a well-known behavior in STP dosimetry (*17*). P = patient.

regression analyses with individual data points (*41*). Thus, the reference TIA was computed through population fitting, using a notably higher parameter-to-data ratio within our dataset, specifically 315 data points and 13 parameters (Table 1). In contrast, individual patient fitting using a monoexponential function uses a significantly lower ratio, such as 3 data points and 2 parameters. This results in a higher uncertainty of the resulting TIA.

In a clinical context, for a new radiopharmaceutical or a new patient population, the STP method introduced here plays a crucial role in the following sequence of steps. The first step is to collect biokinetic activity data during therapy from the patient population of interest. The second is to determine the most suitable fit function based on the data using the PBMS NLME method presented here. This will yield the corresponding fixed-effect and random-effect parameters (Table 2). The third is to conduct STP dosimetry for new patients by applying NLME modeling, using the identified optimal function along with the fixed-effect and random-effect parameters determined in step 2.

Thus, for a known radiopharmaceutical and patient population, step 3 is sufficient, as once the data are obtained in step 2, these can be used for STP dosimetries in every center. Therefore, our results can be used for other studies if the radiopharmaceutical and patient populations are equivalent and appropriate image quantification is ensured.

A prerequisite of NLME modeling is the need for a historical cohort with multiple-time-point [^{177}Lu]Lu-PSMA-617 SPECT/CT data (step 1). Because of the reimbursement policies, the availability of posttreatment SPECT/CT imaging is increasing (*17*). Additionally, promoting data exchange among different health care centers, exemplified by the information offered in this publication, can streamline the model development process.

CONCLUSION

In this study, we developed and implemented an STP dosimetry using NLME modeling and PBMS to calculate kidney-absorbed doses of [^{177}Lu]Lu-PSMA-617. Our results show that a single measurement of SPECT/CT at 2 d after injection might be used to calculate accurate kidney-absorbed doses.

KEY POINTS

QUESTION: Can a nonlinear fixed-effects model with PBMS using many biokinetic data covering a broad postinjection time range provide accurate STP-based kidney-absorbed dose estimates for patients treated with [^{177}Lu]Lu-PSMA-617?

PERTINENT FINDINGS: A single measurement of SPECT/CT at 2 d after injection may be used to calculate accurate kidney-absorbed doses using NLME modeling. The mean RD for STP at 2 d was $-4\% \pm 9\%$, with only 24% of the total number of patients having RDs higher than 10% (15/63 patients) and only 10% of the total number of patients having RDs higher than 20% (6/63 patients).

IMPLICATIONS FOR PATIENT CARE: The STP method presented in this study holds great potential to be integrated into routine clinical practice, thereby increasing the acceptance and use of individualized dosimetry, which will benefit patients by predicting related risks.

DISCLOSURE

This work was supported by a PUTI Q1 grant 2023 from Universitas Indonesia (grant NKB-467/UN2.RST/HKP.05.00/2023). No other potential conflict of interest relevant to this article was reported.

REFERENCES

1. Afshar-Oromieh A, Babich JW, Kratochwil C, et al. The rise of PSMA ligands for diagnosis and therapy of prostate cancer. *J Nucl Med.* 2016;57(suppl 3):79S–89S.
2. Ghosh A, Heston WD. Tumor target prostate specific membrane antigen (PSMA) and its regulation in prostate cancer. *J Cell Biochem.* 2004;91:528–539.
3. Violet J, Sandhu S, Iravani A, et al. Long-term follow-up and outcomes of retreatment in an expanded 50-patient single-center phase II prospective trial of ^{177}Lu-PSMA-617 theranostics in metastatic castration-resistant prostate cancer. *J Nucl Med.* 2020;61:857–865.
4. Rahbar K, Ahmadzadehfar H, Kratochwil C, et al. German multicenter study investigating ^{177}Lu-PSMA-617 radioligand therapy in advanced prostate cancer patients. *J Nucl Med.* 2017;58:85–90.
5. Hofman MS, Emmett L, Sandhu S, et al. [^{177}Lu]Lu-PSMA-617 versus cabazitaxel in patients with metastatic castration-resistant prostate cancer (TheraP): a randomised, open-label, phase 2 trial. *Lancet.* 2021;397:797–804.
6. Sartor O, de Bono J, Chi KN, et al. ^{177}Lutetium–PSMA-617 for metastatic castration-resistant prostate cancer. *N Engl J Med.* 2021;385:1091–1103.
7. Kratochwil C, Fendler WP, Eiber M, et al. EANM procedure guidelines for radionuclide therapy with ^{177}Lu-labelled PSMA-ligands (^{177}Lu-PSMA-RLT). *Eur J Nucl Med Mol Imaging.* 2019;46:2536–2544.
8. Mix M, Renaud T, Kind F, et al. Kidney doses in ^{177}Lu-based radioligand therapy in prostate cancer: is dose estimation based on reduced dosimetry measurements feasible? *J Nucl Med.* 2022;63:253–258.
9. Bodei L, Mueller-Brand J, Baum RP, et al. The joint IAEA, EANM, and SNMMI practical guidance on peptide receptor radionuclide therapy (PRRNT) in neuroendocrine tumours. *Eur J Nucl Med Mol Imaging.* 2013;40:800–816.
10. Bolch WE, Eckerman KF, Sgouros G, Thomas SR. MIRD pamphlet no. 21: a generalized schema for radiopharmaceutical dosimetry—standardization of nomenclature. *J Nucl Med.* 2009;50:477–484.
11. Hardiansyah D, Riana A, Beer A, Glatting G. Single-time-point estimation of absorbed doses in PRRT using a non-linear mixed-effects model. *Z Med Phys.* 2023;33:70–81.
12. Zvereva A, Kamp F, Schlattl H, Zankl M, Parodi K. Impact of interpatient variability on organ dose estimates according to MIRD schema: uncertainty and variance-based sensitivity analysis. *Med Phys.* 2018;45:3391–3403.
13. Jackson PA, Hofman MS, Hicks RJ, Scalzo M, Violet JA. Radiation dosimetry in ^{177}Lu-PSMA-617 therapy using a single posttreatment SPECT/CT scan: a novel methodology to generate time- and tissue-specific dose factors. *J Nucl Med.* 2020;61:1030–1036.
14. Rinscheid A, Kletting P, Eiber M, Beer AJ, Glatting G. Influence of sampling schedules on ^{177}Lu-PSMA dosimetry. *EJNMMI Phys.* 2020;7:41.
15. Chicheportiche A, Sason M, Zidan M, et al. Impact of single-time-point estimates of ^{177}Lu-PRRT absorbed doses on patient management: validation of a trained multiple-linear-regression model in 159 patients and 477 therapy cycles. *J Nucl Med.* 2023;64:1610–1616.
16. Wang C, Peterson AB, Wong KK, Roseland ME, Schipper MJ, Dewaraja YK. Single-time-point imaging for dosimetry after [^{177}Lu]Lu-DOTATATE: accuracy of existing methods and novel data-driven models for reducing sensitivity to time-point selection. *J Nucl Med.* 2023;64:1463–1470.
17. Devasia TP, Dewaraja YK, Frey KA, Wong KK, Schipper MJ. A novel time-activity information sharing approach using nonlinear mixed models for patient-specific dosimetry with reduced imaging time points: application in SPECT/CT imaging post ^{177}Lu-DOTATATE. *J Nucl Med.* 2021;62:1118–1125.
18. Hänscheid H, Lapa C, Buck AK, Lassmann M, Werner RA. Dose mapping after endoradiotherapy with ^{177}Lu-DOTATATE/DOTATOC by a single measurement after 4 days. *J Nucl Med.* 2018;59:75–81.
19. Hardiansyah D, Maass C, Attarwala AA, et al. The role of patient-based treatment planning in peptide receptor radionuclide therapy. *Eur J Nucl Med Mol Imaging.* 2016;43:871–880.
20. Hou X, Brosch J, Uribe C, et al. Feasibility of single-time-point dosimetry for radiopharmaceutical therapies. *J Nucl Med.* 2021;62:1006–1011.

21. Maaß C, Sachs JP, Hardiansyah D, Mottaghy FM, Kletting P, Glatting G. Dependence of treatment planning accuracy in peptide receptor radionuclide therapy on the sampling schedule. *EJNMMI Res.* 2016;6:30.
22. Sundlöv A, Gustafsson J, Brolin G, et al. Feasibility of simplifying renal dosimetry in ^{177}Lu peptide receptor radionuclide therapy. *EJNMMI Phys.* 2018;5:12.
23. Madsen MT, Menda Y, O'Dorisio TM, O'Dorisio MS. Technical note: single time point dose estimate for exponential clearance. *Med Phys.* 2018;45:2318–2324.
24. Willowson KP, Eslick E, Ryu H, Poon A, Bernard EJ, Bailey DL. Feasibility and accuracy of single time point imaging for renal dosimetry following ^{177}Lu-DOTATATE ('Lutate') therapy. *EJNMMI Phys.* 2018;5:33.
25. Merrill S, Horowitz J, Traino AC, Chipkin SR, Hollot CV, Chait Y. Accuracy and optimal timing of activity measurements in estimating the absorbed dose of radioiodine in the treatment of Graves' disease. *Phys Med Biol.* 2011;56:557–571.
26. Melgar Pérez J, Orellana Salas A, Santaella Guardiola Y, Antoranz Callejo JC. Improving individualised dosimetry in radioiodine therapy for hyperthyroidism using population biokinetic modelling. *Phys Med.* 2019;62:33–40.
27. Glatting G, Kull T, Blumstein NM, et al. Dosimetry with ^{188}Re-labelled monoclonal anti-CD66 antibodies. A simplified approach based on a single measurement 3 h p.i. *Nuklearmedizin.* 2006;45:134–138.
28. Siebinga H, de Wit-van der Veen BJ, Stokkel MDM, Huitema ADR, Hendrikx J. Current use and future potential of (physiologically based) pharmacokinetic modelling of radiopharmaceuticals: a review. *Theranostics.* 2022;12:7804–7820.
29. Hardiansyah D, Riana A, Beer AJ, Glatting G. Single-time-point dosimetry using model selection and nonlinear mixed-effects modelling: a proof of concept. *EJNMMI Phys.* 2023;10:12.
30. Harzmann S, Garcia-Aviles CA, Nemer U, Ruf J, Meyer P, Mix M. Comparison of dead time behaviour of two SPECT/CT systems for Lu-177. *Nuklearmedizin.* 2016; 55:A68.
31. Kadrmas DJ, Frey EC, Karimi SS, Tsui BM. Fast implementations of reconstruction-based scatter compensation in fully 3D SPECT image reconstruction. *Phys Med Biol.* 1998;43:857–873.
32. Hofheinz F, Pötzsch C, Oehme L, et al. Automatic volume delineation in oncological PET. Evaluation of a dedicated software tool and comparison with manual delineation in clinical data sets. *Nuklearmedizin.* 2012;51:9–16.
33. Kondev FG. Nuclear data sheets for A=177. *Nucl Data Sheets.* 2019;159:1–412.
34. Burnham KP, Anderson DR. *Model Selection and Multimodel Inference: A Practical Information-Theoretic Approach.* Springer-Verlag; 2002:1–48.
35. Kletting P, Schimmel S, Kestler HA, et al. Molecular radiotherapy: the NUKFIT software for calculating the time-integrated activity coefficient. *Med Phys.* 2013; 40:102504.
36. Strand SE, Zanzonico P, Johnson TK. Pharmacokinetic modeling. *Med Phys.* 1993;20:515–527.
37. Ivashchenko OV, O'Doherty J, Hardiansyah D, et al. Time-activity data fitting in molecular radiotherapy: methodology and pitfalls. *Phys Med.* 2024:117:103192.
38. Glatting G, Reske SN. Treatment of radioactive decay in pharmacokinetic modeling: influence on parameter estimation in cardiac ^{13}N-PET. *Med Phys.* 1999;26: 616–621.
39. Hardiansyah D, Riana A, Kletting P, et al. A population-based method to determine the time-integrated activity in molecular radiotherapy. *EJNMMI Phys.* 2021;8:82.
40. Williams LE, Odom-Maryon TL, Liu A, et al. On the correction for radioactive decay in pharmacokinetic modeling. *Med Phys.* 1995;22:1619–1626.
41. Bonate PL. *Pharmacokinetic-Pharmacodynamic Modeling and Simulation.* Springer; 2011:205–265.
42. Mould DR, Upton RN. Basic concepts in population modeling, simulation, and model-based drug development: part 2—introduction to pharmacokinetic modeling methods. *CPT Pharmacometrics Syst Pharmacol.* 2013;2:e38.
43. Hardiansyah D, Riana A, Eiber M, Beer A, Glatting G. Population-based model selection for an accurate estimation of time-integrated activity using non-linear mixed-effects modelling. *Z Med Phys.* February 20, 2023 [Epub ahead of print].
44. Anscombe FJ. Graphs in statistical analysis. *Am Stat.* 1973;27:17–21.
45. Jiménez-Franco LD, Kletting P, Beer AJ, Glatting G. Treatment planning algorithm for peptide receptor radionuclide therapy considering multiple tumor lesions and organs at risk. *Med Phys.* 2018;45:3516–3523.
46. Kletting P, Kull T, Maass C, et al. Optimized peptide amount and activity for ^{90}Y-labeled DOTATATE therapy. *J Nucl Med.* 2016;57:503–508.
47. Kletting P, Muller B, Erentok B, et al. Differences in predicted and actually absorbed doses in peptide receptor radionuclide therapy. *Med Phys.* 2012;39:5708–5717.
48. Kletting P, Glatting G. Model selection for time-activity curves: the corrected Akaike information criterion and the F-test. *Z Med Phys.* 2009;19:200–206.
49. Brosch-Lenz J, Delker A, Völter F, et al. Toward single-time-point image-based dosimetry of ^{177}Lu-PSMA-617 therapy. *J Nucl Med.* 2023;64:767–774.
50. Sandström M, Freedman N, Fröss-Baron K, Kahn T, Sundin A. Kidney dosimetry in 777 patients during ^{177}Lu-DOTATATE therapy: aspects on extrapolations and measurement time points. *EJNMMI Phys.* 2020;7:73.
51. Peterson AB, Mirando DM, Dewaraja YK. Accuracy and uncertainty analysis of reduced time point imaging effect on time-integrated activity for ^{177}Lu-DOTATATE PRRT in patients and clinically realistic simulations. *EJNMMI Res.* 2023; 13:57.
52. Stabin MG, Sparks RB, Crowe E. OLINDA/EXM: the second-generation personal computer software for internal dose assessment in nuclear medicine. *J Nucl Med.* 2005;46:1023–1027.
53. Sandström M, Garske-Román U, Johansson S, Granberg D, Sundin A, Freedman N. Kidney dosimetry during ^{177}Lu-DOTATATE therapy in patients with neuroendocrine tumors: aspects on calculation and tolerance. *Acta Oncol.* 2018;57:516–521.

Radiolabeled Somatostatin Receptor Antagonist Versus Agonist for Peptide Receptor Radionuclide Therapy in Patients with Therapy-Resistant Meningioma: PROMENADE Phase 0 Study

Christopher Eigler[1], Lisa McDougall[1], Andreas Bauman[1], Peter Bernhardt[2], Michael Hentschel[1], Kristine A. Blackham[1], Guillaume Nicolas[1], Melpomeni Fani[1], Damian Wild*[1], and Dominik Cordier*[3]

[1]*Clinic for Radiology and Nuclear Medicine, University Hospital Basel, Basel, Switzerland;* [2]*Department of Medical Radiation Sciences, Institution of Clinical Science, University of Gothenburg, Gothenburg, Sweden; and* [3]*Department of Neurosurgery, University Hospital Basel, Basel, Switzerland*

Our primary aim was to compare the therapeutic index (tumor–to–bone marrow and tumor-to-kidney absorbed-dose ratios) of the new radiolabeled somatostatin receptor antagonist [^{177}Lu]Lu-DOTA-JR11 with the established radiolabeled somatostatin receptor agonist [^{177}Lu]Lu-DOTATOC in the same patients with progressive, standard therapy-refractory meningioma. **Methods:** In this prospective, single-center, open-label phase 0 study (NCT04997317), 6 consecutive patients were included: 3 men and 3 women (mean age, 63.5 y). Patients received 6.9–7.3 GBq (standard injected radioactivity) of [^{177}Lu]Lu-DOTATOC followed by 3.3–4.9 GBq (2 GBq/m^2 × body surface area) of [^{177}Lu]Lu-DOTA-JR11 at an interval of 10 ± 1 wk. In total, 1 [^{177}Lu]Lu-DOTATOC and 2–3 [^{177}Lu]Lu-DOTA-JR11 treatment cycles were performed. Quantitative SPECT/CT was done at approximately 24, 48, and 168 h after injection of both radiopharmaceuticals to calculate meningioma and organ absorbed doses as well as tumor-to-organ absorbed-dose ratios (3-dimensional segmentation approach for meningioma, kidneys, liver, bone marrow, and spleen). **Results:** The median of the meningioma absorbed dose of 1 treatment cycle was 3.4 Gy (range, 0.8–10.2 Gy) for [^{177}Lu]Lu-DOTATOC and 11.5 Gy (range, 4.7–22.7 Gy) for [^{177}Lu]Lu-DOTA-JR11. The median bone marrow and kidney absorbed doses after 1 treatment cycle were 0.11 Gy (range, 0.05–0.17 Gy) and 2.7 Gy (range, 1.3–5.3 Gy) for [^{177}Lu]Lu-DOTATOC and 0.29 Gy (range, 0.16–0.39 Gy) and 3.3 Gy (range, 1.6–5.9 Gy) for [^{177}Lu]Lu-DOTA-JR11, resulting in a 1.4 (range, 0.9–1.9) times higher median tumor–to–bone marrow absorbed-dose ratio and a 2.9 (range, 2.0–4.8) times higher median tumor-to-kidney absorbed-dose ratio with [^{177}Lu]Lu-DOTA-JR11. According to the Common Terminology Criteria for Adverse Events version 5.0, 2 patients developed reversible grade 2 lymphopenia after 1 cycle of [^{177}Lu]Lu-DOTATOC. Afterward, 2 patients developed reversible grade 3 lymphopenia and 1 patient developed reversible grade 3 lymphopenia and neutropenia after 2–3 cycles of [^{177}Lu]Lu-DOTA-JR11. No grade 4 or 5 adverse events were observed at 15 mo or more after the start of therapy. The disease control rate was 83% (95% CI, 53%–100%) at 12 mo or more after inclusion. **Conclusion:** Treatment with 1 cycle of [^{177}Lu]Lu-DOTA-JR11 showed 2.2–5.7 times higher meningioma absorbed doses and a favorable therapeutic index compared with [^{177}Lu]Lu-DOTATOC after injection of 1.4–2.1 times lower activities. The first efficacy results demonstrated a high disease control rate with an acceptable safety profile in the standard therapy for refractory meningioma patients. Therefore, larger studies with [^{177}Lu]Lu-DOTA-JR11 are warranted in meningioma patients.

Key Words: meningioma; peptide receptor radionuclide therapy; DOTA-JR11; DOTATOC

J Nucl Med 2024; 65:573–579
DOI: 10.2967/jnumed.123.266817

Meningiomas are among the intracranial tumors with the highest prevalence. They arise from the dura mater and occur in World Health Organization grades I–III. Sparse improvement in treatment results over recent decades is reflected by a 5-y survival between 55% and 70% (*1*). Surgery, as the main treatment option, is limited in a subgroup of patients because of anatomic involvement of critical neural or vascular structures or a diffuse growth pattern (*2*). Adjuvant external-beam radiotherapy improves recurrence rates (*3*) but may induce neurologic morbidity (*4*).

About 70% of meningiomas express somatostatin receptor subtype 2 (SST2) at a high density, and SST2 acts as a target for peptide receptor radionuclide therapy (*5*). Peptide receptor radionuclide therapy with the SST2 agonists [^{90}Y]Y-DOTATOC, [^{177}Lu]Lu-DOTATOC, and [^{177}Lu]Lu-DOTATATE (Lutathera; Novartis) has been used as second- or third-line therapy for meningiomas that, on the basis of a poor risk–benefit ratio, are not treatable with standard therapies (*6–10*). Gerster-Gilliéron et al. demonstrated a median progression-free survival of 24 mo and a stabilization of the disease in 87% of patients after treatment with 1.7–14.8 GBq of [^{90}Y]Y-DOTATOC (*7*). Because of severe renal toxicity (grades 4 and 5) in about 10% of patients (*11*), [^{90}Y]Y-DOTATOC is hardly used anymore and has been replaced by [^{177}Lu]Lu-DOTATOC and [^{177}Lu]Lu-DOTATATE, which are less toxic to kidneys. Although peptide receptor radionuclide therapy is efficient for the management of World Health Organization grade I and II meningiomas at an advanced stage, it stabilizes the disease for only up to 24 mo (*7,9,12*). Thus, there is an unmet need to develop more effective radiopharmaceuticals to improve the treatment of patients with advanced meningioma.

Until recently, it was assumed that internalization of the radiolabeled agonists was mandatory for somatostatin receptor–targeted

Received Oct. 5, 2023; revision accepted Jan. 5, 2024.
For correspondence or reprints, contact Damian Wild (damian.wild@usb.ch).
*Contributed equally to this work.
Published online Feb. 29, 2024.

therapy. About 20 y ago, Ginj et al. hypothesized that radiolabeled somatostatin receptor antagonists may perform better than agonists despite lacking internalization (*13*). In the meantime, there has been compelling evidence that ^{177}Lu-labeled SST2 antagonists (e.g., [^{177}Lu]Lu-DOTA-JR11, [^{177}Lu]Lu-OPS201, and [^{177}Lu]Lu-satoreotide tetraxetan) bind to many more SST2-binding sites on the cell surface, resulting in higher tumor absorbed doses (*14*). For example, the SST2 antagonist [^{177}Lu]Lu-DOTA-JR11 was superior to the SST2 agonist [^{177}Lu]Lu-DOTATATE in a single-center, prospective first-in-humans phase 0 study with 4 patients who had advanced metastatic neuroendocrine tumors (*15*). The most relevant findings of this study were the 3.5-fold higher median tumor absorbed dose, the more than 2-fold higher tumor–to–bone marrow absorbed-dose ratio with [^{177}Lu]Lu-DOTA-JR11 than with [^{177}Lu]Lu-DOTATATE, and moderate adverse events with 1 grade 3 thrombocytopenia after treatment with 3 cycles of approximately 5 GBq (15.2 GBq total) of [^{177}Lu]Lu-DOTA-JR11.

Therefore, we hypothesized that [^{177}Lu]Lu-DOTA-JR11 would also have a favorable therapeutic index in meningioma patients compared with [^{177}Lu]Lu-DOTATOC. The primary aim was to compare the therapeutic index (tumor–to–bone marrow and tumor-to-kidney absorbed-dose ratios) of the radiolabeled SST2 antagonist [^{177}Lu]Lu-DOTA-JR11 with the established radiolabeled SST2 agonist [^{177}Lu]Lu-DOTATOC in the same patients with progressive meningiomas that were refractory to standard treatment.

MATERIALS AND METHODS

Study Design and Patients

Six consecutive meningioma patients were included for this prospective, phase 0, single-center, open-label, dosimetry comparison study (ClinicalTrials.gov; NCT04997317). The ethics committee of Northwest and Central Switzerland approved this study, and all patients signed an informed consent form. The main inclusion criteria were a histologically confirmed meningioma that was progressive within less than 30 mo before inclusion, a lack of efficient standard treatment (assessment by the local multidisciplinary neurooncologic tumor board), a Karnofsky index of at least 60, a meningioma measurable in 3 dimensions, and confirmed expression of SST2 on [^{68}Ga]Ga-DOTATOC and [^{68}Ga]Ga-DOTATATE PET/CT imaging. The main exclusion criterion was the administration of another therapeutic substance 30 d before or during the ongoing study. Further inclusion and exclusion criteria are provided in the supplemental materials (available at http://jnm.snmjournals.org) (*16–18*).

Preparation of Radiotracers, SPECT/CT Imaging, and Therapy Protocol

DOTA-JR11 (*15*) and DOTATOC were synthesized according to good manufacturing practices established by piChEM GmbH and Bachem AG, respectively. [^{177}Lu]Lu-DOTA-JR11 was produced on an automated synthesis module (Pharmtracer; Eckert & Ziegler Medical). Briefly, 300 μg of DOTA-JR11 were dissolved in sodium acetate and ascorbic acid buffer (pH 4.5) and reacted with 4–6 GBq of no-carrier-added [^{177}Lu]$LuCl_3$ (EndolucinBeta; ITM) at 83°C for 20 min, followed by C18 solid-phase extraction. The final product was formulated in a physiologic saline solution containing ascorbic acid as the radioprotectant, calcium-diethylenetriamine pentaacetate as the radioisotope scavenger, and ethanol as the excipient. Radiochemical purity was assessed by radio–high-performance liquid chromatography and was 95% or better. The incorporation yield was measured by radio–thin-layer chromatography with levels of unbound ^{177}Lu of no more than 0.2%.

[^{177}Lu]Lu-DOTATOC was produced in a kit-labeling procedure by adding 240 μg of DOTATOC dissolved in sodium ascorbate buffer (pH 5) to a vial containing 8 GBq of no-carrier-added [^{177}Lu]Cl_3 and subsequently heating at 95°C for 30 min. The final product was formulated in a physiologic saline solution containing calcium-diethylenetriamine pentaacetate as the radioisotope scavenger. Radiochemical purity was assessed by radio–high-performance liquid chromatography and was 95% or better. The incorporation yield was measured by radio–thin-layer chromatography with levels of unbound ^{177}Lu of no more than 0.5%.

Patients received [^{177}Lu]Lu-DOTATOC (~7.4 GBq) followed by [^{177}Lu]Lu-DOTA-JR11 (2 GBq/m^2 × body surface area) at an interval of about 10 wk. Quantitative SPECT/CT scans were performed at approximately 24, 48, and 168 h after injection of both compounds using a Symbia Intevo 16 system (Siemens Healthineers) equipped with a medium-energy, low-penetration collimator (supplemental materials).

Meningioma Volumetry and Treatment Response Evaluation with MRI

All external and internal MRI studies were viewed with our institution's PACS, and the T1-weighted postcontrast 3-dimensional sequences were uploaded to mint Lesion software (Mint Medical GmbH). Meningioma volumetry was measured by a U.S. board-certified neuroradiologist with 20 y of experience. Meningioma response assessment was determined by comparison with the inclusion MRI study: progressive disease was defined as at least a 40% increase of meningioma volume or the appearance of new lesions, and stable disease was defined as less than a 40% increase in volume (*19*).

Dosimetry

All meningioma volumetry was based on MRI segmentation. The volume of kidneys, liver, bone marrow (red marrow), and spleen was determined by segmentation of CT images acquired from posttherapy SPECT/CT scans. The number of disintegrations and the absorbed doses were calculated with OLINDA 1.0 (Hermes Medical Solutions). The phantom organ weight was adjusted to the patient organ weight for kidneys, liver, and spleen. The meningioma absorbed dose was calculated using the spheres model in OLINDA. The red marrow activity was determined by drawing 4-mL volumes of interest in each vertebra from T2 to L5 for each time point. If needed, the volume of interest was adjusted to include only the bone marrow and no cortical bone, as the uptake in the vertebrae was assumed to be in the red marrow compartment of the cancellous bone. The red marrow compartment of the ilium was segmented as visible in the CT images. The red marrow absorbed dose was calculated by multiplying the absorbed energy from a ^{177}Lu decay by the time-integrated activity concentration in the red marrow. More details are available in the supplemental materials.

Toxicity

To reduce the risk of nephrotoxicity, the patients received a continuous infusion of 1,000 mL of physiologic NaCl solution containing 20.0 mg/mL of lysine and 20.7 mg/mL of arginine over 5 h (*15*). One hour after the start of this infusion, [^{177}Lu]Lu-DOTATOC or [^{177}Lu]Lu-DOTA-JR11 was infused over 1 min or 2 h, respectively. Two hours of slow infusion of [^{177}Lu]Lu-DOTA-JR11 was well tolerated without relevant nausea and hypotension as found in a previous study (*20*). Vital parameters (blood pressure, heart frequency, and oxygen saturation) were monitored every 15 min during the 2-h infusion of [^{177}Lu]Lu-DOTA-JR11. A full blood count and a comprehensive metabolic panel were performed on the day of each therapy cycle as well as 2, 4, and 6 wk after treatment. Common Terminology Criteria for Adverse Events version 5.0 was used to evaluate possible negative effects.

TABLE 1
Summary of Patient Characteristics, Treatment Protocol, Remission Status, and Adverse Events

Parameter	Patient 1	Patient 2	Patient 3	Patient 4	Patient 5	Patient 6
Baseline characteristics						
Sex	Male	Female	Male	Male	Female	Female
Age (y)	52	58	83	73	75	39
Meningioma WHO grade	III	II	II	II	II	I
First diagnosed (mo before inclusion)	20	89	192	60	60	96
Previous therapy						
Last surgical treatment (mo before inclusion)	8	64	31	7	59	83
Last radiation therapy (mo before inclusion)	16	ND	13	54	55	54
Last systemic treatment (mo before inclusion)	1	ND	ND	ND	ND	ND
Treatment protocol						
[^{177}Lu]Lu-DOTATOC therapy						
Number of cycles	1	1	1	1	1	1
Total injected activity (GBq)	7.1	7.1	6.9	7.3	7.3	7.0
[^{177}Lu]Lu-DOTA-JR11 therapy						
Injected activity at first cycle (GBq)	4.5	4.9	3.3	4.0	4.1	3.7
Number of cycles	2	2	2	3	3	2
Total injected activity (GBq)	9.0	8.9	7.4	11.6	10.4	7.1
Remission status*						
Remission status before inclusion	PD	PD	PD	PD	PD	PD
Progression interval before inclusion (mo)	4	27	27	4	23	5
Meningioma volume change before inclusion (%)	+8,280	+45	+88	+50	+40	+61
Remission status after maximum follow-up	PD	SD	SD	SD	SD	SD
Additional treatments after inclusion†	Yes	Yes	No	No	No	No
Maximum follow-up after inclusion (mo)	15	22	16	15	17	12
Meningioma volume change at maximum follow-up (%)	+778	+9	+31	+19	0	−3
Adverse events (grade)						
Up to 10 wk after [^{177}Lu]Lu-DOTATOC						
Anemia	0	0	0	0	0	0
Neutropenia	0	0	0	0	0	0
Lymphopenia	0	2	0	0	1	2
Thrombocytopenia	0	0	0	0	0	0
Up to 10 wk after first cycle of [^{177}Lu]Lu-DOTA-JR11						
Anemia	0	0	0	0	0	0
Neutropenia	0	0	0	0	3	0
Lymphopenia	0	2	0	0	2	3
Thrombocytopenia	0	0	0	0	0	0
Up to 13 mo after first cycle of [^{177}Lu]Lu-DOTA-JR11						
Anemia	0	0	0	0	0	0
Neutropenia	0	0	0	0	0	2
Lymphopenia	0	3	0	0	3	3
Thrombocytopenia	0	0	0	0	0	0

*Remission status of meningiomas assessed with MRI volumetry.

†Patient 1 received high-dose chemotherapy with ifosamid 7 mo after termination of [^{177}Lu]Lu-DOTA-JR11 therapy followed by therapy with mitogen-activated extracellular signal-regulated kinase inhibitor (cobimetinib). Patient 2 was treated with humanized monoclonal antibody (bevacizumab) 6 mo after termination of [-Lu]Lu-DOTA-JR11 therapy.

ND = not done; PD = progressive disease; SD = stable disease.

TABLE 2
Summary of Tumor Radiation Dose Estimations

	[^{177}Lu]Lu-DOTATOC, 1 cycle*				[^{177}Lu]Lu-DOTA-JR11, 1 cycle†				2–3 cycles†
Patient	Meningioma dose (Gy/cycle)	Red marrow dose (Gy/cycle)	T/BM	T/K	Meningioma dose (Gy/cycle)	Red marrow dose (Gy/cycle)	T/BM ratio	T/K ratio	Meningioma dose (Gy)
1	0.8	0.05	16	0.6	4.7	0.16	30	3.0	9.5
2	1.9	0.10	19	0.6	8.4	0.31	27	1.8	15.3
3	4.4	0.15	28	1.5	14.5	0.27	54	4.6	32.3
4	5.0	0.17	30	0.9	15.0	0.39	38	2.5	43.4
5	10.2	0.13	78	4.0	22.7	0.34	66	8.1	57.7
6	2.5	0.08	29	1.0	7.1	0.24	30	2.0	13.5
Median	3.4	0.11	29	1.0	11.5	0.29	34	2.8	23.8
Range	0.8–10.2	0.05–0.17	16–78	0.6–4.0	4.7–22.7	0.16–0.39	25–66	1.8–8.1	9.5–57.7

*First therapy cycle was performed with 7.4 GBq ± 10% [^{177}Lu]Lu-DOTATOC.
†All [^{177}Lu]Lu-DOTA-JR11 therapy cycles were conducted with 2 GBq × body surface area ± 10% per cycle.
T/BM = tumor-to-red bone marrow ratio; T/K = tumor-to-kidney ratio.

Statistical Analysis

For this phase 0 study, no sample size calculation was performed. All data were summarized using descriptive statistics. Unless otherwise stated, all data are expressed as median with range.

RESULTS

Dosimetry Results and Response

In total, 7 patients were recruited between May 2021 and March 2022. The first patient without histologic proof of a meningioma did not meet the inclusion criteria. Therefore, 6 patients received 1 cycle of [^{177}Lu]Lu-DOTATOC at an activity of 6.9–7.3 GBq (peptide amount, ~190 μg) followed by 1 cycle of [^{177}Lu]Lu-DOTA-JR11 at an activity of 3.3–4.9 GBq (peptide amount, ~240 μg) at an interval of 10 ± 1 wk. Afterward, additional [^{177}Lu]Lu-DOTA-JR11 treatment cycles were performed according to clinical needs (patient characteristics and treatment protocol in Table 1). Table 2 shows the results of tumor and bone marrow absorbed-dose estimations as well as tumor–to–bone marrow and tumor-to-kidney absorbed-dose ratios for all 6 patients. The effective tumor half-life was considerably higher with [^{177}Lu]Lu-DOTA-JR11 (half-life, 71.7 h; range, 56.4–87.0 h) than with [^{177}Lu]Lu-DOTATOC (half-life, 51.7 h; range, 49.2–64.2 h). Furthermore, the median tumor–to–bone marrow absorbed-dose ratio was 1.4 (range, 0.9–1.9) times higher with [^{177}Lu]Lu-DOTA-JR11. Only 1 of 6 patients showed a slightly lower tumor–to–bone marrow absorbed-dose ratio with [^{177}Lu]Lu-DOTA-JR11 than with [^{177}Lu]Lu-DOTATOC. Absorbed-dose estimations for most relevant organs with [^{177}Lu]Lu-DOTATOC and [^{177}Lu]Lu-DOTA-JR11 are summarized in Supplemental Table 1. In correlation with the dosimetry results, quantitative posttreatment SPECT scans showed more pronounced accumulation in meningioma lesions and in the bone marrow with [^{177}Lu]Lu-DOTA-JR11 than with [^{177}Lu]Lu-DOTATOC. Figure 1 shows the maximum-intensity projection SPECT images of all patients. Because of the favorable dosimetry results for the SST2 antagonist, 1–2 additional treatment cycles were performed with [^{177}Lu]Lu-DOTA-JR11, resulting in a disease control rate of 83% (95% CI, 53%–100%) at least 12 mo after inclusion. Remission status is provided in Table 2. Figure 2 shows the treatment response of patient 4.

Toxicity

All adverse events are summarized in Table 1. There was no nausea, vomiting, or hypotension after injection of either compound. In all patients, the reported adverse events resolved after a few weeks and there were no grade 4 or 5 adverse events. Up to 13 mo after the first therapy cycle with [^{177}Lu]Lu-DOTA-JR11, there was no worsening of kidney function and no evidence for myelodysplastic syndrome or other neoplasms.

DISCUSSION

The main results of this study can be summarized as follows. First, although [^{177}Lu]Lu-DOTA-JR11 therapy was performed with 1.4–2.1 times lower activity, the meningioma absorbed dose per treatment cycle was 2.2–5.7 times higher than that with [^{177}Lu]Lu-DOTATOC, resulting in promising efficacy results (disease control rate of 83% at ≥12 mo) in these therapy-resistant meningioma patients. Second, the therapeutic index indicates that [^{177}Lu]Lu-DOTA-JR11 is favorable for the treatment of meningioma patients because the tumor–to–bone marrow and tumor-to-kidney absorbed-dose ratios are 0.9–1.9 and 2.0–4.8 times higher with [^{177}Lu]Lu-DOTA-JR11 than with [^{177}Lu]Lu-DOTATOC. Third, renal toxicity is expected to be negligible with [^{177}Lu]Lu-DOTA-JR11 because of the several times higher tumor-to-kidney absorbed-dose ratios; in fact, there was no observed renal toxicity for up to 13 mo after the start of [^{177}Lu]Lu-DOTA-JR11 therapy. Lastly, although the estimated absorbed bone marrow dose was 1.7–3.1 times higher with [^{177}Lu]Lu-DOTA-JR11 than with [^{177}Lu]Lu-DOTATOC, bone marrow toxicity was only moderate, with reversible grade 3 lymphopenia and neutropenia, respectively, in 33% of patients after treatment with 1 cycle of [^{177}Lu]Lu-DOTATOC and 2 or 3 cycles of [^{177}Lu]Lu-DOTA-JR11.

These observations give rise to the expectation that the higher meningioma absorbed dose delivered by [^{177}Lu]Lu-DOTA-JR11

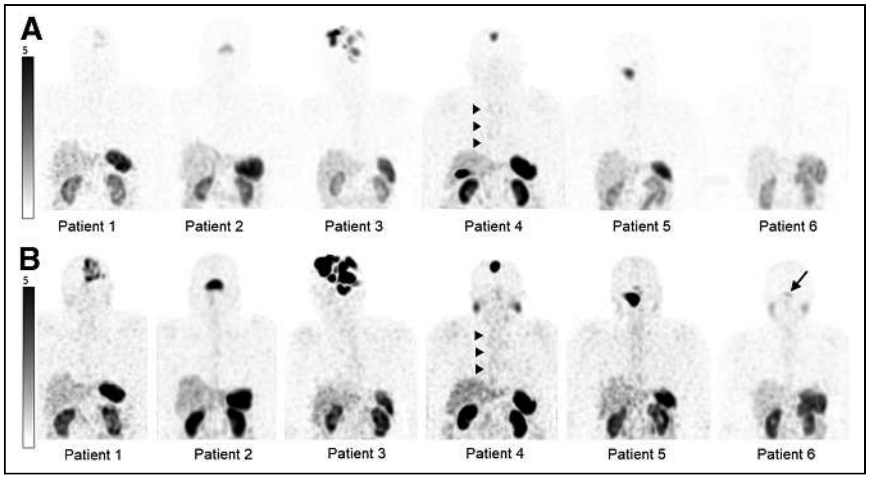

FIGURE 1. Posttreatment maximum-intensity projection of quantitative SPECT images acquired 48 h after injection of [^{177}Lu]Lu-DOTATOC (A) and [^{177}Lu]Lu-DOTA-JR11 (B) in same patients 10 ± 1 wk apart. SUV window threshold was set at 5 for all images, and scales indicate SUVs. In all patients, bone marrow uptake in spine was more pronounced with [^{177}Lu]Lu-DOTA-JR11 than with [^{177}Lu]Lu-DOTATOC (arrowheads in patient 4). In patient 6, small meningioma with volume of 0.3 cm^3 was visible only in posttreatment [^{177}Lu]Lu-DOTA-JR11 SPECT image (arrow).

may result in higher tumor control rates, at least in advanced World Health Organization grade I and II meningiomas. Unlike [^{90}Y]Y-DOTATOC, in which the maximum injected activity was limited by renal or hematologic adverse effects, [^{177}Lu]Lu-DOTA-JR11 is likely to overcome renal toxicity and, furthermore, may improve the bone marrow toxicity profile by enabling higher meningioma doses at a lower injected activity than is possible with [^{177}Lu]Lu-DOTATOC. [^{177}Lu]Lu-DOTA-JR11 administered at less than 5 GBq (2 GBq/m^2 × body surface area) per cycle for 3 cycles appears to offer additional advantages such as reduction of radioactive waste and radionuclide costs.

Nevertheless, bone marrow toxicity remains the dose-limiting adverse effect for the application of [^{177}Lu]Lu-DOTA-JR11 and other radiolabeled SST2 antagonists. This is of particular importance because there is no established bone marrow protection strategy. According to current clinical data, SST2 antagonists such as [^{177}Lu]Lu-DOTA-JR11 and [^{177}Lu]Lu-DOTA-LM3 have induced grade 3 or worse hematologic toxicity (according to the Common Terminology Criteria for Adverse Events) in 20%–23% of patients (*20,21*), which was more than the 9%–13% toxicity induced by [^{177}Lu]Lu-DOTATATE (NETTER-1 study) or [^{90}Y]Y-DOTATOC (*11,22*). For example, Reidy-Lagunes et al. described grade 4 hematotoxicity (leukopenia, neutropenia, and thrombocytopenia) in 4 of the first 7 patients with neuroendocrine tumors treated with 2 cycles of approximately 7.4 GBq (50–100 μg) of [^{177}Lu]Lu-DOTA-JR11 (cumulative radioactivity between 10.5 and 15.0 GBq) (*21*). Hence, their single-center phase I study was suspended, and the protocol was modified to limit the cumulative absorbed bone marrow dose. Importantly, there is evidence that a subpopulation of the hematopoietic cells, especially CD34-positive stem cells, shows some SST2 expression in red marrow (*23*). This is likely the reason for the more pronounced hematotoxicity of [^{177}Lu]Lu-DOTA-JR11 and [^{177}Lu]Lu-DOTA-LM3, as both compounds exhibit an SST2 binding capacity higher than that of [^{177}Lu]Lu-DOTATOC and [^{177}Lu]Lu-DOTATATE (*24*). Furthermore, SPECT images (Fig. 1) of our study show higher accumulation of [^{177}Lu]Lu-DOTA-JR11 than of [^{177}Lu]Lu-DOTATOC in the bone marrow, further supporting the evidence of a more pronounced SST2-mediated accumulation of [^{177}Lu]Lu-DOTA-JR11 in hematopoietic cells. Consequently, blood-based bone marrow dosimetry of SST2-targeting radioligands should be replaced by imaging-based bone marrow dosimetry because the former does not consider specific accumulation of radioligands in red bone marrow (*25*). The only limitation of imaging-based bone marrow dosimetry might be the presence of bone metastases, which is not relevant to meningioma.

One reason for the lower hematologic toxicity in our study than in the 2 other clinical [^{177}Lu]Lu-DOTA-JR11 studies (*20,21*) could be that the injected activities of [^{177}Lu]Lu-DOTA-JR11 in our study were adapted to the body surface area and were generally lower (2.9–4.9 GBq per cycle) than in the 2 other studies (~4.5 and 6.2–7.9 GBq

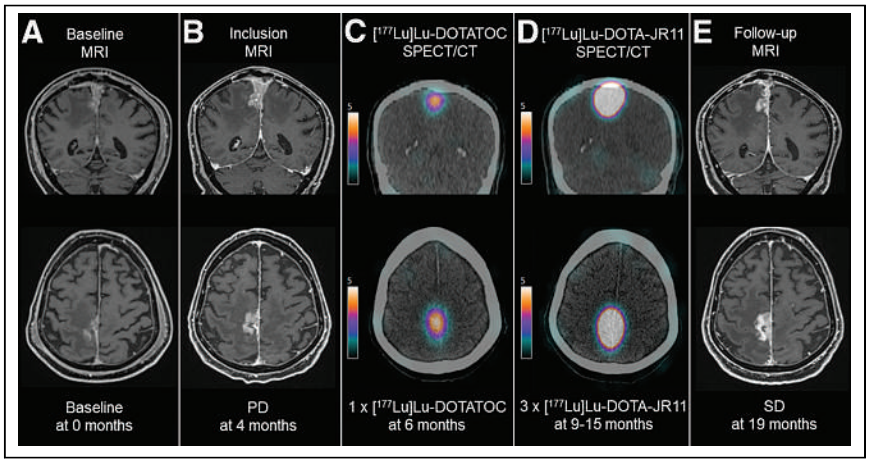

FIGURE 2. Patient 4 with therapy-resistant World Health Organization grade II meningioma. Baseline MRI (A) at 0 mo, inclusion MRI (B) 4 mo after baseline, [^{177}Lu]Lu-DOTATOC SPECT/CT (C) 6 mo after treatment, and [^{177}Lu]Lu-DOTA-JR11 SPECT/CT (D) 9 mo after treatment are shown. Follow-up MRI (E) was performed 19 mo after baseline MRI. Top row shows corresponding coronal images, and bottom row shows corresponding axial images. All MRI examinations were contrast-enhanced T1-weighted volumetric interpolated breath-hold examination sequences, and SPECT/CT scans were acquired 48 h after injection of 7.3 GBq of [^{177}Lu]Lu-DOTATOC and 4.0 GBq of [^{177}Lu]Lu-DOTA-JR11. SUV window threshold was set at 5 for all SPECT images. Patient had progressive disease (PD) with 50% meningioma volume increase within 4 mo at time of inclusion and received 1 cycle of [^{177}Lu]Lu-DOTATOC and 3 cycles of [^{177}Lu]Lu-DOTA-JR11. Follow-up MRI 15 mo after inclusion indicated stable disease (SD) with only 19% meningioma volume increase in comparison to inclusion MRI.

per cycle), resulting in a maximum bone marrow absorbed dose of 0.39 Gy per cycle and 1.13 Gy in total. Another possibility is that the injected amount of DOTA-JR11 (peptide amount) per cycle was approximately 240 μg, resulting in specific activities of between 26 and 35 GBq/μmol for [^{177}Lu]Lu-DOTA-JR11, 4–10 times lower than in the study of Reidy-Lagunes et al. This could be relevant for bone marrow protection, as a lower specific activity (lower ratio of radioactive to nonradioactive compound) causes better saturation of SST2-expressing CD34-positive stem cells, which account for only approximately 2% of total bone marrow cells. In fact, the mean bone marrow absorbed dose and absorbed dose in other SST2-positive organs were lower in our study than in the study of Reidy-Lagunes et al.: the bone marrow dose was 0.07 Gy/GBq (0.04–0.10) versus 0.09 Gy/GBq (0.06–0.15), respectively. Of note, the comparability of dosimetry results is limited by differences in equipment and calculation. Nevertheless, in a preclinical study, Nicolas et al. showed a decrease of bone marrow absorbed dose and absorbed dose in other SST2-positive organs after injection of [^{177}Lu]Lu-DOTA-JR11 at a lower specific activity (*26*). Future clinical studies will be necessary to confirm the protective effect of a lower specific activity to the bone marrow. However, our study showed that 2 or 3 cycles of [^{177}Lu]Lu-DOTA-JR11 with an injected radioactivity of 2 GBq/m^2 times the body surface area and a peptide amount of approximately 240 μg seem to be safe in not only meningioma patients but also other patients (e.g., neuroendocrine tumor patients) who qualify for the treatment with [^{177}Lu]Lu-DOTA-JR11 (*24*).

Previous results with radiolabeled somatostatin receptor agonists demonstrate feasibility and tolerance in the setting of ineffective external-beam radiotherapy followed by radiolabeled SST2 agonists (*27*); however, with the higher doses delivered by radiolabeled SST2 antagonists, the question of tolerance and feasibility should be addressed again.

One main limitation to this study is the application of therapeutic amounts of [^{177}Lu]Lu-DOTATOC and then [^{177}Lu]Lu-DOTA-JR11 10 wk later without using a crossover study design, resulting in a potential carry-over effect (treatment effect) from the first treatment with [^{177}Lu]Lu-DOTATOC onto the [^{177}Lu]Lu-DOTA-JR11 biodistribution. Thus, the dosimetry calculation could reflect a falsely lower meningioma absorbed-dose estimation of [^{177}Lu]Lu-DOTA-JR11. However, the risk for such a carry-over effect is low because the meningioma maximum absorbed dose was only 10.2 Gy with [^{177}Lu]Lu-DOTATOC. A second limitation is the small phase 0 study design that, nevertheless, produced direct comparison data with only 6 patients.

CONCLUSION

This phase 0 study provides, to our knowledge, the first clinical evidence that radiolabeled SST2 antagonists such as [^{177}Lu]Lu-DOTA-JR11 exhibit, in meningiomas, absorbed doses higher than those of standard peptide receptor radionuclide therapy with [^{177}Lu]Lu-DOTATOC despite application of lower activities. Furthermore, SPECT imaging indicates higher accumulation of [^{177}Lu]Lu-DOTA-JR11 than of [^{177}Lu]Lu-DOTATOC in the dose-limiting bone marrow, resulting in higher bone marrow absorbed doses with [^{177}Lu]Lu-DOTA-JR11. At the same time, a favorable therapeutic index was observed with [^{177}Lu]Lu-DOTA-JR11 without relevant hematologic toxicity. Preliminary data on disease control rates are encouraging and support a possible therapeutic role for radiolabeled SST2 antagonists in the treatment of otherwise therapy-refractory meningiomas. Further evaluation of [^{177}Lu]Lu-DOTA-JR11 in meningioma patients is planned in a PROMENADE phase I/II study (ClinicalTrials.gov; NCT04997317).

DISCLOSURE

The study was supported by Swiss Cancer Research foundation (KFS-3712-08-2015), which had no role in the conduct of the study. Peter Bernhardt received funding from the Swedish Cancer Society, the Jubilee Clinic Cancer Research Foundation, and the ALF agreement. No other potential conflict of interest relevant to this article was reported.

ACKNOWLEDGMENTS

We thank Virginie Wersinger and Sujeanthraa Thanabalasingam for excellent assistance.

KEY POINTS

QUESTION: Is the therapeutic index (tumor–to–bone marrow and tumor-to-kidney absorbed-dose ratios) of the SST2 antagonist [^{177}Lu]Lu-DOTA-JR11 superior to that of the established radiolabeled SST2 agonist [^{177}Lu]Lu-DOTATOC in standard therapy-resistant meningioma?

PERTINENT FINDINGS: In this single-center, phase 0 study, [^{177}Lu]Lu-DOTA-JR11 showed much higher meningioma absorbed doses despite application of lower activities in all 6 patients. At the same time, a favorable therapeutic index and no relevant hematologic toxicity were observed after body surface area–based dosing of [^{177}Lu]Lu-DOTA-JR11.

IMPLICATIONS FOR PATIENT CARE: For the treatment of meningioma, [^{177}Lu]Lu-DOTA-JR11 is a promising and safe radiopharmaceutical that needs further clinical evaluation.

REFERENCES

1. Saraf S, McCarthy BJ, Villano JL. Update on meningiomas. *Oncologist.* 2011;16:1604–1613.
2. Schneider M, Schuss P, Guresir A, et al. Cranial nerve outcomes after surgery for frontal skull base meningiomas: the eternal quest of the maximum-safe resection with the lowest morbidity. *World Neurosurg.* 2019;125:e790–e796.
3. Bagshaw HP, Burt LM, Jensen RL, et al. Adjuvant radiotherapy for atypical meningiomas. *J Neurosurg.* 2017;126:1822–1828.
4. Mathiesen T, Kihlstrom L, Karlsson B, et al. Potential complications following radiotherapy for meningiomas. *Surg Neurol.* 2003;60:193–200.
5. Schulz S, Pauli SU, Schulz S, et al. Immunohistochemical determination of five somatostatin receptors in meningioma reveals frequent overexpression of somatostatin receptor subtype sst2A. *Clin Cancer Res.* 2000;6:1865–1874.
6. Bartolomei M, Bodei L, De Cicco C, et al. Peptide receptor radionuclide therapy with ^{90}Y-DOTATOC in recurrent meningioma. *Eur J Nucl Med Mol Imaging.* 2009;36:1407–1416.
7. Gerster-Gilliéron K, Forrer F, Maecke H, et al. ^{90}Y-DOTATOC as a therapeutic option for complex recurrent or progressive meningiomas. *J Nucl Med.* 2015;56:1748–1751.
8. Marincek N, Radojewski P, Dumont RA, et al. Somatostatin receptor-targeted radiopeptide therapy with ^{90}Y-DOTATOC and ^{177}Lu-DOTATOC in progressive meningioma: long-term results of a phase II clinical trial. *J Nucl Med.* 2015;56:171–176.
9. Kurz S, Zan E, Cordova C, et al. CTN1-57. Radionuclide therapy with ^{177}Lu-DOTATATE (Lutathera) in adults with advanced intracranial meningioma: interim analysis results of a single-arm, open-label, multicenter phase II study. *Neuro Oncol.* 2022;24(suppl 7):vii85.
10. Mirian C, Duun-Henriksen AK, Maier A, et al. Somatostatin receptor-targeted radiopeptide therapy in treatment-refractory meningioma: individual patient data meta-analysis. *J Nucl Med.* 2021;62:507–513.

11. Imhof A, Brunner P, Marincek N, et al. Response, survival, and long-term toxicity after therapy with the radiolabeled somatostatin analogue [^{90}Y-DOTA]-TOC in metastasized neuroendocrine cancers. *J Clin Oncol.* 2011;29:2416–2423.
12. Fodi CK, Schittenhelm J, Honegger J, et al. The current role of peptide receptor radionuclide therapy in meningiomas. *J Clin Med.* 2022;11:2364.
13. Ginj M, Zhang H, Waser B, et al. Radiolabeled somatostatin receptor antagonists are preferable to agonists for in vivo peptide receptor targeting of tumors. *Proc Natl Acad Sci USA.* 2006;103:16436–16441.
14. Mansi R, Plas P, Vauquelin G, et al. Distinct in vitro binding profile of the somatostatin receptor subtype 2 antagonist [^{177}Lu]Lu-OPS201 compared to the agonist [^{177}Lu]Lu-DOTA-TATE. *Pharmaceuticals (Basel).* 2021;14:1265.
15. Wild D, Fani M, Fischer R, et al. Comparison of somatostatin receptor agonist and antagonist for peptide receptor radionuclide therapy: a pilot study. *J Nucl Med.* 2014;55:1248–1252.
16. Tran-Gia J, Lassmann M. Characterization of noise and resolution for quantitative ^{177}Lu SPECT/CT with xSPECT Quant. *J Nucl Med.* 2019;60:50–59.
17. Hough M, Johnson P, Rajon D, et al. An image-based skeletal dosimetry model for the ICRP reference adult male: internal electron sources. *Phys Med Biol.* 2011;56:2309–2346.
18. Eckerman K, Endo A. ICRP publication 107. Nuclear decay data for dosimetric calculations. *Ann ICRP.* 2008;38:7–96.
19. Huang RY, Unadkat P, Bi WL, et al. Response assessment of meningioma: 1D, 2D, and volumetric criteria for treatment response and tumor progression. *Neuro Oncol.* 2019;21:234–241.
20. Wild D, Gronbaek H, Navalkissoor S, et al. A phase I/II study of the safety and efficacy of [^{177}Lu]Lu-satoreotide tetraxetan in advanced somatostatin receptor-positive neuroendocrine tumours. *Eur J Nucl Med Mol Imaging.* 2023;51:183–195.
21. Reidy-Lagunes D, Pandit-Taskar N, O'Donoghue JA, et al. Phase I trial of well-differentiated neuroendocrine tumors (NETs) with radiolabeled somatostatin antagonist ^{177}Lu-satoreotide tetraxetan. *Clin Cancer Res.* 2019;25:6939–6947.
22. Strosberg J, El-Haddad G, Wolin E, et al. Phase 3 trial of ^{177}Lu-Dotatate for midgut neuroendocrine tumors. *N Engl J Med.* 2017;376:125–135.
23. Oomen SP, van Hennik PB, Antonissen C, et al. Somatostatin is a selective chemoattractant for primitive (CD34^{+}) hematopoietic progenitor cells. *Exp Hematol.* 2002;30:116–125.
24. Fani M, Mansi R, Nicolas GP, et al. Radiolabeled somatostatin analogs: a continuously evolving class of radiopharmaceuticals. *Cancers (Basel).* 2022;14:1172.
25. Hemmingsson J, Svensson J, Hallqvist A, et al. Specific uptake in the bone marrow causes high absorbed red marrow doses during [^{177}Lu]Lu-DOTATATE treatment. *J Nucl Med.* 2023;64:1456–1462.
26. Nicolas GP, Mansi R, McDougall L, et al. Biodistribution, pharmacokinetics, and dosimetry of ^{177}Lu-, ^{90}Y-, and ^{111}In-labeled somatostatin receptor antagonist OPS201 in comparison to the agonist ^{177}Lu-DOTATATE: the mass effect. *J Nucl Med.* 2017;58:1435–1441.
27. Kreissl MC, Hanscheid H, Lohr M, et al. Combination of peptide receptor radionuclide therapy with fractionated external beam radiotherapy for treatment of advanced symptomatic meningioma. *Radiat Oncol.* 2012;7:99.

Interrogating the Theranostic Capacity of a MUC16-Targeted Antibody for Ovarian Cancer

Kyeara N. Mack[1,2], Zachary V. Samuels[1], Lukas M. Carter[1], Tara D. Viray[1], Komal Mandleywala[1], Cory L. Brooks[3], Michael A. Hollingsworth[4], Prakash Radhakrishnan[4], and Jason S. Lewis[1,2,5]

[1]Department of Radiology, Memorial Sloan Kettering Cancer Center, New York, New York; [2]Department of Pharmacology, Weill Cornell Graduate School of Medical Sciences, Weill Cornell Medicine, New York, New York; [3]Department of Chemistry and Biochemistry, California State University, Fresno, California; [4]Eppley Institute for Research in Cancer and Allied Diseases, University of Nebraska Medical Center, Omaha, Nebraska; and [5]Molecular Pharmacology Program, Memorial Sloan Kettering Cancer Center, New York, New York

Aberrantly expressed glycans on mucins such as mucin-16 (MUC16) are implicated in the biology that promotes ovarian cancer (OC) malignancy. Here, we investigated the theranostic potential of a humanized antibody, huAR9.6, targeting fully glycosylated and hypoglycosylated MUC16 isoforms. **Methods:** In vitro and in vivo targeting of the diagnostic radiotracer [^{89}Zr]Zr-DFO-huAR9.6 was investigated via binding experiments, immuno-PET imaging, and biodistribution studies on OC mouse models. Ovarian xenografts were used to determine the safety and efficacy of the therapeutic version, [^{177}Lu]Lu-CHX-A″-DTPA-huAR9.6. **Results:** In vivo uptake of [^{89}Zr]Zr-DFO-huAR9.6 supported in vitro–determined expression levels: high uptake in OVCAR3 and OVCAR4 tumors, low uptake in OVCAR5 tumors, and no uptake in OVCAR8 tumors. Accordingly, [^{177}Lu]Lu-CHX-A″-DTPA-huAR9.6 displayed strong antitumor effects in the OVCAR3 model and improved overall survival in the OVCAR3 and OVCAR5 models in comparison to the saline control. Hematologic toxicity was transient in both models. **Conclusion:** PET imaging of OC xenografts showed that [^{89}Zr]Zr-DFO-huAR9.6 delineated MUC16 expression levels, which correlated with in vitro results. Additionally, we showed that [^{177}Lu]Lu-CHX-A″-DTPA-huAR9.6 displayed strong antitumor effects in highly MUC16-expressing tumors. These findings demonstrate great potential for ^{89}Zr- and ^{177}Lu-labeled huAR9.6 as theranostic tools for the diagnosis and treatment of OC.

Key Words: PET imaging; radioimmunotherapy; MUC16; huAR9.6; ovarian cancer

J Nucl Med 2024; 65:580–585
DOI: 10.2967/jnumed.123.266524

Ovarian cancer (OC) causes more deaths than any other gynecologic malignancy, with a 5-y survival rate below 30% for patients diagnosed at advanced stages (*1*,*2*). The current standard of care for OC consists of surgery followed by platinum-based chemotherapy; however, these methods have failed to increase overall survival rates in patients because of tumor recurrence and chemoresistance (*2*,*3*). Cancer antigen 125 (CA125)—an epitope on mucin-16 (MUC16)—is a common and widely used serum biomarker for OC diagnosis. However, serum CA125 levels do not sufficiently detect all occurrences of early-stage disease (*4*). Therefore, there is a critical need for both additional detection methods and new targeted therapies that can improve patient survival.

Among the factors contributing to the lethality of OC is the aberrant glycosylation of carbohydrate residues on mucins, which promote metastasis and reduce overall survival (*5*). Membrane-bound mucins with aberrantly expressed *O*-linked glycans are emerging as promising targets for OC diagnosis and treatment because they are expressed solely on epithelial cancer cells (*6*). Studies have shown that elevated levels of hypoglycosylated MUC16 isoforms in OC patients correlate with disease stage and tumor volume (TV) better than the CA125 epitope (*7*). Thus, hypoglycosylated MUC16 could be a potential target for tumor detection via immuno-PET imaging.

Immuno-PET imaging offers a noninvasive approach to OC detection because it combines the tumor-targeting specificity of antibodies with the high sensitivity of PET imaging (*8*). This approach was evaluated with huAR9.6—a humanized antibody that binds to hypoglycosylated residues on MUC16 (*9*). Our previous work validated huAR9.6 as an immuno-PET radiopharmaceutical for OC detection (*10*). Expanding on these findings, we sought to further develop a radiotheranostic system using ^{89}Zr-labeled huAR9.6 to diagnose—and ^{177}Lu-labeled huAR9.6 to subsequently treat—OC.^{89}Zr is a favorable positron-emitting radionuclide, as its half-life (3.3 d) complements the circulation half-life of full-length antibodies. ^{177}Lu is an ideal therapeutic β^--emitting radionuclide because of its favorable half-life (6.6 d) and short tissue penetration range (mean, 670 μm) relative to other β^--emitting radionuclides used in the clinic (*11*).

Clinical imaging for OC patients has largely focused on the OC125 murine antibody that binds to CA125 (*12–14*). However, radiolabeled OC125 demonstrated uptake in noncancerous tissues, thus limiting its specificity for the detection of OC lesions (*15–17*) while additionally causing human antimurine antibody responses, which increase off-target toxicities (*18–20*). We reasoned that a humanized antibody that binds to hypoglycosylated MUC16 isoforms will provide superior specificity for the detection and treatment of OC lesions while simultaneously overcoming the limitations of using murine antibodies in patients. Here, we present a promising radiotheranostic system to detect hypoglycosylated MUC16 and deliver therapeutic levels of radiation in human OC mouse models.

Received Aug. 11, 2023; revision accepted Jan. 29, 2024.
For correspondence or reprints, contact Jason S. Lewis (lewisj2@mskcc.org).
Published online Mar. 14, 2024.

MATERIALS AND METHODS

The supplemental materials (available at http://jnm.snmjournals.org) provide information on cell lines, quantitative real-time polymerase chain reaction, flow cytometry, antibody functionalization and radiolabeling, binding assays, serum stability, dosimetry, and immunohistochemistry.

Xenograft Models

All in vivo experiments were approved by the Research Animal Resource Center and Institutional Animal Care and Use Committee (approval 08-07-013) at Memorial Sloan Kettering. Seven- to 8-wk-old CRL:NU-*Foxn1*^{nu} (Nu/Nu; Charles River Laboratories) female mice were purchased. The animals were housed in ventilated cages and given food and water ad libitum. For PET imaging studies with [^{89}Zr]Zr-DFO-huAR9.6, 7- to 8-wk-old Nu/Nu mice were xenografted subcutaneously with OVCAR3, OVCAR4, OVCAR5, and OVCAR8 tumors. OVCAR3 tumors were induced on the right shoulder by injection of 10 million cells followed by another injection of 5 million cells 1 wk later in a 150-μL cell suspension of a 1:1 (v/v) mixture of fresh medium to BD Matrigel (BD Biosciences). OVCAR4, OVCAR5, and OVCAR8 tumors were induced on the right flank by injection of 5 million cells in a 150-μL cell suspension of a 1:1 (v/v) mixture of fresh medium to BD Matrigel. For therapy and biodistribution studies with [^{177}Lu]Lu-DTPA-huAR9.6, 7- to 8-wk-old B6;129-*Rag2*^{tm1Fwa} *IL2rg*^{tm1Rsky}/DwlHsd (R2G2; Envigo) female mice were purchased. OVCAR3, OVCAR5, and OVCAR8 tumors were induced on the right flank of R2G2 mice by injection of 5 million cells in a 100-μL cell suspension of a 1:1 (v/v) mixture of fresh medium to BD Matrigel. Subcutaneous xenografts were used for in vivo imaging and biodistribution studies when TV reached about 150–300 mm^3.

PET and SPECT Imaging

PET/CT images were acquired on an Inveon PET/CT scanner (Siemens Healthcare). For PET imaging studies, [^{89}Zr]Zr-DFO-huAR9.6 in 150 μL of Chelex (Bio-Rad)-treated phosphate-buffered saline was injected via the lateral tail vein into OVCAR3-, OVCAR4-, OVCAR5-, and OVCAR8-bearing mice. OVCAR3-bearing Nu/Nu mice (n = 4) were injected with 7.73 ± 0.34 MBq (20 μg), OVCAR4-bearing Nu/Nu mice (n = 3) were injected with 7.07 ± 0.19 MBq (20 μg), OVCAR5-bearing Nu/Nu mice (n = 4) were injected with 7.12 ± 0.18 MBq (20 μg), and OVCAR8-bearing Nu/Nu mice (n = 3) were injected with 8.58 ± 0.19 MBq (20 μg). Each tumor model was imaged in independent experiments. For PET imaging studies of recurrent OVCAR3 tumors (n = 3), R2G2 mice were injected with [^{89}Zr]Zr-DFO-huAR9.6 (20 μg, 7.62 ± 0.11 MBq). SPECT/CT images were acquired on a NanoSPECT (Siemens Healthcare). OVCAR3-bearing R2G2 mice (n = 4) with recurrent tumors were injected with a second dose of [^{177}Lu]Lu-DTPA-huAR9.6 (9.87 ± 0.47 MBq, 60 μg) in 150 μL of Chelex-treated phosphate-buffered saline. All image analysis was performed using VivoQuant analysis software (Invicro).

Ex Vivo Biodistribution

For each tumor model, ex vivo biodistribution analyses were performed on separate cohorts of xenografted mice that were administered [^{89}Zr]Zr-DFO-huAR9.6 or [^{177}Lu]Lu-DTPA-huAR9.6. After serial PET/CT imaging, 144-h terminal biodistribution studies were conducted on OVCAR3-, OVCAR4-, OVCAR5-, and OVCAR8-bearing Nu/Nu mice. For serial biodistribution studies with [^{89}Zr]Zr-DFO-huAR9.6 (3 μg), OVCAR3-bearing R2G2 mice were injected with 1.06 ± 0.11 MBq, OVCAR4-bearing Nu/Nu mice were injected with 1.11 ± 0.05 MBq, OVCAR5-bearing Nu/Nu mice were injected with 1.11 ± 0.05 MBq, and OVCAR8-bearing Nu/Nu mice were injected with 1.22 ± 0.05 MBq. In blockade cohorts, mice were injected with a mixture of [^{89}Zr]Zr-DFO-huAR9.6 and a 100-fold excess (mass) of unlabeled huAR9.6. For serial biodistribution studies with [^{177}Lu]Lu-CHX-A″-DTPA-huAR9.6 (3 μg), OVCAR3-bearing R2G2 mice were injected with 1.17 ± 0.08 MBq. Radiotracer injections (150 μL diluted with Chelex-treated phosphate-buffered saline) were administered via the lateral tail vein.

Radioimmunotherapy

All mice were administered 60 μg of [^{177}Lu]Lu-CHX-A″-DTPA-huAR9.6 for therapy studies. R2G2 mice bearing OVCAR3 tumors were separated into 3 cohorts for administration of 9.25 MBq (TV, 247.4 ± 128.70 mm^3; n = 15), 18.5 MBq (TV, 398.40 ± 135.10 mm^3; n = 5), or 27.75 MBq (TV, 356.05 ± 127.12 mm^3; n = 5) of [^{177}Lu]Lu-CHX-A″-DTPA-huAR9.6 to determine the most efficacious dose. Two additional cohorts were used as controls: saline (TV, 247.73 ± 157.65 mm^3; n = 10) and [^{177}Lu]Lu-CHX-A″-DTPA-IgG1 isotype control (9.25 MBq; TV, 186.36 ± 102.67 mm^3; n = 10). The average body weight for mice bearing OVCAR3 xenografts was 29.3 ± 3.1 g. R2G2 mice bearing OVCAR5 and OVCAR8 tumors were separated into 3 cohorts: saline (OVCAR5 TV, 146.78 ± 68.36 mm^3 [n = 10], and OVCAR8 TV, 184.66 ± 42.48 mm^3 [n = 5]), 9.25 MBq of [^{177}Lu]Lu-CHX-A″-DTPA-IgG1 isotype control (OVCAR5 TV, 184.66 ± 62.59 mm^3 [n = 10], and OVCAR8 TV, 207.52 ± 79.77 mm^3 [n = 5]), and 9.25 MBq of [^{177}Lu]Lu-CHX-A″-DTPA-huAR9.6 (OVCAR5 TV, 182.99 ± 94.71 mm^3 [n = 10], and OVCAR8 TV, 388.48 ± 118.91 [n = 5]). The average body weight was 22.0 ± 1.4 g for mice bearing OVCAR5 xenografts and 26.0 ± 1.6 g for mice bearing OVCAR8 xenografts. Tumor measurements were taken twice a week, and weekly blood draws were obtained for analysis on the element HT5 hematology analyzer (HESKA). The endpoints were a tumor size of more than 2,000 mm^3, tumor ulceration or necrosis, severe petechiae, and a 20% weight loss if food or fluid did not improve the health status of the animal after the start of weight loss. Mice whose weight decreased received supplemental DietGel (ClearH$_2$O). Vernier calipers were used to measure the tumor dimensions, and the following equation was used to calculate TV (mm)^3:

$$\mathrm{TV} = \left(\frac{4\pi}{3}\right)\left(\frac{\alpha}{2}\right)^2\left(\frac{b}{2}\right),$$

where α is the longest axis of the tumor (mm) and b is the axis perpendicular to the longest axis (mm).

Statistical Analysis

Statistical analyses were performed using GraphPad Prism, version 10. Unpaired, 2-tailed t tests were used to analyze cell-binding assays. A 1-way ANOVA was used for analysis of organ uptake in biodistribution experiments. A correction for multiple comparisons was performed using the Tukey–Kramer method. Analysis of survival experiments was performed via a log rank (Mantel–Cox) test. A P value of less than 0.05 was considered significant.

Data Availability

The data generated in this study are available on request from the corresponding author.

RESULTS

HuAR9.6 Can Delineate Varying MUC16 Expression Levels in OC

[^{89}Zr]Zr-DFO-huAR9.6 was synthesized with high radiochemical purity (>98%), high specific activity (~0.37 MBq/μg), and was shown to be stable in human serum (Supplemental Figs. 1, 2, 3A, and 3B) (*21*,*22*). To assess the in vitro binding of huAR9.6, we conducted radioligand bead–based (*23*), saturation-binding,

cell-binding, and flow cytometry assays. [^{89}Zr]Zr-DFO-huAR9.6 showed high and specific binding to MUC16 in the bead-based assay (Supplemental Fig. 3C) and bound to the highly MUC16-expressing OVCAR3 cells with high affinity (dissociation constant, 6.2 nM) (Supplemental Fig. 4). The cell-binding assay with OVCAR3 (MUC16-positive/high), OVCAR4 (MUC16-positive/high), OVCAR5 (MUC16-positive/low), and OVCAR8 (MUC16-negative) showed strong binding to OVCAR3 (~76%) and OVCAR4 (~75%), minimal binding to OVCAR5 (~20%), and no binding to OVCAR8 (Fig. 1A). Flow cytometry analysis with huAR9.6 correlated with cell-binding data showing high binding to OVCAR3 and OVCAR4, marginal binding to OVCAR5, and no binding to OVCAR8 (Fig. 1B; Supplemental Fig. 5). Additionally, we analyzed *MUC16* messenger RNA expression levels in each cell line via real-time polymerase chain reaction. The results demonstrated varying *MUC16* messenger RNA expression levels, with the highest messenger RNA expression seen in the OVCAR4 cell line (Supplemental Fig. 6). To further investigate the binding of huAR9.6, nude mice were xenografted with OVCAR3, OVCAR4, OVCAR5, or OVCAR8 subcutaneous tumors, and ex vivo immunohistochemical analysis on tissue slices from these tumors was performed. Staining with huAR9.6 confirmed high expression in OVCAR3 and OVCAR4, minimal expression in OVCAR5, and no expression in OVCAR8 (Fig. 1C).

Building on our previous work with [^{89}Zr]Zr-DFO-huAR9.6 (*10*), we analyzed the behavior of [^{89}Zr]Zr-DFO-huAR9.6 in nude mice bearing OVCAR3, OVCAR4, OVCAR5, and OVCAR8 subcutaneous xenografts. Immuno-PET imaging showed high uptake of the radiotracer at 144 h after injection in OVCAR3 and OVCAR4 tumors, low uptake in OVCAR5 tumors, and minimal signal in OVCAR8 tumors (Fig. 1D). Biodistribution data at 144 h confirmed the uptake seen in the PET images, reaching approximately 35%, 30%, 13%, and 1% in OVCAR3, OVCAR4, OVCAR5, and OVCAR8 tumors, respectively (Fig. 1E; Supplemental Figs. 7–10). [^{89}Zr]Zr-DFO-huAR9.6 was also analyzed in R2G2 mice in preparation for therapy studies. R2G2 mice have a higher subcutaneous uptake rate by OC tumors than do nude mice and are more radioresistant than NSG mice (Jackson Laboratory). Biodistribution studies on R2G2 mice with [^{89}Zr]Zr-DFO-huAR9.6 confirmed significant tumor uptake by 72 h, which could be blocked with the addition of unlabeled huAR9.6 (Supplemental Fig. 11).

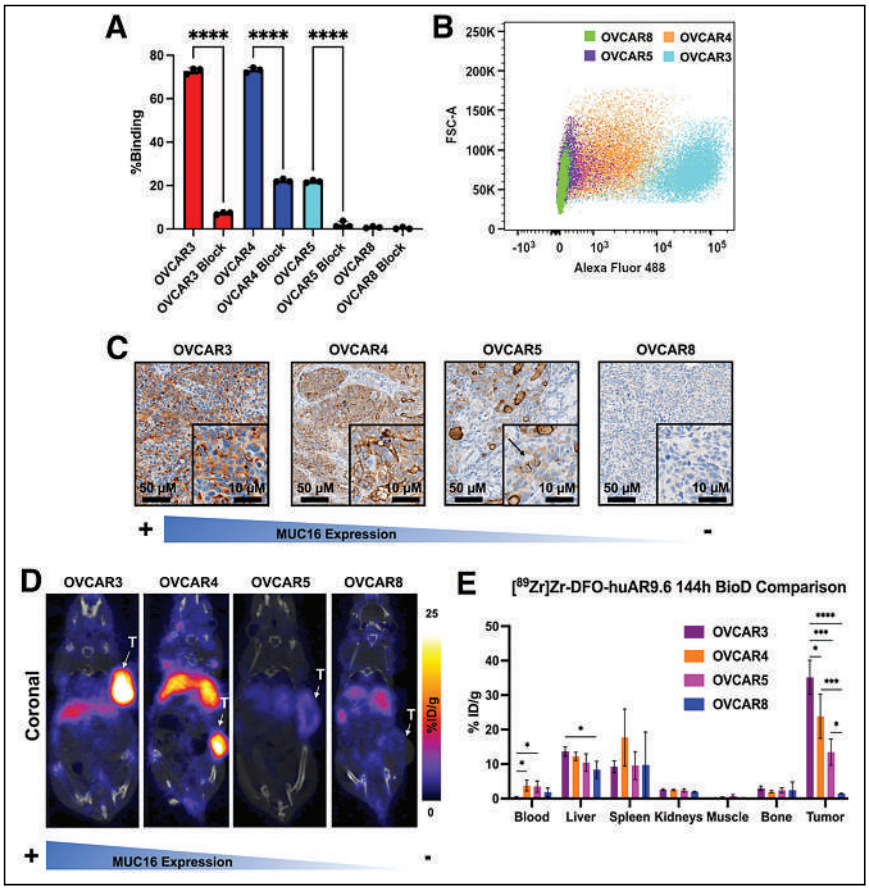

FIGURE 1. huAR9.6 can differentiate between OC cells with high and low MUC16 expression in vitro and in vivo. (A) Radioligand cell-binding assay with [^{89}Zr]Zr-DFO-huAR9.6 in cell lines with varying levels of MUC16 expression. Binding was significantly reduced with administration of 1,000-fold excess blocking dose of nonlabeled huAR9.6. (B) In vitro validation of huAR9.6-AF488 binding in OC cells via flow cytometry. (C) huAR9.6 immunohistochemical staining images of harvested OVCAR3, OVCAR4, OVCAR5, and OVCAR8 subcutaneous tumors. Arrow indicates MUC16 expression on surface of OVCAR5 cells. (D) Female nude mice containing subcutaneous tumors that were injected with 7.4–9.25 MBq (20–25 μg) of [^{89}Zr]Zr-DFO-huAR9.6 followed by PET imaging. (E) Terminal biodistributions at 144 h after injection. n = 3 for OVCAR4 and OVCAR8; n = 4 for OVCAR3 and OVCAR5. *$P \leq 0.05$. ***$P \leq 0.001$. ****$P \leq 0.0001$. %ID = percentage injected dose; FSC-A = forward scatter area; T = tumor.

[^{177}Lu]Lu-CHX-A″-DTPA-huAR9.6 Demonstrates Robust Antitumor Effects in OC Mouse Model

[^{177}Lu]Lu-CHX-A″-DTPA-huAR9.6 was synthesized at high radiochemical purity and was stable in human serum over 7 d (Supplemental Figs. 12, 13, 14A, and 14B). The radioimmunoconjugate maintained highly specific binding to the OVCAR3 cell line (Supplemental Figs. 14C and 15) and significant tumor uptake in the R2G2 model (Supplemental Fig. 16). A radioimmunotherapy study was performed on OVCAR3 tumor–bearing R2G2 mice. The mice were divided into 3 cohorts of [^{177}Lu]Lu-CHX-A″-DTPA-huAR9.6 with different specific activities: 9.25, 18.5, and 27.75 MBq. [^{177}Lu]Lu-CHX-A″-DTPA-huAR9.6 doses were confirmed by dosimetry estimates that were generated from xenografted OVCAR3 mouse biodistribution studies (Supplemental Fig. 17) (*24–28*). The dosimetry estimates indicated the appropriate dose to achieve tumor response while maintaining tolerable radiation exposure of healthy tissues (*29*,*30*). This study also included 2 control groups: saline and a 9.25-MBq [^{177}Lu]Lu-CHX-A″-DTPA-IgG isotype control. Overall survival in the 9.25- and 18.5-MBq cohorts was significantly higher than in the saline and IgG control groups (Fig. 2A). Potent antitumor effects were seen in all cohorts in comparison to control groups (Fig. 2B; Supplemental Fig. 18). All 5 mice in the 18.5-MBq cohort

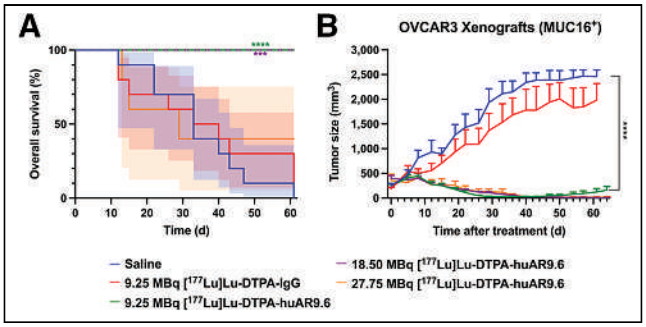

FIGURE 2. [^{177}Lu]Lu-CHX-A″-DTPA-huAR9.6 treatment improves overall survival and inhibits tumor growth in OVCAR3-bearing mice. (A and B) Overall survival percentage (A) and TV (mm^3) growth curves (B) of R2G2 OVCAR3-bearing mice after treatment. Significant tumor growth inhibition was observed in all treated mice in comparison to saline and IgG isotype controls. Shading represents 95% CI. ***$P \leq 0.001$. ****$P \leq 0.0001$.

and 2 of 5 mice in 27.75-MBq cohort had complete and durable responses after a single dose of [^{177}Lu]Lu-CHX-A″-DTPA-huAR9.6. Two mice in the 27.75-MBq group died of undetermined causes (days 13 and 15 after injection); however, these mice were experiencing decreases in body weight and blood cell counts before death. The third mouse was euthanized because it lost more than 20% of its initial body weight (day 29 after injection).

Nine of 15 tumors in the lowest-dose [^{177}Lu]Lu-CHX-A″-DTPA-huAR9.6 cohort demonstrated recurrence at an approximate range of 5–10 wk after treatment. Mouse 2 was not retreated, because it developed a severe skin infection, and mouse 12 was euthanized to harvest the tumor for analysis. Immunohistochemical analysis with huAR9.6 was performed to confirm maintenance of MUC16 expression (Supplemental Fig. 19). Three mice with recurrent tumors (mice *6–8*) were injected with [^{89}Zr]Zr-DFO-huAR9.6 (day 60 after treatment). PET/CT imaging confirmed MUC16 expression (Fig. 3A), suggesting the opportunity for retreatment with [^{177}Lu]Lu-CHX-A″-DTPA-huAR9.6. The mice received 9.25 MBq of [^{177}Lu]Lu-CHX-A″-DTPA-huAR9.6 (day 75 after initial treatment), which led to a complete response by approximately 6 wk after injection (Fig. 3B). The remaining 4 mice (mice *11* and *13–15*) with recurrent tumors were also injected with another 9.25-MBq dose of [^{177}Lu]Lu-CHX-A″-DTPA-huAR9.6 (day 121 after initial treatment), and uptake of the radiopharmaceutical was confirmed via SPECT/CT (Supplemental Fig. 20A). The tumors completely regressed by approximately 6 wk after retreatment (Supplemental Fig. 20B) but recurred at about 8 wk.

Additional radioimmunotherapy studies were performed on OVCAR5 (MUC16-positive/low) and OVCAR8 (MUC16-negative) xenografts. Both studies consisted of a group receiving a single 9.25-MBq dose of [^{177}Lu]Lu-CHX-A″-DTPA-huAR9.6, a saline control group, and a group receiving a single 9.25-MBq dose of [^{177}Lu]Lu-CHX-A″-DTPA-IgG. [^{177}Lu]Lu-CHX-A″-DTPA-huAR9.6 delayed tumor growth in the OVCAR5 xenografts in comparison to the saline control; however, this effect was not significant in comparison to the [^{177}Lu]Lu-CHX-A″-DTPA-IgG group (Supplemental Fig. 21A). This result is likely attributable to the low MUC16 expression of OVCAR5 tumors. In addition, the delayed tumor growth seen in the [^{177}Lu]Lu-CHX-A″-DTPA-IgG group was likely due to the enhanced permeability and retention effect, which allows for nonspecific accumulation in the tumor. Although the antitumor effect of [^{177}Lu]Lu-CHX-A″-DTPA-huAR9.6 was not significant in comparison to [^{177}Lu]Lu-CHX-A″-DTPA-IgG, mice in the treatment group showed improved overall survival in comparison to the saline control group, whereas the [^{177}Lu]Lu-CHX-A″-DTPA-IgG group did not show improved survival (Supplemental Figs. 21B and 22). No significant antitumor effects were seen in the OVCAR8 xenografts in comparison to controls, as expected from the lack of MUC16 expression in this model (Supplemental Fig. 23).

Hematologic Toxicity Is Transient in [^{177}Lu]Lu-CHX-A″-DTPA-huAR9.6–Treated Mice

Estimates of murine dosimetry implicated hematologic toxicity as the likely predominant radiogenic toxicity for radioimmunotherapy (Supplemental Fig. 17). To test the significance of hematologic toxicity, weekly blood analysis was implemented throughout the study in OVCAR3, OVCAR5, and OVCAR8 xenografts (Supplemental Figs. 24–26). The mean white blood cell, red blood cell, and platelet counts in OVCAR3 xenografts showed a dose-dependent decrease (Figs. 4A–4C). Platelet and white blood cell counts were most sensitive to radiation, but all cell counts recovered close to pretherapy levels or ranges after therapy initiation. Overall, hematologic toxicity was transient, with a nadir at 2–3 wk. Recovery to pretherapy values was achieved; that is, values recovered to ±1 SD of the average pretherapy values. To assess outward signs of toxicity, the mice were weighted twice weekly and monitored for observable symptoms, including changes in behavior and appearance. Significant weight loss was seen in 1 OVCAR3-bearing mouse in both the 18.5-MBq and the 27.75-MBq [^{177}Lu]Lu-CHX-A″-DTPA-huAR9.6 groups (Fig. 4D; Supplemental Fig. 27). Mice in the 27.75-MBq [^{177}Lu]Lu-CHX-A″-DTPA-huAR9.6 group demonstrated greater weight loss than mice in the lower-dose groups, indicating a dose-dependent toxicity response, with a nadir at about 2 wk. Mild petechia was also observed in the 27.75-MBq cohort. Similarly, weight loss was seen in OVCAR5 xenografts that received 9.25 MBq of [^{177}Lu]Lu-CHX-A″-DTPA-huAR9.6 or [^{177}Lu]Lu-CHX-A″-DTPA-IgG. However, average weight loss in those 2 groups did not exceed the 20% cutoff, with a nadir at about 2 wk (Supplemental Figs. 28 and 29).

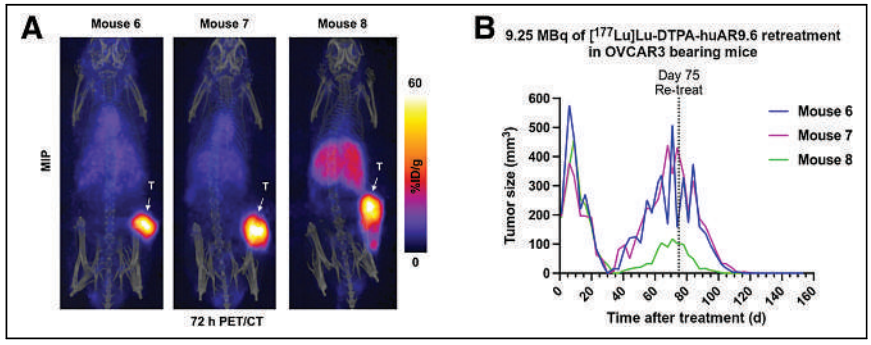

FIGURE 3. [^{177}Lu]Lu-CHX-A″-DTPA-huAR9.6 still shows strong antitumor effects in recurrent tumors. (A) 72-h PET/CT imaging with [^{89}Zr]Zr-DFO-huAR9.6 shows that OVCAR3 recurrent tumors still strongly express MUC16. Images are represented as maximum-intensity projections. (B) Individual TVs for recurrent OVCAR3 tumors. Mice were retreated with 9.25 MBq of [^{177}Lu]Lu-CHX-A″-DTPA-huAR9.6 at day 75 of therapy. %ID = percentage injected dose; MIP = maximum-intensity projection; T = tumor.

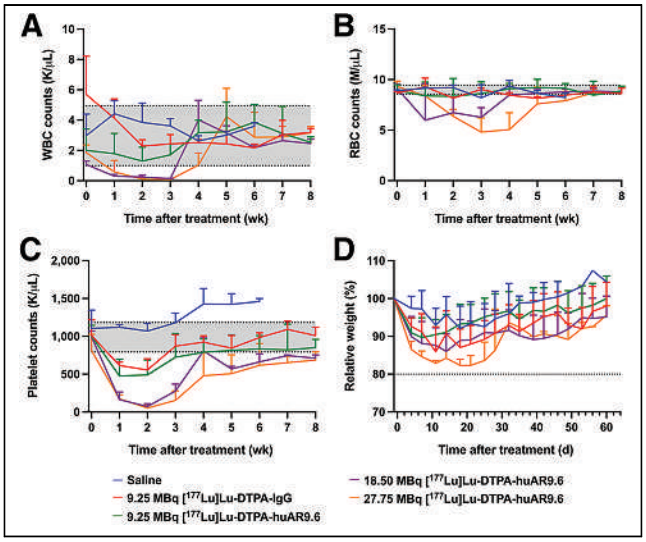

FIGURE 4. Hematologic toxicity is transient in [^{177}Lu]Lu-CHX-A″-DTPA-huAR9.6–treated mice with OVCAR3 tumors. (A–C) White blood cell counts (A), red blood cell counts (B), and platelet counts (C) in OVCAR3-bearing mice that received [^{177}Lu]Lu-CHX-A″-DTPA-huAR9.6 treatment. Shading indicates mean ± SD of values collected from entire cohort of OVCAR3-bearing mice before therapy initiation (week 0). (D) Mean relative weight percentages for OVCAR3-bearing mice in each cohort. RBC = red blood cell; WBC = white blood cell.

DISCUSSION

A theranostic approach integrates the diagnostic and therapeutic agent into a single platform (*31*). This method offers great potential to solve the challenges presented by late-stage diagnosis and poor therapeutic response. There is a critical need for earlier detection methods and additional precision-based therapies against novel targets for OC patients; therefore, we proposed the use of a radiotheranostic approach using huAR9.6.

huAR9.6 has a novel mechanism of action in comparison to other MUC16-targeting antibodies (*9*,*32*,*33*). In addition, huAR9.6 is a humanized antibody, allowing for higher tolerance and decreased immunogenicity in comparison to murine antibodies. We validated the diagnostic agent, [^{89}Zr]Zr-DFO-huAR9.6, in OC xenografts with varying MUC16 expression levels. Off-target uptake was identified within the liver and spleen, as may be attributed to MUC16 being a shed antigen, clearance of immunocomplexes by the reticuloendothelial system, or nonspecific binding of huAR9.6 to hepatic Fc receptors. In an OC patient study, the MUC16-targeting antibody (B43.13) showed binding to circulating MUC16 in the serum of patients, and the radioimmunoconjugate accumulated within the reticuloendothelial system (*34*,*35*). For our studies, serum levels of MUC16 were not detected via enzyme-linked immunosorbent assay. This can be attributed to a lack of high levels of MUC16 shed into the bloodstream in subcutaneous mouse models. Nonspecific binding to Fc receptors in the liver is common for radiolabeled full-length IgG antibodies because these antibodies still have an intact Fc region (*36*,*37*). Nonspecific uptake in these organs did not significantly affect tumor uptake; however, nonspecific uptake could potentially be blocked with the administration of an excess of unlabeled antibody before administration of its radiolabeled counterpart (*38*,*39*). Antibodies targeting shed antigen have been successfully used in the clinic for immuno-PET imaging with this approach (*40*).

Tumor uptake in OVCAR3, OVCAR5, and OVCAR8 xenografts correlated with [^{177}Lu]Lu-CHX-A″-DTPA-huAR9.6 therapy response. [^{177}Lu]Lu-CHX-A″-DTPA-huAR9.6 portrayed strong antitumor effects in all 3 tested doses in OVCAR3 xenografts. The maximum efficacious dose was 27.75 MBq; however, this dose did cause significant toxicity in 3 of the 5 mice. The 9.25- and 18.5-MBq [^{177}Lu]Lu-CHX-A″-DTPA-huAR9.6 cohorts experienced significantly improved overall survival in comparison to the saline control. Therapy with a single dose of [^{177}Lu]Lu-CHX-A″-DTPA-huAR9.6 did not have strong antitumor effects in OVCAR5 xenografts. It is possible that a single dose of [^{177}Lu]Lu-CHX-A″-DTPA-huAR9.6 is not sufficient to treat tumors with low MUC16 expression. Additional studies are warranted to investigate whether multiple doses would be beneficial in this model.

Tumor recurrence after a single low dose of [^{177}Lu]Lu-CHX-A″-DTPA-huAR9.6 did occur in a few OVCAR3-bearing mice. We hypothesized that a second administration of [^{177}Lu]Lu-CHX-A″-DTPA-huAR9.6 could be beneficial for retreating the recurrent tumors. The diagnostic agent, [^{89}Zr]Zr-DFO-huAR9.6, allowed us to predict whether the mice with recurrent tumors could benefit from a second administration of the radioimmunotherapy. Recurrent tumor burden was completely regressed with a second dose of [^{177}Lu]Lu-CHX-A″-DTPA-huAR9.6, indicating that multiple doses are beneficial for retreatment. However, tumor recurrence did occur about 60 d after the second dose in 2 of 7 retreated mice, and a third dose was not tested.

Radioimmunotherapy is often limited by hematologic toxicity due to slow clearance of the radiotracer from the blood (*41*). The treatment cohorts demonstrated dose-dependent toxicity, with the most severe reduction in platelet and white blood cell counts seen in the highest-dose cohort (27.75 MBq). However, hematologic effects from the radioimmunotherapy were transient, and blood counts rebounded over time.

CONCLUSION

The combination of the highly specific huAR9.6 antibody with a PET or therapeutic radionuclide allowed us to identify and treat tumors noninvasively. In this work, we validated the theranostic capability of [^{89}Zr]Zr-DFO-huAR9.6 in OC models. Furthermore, we demonstrated the strong antitumor effects of [^{177}Lu]Lu-CHX-A″-DTPA-huAR9.6 in highly MUC16-expressing tumors. These findings demonstrate great potential for using ^{89}Zr- and ^{177}Lu-labeled huAR9.6 as a theranostic pair for the identification and personalized treatment of MUC16-positive OC.

DISCLOSURE

The humanization of AR9.6 was funded by a private research contract to Cory Brooks from Quest Pharmatech Inc. during the conduct of the study. Jason Lewis reports grants from the NIH (R35 CA232130), Emerson Collective Cancer Research Fund, Tow Foundation, and IMRAS Memorial Sloan Kettering Cancer Center during this study. This study was also supported in part by the NIH R35 CA232130-S2 Diversity Supplement, awarded to Kyeara Mack. The Radiochemistry and Molecular Imaging Probes Core Facility, the Small Animal Imaging Facility, and the Molecular Cytology Core Facility were supported in part by NIH P30 CA08748. Prakash Radhakrishnan and Michael Hollingsworth acknowledge the NIH for support (CA208108 and P01CA217798). No other potential conflict of interest relevant to this article was reported.

ACKNOWLEDGMENTS

We gratefully acknowledge the support of the Radiochemistry and Molecular Imaging Probes Core Facility (Memorial Sloan Kettering), the Small Animal Imaging Facility (Memorial Sloan Kettering), and the Tri-Institutional Laboratory of Comparative Pathology. The Medical Graphics Department at Memorial Sloan Kettering Cancer Center is acknowledged. Dr. Sebastien Monette and Maria S. Jiao are gratefully acknowledged for assistance with ex vivo histopathologic examination. Quest Pharmatech is acknowledged for providing the AR9.6 antibody.

KEY POINTS

QUESTION: Can ^{89}Zr- and ^{177}Lu-labeled huAR9.6 be used as a theranostic platform for the diagnosis and treatment of OC?

PERTINENT FINDINGS: Hypoglycosylated MUC16 isoforms in OC can be detected via immuno-PET imaging with the MUC16-targeting radiotracer [^{89}Zr]Zr-DFO-huAR9.6. In vivo studies showed that [^{89}Zr]Zr-DFO-huAR9.6 could successfully delineate varying MUC16 expression levels in OC mouse models. Subsequent radioimmunotherapy studies with [^{177}Lu]Lu-CHX-A″-DTPA-huAR9.6 demonstrated improved overall survival and strong antitumor responses in highly MUC16-expressing models.

IMPLICATIONS FOR PATIENT CARE: Immuno-PET imaging of MUC16 with the huAR9.6 mAb may allow for noninvasive diagnosis and treatment monitoring of OC lesions in patients. This theranostic platform may be used to stratify and select patients who would benefit from the targeted radioimmunotherapy.

REFERENCES

1. Torre LA, Trabert B, DeSantis CE, et al. Ovarian cancer statistics, 2018. *CA Cancer J Clin.* 2018;68:284–296.
2. Special section: ovarian cancer. In: *Cancer Facts & Figures: 2018.* American Cancer Society; 2018:28–43.
3. Li SS, Ma J, Wong AST. Chemoresistance in ovarian cancer: exploiting cancer stem cell metabolism. *J Gynecol Oncol.* 2018;29:e32.
4. Scholler N, Urban N. CA125 in ovarian cancer. *Biomark Med.* 2007;1:513–523.
5. Radhakrishnan P, Dabelsteen S, Madsen FB, et al. Immature truncated O-glycophenotype of cancer directly induces oncogenic features. *Proc Natl Acad Sci USA.* 2014;111:E4066–E4075.
6. Akita K, Yoshida S, Ikehara Y, et al. Different levels of sialyl-Tn antigen expressed on MUC16 in patients with endometriosis and ovarian cancer. *Int J Gynecol Cancer.* 2012;22:531–538.
7. Kobayashi H, Terao T, Kawashima Y. Serum sialyl Tn antigen as a prognostic marker in patients with epithelial ovarian cancer. *Nippon Sanka Fujinka Gakkai Zasshi.* 1992;44:14–20.
8. Heskamp S, Raavé R, Boerman O, et al. ^{89}Zr-immuno-positron emission tomography in oncology: state-of-the-art ^{89}Zr radiochemistry. *Bioconjug Chem.* 2017;28:2211–2223.
9. Thomas D, Sagar S, Liu X, et al. Isoforms of MUC16 activate oncogenic signaling through EGF receptors to enhance the progression of pancreatic cancer. *Mol Ther.* 2021;29:1557–1571.
10. Sharma SK, Mack KN, Piersigilli A, et al. ImmunoPET of ovarian and pancreatic cancer with AR9.6, a novel MUC16-targeted therapeutic antibody. *Clin Cancer Res.* 2022;28:948–959.
11. Dash A, Pillai MR, Knapp FF Jr. Production of ^{177}Lu for targeted radionuclide therapy: available options. *Nucl Med Mol Imaging.* 2015;49:85–107.
12. Maughan TS, Haylock B, Hayward M, et al. OC125 immunoscintigraphy in ovarian carcinoma: a comparison with alternative methods of assessment. *Clin Oncol (R Coll Radiol).* 1990;2:199–205.
13. Papazefkos V, Michalas S, Papantoniou V, et al. Comparative study of RIS with the ^{131}I-OC 125 F(ab′)2 Mab and CT scan prior to second look operation for ovarian cancer. *Eur J Obstet Gynecol Reprod Biol.* 1990;37:271–277.
14. Perkins AC, Powell MC, Wastie ML, et al. A prospective evaluation of OC125 and magnetic resonance imaging in patients with ovarian carcinoma. *Eur J Nucl Med.* 1990;16:311–316.
15. Barzen G, Mayr AC, Langer M, et al. Radioimmunoscintigraphy of ovarian cancer with 131-iodine labeled OC-125 antibody fragments. *Eur J Nucl Med.* 1989;15:42–48.
16. Peltier P, Dutin JP, Chatal JF, et al. Usefulness of imaging ovarian cancer recurrence with In-111-labeled monoclonal antibody (OC 125) specific for CA 125 antigen. The INSERM Research Network (Nantes, Rennes, Reims, Vuillejuif, Saclay. *Ann Oncol.* 1993;4:307–311.
17. Vuillez JP, Levrot E, Mousseau M, et al. Evaluation of the diagnostic usefulness of CA125 immunoscintigraphy for ovarian carcinoma follow-up after treatment: contribution of this technique in Grenoble University Medical Center. *Bull Cancer.* 1997;84:1033–1042.
18. Finkler NJ, Muto MG, Kassis AI, et al. Intraperitoneal radiolabeled OC 125 in patients with advanced ovarian cancer. *Gynecol Oncol.* 1989;34:339–344.
19. Mahé MA, Fumoleau P, Fabbro M, et al. A phase II study of intraperitoneal radioimmunotherapy with iodine-131-labeled monoclonal antibody OC-125 in patients with residual ovarian carcinoma. *Clin Cancer Res.* 1999;5:3249s–3253s.
20. Muto MG, Finkler NJ, Kassis AI, et al. Human anti-murine antibody responses in ovarian cancer patients undergoing radioimmunotherapy with the murine monoclonal antibody OC-125. *Gynecol Oncol.* 1990;38:244–248.
21. Holland JP, Sheh Y, Lewis JS. Standardized methods for the production of high specific-activity zirconium-89. *Nucl Med Biol.* 2009;36:729–739.
22. Vosjan MJ, Perk LR, Visser GW, et al. Conjugation and radiolabeling of monoclonal antibodies with zirconium-89 for PET imaging using the bifunctional chelate p-isothiocyanatobenzyl-desferrioxamine. *Nat Protoc.* 2010;5:739–743.
23. Sharma SK, Lyashchenko SK, Park HA, et al. A rapid bead-based radioligand binding assay for the determination of target-binding fraction and quality control of radiopharmaceuticals. *Nucl Med Biol.* 2019;71:32–38.
24. Comuzzi C, Polese P, Melchior A, et al. SOLVERSTAT: a new utility for multipurpose analysis. An application to the investigation of dioxygenated Co(II) complex formation in dimethylsulfoxide solution. *Talanta.* 2003;59:67–80.
25. Bolch WE, Eckerman KF, Sgouros G, et al. MIRD pamphlet no. 21: a generalized schema for radiopharmaceutical dosimetry—standardization of nomenclature. *J Nucl Med.* 2009;50:477–484.
26. Carter LM, Crawford TM, Sato T, et al. PARaDIM: A PHITS-based Monte Carlo tool for internal dosimetry with tetrahedral mesh computational phantoms. *J Nucl Med.* 2019;60:1802–1811.
27. Sato T, Niita K, Matsuda N, et al. Overview of particle and heavy ion transport code system PHITS. *Ann Nucl Energy.* 2015;82:110–115.
28. Kesner A, Olguin E, Zanzonico P, et al. MIRDCalc V 1.0: a community spreadsheet tool for organ-level radiopharmaceutical absorbed dose calculations [abstract]. *J Nucl Med.* 2018;59(suppl 1):473.
29. Larson SM, Carrasquillo JA, Cheung NK, Press OW. Radioimmunotherapy of human tumours. *Nat Rev Cancer.* 2015;15:347–360.
30. Emami B, Lyman J, Brown A, et al. Tolerance of normal tissue to therapeutic irradiation. *Int J Radiat Oncol Biol Phys.* 1991;21:109–122.
31. Bodei L, Herrmann K, Schöder H, et al. Radiotheranostics in oncology: current challenges and emerging opportunities. *Nat Rev Clin Oncol.* 2022;19:534–550.
32. Nemieboka B, Sharma SK, Rao TD, et al. Radiopharmacologic screening of antibodies to the unshed ectodomain of MUC16 in ovarian cancer identifies a lead candidate for clinical translation. *Nucl Med Biol.* 2020;86-87:9–19.
33. Sharma SK, Wuest M, Wang M, et al. Immuno-PET of epithelial ovarian cancer: harnessing the potential of CA125 for non-invasive imaging. *EJNMMI Res.* 2014;4:60.
34. McQuarrie SA, Baum RP, Niesen A, et al. Pharmacokinetics and radiation dosimetry of ^{99}Tc^{m}-labelled monoclonal antibody B43.13 in ovarian cancer patients. *Nucl Med Commun.* 1997;18:878–886.
35. McQuarrie SA, Riauka T, Baum RP, et al. The effects of circulating antigen on the pharmacokinetics and radioimmunoscintigraphic properties of ^{99m}Tc labelled monoclonal antibodies in cancer patients. *J Pharm Pharm Sci.* 1998;1:115–125.
36. Boyle CC, Paine AJ, Mather SJ. The mechanism of hepatic uptake of a radiolabelled monoclonal antibody. *Int J Cancer.* 1992;50:912–917.
37. Hosseinimehr SJ, Tolmachev V, Orlova A. Liver uptake of radiolabeled targeting proteins and peptides: considerations for targeting peptide conjugate design. *Drug Discov Today.* 2012;17:1224–1232.
38. Houghton JL, Abdel-Atti D, Scholz WW, Lewis JS. Preloading with unlabeled CA19.9 targeted human monoclonal antibody leads to improved PET imaging with ^{89}Zr-5B1. *Mol Pharm.* 2017;14:908–915.
39. Henry KE, Shaffer TM, Mack KN, et al. Exploiting the MUC5AC antigen for noninvasive identification of pancreatic cancer. *J Nucl Med.* 2021;62:1384–1390.
40. Lohrmann C, O'Reilly EM, O'Donoghue JA, et al. Retooling a blood-based biomarker: phase I assessment of the high-affinity CA19-9 antibody HuMab-5B1 for immuno-PET imaging of pancreatic cancer. *Clin Cancer Res.* 2019;25:7014–7023.
41. Sharkey RM, Goldenberg DM. Cancer radioimmunotherapy. *Immunotherapy.* 2011;3:349–370.

Peptide Binder to Glypican-3 as a Theranostic Agent for Hepatocellular Carcinoma

Fanching Lin*[1], Renee Clift*[1], Takeru Ehara[2], Hayato Yanagida[2], Steven Horton[1], Alain Noncovich[1], Matt Guest[1], Daniel Kim[1], Katrina Salvador[1], Samantha Richardson[1], Terra Miller[1], Guangzhou Han[1], Abhijit Bhat[1], Kenneth Song[1], and Gary Li[1]

[1]*RayzeBio, Inc., San Diego, California; and* [2]*PeptiDream Inc., Kanagawa, Japan*

Glypican-3 (GPC3) is a membrane-associated glycoprotein that is significantly upregulated in hepatocellular carcinomas (HCC) with minimal to no expression in normal tissues. The differential expression of GPC3 between tumor and normal tissues provides an opportunity for targeted radiopharmaceutical therapy to treat HCC, a leading cause of cancer-related deaths worldwide. **Methods**: DOTA-RYZ-GPC3 (RAYZ-8009) comprises a novel macrocyclic peptide binder to GPC3, a linker, and a chelator that can be complexed with different radioisotopes. The binding affinity was determined by surface plasma resonance and radioligand binding assays. Target-mediated cellular internalization was radiometrically measured at multiple time points. In vivo biodistribution, monotherapy, and combination treatments with ^{177}Lu or ^{225}Ac were performed on HCC xenografts. **Results:** RAYZ-8009 showed high binding affinity to GPC3 protein of human, mouse, canine, and cynomolgus monkey origins and no binding to other glypican family members. Potent cellular binding was confirmed in GPC3-positive HepG2 cells and was not affected by isotope switching. RAYZ-8009 achieved efficient internalization on binding to HepG2 cells. Biodistribution study of ^{177}Lu-RAYZ-8009 showed sustained tumor uptake and fast renal clearance, with minimal or no uptake in other normal tissues. Tumor-specific uptake was also demonstrated in orthotopic HCC tumors, with no uptake in surrounding liver tissue. Therapeutically, significant and durable tumor regression and survival benefit were achieved with ^{177}Lu- and ^{225}Ac-labeled RAYZ-8009, as single agents and in combination with lenvatinib, in GPC3-positive HCC xenografts. **Conclusion:** Preclinical in vitro and in vivo data demonstrate the potential of RAYZ-8009 as a theranostic agent for the treatment of patients with GPC3-positive HCC.

Key Words: GPC3; HCC; targeted radiotherapy; actinium; theranostics

J Nucl Med 2024; 65:586–592
DOI: 10.2967/jnumed.123.266766

Liver cancer is the sixth most diagnosed cancer and third most common cause of cancer deaths globally. In 2020, there were an estimated 905,677 new diagnoses and 830,180 deaths worldwide (*1*), and the incidence and mortality continue to worsen, likely because of an increase in nonalcoholic fatty liver disease (*2*). Of all liver cancer cases, hepatocellular carcinoma (HCC) accounts for approximately 85%. Although first-line systemic treatments such as atezolizumab/bevacizumab, tremelimumab-acti/durvalumab, and lenvatinib have shown encouraging clinical benefits in patients with unresectable HCC, more work is urgently needed to identify and exploit the vulnerabilities of HCC and improve treatment outcomes.

Glypican-3 (GPC3) is a membrane-associated heparan sulfate proteoglycan (*3*), involved primarily in embryonic development, and its expression levels decrease significantly after birth (*3*). Although barely detectable in normal adult tissues (*4*), a significant upregulation of GPC3 in HCC has been observed in up to 75% of cases (*5*–*7*) and appears to correlate with a poor prognosis (*8*,*9*). The expression of GPC3 can potentially be used to distinguish HCC from noncancerous pathologies such as focal nodular hyperplasia or cirrhosis (*10*,*11*). Besides HCC, GPC3 expression has also been observed in other adult and pediatric cancers, such as lung adenocarcinoma and squamous cell carcinoma (*12*,*13*), embryonal tumors (*14*), testicular germ cell tumors (*15*), and liposarcoma (*16*).

Because of its high expression in cancer and minimum expression in normal tissues, GPC3 is considered an attractive target for tumor-directed cancer therapy (*17*). Particularly, GPC3 CAR T-cell treatments have yielded promising results in both adult (*18*) and pediatric (*19*) HCC patients. Similarly, the differential expression also provides a basis for discovering and developing GPC3-targeted radiopharmaceutical therapy, especially for treatment-resistant or -refractory patients after first-line therapy to address disseminated disease and metastases (*20*). Previously, imaging studies with GPC3-targeted antibodies labeled with ^{124}I (*21*) or ^{89}Zr (*22*) have shown tumor-specific uptake with low background uptake. In this report, we describe in vitro, in vivo, and ex vivo characteristics of DOTA-RYZ-GPC3 (RAYZ-8009), a potent and selective GPC3 peptide binder, for treatment of HCC.

MATERIALS AND METHODS

Detailed reagents and experimental procedures are included in the supplemental materials and methods (supplemental materials are available at http://jnm.snmjournals.org).

Discovery of RAYZ-8009. RAYZ-8009 comprises a novel macrocyclic peptide binder to GPC3 and a chelator that binds radiometal isotopes. The GPC3 binder was discovered using the Peptide Discovery Platform System, a proprietary screening system of PeptiDream Inc. (*23*). From the initial library consisting of more than 1,013 unique peptides, GPC3-specific binders were enriched using His-tagged GPC3 (catalog no. 2119-GP; R&D Systems) immobilized on cobalt magnetic beads (Dynabeads [catalog no. 10103D]; Life Technologies Corp.) via iterative selection rounds (*24*,*25*). One of the enriched

Received Oct. 16, 2023; revision accepted Jan. 23, 2024.
For correspondence or reprints, contact Gary Li (gli@rayzebio.com).
*Contributed equally to this work.
Published online Feb. 29, 2024.

TABLE 1
Binding of RAYZ-8009 Conjugated with Different Stable Isotopes to HepG2 Cells

Compound	Inhibition constant (nM)	Half-maximal inhibitory concentration (nM)
^{175}Lu-RAYZ-8009	6.73	9.35
^{139}La-RAYZ-8009	11.19	15.67
^{69}Ga-RAYZ-8009	9.77	13.67

Binding affinity of ^{139}La-RAYZ-8009 and ^{69}Ga-RAYZ-8009 to human GPC3 was determined using competitive radioligand binding assay in HepG2 human HCC cells. ^{177}Lu-RAYZ-8009 was used as competitive radioligand, and ^{175}Lu-RAYZ-8009 was used as reference ligand.

peptides was further optimized chemically, and subsequent installation of a metal chelator afforded RAYZ-8009.

Cell Lines and Cell Culture. Human HCC cell lines were obtained from American Type Culture Collection, and the authentication and pathogen testing were performed at IDEXX Bio Research. Cells passaged fewer than 4 times were used for in vivo experiments.

Use of ^{139}La as Surrogate for ^{225}Ac. ^{139}La was used in place of ^{225}Ac in some nonclinical studies, as there is no stable isotope in the lanthanide series and La^{3+} is regarded as an appropriate surrogate for ^{225}Ac in preclinical studies (*26–28*).

Preparation of ^{177}Lu-RAYZ-8009 and ^{225}Ac-RAYZ-8009. RAYZ-8009 was labeled at a molar activity of 3.7 MBq/nmol (for in vitro and biodistribution studies) or 55.5 MBq/nmol (for efficacy studies) with [^{177}Lu]$LuCl_3$ (Isotopia). Quality control of ^{177}Lu-RAYZ-8009 was performed by radio–high-performance liquid chromatography with a reverse-phase C18 column at the end of synthesis. The ^{225}Ac ([^{225}Ac]$Ac(NO_3)_3$) was provided by the U.S. Department of Energy (managed by the National Isotope Development Center) and dissolved in 0.5 M HCl to form [^{225}Ac]$AcCl_3$. The [^{225}Ac]$AcCl_3$ solution was added to a reaction mixture consisting of sodium acetate (0.4 M) in water at pH 6.5. After the addition of RAYZ-8009, the reaction was incubated for 15 min at 90°C. Quality control of ^{225}Ac-RAYZ-8009 was performed by radio–thin-layer chromatography analysis, with silicic acid thin-layer chromatography plates as the solid phase and diethylenetriaminepentaacetic acid in water as the mobile phase, at the end of synthesis.

Biodistribution of ^{177}Lu-RAYZ-8009 in HepG2 Tumor–Bearing Mice. Animal studies were conducted under RayzeBio's animal care and use protocols. Biodistribution was studied on athymic nude mice harboring subcutaneously implanted HepG2 tumor. After single intravenous injections of 3.7 MBq (3.7 MBq/mmol) of ^{177}Lu-RAYZ-8009, tumor and normal tissues ($n = 3$) were collected at various time points and weighed, and the radioactivities were analyzed by γ-counting (Hidex). For dosimetry estimation, the time-integrated activity coefficient was obtained with monoexponential direct fitting and manual relative mass scaling and was used to estimate organ-specific absorbed doses in OLINDA.

SPECT Imaging. Static tumor images were acquired using the nanoSPECT imaging system (Mediso Imaging Systems). A whole-body CT scan was acquired (7 min, 50 kVp, and exposure time of 300 ms), followed by a static SPECT image (~20 min, multipinhole) with primary ^{177}Lu energy windows of 208 keV ± 10% (187–228 keV), 112 keV ± 10% (101–124 keV), and 56 keV (tertiary peak). For the subcutaneous HepG2 xenograft model, tumor-bearing mice received a bolus intravenous dose of 3.7 MBq of ^{177}Lu-RAYZ-8009 and were scanned 72 and 96 h after injection. For the orthotopic HepG2 model, tumor-bearing mice received a bolus intravenous dose of 3.7 MBq of ^{177}Lu-RAYZ-8009 and were scanned 2, 48, and 240 h after injection.

In Vivo Efficacy Studies. For the cell line–derived xenograft model, a cell suspension was diluted with RPMI medium containing 50% Matrigel (catalog no. 354234; Corning) to a concentration of 5×10^7 cells/mL. Athymic female nude mice were subcutaneously inoculated in the right hind flank with 5×10^6 cells per mouse. Tumor volume (mm^3) was assessed twice weekly and calculated as $width^2 \cdot length \cdot 0.5$. Animals were weighed individually on the days indicated in the graphs. Cage-side observations were performed daily on animals from the date of inoculation through study termination. Individual animals were killed when tumor volume reached about 2,000 mm^3, tumors became ulcerated, or the mice became moribund or had more than a 20% net weight loss lasting 3 d.

RESULTS

Binding Affinity and Specificity of RAYZ-8009 to GPC3

By surface plasma resonance, the binding equilibrium dissociation constant values of RAYZ-8009 were 0.35 and 0.42 nM for human and mouse GPC3, respectively (Supplemental Fig. 1).^{177}Lu-RAYZ-8009 bound to GPC3-expressing HepG2 cells with a dissociation constant of 10.8 nM as determined by a saturation radioligand binding assay (Supplemental Fig. 2). The binding between RAYZ-8009 and human GPC3 was not affected by the chelated isotopes ^{175}Lu, ^{139}La, or ^{69}Ga, as shown in Table 1 and Supplemental Figure 3, with comparable inhibition constants and half-maximal inhibitory concentrations measured by a competitive radioligand binding assay on HepG2 cells. Furthermore, RAYZ-8009 showed similar binding potencies to human, mouse, canine, and cynomolgus monkey GPC3 proteins (Table 2; Supplemental Fig. 4), which enables nonclinical pharmacokinetic and toxicity studies. In addition, ^{177}Lu-RAYZ-8009 exhibited binding specificity to GPC3, with no cross-reactivity to other human glypican family member proteins (Fig. 1).

Internalization of ^{177}Lu-RAYZ-8009

The internalized and surface-bound fractions of radioactivity were measured using a Microbeta counter (Perkin Elmer) at 20,

TABLE 2
Cross-Species Binding of ^{177}Lu-RAYZ-8009 to Recombinant Human, Mouse, Canine, and Cynomolgus Monkey GPC3

Parameter	Human GPC3	Mouse GPC3	Canine GPC3	Cynomolgus GPC3
Half-maximal effective concentration (nM)	1.92	1.33	5.73	4.42
Dissociation constant (nM)	2.08	1.37	5.40	3.97

Cross-species GPC3 binding of ^{177}Lu-RAYZ-8009 was evaluated in radioligand binding assay with recombinant mouse, canine, and cynomolgus monkey GPC3. Recombinant human GPC3 was used as positive control.

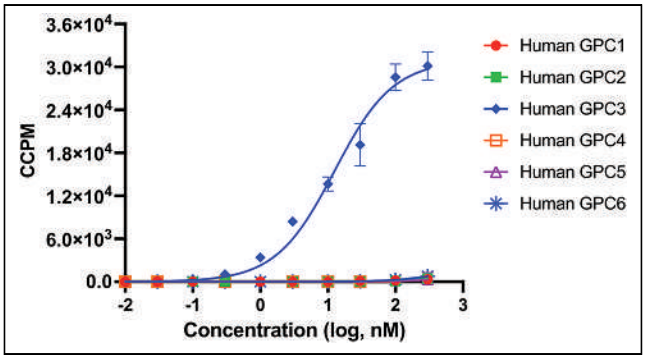

FIGURE 1. Binding specificity of ^{177}Lu-RAYZ-8009 among human glypican family proteins. Radioligand saturation binding of ^{177}Lu-RAYZ-8009 was determined with 5 μg/mL concentration of recombinant human GPC1, GPC2, GPC3, GPC4, GPC5, and GPC6 proteins. ^{177}Lu-RAYZ-8009 exhibited binding specificity to GPC3 with half-maximal effective concentration of 12.5 nM, without cross-reactivity to other human glypican proteins. CCPM = corrected counts per minute.

40, 60, 90, and 120 min after incubation of ^{177}Lu-RAYZ-8009 with HepG2 cells at 37°C. ^{177}Lu-RAYZ-8009 showed rapid internalization on binding to GPC3, with 41.6% internalized within 20 min and a peak internalization of 58.6% observed at 90 min (Fig. 2).

Pharmacokinetics in Mice

Plasma concentration–time curves for RAYZ-8009 are shown in Supplemental Figure 5. After intravenous administration at 5 mg/kg in female athymic nude mice, RAYZ-8009 showed a plasma clearance of 7.63 mL/min/kg and a half-life of 0.30 h. The volume of distribution was 0.172 L/kg, and the area under the plasma concentration–time curve from time zero to the last quantifiable concentration was 10,891 ng·h/mL. In both male and female C57BL/6 mice at 2 and 20 mg/kg doses of RAYZ-8009, the exposure appeared to be dose-proportional and independent of sex. The projected half-life in humans based on the mouse pharmacokinetic studies is about 2.2 h.

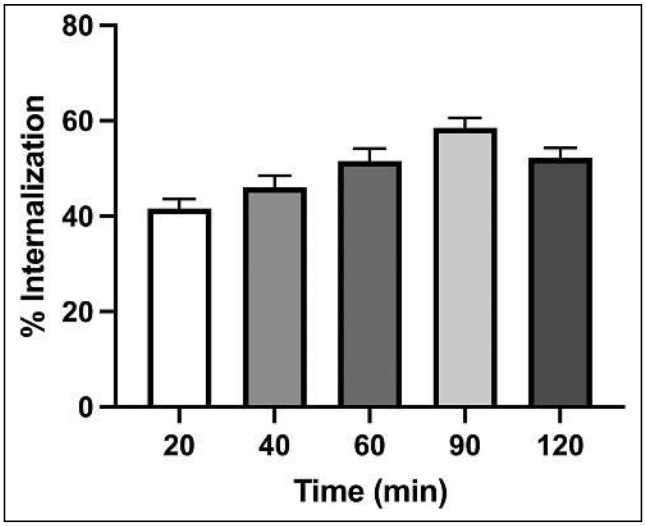

FIGURE 2. Internalization kinetics of ^{177}Lu-RAYZ-8009 in HepG2 cells. Internalized and surface-bound fractions of radioactivity were measured at indicated time points after incubation of ^{177}Lu-RAYZ-8009 with HepG2 cells at 37°C. Percentage internalization was calculated as ratio of internalized radioactivity to total (surface bound + internalized) activity. ^{177}Lu-RAYZ-8009 showed rapid internalization, with peak of 58.6% at 90 min.

Biodistribution and SPECT of ^{177}Lu-RAYZ-8009 in HepG2 Tumor–Bearing Mice

HepG2 tumor–bearing female athymic nude mice were intravenously dosed with a single injection of ^{177}Lu-RAYZ-8009 at a molar activity of 3.7 MBq/nmol. The mean injected activity was 3.9 MBq (3.7 MBq planned). Animals (3 per time point) were euthanized at 1, 2, 6, 24, 48, 96, 192, and 288 h after injection (Fig. 3A). The tumor-to-kidney ratios were 3.69, 11.33, 15.04, 22.29, and 12.37, with a tumoral percent injected dose per gram (%ID/g) of 16.63, 16.39, 8.76, 2.56, and 2.38, at 24, 48, 96, 192, and 288 h after dosing, respectively (Table 3). Kidney uptake was highest at 1 h after dosing and steadily declined throughout the 288-h study. By 96 h, the kidney levels dropped to 0.67 ± 0.16 %ID/g. The activity injected was cleared primarily in the first 24 h after dosing via excretion (71.40 %ID/g), with a smaller percentage recovered in kidneys (4.67 %ID/g) and other normal tissues (5.47 %ID/g) and the remainder retained in the tumor (16.63 %ID/g) (Table 3). Additionally, static tumor images were acquired at 72 and 96 h after dosing (Fig. 3B), confirming sustained tumor

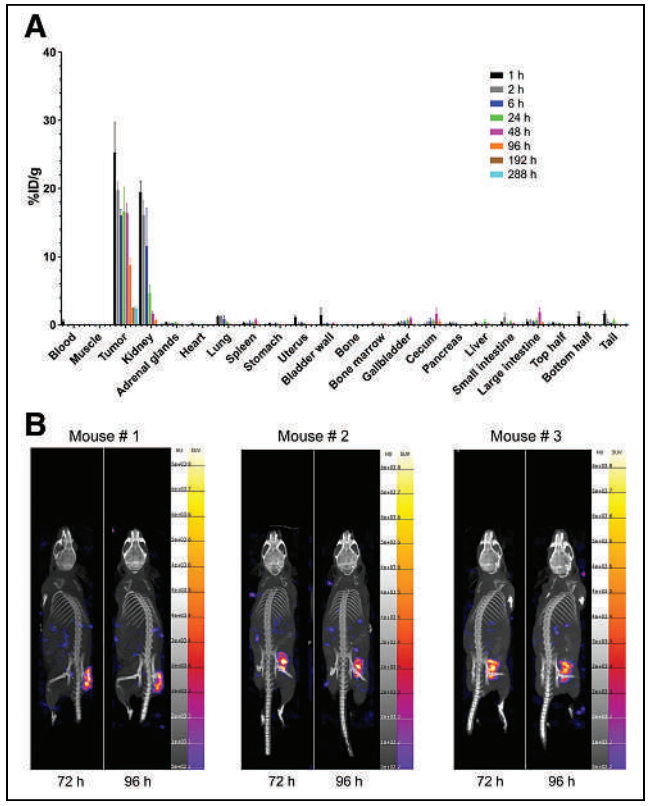

FIGURE 3. Biodistribution of ^{177}Lu-RAYZ-8009 in HepG2 xenograft model after single intravenous injection. (A) HepG2 tumor–bearing mice were intravenously dosed with ^{177}Lu-RAYZ-8009 (3.9 MBq, 3.7 MBq/nmol). Animals (3 per time point) were euthanized at indicated time points after injection. Various tissues were weighed, and radioactivities were measured by γ-counting. (B) Static tumor SPECT images were acquired at 72 and 96 h after dosing. %ID/g = percentage injected activity per gram; bottom half = remaining tissues not collected from directly below diaphragm to base of tail; top half = remaining tissues not collected from diaphragm to top of head.

TABLE 3
Ex Vivo Biodistribution After Single Intravenous Injection of ^{177}Lu-RAYZ-8009 to Female Nude Mice Bearing HepG2 Xenografted Tumor

	Average %ID/g							
Organ	1 h	2 h	6 h	24 h	48 h	96 h	192 h	288 h
Blood	0.54	0.03	0.01	0.01	0.01	0.00	0.00	0.00
Muscle	0.077	0.051	0.049	0.026	0.007	0.02	0.00	0.00
Tumor	25.28	19.77	16.08	16.63	16.39	8.76	2.56	2.38
Kidney	19.50	16.14	11.56	4.67	1.60	0.67	0.11	0.19
Adrenal glands	0.374	0.284	0.201	0.315	0.102	0.071	0.014	0.014
Heart	0.197	0.103	0.080	0.047	0.022	0.008	0.001	0.001
Lung	1.234	1.266	0.839	0.377	0.107	0.050	0.007	0.009
Spleen	0.314	0.273	0.348	0.285	0.740	0.075	0.028	0.116
Stomach	0.257	0.117	0.173	0.102	0.028	0.018	0.002	0.003
Uterus	1.097	0.269	0.325	0.189	0.071	0.058	0.026	0.043
Bladder wall	1.451	0.151	0.207	0.054	0.241	0.057	0.018	0.018
Bone	0.086	0.048	0.055	0.036	0.021	0.008	0.004	0.002
Bone marrow	0.228	0.104	0.067	0.176	0.139	0.025	0.003	0.000
Gallbladder	0.298	0.463	0.411	0.709	0.928	0.080	0.023	0.009
Cecum	0.106	0.402	0.573	0.575	1.621	0.456	0.095	0.159
Pancreas	0.279	0.308	0.175	0.076	0.023	0.009	0.001	0.000
Liver	0.263	0.133	0.090	0.463	0.159	0.060	0.020	0.044
Small intestine	0.403	1.126	0.138	0.415	0.208	0.077	0.022	0.184
Large intestine	0.532	0.621	0.451	0.634	1.872	0.306	0.107	0.248
Top half	0.326	0.227	0.186	0.143	0.047	0.016	0.003	0.006
Bottom half	1.235	0.250	0.183	0.246	0.097	0.055	0.012	0.017
Tail	1.645	0.506	0.234	0.593	0.120	0.057	0.015	0.166
Tumor-to-kidney ratio	1.29	1.25	1.76	3.69	11.33	15.04	22.29	12.37
Tumor-to-liver ratio	108.74	244.41	189.66	62.96	104.80	148.36	145.51	55.89

Top half = remaining tissues not collected from diaphragm to top of head; bottom half = remaining tissues not collected from directly below diaphragm to base of tail.

retention with minimal normal-tissue background uptake. Preliminary human dosimetry estimation based on HepG2 ex vivo biodistribution data indicated kidneys to be the dose-limiting organ (0.0858 Gy/GBq, vs. tumor at 0.779 G/GBq). When 23 Gy were used as the dose limit for kidneys, the maximal tumor dose was estimated to be about 209 Gy.

Tumor-Specific Uptake of ^{177}Lu-RAYZ-8009 in Orthotopic HepG2 HCC Model

Mice bearing orthotopically implanted HepG2 tumors were intravenously dosed with ^{177}Lu-RAYZ-8009 at 3.7 MBq/animal. Images were acquired at 2 h, 48 h, and 10 d after dosing (Supplemental Fig. 6). ^{177}Lu-RAYZ-8009 was confirmed to bind specifically to the tumor while sparing the surrounding normal liver tissue.

Antitumor Activity of ^{177}Lu- and ^{225}Ac-RAYZ-8009 in HepG2 Xenografts

HepG2 tumor–bearing mice (10/group) were administered a single intravenous dose of either ^{177}Lu-RAYZ-8009 (55.5 MBq/nmol) at 37 MBq/mouse or ^{225}Ac-RAYZ-8009 (0.185 MBq/nmol) at 0.0111, 0.0185, or 0.037 MBq/mouse. On day 26 (time of termination of vehicle group), ^{177}Lu-RAYZ-8009 exhibited 87.5% tumor growth inhibition (TGI) relative to vehicle, and ^{225}Ac-RAYZ-8009 achieved a 76.4%, 79.5%, or 85.1% TGI at 0.0111, 0.0185, or 0.037 MBq, respectively (Fig. 4A). At a dose 1,000 times lower, ^{225}Ac-RAYZ-8009 (0.037 MBq) was as efficacious in TGI as ^{177}Lu-RAYZ-8009 (37 MBq). No significant body weight change or clinical signs of stress were observed in any groups.

Antitumor Activity of ^{177}Lu- and ^{225}Ac-RAYZ-8009 in Hep3B Xenografts

Hep3B tumor–bearing mice (10/group) were dosed with ^{225}Ac-RAYZ-8009 (0.185 MBq/nmol) at 0.037 or 0.111 MBq/mouse or with ^{177}Lu-RAYZ-8009 (55.5 MBq/nmol) at 111 MBq/mouse. Treatment with RAYZ-8009 labeled with either isotope resulted in prolonged tumor regression (Fig. 4B). On day 22 after dosing (at the time of termination of the vehicle group), ^{177}Lu-RAYZ-8009 at 111 MBq resulted in a TGI of 109.8% relative to vehicle control, whereas ^{225}Ac-RAYZ-8009 at 0.111 or 0.037 MBq/mouse resulted in a TGI of 102.3% and 89.2%, respectively. At a dose 1,000 times lower, ^{225}Ac-RAYZ-8009 (0.111 MBq) was as efficacious in TGI as ^{177}Lu-RAYZ-8009 (111 MBq). Further tumor

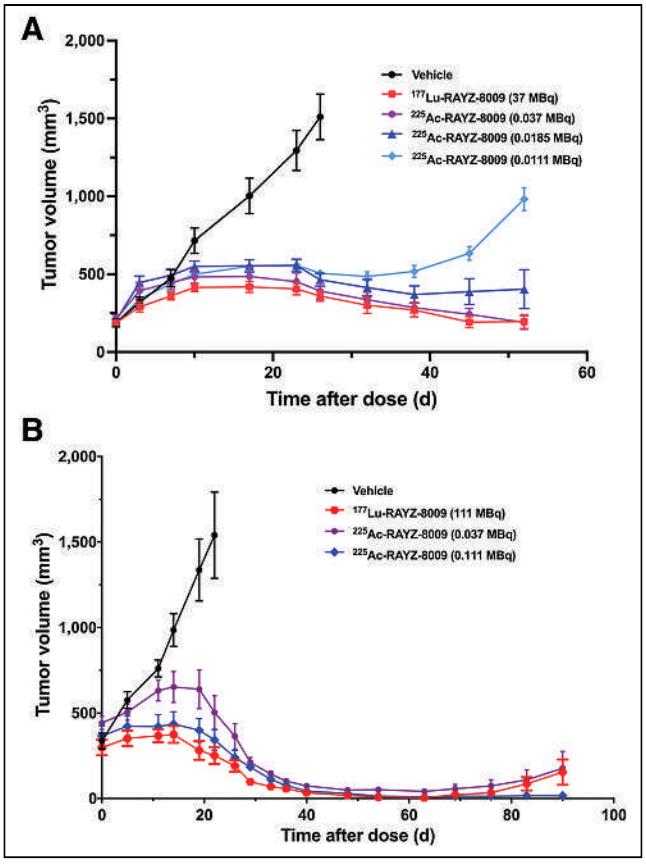

FIGURE 4. Antitumor activity of radiolabeled RAYZ-8009. (A) Antitumor activity of ^{177}Lu-RAYZ-8009 and ^{225}Ac-RAYZ-8009 in HepG2 xenografts that received single intravenous dose of either ^{177}Lu-RAYZ-8009 at 37 MBq/mouse or ^{225}Ac-RAYZ-8009 at 0.0111, 0.0185, or 0.037 MBq/mouse. (B) Antitumor activity of ^{177}Lu-RAYZ-8009 and ^{225}Ac-RAYZ-8009 in Hep3B xenografts that received single dose of ^{225}Ac-RAYZ-8009 at 0.037 or 0.111 MBq/mouse or ^{177}Lu-RAYZ-8009 at 111 MBq/mouse.

regression was observed in all treatment groups after day 22 for an additional 68 d. The most durable response was achieved with 0.111 MBq of ^{225}Ac-RAYZ-8009. No significant body weight change or clinical signs of stress were observed in any groups.

Antitumor Activity of ^{177}Lu- and ^{225}Ac-RAYZ-8009 When Combined with Lenvatinib

Lenvatinib is a standard-of-care therapy for advanced HCC. To study the potential of combining lenvatinib with RAYZ-8009, HepG2 tumor–bearing mice (10/group) were dosed with either vehicle, ^{177}Lu-RAYZ-8009 alone (11.1 MBq/mouse intravenously), lenvatinib alone (30 mg/kg orally every day for 10 d), or a combination of ^{177}Lu-RAYZ-8009 with lenvatinib. Treatment with lenvatinib alone and ^{177}Lu-RAYZ-8009 alone resulted in a 32% and 49% TGI, respectively, on day 36 after dosing (time of termination for the vehicle group), whereas the lenvatinib–^{177}Lu-RAYZ-8009 combination led to an improved TGI of 86% ($P < 0.0007$; Fig. 5A). In a separate study with Hep3B xenograft mice (10/group), treatment with lenvatinib alone (30 mg/kg orally every day for 10 d) and ^{225}Ac-RAYZ-8009 alone (0.0111 MBq/mouse) resulted in a 75% and 94% TGI, respectively, on day 24 after dosing (time of termination for the vehicle group), whereas the lenvatinib–^{225}Ac-RAYZ-8009 combination resulted in a TGI of 97% compared with vehicle alone

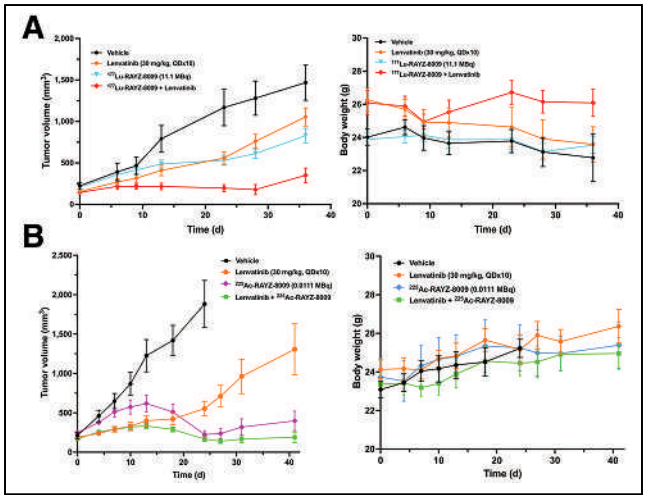

FIGURE 5. Antitumor activity of radiolabeled RAYZ-8009 in combination with lenvatinib. (A) Combination of ^{177}Lu-RAYZ-8009 and lenvatinib in HepG2 xenografts. Tumor-bearing mice were dosed with single intravenous injection of vehicle, ^{177}Lu-RAYZ-8009 alone (11.1 MBq/mouse), lenvatinib alone (30 mg/kg orally every day for 10 d), or combination of ^{177}Lu-RAYZ-8009 with lenvatinib. (B) Combination of ^{225}Ac-RAYZ-8009 and lenvatinib in Hep3B xenografts. Tumor-bearing mice were dosed with single intravenous injection of vehicle, ^{225}Ac-RAYZ-8009 alone (0.0111 MBq/mouse), lenvatinib alone (30 mg/kg orally every day for 10 d), or combination of ^{225}Ac-RAYZ-8009 with lenvatinib.

($P < 0.0009$; Fig. 5B). No significant body weight change or clinical signs of stress were observed in any groups.

DISCUSSION

Although many HCC cases can be attributed to liver cirrhosis and chronic liver diseases (*29*,*30*), GPC3 is detected only in HCC and not in cirrhotic liver tissue or other benign conditions (Supplemental Fig. 7) (*31*,*32*). Therefore, GPC3 can potentially serve as a diagnostic marker for distinguishing HCC from other non-HCC conditions (*10*,*11*). Besides HCC, other adult (*33*) and pediatric (*34*) cancer types that express GPC3 and can potentially benefit from a GPC3-directed theranostic approach include squamous lung cancer (*12*), embryonal tumors (*14*), testicular germ cell tumors (*15*), and liposarcoma (*16*).

Radiopharmaceutical therapy is a rapidly growing area in cancer drug development, with 2 agents (^{177}Lu-DOTATATE [Lutathera; Novartis] and ^{177}Lu-vipivotide tetraxetan [Pluvicto; Novartis]) having recently been approved by the Food and Drug Administration (*35*,*36*) and an ^{225}Ac-based radiopharmaceutical therapy being in phase 3 clinical evaluation (*37*,*38*). Peptide-based radiopharmaceuticals are preferred over antibodies because of several advantages, including better tumor penetration, ease of synthesis and modification, and low immunogenicity (*39*). However, previously reported GPC3 peptide binders appear to lack specificity or potency suitable for radiopharmaceutical therapy applications (*40*–*42*). In this study, RAYZ-8009 showed significantly higher affinity to GPC3 than other reported binders (*41*,*43*–*45*), an exquisite specificity to GPC3 with no binding to any other glypican family proteins, and compatibility with multiple radiometal isotopes. These properties make RAYZ-8009 suitable for theranostic development.

In tumor-bearing animals, ^{177}Lu-RAYZ-8009 exhibited sustained tumor-specific uptake and fast renal clearance. The sustained tumor

retention is likely the result of high binding affinity to GPC3 and efficient internalization. In line with minimal GPC3 expression in normal tissues by immunohistochemistry, there are minimal or undetectable signals in other normal tissues and organs except for the kidney, the primary route of clearance. Peptide uptake in the kidneys can also be due to kidney-expressed amino acid transporters and organic anion/cation transporters transiently binding the peptide (*46*,*47*). Even so, the HepG2 tumor signals were consistently higher than those in kidneys at all time points, with increasing tumor-to-kidney ratios ranging from 1.25 at 2 h to 22.29 at 192 h after injection.

In both HCC xenograft models, ^{225}Ac-RAYZ-8009 as a single agent demonstrated dose-dependent antitumor activities including sustained tumor regression. Compared with ^{177}Lu-RAYZ-8009, ^{225}Ac-RAYZ-8009 treatment yielded comparable TGI with an injected activity 1,000 times lower. The α-emitter ^{225}Ac-labeled binder may offer several advantages over the β-emitter ^{177}Lu-labeled binder. α-emitters typically have a short path in human tissue (40–100 μm), equivalent to the thickness of 1–3 cell widths, allowing for selective killing of targeted cancer cells while sparing surrounding healthy tissue (*48*). Additionally, α-emitters can generate linear energy transfer several magnitudes higher than β-emitters, causing double-stranded DNA breaks and subsequent cancer cell death with high efficiency (*49*,*50*). Along with higher linear energy transfer, the cell-killing effect of α-particles is not dependent on tumor oxidization status, whereas β-emitters are dependent on oxygen for maximal effect (*51*). Besides single-agent activity, RAYZ-8009 showed superior antitumor efficacy when combined with lenvatinib, one of the approved first-line therapies for unresectable HCC.

CONCLUSION

RAYZ-8009 is a peptide-based, potent, and selective radiopharmaceutical agent targeting GPC3-expression tumors. The favorable preclinical pharmacokinetic and biodistribution profiles, and durable antitumor efficacy either as a single agent or in combination with standard-of-care TKI inhibitor, demonstrate the potential of RAYZ-8009 as a theranostic agent for the treatment of patients with GPC3-positive HCC.

KEY POINTS

QUESTION: Does targeting of GPC3 overexpression with a radiopharmaceutical agent represent a promising therapeutic strategy for HCC?

PERTINENT FINDINGS: Treatment with the highly potent and selective GPC3-targeted peptide binder RAYZ-8009 conjugated with either ^{177}Lu or ^{225}Ac led to tumor-specific uptake of the agent, resulting in sustained tumor regression in HCC xenograft models.

IMPLICATIONS FOR PATIENT CARE: Preclinical data support clinical development of RAYZ-8009 as a theranostic agent for patients with HCC.

DISCLOSURE

Fanching Lin, Renee Clift, Steven Horton, Alain Noncovich, Matt Guest, Daniel Kim, Katrina Salvador, Samantha Richardson, Terra Miller, Guangzhou Han, Abhijit Bhat, Kenneth Song, and Gary Li are employees and stock option holders of RayzeBio, Inc. Takeru Ehara and Hayato Yanagida are employees of PeptiDream Inc. No other potential conflict of interest relevant to this article was reported.

ACKNOWLEDGMENTS

We thank Anna Karmann, Jessica Rearden, and Susan Moran for scientific and clinical input.

REFERENCES

1. Sung H, Ferlay J, Siegel RL, et al. Global cancer statistics 2020: GLOBOCAN estimates of incidence and mortality worldwide for 36 cancers in 185 countries. *CA Cancer J Clin.* 2021;71:209–249.
2. Eslam M, George J. Genetic contributions to NAFLD: leveraging shared genetics to uncover systems biology. *Nat Rev Gastroenterol Hepatol.* 2020;17:40–52.
3. Filmus J, Capurro M, Rast J. Glypicans. *Genome Biol.* 2008;9:224.
4. Haruyama Y, Kataoka H. Glypican-3 is a prognostic factor and an immunotherapeutic target in hepatocellular carcinoma. *World J Gastroenterol.* 2016;22:275–283.
5. Bell MM, Gutsche NT, King AP, et al. Glypican-3-targeted alpha particle therapy for hepatocellular carcinoma. *Molecules.* 2020;26:4.
6. Hsu H, Cheng W, Lai P. Cloning and expression of a developmentally regulated transcript MXR7 in hepatocellular carcinoma: biological significance and temporospatial distribution. *Cancer Res.* 1997;57:5179–5184.
7. Shih TC, Wang L, Wang HC, Wan YY. Glypican-3: a molecular marker for the detection and treatment of hepatocellular carcinoma. *Liver Res.* 2020;4:168–172.
8. Kaseb AO, Hassan M, Lacin S, et al. Evaluating clinical and prognostic implications of Glypican-3 in hepatocellular carcinoma. Vol 7; 2016:69916-69926.
9. Shirakawa H, Suzuki H, Shimomura M, et al. Glypican-3 expression is correlated with poor prognosis in hepatocellular carcinoma. *Cancer Sci.* 2009;100:1403–1407.
10. Capurro M, Wanless IR, Sherman M, et al. Glypican-3: a novel serum and histochemical marker for hepatocellular carcinoma. *Gastroenterology.* 2003;125:89–97.
11. Zhu ZW, Friess H, Wang L, et al. Enhanced glypican-3 expression differentiates the majority of hepatocellular carcinomas from benign hepatic disorders. *Gut.* 2001;48:558–564.
12. Aviel-Ronen S, Lau SK, Pintilie M, et al. Glypican-3 is overexpressed in lung squamous cell carcinoma, but not in adenocarcinoma. *Mod Pathol.* 2008;21:817–825.
13. Ning J, Jiang S, Li X, et al. GPC3 affects the prognosis of lung adenocarcinoma and lung squamous cell carcinoma. *BMC Pulm Med.* 2021;21:199.
14. Saikali Z, Sinnett D. Expression of glypican 3 (GPC3) in embryonal tumors. *Int J Cancer.* 2000;89:418–422.
15. Zynger DL, Dimov ND, Luan C, Teh BT, Yang XJ. Glypican 3: a novel marker in testicular germ cell tumors. *Am J Surg Pathol.* 2006;30:1570–1575.
16. Baumhoer D, Tornillo L, Stadlmann S, Roncalli M, Diamantis EK, Terracciano LM. Glypican 3 expression in human nonneoplastic, preneoplastic, and neoplastic tissues: a tissue microarray analysis of 4,387 tissue samples. *Am J Clin Pathol.* 2008;129:899–906.
17. Shimizu Y, Suzuki T, Yoshikawa T, Endo I, Nakatsura T. Next-generation cancer immunotherapy targeting glypican-3. *Front Oncol.* 2019;9:248.
18. Zhang Q, Fu Q, Cao W, et al. First report of preliminary safety, efficacy, and pharmacokinetics of C-CAR031 (GPC3-specific TGFβRIIDN CAR-T) in patients with advanced HCC [abstract]. *Cancer Res.* 2023;83(suppl):CT097.
19. Steffin DHM, Ghatwai N, Batra S, et al. A phase 1 clinical trial using armored GPC3-car T cells for children with relapsed/refractory liver tumors [abstract]. *J Clin Oncol.* 2020;37(suppl):TPS2647.
20. Pouget JP, Lozza C, Deshayes E, Boudousq V, Navarro-Teulon I. Introduction to radiobiology of targeted radionuclide therapy. *Front Med (Lausanne).* 2015;2:12.
21. Carrasquillo JA, O'Donoghue JA, Beylergil V, et al. I-124 codrituzumab imaging and biodistribution in patients with hepatocellular carcinoma. *EJNMMI Res.* 2018;8:20.
22. Fayn S, King AP, Gutsche NT, et al. Site-specifically conjugated single-domain antibody successfully identifies glypican-3-expressing liver cancer by immuno-PET. *J Nucl Med.* 2023;64:1017–1023.
23. Kashiwagi K, Reid CP, inventors; Peptidream Inc., assignee. Rapid display method in translational synthesis of peptide. Patent WO2011049157. April 28, 2011.
24. Goto Y, Katoh T, Suga H. Flexizymes for genetic code reprogramming. *Nat Protoc.* 2011;6:779–790.
25. Ishizawa T, Kawakami T, Reid PC, Murakami H. TRAP display: a high-speed selection method for the generation of functional polypeptides. *J Am Chem Soc.* 2013;135:5433–5440.
26. Nelson B, Andersson J, Wuest F. Targeted alpha therapy: progress in radionuclide production, radiochemistry and applications. *Pharmaceutics.* 2020;13:49.

27. Pandya DN, Hantgan R, Budzevich MM, et al. Preliminary therapy evaluation of ^{225}Ac-DOTA-c(RGDyK) demonstrates that Cerenkov radiation derived from ^{225}Ac daughter decay can be detected by optical imaging for in vivo tumor visualization. *Theranostics.* 2016;6:698–709.
28. Thiele NA, Wilson JJ. Actinium-225 for targeted alpha therapy: coordination chemistry and current chelation approaches. *Cancer Biother Radiopharm.* 2018;33:336–348.
29. McGlynn KA, Petrick JL, El-Serag HB. Epidemiology of hepatocellular carcinoma. *Hepatology.* 2021;73(suppl 1):4–13.
30. Chidambaranathan-Reghupaty S, Fisher PB, Sarkar D. Hepatocellular carcinoma (HCC): epidemiology, etiology and molecular classification. *Adv Cancer Res.* 2021;149:1–61.
31. Libbrecht L, Severi T, Cassiman D, et al. Glypican-3 expression distinguishes small hepatocellular carcinomas from cirrhosis, dysplastic nodules, and focal nodular hyperplasia-like nodules. *Am J Surg Pathol.* 2006;30:1405–1411.
32. Wang HL, Anatelli F, Zhai QJ, Adley B, Chuang ST, Yang XJ. Glypican-3 as a useful diagnostic marker that distinguishes hepatocellular carcinoma from benign hepatocellular mass lesions. *Arch Pathol Lab Med.* 2008;132:1723–1728.
33. Moek KL, Fehrmann RSN, van der Vegt B, de Vries EGE, de Groot DJA. Glypican 3 overexpression across a broad spectrum of tumor types discovered with functional genomic mRNA profiling of a large cancer database. *Am J Pathol.* 2018;188:1973–1981.
34. Ortiz MV, Roberts SS, Glade Bender J, Shukla N, Wexler LH. Immunotherapeutic targeting of GPC3 in pediatric solid embryonal tumors. *Front Oncol.* 2019;9:108.
35. Hennrich U, Kopka K. Lutathera®: the first FDA- and EMA-approved radiopharmaceutical for peptide receptor radionuclide therapy. *Pharmaceuticals (Basel).* 2019;12:114.
36. Hennrich U, Eder M. [^{177}Lu]Lu-PSMA-617 (Pluvicto™): the first FDA-approved radiotherapeutical for treatment of prostate cancer. *Pharmaceuticals (Basel).* 2022;15:1292.
37. Han G, Hwang E, Lin F, et al. RYZ101 (Ac-225 DOTATATE) opportunity beyond gastroenteropancreatic neuroendocrine tumors: preclinical efficacy in small cell lung cancer. *Mol Cancer Ther.* 2023;22:1434–1443.
38. Morris M, Ulaner GA, Halperin DM, et al. ACTION-1 phase Ib/3 trial of RYZ101 in somatostatin receptor subtype 2–expressing (SSTR2+) gastroenteropancreatic neuroendocrine tumors (GEP-NET) progressing after ^{177}Lu somatostatin analogue (SSA) therapy: initial safety analysis [abstract]. *J Clin Oncol.* 2023;41(suppl):4132.
39. Okarvi SM. Peptide-based radiopharmaceuticals and cytotoxic conjugates: potential tools against cancer. *Cancer Treat Rev.* 2008;34:13–26.
40. Berman RM, Kelada OJ, Gutsche NT, et al. In vitro performance of published glypican 3-targeting peptides TJ12P1 and L5 indicates lack of specificity and potency. *Cancer Biother Radiopharm.* 2019;34:498–503.
41. Wang S, Kalim M, Liang K, Zhan J. Polyclonal antibody production against rGPC3 and their application in diagnosis of hepatocellular carcinoma. *Prep Biochem Biotechnol.* 2018;48:435–445.
42. Li D, Li N, Zhang YF, et al. Persistent polyfunctional chimeric antigen receptor T cells that target glypican 3 eliminate orthotopic hepatocellular carcinomas in mice. *Gastroenterology.* 2020;158:2250–2265.e20.
43. Zhu D, Qin Y, Wang J, et al. Novel glypican-3-binding peptide for in vivo hepatocellular carcinoma fluorescent imaging. *Bioconjug Chem.* 2016;27:831–839.
44. Qin Z, Wang J, Wang Y, et al. Identification of a glypican-3-binding peptide for in vivo non-invasive human hepatocellular carcinoma detection. *Macromol Biosci.* 2017;17(4).
45. Zhang Q, Han Z, Tao J, et al. An innovative peptide with high affinity to GPC3 for hepatocellular carcinoma diagnosis. *Biomater Sci.* 2018;7:159–167.
46. Ganapathy V, Leibach FH. Carrier-mediated reabsorption of small peptides in renal proximal tubule. *Am J Physiol.* 1986;251:F945–F953.
47. van Montfoort JE, Hagenbuch B, Groothuis GM, Koepsell H, Meier PJ, Meijer DK. Drug uptake systems in liver and kidney. *Curr Drug Metab.* 2003;4:185–211.
48. Shi M, Jakobsson V, Greifenstein L, et al. Alpha-peptide receptor radionuclide therapy using actinium-225 labeled somatostatin receptor agonists and antagonists. *Front Med (Lausanne).* 2022;9:1034315.
49. Sgouros G. Dosimetry, radiobiology and synthetic lethality: radiopharmaceutical therapy (RPT) with alpha-particle-emitters. *Semin Nucl Med.* 2020;50:124–132.
50. Makvandi M, Dupis E, Engle JW, et al. Alpha-emitters and targeted alpha therapy in oncology: from basic science to clinical investigations. *Target Oncol.* 2018;13:189–203.
51. Wang H, Jiang H, Van De Gucht M, De Ridder M. Hypoxic radioresistance: can ROS be the key to overcome it? *Cancers (Basel).* 2019;11:112.

Development and Preclinical Evaluation of [^{211}At]PSAt-3-Ga: An Inhibitor for Targeted α-Therapy of Prostate Cancer

Mohamed El Fakiri*[1–6], Nawal Ayada*[1–4,6], Marius Müller[6,7], Lars Hvass[7,8], Teodor H. Gamzov[6], Anne Skovsbo Clausen[7,8], Nicolas M. Geis[1–5], Nils Steinacker[1–4], Ellinor Hansson[9], Sture Lindegren[9,10], Emma Aneheim[9,10], Holger Jensen[7], Ann-Christin Eder[1–4], Andreas I. Jensen[11], Christian B.M. Poulie[†6], Andreas Kjaer[†7,8], Matthias Eder[†1–4], and Matthias M. Herth[†6,7]

[1]Department of Nuclear Medicine, University Medical Center Freiburg, Freiburg, Germany; [2]Faculty of Medicine, University of Freiburg, Freiburg, Germany; [3]Division of Radiopharmaceutical Development, German Cancer Consortium Partner Site, Freiburg, Germany; [4]German Cancer Research Center, Heidelberg, Germany; [5]Faculty of Biology, University of Freiburg, Freiburg, Germany; [6]Department of Drug Design and Pharmacology, Faculty of Health and Medical Sciences, University of Copenhagen, Copenhagen, Denmark; [7]Department of Clinical Physiology, Nuclear Medicine and PET, Rigshospitalet, Copenhagen, Denmark; [8]Cluster for Molecular Imaging, Department of Biomedical Sciences, University of Copenhagen, Copenhagen, Denmark; [9]Atley Solutions AB, Gothenburg, Sweden; [10]Department of Radiation Physics, Institute of Clinical Sciences, Sahlgrenska Academy, University of Gothenburg, Gothenburg, Sweden; and [11]Center for Nanomedicine and Theranostics, DTU Health Technology, DTU, Lyngby, Denmark

The application of prostate-specific membrane antigen (PSMA)–targeted α-therapy is a promising alternative to β$^-$-particle–based treatments. ^{211}At is among the potential α-emitters that are favorable for this concept. Herein, ^{211}At-based PSMA radiopharmaceuticals were designed, developed, and evaluated. **Methods:** To identify a ^{211}At-labeled lead, a surrogate strategy was applied. Because astatine does not exist as a stable nuclide, it is commonly replaced with iodine to mimic the pharmacokinetic behavior of the corresponding ^{211}At-labeled compounds. To facilitate the process of structural design, iodine-based candidates were radiolabeled with the PET radionuclide ^{68}Ga to study their preliminary in vitro and in vivo properties before the desired ^{211}At-labeled lead compound was formed. The most promising candidate from this evaluation was chosen to be ^{211}At-labeled and tested in biodistribution studies. **Results:** All ^{68}Ga-labeled surrogates displayed affinities in the nanomolar range and specific internalization in PSMA-positive LNCaP cells. PET imaging of these compounds identified [^{68}Ga]PSGa-**3** as the lead compound. Subsequently, [^{211}At]PSAt-**3**-Ga was synthesized in a radiochemical yield of 35% and showed tumor uptake of 19 ± 8 percentage injected dose per gram of tissue (%ID/g) at 1 h after injection and 7.6 ± 2.9 %ID/g after 24 h. Uptake in off-target tissues such as the thyroid (2.0 ± 1.1 %ID/g), spleen (3.0 ± 0.6 %ID/g), or stomach (2.0 ± 0.4 %ID/g) was low, indicating low in vivo deastatination of [^{211}At]PSAt-**3**-Ga. **Conclusion:** The reported findings support the use of iodine-based and ^{68}Ga-labeled variants as a convenient strategy for developing astatinated compounds and confirm [^{211}At]PSAt-**3** as a promising radiopharmaceutical for targeted α-therapy.

Key Words: PSMA; prostate cancer; ^{211}At; targeted α-therapy; α-emitters

J Nucl Med 2024; 65:593–599
DOI: 10.2967/jnumed.123.267043

Metastatic castration-resistant prostate cancer is a disease with poor prognosis and median survival times no longer than 12 mo (*1–3*). However, the recent approval by regulatory agencies of the prostate-specific membrane antigen (PSMA)–targeted radiopharmaceutical [^{177}Lu]Lu-PSMA-617 (Pluvicto; Novartis) is raising hope (*4*). Nevertheless, [^{177}Lu]Lu-PSMA-617 is able to treat only 50%–60% of late-stage metastatic castration-resistant prostate cancer patients (*5–7*). It has been shown that PSMA-targeted α-radiotherapy is an effective and promising alternative to β$^-$-based approaches (*8,9*). For example, the application of ^{225}Ac-labeled PSMA ligands resulted in positive outcomes for patients who did not respond to ^{177}Lu-based therapy (*10,11*).

One of the most promising α-emitters is ^{211}At. Its production is scalable, and its relatively short half-life (7.2 h) matches the tumor retention time of many targeting vectors (*12*). Radionuclides with half-lives that fit the biological tumor retention time of the targeting vector, such as ^{211}At, should optimize the dose that can be delivered, maximizing the therapeutic effect (*13*). In addition, using nuclides with half-lives shorter than that of, for example, ^{225}Ac can result in a lower radiation burden on nontarget tissues. In addition, efforts have been made to explain the relative ineffectiveness of therapeutic fibroblast activation protein inhibitor derivatives using longer-lived radionuclides such as ^{177}Lu and ^{90}Y (*14,15*). Thus, it is not surprising that several ^{211}At-based radiopharmaceuticals targeting PSMA have been developed (*16–19*).

In this work, a class of ^{211}At-labeled PSMA-targeting structures based on the successful glutamate–urea–lysine construct was developed. The main aim was to possibly reduce deastatination and mimic the biodistribution pattern of PSMA-617, including its ability to internalize into cells—a relevant feature, because cell internalization has been shown to positively correlate with therapeutic effect for PSMA-targeting radiopharmaceuticals (*20,21*). Figure 1 displays the design rationale of the compounds. The glutamate–urea–lysine construct was chosen to promote specificity and nanomolar affinity toward PSMA. Aromatic amino acids in the linker region were inserted to promote internalization via lipophilic interaction with the S1 aromatic region deep inside the PSMA binding

Received Nov. 15, 2023; revision accepted Jan. 23, 2024.
For correspondence or reprints, contact Matthias M. Herth (matthias.herth@sund.ku.dk).
*Contributed equally to this work.
†Contributed equally to this work.
Published online Feb. 29, 2024.

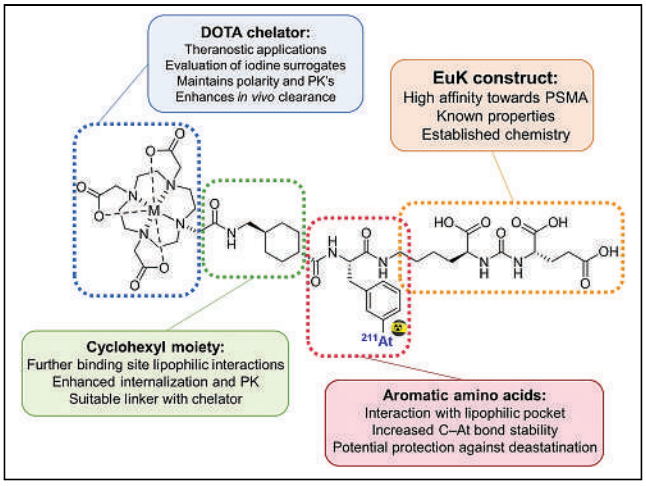

FIGURE 1. Design rationale of reported series. Compound selected as lead candidate, [^{211}At]-PSAt-**3,** is used as example. EuK = glutamate–urea–lysine; PK = pharmacokinetics.

pocket (*22*). It was also chosen to ^{211}At-astatinate the inhibitors within this lipophilic linker region, because it was hypothesized that this could shield ^{211}At from oxidative species, which are supposed to be responsible for deastatination processes (*23*). Consequently, achievement of higher in vivo stability was expected using this labeling approach. Finally, the DOTA chelator was preserved in the structures to promote excretion because of the intrinsic polarity of this moiety (*24*) and to have the possibility of radiolabeling with ^{68}Ga, which allowed more convenient in vitro and in vivo evaluation. Therefore, ^{68}Ga-labeled iodine-based surrogates were evaluated to approximate the in vivo behavior of their ^{211}At-labeled counterparts. This strategy was used because astatine does not exist in a nonradioactive form; in addition, its scarce availability would have made the evaluation studies even more challenging.

MATERIALS AND METHODS

Chemistry and Radiochemistry

The series of synthesized compounds is depicted in Figure 2. The chemical synthesis of all derivatives was performed via standard solid phase peptide synthesis (SPPS) or solution phase peptide synthesis (*25*). All building blocks for peptide chemistry were from commercial sources, except for silyl-containing amino acid **9,** which was synthesized using palladium-mediated chemistry (*26*). The precursor for [^{68}Ga]Ga-PSMA-617 was obtained from commercial sources. Figure 3 outlines the general synthetic pathway for amino acid **9** and precursors **18** and **11.** Details on the syntheses and purifications are available in the supplemental materials (supplemental materials are available at http://jnm.snmjournals.org). Labeling with ^{68}Ga was performed using standard procedures; details are available in the supplemental materials.

^{211}At was produced on a Scanditronix MC32 cyclotron (Copenhagen University Hospital) via the ^{209}Bi(α,2n)^{211}At reaction. Thereafter, ^{211}At was isolated through dry distillation (Atley C100; Atley Solutions) and recovered in chloroform for further processing.

For ^{211}At labeling, ^{211}At in chloroform (50–200 MBq) was poured into a V-shaped glass vial, and solvent was evaporated with a flow of nitrogen. Afterward, a solution of the trimethylsilane precursor (precursor **18,** PSTMS-3) in methanol was added (5 μL, 50 nmol), followed by the addition of *N*-chlorosuccinimide (400 μg, 3.0 μmol) in 20 μL of methanol and a 0.3 M methanol–acetic acid solution (20 μL). The whole mixture was then evaporated to dryness with a gentle nitrogen flow. Thereafter, trifluoroacetic acid (20 μL) was added to the mixture and heated to 70°C for 10 min (*27*). Directly after labeling, the mixture was evaporated to dryness and redissolved in sodium acetate buffer (80 μL, pH 5.5), followed by addition of an excess of $^{nat}GaNO_3$. The solution was heated to 70°C for an additional 10 min to ensure complete complexation. After radiolabeling and cold complexation, the mixture was diluted to 200 μL by the addition of an acetonitrile–water–trifluoroacetic acid mixture (20:80:0.1) and subsequently purified by high-performance liquid chromatography. Collected fractions containing [^{211}At]PSAt-**3**-Ga were diluted with water (10 mL) and loaded onto a preconditioned hydrophilic lipophilic balanced cartridge (Chromafix HLB Small 60 μm; Macherey-Nagel). A solid phase extraction cartridge was washed with water (5 mL), dried with air, and [^{211}At]PSAt-**3**-Ga–eluted with 0.5 mL of absolute ethanol. The ethanol was evaporated under a stream of nitrogen, and the compound was reconstituted in phosphate-buffered saline (pH 7.4) containing 5% ethanol.

Cell Culture and In Vitro Assays

For in vitro and in vivo evaluation of the compounds, the PSMA-positive cell line LNCaP was used (CRL-17400; American Type Culture Collection). To this end, cells were cultured in RPMI medium supplemented with 10% fetal calf serum, 1% sodium pyruvate, and 1% penicillin–streptomycin to avoid bacterial growth. Cells were kept at 37°C in humidified air supplemented with 5% carbon dioxide; when a confluence of at least 80% was reached, cells were harvested using trypsin–ethylenediaminetetraacetic acid and subsequently processed. Cells were regularly authenticated (last authentication April 2023) and were *Mycoplasma*-free.

Internalization, plasma protein binding, lipophilicity, and binding affinity assays were performed as described previously (*28*). Details on the methodologies are provided in the supplemental materials.

In Vivo Evaluation

For PET imaging, 7- to 8-wk-old BALC/c *nu/nu* mice (Janvier) were subcutaneously inoculated on their right flank with 5×10^6 LNCaP cells (in a 1:1 ratio of phosphate-buffered saline to Matrigel; Corning). Once the tumor size was about 1 cm^3, mice were injected via the tail vein with 500 pmol of the ^{68}Ga-labeled compounds (10–15 MBq). A dynamic PET scan spanning 0–60 min after injection was recorded (30 frames), followed by a nontriggered localizer and a 3-step, whole-body, T1-weighed, 3-dimensional MR scan (PET/MR 3T; Bruker BioSpin). In addition, static images (10-min scan time) were recorded at 2 h after injection, also followed by a nontriggered localizer and a 3-step, T1-weighed, 3-dimensional MR image. PET/MR data were obtained via ParaVision version 3.0 (ParaVision) and reconstructed through a maximum-likelihood expectation maximization algorithm at 0.5 mm for 18 iterations. MR-based attenuation correction was applied to the reconstruction.

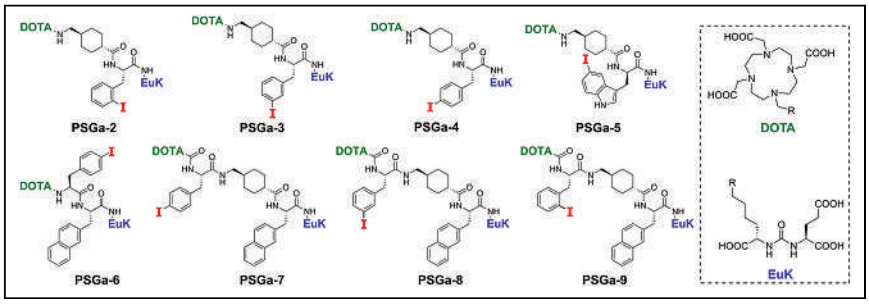

FIGURE 2. Series of compounds synthesized for preliminary evaluation through their ^{68}Ga-labeled versions. Note presence of cold iodine in various strategic positions. EuK = glutamate–urea–lysine.

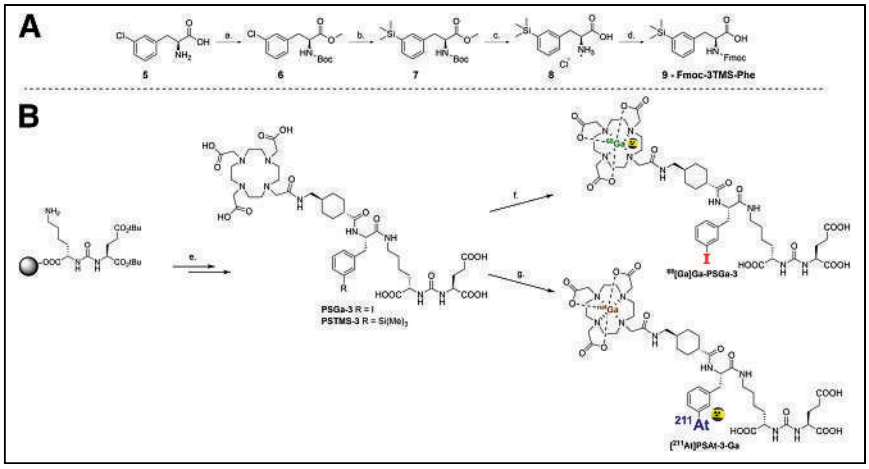

FIGURE 3. (A) Synthetic pathway toward key amino acid **9** (*Fmoc*-3TMS-Phe). (a) AcCl, methanol, 80°C, 5 h (i); Boc_2O, Et_3N, tetrahydrofuran, room temperature (r.t.), overnight (o.n.) (ii). (b) $Pd_2(dba)_3$, Me_3Si_2, water, $KHCO_3$, ^{me}CgPPh, dimethylformamide, 100°C, 72 h. (c) LiOH, tetrahydrofuran/water, r.t., 1.5 h (i); 4 M HCl, dioxane, r.t., 30 min (ii). (d) Fmoc-Cl, 10% $NaHCO_{3(aqueous)}$/dioxane, 0°C, 2 h. (B) Synthesis and subsequent radiolabeling of lead candidate precursors PSGa-**3** and PSTMS-**3.** (e) Standard solid-phase peptide synthesis: hexafluorophosphate azabenzotriazole tetramethyl uronium, *N,N*-diisopropylethylamine, dimethylformamide, 35°C, 60 min to o.n. (i); 20% piperidine in dimethylformamide, 35°C, 10 min (ii); trifluoroacetic acid–water–triisopropylsilane (94:3:3), r.t., 2 h, or 4 M HCl, dioxane, r.t., 2 h (iii). (f) $^{68}Ga^{3+}$, (4-(2-hydroxyethyl)-1-piperazineethanesulfonic acid) (1.0 M, pH 4.0), 95°C, 5 min. (g) ^{211}At, methanol, trifluoroacetic acid, 70°C, 10 min (i); 10 mM $^{nat}Ga(NO)_3$ in 0.1 M HCl, NaOAc buffer (pH 4.5), 70°C, 10 min (ii).

For biodistribution of [^{211}At]PSAt-**3**-Ga, the same tumor model was used. Once the tumors were sizable, mice were injected via the tail vein with approximately 100 kBq of [^{211}At]PSAt-**3**-Ga. Mice were killed at 2, 6, and 24 h after injection (n = 4–6 per time point), and organs of interest were harvested. Organs included heart, lungs, liver, salivary glands, thyroid (trachea), spleen, stomach, small intestine, and kidneys; blood, tail, and grafted LNCaP tumor were also harvested. After weighing, each organ was measured in an automated γ-counter (Hidex AMG) with an energy window of 60–100 keV. The percentage injected dose per gram of tissue (%ID/g) was calculated using the amount of solution injected and the animal or organ weight. All counts were decay-corrected and standardized to the injection solution.

All animal experiments were performed according to the directive 2010/63/EU of the European Parliament and the European Council on the protection of animals used for scientific purposes and approved by the Danish Animal Experiments Inspectorate under an approved animal license (2021-15-0201-01041, approved December 2021, biodistribution studies), as well as the Federal Republic of Germany, Regional Council Freiburg (35-9185.81/G18/04, approved February 2018, PET/MR studies). In all cases, mice were housed upon arrival in groups to acclimatize them for a week with a light-to-dark period of 12:12 h and under controlled environmental conditions. Access to fresh water and standard pellet diet was provided ad libitum.

Statistics

All experiments were performed at least in triplicate, with the exception of PET/MRI (n = 1). All multiple measurement results are expressed as mean ± SD. Data were analyzed and plotted using Prism (version 8.0.1; GraphPad Software). Applicable P values were determined by Student t test and were considered significant when smaller than 0.05.

RESULTS

Chemistry

Reference Compounds. Eight PSMA iodine-bearing derivatives (PSGa-**2** through PSGa-**9**) were successfully synthesized (Fig. 2). These compounds were used as surrogates to study the pharmacokinetic behavior of their corresponding ^{211}At-labeled counterparts. They were synthesized according to reported procedures (*25,28*), with overall yields of 2%–15%. In all cases, the key intermediate was the dissolved or resin-supported lysine–urea–glutamate construct, and syntheses were performed using single-peptide coupling steps that led to overall yields of 4%–15%, typical for SPPS procedures. More details on the syntheses and analytic data are shown in the supplemental materials.

Precursor. Synthesis of silyl precursor **18** was successful in a 6-step SPPS sequence with an overall yield of 2%. The key intermediate, nonnatural amino acid **9,** could be obtained in an overall yield of 10% over 4 steps. Figure 3 displays the synthetic strategy. Details on the synthetic procedures, along with analytic data, are shown in the supplemental materials.

Radiochemistry

Labeling with ^{211}At was performed through trimethylsilyl-bearing precursors (*27*). The radiolabeling of precursor **18** was successful, with a radiochemical conversion of 75% and a radiochemical yield of 35% after $^{nat}Ga^{3+}$ complexation and high-performance liquid chromatography purification. ^{68}Ga labeling was performed following conditions described in the supplemental materials and resulted in radiochemical conversions of at least 98% for all iodine-bearing analogs. Radiochemical conversion and radiochemical yield were determined according to consensus guidelines (*29*).

In Vitro Evaluation

Physicochemical properties such as lipophilicity ($\log D_{pH7.4}$ in n-octanol and phosphate-buffered saline) of the ^{68}Ga-labeled derivatives and plasma protein binding were determined, with results in the expected ranges. These are summarized in Table 1.

Internalization studies of the ^{68}Ga-labeled derivatives showed specific uptake within LNCaP cells (Table 1) after 45 min of incubation. Uptake was specific as proven by blocking experiments with 2-phosphonomethyl pentanedioic acid. Binding affinities were in the nanomolar range for all tested ^{68}Ga-labeled inhibitors (Table 1). [^{68}Ga]Ga-PSGa-**4** or [^{68}Ga]Ga-PSGa-**5** and [^{68}Ga]Ga-PSGa-**6** showed an inhibitor constant 2-fold lower than that of [^{68}Ga]Ga-PSMA-617. Other compounds displayed binding affinities similar to that of [^{68}Ga]Ga-PSMA-617 ($P > 0.05$). With regard to internalization, [^{68}Ga]Ga-PSGa-**6** internalization was significantly lower than that of [^{68}Ga]Ga-PSMA-617 ($P = 0.046$), whereas the rest of the tested compounds showed nonsignificant differences compared with [^{68}Ga]Ga-PSMA-617 ($P > 0.05$).

PET/MRI

PET imaging in LNCaP xenograft mice revealed fast tumor uptake accompanied by rapid clearance through renal pathways for all ^{68}Ga-labeled compounds. All tracers showed uptake higher than or similar to that of [^{68}Ga]Ga-PSMA-617, with peak tumor accumulation of 0.4–0.6 SUV (g/mL) within 0–60 min after injection. Tumor uptake slightly decreased over time, resulting in tumor

TABLE 1
In Vitro Characterization Data of ^{68}Ga-Labeled Surrogate Compounds (n = 3)

Compound	Specific internalization (%AA/10^5 cells)*	K_i (nM)†	Lipophilicity‡	Plasma protein binding (%)	
				Mouse	Human
PSMA-617	0.14 ± 0.04	17.8 ± 5.9	−3.5 ± 0.1	63.3 ± 2.4	76.7 ± 3.2
PSGa-**2**	0.15 ± 0.06	27.4 ± 3.0	−3.4 ± 0.1	66.6 ± 0.5	76.4 ± 0.9
PSGa-**3**	0.16 ± 0.03	28.7 ± 4.4	−3.8 ± 0.1	55.8 ± 2.3	67.5 ± 4.2
PSGa-**4**	0.05 ± 0.01	14.7 ± 4.6	−3.7 ± 0.2	55.9 ± 0.9	70.5 ± 3.5
PSGa-**5**	0.14 ± 0.05	12.9 ± 1.8	−3.6 ± 0.1	66.2 ± 4.7	71.8 ± 1.1
PSGa-**6**	0.02 ± 0.01	14.1 ± 3.8	−2.5 ± 0.2	51.5 ± 1.5	65.6 ± 3.2
PSGa-**7**	0.16 ± 0.02	30.5 ± 8.9	−2.1 ± 0.1	83.7 ± 1.0	87.3 ± 0.8
PSGa-**8**	0.15 ± 0.03	17.7 ± 2.2	−3.0 ± 0.2	81.5 ± 1.2	96.7 ± 1.8
PSGa-**9**	0.13 ± 0.04	23.4 ± 3.7	−2.9 ± 0.1	84.2 ± 1.1	94.0 ± 1.0

*Specific internalization refers to total internalization (n = 3) corrected with blocked internalization in presence of 500 μM 2-phosphonomethyl pentanedioic acid, expressed as percentage applied activity (%AA) per 10^5 cells.
†Inhibitor constant (K_i) is determined through Cheng–Prusoff method in competition assay (n = 3) with 0.75 nM [^{68}Ga]Ga-PSMA-10 (K_d = 3.8 ± 1.8 nM).
‡Lipophilicity is log$D_{oct/PBS}$.
oct = n-octanol; PBS = phosphate-buffered saline.

retention at 2 h after injection of 0.2–0.5 SUV (g/mL), with the highest SUV for [^{68}Ga]Ga-PSGa-**9**. The highest tumor uptake was observed for [^{68}Ga]Ga-PSGa-**7**, with SUV_{max} (g/mL) of 0.7 at 15 min after injection. High imaging contrast (tumor-to-muscle ratios of 3.6–6.6 at 1 h after injection) could be detected at early time points (Fig. 4). PET scan data showed the best tumor accumulation values for compounds [^{68}Ga]Ga-PSGa-**7** to [^{68}Ga]Ga-PSGa-**9**; however, these compounds were accompanied by higher kidney retention. Compounds [^{68}Ga]Ga-PSGa-**2** to [^{68}Ga]Ga-PSGa-**5** showed marginally lower SUVs in the tumor but quicker renal clearance.

[^{211}At]PSAt-3 Biodistribution

Figure 5 shows the biodistribution of [^{211}At]PSAt-**3**-Ga in the LNCaP mouse xenograft (supplemental materials include a table with detailed values). Tumor enrichment of [^{211}At]PSAt-**3**-Ga was high, with 19 ± 8 %ID/g at 1 h after injection. Uptake was reduced over 24 h to 7.6 ± 2.9 %ID/g. In comparison, the gold standard PSMA-617 showed similar pharmacokinetic behavior but with higher retention at 24 h after injection (supplemental materials). Deastatination occurred only to a minor extent, as exemplified by low uptake in organs such as the stomach (1.6 ± 0.4 %ID/g), spleen (3.1 ± 0.6 %ID/g), and thyroid or trachea (1.6 ± 1.1 %ID/g) at 1 h after injection. The clearance of [^{211}At]PSAt-**3**-Ga was through renal pathways, with high kidney uptake at early time points (82 ± 15 %ID/g at 1 h after injection and 44 ± 8 %ID/g at 6 h after injection), followed by rapid washout over 24 h, leading to 8.0 ± 4.2 %ID/g. Uptake of [^{211}At]PSAt-**3**-Ga in salivary glands was low (2.0 ± 0.7 %ID/g at 1 h after injection and 0.4 ± 0.1 %ID/g at 24 h after injection) and did not increase over time.

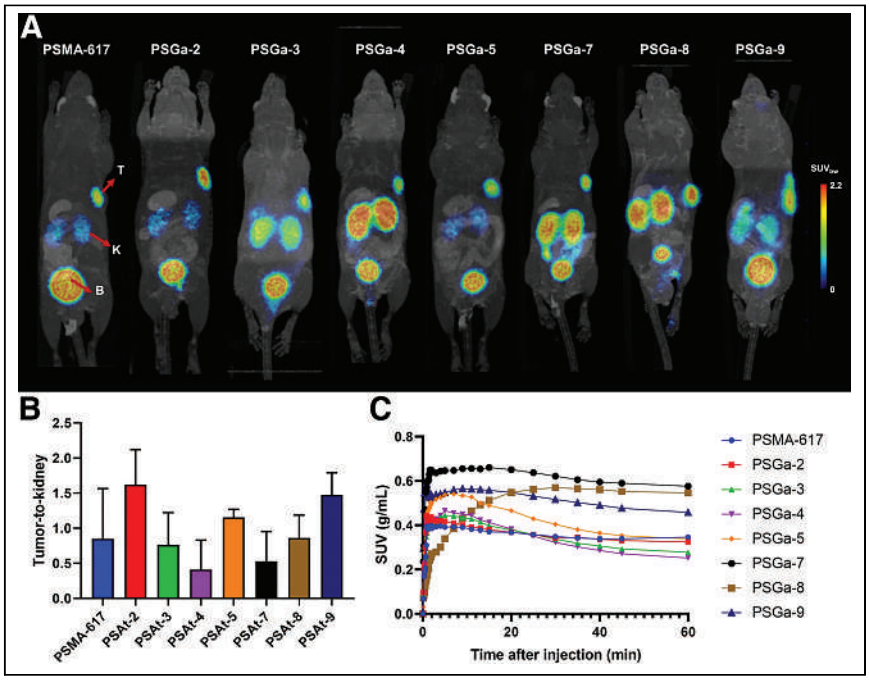

FIGURE 4. (A) PET/MRI maximum intensity projections 2 h after injection of 0.5 nmol of ^{68}Ga-labeled surrogate compounds and reference PSMA-617. (B) Tumor-to-kidney ratios 2 h after injection. (C) Tumor accumulation (SUV) 0–60 min after injection in LNCaP nude mouse (BALB/c *nu/nu*) model (n = 1). B = bladder; K = kidney; T = tumor.

DISCUSSION

The compounds in the reported series are based on preclinically and clinically successful PSMA-targeting compounds

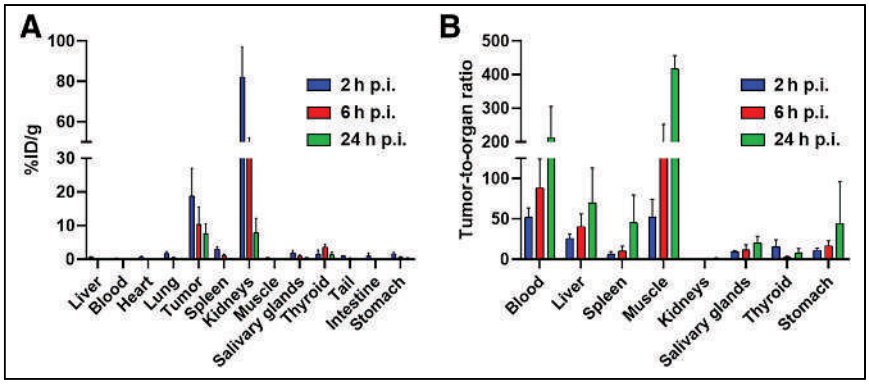

FIGURE 5. (A) Biodistribution (%ID/g) of [^{211}At]PSAt-**3**-Ga in dissected organs (n = 4 for 2 h after injection; n = 6 for 6 and 24 h after injection). (B) Tumor-to-organ ratios (n = 4 for 2 h after injection; n = 6 for 6 and 24 h after injection). Detailed values in supplemental materials. p.i. = postinjection.

that show sufficient tumor uptake, tumor retention, high cell internalization, and rapid excretion. The main goal of this study was to design radiopharmaceuticals that can accommodate a halogen and do so without causing a significant change in the pharmacokinetic profile of the radioligand while decreasing deastatination (Figs. 1 and 2). To this end, 2 strategies were followed. First, the aim was to replace or complement the 2-naphthyl-L-alanine aromatic system with iodine-bearing L-phenylalanine derivatives. It was hypothesized that this strategy would not significantly modify the binding and internalization properties of the ligands (*30*). Second, it is known that the 2-naphthyl-L-alanine aromatic system interacts with the accessory PSMA lipophilic site, improving binding (*31*). By placing the carbon–astatine bond in this lipophilic site, its stability could be potentially increased as its exposure to oxidative species was reduced (*23*). To modulate the polarity of the compounds and thereby influence their pharmacokinetic profile, especially with regard to their clearance, they were conjugated to a DOTA chelator. This addition allows imaging of surrogate compounds by replacing astatine with iodine—for example, labeling DOTA with ^{68}Ga or ^{111}In—whereas the astatinated versions could serve therapeutic purposes.

In this respect and for ease of handling, the compound series was initially evaluated as the ^{68}Ga-labeled version. This served as a starting point for the full in vitro characterization of the inhibitors, as well as a preliminary pharmacokinetic study through PET imaging. In vitro evaluation of the ^{68}Ga-labeled compounds involved internalization and competitive binding affinity assays. The results from the internalization assays showed that the chemical modifications did not affect the ability of the ligands to internalize, with one exception. [^{68}Ga]Ga-PSGa-**4** had a surprisingly low rate of internalization. The reason for this unexpected behavior is unknown. Furthermore, it was confirmed that the cyclohexyl moiety is essential to promote internalization. [^{68}Ga]Ga-PSGa-**6,** which lacks this aliphatic cycle, showed very low uptake in PSMA-positive LNCaP cells. Binding affinities were in the same nanomolar range as for the gold standard [^{68}Ga]Ga-PSMA-617. These findings were expected, because the binding affinity is mainly driven by the glutamate–urea–lysine construct (*32*). Log$D_{pH7.4}$ determination confirmed the hydrophilic nature of the compounds. As expected, the slightly more lipophilic compounds PSGa-**7** to PSGa-**9** displayed higher binding toward plasma proteins than did their more hydrophilic counterparts (Table 1). As such, they were expected not only to result in marginally higher tumor uptake but also to be excreted somewhat more slowly (*33*).

Encouraged by these results, the ^{68}Ga-labeled compounds (besides [^{68}Ga]Ga-PSGa-**6,** because of its poor internalization rate) were progressed to PET imaging studies in an LNCaP mouse xenograft. Dynamic scans of the compounds were recorded 0–60 min after injection. For all structures, time–activity curves (Fig. 4; supplemental materials) revealed a fast pharmacokinetic profile with peak tumor accumulation of 0.4–0.7 SUV (g/mL) and excretion through renal pathways. As expected, clearance for [^{68}Ga]Ga-PSGa-**7** to [^{68}Ga]Ga-PSGa-**9** was slightly slower, along with narrowly higher tumor accumulation. Additional static images at 2 h after injection confirmed the pharmacokinetic behavior of the series (Figs. 4A and 4B). Tumor uptake and retention of the compounds were high for all candidates, with slightly increased values for [^{68}Ga]Ga-PSGa-**7** to [^{68}Ga]Ga-PSGa-**9**. However, these compounds also showed lowered kidney-to-tumor ratios—most likely because of their slower clearance rate. Because high kidney retention has been shown to be detrimental for targeted α-radiotherapy (*16*), PSGa-**7** to PSGa-**9** were excluded from further studies using ^{211}At. Because compounds PSGa-**2,** PSGa-**3,** and PSGa-**5** showed similar pharmacokinetic profiles, similar internalization rates, and affinities in the same nanomolar order, it was decided to furnish [^{211}At]PSAt-**3.** This decision was mainly driven by the synthetic accessibility of [^{211}At]PSAt-**3** and its precursor compared with PSAt-**2** and PSAt-**5** (supplemental materials provide detailed information).

The chosen evaluation strategy, based on the short-lived radionuclide ^{68}Ga, can assess only early biodistribution time points, and as such, this strategy cannot predict the residence time of the tested compounds, which in turn is positively correlated with therapeutic outcomes. Because ^{211}At also possesses a relatively short half-life, early biodistribution might be sufficient to select the most promising candidate for ^{211}At labeling. Consequently, the trimethylsilyl-containing precursor **18** of [^{211}At]PSAt-**3** was synthesized. The choice of a trimethylsilyl over a stannyl-leaving group was mainly based on the higher stability of the silyl moiety compared with stannanes, as organotin compounds are sensitive to acidic conditions and cannot be easily applied to standard SPPS procedures (*34*). In contrast, the trimethylsilyl group allowed the introduction of amino acid **9** into standard SPPS procedures. Amino acid **9** is the key intermediate to introduce the silyl-based precursor moiety into precursor **18.** However, the use of trimethylsilyl is not exempt of shortcomings, because its reactivity is relatively low toward electrophilic aromatic substitutions. Higher temperatures (around 70°C) in neat trifluoroacetic acid have to be used (*27*). As these conditions lead to cyclization of the unprotected glutamate–urea–lysine structural motif (*35*), a relatively complex product mixture was observed after radiolabeling of [^{211}At]PSAt-**3** (supplemental materials). However, [^{211}At]PSAt-**3** was successfully isolated in sufficient radiochemical yield (35%) and radiochemical purity (≥98%).

To mimic the pharmacokinetic behavior of [^{68}Ga]Ga-PSGa-**3,** ^{nat}Ga^{3+} was chelated into the DOTA moiety of [^{211}At]PSAt-**3.** Omission of the metal in the chelator moiety can have an effect on the pharmacokinetic profile of the ligand (*36*). Afterward, biodistribution studies of [^{211}At]PSAt-**3**-Ga were performed in an LNCaP xenograft model and revealed that [^{211}At]PSAt-**3**-Ga

exhibited favorable tumor-targeting properties (Fig. 5), as evidenced by tumor accumulation of 19 ± 8 %ID/g at 1 h and 7.6 ± 2.9 %ID/g at 24 h after injection. These values are comparable to those reported for other ^{211}At-labeled PSMA-targeting compounds (*17*). For both [^{211}At]PSAt-**3**-Ga and the previously reported compounds, tumor retention decreases around 50% at 24 h after injection compared with that of [^{177}Lu]Lu-PSMA-617 (supplemental materials) when a similar dose (~100 kBq) is administered to the tumor-bearing mice. A potential explanation for the decrease in tumor uptake would be the effect of an α-emitter, such as ^{211}At, on tumor cells compared with the weaker β-emitter. A lower dose of ^{211}At might already be sufficient to eradicate some tumorous cells and therefore decrease the %ID/g at 24 h after injection. Such effectivity of α-emitters has been proven with similar single doses of ^{225}Ac-labeled radiopharmaceuticals (*37,38*). In addition, kidney retention for [^{211}At]PSAt-**3**-Ga compared with [^{177}Lu]Lu-PSMA-617 is similar at early time points, albeit slightly higher at 24 h after injection. [^{211}At]PSAt-**3**-Ga also showed low accumulation in organs related to deastatination, with a maximum of 3.6 ± 0.8 %ID/g in the thyroid at 6 h after injection. This is in line with the initial hypothesis that positioning the astatine in the PSMA lipophilic accessory pocket prevents deastatination, highlighting the need for careful design of astatinated radiopharmaceuticals to prevent deastatination. However, careful validation studies need to be performed to better assert deastatination, especially in animals such as mice, in which the small size of the deastatination organ markers could lead to increased errors in the %ID/g determinations.

CONCLUSION

In this study, a series of compounds was synthesized and evaluated in vitro and through PET imaging using ^{68}Ga-labeled and iodine-substituted versions to identify a lead compound and then develop a ^{211}At-labeled PSMA radiopharmaceutical. This lead compound was finally radiolabeled with ^{211}At for biodistribution studies in an LNCaP xenograft model. [^{211}At]PSAt-**3**-Ga demonstrated favorable distribution, with good tumor accumulation, adequate renal-mediated clearance, and negligible deastatination. The results highlight [^{211}At]PSAt-**3**-Ga as a compound not inferior to the previously reported ^{211}At-labeled PSMA-targeting compounds and emphasize the need for a head-to-head comparison using the same animal model to identify the best candidate. Nevertheless, the findings herein described establish [^{211}At]PSAt-**3**-Ga among the leading candidates for PSMA-targeted α-radiotherapy and preclinical efficacy, as well as comparison studies with other compounds or radionuclides that are under way.

DISCLOSURE

This work received financial support from Deutsche Forschungsgemeinschaft (423813989/GRK2606) and from the Independent Research Fund Denmark (1032-00177B). Matthias Herth, Andreas Kjaer, Andreas Jensen, Ann-Christin Eder, and Matthias Eder are inventors on a patent application for the compounds described herein. No other potential conflict of interest relevant to this article was reported.

ACKNOWLEDGMENTS

We thank Lisa Domogalla for technical assistance during the PET/MRI study. The graphical abstract was created with BioRender (Science Suite).

KEY POINTS

QUESTION: Can clinically relevant PSMA-targeting compounds be used as a good platform for developing an α-emitting inhibitor, with their similar favorable pharmacokinetic properties?

PERTINENT FINDINGS: The rationally designed [^{211}At]PSAt-**3**-Ga showed a satisfactory pharmacokinetic profile with good tumor uptake and negligible nontarget tissue accumulation.

IMPLICATIONS FOR PATIENT CARE: If proven effective in controlling tumor growth or eradicating tumors in preclinical models, [^{211}At]PSAt-**3**-Ga could be translated into clinical settings for application in targeted α-therapy. In addition, this work strengthens the theses of bringing ^{211}At into clinical practice as a better and more efficient alternative to current α-emitting radionuclides.

REFERENCES

1. Cancer today. International Agency for Research, World Health Organization website. https://gco.iarc.fr/today/home. Updated 2020. Accessed September 30, 2023.
2. Mehtälä J, Zong J, Vassilev Z, et al. Overall survival and second primary malignancies in men with metastatic prostate cancer. *PLoS One.* 2020;15:e0227552.
3. He L, Fang H, Chen C, et al. Metastatic castration-resistant prostate cancer: academic insights and perspectives through bibliometric analysis. *Medicine (Baltimore).* 2020;99:e19760.
4. Fallah J, Agrawal S, Gittleman H, et al. FDA approval summary: lutetium Lu 177 vipivotide tetraxetan for patients with metastatic castration-resistant prostate cancer. *Clin Cancer Res.* 2023;29:1651–1657.
5. Rahbar K, Schmidt M, Heinzel A, et al. Response and tolerability of a single dose of ^{177}Lu-PSMA-617 in patients with metastatic castration-resistant prostate cancer: a multicenter retrospective analysis. *J Nucl Med.* 2016;57:1334–1338.
6. Sun M, Niaz MOJ, Nelson A, Skafida M, Niaz MOJ. Review of ^{177}Lu-PSMA-617 in patients with metastatic castration-resistant prostate cancer. *Cureus.* 2020; 12:e8921.
7. El Fakiri M, Geis NM, Ayada N, Eder M, Eder AC. PSMA-targeting radiopharmaceuticals for prostate cancer therapy: recent developments and future perspectives. *Cancers (Basel).* 2021;13:3967.
8. Graf F, Fahrer J, Maus S, et al. DNA double strand breaks as predictor of efficacy of the alpha-particle emitter Ac-225 and the electron emitter Lu-177 for somatostatin receptor targeted radiotherapy. *PLoS One.* 2014;9:e88239.
9. Chakravarty R, Siamof CM, Dash A, Cai W. Targeted α-therapy of prostate cancer using radiolabeled PSMA inhibitors: a game changer in nuclear medicine. *Am J Nucl Med Mol Imaging.* 2018;8:247–267.
10. Kratochwil C, Bruchertseifer F, Giesel FL, et al. ^{225}Ac-PSMA-617 for PSMA-targeted α-radiation therapy of metastatic castration-resistant prostate cancer. *J Nucl Med.* 2016;57:1941–1944.
11. Zacherl MJ, Gildehaus FJ, Mittlmeier L, et al. First clinical results for PSMA-targeted α-therapy using ^{225}Ac-PSMA-I&T in advanced-mCRPC patients. *J Nucl Med.* 2021;62:669–674.
12. Lindegren S, Albertsson P, Bäck T, Jensen H, Palm S, Aneheim E. Realizing clinical trials with astatine-211: the chemistry infrastructure. *Cancer Biother Radiopharm.* 2020;35:425–436.
13. Vaziri B, Wu H, Dhawan AP, et al. MIRD pamphlet no. 25: MIRDcell V2.0 software tool for dosimetric analysis of biologic response of multicellular populations. *J Nucl Med.* 2014;55:1557–1564.
14. Privé BM, Boussihmad MA, Timmermans B, et al. Fibroblast activation protein-targeted radionuclide therapy: background, opportunities, and challenges of first (pre)clinical studies. *Eur J Nucl Med Mol Imaging.* 2023;50:1906–1918.
15. Sidrak MMA, De Feo MS, Corica F, et al. Fibroblast activation protein inhibitor (FAPI)-based theranostics: where we are at and where we are heading—a systematic review. *Int J Mol Sci.* 2023;24:3863.
16. Kiess AP, Minn I, Vaidyanathan G, et al. (2S)-2-(3-(1-carboxy-5-(4-^{211}At-astatobenzamido)pentyl)ureido)-pentanedioic acid for PSMA-targeted α-particle radiopharmaceutical therapy. *J Nucl Med.* 2016;57:1569–1575.
17. Mease RC, Kang C, Kumar V, et al. An improved ^{211}At-labeled agent for PSMA-targeted α-therapy. *J Nucl Med.* 2022;63:259–267.
18. Vaidyanathan G, Mease RC, Minn I, et al. Synthesis and preliminary evaluation of ^{211}At-labeled inhibitors of prostate-specific membrane antigen for targeted alpha particle therapy of prostate cancer. *Nucl Med Biol.* 2021;94-95:67–80.

19. Watabe T, Kaneda-Nakashima K, Shirakami Y, et al. Targeted α-therapy using astatine ^{211}At-labeled PSMA1, 5, and 6: a preclinical evaluation as a novel compound. *Eur J Nucl Med Mol Imaging.* 2023;50:849–858.
20. Matthias J, Engelhardt J, Schäfer M, et al. Cytoplasmic localization of prostate-specific membrane antigen inhibitors may confer advantages for targeted cancer therapies. *Cancer Res.* 2021;81:2234–2245.
21. Stenberg VY, Tornes AJK, Nilsen HR, et al. Factors influencing the therapeutic efficacy of the PSMA targeting radioligand ^{212}Pb-NG001. *Cancers (Basel).* 2022; 14:2784.
22. Davis MI, Bennett MJ, Thomas LM, Bjorkman PJ. Crystal structure of prostate-specific membrane antigen, a tumor marker and peptidase. *Proc Natl Acad Sci USA.* 2005;102:5981–5986.
23. Teze D, Sergentu DC, Kalichuk V, et al. Targeted radionuclide therapy with astatine-211: oxidative dehalogenation of astatobenzoate conjugates. *Sci Rep.* 2017;7:2579.
24. Eder M, Schäfer M, Bauder-Wüst U, et al. ^{68}Ga-complex lipophilicity and the targeting property of a urea-based PSMA inhibitor for PET imaging. *Bioconjug Chem.* 2012;23:688–697.
25. Lowe PT, Dall'Angelo S, Fleming IN, Piras M, Zanda M, O'Hagan D. Enzymatic radiosynthesis of a ^{18}F-Glu-ureido-Lys ligand for the prostate-specific membrane antigen (PSMA). *Org Biomol Chem.* 2019;17:1480–1486.
26. Meyer FM, Liras S, Guzman-Perez A, Perreault C, Bian J, James K. Functionalization of aromatic amino acids via direct C-H activation: generation of versatile building blocks for accessing novel peptide space. *Org Lett.* 2010;12:3870–3873.
27. Watanabe S, Azim MAU, Nishinaka I, et al. A convenient and reproducible method for the synthesis of astatinated 4-[^{211}At]astato-l-phenylalanine via electrophilic desilylation. *Org Biomol Chem.* 2018;17:165–171.
28. Benešová M, Bauder-Wüst U, Schäfer M, et al. Linker modification strategies to control the prostate-specific membrane antigen (PSMA)-targeting and pharmacokinetic properties of DOTA-conjugated PSMA inhibitors. *J Med Chem.* 2016;59: 1761–1775.
29. Herth MM, Ametamey S, Antuganov D, et al. On the consensus nomenclature rules for radiopharmaceutical chemistry: reconsideration of radiochemical conversion. *Nucl Med Biol.* 2021;93:19–21.
30. Kuo HT, Pan J, Zhang Z, et al. Effects of linker modification on tumor-to-kidney contrast of ^{68}Ga-labeled PSMA-targeted imaging probes. *Mol Pharm.* 2018;15: 3502–3511.
31. Kopka K, Benešová M, Bařinka C, Haberkorn U, Babich J. Glu-ureido-based inhibitors of prostate-specific membrane antigen: lessons learned during the development of a novel class of low-molecular-weight theranostic radiotracers. *J Nucl Med.* 2017;58(suppl 2):17S–26S.
32. Felber VB, Valentin MA, Wester HJ. Design of PSMA ligands with modifications at the inhibitor part: an approach to reduce the salivary gland uptake of radiolabeled PSMA inhibitors? *EJNMMI Radiopharm Chem.* 2021;6:10.
33. Benešová M, Umbricht CA, Schibli R, Müller C. Albumin-binding PSMA ligands: optimization of the tissue distribution profile. *Mol Pharm.* 2018;15:934–946.
34. Kraus CA, Sessions WV. Chemistry of the trimethyltin group. *J Am Chem Soc.* 1925;47:2361–2368.
35. Martin S, Tönnesmann R, Hierlmeier I, et al. Identification, characterization, and suppression of side products formed during the synthesis of [^{177}Lu]Lu-PSMA-617. *J Med Chem.* 2021;64:4960–4971.
36. Delage JA, Faivre-Chauvet A, Barbet J, et al. Impact of DOTA conjugation on pharmacokinetics and immunoreactivity of [^{177}Lu]Lu-1C1m-Fc, an anti TEM-1 fusion protein antibody in a TEM-1 positive tumor mouse model. *Pharmaceutics.* 2021;13:96.
37. Tafreshi NK, Pandya DN, Tichacek CJ, et al. Preclinical evaluation of [^{225}Ac]Ac-DOTA-TATE for treatment of lung neuroendocrine neoplasms. *Eur J Nucl Med Mol Imaging.* 2021;48:3408–3421.
38. Rodak M, Dekempeneer Y, Wojewódzka M, et al. Preclinical evaluation of ^{225}Ac-labeled single-domain antibody for the treatment of HER2pos cancer. *Mol Cancer Ther.* 2022;21:1835–1845.

Can Internal Carotid Arteries Be Used for Noninvasive Quantification of Brain PET Studies?

Laura Providência, Chris W.J. van der Weijden, Philipp Mohr, Joyce van Sluis, Johannes H. van Snick, Riemer H.J.A. Slart, Rudi A.J.O. Dierckx, Adriaan A. Lammertsma, and Charalampos Tsoumpas

Department of Nuclear Medicine and Molecular Imaging, University Medical Center Groningen, University of Groningen, Groningen, The Netherlands

Because of the limited axial field of view of conventional PET scanners, the internal carotid arteries are commonly used to obtain an image-derived input function (IDIF) in quantitative brain PET. However, time–activity curves extracted from the internal carotids are prone to partial-volume effects due to the limited PET resolution. This study aimed to assess the use of the internal carotids for quantifying brain glucose metabolism before and after partial-volume correction. **Methods:** Dynamic [^{18}F]FDG images were acquired on a 106-cm-long PET scanner, and quantification was performed with a 2-tissue-compartment model and Patlak analysis using an IDIF extracted from the internal carotids. An IDIF extracted from the ascending aorta was used as ground truth. **Results:** The internal carotid IDIF underestimated the area under the curve by 37% compared with the ascending aorta IDIF, leading to K_i values approximately 17% higher. After partial-volume correction, the mean relative K_i differences calculated with the ascending aorta and internal carotid IDIFs dropped to 7.5% and 0.05%, when using a 2-tissue-compartment model and Patlak analysis, respectively. However, microparameters (K_1, k_2, k_3) derived from the corrected internal carotid curve differed significantly from those obtained using the ascending aorta. **Conclusion:** These results suggest that partial-volume–corrected internal carotids may be used to estimate K_i but not kinetic microparameters. Further validation in a larger patient cohort with more variable kinetics is needed for more definitive conclusions.

Key Words: cerebral glucose consumption; image-derived input function; PET; kinetic modeling; partial-volume correction

J Nucl Med 2024; 65:600–606
DOI: 10.2967/jnumed.123.266675

Fully quantitative PET studies of the brain provide a more accurate assessment of the underlying physiologic processes than SUV analyses. In contrast to SUV analysis, kinetic modeling corrects for confounding factors that contribute to the PET signal, such as variations in tissue perfusion, transport rate, and tracer clearance over time (*1*).

In general, kinetic modeling requires an arterial input function, describing the concentration of parent tracer in arterial plasma over time. The gold-standard technique for obtaining this function is through continuous arterial sampling after arterial catheterization. This is, however, an invasive and laborious procedure, making it less practical for clinical routine (*2*), and it may discourage some subjects from participating in research studies because of the discomfort of placing an arterial line (*3*). To avoid arterial cannulation, image-derived input functions (IDIFs) have emerged (*4*,*5*) as an alternative noninvasive approach to obtain the arterial input function.

Extracting an IDIF from large blood pools such as the left ventricle and the aorta has been widely validated since the 1990s (*6*), making this method suitable for cardiac PET and quantification of regions within the thorax (*2*). Such large vessels are, however, not available in or near the brain, as conventional PET systems have a relatively short axial field of view ranging from 15 to 30 cm. The largest arteries found near the brain, and that are still included in the field of view, are the internal carotids, with a diameter of 3.9–6.0 mm (*7*), making them the best candidate for IDIF extraction in quantitative brain studies (*8*–*10*). However, the internal carotids' size is comparable to the spatial resolution of PET, and therefore extraction of tracer concentrations from these vessels is prone to partial-volume effects (*2*,*3*). Even though the use of the internal carotids has been validated in several studies (*8*,*11*,*12*), laborious and complex procedures are needed to correct the raw time–activity curves for partial-volume effects. In addition, these methods for partial-volume correction (PVC) often are tailor-made for a specific cohort of patients or radiotracers and cannot be easily extended for general use. Examples of PVC methods include count recovery models (*11*), blood-based techniques (*8*), and methods based on segmentation of the carotids using coregistered MR images or MR angiography (*12*). A purely PET-based noninvasive PVC method that does not require additional medical images or blood sampling is necessary for the wider translation of kinetic analysis using IDIFs in both research and clinical practice.

Iterative deconvolution methods (IDMs) have emerged as a PVC technique that relies solely on PET images and can be used to increase image resolution (*13*,*14*). Until now, IDMs have been investigated for correcting partial-volume effects only in brain tissue, and not in the carotid arteries. Their performance regarding PVC in the internal carotids is, therefore, still unknown.

The introduction of systems with a long axial field of view provides a solution to the problem of noninvasive brain quantification, allowing for simultaneous imaging of brain and thoracic regions. The IDIF can be derived from a large vascular structure, such as the ascending aorta, which is large enough (25–38 mm) to minimize partial-volume effects. The purpose of this study was to assess the use of the internal carotids for quantification of the metabolic rate of glucose, before and after applying PET-based PVC, using the ascending aorta as the gold standard.

Received Sep. 19, 2023; revision accepted Jan. 23, 2024.
For correspondence or reprints, contact Laura Providência (l.lopes.goncalves.da.providencia@umcg.nl).
Published online Mar. 14, 2024.

MATERIALS AND METHODS

Patient Population

Eight oncology patients (4 men, 4 women; age range, 61–81 y; mean ± SD, 75 ± 4 y) with suspected lung malignancy, referred for clinical diagnosis, were included in this study. The local Medical Ethics Review Committee of the University Medical Center Groningen waived the need for formal ethical review (waiver METc2020/554).

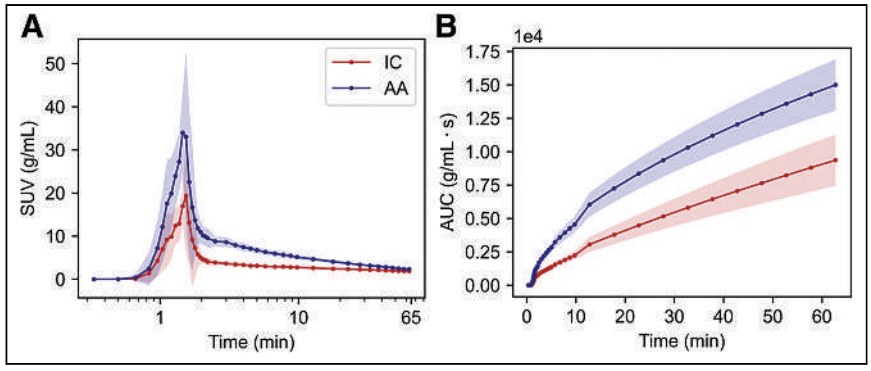

FIGURE 1. Time–activity curves (mean of 8 patients) derived from ascending aorta (AA) and internal carotids (IC): complete curve with time in logarithmic scale (A) and AUC (B). Shadows represent SD for each time point across studied population.

Data Acquisition

After a delay of 10 s after automated [^{18}F]FDG bolus injection and a saline flush of 30 mL, list-mode PET data were acquired on a long-axial-field-of-view Siemens Biograph Vision Quadra (axial field of view of 106 cm) for 65 min. Patients received a standard weight-based injection of 3 MBq/kg (±10). Data were binned over 42 frames (4 × 10, 16 × 5, 6 × 30, 5 × 60, and 11 × 300 s), and images were reconstructed using an ordered-subset expectation maximization algorithm (4 iterations, 5 subsets) with time of flight and resolution modeling (point-spread function). Data were corrected for attenuation, random coincidences, scattered radiation, dead time, and decay. Reconstructed images consisted of 645 planes of 440 × 440 voxels (voxel size, 1.65 × 1.65 × 1.645 mm) and image resolution of approximately 3.5 mm in the center of the field of view (*15*). No filter was applied. Image reconstructions were performed using e7tools, a prototype research software package from Siemens Healthineers.

Motion Correction and Interframe Alignment

Dynamic images were originally reconstructed without attenuation correction. Subsequently, the attenuation correction CT was registered to each non–attenuation-corrected PET frame to correct for potential CT-to-PET mismatches, therefore creating a motion-corrected CT frame for each PET frame. This was done using a deep learning–based tool (*16*) and the open-source software NiftyReg (*17*) (further details in the supplemental materials, available at http://jnm.snmjournals.org). The motion-corrected CT images were used for reconstruction of the final PET images. Postreconstruction interframe alignment was performed on the slices comprising the head region (~24 cm) using a cubic spline interpolation. The correction was applied when motion was larger than 3 mm.

PVC

PVC was performed with the reblurred Van Cittert iterative deconvolution technique (*18*) (details regarding the choice of this method in the supplemental materials). The reblurred Van Cittert technique was used as implemented in the open-source toolbox PETPVC (*14*). A point-spread function of 4.4 × 4.4 × 3.8 mm (transverse × axial) was chosen on the basis of system acceptance measurements. To identify the most suitable number of PVC iterations for the present data, reblurred Van Cittert technique was used with 4, 8, 12, and 16 iterations. The number of iterations for which the internal carotid time–activity curve had the best correspondence with the ascending aorta time–activity curve was considered as the most suitable for performing IDM. IDM with the selected parameters was applied to the complete dataset, and the resultant images were used to extract corrected internal carotid time–activity curves.

IDIF

The volumes of interest for extracting the internal carotid time–activity curve were obtained by choosing the 4 highest-intensity pixels over 16 consecutive planes for both left and right internal carotids (*9*). Volumes of interest were defined on an image corresponding to the average of earlier frames (~60–110 s). Subsequently, these volumes of interest were applied to all frames to generate an IDIF from the internal carotids ($IDIF_{IC}$). As ground truth, an IDIF from the ascending aorta ($IDIF_{AA}$) was obtained by placing a 15-mm diameter (~9 planes) sphere in the center of this structure. The ascending aorta has previously been validated as an alternative to arterial blood sampling showing excellent agreement with the blood time–activity curve (*19*) and the resulting quantitative parameters (*6*).

Kinetic Modeling

Volumes of interest in the brain were extracted using the Hammers maximum-probability atlas within PMOD's PET-only workflow (version 4.105; PMOD Technologies LLC). Regional time–activity curves were generated for whole brain, gray matter (union of parietal lobe, frontal lobe, temporal lobe, and occipital cortex), and white matter (corpus callosum). For each segmented region, quantification was performed using an irreversible 2-tissue-compartment model (2T3k_V_B) with 3 rate constants, K_1 (mL · cm^{-3} · min^{-1}), k_2 (min^{-1}), and k_3 (min^{-1}), and a blood volume parameter, V_B. In addition, Patlak graphical analysis was performed, assuming that steady-state conditions apply after 30 min (t* = 30 min). Net tracer influx, K_i (mL · cm^{-3} · min^{-1}), was calculated

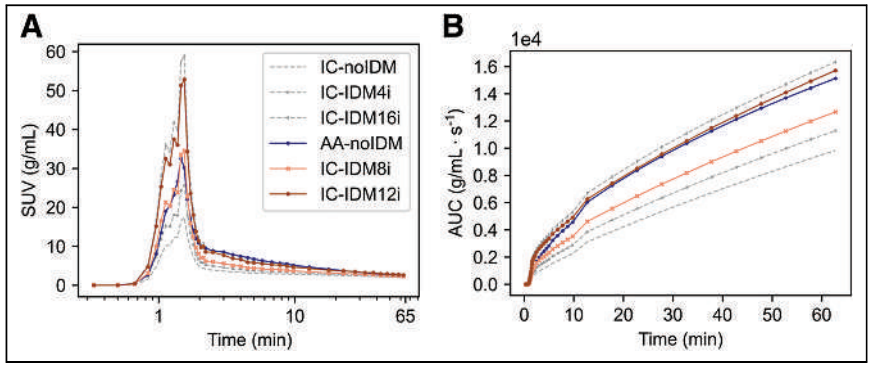

FIGURE 2. Time–activity curves (mean of 8 patients) derived from ascending aorta (AA-noIDM) and internal carotids before (IC-noIDM) and after application of IDM with 4 (IC-IDM4i), 8 (IC-IDM8i), 12 (IC-IDM12i), and 16 (IC-IDM16i) iterations: complete curve with time in logarithmic scale (A) and AUC (B).

TABLE 1
Mean AUCs of Ascending Aorta and Internal Carotid Curves for [^{18}F]FDG

AUC	$IDIF_{AA}$	$IDIF_{IC}$	$IDIF_{IC\text{-}IDM8i}$	$IDIF_{IC\text{-}IDM12i}$
Full curve (g/mL · s $\times 10^4$)	1.50 (0.19)	0.94 (0.20)	1.22 (0.19)	1.51 (0.25)
Peak (g/mL · s $\times 10^3$)	1.32 (022)	0.70 (0.12)	1.33 (0.16)	2.01 (0.26)
Tail (g/mL · s $\times 10^3$)	1.38 (0.20)	0.91 (0.14)	1.13 (0.15)	1.40 (0.19)

Data in parentheses are SDs.

using both the compartment model and Patlak analysis. Additionally, the Patlak intercept was calculated.

Statistical Analysis

Internal carotids and ascending aorta time–activity curves were compared by calculating the areas under the curve (AUC). Differences in model parameters obtained with $IDIF_{IC}$ and $IDIF_{AA}$ were assessed using the paired Student *t* test or a Wilcoxon signed-rank test, depending on the result of the Shapiro–Wilk test for normality. Agreement between K_i derived with $IDIF_{IC}$ and $IDIF_{AA}$ was analyzed using a Bland–Altman plot. In addition, the correlation of these K_i values was evaluated using Pearson correlation analysis, and values of slope, intercept, intraclass correlation coefficient, and coefficient of determination (R^2) were reported. *P* values lower than 0.05 were considered as statistically significant.

RESULTS

No PVC

Figure 1 shows time–activity curves extracted from the internal carotids and ascending aorta for all 8 patients (SUV_{mean} ± SD per time point). In all patients, the internal carotids significantly underestimated the activity compared with the ascending aorta. The mean AUCs of the full curves, peaks, and tails are shown in Table 1. Overall, the AUC of the internal carotids showed an underestimation of 37%, 47%, and 34% for full curve, peak, and tail, respectively, compared with the ascending aorta.

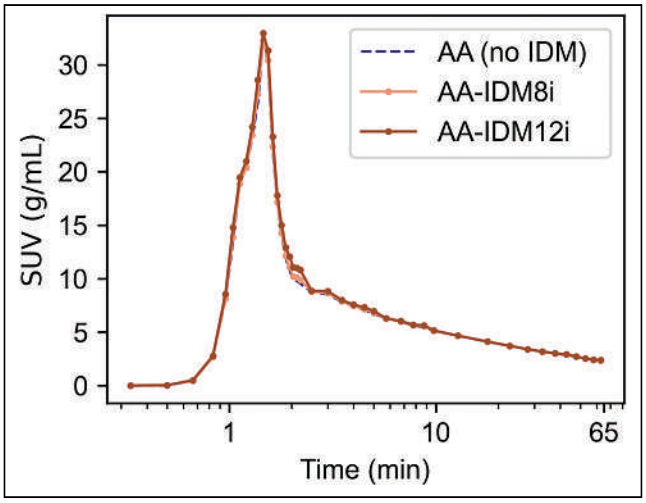

FIGURE 3. Time–activity curves (mean of 8 patients) of ascending aorta time–activity curves before IDM and after application of IDM with 8 (AA-IDM8i) and 12 (AA-IDM12i) iterations.

Mean kinetic parameters for white matter, gray matter, and whole brain obtained using $IDIF_{IC}$ and $IDIF_{AA}$ are shown in Table 2. In the case of the 2T3k_V_B model and for all 3 brain regions, K_1, k_3, and K_i derived using $IDIF_{IC}$ were significantly different from those obtained using $IDIF_{AA}$, with K_1 and K_i being systematically overestimated by the internal carotids and k_3 underestimated. No significant difference was observed for k_2. For the Patlak analysis of all 3 brain regions, both K_i and intercept derived using $IDIF_{IC}$ were significantly different (overestimated) from those obtained using $IDIF_{AA}$.

PVC: Parameter Optimization

Figure 2 shows the time–activity curves extracted from the internal carotids (mean ± SD per time point) after applying IDM with 4 (IDM4i), 8 (IDM8i), 12 (IDM12i), and 16 (IDM16i) iterations to the original images. Both internal carotids and ascending aorta time–activity curves extracted from the original images (i.e., no IDM) are also shown for comparison. The internal carotid time–activity curves before and after IDM (referred to as IC and IC-IDM, respectively), were compared with the original ascending aorta time–activity curves, for which no IDM was applied: as demonstrated in Figure 3, larger structures such as the ascending aorta are not affected by partial-volume effects. The internal carotid time–activity curve after IDM4i underestimated the activity compared with the ascending aorta time–activity curve, both for the peak and for the tail. After IDM8i, the peak of the internal carotids showed good recovery, but the tail was still underestimated. In contrast, after IDM12i and IDM16i, the internal carotid time–activity curves overestimated the peak, but the tail came closer to those of the ascending aorta time–activity curves. On the basis of these results, it was concluded that 4 iterations were not enough to correct the internal carotid time–activity curves. The reconstruction with 16 iterations was also discarded as it provided very similar results to the one with 12 iterations but with the disadvantage of adding more noise due to the additional iterations. The internal carotid curves corrected using IDM8i ($IDIF_{IC\text{-}IDM8i}$) and IDM12i ($IDIF_{IC\text{-}IDM12i}$) were therefore selected for further kinetic analysis.

PVC

After parameter optimization, IDM8i and IDM12i were applied to the original images of all patients. The mean AUCs of the full curve, peak, and tail of $IDIF_{IC\text{-}IDM8i}$ and $IDIF_{IC\text{-}IDM12i}$ are shown in Table 1. After IDM8i, the internal carotid AUC was overestimated by 0.8% in the peak and underestimated by 18% in the tail. With IDM12i, the internal carotid AUC was overestimated by 52% in the peak and underestimated by 1% in the tail.

TABLE 2
Mean Model Parameters Obtained with 2T3k_V_B and Patlak Analysis Using [^{18}F]FDG, Derived with $IDIF_{AA}$ and $IDIF_{IC}$

		2T3k_V_B					Patlak	
Region	IDIF	V_B	K_1 (mL · cm^{-3} · min^{-1})	k_2 (min^{-1})	k_3 (min^{-1})	K_i (mL · cm^{-3} · min^{-1})	K_i (mL · cm^{-3} · min^{-1})	Y_0 (mL · cm^{-3})
White matter	$IDIF_{AA}$	0.020 (0.008)	0.04 (0.02)	0.09 (0.02)	0.036 (0.008)	0.010 (0.003)	0.008 (0.003)	0.33 (0.14)
	$IDIF_{IC}$	0.03 (0.01)†	0.08 (0.04)†	0.10 (0.02)	0.016 (0.003)‡	0.011 (0.004)*	0.010 (0.003)*	0.66 (0.24)‡
Gray matter	$IDIF_{AA}$	0.040 (0.005)	0.10 (0.01)	0.14(0.02)	0.055 (0.005)	0.027 (0.004)	0.023 (0.003)	0.65 (0.08)
	$IDIF_{IC}$	0.06 (0.01)‡	0.20 (0.04)‡	0.12 (0.01)	0.024 (0.004)‡	0.033 (0.006)†	0.027 (0.005)*	1.4 (0.18)‡
Whole brain	$IDIF_{AA}$	0.039 (0.004)	0.08 (0.01)	0.14 (0.02)	0.052 (0.005)	0.022 (0.003)	0.018 (0.002)	0.58 (0.06)
	$IDIF_{IC}$	0.061 (0.009)‡	0.18 (0.03)‡	0.13 (0.02)	0.023 (0.004)‡	0.026 (0.004)†	0.021 (0.004)*	1.21 (0.16)‡

*$P < 0.05$, $IDIF_{AA}$ vs. $IDIF_{IC}$.
†$P < 0.01$, $IDIF_{AA}$ vs. $IDIF_{IC}$.
‡$P < 0.001$, $IDIF_{AA}$ vs. $IDIF_{IC}$.
Y_0 = Patlak intercept.
Data in parentheses are SDs.

Kinetic parameters derived using $IDIF_{IC\text{-}IDM8i}$ and $IDIF_{IC\text{-}IDM12i}$ were compared with those obtained using $IDIF_{AA}$ (Table 3). When using $IDIF_{IC\text{-}IDM8i}$, k_2 and k_3 were significantly different from those obtained using $IDIF_{AA}$ for all brain regions, but no significant differences were observed for either K_1 or K_i. Even though the K_i values estimated with $IDIF_{IC\text{-}IDM8i}$ were very close to the ones estimated with $IDIF_{AA}$ (ratio ~1), this is because both the numerator and the denominator of K_i estimated with the $IDIF_{IC\text{-}IDM8i}$ were underestimated by a similar factor, and the errors cancelled out (Supplemental Fig. 1). With the Patlak analysis, and for all brain regions, K_i obtained using $IDIF_{IC\text{-}IDM8i}$ was also not significantly different from the one obtained using $IDIF_{AA}$, but a significant difference was found for the intercept. When $IDIF_{IC\text{-}IDM12i}$ was used as input function (Table 3), significant differences were found for all parameters of both the 2T3k_V_B model and the Patlak analysis in all 3 brain regions, compared with using $IDIF_{AA}$.

Bland–Altman Plots and Correlation Analysis (Before and After PVC)

Bland–Altman relative difference plots and scatterplots were analyzed to assess the agreement and correlation between K_i derived using $IDIF_{IC}$, $IDIF_{IC\text{-}IDM8i}$, and $IDIF_{IC\text{-}IDM12i}$ and K_i obtained using $IDIF_{AA}$. The plots comparing K_i derived with $IDIF_{IC\text{-}IDM12i}$ and $IDIF_{AA}$ are not shown because of the poor results obtained with the $IDIF_{IC\text{-}IDM12i}$ (Table 3) and can be seen in the Supplemental Figures 2 and 3.

Figure 4 shows Bland–Altman plots for both the 2T3k_V_B and Patlak analyses. Without PVC, the Bland–Altman plot revealed a positive bias of 17% in both 2T3k_V_B and Patlak analyses. The Bland–Altman plot comparing K_i values derived using $IDIF_{IC\text{-}IDM8i}$ with those derived using $IDIF_{AA}$ showed average relative errors of −7.5 and −0.5% for 2T3k_V_B and Patlak analyses, respectively.

Figure 5 shows K_i correlation plots. Table 4 gives an overview of the values resulting from the correlation analyses, that is, slope, intercept, intraclass correlation coefficient, and R^2.

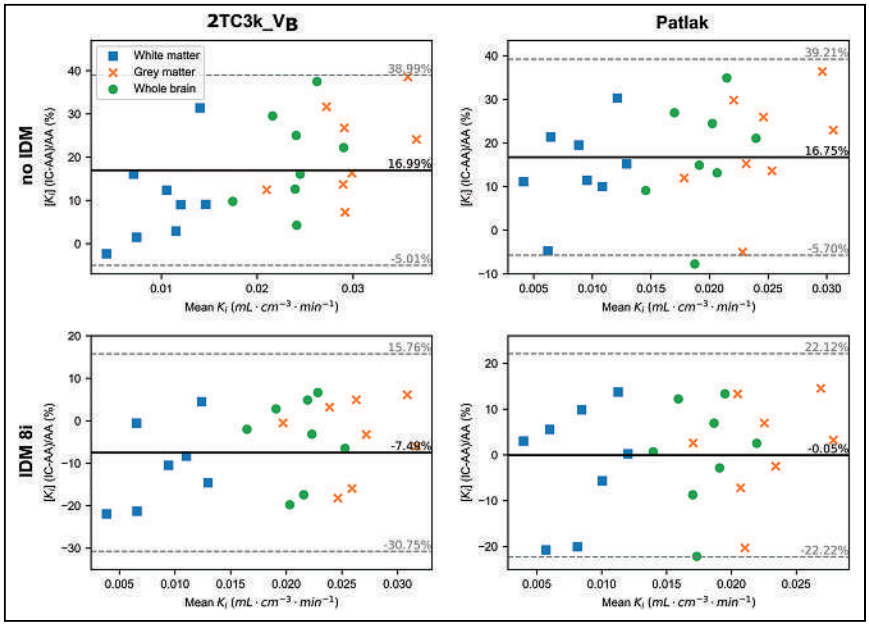

FIGURE 4. Bland–Altman relative difference plots of K_i values derived with internal carotids (IC) and ascending aorta (AA) IDIF. First row: K_i derived using $IDIF_{IC}$ vs. $IDIF_{AA}$ (no IDM). Second row: K_i derived using $IDIF_{IC\text{-}IDM8i}$ vs. $IDIF_{AA}$ (IDM8i). *y*-axis represents relative percentage error of internal carotid K_i compared with that of ascending aorta, that is, $\frac{K_i^{IC} - K_i^{AA}}{K_i^{AA}} \times 100$. Average relative error is represented by solid black line, and upper and lower CI limits are represented by dashed gray lines.

DISCUSSION

This study aimed to assess whether the internal carotids can be used to define an IDIF for noninvasive kinetic analysis of [^{18}F]FDG brain PET. Without PVC, internal carotid time–activity curves underestimated blood concentrations compared with those derived from the ascending

TABLE 3
Mean Model Parameters Obtained with 2T3k_V_B and Patlak Analysis Using [^{18}F]FDG, Derived with $IDIF_{AA}$, $IDIF_{IC\text{-}IDM8i}$, and $IDIF_{IC\text{-}IDM12i}$

		2T3k_V_B					Patlak	
Region	IDIF	V_B	K_1 (mL · cm^{-3} · min^{-1})	k_2 (min^{-1})	k_3 (min^{-1})	K_i (mL · cm^{-3} · min^{-1})	K_i (mL · cm^{-3} · min^{-1})	Y_0 (mL · cm^{-3})
White matter	$IDIF_{AA}$	0.020 (0.008)	0.04 (0.02)	0.09 (0.02)	0.036 (0.008)	0.010 (0.003)	0.008 (0.003)	0.32 (0.13)
	$IDIF_{IC\text{-}IDM8i}$	0.013 (0.006)*	0.04 (0.02)*	0.06 (0.01)†	0.015 (0.005)‡	0.008 (0.003)	0.008 (0.003)	0.50 (0.20)
	$IDIF_{IC\text{-}IDM12i}$	0.008 (0.003)†	0.03 (0.01)*	0.05 (0.01)‡	0.016 (0.006)‡	0.007 (0.003)†	0.007 (0.003)†	0.38 (0.16)*
Gray matter	$IDIF_{AA}$	0.040 (0.005)	0.10 (0.01)	0.14 (0.02)	0.055 (0.005)	0.027 (0.004)	0.023 (0.003)	0.65 (0.08)
	$IDIF_{IC\text{-}IDM8i}$	0.029 (0.005)†	0.10 (0.01)	0.07 (0.01)‡	0.024 (0.005)‡	0.026 (0.004)	0.023 (0.004)	1.04 (0.12)‡
	$IDIF_{IC\text{-}IDM12i}$	0.018 (0.004)‡	0.069 (0.01)†*	0.057 (0.01)‡	0.026 (0.006)‡	0.022 (0.003)†	0.020 (0.003)†	0.78 (0.12)*
Whole brain	$IDIF_{AA}$	0.039 (0.004)	0.08 (0.01 s)	0.14 (0.02)	0.052 (0.005)	0.022 (0.003)	0.018 (0.002)	0.58 (0.06)
	$IDIF_{IC\text{-}IDM8i}$	0.028 (0.004)†	0.09 (0.01)	0.08 (0.01)‡	0.023 (0.005)‡	0.021 (0.003)	0.018 (0.003)	0.91 (0.09)‡
	$IDIF_{IC\text{-}IDM12i}$	0.018 (0.003)‡	0.061 (0.008)†	0.06 (0.01)‡	0.025 (0.005)‡	0.017 (0.002)†	0.015 (0.002)*	0.68 (0.08)†

*$P < 0.05$, $IDIF_{AA}$ vs. $IDIF_{IC}$.
†$P < 0.01$, $IDIF_{AA}$ vs. $IDIF_{IC}$.
‡$P < 0.001$, $IDIF_{AA}$ vs. $IDIF_{IC}$.
Y_0 = Patlak intercept.
Data in parentheses are SDs.

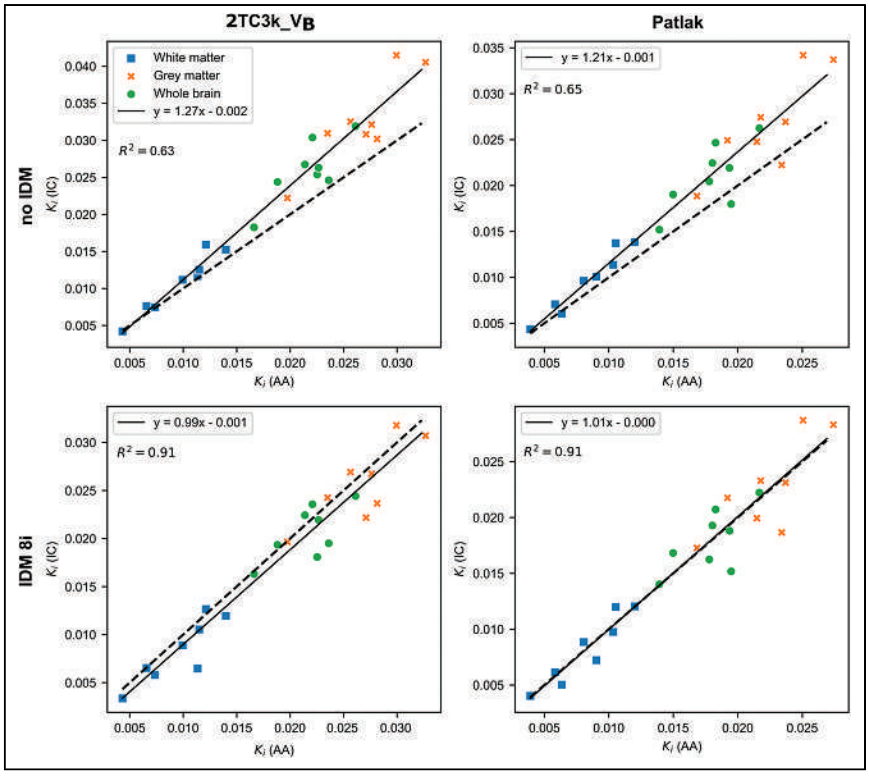

FIGURE 5. Correlation of K_i values derived using internal carotids (IC) IDIF vs. K_i derived using ascending aorta (AA) IDIF. First row: K_i derived using $IDIF_{IC}$ vs. $IDIF_{AA}$ (no IDM). Second row: K_i derived using $IDIF_{IC\text{-}IDM8i}$ vs. $IDIF_{AA}$ (IDM8i). Dashed line corresponds to identity line.

aorta. Consequently, all kinetic parameters derived using $IDIF_{IC}$, except for k_2, were significantly different from those obtained using $IDIF_{AA}$. $IDIF_{IC}$ resulted in a significant overestimation of K_i both for 2T3k_V_B and for Patlak analysis. To correct for partial-volume effects, a postreconstruction PVC technique, the reblurred Van Cittert method (*13*,*18*), was used. The best results with this method were obtained after 8 iterations ($IDIF_{IC\text{-}IDM8i}$), which resulted in a reduction of the error between the internal carotid and ascending aorta AUCs from 47% to −0.8% in the peak and from 34% to 18% in the tail. When $IDIF_{IC\text{-}IDM8i}$ was used as the input function in the 2T3k_V_B analysis, the estimated K_i values were not significantly different from those obtained with $IDIF_{AA}$. However, the microparameters K_1, k_2, and k_3 obtained using $IDIF_{ic\text{-}IDM8i}$ were in general significantly different from those generated using $IDIF_{AA}$. When $IDIF_{IC\text{-}IDM8i}$ was used as the input function in the Patlak analysis, derived K_i values were not significantly different from those obtained using $IDIF_{AA}$.

The overestimation of K_i when using an $IDIF_{IC}$ without PVC is in agreement with previous studies. For example, Sari et al. (*12*) showed that when an uncorrected $IDIF_{IC}$ was used, K_i values in white and gray matter were overestimated by 46.2% and 51.0%, respectively, when compared with an input function based on arterial samples. Interestingly, in the present study, K_i overestimation for the uncorrected $IDIF_{IC}$ was only 10.0% and 17.4% in white and gray matter, respectively. The significant improvement in results obtained with an uncorrected $IDIF_{IC}$ may be attributed to several factors. First, the present study was performed using a Biograph Vision Quadra, which has substantially improved sensitivity compared with older scanners. Apart from an overall decrease in noise, the higher sensitivity of the system also allows for reconstructing the first minutes of the scan with shorter frames (2–5 s), resulting in better recovery of the internal carotid peak than when the frames are longer (10 s). Second, we correct for head motion by aligning the original CT images to the individual frames before the final image reconstruction. When head motion is corrected for only by realigning the frames after reconstruction, the attenuation correction is inaccurate and can lead to erroneous activity values possibly affecting the kinetic parameter estimation. Finally, region-of-interest definition may also play a role in the observed differences.

The results of this study show that an uncorrected curve using the internal carotids leads to significantly biased model parameters and to an overestimation of K_i and, therefore, should not be used for quantification. Although this study was performed using [^{18}F]FDG data, the main results should also be valid for other tracers, as partial-volume effects are inherently linked to the size of the object in relation to the PET resolution. After application of PVC, 2T3k_V_B K_i values were not significantly different from those obtained using $IDIF_{AA}$. Similarly, K_i values estimated using Patlak analysis were also not significantly different from those obtained using $IDIF_{AA}$, and the corresponding Bland–Altman plot showed no bias, indicating that this could be a potential correction method for K_i calculation.

Despite the accurate results obtained for K_i, the microparameters K_1, k_2, and k_3 obtained with 2T3k_V_B were still biased, suggesting that the method used in this study, the reblurred Van Cittert, is insufficient to correct for PVC when full kinetic modeling is needed. In line with the present findings, Sari et al. (*12*) also observed that microparameters K_1 and k_3 derived using a corrected IDIF still were significantly biased. The reason why biased microparameters lead to accurate K_i estimates remains unclear, but it is known that macroparameters are generally more stable than microparameters, as errors in microparameter estimation might cancel out in the calculation of the macroparameters (Supplemental Fig. 1) (*20*,*21*). Nevertheless, compared with previously published values (*22*), K_1, k_2, and K_i values estimated using $IDIF_{IC\text{-}IDM8i}$ are within the reference range in both white and gray matter; k_3, however, is underestimated compared with literature results.

The main limitation of this study is the use of a single point-spread function value to perform deconvolution. Ideally, location-specific measurements of point-spread function for the position of each carotid artery within the field of view should be used when performing IDM. Here, a single value based on system acceptance measurements was used, which may introduce errors when correcting the internal carotids for partial volume. Another limitation is the relatively small sample size used in this study. A larger sample size could potentially yield more robust results.

TABLE 4
Results of Correlation Analyses Between K_i Derived Using $IDIF_{AA}$ and K_i Derived Using $IDIF_{IC}$, $IDIF_{IC\text{-}IDM8i}$, and $IDIF_{IC\text{-}IDM12i}$

	2TCk3_V_B				Patlak			
IDIF	Slope	Intercept	R^2	ICC	Slope	Intercept	R^2	ICC
$IDIF_{IC}$	1.27	-2×10^{-3}	0.63	0.84	1.19	-5×10^{-4}	0.65	0.79
$IDIF_{IC\text{-}IDM8i}$	1.01	-2×10^{-3}	0.91	0.79	1.01	-4×10^{-4}	0.91	0.79
$IDIF_{IC\text{-}IDM12i}$	0.84	-1×10^{-3}	0.65	0.77	0.86	-2×10^{-4}	0.81	0.81

ICC = intraclass correlation coefficient.

CONCLUSION

These findings indicate that using an IDIF measured from the internal carotid curve results in overestimation of K_i as well as biased microparameters and should therefore not be used for brain quantification. With the proposed PVC method, K_i values derived using an internal carotid IDIF closely align with those obtained using the ascending aorta as IDIF, suggesting that this PVC method may be of interest for this specific purpose. However, the underlying microparameters still showed significant bias, indicating that a system with a long axial field of view is the best option for noninvasive brain quantification. In the future, to use the internal carotids as input function, a PET system with high spatial resolution is needed.

DISCLOSURE

No potential conflict of interest relevant to this article was reported.

ACKNOWLEDGMENTS

We thank Siemens Healthineers for providing us with the tool for CT-to-PET motion correction and the e7tools, and we thank Dr. Joshua Schaefferkoetter for his guidance.

KEY POINTS

QUESTION: Does using the internal carotids for brain quantification result in accurate kinetic parameters?

PERTINENT FINDINGS: In a cohort of 8 patients imaged using a scanner with a long axial field of view, the use of the internal carotids—compared with the ascending aorta—as the input function led to biased kinetic parameters. After PVC, K_i values obtained with the internal carotids were not significantly different from the ones obtained with the ascending aorta, but most of the microparameters were.

IMPLICATIONS FOR PATIENT CARE: The internal carotids should not be used for brain quantification without proper PVC for scanners with at least a 3-mm spatial resolution.

REFERENCES

1. Huang SC. Anatomy of SUV. *Nucl Med Biol.* 2000;27:643–646.
2. Vanzi E, Berti V, Polito C, et al. Cerebral metabolic rate of glucose quantification with the aortic image-derived input function and Patlak method: numerical and patient data evaluation. *Nucl Med Commun.* 2016;37:849–859.
3. Zanotti-Fregonara P, Chen K, Liow JS, Fujita M, Innis RB. Image-derived input function for brain PET studies: many challenges and few opportunities. *J Cereb Blood Flow Metab.* 2011;31:1986–1998.
4. van der Weijden CWJ, Mossel P, Bartels AL, et al. Non-invasive kinetic modelling approaches for quantitative analysis of brain PET studies. *Eur J Nucl Med Mol Imaging.* 2023;50:1636–1650.
5. van der Weijden CWJ, van der Hoorn A, Wang Y, et al. Investigation of image-derived input functions for non-invasive quantification of myelin density using [^{11}C]MeDAS PET. *Neuroimage.* 2022;264:119772.
6. Henriksen AC, Lonsdale MN, Fuglø D, Kondziella D, Nersesjan V, Marner L. Non-invasive quantification of cerebral glucose metabolism using Gjedde-Patlak plot and image-derived input function from the aorta. *Neuroimage.* 2022;253:119079.
7. Krejza J, Arkuszewski M, Kasner SE, et al. Carotid artery diameter in men and women and the relation to body and neck size. *Stroke.* 2006;37:1103–1105.
8. Chen K, Bandy D, Reiman E, et al. Noninvasive quantification of the cerebral metabolic rate for glucose using positron emission tomography,^{18}F-fluoro-2-deoxyglucose, the Patlak method, and an image-derived input function. *J Cereb Blood Flow Metab.* 1998;18:716–723.
9. Mourik JEM, Lubberink M, Klumpers UMH, Comans EF, Lammertsma AA, Boellaard R. Partial volume corrected image derived input functions for dynamic PET brain studies: methodology and validation for [^{11}C]flumazenil. *Neuroimage.* 2008;39:1041–1050.
10. Zanotti-Fregonara P, Fadaili EM, Maroy R, et al. Comparison of eight methods for the estimation of the image-derived input function in dynamic [^{18} F]-FDG PET human brain studies. *J Cereb Blood Flow Metab.* 2009;29:1825–1835.
11. Srinivas SM, Dhurairaj T, Basu S, Bural G, Surti S, Alavi A. A recovery coefficient method for partial volume correction of PET images. *Ann Nucl Med.* 2009;23:341–348.
12. Sari H, Erlandsson K, Law I, et al. Estimation of an image derived input function with MR-defined carotid arteries in FDG-PET human studies using a novel partial volume correction method. *J Cereb Blood Flow Metab.* 2017;37:1398–1409.
13. Tohka J, Reilhac A. Deconvolution-based partial volume correction in raclopride-PET and Monte Carlo comparison to MR-based method. *Neuroimage.* 2008;39:1570–1584.
14. Thomas BA, Cuplov V, Bousse A, et al. PETPVC: a toolbox for performing partial volume correction techniques in positron emission tomography. *Phys Med Biol.* 2016;61:7975–7993.
15. Prenosil GA, Sari H, Fürstner M, et al. Performance characteristics of the Biograph Vision Quadra PET/CT system with long axial field of view using the NEMA NU 2-2018 standard. *J Nucl Med.*
16. Schaefferkoetter J, Shah V, Hayden C, Prior JO, Zuehlsdorff S. Deep learning for improving PET/CT attenuation correction by elastic registration of anatomical data. *Eur J Nucl Med Mol Imaging.* 2023;50:2292–2304.
17. Modat M, Cash DM, Daga P, Winston GP, Duncan JS, Ourselin S. Global image registration using a symmetric block-matching approach. *J Med Imaging (Bellingham).* 2014;1:024003.
18. Carasso AS. Linear and nonlinear image deblurring: a documented study. *SIAM J Numer Anal.* 1999;36:1659–1689.
19. van der Weerdt AP, Klein LJ, Boellaard R, Visser CA, Visser FC, Lammertsma AA. Image-derived input functions for determination of MRGlu in cardiac ^{18}F-FDG PET scans. *J Nucl Med.* 2001;42:1622–1629.
20. Aston JAD, Cunningham VJ, Asselin MC, Hammers A, Evans AC, Gunn RN. Positron emission tomography partial volume correction: estimation and algorithms. *J Cereb Blood Flow Metab.* 2002;22:1019–1034.
21. Sari H, Erlandsson K, Marner L, et al. Non-invasive kinetic modelling of PET tracers with radiometabolites using a constrained simultaneous estimation method: evaluation with ^{11}C-SB201745. *EJNMMI Res.* 2018;8:58.
22. Phelps ME, Huang SC, Hoffman EJ, Selin C, Sokoloff L, Kuhl DE. Tomographic measurement of local cerebral glucose metabolic rate in humans with (F-18)2-fluoro-2-deoxy-D-glucose: validation of method. *Ann Neurol.* 1979;6:371–388.

Total-Body PET/CT Applications in Cardiovascular Diseases: A Perspective Document of the SNMMI Cardiovascular Council

Riemer H.J.A. Slart[1,2], Frank M. Bengel[3], Cigdem Akincioglu[4], Jamieson M. Bourque[5], Wengen Chen[6], Marc R. Dweck[7], Marcus Hacker[8], Saurabh Malhotra[9], Edward J. Miller[10], Matthieu Pelletier-Galarneau[11], René R.S. Packard[12], Thomas H. Schindler[13], Richard L. Weinberg[14], Antti Saraste[15], and Piotr J. Slomka[16]

[1]Medical Imaging Centre, Department of Nuclear Medicine and Molecular Imaging, University Medical Center Groningen, University of Groningen, Groningen, The Netherlands; [2]Biomedical Photonic Imaging Group, Faculty of Science and Technology, University of Twente, Enschede, The Netherlands; [3]Department of Nuclear Medicine, Hannover Medical School, Hannover, Germany; [4]Division of Nuclear Medicine, Medical Imaging, Western University, London, Ontario, Canada; [5]Departments of Medicine (Cardiology) and Radiology, University of Virginia, Charlottesville, Virginia; [6]Department of Diagnostic Radiology and Nuclear Medicine, University of Maryland School of Medicine, Baltimore, Maryland; [7]British Heart Foundation Centre for Cardiovascular Science, Edinburgh Heart Centre, University of Edinburgh, Edinburgh, United Kingdom; [8]Division of Nuclear Medicine, Department of Biomedical Imaging and Image-Guided Therapy, Medical University of Vienna, Vienna, Austria; [9]Cook County Health, Rush Medical College, Chicago, Illinois; [10]Department of Biomedical Engineering, Yale University, New Haven, Connecticut; Department of Radiology and Biomedical Imaging, Yale School of Medicine, and Department of Internal Medicine, Yale University, New Haven, Connecticut; [11]Department of Medical Imaging, Montreal Heart Institute, Montreal, Quebec, Canada; [12]Division of Cardiology, Department of Medicine, David Geffen School of Medicine, UCLA, Los Angeles, California; [13]Mallinckrodt Institute of Radiology, Division of Nuclear Medicine, Cardiovascular Medicine, Washington University School of Medicine, St. Louis, Missouri; [14]Division of Cardiology, Feinberg School of Medicine, Northwestern University, Chicago, Illinois; [15]Turku PET Centre and Heart Center, Turku University Hospital and University of Turku, Turku, Finland; and [16]Division of Artificial Intelligence in Medicine, Department of Medicine, Cedars–Sinai Medical Center, Los Angeles, California

Digital PET/CT systems with a long axial field of view have become available and are emerging as the current state of the art. These new camera systems provide wider anatomic coverage, leading to major increases in system sensitivity. Preliminary results have demonstrated improvements in image quality and quantification, as well as substantial advantages in tracer kinetic modeling from dynamic imaging. These systems also potentially allow for low-dose examinations and major reductions in acquisition time. Thereby, they hold great promise to improve PET-based interrogation of cardiac physiology and biology. Additionally, the whole-body coverage enables simultaneous assessment of multiple organs and the large vascular structures of the body, opening new opportunities for imaging systemic mechanisms, disorders, or treatments and their interactions with the cardiovascular system as a whole. The aim of this perspective document is to debate the potential applications, challenges, opportunities, and remaining challenges of applying PET/CT with a long axial field of view to the field of cardiovascular disease.

Key Words: long axial field-of-view PET/CT; cardiovascular diseases; current status; future perspectives

J Nucl Med 2024; 65:607–616
DOI: 10.2967/jnumed.123.266858

Recently, digital PET/CT systems with a long axial field of view (LAFOV) have become available as the current state-of-the-art clinical imaging systems. These new camera systems enable a larger anatomic coverage and a significant increase in system sensitivity, with a factor of 10–40, depending on the volume of detector material, that is, the actual length of the scanner (*1*,*2*). This is due to the numerous, highly performing silicon photomultiplier–based detectors collecting a huge number of coincidence photons, with consequent improvement of signal-to-noise ratio that, in turn, positively impacts image quality. Preliminary results from the clinical application of LAFOV systems therefore demonstrate improved image quality and lesion quantification (*1*,*3*). Low-dose examination protocols and a significant reduction in acquisition time are other potential advantages. These novel scanners also allow quantitative dynamic imaging of the whole body with high temporal resolution in a large field of view (*4*). The whole-body coverage enables simultaneous assessment of multiple organs and large vascular structures, opening new opportunities for imaging cardiovascular disorders.

The aim of this perspective is to discuss the potential applications, opportunities, and challenges of LAFOV PET/CT in the field of cardiovascular disease (CVD).

MULTIORGAN APPROACH IN CARDIOVASCULAR DISORDERS

Driven by the results of an increasing number of clinical trials, cardiovascular medicine is changing and moving beyond a single-organ–centered approach. Contemporary optimal cardiovascular care focuses on the whole body and includes a systems-based

Received Nov. 7, 2023; revision accepted Jan. 11, 2024.
For correspondence or reprints, contact Riemer Slart (r.h.j.a.slart@umcg.nl).
Published online Feb. 22, 2024.

approach in which the heart and circulatory system are embedded in integrated networks (Fig. 1). Despite symptom improvement in chronic coronary syndromes, targeted coronary artery revascularization may not improve patient survival even in the presence of myocardial ischemia (*5*). On the other hand, systemic medical therapy does improve CVD outcomes, and this includes targeted modulation of the neurohumoral, endocrine, and immune systems (*6*,*7*). Likewise, the interplay between heart, vessel wall, and other organs is increasingly emphasized for optimal cardiovascular health. Based on different organ and system interactions, various subdisciplines such as cardioimmunology (*8*), cardioneurology (*9*), or cardiooncology (*10*) have emerged, and the cardiorenal (*11*), cardiohepatic (*12*), cardiopulmonary, and gut–heart axes (*13*,*14*) are being explored to obtain mechanistic insights and identify therapeutically exploitable targets. Accordingly, diagnostic imaging tests, which provide information about the entire body, may be of significant value. Hence, LAFOV PET/CT may provide the diagnostic armamentarium for high-quality, innovative cardiovascular medicine within the overall context of systems medicine.

METHODOLOGY CONCERNING LAFOV PET

Hot-spot cardiovascular PET data are mainly presented by way of weight, activity, and SUV maps, which physicians are trained to interpret in a qualitative and subjective way. The shortcomings of SUV are well known (Table 1). In contrast, there are established and quantitative methods for the analysis of dynamic PET data, which can reveal deeper insights into physiologic parameters that are not possible to measure from single-time-point SUV analysis. Clear benefits to this approach, such as improved lesion detection due to parametric imaging (*15*), could be very helpful in imaging CVDs, particularly for smaller lesions such as those in atherosclerosis.

Further, the large amount of data generated by total-body scanners, and the consequently long reconstruction times (Fig. 1), necessitate high-performance hardware to prevent the need for transferring these datasets over traditional hospital information technology networking systems. Nonetheless, the acquired data offer a wealth of additional information that can be extracted using both conventional methods of mathematical modeling and artificial intelligence. The use of population-based input functions with shorter dynamic ^{18}F-FDG protocols in a LAFOV PET/CT system is a good example of this, decreasing acquisition time from 60 to 10 min (*4*). Further, artificial intelligence is expected to play an increasingly critical role in imaging equipment, reconstruction, and postprocessing pipelines in the field of nuclear medicine (*16*) and likely to have value in LAFOV PET/CT due to its capacity to process and learn from large amounts of data (Fig. 1). Novel deep-learning reconstruction methods may be used to accelerate the process and improve the image quality. Multiorgan artificial intelligence–based segmentation tools will likely aid in the kinetic modeling of cardiovascular data across the entire patient body.

CARDIOVASCULAR APPLICATIONS

Whole-Body PET Perfusion and Myocardial Blood Flow Quantification

PET/CT has become a mainstay in the detection and characterization of subclinical and clinically manifested coronary artery disease (CAD) (*17*) and for viability assessments in ischemic cardiomyopathy (*18*). PET remains the noninvasive gold standard for quantification of myocardial blood flow and cerebral blood flow. Because of the presence of the blood–brain barrier, PET measurements of cerebral blood flow are mostly conducted with the radiotracer ^{15}O-H_2O (*19*–*21*). In the heart, clinical blood flow quantification relies on various radiotracers such as ^{82}Rb-Cl,^{13}N-NH_3, ^{15}O-H_2O, and (in the future) ^{18}F-flurpiridaz (*22*). Myocardial blood flow quantification has well-established clinical applications in epicardial CAD and coronary microvascular dysfunction (*23*,*24*). Studies have demonstrated the feasibility of measuring blood flow in specific organs, such as the kidneys with ^{15}O-H_2O (*25*,*26*), ^{82}Rb-Cl (*27*,*28*), and ^{13}N-NH_3 (*29*). Furthermore, skeletal muscle and splenic blood flow can be measured with PET using ^{15}O-H_2O and ^{82}Rb-Cl (*30*–*34*). There are challenges in the evaluation of blood flow at the whole-body level, such as a wide range of flow levels and variable tracer extraction in different organs. Furthermore, there is more than one input in some organs, such as the lungs and the liver. Initial experiences have been obtained with tracers with high extraction, including ^{15}O-H_2O (Fig. 2) and ^{11}C-butanol (*35*).

With the recent introduction of LAFOV PET/CT, the comprehensive assessment of multiorgan function related to the cardiovascular system appears feasible, opening new avenues and opportunities in research and clinical care. For example, microvascular disease may be determined in virtually all vascular beds concurrently or nearly concurrently, depending on the differences in local radiotracer extraction and tissue kinetics. The dimensionality of the target organs assessed—whole organ, major arterial bed, or segmental arterial bed—may require nuanced evaluations to unmask focal abnormalities in blood flow (*36*).

Many CVD entities are connected to systemic factors such as the immune and neurohumoral systems and endocrine disorders and may need a more comprehensive and systems-based diagnostic and medical treatment approach (*8*–*14*). For example, impaired renal perfusion contributes to cardiorenal syndrome in heart failure, and there is a need for markers that balance the benefits of the renin–angiotensin–aldosterone system blockade and potential adverse effects related to a decreasing glomerular filtration rate in those with significant kidney disease (*11*). There is only limited information on myocardial blood flow responses in the lower extremities in atherosclerotic CVD and the value of perfusion imaging in monitoring treatment of critical limb ischemia (*37*). Data from the REACH registry showed that approximately 10% of patients with CAD present with concomitant peripheral artery disease,

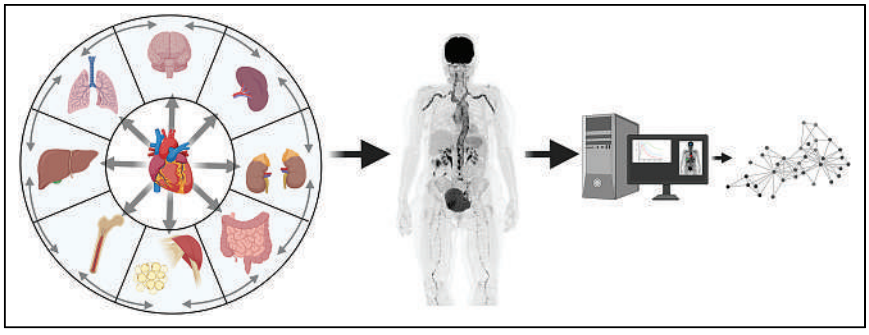

FIGURE 1. Simultaneous cardiovascular multisystem studies with total-body PET and dedicated analysis of dynamic PET data. Arrows in wheel display heart–organ connections and interactions.

TABLE 1
Strengths, Weaknesses, Opportunities, and Threat Analysis of LAFOV Total-Body PET/CT in Cardiovascular Imaging

Parameter	Description
Strengths	Whole-body coverage
	High spatial and temporal resolution
	Dynamic imaging
	Short imaging time
	Low radiation dose
Opportunities	New development in medical imaging
	Clinical cardiovascular trials
	Biodistribution of newly developed (radiolabeled) cardiovascular drugs
	Insights of cardiovascular and multiorgan interaction/cross-talk
	Artificial intelligence implementation
Weaknesses	CT for attenuation correction, as significant limit to dose reduction (although ultra-low-dose CT, time-of-flight correction, or deep-learning approach will be implemented soon)
	Requirement for accurate motion correction
	Data storage and networking infrastructure
	Lack of easy-to-use clinical kinetic software programs
	Number of patient preparation rooms
Threats	Costs
	Not widely available
	Computational times for reconstruction, data corrections, and kinetic modeling

whereas 60% of patients with peripheral artery disease present with concomitant CAD (*38*). Data from large randomized clinical trials consistently showed that the coexistence of CAD and peripheral artery disease is a particularly harmful association, with a heightened risk of major adverse cardiovascular events, including myocardial infarction, stroke, and cardiovascular death, compared with CAD or PAD only (*39*). Open questions are if functional total-body PET perfusion may resolve the clinical observation that some patients have coronary atherosclerotic disease only, whereas others have systemic vascular disease and still others have both. Do we need to focus directly on vascular atherosclerotic activity? In this respect, the LAFOV PET/CT scanner may afford unique and noninvasive insights in the detection and characterization of cardiovascular physiology and metabolism in conjunction with other organs and systemic factors and may result in the development and monitoring of new treatments.

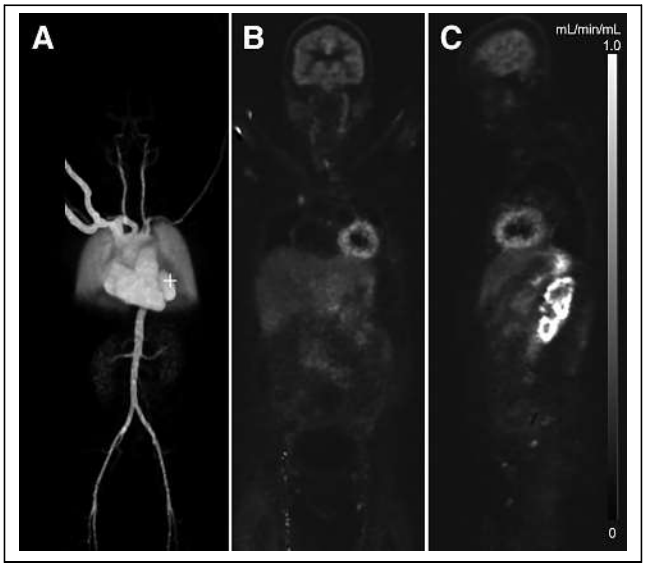

FIGURE 2. Dynamic perfusion imaging with ^{15}O-H_2O with Biograph Vision Quadra system (Siemens) and whole-body PET. (A) 3-dimensional parametric image of arterial blood volume (V_a). (B and C) Parametric images of organ-specific blood flow (k_1, mL/min/mL) in horizontal and sagittal planes, respectively. Images centered in left ventricle show that high flow can be seen in myocardium and kidney.

Atherosclerosis

It remains poorly understood how inflammatory atherosclerotic processes interact in the different vascular beds (e.g., coronary arteries, carotids, aortic arch, peripheral vessels) and with other organ systems (e.g., the brain, gut, hematopoietic tissues). Such systemic interrelations and disease networks could be further determined with LAFOV PET/CT imaging (Fig. 3). Furthermore,

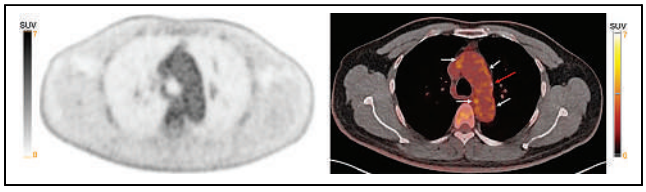

FIGURE 3. ^{18}F-FDG PET/CT of 56-y-old man 3 mo after successful revascularization of acute myocardial infarction. Images were obtained using LAFOV PET/CT (Siemens Vision Quadra) 60 min after injection. ^{18}F-FDG PET (left) and PET/CT (right) images were acquired with high sensitivity and spatial resolution, enabling detection of slightly increased spotty FDG accumulation in arterial wall of aortic arch (white arrows), with only 1 calcified focus (red arrow) indicating increased inflammatory atherosclerotic activity in otherwise less advanced atherosclerotic stage.

ultralow radiation dosing makes multiple-time-point and sequential multitracer studies increasingly feasible. These features are of particular interest in atherosclerosis, which is a systemic condition that changes with time and treatment and involves different pathologic processes including inflammation, calcification, fibrosis, and thrombus formation. Each of them can be targeted with modern PET tracers. For example, ^{18}F-FDG PET has already been used to investigate how large vessel inflammation (aorta) is increased after myocardial infarction and is linked with increases in psychologic stress (amygdala of the brain) and hematopoietic bone marrow activity (*40*). Multitracer studies could be used to investigate how vascular inflammation associates with calcification activity (^{18}F-fluoride) (*41*), fibroblast activation (^{68}Ga-fibroblast activation protein inhibitor [FAPI]) (*42*,*43*), and thrombus formation (^{18}F-glycoprotein 1) (*44*).

Dynamic total-body ^{18}F-FDG images yield a high vessel wall signal and target-to-background ratio, even after several half-life times of decay, allowing the cross-talk between vessel wall and lymphoid organs to be identified, including parametric imaging of metabolic rate of ^{18}F-FDG (*45*). Novel and inexpensive radiopharmaceuticals with higher patient throughput may hold promise in advancing our understanding of atherosclerosis as well as a range of other cardiovascular conditions and in improving patient assessment and treatment.

Myocardial and Peripheral Muscular Metabolism

A variety of radiotracers informs cardiac metabolism. ^{18}F-FDG is a glucose analog, of which uptake provides a surrogate for glucose metabolism in cardiac myocytes. Radiolabeled long-chain fatty acids and fatty acid analogs, such as ^{11}C-palmitate and ^{18}F-fluoroheptadecanoic acid, allow imaging of fatty acid metabolism, including oxidation and lipid storage (*46*,*47*). Oxidative metabolism can be evaluated with ^{11}C-acetate, in which washout reflects myocardial oxygen consumption (*48*,*49*).

Studies using metabolic PET tracers have shown distinct alterations in myocardial substrate metabolism and external efficiency in various cardiac diseases including heart failure (*49*,*50*). These relate partially to alterations in systemic metabolism, such as those that occur in obesity and diabetes (*51*). By assessing the metabolism simultaneously in multiple organs, including the heart, skeletal muscles, liver, and adipose tissue, LAFOV PET can contribute to studying organ-specific changes in cardiometabolic diseases and related cardiovascular complications (*52*). For example, cardiac and systemic insulin resistance is a typical feature of heart failure that predicts impaired functional capacity and reduced survival (*53*). However, mechanisms of insulin resistance differ between cardiac and skeletal muscle related to substrate metabolism and hemodynamic stressors (*54*). Metabolic imaging with LAFOV PET/CT may provide answers to the associations between myocardial and peripheral insulin resistance in cardiac disease and diabetes (*55*). Given its superior sensitivity, accurate modeling of multiple compartments in dynamic datasets may become possible to derive new insights into glucose, fatty acid, and oxidative metabolism (*56*). Such an approach has been demonstrated previously to determine the influx rate, fractional blood volume, tracer delivery rate, and volume of distribution of ^{18}F-FDG in tumors (*56*) and in patients recovering from coronavirus disease 2019 infection (*57*).

Involvement of the Heart in Systemic Disease

Sarcoidosis is a multisystem inflammatory condition of unknown etiology and predominantly affects the lungs and lymph nodes; cardiac sarcoidosis is clinically apparent in 5%–10% of patients, and it is the most frequent cause of death in these patients (*58*,*59*). Autopsy data demonstrate cardiac sarcoidosis involvement in 25% of cases, suggesting that many patients with cardiac sarcoidosis are not recognized with current imaging techniques.

^{18}F-FDG PET is currently recommended for the assessment of patients with suspected cardiac sarcoidosis (*60*) and is characterized by intense focal uptake in the myocardium, which corresponds with areas of myocardial injury observed either on rest perfusion nuclear imaging or late gadolinium enhancement sequences from cardiovascular MRI (*61*). This finding provides important prognostic information (*62*) and frequently prompts the prescription of anti-inflammatory agents and consideration of (expensive) cardiac device implantation.

LAFOV PET/CT would potentially improve our assessment of patients with cardiac sarcoidosis, allowing us to better appreciate sarcoidosis involvement across multiple organs (e.g., brain, heart, lungs, gut, skin, eyes, lymph nodes). Given the low sensitivity of myocardial biopsy, histologic proof of extracardiac sarcoidosis guided by imaging findings can also be valuable for diagnosis of cardiac sarcoidosis (*60*). Reduced radiation doses are particularly attractive when considering longitudinal imaging to track disease progression and response to therapy (*60*).

Cardiac amyloidosis is part of a systemic disease in which amyloidogenic proteins deposit in target organs, leading to dysfunction. There are 2 major types of cardiac amyloidosis: transthyretin amyloidosis and amyloidosis where the amyloidogenic proteins are either misfolded transthyretin or misfolded immunoglobulin light chains (amyloid light-chain amyloidosis) (*63*). Over the past decade, imaging of cardiac amyloidosis has undergone a revolution with the adoption of bone scintigraphy imaging using SPECT tracers and techniques that have allowed for the noninvasive diagnosis of transthyretin cardiac amyloidosis. However, there are also multiple unmet needs in the evaluation of amyloidosis that lend themselves to the use of PET-based radiotracers, including quantification of total-body or target organ amyloid disease burden, differentiation between various types of amyloidosis, and determination of treatment response.

By the nature of PET imaging, PET-based radiotracers are more quantitative than their SPECT counterparts. Parametric imaging with PET can be a valuable tool for the quantification of PET tracer uptake (*64*). Therefore, the use of PET imaging for evaluation of cardiac amyloidosis is most likely to center around the qualitative nature of this modality. Four thioflavin analog PET tracers have shown promise for the diagnosis of cardiac amyloidosis. These include ^{11}C-labeled Pittsburg compound B, ^{18}F-florbetapir, ^{18}F-florbetaben, and ^{18}F-flutemetamol (*65*). There are data from these agents that have shown preliminary utility in imaging the heart, including kinetic modeling (*66*,*67*), whole-body or cardiac disease burden (*68*–*70*), and amyloid isotype differentiation (*71*). There is also interest in the use of the bone tracer ^{18}F-NaF for imaging transthyretin cardiac amyloidosis (*72*).

The use of whole-body PET systems may allow for more accurate and earlier diagnosis of cardiac involvement while simultaneously offering the ability to determine the total systemic disease burden, including dynamic and parametric image quantification. Whole-body PET systems could allow for determination of total-body disease burden in response to therapy, which is of particular interest in amyloid light-chain amyloidosis, where various target organs (heart, gastrointestinal tract/liver, kidneys) can be involved and would normally require longer, multiple-bed-position acquisitions with traditional

PET machines. Unlike amyloid light-chain amyloidosis, the role of circulating biomarkers (natriuretic peptides, transthyretin, RNA polymerase II subunit B4) in the diagnosis and management of transthyretin cardiac amyloidosis is much less defined and validated (*73*). The availability of disease-modifying agents highlights the need for new markers capable of addressing correct clinical management and more accurate prognostic stratification (*73*). Markers define the minimum disease threshold to justify starting new treatments and to exclude patients with infiltration so advanced that they would not benefit from therapy or to identify "responders" and "nonresponders" to a specific disease-modifying agent. LAFOV PET/CT could therefore potentially provide new markers of cardiac involvement relative to total-body disease burden and will be relevant in systemic diseases such as amyloidosis.

Large vessel vasculitis (LVV) disorders are defined as chronic inflammatory disorders that affect the arteries, with variants distinguished in giant cell arteritis, Takayasu arteritis, and isolated (noninfectious) aortitis. These often present with nonspecific constitutional symptoms, which make an accurate diagnosis challenging. Timely diagnosis is of the utmost importance to initiate appropriate treatment and to avoid potential life-threatening vascular (stenosis, dilation, rupture) and potential multiorgan complications (*74*). ^{18}F-FDG PET/CT is now widely accepted as a useful tool to aid in the diagnosis of LVV and is included in current guideline recommendations (*75*,*76*). The increased sensitivity of LAFOV PET/CT may provide added value in detecting suppressed arterial wall ^{18}F-FDG PET activity due to glucocorticosteroid use (*77*) or unclear cases where residual or reactivated LVV activity is suspected (Fig. 4). The ability to perform low-dose radiation imaging or short-duration scans is also attractive, particularly when considering the need for repeat imaging in patients. The use of appropriate (multiorgan/vascular) kinetic models will provide a significantly higher target-to-background ratio than is possible with conventional scoring and quantification (*2*,*78*). Dynamic PET angiography can even be reconstructed from early dynamic PET/CT images for the evaluation of arteries, of particular interest as a one-stop-shop approach in LVV (*79*), or may include the use of specific inflammatory tracers with dynamic PET (*80*). The main challenge with systemic vasculitis is the differentiation from widespread atherosclerosis, given the important role inflammation plays in the pathogenesis of atherosclerosis (*81*) and the difficulty differentiating between active and nonactive LVV (smoldering disease) during and after therapy (*82*). Visual differentiation is mainly based on pattern. A pattern that is more heterogeneous (*83*) could further characterize differences in a more precise and less reader-dependent method and may be further improved with specific PET-labeled markers for assessment of remaining LVV activity (*82*). In general, autoimmune diseases are vast, and many are understudied in cardiovascular risk. Various immunotherapies affect the cardiovascular system, and cardiovascular risk in the field of cardiorheumatology is still unknown (*83*). A crucial area of scientific investigation is moving forward in which LAFOV PET/CT can play a central role.

Heart failure with preserved ejection fraction (HFpEF) is increasing in prevalence worldwide, already accounting for at least half of all heart failure. Recently, strong evidence for bidirectional crosstalk between metabolic stress and chronic inflammation has emerged, and alterations in systemic and cardiac immune responses are held to participate in HFpEF pathophysiology (*84*). Given the well-established heterogeneity among HFpEF phenotypes, coupled with the robust complexity and intertwined interactions between metabolic events and inflammation, a comprehensive program of investigation will be required. LAFOV PET/CT may unravel metainflammatory mechanisms contributing to HFpEF pathophysiology and evaluate the systemic effect of new therapeutic (antiinflammatory) approaches (*84*).

FIGURE 4. LAFOV ^{18}F-FDG PET/CT in 55-y-old woman with active large vessel giant cell arteritis and moderate progressive muscle relaxation activity at shoulders and hips. PET acquisition time was 4 min.

Autonomic Nervous System

Using various radiolabeled catecholamines or catecholamine analogs, PET has been successfully applied for interrogation of the cardiac sympathetic nervous system. Global and regional impairments of myocardial innervation have been identified in heart failure, ischemic and structural heart disease, various cardiomyopathies, and systemic diseases affecting the heart, such as diabetes mellitus, amyloidosis, and Parkinson disease (*85*,*86*). Of note, a prognostic value has been established in heart failure, where the severity of innervation impairment is an independent predictor of adverse events, including arrhythmias (*85*,*87*,*88*). Among patients with ischemic cardiomyopathy, the severity of myocardial sympathetic denervation measured on ^{11}C-hydroxyephidrine PET has an established prognostic value for adverse cardiovascular events, including malignant ventricular arrhythmias (*72*,*74*,*75*). Similar clinical applications are being sought from ^{18}F-flubrobenguane or ^{18}F-LMI1195, which will support greater application of myocardial denervation on PET (*89*,*90*). Although a clear-cut clinical indication

has not yet been established for PET imaging of cardiac innervation, it has certainly provided profound mechanistic insights into the interaction between myocardial catecholamine handling, contractile function, electrophysiology, and other pathophysiologic mechanisms in various cardiac diseases (*91*). LAFOV PET/CT now provides the opportunity to expand these mechanistic insights by putting cardiac innervation into the framework of total-body catecholamine handling and by providing information about the simultaneous state of other networking organs. For example, experimental studies have suggested that sympathetic stimulation of hematopoietic organs plays a role in immune-mediated progression of CVD (*92*), whereas richly innervated brown fat may attenuate catecholamine-mediated heart failure progression (*93*). A comprehensive LAFOV total-body PET protocol, which covers catecholamine kinetics sensitively and simultaneously in all relevant organs and considers the effects of circulating catecholamine levels (*94*) and the role of nonspecific tracer signal from some tissues (*95*), may provide answers to questions regarding the interaction between the heart, the autonomic nervous system, and other systems in health and disease. Meta-^{18}F-fluorobenzylguanidine, an analog of meta-iodobenzylguanidine, was recently used to study myocardial sympathetic innervation and was noted to exhibit rapid and sustained uptake in the myocardium (*96*). Although dynamic meta-^{18}F-fluorobenzylguanidine PET allows for quantitation of its volume of distribution, which is a surrogate for norepinephrine transporter-1 density in the myocardium, a LAFOV PET/CT approach would quantitate autonomic function at a more systemic level. Finally, sensory neurons detect invading pathogens and immune cell activation and, in response, relay signals to the central nervous system and act locally to regulate immune cell function. Most exciting are the possibilities of translating our understanding of these neuroimmune communications to new therapies in the cardiovascular field and linking organs, especially given the possibility of repurposing the neuron-specific pharmacologic agents that have already been developed (*97*).

Cardiovascular Infections

The dramatic recent increase in implantation of prosthetic valves, cardiac implantable electronic devices, vascular grafts, and ventricular assist devices has led to a rise in cardiovascular infections with associated high morbidity and mortality and substantial health costs (*98–100*). Accurate diagnosis of cardiovascular infection is challenging. Echocardiography and CT play an important role but have limitations, including acoustic shadowing, metal artifacts, and reduced specificity from noninfected vegetations (*101–103*). ^{18}F-FDG PET/CT allows earlier diagnosis before extensive morphologic damage, as well as the detection of remote septic emboli and other noncardiac manifestations (*104*). These advantages improve diagnostic accuracy to a high level, with metaanalyses showing 73%–100% sensitivity and 71%–100% specificity for prosthetic valve endocarditis and 87% sensitivity and 94% specificity for cardiac implantable electronic device infection (*105*,*106*). In suspected left ventricular assist device infection, ^{18}F-FDG PET/CT can localize the site of infection with a prognostic value (*107*).

LAFOV PET/CT is an emerging tool with advantages that may counteract existing ^{18}F-FDG PET/CT limitations. Full-body coverage and greater signal-to-noise ratio with total-body PET/CT may help detect smaller and low-grade ^{18}F-FDG–avid septic foci, even in the young (Fig. 5) (*108*). LAFOV PET/CT also covers multiple organ systems, including bone marrow, spleen, and lymph node stations that can be involved in cardiovascular infections. In patients with high ^{18}F-FDG uptake in the bone marrow, a cardiovascular or musculoskeletal focus of infection is more likely, typically with gram-negative species. A cardiovascular focus of infection is also more likely in the setting of high splenic ^{18}F-FDG uptake (*109*). A significant challenge for ^{18}F-FDG PET/CT in evaluation of cardiovascular device infection is distinguishing between infection and nonspecific inflammation, particularly in the early postoperative setting or with bioadhesive use (*110*,*111*). Distinct pharmacokinetic patterns of ^{18}F-FDG uptake on dynamic-imaging LAFOV PET/CT may help differentiate foci of infection from inflammation.

Development of novel non–^{18}F-FDG PET tracers that exhibit direct binding to bacteria may direct imaging of infection rather than inflammation as a surrogate. For example, ^{18}F-labeled polysaccharides that target bacteria-specific maltodextrin transporter (^{18}F-sorbitol, ^{18}F-maltohexaose, ^{18}F-maltose, ^{18}F-maltotriose) achieve a high intrabacterial activity due to continuous internalization, facilitating infection imaging with high sensitivity. Other non–^{18}F-FDG infection imaging tracers include radiolabeled antibiotics, antimicrobial peptides, bacterial antibodies, bacteriophages, and bacterial DNA/RNA hybrid nucleotide oligomers (*112*). Nevertheless, these tracers encounter low sensitivity due to bacterial surface binding only, without intrabacterial signal amplification. The high sensitivity of LAFOV PET/CT may allow direct visualization of these bacteria-binding tracers despite a low signal.

RADIOPHARMACEUTICALS AND DRUG DEVELOPMENT

LAFOV PET/CT scanners have exhibited the ability to enhance clinical diagnostics by enabling imaging at delayed time points after injection. This delayed imaging approach holds promise not only for clinical applications but also for advancing research endeavors through improved characterization of tracer biology. Notably, extending imaging to as late as 24 h after injection of a standard ^{18}F-FDG dose has revealed a more pronounced washout of tracer from the circulating blood pool, concomitant with heightened uptake in cardiovascular tissue. Furthermore, using images of the newly introduced long-lived ^{89}Zr-labeled anti-CD8 minibody against T cell CD8+ at the 24-h mark unveiled the potential to longitudinally monitor immune cell (slower) dynamics. This novel application could potentially find utility in cardiovascular imaging, particularly in atherosclerosis research (*113*).

An illustrative instance involves ^{68}Ga- or the longer-lasting ^{64}Cu-labeled DOTATATE, a Food and Drug Administration–approved PET radiotracer known for its binding to somatostatin receptor type 2, primarily used for identifying and tracking somatostatin receptor type 2–positive neuroendocrine tumors. Importantly, this radiotracer is gaining rapid traction in the realm of cardiovascular inflammation imaging (*114*). Further, PET radiotracers targeting fibroblast-activation protein are now being evaluated increasingly beyond oncologic imaging, such as in the heart, where stimuli activate fibroblasts, leading to progressing interstitial fibrosis and resulting in cardiac dysfunction. Recent literature has demonstrated dynamic total-body PET using ^{68}Ga-FAPI-04 in an oncologic setting, showing rapid tracer uptake and a high tracer-to-background ratio (*115*). Data suggest that total-body modeling is feasible for FAPI ligands, and these promising tracers can also be used to investigate the impact of CVD on fibrotic activity throughout the entire body. With the development of novel antifibrotic treatments (*116*,*117*), FAPI PET has the potential to identify suitable subjects by providing insights into the condition of the heart and distant organs. PET radiotracers hold the promise of expediting drug development by facilitating comprehensive

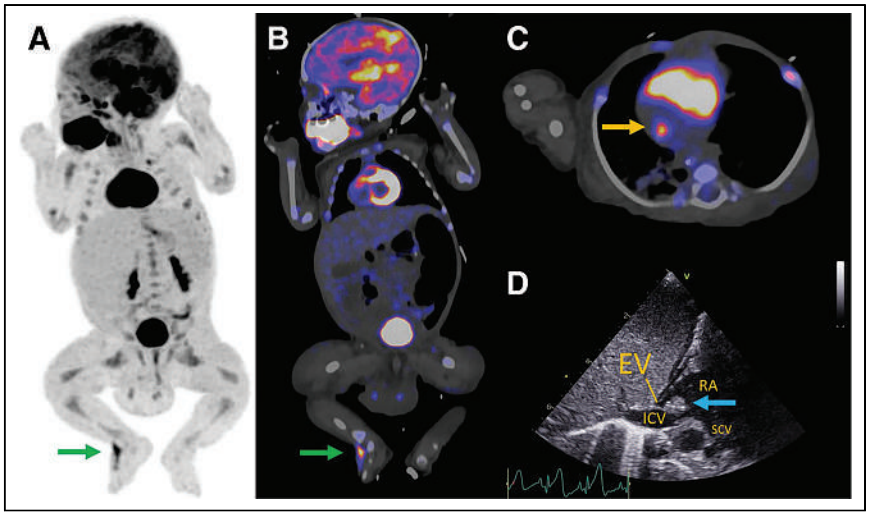

FIGURE 5. 10-wk-old baby presenting with *Staphylococcus aureus* sepsis of unknown origin underwent total-body ^{18}F-FDG PET/CT imaging, which was performed in 3 min (1 bed position) without sedation on Biograph Vision Quadra system (Siemens Healthineers) using only 12 MBq. His medical history consisted of several congenital defects, including Fallot tetralogy and jejunal atresia. Two infectious foci were detected: at dorsum of right foot (A and B, green arrows) around intravenous access line, and at bottom of right atrium near entrance of inferior caval vein (C, arrow). Reactive bone marrow uptake is also visible (A). Ultrasound of foot revealed subcutaneous abscess, which was drained; culturing detected *S. aureus*. ^{18}F-FDG uptake in heart corresponded with solid, echodense structure suggestive of thrombus or vegetation. This is seen on transthoracic echocardiography (D, arrow) at eustachian valve (usually absent by adulthood), indicative of possible endocarditis. Patient improved under antibiotic therapy. (Reprinted with permission of (*124*).)

assessments. This approach enables (guided) therapy monitoring in total-body mode, encompassing critical aspects such as quantifying receptor occupancy, evaluating drug distribution, conducting pharmacokinetic analyses, confirming target engagement, monitoring treatment responses, and gauging compound concentrations.

The potential extends to understanding the spatial distribution of drugs throughout the entire body, offering insights into how agents accumulate in various tissues over time. Although these dimensions are pivotal in cardiovascular studies, they remain relatively underexplored at present (*118*).

DISCUSSION

The future of PET is quantitative and, with the availability of the of LAFOV PET/CT systems, represents an exciting development in the field of medical imaging (*119*). These systems have the potential to not only revolutionize busy clinical services but also enable the investigation of tissue kinetics at multiple levels simultaneously.

From a cardiovascular perspective, this innovative imaging methodology will significantly enhance our understanding of the systemic effects and interactions of various cardiovascular disorders. Until now, these disorders were examined using only single-frame, static, whole-body imaging. In certain cases, imaging at later time points may prove beneficial for achieving a better ratio between the inflammatory lesion and blood-pool activity. For example, it can be useful in conditions such as LVV or cardiac sarcoidosis.

LAFOV PET/CT offers additional advantages such as the ability to perform dynamic scans, which can aid in distinguishing between reactive ^{18}F-FDG uptake and artifact. This feature allows for more accurate visualization of smaller mobile structures in the heart, including suspected endocarditis vegetations, which are frequently missed on conventional PET/CT systems.

Because of the improved sensitivity of a LAFOV PET/CT scanner, scanning even after 4 or 5 half-lives becomes feasible and worth considering. Decreased tracer doses are possible, reducing radiation and creating greater opportunity for serial imaging and therapy monitoring in CVDs. However, the use of CT for attenuation correction in LAFOV PET/CT can contribute significantly to the radiation exposure. Recent CT technology has introduced features such as the tin filter (*120*) or deep learning algorithms, which can substantially reduce the CT radiation dose (*121*).

LAFOV PET/CT imaging of multiorgan involvement in several systemic diseases is of potential value, such as in sarcoidosis, amyloidosis, LVV, and atherosclerosis, as PET can be an early marker of systemic disease activity, prevent disease early, better assess prognosis, and determine the optimal moment of therapy induction. Low radiation might also allow (simultaneous) multitracer imaging to assess the link between cardiovascular inflammation and fibroblast activation in these diseases (*122*). Finally, future research in cardiooncology is an opportunity for LAFOV PET/CT to elucidate the mechanisms involved in cross-talk between cardiac and cancer cells, as cancer cells can promote metabolic remodeling in the heart (*123*). Metabolic changes provide opportunities for novel treatment strategies to prevent heart failure and monitor disease progression through new imaging techniques. However, along with the opportunities presented by LAFOV PET/CT, there are several challenges that need to be addressed (Table 1).

CONCLUSION

LAFOV PET/CT not only introduces a fast imaging acquisition technique with optimal image quality but also facilitates the implementation of quantitative kinetic imaging in clinical settings. It significantly enhances our knowledge of systemic CVD inter(organ) actions and serves as an excellent method for longitudinal imaging and the serial evaluation of disease activity with time, as well as a method to determine the effectiveness of new medical drugs at the whole-body level.

DISCLOSURE

No potential conflict of interest relevant to this article was reported.

ACKNOWLEDGMENT

We thank Nick van Rijsewijk for the use of Figure 5.

REFERENCES

1. Badawi RD, Shi H, Hu P, et al. First human imaging studies with the EXPLORER total-body PET scanner. *J Nucl Med.* 2019;60:299–303.
2. Slart RH, Tsoumpas C, Glaudemans A, et al. Long axial field of view PET scanners: a road map to implementation and new possibilities. *Eur J Nucl Med Mol Imaging.* 2021;48:4236–4245.

3. van Sluis J, van Snick JH, Brouwers AH, et al. EARL compliance and imaging optimisation on the Biograph Vision Quadra PET/CT using phantom and clinical data. *Eur J Nucl Med Mol Imaging.* 2022;49:4652–4660.
4. van Sluis J, van Snick JH, Brouwers AH, et al. Shortened duration whole body ^{18}F-FDG PET Patlak imaging on the Biograph Vision Quadra PET/CT using a population-averaged input function. *EJNMMI Phys.* 2022;9:74.
5. Maron DJ, Hochman JS, Reynolds HR, et al. Initial invasive or conservative strategy for stable coronary disease. *N Engl J Med.* 2020;382:1395–1407.
6. Ridker PM, Everett BM, Thuren T, et al. Antiinflammatory therapy with canakinumab for atherosclerotic disease. *N Engl J Med.* 2017;377:1119–1131.
7. Roshandel G, Khoshnia M, Poustchi H, et al. Effectiveness of polypill for primary and secondary prevention of cardiovascular diseases (PolyIran): a pragmatic, cluster-randomised trial. *Lancet.* 2019;394:672–683.
8. Swirski FK, Nahrendorf M. Cardioimmunology: the immune system in cardiac homeostasis and disease. *Nat Rev Immunol.* 2018;18:733–744.
9. Cermakova P, Eriksdotter M, Lund LH, Winblad B, Religa P, Religa D. Heart failure and Alzheimer's disease. *J Intern Med.* 2015;277:406–425.
10. Moslehi JJ. Cardiovascular toxic effects of targeted cancer therapies. *N Engl J Med.* 2016;375:1457–1467.
11. Zannad F, Rossignol P. Cardiorenal syndrome revisited. *Circulation.* 2018;138:929–944.
12. Samsky MD, Patel CB, DeWald TA, et al. Cardiohepatic interactions in heart failure: an overview and clinical implications. *J Am Coll Cardiol.* 2013;61:2397–2405.
13. Oliveira SD. Cardiopulmonary pathogenic networks: unveiling the gut-lung microbiome axis in pulmonary arterial hypertension. *Am J Respir Crit Care Med.* 2023;207:655–657.
14. Tang WH, Kitai T, Hazen SL. Gut microbiota in cardiovascular health and disease. *Circ Res.* 2017;120:1183–1196.
15. Rahmim A, Lodge MA, Karakatsanis NA, et al. Dynamic whole-body PET imaging: principles, potentials and applications. *Eur J Nucl Med Mol Imaging.* 2019;46:501–518.
16. Visvikis D, Lambin P, Beuschau Mauridsen K, et al. Application of artificial intelligence in nuclear medicine and molecular imaging: a review of current status and future perspectives for clinical translation. *Eur J Nucl Med Mol Imaging.* 2022;49:4452–4463.
17. Schindler TH, Bateman TM, Berman DS, et al. Appropriate use criteria for PET myocardial perfusion imaging. *J Nucl Med.* 2020;61:1221–1265.
18. Mielniczuk LM, Toth GG, Xie JX, De Bruyne B, Shaw LJ, Beanlands RS. Can functional testing for ischemia and viability guide revascularization? *JACC Cardiovasc Imaging.* 2017;10:354–364.
19. Mintun MA, Raichle ME, Martin WR, Herscovitch P. Brain oxygen utilization measured with O-15 radiotracers and positron emission tomography. *J Nucl Med.* 1984;25:177–187.
20. Raichle ME, Martin WR, Herscovitch P, Mintun MA, Markham J. Brain blood flow measured with intravenous $H_2{}^{15}O$. II. Implementation and validation. *J Nucl Med.* 1983;24:790–798.
21. Wintermark M, Sesay M, Barbier E, et al. Comparative overview of brain perfusion imaging techniques. *Stroke.* 2005;36:e83–e99.
22. Murthy VL, Bateman TM, Beanlands RS, et al. Clinical quantification of myocardial blood flow using pet: joint position paper of the SNMMI Cardiovascular Council and the ASNC. *J Nucl Med.* 2018;59:273–293.
23. Ngo V, Martineau P, Harel F, Pelletier-Galarneau M. Improving detection of CAD and prognosis with PET/CT quantitative absolute myocardial blood flow measurements. *Curr Cardiol Rep.* 2022;24:1855–1864.
24. Schindler TH, Fearon WF, Pelletier-Galarneau M, et al. Myocardial perfusion PET for the detection and reporting of coronary microvascular dysfunction: a *JACC: Cardiovascular Imaging* Expert Panel Statement. *JACC Cardiovasc Imaging.* 2023;16:536–548.
25. Juillard L, Janier MF, Fouque D, et al. Dynamic renal blood flow measurement by positron emission tomography in patients with CRF. *Am J Kidney Dis.* 2002;40:947–954.
26. Juillard L, Janier MF, Fouque D, et al. Renal blood flow measurement by positron emission tomography using ^{15}O-labeled water. *Kidney Int.* 2000;57:2511–2518.
27. Langaa SS, Lauridsen TG, Mose FH, Fynbo CA, Theil J, Bech JN. Estimation of renal perfusion based on measurement of rubidium-82 clearance by PET/CT scanning in healthy subjects. *EJNMMI Phys.* 2021;8:43.
28. Tahari AK, Bravo PE, Rahmim A, Bengel FM, Szabo Z. Initial human experience with rubidium-82 renal PET/CT imaging. *J Med Imaging Radiat Oncol.* 2014;58:25–31.
29. Nitzsche EU, Choi Y, Killion D, et al. Quantification and parametric imaging of renal cortical blood flow in vivo based on Patlak graphical analysis. *Kidney Int.* 1993;44:985–996.
30. Keramida G, Gregg S, Peters AM. Stimulation of the hepatic arterial buffer response using exogenous adenosine: hepatic rest/stress perfusion imaging. *Eur Radiol.* 2020;30:5852–5861.
31. Mossberg KA, Mullani N, Gould KL, Taegtmeyer H. Skeletal muscle blood flow in vivo: detection with rubidium-82 and effects of glucose, insulin, and exercise. *J Nucl Med.* 1987;28:1155–1163.
32. Oguro A, Taniguchi H, Koyama H, et al. Quantification of human splenic blood flow (quantitative measurement of splenic blood flow with $H_2{}^{15}O$ and a dynamic state method: 1). *Ann Nucl Med.* 1993;7:245–250.
33. Oguro A, Taniguchi H, Koyama H, et al. Relationship between liver function and splenic blood flow (quantitative measurement of splenic blood flow with $H_2{}^{15}O$ and a dynamic state method: 2). *Ann Nucl Med.* 1993;7:251–255.
34. Rudroff T, Weissman JA, Bucci M, et al. Positron emission tomography detects greater blood flow and less blood flow heterogeneity in the exercising skeletal muscles of old compared with young men during fatiguing contractions. *J Physiol (Lond).* 2014;592:337–349.
35. Li EJ, Lopez JE, Spencer BA, et al. Total-body perfusion imaging with [^{11}C]-butanol. *J Nucl Med.* 2023;64:1831–1838.
36. Packard RRS, Votaw JR, Cooke CD, Van Train KF, Garcia EV, Maddahi J. ^{18}F-flurpiridaz positron emission tomography segmental and territory myocardial blood flow metrics: incremental value beyond perfusion for coronary artery disease categorization. *Eur Heart J Cardiovasc Imaging.* 2022;23:1636–1644.
37. Chou TH, Alvelo JL, Janse S, et al. Prognostic value of radiotracer-based perfusion imaging in critical limb ischemia patients undergoing lower extremity revascularization. *JACC Cardiovasc Imaging.* 2021;14:1614–1624.
38. Suárez C, Zeymer U, Limbourg T, et al. Influence of polyvascular disease on cardiovascular event rates. Insights from the REACH Registry. *Vasc Med.* 2010;15:259–265.
39. Hess CN, Bonaca MP. Contemporary review of antithrombotic therapy in peripheral artery disease. *Circ Cardiovasc Interv.* 2020;13:e009584.
40. Tawakol A, Ishai A, Takx RA, et al. Relation between resting amygdalar activity and cardiovascular events: a longitudinal and cohort study. *Lancet.* 2017;389:834–845.
41. Joshi NV, Vesey AT, Williams MC, et al. ^{18}F-fluoride positron emission tomography for identification of ruptured and high-risk coronary atherosclerotic plaques: a prospective clinical trial. *Lancet.* 2014;383:705–713.
42. Diekmann J, Koenig T, Zwadlo C, et al. Molecular imaging identifies fibroblast activation beyond the infarct region after acute myocardial infarction. *J Am Coll Cardiol.* 2021;77:1835–1837.
43. Wu M, Ning J, Li J, et al. Feasibility of in vivo imaging of fibroblast activation protein in human arterial walls. *J Nucl Med.* 2022;63:948–951.
44. Tzolos E, Bing R, Andrews J, et al. Noninvasive in vivo coronary artery thrombus imaging. *JACC Cardiovasc Imaging.* 2023;16:820–832.
45. Derlin T, Werner RA, Weiberg D, Derlin K, Bengel FM. Parametric imaging of biologic activity of atherosclerosis using dynamic whole-body positron emission tomography. *JACC Cardiovasc Imaging.* 2022;15:2098–2108.
46. Ebert A, Herzog H, Stocklin GL, et al. Kinetics of 14(R,S)-fluorine-18-fluoro-6-thia-heptadecanoic acid in normal human hearts at rest, during exercise and after dipyridamole injection. *J Nucl Med.* 1994;35:51–56.
47. McArdle B, Dowsley TF, Cocker MS, et al. Cardiac PET: metabolic and functional imaging of the myocardium. *Semin Nucl Med.* 2013;43:434–448.
48. Lopaschuk GD, Ussher JR. Evolving concepts of myocardial energy metabolism: more than just fats and carbohydrates. *Circ Res.* 2016;119:1173–1176.
49. Sörensen J, Harms HJ, Aalen JM, Baron T, Smiseth OA, Flachskampf FA. Myocardial efficiency: a fundamental physiological concept on the verge of clinical impact. *JACC Cardiovasc Imaging.* 2020;13:1564–1576.
50. Gewirtz H. Cardiac PET: a versatile, quantitative measurement tool for heart failure management. *JACC Cardiovasc Imaging.* 2011;4:292–302.
51. Peterson LR, Gropler RJ. Metabolic and molecular imaging of the diabetic cardiomyopathy. *Circ Res.* 2020;126:1628–1645.
52. Kumar V, Hsueh WA, Raman SV. Multiorgan, Multimodality imaging in cardiometabolic disease. *Circ Cardiovasc Imaging.* 2017;10:e005447.
53. Doehner W, Frenneaux M, Anker SD. Metabolic impairment in heart failure: the myocardial and systemic perspective. *J Am Coll Cardiol.* 2014;64:1388–1400.
54. Lopaschuk GD, Karwi QG, Tian R, Wende AR, Abel ED. Cardiac energy metabolism in heart failure. *Circ Res.* 2021;128:1487–1513.
55. Tuunanen H, Knuuti J. Metabolic remodelling in human heart failure. *Cardiovasc Res.* 2011;90:251–257.
56. Wang G, Nardo L, Parikh M, et al. Total-body PET multiparametric imaging of cancer using a voxelwise strategy of compartmental modeling. *J Nucl Med.* 2022;63:1274–1281.
57. Wang Y, Nardo L, Spencer BA, et al. Total-body multiparametric PET quantification of ^{18}F-FDG delivery and metabolism in the study of coronavirus disease 2019 recovery. *J Nucl Med.* 2023;64:1821–1830.

58. Birnie DH, Nery PB, Ha AC, Beanlands RS. Cardiac sarcoidosis. *J Am Coll Cardiol.* 2016;68:411–421.
59. Iannuzzi MC, Rybicki BA, Teirstein AS. Sarcoidosis. *N Engl J Med.* 2007;357:2153–2165.
60. Slart RH, Glaudemans A, Lancellotti P, et al. A joint procedural position statement on imaging in cardiac sarcoidosis: from the Cardiovascular and Inflammation & Infection Committees of the European Association of Nuclear Medicine, the European Association of Cardiovascular Imaging, and the American Society of Nuclear Cardiology. *J Nucl Cardiol.* 2018;25:298–319.
61. Dweck MR, Abgral R, Trivieri MG, et al. Hybrid magnetic resonance imaging and positron emission tomography with fluorodeoxyglucose to diagnose active cardiac sarcoidosis. *JACC Cardiovasc Imaging.* 2018;11:94–107.
62. Blankstein R, Osborne M, Naya M, et al. Cardiac positron emission tomography enhances prognostic assessments of patients with suspected cardiac sarcoidosis. *J Am Coll Cardiol.* 2014;63:329–336.
63. Kittleson MM, Maurer MS, Ambardekar AV, et al. Cardiac amyloidosis: evolving diagnosis and management: a scientific statement from the American Heart Association. *Circulation.* 2020;142:e7–e22.
64. Yan J, Planeta-Wilson B, Carson RE. Direct 4-D PET list mode parametric reconstruction with a novel EM algorithm. *IEEE Trans Med Imaging.* 2012;31:2213–2223.
65. Gallegos C, Miller EJ. Advances in PET-based cardiac amyloid radiotracers. *Curr Cardiol Rep.* 2020;22:40.
66. Dhoot GK. Identification and changes in the pattern of expression of slow-skeletal-muscle-like myosin heavy chains in a developing fast muscle. *Differentiation.* 1988;37:53–61.
67. Papathanasiou M, Kessler L, Carpinteiro A, et al. ^{18}F-flutemetamol positron emission tomography in cardiac amyloidosis. *J Nucl Cardiol.* 2022;29:779–789.
68. Dietemann S, Nkoulou R. Amyloid PET imaging in cardiac amyloidosis: a pilot study using ^{18}F-flutemetamol positron emission tomography. *Ann Nucl Med.* 2019;33:624–628.
69. Ezawa N, Katoh N, Oguchi K, Yoshinaga T, Yazaki M, Sekijima Y. Visualization of multiple organ amyloid involvement in systemic amyloidosis using ^{11}C-PiB PET imaging. *Eur J Nucl Med Mol Imaging.* 2018;45:452–461.
70. Mestre-Torres J, Lorenzo-Bosquet C, Cuberas-Borros G, et al. Utility of the ^{18}F-florbetapir positron emission tomography in systemic amyloidosis. *Amyloid.* 2018;25:109–114.
71. Takasone K, Katoh N, Takahashi Y, et al. Non-invasive detection and differentiation of cardiac amyloidosis using ^{99m}Tc-pyrophosphate scintigraphy and ^{11}C-Pittsburgh compound B PET imaging. *Amyloid.* 2020;27:266–274.
72. Trivieri MG, Dweck MR, Abgral R, et al. ^{18}F-sodium fluoride PET/MR for the assessment of cardiac amyloidosis. *J Am Coll Cardiol.* 2016;68:2712–2714.
73. Perfetto F, Zampieri M, Fumagalli C, Allinovi M, Cappelli F. Circulating biomarkers in diagnosis and management of cardiac amyloidosis: a review for internist. *Intern Emerg Med.* 2022;17:957–969.
74. Tarkin JM, Gopalan D. Multimodality imaging of large-vessel vasculitis. *Heart.* 2023;109:232–240.
75. Dejaco C, Ramiro S, Duftner C, et al. EULAR recommendations for the use of imaging in large vessel vasculitis in clinical practice. *Ann Rheum Dis.* 2018;77:636–643.
76. Slart RH, Writing Group, Reviewer Group, et al. FDG-PET/CT(A) imaging in large vessel vasculitis and polymyalgia rheumatica: joint procedural recommendation of the EANM, SNMMI, and the PET Interest Group (PIG), and endorsed by the ASNC. *Eur J Nucl Med Mol Imaging.* 2018;45:1250–1269.
77. Nielsen BD, Gormsen LC, Hansen IT, Keller KK, Therkildsen P, Hauge EM. Three days of high-dose glucocorticoid treatment attenuates large-vessel ^{18}F-FDG uptake in large-vessel giant cell arteritis but with a limited impact on diagnostic accuracy. *Eur J Nucl Med Mol Imaging.* 2018;45:1119–1128.
78. Sari H, Mingels C, Alberts I, et al. First results on kinetic modelling and parametric imaging of dynamic ^{18}F-FDG datasets from a long axial FOV PET scanner in oncological patients. *Eur J Nucl Med Mol Imaging.* 2022;49:1997–2009.
79. Drescher R, Freesmeyer M. PET angiography: application of early dynamic PET/CT to the evaluation of arteries. *AJR.* 2013;201:908–911.
80. Lamare F, Hinz R, Gaemperli O, et al. Detection and quantification of large-vessel inflammation with ^{11}C-(*R*)-PK11195 PET/CT. *J Nucl Med.* 2011;52:33–39.
81. Nienhuis PH, van Praagh GD, Glaudemans A, Brouwer E, Slart R. A review on the value of imaging in differentiating between large vessel vasculitis and atherosclerosis. *J Pers Med.* 2021;11:236.
82. van der Geest KSM, Sandovici M, Nienhuis PH, et al. Novel PET imaging of inflammatory targets and cells for the diagnosis and monitoring of giant cell arteritis and polymyalgia rheumatica. *Front Med (Lausanne).* 2022;9:902155.
83. Weber B, Garshick M, Liao KP, Di Carli M. Sore, hot, and at risk: the emerging specialty of cardio-rheumatology. *J Am Heart Assoc.* 2023;12:e027846.
84. Schiattarella GG, Alcaide P, Condorelli G, et al. Immunometabolic mechanisms of heart failure with preserved ejection fraction. *Nat Cardiovasc Res.* 2022;1:211–222.
85. Malhotra S, Fernandez SF, Fallavollita JA, Canty JM Jr. Prognostic significance of imaging myocardial sympathetic innervation. *Curr Cardiol Rep.* 2015;17:62.
86. Thackeray JT, Bengel FM. Assessment of cardiac autonomic neuronal function using PET imaging. *J Nucl Cardiol.* 2013;20:150–165.
87. Fallavollita JA, Heavey BM, Luisi AJ Jr, et al. Regional myocardial sympathetic denervation predicts the risk of sudden cardiac arrest in ischemic cardiomyopathy. *J Am Coll Cardiol.* 2014;63:141–149.
88. Malhotra S, Singh V, Fallavollita JA, Canty JM Jr. Myocardial denervation and left ventricular volume predict ventricular arrhythmias in patients with ischemic cardiomyopathy. *JACC Cardiovasc Imaging.* 2022;15:1164–1166.
89. Mu L, Kramer SD, Warnock GI, et al. [^{11}C]mHED PET follows a two-tissue compartment model in mouse myocardium with norepinephrine transporter (NET)-dependent uptake, while [^{18}F]LMI1195 uptake is NET-independent. *EJNMMI Res.* 2020;10:114.
90. Zelt JGE, Britt D, Mair BA, et al. Regional distribution of fluorine-18-flubrobenguane and carbon-11-hydroxyephedrine for cardiac PET imaging of sympathetic innervation. *JACC Cardiovasc Imaging.* 2021;14:1425–1436.
91. Bengel FM. Imaging targets of the sympathetic nervous system of the heart: translational considerations. *J Nucl Med.* 2011;52:1167–1170.
92. Dutta P, Courties G, Wei Y, et al. Myocardial infarction accelerates atherosclerosis. *Nature.* 2012;487:325–329.
93. Thoonen R, Ernande L, Cheng J, et al. Functional brown adipose tissue limits cardiomyocyte injury and adverse remodeling in catecholamine-induced cardiomyopathy. *J Mol Cell Cardiol.* 2015;84:202–211.
94. DeGrado TR, Hutchins GD, Toorongian SA, Wieland DM, Schwaiger M. Myocardial kinetics of carbon-11-meta-hydroxyephedrine: retention mechanisms and effects of norepinephrine. *J Nucl Med.* 1993;34:1287–1293.
95. Thackeray JT, Beanlands RS, Dasilva JN. Presence of specific ^{11}C-meta-hydroxyephedrine retention in heart, lung, pancreas, and brown adipose tissue. *J Nucl Med.* 2007;48:1733–1740.
96. Grkovski M, Zanzonico PB, Modak S, Humm JL, Narula J, Pandit-Taskar N. F-18 meta-fluorobenzylguanidine PET imaging of myocardial sympathetic innervation. *J Nucl Cardiol.* 2022;29:3179–3188.
97. Udit S, Blake K, Chiu IM. Somatosensory and autonomic neuronal regulation of the immune response. *Nat Rev Neurosci.* 2022;23:157–171.
98. Bin Abdulhak AA, Baddour LM, Erwin PJ, et al. Global and regional burden of infective endocarditis, 1990-2010: a systematic review of the literature. *Glob Heart.* 2014;9:131–143.
99. Morita Y, Haruna T, Haruna Y, et al. Thirty-day readmission after infective endocarditis: analysis from a nationwide readmission database. *J Am Heart Assoc.* 2019;8:e011598.
100. Pant S, Patel NJ, Deshmukh A, et al. Trends in infective endocarditis incidence, microbiology, and valve replacement in the United States from 2000 to 2011. *J Am Coll Cardiol.* 2015;65:2070–2076.
101. Habib G, Badano L, Tribouilloy C, et al. Recommendations for the practice of echocardiography in infective endocarditis. *Eur J Echocardiogr.* 2010;11:202–219.
102. Habib G, Lancellotti P, Antunes MJ, et al. 2015 ESC guidelines for the management of infective endocarditis: the Task Force for the Management of Infective Endocarditis of the European Society of Cardiology (ESC). Endorsed by: European Association for Cardio-Thoracic Surgery (EACTS), the European Association of Nuclear Medicine (EANM). *Eur Heart J.* 2015;36:3075–3128.
103. Lindner JR, Case RA, Dent JM, Abbott RD, Scheld WM, Kaul S. Diagnostic value of echocardiography in suspected endocarditis. An evaluation based on the pretest probability of disease. *Circulation.* 1996;93:730–736.
104. Chen W, Sajadi MM, Dilsizian V. Merits of FDG PET/CT and functional molecular imaging over anatomic imaging with echocardiography and CT angiography for the diagnosis of cardiac device infections. *JACC Cardiovasc Imaging.* 2018;11:1679–1691.
105. Gomes A, Glaudemans A, Touw DJ, et al. Diagnostic value of imaging in infective endocarditis: a systematic review. *Lancet Infect Dis.* 2017;17:e1–e14.
106. Juneau D, Golfam M, Hazra S, et al. Positron emission tomography and single-photon emission computed tomography imaging in the diagnosis of cardiac implantable electronic device infection: a systematic review and meta-analysis. *Circ Cardiovasc Imaging.* 2017;10:e005772.
107. Kim J, Feller ED, Chen W, Liang Y, Dilsizian V. FDG PET/CT for early detection and localization of left ventricular assist device infection: impact on patient management and outcome. *JACC Cardiovasc Imaging.* 2019;12:722–729.
108. Feng T, Zhao Y, Shi H, et al. Total-body quantitative parametric imaging of early kinetics of ^{18}F-FDG. *J Nucl Med.* 2021;62:738–744.
109. Pijl JP, Kwee TC, Slart R, Yakar D, Wouthuyzen-Bakker M, Glaudemans A. Clinical implications of increased uptake in bone marrow and spleen on

FDG-PET in patients with bacteremia. *Eur J Nucl Med Mol Imaging.* 2021;48: 1467–1477.
110. Roque A, Pizzi MN, Fernandez-Hidalgo N, et al. Mosaic bioprostheses may mimic infective endocarditis by PET/CTA: trust the uptake pattern to avoid misdiagnosis. *JACC Cardiovasc Imaging.* 2020;13:2239–2244.
111. Scholtens AM, Swart LE, Verberne HJ, Tanis W, Lam MG, Budde RP. Confounders in FDG-PET/CT imaging of suspected prosthetic valve endocarditis. *JACC Cardiovasc Imaging.* 2016;9:1462–1465.
112. Chen W, Dilsizian V. Molecular imaging of cardiovascular device infection: targeting the bacteria or the host-pathogen immune response? *J Nucl Med.* 2020;61:319–326.
113. Omidvari N, Jones T, Price PM, et al. First-in-human immunoPET imaging of COVID-19 convalescent patients using dynamic total-body PET and a CD8-targeted minibody. *Sci Adv.* 2023;19:eadh7968.
114. Ćorović A, Wall C, Nus M, et al. Somatostatin receptor PET/MR imaging of inflammation in patients with large vessel vasculitis and atherosclerosis. *J Am Coll Cardiol.* 2023;81:336–354.
115. Chen R, Yang X, Yu X, et al. The feasibility of ultra-early and fast total-body [^{68}Ga]Ga-FAPI-04 PET/CT scan. *Eur J Nucl Med Mol Imaging.* 2023;50: 661–666.
116. Ishikane S, Arioka M, Takahashi-Yanaga F. Promising small molecule antifibrotic agents: newly developed or repositioned drugs targeting myofibroblast transdifferentiation. *Biochem Pharmacol.* 2023;214:115663.
117. Morfino P, Aimo A, Castiglione V, Galvez-Monton C, Emdin M, Bayes-Genis A. Treatment of cardiac fibrosis: from neuro-hormonal inhibitors to CAR-T cell therapy. *Heart Fail Rev.* 2023;28:555–569.
118. Ghosh KK, Padmanabhan P, Yang CT, et al. Positron emission tomographic imaging in drug discovery. *Drug Discov Today.* 2022;27:280–291.
119. Cherry SR, Diekmann J, Bengel FM. Total-body positron emission tomography: adding new perspectives to cardiovascular research. *JACC Cardiovasc Imaging.* 2023;16:1335–1347.
120. Shiri I, Arabi H, Geramifar P, et al. Deep-JASC: joint attenuation and scatter correction in whole-body ^{18}F-FDG PET using a deep residual network. *Eur J Nucl Med Mol Imaging.* 2020;47:2533–2548.
121. Mostafapour S, Greuter M, van Snick JH, et al. Ultra-low dose CT scanning for PET/CT. *Med Phys.* 2024;51:139–155.
122. Zeng F, Fang J, Muhashi A, Liu H. Direct reconstruction for simultaneous dual-tracer PET imaging based on multi-task learning. *EJNMMI Res.* 2023; 13:7.
123. Karlstaedt A, Barrett M, Hu R, Gammons ST, Ky B. Cardio-oncology: understanding the intersections between cardiac metabolism and cancer biology. *JACC Basic Transl Sci.* 2021;6:705–718.
124. van Rijsewijk ND, van Leer B, Ivashchenko OV, et al. Ultra-low dose infection imaging of a newborn without sedation using long axial field-of-view PET/CT. *Eur J Nucl Med Mol Imaging.* 2023;50:622–623.

[^{18}F]FDG PET/CT Signal Correlates with Neoangiogenesis Markers in Patients with Fibrotic Interstitial Lung Disease Who Underwent Lung Biopsy: Implication for the Use of PET/CT in Diffuse Lung Diseases

Joanna C. Porter[1,2], Balaji Ganeshan[3], Thida Win[4], Francesco Fraioli[3], Saif Khan[5], Manuel Rodriguez-Justo[5], Raymond Endozo[3], Robert I. Shortman[3], Luke R. Hoy[3], Toby M. Maher[6], and Ashley M. Groves[3]

[1]CITR, UCL Respiratory, University College London, London, United Kingdom; [2]Interstitial Lung Disease Centre, University College London Hospital, London, United Kingdom; [3]Institute of Nuclear Medicine, University College London and University College London Hospital, London, United Kingdom; [4]Lister Hospital, North East Herts Trust, Stevenage, United Kingdom; [5]Research Department of Pathology, University College London, and Department of Histopathology, University College London Hospital, London, United Kingdom; and [6]Keck School of Medicine, University of Southern California, Los Angeles, California

The use of [^{18}F]FDG PET/CT as a biomarker in diffuse lung diseases is increasingly recognized. We investigated the correlation between [^{18}F]FDG uptake with histologic markers on lung biopsy of patients with fibrotic interstitial lung disease (fILD). **Methods:** We recruited 18 patients with fILD awaiting lung biopsy for [^{18}F]FDG PET/CT. We derived a target-to-background ratio (TBR) of maximum pulmonary uptake of [^{18}F]FDG (SUV_{max}) divided by the lung background (SUV_{min}). Consecutive paraffin-embedded lung biopsy sections were immunostained for alveolar and interstitial macrophages (CD68), microvessel density (MVD) (CD31 and CD105/endoglin), and glucose transporter 1. MVD was expressed as vessel area percentage per high-power field (Va%/hpf). Differences in imaging and angiogenesis markers between histologic usual interstitial pneumonia (UIP) and non-UIP were assessed using a nonparametric Mann–Whitney test. Correlation of imaging with angiogenesis markers was assessed using the nonparametric Spearman rank correlation. Univariate Kaplan–Meier survival analysis assessed the difference in the survival curves for each of the angiogenesis markers (separated by their respective optimal cutoff) using the log-rank test. Statistical analysis was performed using SPSS. **Results:** In total, 18 patients were followed for an average of 41.36 mo (range, 5.69–132.46 mo; median, 30.07 mo). Only CD105 MVD showed a significantly positive correlation with [^{18}F]FDG TBR (Spearman rank correlation, 0.556; $P < 0.05$, $n = 13$). There was no correlation between [^{18}F]FDG uptake and macrophage expression of glucose transporter 1. CD105 and CD31 were higher for UIP than for non-UIP, with CD105 reaching statistical significance ($P = 0.011$). In all patients, MVD assessed with either CD105 or CD31 quantification on biopsy predicted overall survival. Patients with CD105 MVD of less than 12 Va%/hpf or CD31 MVD of less than 35 Va%/hpf had a significantly better prognosis (no deaths during follow-up in the case of CD105) than did patients with higher scores of CD105 MVD (median survival, 35 mo; $P = 0.041$, $n = 13$) or CD31 MVD (median survival, 28 mo; $P = 0.014$, $n = 13$). **Conclusion:** Previous work has used [^{18}F]FDG uptake in PET/CT as a biomarker in fILD. Here, we highlight a correlation between angiogenesis and [^{18}F]FDG TBR. We show that MVD is higher for UIP than for non-UIP and is associated with mortality in patients with fILD. These data set the scene to investigate the potential role of vasculature and angiogenesis in fibrosis.

Key Words: [^{18}F]FDG PET/CT; ILD; fibrosis; angiogenesis; microvessel

J Nucl Med 2024; 65:617–622
DOI: 10.2967/jnumed.123.266445

There is an urgent clinical need for better biomarkers in interstitial lung disease (ILD) for both patient management and as surrogate endpoints for clinical trials (*1*). The potential role of PET/CT in guiding the management of patients with ILD has been recognized for some time (*2*). We have previously shown that [^{18}F]FDG uptake on PET/CT is a prognostic biomarker in idiopathic pulmonary fibrosis (IPF) that can improve the ability of the clinical sex, age, and physiology score to predict outcomes (*3*). Determining the basis of this signal may improve the clinical utility of [^{18}F]FDG PET/CT through patient stratification, the assessment of treatment response, and potentially valuable mechanistic and therapeutic insights into fibrotic ILD (fILD).

Vessel volume and vessel density, as determined by tissue-density measurements on CT imaging, correlate positively with both physiologic measures (*4*) and outcomes in IPF (*5*). Unfortunately, the prognostic value of lung vascularity, reflected by either microvessel density (MVD) or its correlation with [^{18}F]FDG uptake, has not been explored, and there remains contention over whether there is a paucity or an excess of blood vessels in the fibrotic lung (*6*).

In this study, we investigated the hypothesis that MVD and macrophage phenotype/glucose transporter 1 (GLUT-1) expression on immunohistochemistry were potential predictors of mortality in fILD and examined the correlation between [^{18}F]FDG uptake on PET imaging and angiogenesis and macrophage subsets for different histologic presentations of disease (usual interstitial pneumonia [UIP] vs. non-UIP).

Received Aug. 23, 2023; revision accepted Jan. 11, 2024.
For correspondence or reprints, contact Joanna C. Porter (joanna.porter@ucl.ac.uk).
Published online Mar. 14, 2024.

MATERIALS AND METHODS

Patients

This prospective, single-center study was approved by the London-Harrow Research Ethics Committee (reference 06/Q0505/22), and all participants signed an informed consent form. In total, 18 patients were included in the study on the basis of having a radiologic diagnosis of fILD and either having had or being scheduled to have a clinically required biopsy of an area of lung determined radiographically. Patients were excluded if they had ongoing inflammatory or malignant disease or had been on treatment (immunosuppression or antifibrotics) for ILD in the previous 3 mo. Each participant had an [^{18}F]FDG PET/CT scan that was performed an average of 184 ± 692 d after the biopsy. Pulmonary function tests were undertaken in all patients where possible and quantified as forced vital capacity and transfer factor of the lung for carbon monoxide.

PET/CT Image Acquisition

The methodology we used is described in detail elsewhere (*7–10*). All images were acquired on the same PET/CT scanner (VCT PET/64-detector CT instrument; GE Healthcare). Participants were each injected with 200 MBq of [^{18}F]FDG and allowed to rest peacefully in a private cubicle during the 1-h uptake time. The participants were positioned supine on the CT table with their arms held above their head and were instructed to keep still throughout the procedure, which took approximately 20 min. The first scan was a CT attenuation-correction scan of the thorax, immediately followed by a PET emission scan (8 min per bed position) with identical anatomic coverage. The final scan was a high-resolution CT scan of the lungs that was performed on a deep inspiratory breath-hold, using the following CT parameters: 64 × 1.25 mm detectors, a pitch of 0.53, and a 1.25-mm collimation (120 kVp and 100 mAs).

PET/CT Image Analysis

PET images were analyzed by a dual-trained nuclear medicine physician and a nuclear medicine technologist with more than 5 y of experience in quantifying pulmonary uptake in [^{18}F]FDG PET/CT imaging of ILD. CT images were reviewed independently of the PET/CT analysis by a dedicated thoracic radiologist.

All images were loaded onto an ADW workstation (GE Healthcare). All datasets underwent image processing that has been previously described in detail and has been shown to have high inter- and intraobserver reproducibility (*2*). The area of most intense pulmonary [^{18}F]FDG uptake was identified visually, and then a 2-dimensional region of interest was drawn over the area and the highest pixel value (SUV_{max}) measured.

The region of pulmonary parenchyma with the lowest uptake (SUV_{min}) was similarly identified and confirmed by the dedicated thoracic radiologist to be morphologically normal lung parenchyma on coregistered CT. The SUV_{min} was considered a measure of the background lung uptake and was used to calculate the lung target-to-background ratio ($TBR = SUV_{max}/SUV_{min}$) (*2*).

Histologic Image Analysis

Biopsy samples were taken from affected lung at the discretion of the thoracic surgeon or bronchoscopist, but biopsies were not specifically targeted to PET-avid areas when that information was available. Immunostaining was performed for CD31, a panendothelial cell marker expressed on mature and immature vessels; CD105/endoglin, a proliferation-related endothelial cell marker that is more specific for new immature vessels (*11*); CD68/CD80 for M1-like macrophages; and CD68/CD163 for M2-like macrophages and GLUT-1 expression. Consecutive paraffin-embedded sections obtained from biopsy were immunostained for CD68 (514H12; Leica Biosystems) (alveolar and interstitial macrophages), CD31 (1A10; Novocastra) (panendothelial marker), CD105 (4G11; Novocastra) (endoglin, a protein expressed in angiogenic endothelial cells), and GLUT-1 (polyclonal; Millipore) (the receptor for glucose uptake). Quantification of CD31, CD105, and GLUT-1/CD68 was performed by a single observer (with >20 y of experience) masked to the [^{18}F]FDG PET/CT imaging findings through a semiquantitative analysis of immunoreactivity of the markers. For CD31 and CD105, four 1.060 mm^2 fibrous areas of highest vascularization (hot spots) were counted at a ×20 magnification on an Olympus BX51 microscope (*12*). Figure 1 shows immunohistochemical images of CD105 staining of microvessels in UIP (Figs. 1A and 1B) and non-UIP (Figs. 1C and 1D) at a ×200 magnification (digital-based platform).

CD31 and CD105 are expressed as vessel area percentage per high-power field (Va%/hpf); GLUT-1 staining of CD68 macrophages was scored as absent (0), intermediate (1), or high (2) (*8*). CD68 macrophages were also costained for CD80 as a marker of M1-like macrophages and CD163 to distinguish the M2-like subtypes. Figure 2 shows typical examples of histologic staining and [^{18}F]FDG PET/CT scans in different participants.

Follow-up

The follow-up period was defined as the period between the date of the participant's [^{18}F]FDG PET/CT scan and the date of the patient's death or of the patient's last living contact with medical services, calculated in months.

Statistical Analysis

Statistical analysis was performed using SPSS (version 27.0; IBM Corp.), with a P value of less than 0.05 considered to be significant. Differences in imaging and angiogenesis markers between the histology were assessed using a nonparametric Mann–Whitney test. Univariate Kaplan–Meier survival analysis assessed the difference in the survival curves for each of the angiogenesis markers (separated by their respective optimal cutoff) using the log-rank test. The statistical methodology for determining the optimal cutoff (maximum log-rank or minimum P value) in univariate survival analysis was performed as previously reported (*13*). This methodology has previously been used in prognostication of IPF patients (*3*). Correlation between the imaging and angiogenesis markers was assessed using nonparametric Spearman rank correlation.

RESULTS

In total, 18 patients with fILD were followed for an average of 41.36 mo (range, 5.69–132.46 mo; median, 30.07 mo). Histologic information was available for all 18 participants, of whom 72% (13/18) had histologic UIP and met the clinical criteria for IPF (*14*) and 28% (5/18) had non-UIP findings, of which 4 were considered fibrotic nonspecific interstitial pneumonia and 1 was thought to be fibrotic organizing pneumonia. Technical factors, mainly due to insufficient tissue volume, prevented CD105 staining in 5 of 18 cases. Table 1 illustrates the pulmonary function test results, histology, treatment, neoangiogenesis, vasculature, macrophages, and PET uptake markers for each patient in the study population.

On biopsy, only CD105 was significantly higher ($P = 0.011$; Fig. 3) for UIP ($n = 9$) than for non-UIP ($n = 4$). CD31 was higher for UIP histology but did not reach statistical significance ($P = 0.08$, $n = 13$).

In all participants, both CD105 MVD and CD31 MVD staining on biopsy predicted overall survival in fILD patients. Patients with a CD105 MVD of less than 12 Va%/hpf had no deaths during their follow-up, and patients with a CD31 MVD of less than 35 Va%/hpf had improved survival than that seen with a higher CD31

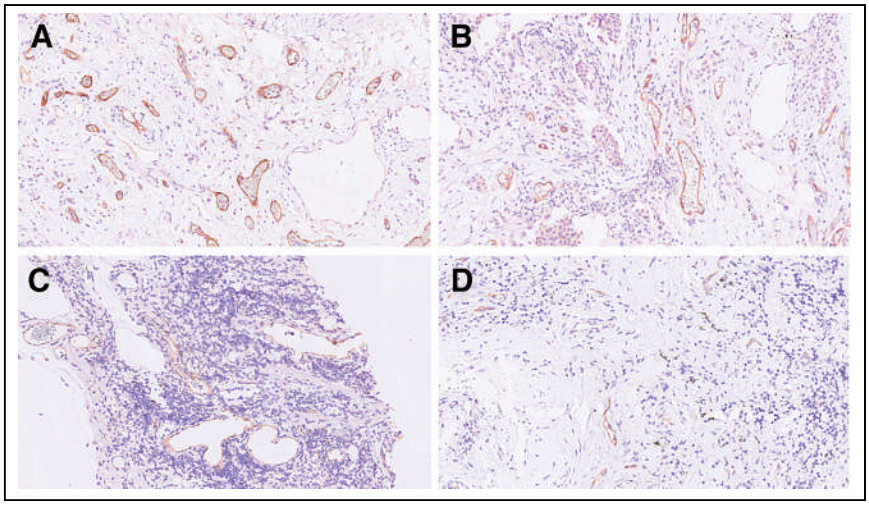

FIGURE 1. Immunohistochemical images of CD105 staining of microvessels in UIP (A and B) and non-UIP (C and D) at ×200 magnification (digital-based platform).

MVD. The median survival of patients with a CD105 MVD of at least 12 Va%/hpf and a CD31 MVD of at least 35 Va%/hpf was 35 mo ($P = 0.041$, $n = 13$; Fig. 4) and 28 mo ($P = 0.014$, $n = 13$; Fig. 5), respectively. There was no correlation between macrophage numbers, M1 or M2 subtypes, or M1:M2 ratios with survival.

The [^{18}F]FDG PET/CT signal in the 13 participants with UIP histology and IPF was found to be similar to that of the 5 participants with non-UIP histology, with no significant difference in TBR ($P = 0.29$). However, the TBR did have a significant positive correlation with the angiogenesis marker CD105 MVD (Spearman rank correlation, 0.556; $P < 0.05$, $n = 13$; Fig. 6). The CD31 MVD was not significantly correlated with TBR (Spearman rank correlation, 0.479; $P = 0.097$, $n = 13$), and there was no correlation between [^{18}F]FDG uptake and either macrophage expression of GLUT-1 or macrophage subsets.

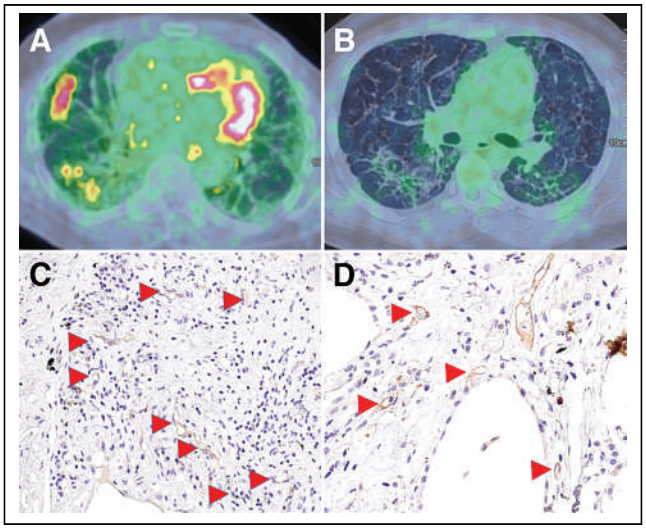

FIGURE 2. Representative participant [^{18}F]FDG PET/CT scans showing high (A) and low (B) TBR of [^{18}F]FDG uptake. Immunohistochemistry images of stained patient biopsies show high (C) and low (D) expression of CD105/endoglin (arrowheads).

DISCUSSION

In this study, we found CD105 MVD as a marker of neoangiogenesis that was significantly correlated positively with mortality, UIP histology, and [^{18}F]FDG TBR in patients with fILD. CD31, a marker of established vasculature, significantly correlated positively with mortality but not with PET signal or histology. We also found no correlation between GLUT-1 expression on macrophages and [^{18}F]FDG PET/CT or with macrophage subsets, as determined by CD68 (M1) and CD103 (M2).

We have previously shown using cross-validation in a cohort of 113 patients that TBR derived from [^{18}F]FDG PET/CT is predictive of the outcome in patients with IPF (*3*) and that a high percentage of vessels on quantitative CT, measured as pulmonary vessel volume (*4*) or as vessel percentage (*5*), in relatively unaffected parts of the lung enables identification of IPF patients who have worse health outcomes. Although the biologic basis for this is unclear, Jacob et al. (*4*) offered 3 plausible explanations: blood-flow diversion from advanced fibrotic areas to relatively spared lung regions; a dilatation effect on blood vessels due to increased negative inspiratory pressure, secondary to increased lung stiffness; and the effect of pleuroparenchymal and bronchopulmonary arterial anastomosis. To reconcile these findings, we suggest that, despite active neoangiogenesis in fibrotic areas, these vessels may not significantly contribute to blood flow.

Angiogenesis may be driven by hypoxia and hypoxia-inducible factor transcriptional regulators, but our previous work shows very little hypoxia-inducible factor activation in the IPF lung (*9*). Transforming growth factor-β is a key cytokine in fibrosis and angiogenesis, and endoglin/CD105 acts as a transforming growth factor-β coreceptor to bind leucine-rich glycoprotein 1 and drive aberrant vessel formation during neoangiogenesis (*15*).

GLUT-1, the main transporter for [^{18}F]FDG, is found in erythrocytes and alveolar macrophages in the fibrotic lung, which has led to the suggestion that the [^{18}F]FDG PET/CT signal in ILD may reflect inflammation or neoangiogenesis (*16*). Macrophages play a role in ILD, with monocyte-derived macrophages contributing to fibrotic potential, and can be broadly considered to exist on a spectrum of inflammatory (M1-like) or antiinflammatory and fibrotic (M2-like) behavior, dependent on their cell surface molecule expression and cytokine production profiles (*17*). However, there are inconsistencies with this view, and a recent attempt has been made to provide a consensus classification (*18*). In general, M1-like or classically activated macrophages show enhanced glycolysis and GLUT-1 expression (*19*) and are thought to be elevated during inflammation, with M2-like or alternatively activated macrophages increased in the fibrotic stage of disease. This view has given rise to the targeting of M2-like macrophages as a possible treatment strategy in IPF (*20*). Distinguishing these populations on immunohistochemistry is difficult (*21*), and with these limitations in mind, we used CD80 and CD163 surface staining to distinguish the M1-like (CD68-positive/CD80high/CD163low) and M2-like (CD68-positive/CD80low/CD163high) phenotypes, respectively. Although we found no differences in [^{18}F]FDG PET

TABLE 1
Participant Characteristics, Immunohistochemistry Results, and [^{18}F]FDG PET/CT Quantification*

Patient	Forced vital capacity prediction (%)	Transfer factor of lung for carbon monoxide prediction (%)	Histology	Treatment for ILD	CD105 (Va%/hpf)	CD31 (Va%/hpf)	GLUT-1 macrophage score	TBR	CD80 average of hpf counts	CD163 average of hpf counts	CD163:CD80 ratio
1	65	57	UIP	No	22	26	0	5.29	42.5	57.5	1.35
2	54	27	NSIP	No	19	23	1	7.71	NA	NA	NA
3	47	33	OP	No	10	15	1	3	NA	NA	NA
4	57	29	NSIP	No	10	34	0	4.6	16.5	75	4.55
5	99	79	UIP	No	23	30	0	4.29	9.5	34	3.58
6	73	41	UIP	No	44	NA	0	4.67	1.5	31.5	21
7	NA	45	UIP	No	NA	NA	2	6	2.5	58.5	23.4
8	95	64	UIP	No	18	38	0	3.86	32.5	52.5	1.62
9	91	66	NSIP	No	NA	29	1	5.29	33	36	1.09
10	77	47	NSIP	No	14	NA	0	3.33	20.5	51	2.49
11	104	70	UIP	No	25	NA	1	4.6	4.5	85	18.89
12	99	63	UIP	No	34	70	0	5.86	18.5	65	3.51
13	75	54	UIP	No	17	21	0	3.75	10.5	56	5.33
14	99	NA	UIP	No	NA	55	2	6.33	7.5	31.5	4.2
15	43	43	UIP	No	NA	45	0	5.17	3	51.5	17.17
16	63	63	UIP	No	24	35	0	10.29	1	42.5	42.5
17	NA	NA	UIP	No	NA	NA	2	6.17	NA	NA	NA
18	58	40	UIP	No	19	45	1	12	11.5	38	3.3

*Lung function results were within 10 d of [^{18}F]FDG PET/CT scan.
NSIP = nonspecific interstitial pneumonia; NA = not available; OP = organizing pneumonia.

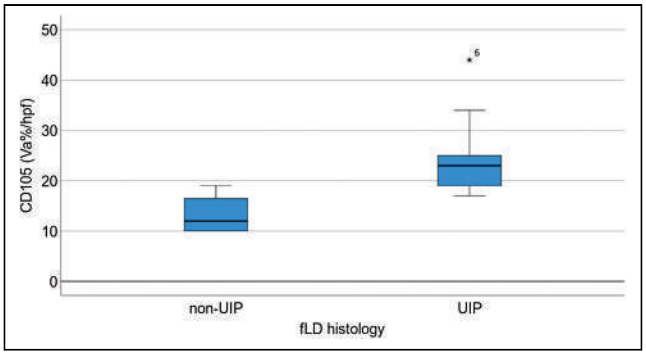

FIGURE 3. Box plot highlighting increased distribution of CD105 in UIP vs. non-UIP histology ($P = 0.011$). *Patient 6 outlier (CD105 = 44). fLD = fibrotic lung disease.

uptake parameters with differing macrophage populations on immunohistochemistry, further study may be warranted using more specific markers of transcription and other factors (*21*).

Although our study population was limited in size, only a small minority of ILD patients have lung biopsies, and therefore, our cohort of 18 fILD patients with matched [^{18}F]FDG PET/CT images and immunohistochemistry is the largest reported to the best of our knowledge. Unfortunately, it was difficult to control the time between the biopsy and the [^{18}F]FDG PET/CT scan, causing a large variation in the biopsy–scan interval, which is a limitation of this study. In addition, the association between MVD and survival in such a small group is open to valid criticism. Although the determination of optimal cutoff points in our univariate survival analysis followed a statistically recognized methodology previously reported (*13*), it is important to note that this is a pilot study and future studies should include robust validation procedures to confirm and generalize the findings. Although perfect registration between the biopsy location and PET measurements was not possible, it is less problematic in diffuse lung disease than with focal lesions such as lung cancer. Using a volume of interest

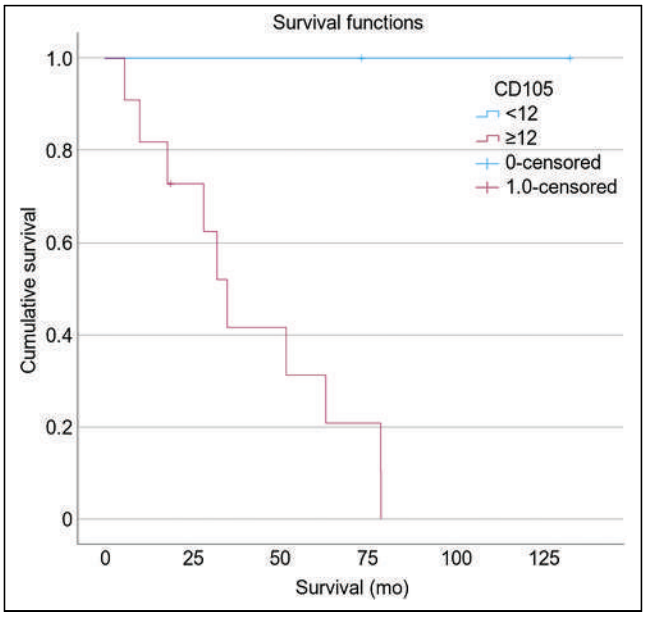

FIGURE 4. Kaplan–Meier survival curve showing how neoangiogenic marker CD105 predicts overall survival ($P = 0.041$).

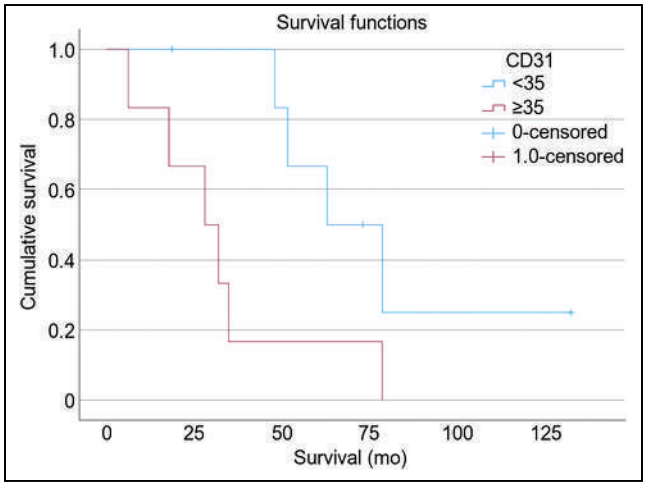

FIGURE 5. Kaplan–Meier survival curve showing how vasculature marker CD31 predicts overall survival ($P = 0.014$).

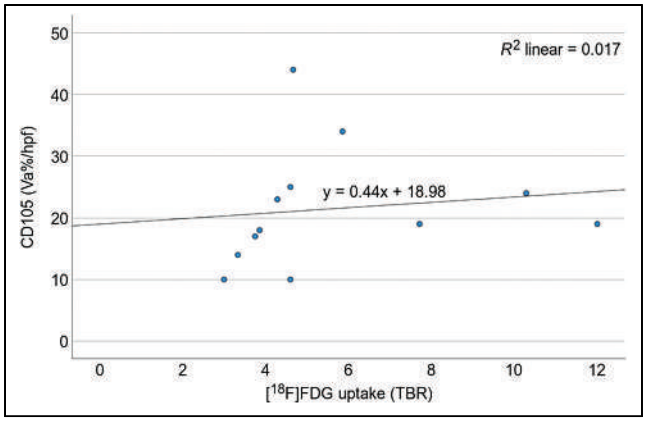

FIGURE 6. Scatterplot demonstrating positive correlation (Spearman rank correlation, 0.556; $P < 0.05$) between CD105 and [^{18}F]FDG uptake (TBR).

near the biopsy location rather than a 2-dimensional region of interest for PET uptake measurements may be a better reflection of the underlying lung biology and could be the subject of a future study, but it is the inherent heterogeneity of both immunochemistry and radiologic appearance that makes quantification of ILD difficult. This challenge is being increasingly met through computer-aided quantitative analysis, and CT texture has already been shown to be a significant predicator of IPF mortality that is independent of lung parenchymal patterns (*22*). It is plausible that CT texture analysis could provide useful information about pulmonary vasculature and PET uptake in the future.

CONCLUSION

Previous work has used [^{18}F]FDG PET/CT as a biomarker for guiding personalized treatment and prognostication in IPF, and its utility is increasingly recognized in other conditions such as in post–coronavirus disease 2019 lung disease (*10*). Understanding the basis of the [^{18}F]FDG PET/CT signal may offer mechanistic insights into ILD and identify novel pharmacologic targets around fibrosis. In this study, we highlight a marker of neoangiogenesis and one of established vasculature as a predictor of mortality and possible associations between neoangiogenesis and [^{18}F]FDG

uptake (TBR) and histology in patients with fILD. Whether such positive correlations reflect a direct causal link is unknown, but they do set the scene to investigate the potential role of vasculature and angiogenesis in fibrosis.

DISCLOSURE

Joanna Porter was funded by a Medical Research Council new investigator award and by Breathing Matters; this work was undertaken at UCLH/UCL, which received a proportion of funding from the U.K.'s Department of Health's National Institute of Health Research Biomedical Research Centres' funding scheme. No other potential conflict of interest relevant to this article was reported.

KEY POINTS

QUESTION: Does the lung uptake of [^{18}F]FDG on PET/CT correlate with histologic markers in patients with fILD?

PERTINENT FINDINGS: This study revealed a positive correlation between lung uptake of [^{18}F]FDG and MVD (CD105 MVD) in fILD patients. Higher CD105 MVD in UIP cases than in non-UIP cases was associated with increased mortality.

IMPLICATIONS FOR PATIENT CARE: The findings emphasize the potential significance of angiogenesis, particularly CD105 MVD, in fILD, suggesting avenues for further research and therapeutic exploration.

REFERENCES

1. Sgalla G, Wijsenbeek MS, Richeldi L. The shorter, the better: can we improve efficiency of idiopathic pulmonary fibrosis trials? *Am J Respir Crit Care Med.* 2022; 205:867–869.
2. Groves AM, Win T, Screaton NJ, et al. Idiopathic pulmonary fibrosis and diffuse parenchymal lung disease: implications from initial experience with ^{18}F-FDG PET/CT. *J Nucl Med.* 2009;50:538–545.
3. Win T, Screaton NJ, Porter JC, et al. Pulmonary ^{18}F-FDG uptake helps refine current risk stratification in idiopathic pulmonary fibrosis (IPF). *Eur J Nucl Med Mol Imaging.* 2018;45:806–815.
4. Jacob J, Bartholmai BJ, Rajagopalan S, et al. Mortality prediction in idiopathic pulmonary fibrosis: evaluation of computer-based CT analysis with conventional severity measures. *Eur Respir J.* 2017;49:1601011.
5. Fraioli F, Lyasheva M, Porter JC, et al. Synergistic application of pulmonary ^{18}F-FDG PET/HRCT and computer-based CT analysis with conventional severity measures to refine current risk stratification in idiopathic pulmonary fibrosis (IPF). *Eur J Nucl Med Mol Imaging.* 2019;46:2023–2031.
6. Hanumegowda C, Farkas L, Kolb M. Angiogenesis in pulmonary fibrosis: too much or not enough? *Chest.* 2012;142:200–207.
7. Chen DL, Ballout S, Chen L, et al. Consensus recommendations on the use of ^{18}F-FDG PET/CT in lung disease. *J Nucl Med.* 2020;61:1701–1707.
8. Groves AM, Shastry M, Rodriguez-Justo M, et al. ^{18}F-FDG PET and biomarkers for tumour angiogenesis in early breast cancer. *Eur J Nucl Med Mol Imaging.* 2011;38:46–52.
9. Porter JC, Win T, Erlandsson K, et al. Measurement of hypoxia in the lung in idiopathic pulmonary fibrosis: an F-MISO PET/CT study. *Eur Respir J.* 2021;58: 2004584.
10. Thornton A, Fraioli F, Wan S, et al. Evolution of ^{18}F-FDG PET/CT findings in patients after COVID-19: an initial investigation. *J Nucl Med.* 2022;63:270–273.
11. Beresford MJ, Harris AL, Ah-See M, Daley F, Padhani AR, Makris A. The relationship of the neo-angiogenic marker, endoglin, with response to neoadjuvant chemotherapy in breast cancer. *Br J Cancer.* 2006;95:1683–1688.
12. Goh V, Rodriguez-Justo M, Engledow A, et al. Assessment of the metabolic flow phenotype of primary colorectal cancer: correlations with microvessel density are influenced by the histological scoring method. *Eur Radiol.* 2012;22:1687–1692.
13. Faraggi D, Simon R. A simulation study of cross-validation for selecting an optimal cutpoint in univariate survival analysis. *Stat Med.* 1996;15:2203–2213.
14. Raghu G, Remy-Jardin M, Myers JL, et al. Diagnosis of idiopathic pulmonary fibrosis: an official ATS/ERS/JRS/ALAT clinical practice guideline. *Am J Respir Crit Care Med.* 2018;198:e44–e68.
15. Wang X, Abraham S, McKenzie JAG, et al. LRG1 promotes angiogenesis by modulating endothelial TGF-beta signalling. *Nature.* 2013;499:306–311.
16. El-Chemaly S, Malide D, Yao J, et al. Glucose transporter-1 distribution in fibrotic lung disease: association with ^{18}F-2-fluoro-2-deoxyglucose-PET scan uptake, inflammation, and neovascularization. *Chest.* 2013;143:1685–1691.
17. Lawrence T, Natoli G. Transcriptional regulation of macrophage polarization: enabling diversity with identity. *Nat Rev Immunol.* 2011;11:750–761.
18. Murray PJ, Allen JE, Biswas SK, et al. Macrophage activation and polarization: nomenclature and experimental guidelines. *Immunity.* 2014;41:14–20.
19. Jha AK, Huang SC, Sergushichev A, et al. Network integration of parallel metabolic and transcriptional data reveals metabolic modules that regulate macrophage polarization. *Immunity.* 2015;42:419–430.
20. Singh A, Chakraborty S, Wong SW, et al. Nanoparticle targeting of de novo profibrotic macrophages mitigates lung fibrosis. *Proc Natl Acad Sci USA.* 2022;119: e2121098119.
21. Barros MH, Hauck F, Dreyer JH, Kempkes B, Niedobitek G. Macrophage polarisation: an immunohistochemical approach for identifying M1 and M2 macrophages. *PLoS One.* 2013;8:e80908.
22. AlDalilah Y, Ganeshan B, Endozo R, et al. Filtration-histogram based texture analysis and CALIPER based pattern analysis as quantitative CT techniques in idiopathic pulmonary fibrosis: head-to-head comparison. *Br J Radiol.* 2022;95: 20210957.

Clinical Evaluation of Deep Learning for Tumor Delineation on ^{18}F-FDG PET/CT of Head and Neck Cancer

David G. Kovacs[1,2], Claes N. Ladefoged[1,3], Kim F. Andersen[1], Jane M. Brittain[1], Charlotte B. Christensen[4], Danijela Dejanovic[1], Naja L. Hansen[1], Annika Loft[1], Jørgen H. Petersen[5], Michala Reichkendler[1], Flemming L. Andersen[1,2], and Barbara M. Fischer[1,2,6]

[1]*Department of Clinical Physiology and Nuclear Medicine, Rigshospitalet, University of Copenhagen, Copenhagen, Denmark;* [2]*Department of Clinical Medicine, Faculty of Health and Medical Sciences, University of Copenhagen, Copenhagen, Denmark;* [3]*Department of Applied Mathematics and Computer Science, Technical University of Denmark, Lyngby, Denmark;* [4]*Department of Clinical Physiology and Nuclear Medicine, Herlev Hospital, University of Copenhagen, Copenhagen, Denmark;* [5]*Section of Biostatistics, Institute of Public Health, Faculty of Health Sciences, University of Copenhagen, Denmark; and* [6]*PET Centre, School of Biomedical Engineering and Imaging Science, King's College London, London, United Kingdom*

Artificial intelligence (AI) may decrease ^{18}F-FDG PET/CT–based gross tumor volume (GTV) delineation variability and automate tumor-volume–derived image biomarker extraction. Hence, we aimed to identify and evaluate promising state-of-the-art deep learning methods for head and neck cancer (HNC) PET GTV delineation. **Methods:** We trained and evaluated deep learning methods using retrospectively included scans of HNC patients referred for radiotherapy between January 2014 and December 2019 (ISRCTN16907234). We used 3 test datasets: an internal set to compare methods, another internal set to compare AI-to-expert variability and expert interobserver variability (IOV), and an external set to compare internal and external AI-to-expert variability. Expert PET GTVs were used as the reference standard. Our benchmark IOV was measured using the PET GTV of 6 experts. The primary outcome was the Dice similarity coefficient (DSC). ANOVA was used to compare methods, a paired *t* test was used to compare AI-to-expert variability and expert IOV, an unpaired *t* test was used to compare internal and external AI-to-expert variability, and post hoc Bland–Altman analysis was used to evaluate biomarker agreement. **Results:** In total, 1,220 ^{18}F-FDG PET/CT scans of 1,190 patients (mean age ± SD, 63 ± 10 y; 858 men) were included, and 5 deep learning methods were trained using 5-fold cross-validation (n = 805). The nnU-Net method achieved the highest similarity (DSC, 0.80 [95% CI, 0.77–0.86]; n = 196). We found no evidence of a difference between expert IOV and AI-to-expert variability (DSC, 0.78 for AI vs. 0.82 for experts; mean difference of 0.04 [95% CI, −0.01 to 0.09]; P = 0.12; n = 64). We found no evidence of a difference between the internal and external AI-to-expert variability (DSC, 0.80 internally vs. 0.81 externally; mean difference of 0.004 [95% CI, −0.05 to 0.04]; P = 0.87; n = 125). PET GTV–derived biomarkers of AI were in good agreement with experts. **Conclusion:** Deep learning can be used to automate ^{18}F-FDG PET/CT tumor-volume–derived imaging biomarkers, and the deep-learning–based volumes have the potential to assist clinical tumor volume delineation in radiation oncology.

Received Aug. 23, 2023; revision accepted Jan. 29, 2024.

For correspondence or reprints, contact David G. Kovacs (dkov0001@regionh.dk).

Published online Feb. 22, 2024.

Key Words: ^{18}F-FDG PET/CT; head and neck cancer; tumor volume delineation; imaging biomarkers; deep learning

J Nucl Med 2024; 65:623–629
DOI: 10.2967/jnumed.123.266574

PET/CT with ^{18}F-FDG is integral to the oncologic evaluation of nodal involvement, identification of distant metastases, radiotherapy planning, response assessment, and patient follow-up (*1–4*). This applies to several types of cancer, including head and neck cancer (HNC). HNC was the seventh most common cancer worldwide in 2018, with 890,000 new cases and 450,000 deaths (*5*). Modern chemo-, immuno-, and high-precision radiotherapy have increased survival; however, these treatments depend on advanced image analysis, including tumor delineation by expert specialists on functional and anatomic images (*6*).

Delineation of ^{18}F-FDG PET/CT–based gross tumor volume (GTV) to guide radiotherapy involves distinguishing healthy from pathologic metabolic activity with high accuracy. This task is complex in assessing nodal involvement and distinguishing healthy metabolic activity in the proximity of malignant tissue. Furthermore, the anatomic closeness between organs at risk, lymph nodes, and malignant tissues can make HNC PET GTV delineation particularly challenging. Here, a high-quality automated tumor delineation method could lead to more consistent and repeatable image evaluation. Additionally, treatment delay in radiotherapy leads to a decreased chance of tumor control and an increased risk of metastases. In this context, the time savings made possible by automated contouring in ^{18}F-FDG PET/CT–guided radiotherapy planning holds a potentially tangible clinical impact (*7*).

Artificial intelligence (AI) deep learning methods are currently the state of the art for semantic segmentation on medical images (*8*). Although lack of clinical evaluation has hampered AI implementation in practice, there is good evidence that predefined deep learning methods can solve advanced, previously unseen problems (*9–11*). Considering the success of predefined deep learning methods with novel problems, we hypothesized that these algorithms could delineate PET GTV to a standard comparable to our current clinical methods.

In this study, we identified promising, reproducible, predefined AI deep learning methods in a systematic literature review and

trained them on a large clinical dataset. We investigated how the methods compared with clinical PET GTVs. We evaluated AI on internal and external test scans, using expert-delineated PET GTVs as the reference. Finally, we investigated whether PET GTV–derived metabolic biomarkers were reliable. We aimed to identify, train, and evaluate promising state-of-the-art deep learning methods for HNC PET GTV delineation and PET GTV–derived biomarker extraction.

MATERIALS AND METHODS

This retrospective clinical evaluation was approved by the Danish Patient Safety Authority (approval 31-1521-340, reference no. SMMO) and the Danish Data Protection Agency (approval P-2020-427).

Observer evaluations were conducted from January to October 2022, the analysis was performed from October 2022 to March 2023, and the statistical analysis plan was published in September 2022 before looking at any data at the registry (www.isrctn.com/: ISRCTN16907234). After internal results became available, the decision was made to test deep learning on an external dataset.

A full version of the Materials and Methods section is available as Supplemental Appendix A (*12–15*). Supplemental Appendix B and Supplemental Table 1 list image acquisition and preprocessing details. Hardware and software specifications are listed in Supplemental Table 2 (supplemental materials are available at http://jnm.snmjournals.org).

Study Design and Patient Population

Scans were included of patients with HNC referred for ^{18}F-FDG PET/CT–guided radiotherapy at our institution (internal) between 2014 and 2019 and an external institution between 2018 and 2019. The reasons for exclusion were incomplete data or failure to pass visual validation (Fig. 1). No patients were below 18 y of age. The selected scans were divided into training, validation, and test subsets. Three test sets, including an external one, were created with sample sizes based on power considerations.

The institutional review boards at the involved hospitals approved this retrospective study, and the requirement to obtain informed consent was waived.

Clinical Evaluation and Reference Delineations

The clinical PET GTVs used for radiotherapy were applied for model training and methods comparison. In our clinical routine, the PET GTV delineated by nuclear medicine specialists is sent to a radiation oncologist or radiologist, who uses the volume to guide the final GTV delineation. Hence, for clinical evaluation, PET GTV was independently delineated on the test sets for this study by 7 nuclear medicine specialists: 6 internally and 1 externally (board-certified specialists with 3.5 to >15 y of experience). The PET GTV region was delineated on the PET image with an optionally underlying CT image. A visually adapted isocontour without a fixed threshold was used to fit the steepest gradient between the ^{18}F-FDG–avid malignant region and the surrounding tissue, excluding areas with nonmalignant uptake.

Interobserver variability (IOV) was evaluated by 2 randomly selected experts from a group of 6 delineating the PET GTV on each scan (Fig. 2). The randomization was blocked; each expert therefore contributed equally. Scans were uploaded to clinical systems twice under different anonymous identities to ensure that experts could not review previous PET GTVs. To resemble clinical practice, where it is random which of our experts delineate each scan, 1 of the 2 experts was randomly selected as the reference. The patients were anonymized to mask the experts. Hence, the internal experts could not look up contextual patient journal information. Instead, they were provided with a brief text containing the causes of the referral. The external expert had access to the same information as in clinical routine, except for the PET GTV used for treatment.

Statistical Analysis

We selected the Dice similarity coefficient (DSC) expressing the degree of overlap (0, no overlap; 1, complete overlap) between 2 volumes because it is the most widely used metric in the deep learning literature, allowing for comparison to other studies. The Hausdorff distance, F1 score, PET GTV–derived tumor volume (cm^3), SUV_{mean}, and SUV_{max} were secondary outcomes. We used a significance level of 0.05 in all statistical testing.

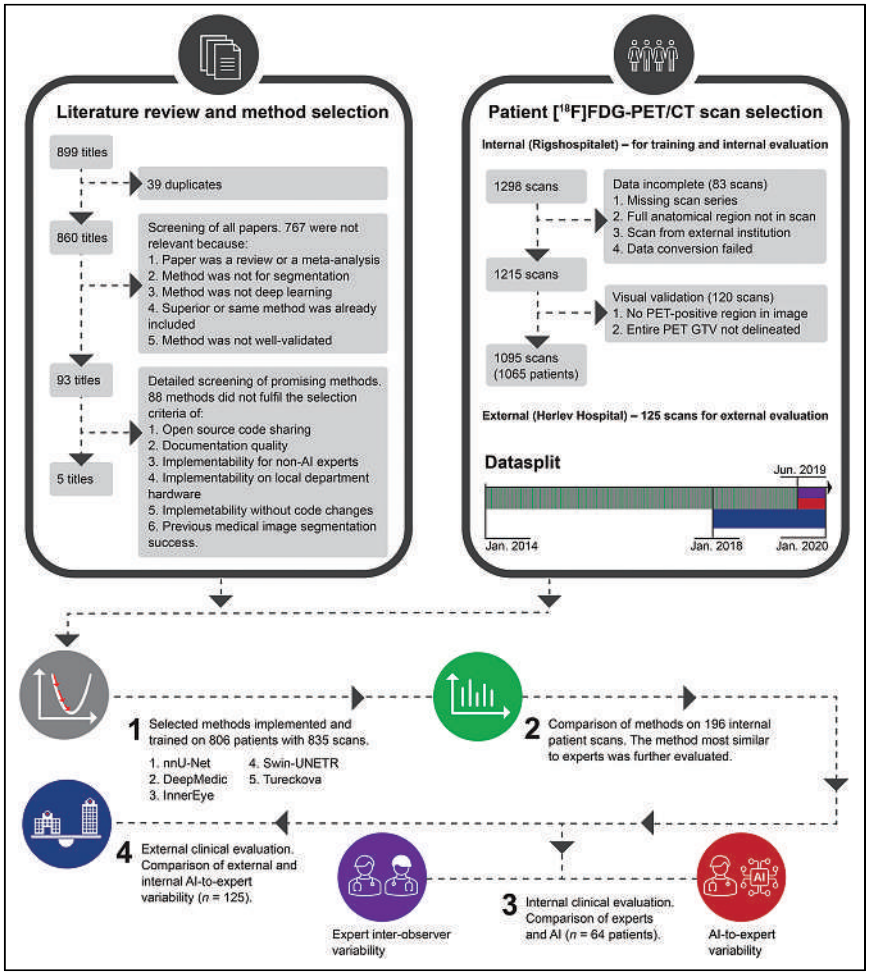

FIGURE 1. Summary of study. Causes of exclusion were data incompleteness and failure to pass visual validation. No external scans were excluded to these criteria. Model training used 805 patients (835 scans). Each scan represented unique patient in steps 2, 3, and 4.

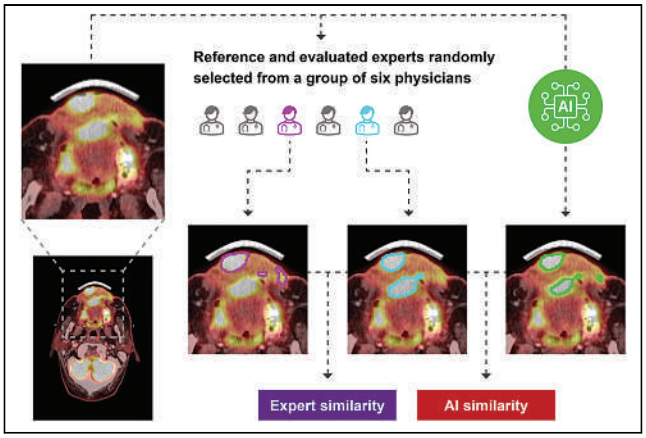

FIGURE 2. Study design comparing expert IOV and AI-to-expert variability. Delineations are exemplified on random patient's axial ^{18}F-FDG PET/CT intravenous contrast scan slice.

The sample sizes were based on power calculations in R using a power of 0.8, a significance level of 0.05, and an expected SD of 0.14, based on measurements published by Gudi et al. (*14*). In the ANOVA, we aimed to show a DSC difference of at least 0.025. The *t* test power calculations used a 2-sided alternative hypothesis. We aimed to show a DSC difference of at least 0.05. The intended sample sizes were 196 to compare methods' AI-to-expert variability using 1-way ANOVA, 64 to compare AI-to-expert variability and expert IOV using a paired *t* test, and 125 to compare internal to external AI-to-expert variability using an unpaired *t* test (the latter comparing 2 different patient groups). A significance level of 0.05 was used in all statistical evaluations. Post hoc Bland–Altman analysis was used to evaluate biomarker agreement.

The tumor volumes were modeled as a sphere, of which we calculated the radius to achieve interpretable yet normally distributed differences. We selected and described cases in which AI or experts failed.

RESULTS

Patient Characteristics

We found 1,298 ^{18}F-FDG PET/CT scans for radiotherapy planning from servers at Rigshospitalet (the internal institution). Of these, 83 were excluded because of incomplete data, and 120 failed to pass visual validation (Fig. 1). This left 1,095 scans from 1,065 patients. All 125 scans from the external institution (Herlev Hospital) were included, leading to a total of 1,190 patients studied (mean age ± SD, 63 ± 10 y; 858 men; Table 1).

We allocated 4 patient cohorts for this study: 1 cohort for training/validation (n = 835) trained with 5-fold cross-validation and 3 cohorts for testing (Table 2). Test 1 (n = 196) was used for model evaluation and selection of the optimal model. The model achieving the highest performance was used in subsequent tests. Test 2 (n = 64) was used to compare this model with human experts. All subjects in the test 2 cohort were scanned at a later date than the training and test 1 cohort (Table 2) to ensure no model selection bias based on subjects. Finally, in test 3 (n = 125), an external evaluation was performed with externally acquired data.

Description of Included Methods

Of 860 unique results, 767 were excluded because of lack of direct relevance to this study (metaanalyses, task not segmentation, method not deep learning, superior method included, or method not well validated). Of the remaining 93 titles, 88 were excluded because of lack of open-source, documentation, and implementability (further details and search key words in Supplemental Appendix A and Fig. 1).

TABLE 1
Summary of Patient Demographics and Key Clinical Characteristics in Each Dataset

Characteristic	Training and validation	Method comparison	Internal clinical evaluation	External clinical evaluation
Number of patients	805	196	64	125
Age (y)	62.6 ± 10.5	62.8 ± 9.3	65.6 ± 10.0	64.2 ± 8.6
Weight (kg)	75.0 ± 18.1	76.3 ± 18.7	71.8 ± 16.9	74.8 ± 18.6
Dose (MBq)	300.4 ± 72.1	306.8 ± 72.9	283.1 ± 67.6	289.1 ± 61.5
Injection-to-scan time (h)	1.1 ± 2	1.1 ± 3	1.1 ± 1	1.1 ± 1
Sex	584 (73%) men	141 (72%) men	42 (66%) men	90 (72%) men
Oropharynx	301/805 (37%)	78/196 (40%)	23/64 (40%)	76/125 (61%)
Larynx	123/805 (15%)	30/196 (15%)	9/64 (15%)	7/125 (6%)
Cavum oris	87/805 (11%)	22/196 (11%)	7/64 (11%)	8/125 (6%)
Hypopharynx	84/805 (10%)	21/196 (11%)	5/64 (8%)	22/125 (18%)
Rhinopharynx	50/805 (6%)	12/196 (6%)	6/64 (9%)	5/125 (4%)
Vestibulum nasi or sinus paranasalis	33/805 (4%)	6/196 (3%)	3/64 (2%)	1/125 (1%)
Unknown primary with lymph nodes	18/805 (2%)	3/196 (2%)	0/64 (0%)	6/125 (5%)
Salivary gland tumor	10/805 (1%)	0/196 (0%)	0/64 (0%)	0/125 (0%)
Unspecified	99/805 (12%)	24/196 (12%)	12/64 (19%)	0/125 (0%)

Qualitative data are number and percentage; continuous data are mean and SD (total n = 1,190). There was no difference in age between men and women in any of 4 datasets (all $P > 0.05$). Mean age was higher in internal clinical evaluation test set than in training data ($P = 0.01$). At same time, there was no evidence of age differences from training data in 2 other test sets ($P = 0.74$ for method comparison test set and $P = 0.10$ for external test set).

TABLE 2
Summary of Datasets for Model Training, Validation, and Independent Testing

Set	Start	End	Source	*n*	Purpose
Training by cross-validation					
Training folds (80%)	2014 January	2019 June	Internal	668	Train model
Validation fold (20%)	2014 January	2019 June	Internal	167	Validate model
Test					
1	2014 January	2019 June	Internal	196	Compare models performance
2	2019 July	2019 December	Internal	64	Compare models with experts' IOV
3	2018 January	2019 December	External	125	Compare internal with external model performance

All methods were trained with a 2-channel PET and CT input against PET GTV as the output.

Five methods met our inclusion criteria (Fig. 1): nnU-Net, DeepMedic, InnerEye, Swin-UNETR, and Tureckova. nnU-Net (version 1) (*16*) is based on the U-Net (*17*), characterized by a U-shaped architecture consisting of convolutional and pooling layers mirrored to form the output. nnU-Net is designed to deal with dataset diversity by fully standardizing and automating the pre- and postprocessing design decisions based on training data features. DeepMedic (*18*) uses a dual pathway of convolutional layers that simultaneously process the image at normal and low resolution to incorporate local and contextual information. Subsequently, it uses a 3-dimensional fully connected conditional random field model to remove false positives. InnerEye (*19*) features a HeadAndNeckBase class used in a previous publication about HNC tumor segmentation. This was used in our implementation. The method uses a 3-dimensional U-Net with strided convolutions instead of max-pooling operations, nonlinear activation of upsampled tensors, residual connections, and dilated convolution kernels in the encoder to preserve more contextual information. Swin-UNETR (*20*) attempts to solve the challenge of modeling long-range information using shifting window transformers that compute self-attention in an efficient shifted window partitioning scheme. It utilizes the U-shaped architecture with a shifting window transformer as the encoder and connects it to a convolutional neural network–based decoder at different resolutions via skip connections. Finally, Tureckova (*21*) is an extension to nnU-Net featuring a V-Net architecture with attention gates designed to help the network focus on a desired scan area by learning to focus on a subset of target structures.

Comparison of AI Methods

nnU-Net achieved the highest mean DSC (Fig. 3A, clinical example in Fig. 4). The DSCs of DeepMedic, InnerEye, and Swin-UNETR were lower (all $P \leq 0.05$, exact values in Fig. 3), whereas we found no evidence of a difference from Tureckova ($P = 0.19$). Complete delineation disagreement (DSC, 0) between clinical and AI-based delineations occurred in 4 of 196 patients (2%) for DeepMedic; 6 of 196 patients (3%) for nnU-Net, Swin-UNETR, and Tureckova; and 35 of 196 patients (18%) for InnerEye. nnU-Net achieved a higher F1 score than Tureckova. Hence, nnU-Net, hereafter referred to as AI in this Results section, was further evaluated.

Internal Clinical Evaluation

The internal clinical evaluation showed no evidence of differences between AI-to-expert variability (DSC, 0.78) and expert IOV (DSC, 0.82, a mean difference of 0.04 [95% CI, −0.01 to 0.09]; $P = 0.12$; Fig. 3B). In 1 patient, AI included no volume, whereas the experts did. The reference expert included no volume in 2 cases, whereas the other expert and AI did.

AI and expert PET GTV–based biomarker agreement was acceptable (Figs. 5A and 5B). The 3 scans with no PET GTV detected

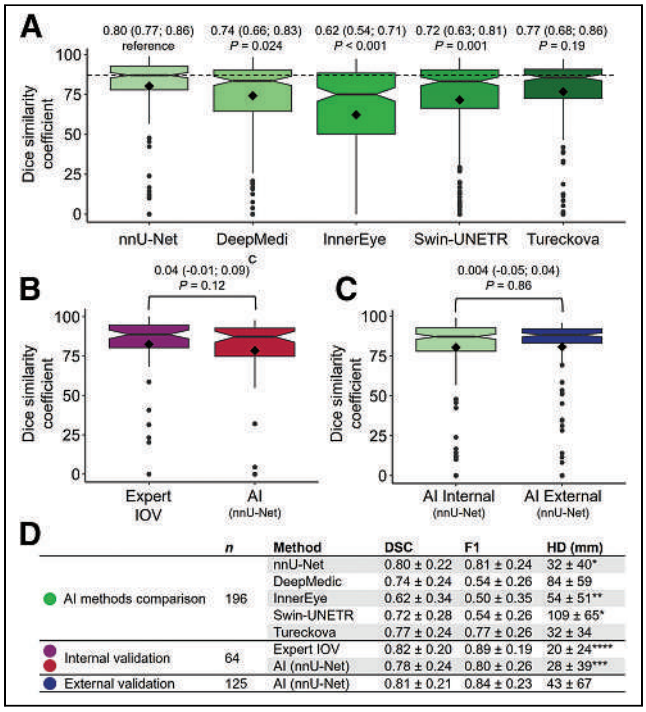

	n	Method	DSC	F1	HD (mm)
AI methods comparison	196	nnU-Net	0.80 ± 0.22	0.81 ± 0.24	32 ± 40*
		DeepMedic	0.74 ± 0.24	0.54 ± 0.26	84 ± 59
		InnerEye	0.62 ± 0.34	0.50 ± 0.35	54 ± 51**
		Swin-UNETR	0.72 ± 0.28	0.54 ± 0.26	109 ± 65*
		Tureckova	0.77 ± 0.24	0.77 ± 0.26	32 ± 34
Internal validation	64	Expert IOV	0.82 ± 0.20	0.89 ± 0.19	20 ± 24****
		AI (nnU-Net)	0.78 ± 0.24	0.80 ± 0.26	28 ± 39***
External validation	125	AI (nnU-Net)	0.81 ± 0.21	0.84 ± 0.23	43 ± 67

FIGURE 3. (A) Comparison of 5 implemented methods trained on 196 patient scans based on DSC. Values above boxes are mean followed by 95% CI in parentheses, with *P* values below. nnU-Net achieved highest DSC and was further analyzed (denoted AI). (B) Paired comparison of AI-to-expert variability and expert IOV on 64 independent internal test scans. (C) Comparison of AI-to-expert variability on 196 internal (same as nnU-Net in A) and 125 external patients. All 3 comparisons used expert-delineated tumor volumes as reference. Values above boxes in B and C are mean difference followed by 95% CI in parentheses, with *P* values below. Rhombus shape indicates mean value, and central line represents median. Boxes enclose interquartile range. Whiskers extend to most significant measurement no further than 1.5 × interquartile range from hinge. Data beyond whiskers are plotted individually. Notch roughly represents 95% CI around median. (D) DSC, F1 score (F1), and Hausdorff distance (HD) summary statistics in mean ± SD. Hausdorff distance is undefined when expert or AI includes no volume. Hence, numbers marked with *, **, ***, and **** were based on $n = 195$, 186, 61, and 63, respectively.

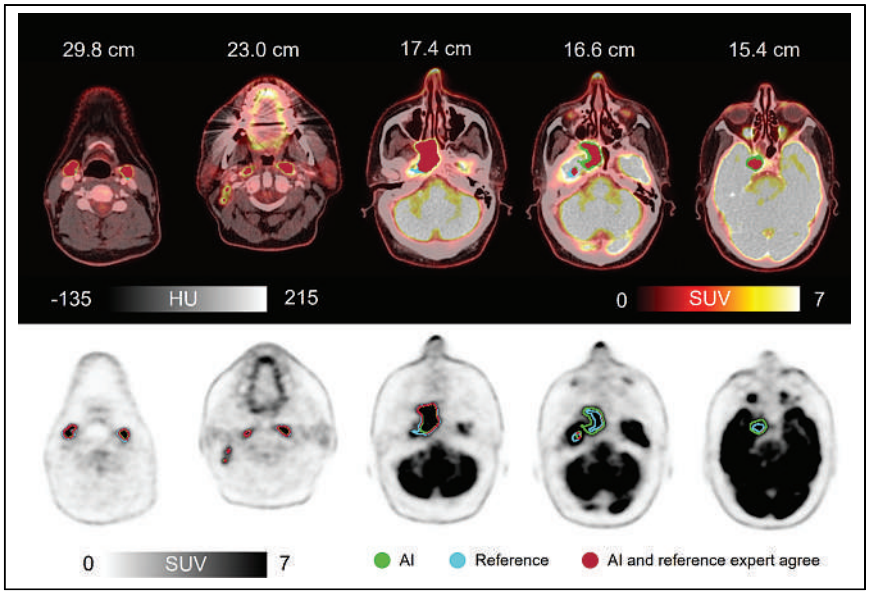

FIGURE 4. Clinical scan delineated by expert (reference) and by AI, along with AI-to-expert agreement (DSC, 0.92). Shown are axial images of 50-y-old man with HNC of rhinopharynx. ^{18}F-FDG PET/CT with intravenous contrast agent showed greatly increased activity corresponding to large tumor process in right rhinopharynx, crossing midline and growing frontally into cavum nasi on right, intracranially on right, medially in fossa media, and along dura laterally. In addition, multiple lymph nodes in neck had greatly increased activity bilaterally. AI correctly avoided including physiologically active areas such as saliva, metal artifact–induced activity, nose tip, brain, and optic nerve. HU = Hounsfield units.

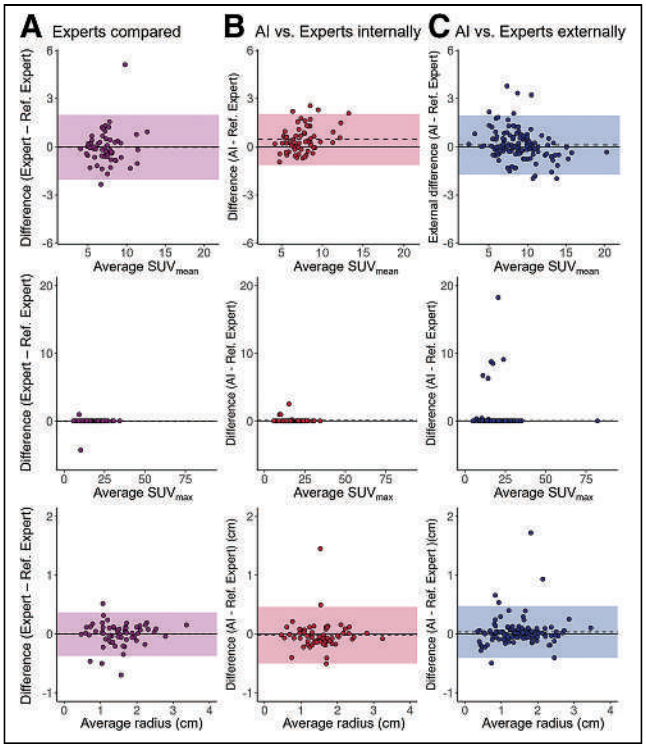

FIGURE 5. Tumor-volume–derived biomarkers based on AI delineation in good agreement with experts. Shown are Bland–Altman plots for agreement between AI and expert PET GTV–derived biomarkers. Shaded regions and dashed lines represent LoA and mean bias, respectively. Limits of agreement for SUV_{max} were not included because of violation of normality assumption. To improve visualization, single outlier with extreme SUV_{max} of 151 in B was excluded from plot.

were excluded, leaving 61 patients for analysis. For SUV_{mean}, AI showed narrower limits of agreement (LoAs) than experts compared (lower to upper, −1.1 to 2.1 for AI and −2.1 to 2.0 for experts). We found no evidence of bias between experts (P = 0.83), whereas AI overestimated values by 0.5 (95% CI, 0.2–0.7) ($P \leq 0.001$). Tumor radius LoAs of AI were broader than experts' (lower to upper, −0.5 to 0.5 cm for AI and −0.4 to 0.4 cm for experts), and we observed no evidence of biases (0.004 cm [95% CI, −0.05 to 0.05 cm; P = 0.88] for the experts and 0.02 cm [95% CI, −0.08 to 0.04 cm; P = 0.51] for AI). SUV_{max} was not analyzed statistically because of violation of the normality assumption; however, AI and experts found the same value in all except 3 patients (Supplemental Fig. 2), whereas experts found the same value in all but 2 patients.

External Clinical Evaluation

The external clinical evaluation showed no evidence of a difference between internal and external AI-to-expert variability (mean DSC difference of 0.004 [95% CI, −0.05 to 0.04; P = 0.86], Fig. 3C). Both the expert and AI identified PET GTV in all patients.

External biomarker agreement between AI and experts was acceptable (Fig. 5C). For SUV_{mean}, the LoA was narrower externally than that of internal experts (lower to upper, −1.7 to 2.0 externally and −2.1 to 2.0 internally), whereas no bias was detected (0.1 [95% CI, −0.1 to 0.3]; P = 0.18). For the tumor volume radius, Lower and upper LoAs for the PET GTV were −0.4 to 0.5 cm externally and −0.5 to 0.5 cm internally, and there was no evidence of bias (0.03 cm [95% CI, −0.007 to 0.07 cm]; P = 0.10). Because of violation of the normality assumption, SUV_{max} was not analyzed statistically; however, experts and AI found the same value in 116 of 125 patients.

Failure Analysis

We identified 11 patients for whom either AI or experts failed (Supplemental Fig. 1). The main causes of delineation failure for AI and experts were postsurgical inflammation (4 patients) and lymph node inclusion disagreements (4 patients). In addition, rare situations not represented in the training scans could have led AI to fail (2 patients): one in which physicians included a tonsil with borderline activity and one in which the patient was lying in a nonstandard position in the scanner. Finally, for a single patient, the reference physician incorrectly included a region in the patient's orbita. Six of the 11 test scans were postsurgical (55%). The test set featured 10 of 64 postsurgical patients (16%). In postsurgical patients, expert DSC dropped from 0.82 to 0.58. AI DSC dropped from 0.78 to 0.46. Excluding postsurgical patients and repeating the paired t test to compare AI-to-expert variability and expert IOV, the lack of a significant difference between the AI-to-expert variability and expert IOV remained (DSC, 0.87 for AI-to-expert vs. 0.84 for expert IOV, a difference of 0.03 [95% CI, −0.02 to 0.07]; P = 0.24).

DISCUSSION

This study was conducted to identify and evaluate state-of-the-art deep learning for delineating PET GTV in HNC and for PET GTV–derived biomarker extraction. We demonstrated that deep learning could delineate volumes similar to clinical quality (AI-to-expert DSC, 0.78, and IOV of 6 experts' DSC, 0.82; $P = 0.12$) and that resulting PET GTV–derived biomarkers were reliable (tumor volume radius upper and lower limits of agreement, −0.5 to 0.5 cm for AI and −0.4 to 0.4 cm for experts). We suspect most clinics will find these limits of agreement acceptable for clinical use. Further, our results warrant further investigation into how deep learning could reduce clinical tumor delineation variability.

During our survey of deep learning methods, we encountered 93 promising titles. Of these, 88 lacked shared code, proper documentation, or accessible implementability. nnU-net achieved the highest level of similarity to our experts. This method has had a significant impact in recent years, winning challenges such as the Brain Tumor Image Segmentation Benchmark and the Medical Segmentation Decathlon (*11*,*22*). Notably, since 2022, the leading method of the latter challenge has been the Swin-UNETR method, which we expected would be superior to nnU-Net. However, this was not the case. This difference may imply that nnU-Net is the more robust method when pretraining data are unavailable; however, the results may be specific to our setting. Compared with other models, nnU-Net has the benefit of flexibility enabled by integrated self-configuring pre- and postprocessing, enabling reliable results for various tasks. Conversely, the main weakness of nnU-Net is its computational demand. Like other deep learning models, nnU-Net lacks inherent interpretability and depends on high data quality. Although the Head and Neck Tumor Segmentation Challenge (HECKTOR) is not directly comparable because of segmentation task differences, it resembles our work. Here, the nnU-Net achieved a similarity in our study as observed in the latest results of HECKTOR (DSC, 0.8). Finally, although we have not explicitly tested model performance using CT or PET alone, it has previously been shown that a multimodal PET/CT input is superior to either modality used alone (*23*).

If a method has limited precision, even a perfect new method will not agree with it (*24*). Hence, the AI-to-expert similarity can exceed the expert IOV only by random effect, making IOV measurements important to understand the level of similarity to experts that AI can theoretically achieve. Although some authors provide IOV and find similar results to this work (*25*), such data are often unavailable. With a DSC of 0.82, our experts achieved a higher similarity than other groups (DSC, 0.61–0.69) (*14*,*26*). Notably, we used the delineation of a random expert as the reference for each patient, which we consider a considerable strength because the resulting variability represents what patients are exposed to in practice (for instance, consensus delineations are not used in clinical practice).

We do not know of others evaluating deep learning–based biomarker extraction from PET/CT scans of HNC. However, there is evidence that PET/CT biomarkers can be extracted for ^{68}Ga-PSMA PET/CT scans of prostate cancer (total lesion volume and uptake) and ^{18}F-FDG PET/CT scans of lymphoma (total metabolic tumor volume) (*27*,*28*). These results support the indication of this work that AI can safely be used for PET/CT biomarker extraction.

Our failure analysis showed that expert IOV and AI-to-expert variability increased in postsurgical scans. In addition, AI tended to include more lymph nodes than physicians did. Concerning postsurgical patient scans, our observation is consistent with the literature (*29*). Furthermore, the observation matches our clinical experience: scans taken after surgery complicate the classification of ^{18}F-FDG–avid regions. Concerning lymph nodes, the clinical decision of inclusion relies on the optimal balance between including too much or too little tissue. Hence, the final delineation result depends on a clinical risk assessment of contextual information. Considering this information in a deep learning model requires methodologic developments before being tested in a clinical context.

Our study had limitations. We confined the inclusion of methods to those reproducible in our context, which could lead to the exclusion of leading methods. For example, the 2022 HECKTOR winner did not meet our method selection criteria (*30*). Furthermore, because of masking, the internal experts did not have access to routine contextual information, a necessary precaution to avoid the potential bias from seeing tumor-volume delineations of other experts. Finally, although several scanners were represented, scans were performed mostly on the same model (Siemens Biograph 64), which could limit generalization.

Our findings indicate that AI-based PET GTV delineations are on a par with human delineations, bearing significant implications for clinical practice. First, it could reduce delineation time for nuclear medicine physicians, radiologists, and radiation oncologists. Second, AI's consistency could reduce physician IOV. Consequently, this points to potential improvements in the speed and consistency of treatment planning and increased biomarker stability.

CONCLUSION

Deep learning can be used for automated PET GTV–derived biomarker extraction and large imaging biomarker studies. Furthermore, deep learning can delineate PET GTVs similar to clinical volumes, holding potential for radiotherapy planning.

DISCLOSURE

David Kovacs received research funding from Brødrene Hartmanns Fond. Barbara Fischer received research funding from Aage and Johanne Louis-Hansen Fonden and has received support from Siemens Healthineers to attend meetings. No other potential conflict of interest relevant to this article was reported.

KEY POINTS

QUESTION: Can AI deep learning automate ^{18}F-FDG PET/CT HNC tumor volume delineation and image biomarker extraction?

PERTINENT FINDINGS: We retrospectively developed 5 deep learning models using 5-fold cross-validation and compared them using the DSC as the primary outcome. The AI-to-expert similarity (DSC, 0.78) was not significantly different from expert-to-expert similarity (DSC, 0.82), and when evaluated in Bland–Altman analysis, the AI imaging biomarker limits of agreement were in the same range as the uncertainty between experts.

IMPLICATIONS FOR PATIENT CARE: Deep learning can automate ^{18}F-FDG PET/CT biomarker extraction in HNC. It can potentially assist tumor delineation in radiotherapy planning.

REFERENCES

1. Fahim-Ul-Hassan, Cook GJ. PET/CT in oncology. *Clin Med (Lond).* 2012;12:368–372.

2. Hillner BE, Siegel BA, Liu D, et al. Impact of positron emission tomography/computed tomography and positron emission tomography (PET) alone on expected management of patients with cancer: initial results from the National Oncologic PET Registry. *J Clin Oncol.* 2008;26:2155–2161.
3. Bussink J, van Herpen CM, Kaanders JH, Oyen WJ. PET-CT for response assessment and treatment adaptation in head and neck cancer. *Lancet Oncol.* 2010;11:661–669.
4. Pike LC, Thomas CM, Guerrero-Urbano T, et al. Guidance on the use of PET for treatment planning in radiotherapy clinical trials. *Br J Radiol.* 2019;92:20190180.
5. Bray F, Ferlay J, Soerjomataram I, Siegel RL, Torre LA, Jemal A. Global cancer statistics 2018: GLOBOCAN estimates of incidence and mortality worldwide for 36 cancers in 185 countries. *CA Cancer J Clin.* 2018;68:394–424.
6. Chow LQM. Head and neck cancer. *N Engl J Med.* 2020;382:60–72.
7. Fonti R, Conson M, Del Vecchio S. PET/CT in radiation oncology. *Semin Oncol.* 2019;46:202–209.
8. Litjens G, Kooi T, Bejnordi BE, et al. A survey on deep learning in medical image analysis. *Med Image Anal.* 2017;42:60–88.
9. Kleppe A, Skrede OJ, De Raedt S, Liestøl K, Kerr DJ, Danielsen HE. Designing deep learning studies in cancer diagnostics. *Nat Rev Cancer.* 2021;21:199–211.
10. Hosny A, Bitterman DS, Guthier CV, et al. Clinical validation of deep learning algorithms for radiotherapy targeting of non-small-cell lung cancer: an observational study. *Lancet Digit Health.* 2022;4:e657–e666.
11. Antonelli M, Reinke A, Bakas S, et al. The medical segmentation decathlon. *Nat Commun.* 2022;13:4128.
12. Mongan J, Moy L, Kahn CE Jr. Checklist for artificial intelligence in medical imaging (CLAIM): a guide for authors and reviewers. *Radiol Artif Intell.* 2020;2:e200029.
13. Mayo CS, Moran JM, Bosch W, et al. American Association of Physicists in Medicine Task Group 263: standardizing nomenclatures in radiation oncology. *Int J Radiat Oncol Biol Phys.* 2018;100:1057–1066.
14. Gudi S, Ghosh-Laskar S, Agarwal JP, et al. Interobserver variability in the delineation of gross tumour volume and specified organs-at-risk during IMRT for head and neck cancers and the impact of FDG-PET/CT on such variability at the primary site. *J Med Imaging Radiat Sci.* 2017;48:184–192.
15. Li X, Morgan PS, Ashburner J, Smith J, Rorden C. The first step for neuroimaging data analysis: DICOM to NIfTI conversion. *J Neurosci Methods.* 2016;264:47–56.
16. Isensee F, Jaeger PF, Kohl SAA, Petersen J, Maier-Hein KH. nnU-Net: a self-configuring method for deep learning-based biomedical image segmentation. *Nat Methods.* 2021;18:203–211.
17. Ronneberger O, Fischer P, Brox T. U-Net: convolutional networks for biomedical image segmentation. *MICCAI.* 2015;9351:234–241.
18. Kamnitsas K, Ledig C, Newcombe VFJ. Efficient multi-scale 3D CNN with fully connected CRF for accurate brain lesion segmentation. *Med Image Anal.* 2017;36:61–78.
19. Oktay O, Nanavati J, Schwaighofer A. Evaluation of deep learning to augment image-guided radiotherapy for head and neck and prostate cancers. *JAMA Netw Open.* 2020;3:e2027426.
20. Hatamizadeh A, Nath V, Tang Y, Yang D, Roth H, Xu D. Swin UNETR: Swin transformers for semantic segmentation of brain tumors in MRI images. arXiv website. https://doi.org/10.48550/arXiv.2201.01266. Published January 4, 2022. Accessed February 7, 2024.
21. Turečková A, Tureček T, Komínková Oplatková Z, Rodríguez-Sánchez A. Improving CT image tumor segmentation through deep supervision and attentional gates. *Front Robot AI.* 2020;7:106.
22. Menze BH, Jakab A, Bauer S, et al. The multimodal brain tumor image segmentation benchmark (BRATS). *IEEE Trans Med Imaging.* 2015;34:1993–2024.
23. Groendahl AR, Skjei Knudtsen I, Huynh BN, et al. A comparison of methods for fully automatic segmentation of tumors and involved nodes in PET/CT of head and neck cancers. *Phys Med Biol.* 2021;66:065012.
24. Bland JM, Altman DG. Statistical methods for assessing agreement between two methods of clinical measurement. *Lancet.* 1986;1:307–310.
25. Heller N, Isensee F, Maier-Hein KH, et al. The state of the art in kidney and kidney tumor segmentation in contrast-enhanced CT imaging: results of the KiTS19 challenge. *Med Image Anal.* 2021;67:101821.
26. Oreiller V, Andrearczyk V, Jreige M, et al. Head and neck tumor segmentation in PET/CT: the HECKTOR challenge. *Med Image Anal.* 2022;77:102336.
27. Kendrick J, Francis RJ, Hassan GM, Rowshanfarzad P, Ong JSL, Ebert MA. Fully automatic prognostic biomarker extraction from metastatic prostate lesion segmentations in whole-body [^{68}Ga]Ga-PSMA-11 PET/CT images. *Eur J Nucl Med Mol Imaging.* 2022;50:67–79.
28. Veziroglu EM, Farhadi F, Hasani N. Role of artificial intelligence in PET/CT imaging for management of lymphoma. *Semin Nucl Med.* 2023;53:426–448.
29. Evans M, Beasley M. Target delineation for postoperative treatment of head and neck cancer. *Oral Oncol.* 2018;86:288–295.
30. Myronenko A, Siddiquee MMR, Yang D, He Y, Xu D. Automated head and neck tumor segmentation from 3D PET/CT. arXiv website. https://doi.org/10.48550/arXiv.2209.10809. Published September 22, 2022. Accessed February 7, 2024.

PET/CT-Based Radiogenomics Supports KEAP1/NFE2L2 Pathway Targeting for Non–Small Cell Lung Cancer Treated with Curative Radiotherapy

Vincent Bourbonne[1,2], Moncef Morjani[1], Olivier Pradier[1,2], Mathieu Hatt[2], Vincent Jaouen[2,3], Solène Querellou[4,5], Dimitris Visvikis[2], François Lucia[1,2], and Ulrike Schick[1,2]

[1]*Department of Radiation Oncology, University Hospital, Brest, France;* [2]*LaTIM UMR 1101 INSERM, University Brest, Brest, France;* [3]*Institut Mines-Télécom Atlantique, Brest, France;* [4]*Nuclear Medicine Department, University Hospital, Brest, France; and* [5]*Groupe d'Étude de la Thrombose Occidentale GETBO (INSERM UMR 1304), Université de Bretagne Occidentale, Brest, France*

In lung cancer patients, radiotherapy is associated with a increased risk of local relapse (LR) when compared with surgery but with a preferable toxicity profile. The KEAP1/NFE2L2 mutational status ($Mut_{KEAP1/NFE2L2}$) is significantly correlated with LR in patients treated with radiotherapy but is rarely available. Prediction of $Mut_{KEAP1/NFE2L2}$ with noninvasive modalities could help to further personalize each therapeutic strategy. **Methods:** Based on a public cohort of 770 patients, model RNA (M-RNA) was first developed using continuous gene expression levels to predict $Mut_{KEAP1/NFE2L2}$, resulting in a binary output. The model PET/CT (M-PET/CT) was then built to predict M-RNA binary output using PET/CT-extracted radiomics features. M-PET/CT was validated on an external cohort of 151 patients treated with curative volumetric modulated arc radiotherapy. Each model was built, internally validated, and evaluated on a separate cohort using a multilayer perceptron network approach. **Results:** The M-RNA resulted in a C statistic of 0.82 in the testing cohort. With a training cohort of 101 patients, the retained M-PET/CT resulted in an area under the curve of 0.90 ($P < 0.001$). With a probability threshold of 20% applied to the testing cohort, M-PET/CT achieved a C statistic of 0.7. The same radiomics model was validated on the volumetric modulated arc radiotherapy cohort as patients were significantly stratified on the basis of their risk of LR with a hazard ratio of 2.61 ($P = 0.02$). **Conclusion:** Our approach enables the prediction of $Mut_{KEAP1/NFE2L2}$ using PET/CT-extracted radiomics features and efficiently classifies patients at risk of LR in an external cohort treated with radiotherapy.

Key Words: radiation sensitivity; KEAP1/NFE2L2; PET; lung cancer; radiomics

J Nucl Med 2024; 65:630–634
DOI: 10.2967/jnumed.123.266749

Radiotherapy is a major treatment option for localized lung cancer (*1*). Depending on the clinical setting, radiotherapy can be delivered alone or in combination with systemic treatments such as chemotherapy, immunotherapy, or other drugs (*1*). Fractionation and dose prescription are tailored for each patient depending on the histology and the tumor stage. For patients with locally advanced non–small cell lung cancer (NSCLC) who cannot undergo surgery, chemoradiotherapy followed by durvalumab is the preferred option (*2*,*3*). For patients with stage I NSCLC, stereotactic radiotherapy challenges surgery as the upfront treatment (*4*–*6*). Radiotherapy requires an extensive staging with ^{18}F-FDG PET/CT (*7*). Local relapse (LR) rates slightly differ after the 2 treatment options, with a higher LR rate in patients treated with radiotherapy than in those treated with surgery (*8*). The KEAP1/NFE2L2 pathway regulates the response to radiotherapy with several involvements in the oxidative cascade (*9*–*12*). Patients who harbored a mutation in the KEAP1 or NFE2L2 gene are more likely to present a postradiotherapy LR than patients who are mutation-naïve (*13*,*14*). Establishing the mutational status could thus have a substantial therapeutic impact, with some patients being possibly recommended for surgery rather than radiotherapy when a mutation is found. When surgery is not feasible, dose escalation or radiosensitization through systemic agents could be an option. Results could even be extrapolated to patients treated with immunotherapy or chemotherapy, as KEAP1/NFE2L2 mutations are also associated with response to systemic treatments (*15*,*16*).

KEAP1/NFE2L2 mutations are not part of the usual tested biomarkers for lung cancer. Noninvasive assessment of the KEAP1/NFE2L2 mutational status ($Mut_{KEAP1/NFE2L2}$) could have the same impact as genetic sequencing but with added advantages such as early diagnosis, decreased costs, and eventual longitudinal monitoring for a more accurate follow-up.

Radiomics features are statistical, geometric, or textural metrics designed to provide quantitative measurements of intensity, shape, or heterogeneity of a given volume of interest in medical images and have been a great field of interest for several years. Radiomics are thought to noninvasively apprehend intratumoral heterogeneity and fully characterize a tumor and were previously used for the prediction of biomarkers such as a mutation in the epidermal growth factor (*17*). To our knowledge, it was never used for the prediction of KEAP1/NFE2L2 mutations.

The aim of this study was to develop and externally validate a PET/CT-based radiomics model for the prediction of $Mut_{KEAP1/NFE2L2}$.

MATERIALS AND METHODS

Population

Our goal was to develop a prediction model for $Mut_{KEAP1/NFE2L2}$ using only PET/CT features. Of the 1,374 available patients in the cohorts of The Cancer Genome Atlas–Lung Squamous Cell Carcinoma

Received Sep. 25, 2023; revision accepted Jan. 2, 2024.
For correspondence or reprints, contact Vincent Bourbonne (vincent.bourbonne@chu-brest.fr).
Published online Feb. 15, 2024.

(*18*) (n = 522), The Cancer Genome Atlas–Lung Adenocarcinoma (*19*) (n = 504), Clinical Proteomic Tumor Analysis Consortium–Lung Squamous Cell Carcinoma (*20*) (n = 108), Clinical Proteomic Tumor Analysis Consortium–Lung Adenocarcinoma (*21*) (n = 110), and NSCLC-Radiogenomics (*22*) (n = 130), $Mut_{KEAP1/NFE2L2}$ was known for 770 patients, of which only 41 had an available PET/CT image. Because of the low number of cases, direct prediction of the mutational status using PET/CT features was deemed not feasible and prone to overfitting. Transcriptomics via sequencing of the RNA could give an insight on $Mut_{KEAP1/NFE2L2}$, with 33 genes being upregulated in the case of $Mut_{KEAP1/NFE2L2}$ (*23*) and thus leading to highly activated metabolic pathways such as glutathione metabolism. Genomics (exome sequencing data) and transcriptomics data were thus available for 770 patients (cohort 1), whereas transcriptomics (Illumina HiSeq platform) and PET/CT data were available for 158 patients (cohort 2).

A 3-step approach was proposed. First, using cohort 1, the first model RNA (M-RNA) using continuous gene expression levels was developed to predict $Mut_{KEAP1/NFE2L2}$. Gene expression levels were normalized as reads per kilobase million. The outputs of the M-RNA were continuous-probability M-RNA and binary-outcome M-RNA (M-RNA-B). Second, another model (model PET/CT [M-PET/CT]) using radiomics data was built with a focus on cohort 2 for the prediction of M-RNA-B. The outputs of the M-PET/CT were thus M-PET/CT-C as a continuous probability and M-PET/CT-B as a binary output. Third, in the final step, 2 cohorts were used for clinical validation, testing the impact of M-PET/CT-B on LR-free survival (LRFS). Crude incidence rates were used. Survival analysis was based on a Kaplan–Meier curve using 2 cohorts: the NSCLC-Radiogenomics cohort, with 123 patients being analyzable (available clinical data and PET/CT), and an external cohort of 151 patients (cohort 3; NCT04545658 and NCT03931356) (*24*,*25*) treated with curative volumetric modulated arc radiotherapy.

The institutional review board of the University Hospital of Brest approved this retrospective study, and all subjects received a nonopposition form. The research was performed in accordance with the declaration of Helsinki. The section below (Model Building) shows the dichotomization of the continuous-probability M-RNA outputs to M-RNA-B ones.

Figure 1 provides a flowchart summarizing the different statistical steps, and a second flowchart explaining the patients' selection is presented in Supplemental Figure 1 (supplemental materials are available at http://jnm.snmjournals.org).

As an additional statistical validation, direct prediction of $Mut_{KEAP1/NFE2L2}$ using M-PET/CT-C was also assessed in the 41 patients for whom both mutational status and PET/CT were available.

Model Building

Each model was built, internally validated, and evaluated on a separate cohort using a multilayer perceptron network approach, as previously reported (*24*,*26*). In-depth explanations regarding the model building are available as Supplemental Protocol 1 (*18*–*25*,*27*–*29*). Briefly, transcriptomics or radiomics features were first selected using the Mann–Whitney test. Only statistically different features about the $Mut_{KEAP1/NFE2L2}$ (step 1) or the M-RNA-B (step 2) were retained. Correlation between the retained features was then assessed with the Spearman correlation coefficient, keeping only the most significant feature in the case of a Spearman coefficient greater than 0.7. Selected features were then combined using a decremental neural network approach based on each feature's ranking, with the ranking being set by the importance of the feature in the proposed model. For each model, the least important feature is put apart and the remaining features are provided for the development of the next model. The chosen model was the one maximizing the mean accuracy based on 1,000 replications of bootstrapping.

For the development of the M-RNA, cohort 1 was randomly split into 3 independent sets: training (50%, 381/770), validation (20%, 159/770), and testing (30%, 230/770). For the development of the M-PET/CT, cohort 2 was randomly split into a training set (~60%, n = 151) and a testing set (~40%, n = 57). Each model was associated with a probability cutoff based on the Youden index, thus classifying patients at high or low risk of mutation. For the M-RNA, the probability threshold was defined using the validation cohort, resulting in M-RNA-B. For the M-PET/CT, the probability threshold was determined on the training set, resulting in M-PET/CT-B.

Both models were evaluated on the testing and validation cohorts using receiver-operating characteristics such as the area under the curve (AUC), sensitivity, specificity, interrater agreement statistic (κ), balanced accuracy (BACC), and F1 score. Negative and positive predictive values were calculated. Decision curves were also used for the models' evaluation. The impact of the probability threshold was assessed by changing its value and observing the shifts in sensitivity, specificity, negative predictive values, positive predictive values, and κ for the M-PET/CT. The research was performed in accordance with the Standards for Reporting of Diagnostic Accuracy guidelines.

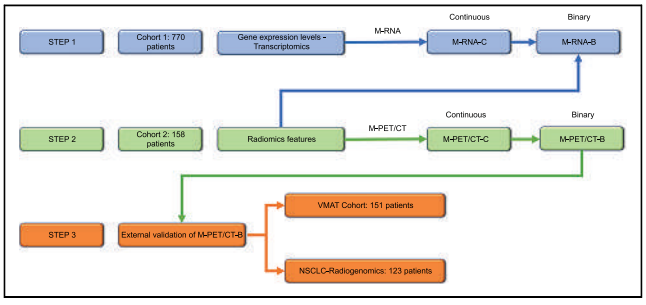

FIGURE 1. Flowchart summarizing different statistical steps. M-RNA-C = continuous-probability M-RNA; VMAT = volumetric modulated arc radiotherapy.

RESULTS

Prediction of $Mut_{KEAP1/NFE2L2}$ Using Transcriptomics Data

A mutation of either KEAP1 or NFE2L2 was found in 175 of 770 patients (22.7%). The best M-RNA reached a mean accuracy of 91.6% in the training cohort (Supplemental Fig. 2). When 9 transcriptomics features were combined (CBR1, G6PD, GCLM, NQO1, PGD, SRXN1, TRIM16, TXNRD1, and UGDH), the M-RNA reached an AUC of 0.99 ($P < 0.001$). The importance of each transcriptomics feature in the M-RNA is shown in Supplemental Table 1.

In the training set and with a 15% probability cutoff, the M-RNA resulted in a BACC of 96.8%, a sensitivity of 96.3%, a specificity of 97.3%, and a κ of 0.90. With the same probability threshold, the BACC was 78.8% and 81.9% in the validation and testing cohorts, respectively.

The receiver-operating-characteristic curves for each cohort are available in Figures 2A and 2C, and the results according to the cohort are detailed in Table 1.

Decision curve analysis showed the efficiency of the M-RNA, especially for higher predicted probabilities mainly in the testing cohort (Supplemental Figs. 3A–3C).

Prediction of M-RNA-B Using Radiomics Features

On the basis of the 101 patients from the training cohort, only 5 features harbored a significant differential distribution between the 2 M-RNA-B groups: 4 features extracted from PET and 1 extracted from CT (Supplemental Table 2). Selected radiomics features harbored a significant correlation with 7 of 9 retained

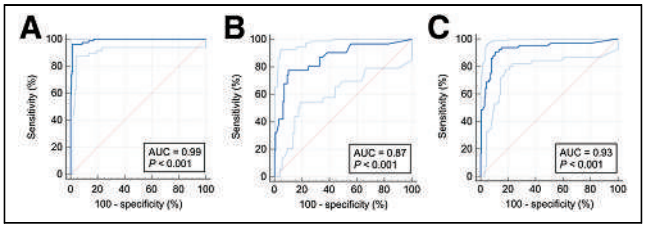

FIGURE 2. Prediction of $MUT_{KEAP1/NFE2L2}$ using continuous-probability M-RNA (receiver-operating-characteristic curve) in training cohort (A), validation cohort (B), and testing cohort (C).

transcriptomics features as shown in Supplemental Table 3. A positive M-RNA-B status was seen for 29.7% and 17.5% ($P = 0.09$) of the training and testing cohorts, respectively (Supplemental Table 4).

In the training cohort, the M-PET/CT combined the 5 previously presented radiomics features, resulting in a mean accuracy of 74.1%. The most important feature was the Wavelet-HLH_glcm_MaximumProbability, with an importance of 82.0%. In the training cohort, M-PET/CT-C achieved an AUC of 0.90 ($P < 0.001$). When the 20% probability threshold maximizing the Youden index was applied, M-PET/CT-B resulted in a BACC of 80.4%, a sensitivity of 83.3%, a specificity of 77.5%, and a κ of 0.55. On the testing cohort, M-PET/CT decreased to an AUC of 0.71 ($P = 0.02$), a κ of 0.34, a BACC of 70.5%, a sensitivity of 60%, and a specificity of 80.9%. In the training and testing cohorts, respectively, M-PET/CT-B resulted in negative predictive values of 91.7% and 90.5% and positive predictive values of 61.0% and 40.0% (Table 2).

The receiver-operating-characteristic curves for each cohort (training and testing cohorts) are available in Figures 3A and 3B, and the mean accuracy for M-PET/CT is presented as Supplemental Figure 4.

In the testing cohort, analysis of the decision curve for M-PET/CT-C showed a positive net clinical benefit for probabilities ranging between 0% and 33% (Supplemental Fig. 5).

Prediction of $Mut_{KEAP1/NFE2L2}$ Using M-PET/CT-C

An exploratory analysis regarding the prediction of $Mut_{KEAP1/NFE2L2}$ using M-PET/CT-C was performed. For the 26 patients included in the training cohort, M-PET/CT-C reached an AUC of 0.71 ($P = 0.06$), whereas the AUC changed to 0.80 for the 15 patients in the testing cohort.

Impact on LRFS

Prediction of LRFS in NSCLC-Operated Patients Using M-PET/CT-B. With a median follow-up of 58.8 mo (95% CI, 43.4–64.6 mo), the LR rate was as low as 4.6% (6 of 123 patients from the NSCLC-Radiogenomics cohort). No significant difference was found according to the M-PET/CT-B as shown in Figure 4A.

Prediction of LRFS in NSCLC Patients Treated with Curative Radiotherapy Using M-PET/CT-B. In a retrospective cohort of 151 patients with a median follow-up of 28.9 mo (95% CI, 21.1–35.1 mo), LR occurred in 15.1% of the patients. M-PET/CT-B significantly stratified patients regarding their risk of LR, with a hazard ratio of 2.61 (95% CI, 1.07–6.40; $P = 0.02$) with a LR rate of 15.1% as shown in Figure 4B.

DISCUSSION

To our knowledge, this study is the first to focus on the prediction of the KEAP1/NFE2L2 mutation. Not being available in the clinical practice because of its cost and novelty, noninvasive prediction could have a significant therapeutic impact given the shorter LRFS in patients harboring such mutations. When 5 PET/CT radiomics features were combined, the M-PET/CT was predictive of LRFS in an external cohort of 151 patients treated with radiotherapy.

The KEAP1/NFE2L2 molecular pathway is of growing interest given recent data, making it a potential biomarker of radioresistance (*14*). Our model could have a substantial impact on the treatment of NSCLC. With a negative predictive value of 90.5%, patients with a M-PET/CT-C of 20% or less could thus continue with their radiotherapy plan, whereas patients with a M-PET/CT-C of more than 20% could be proposed for either tumor RNA or genome sequencing. In the testing cohort alone, this would avoid such genetic tests for 73.7% (42/57) of the testing cohort. In the overall cohort, the M-PET/CT would avoid unnecessary genetic testing for 64.6% of the cohort, with the risk of only 9 false-negative patients (5.7%). The BACC decreased in the testing set, especially with a lower sensitivity. Apart from the performance of the M-PET/CT itself, this can partly be explained by the lower rate of M-RNA-B–positive patients in the testing set.

In the case of a proven mutation affecting the KEAP1/NFE2L2 pathway, management remains unclear to this day. Operable patients could be referred to a thoracic surgeon. However, a significant number of patients are probably not suitable for surgery. For this subset of patients, dose escalation or treatment combination could be proposed. Use of radiosensitization agents such as glutaminase inhibitors could lower the risk of LR (*13*,*14*).

The second major finding in our work is the significant stratification allowed by M-PET/CT-C regarding the LR risk in patients treated with radiotherapy. Patients with a M-PET/CT-C greater than 20% were 2.6 times more likely to present with LR in an

TABLE 1
Prediction of $MUT_{KEAP1/NFE2L2}$ Using Continuous-Probability M-RNA

Probability threshold	Partition	Mean accuracy*	AUC_ RecallCurve	F1 score	AUC	κ	SE	SP	BACC
>15%	Training	91.6%	0.97	0.96	0.99	0.90	96.3%	97.3%	96.8%
	Validation		0.69	0.71	0.87	0.32	64.5%	93.0%	78.8%
	Testing		0.87	0.87	0.93	0.49	70.3%	93.4%	81.9%

*Based on 1,000 bootstrap replications.
SE = sensitivity; SP = specificity.

TABLE 2
Receiver-Operating Characteristics of M-RNA-B Using M-PET/CT-C in Each Cohort

	Training cohort (n = 101 patients)										Testing cohort (n = 57 patients)									
			ROC results				Patients under the threshold		Patients above the threshold				ROC results				Patients under the threshold		Patients above the threshold	
Probability threshold	Mean accuracy*	κ	SE	SP	BACC	F1 score	No M-RNA-B†	M-RNA-B	No M-RNA-B	M-RNA-B‡	κ	SE	SP	BACC	F1 score	No M-RNA-B†	M-RNA-B	No M-RNA-B	M-RNA-B‡
>10%	74.1%	0.28	100%	39.4%	69.7%	0.58	28 (100.0%)	0 (0.0%)	43 (58.9%)	30 (41.1%)	0.11	90.0%	34.0%	62.0%	0.36	16 (94.1%)	1 (5.9%)	31 (77.5%)	9 (22.5%)
>20%		**0.55**	**83.3%**	**77.5%**	**80.4%**	**0.70**	**55 (91.7%)**	**5 (8.3%)**	**16 (39.0%)**	**25 (61.0%)**	**0.34**	**60.0%**	**80.9%**	**70.5%**	**0.48**	**38 (90.5%)**	**4 (9.5%)**	**9 (60.0%)**	**6 (40.0%)**
>30%		0.52	43.3%	100%	71.7%	0.61	71 (80.7%)	17 (19.3%)	0 (0.0%)	13 (100.0%)	0.14	20.0%	91.5%	55.8%	0.30	43 (84.3%)	8 (15.7%)	4 (66.7%)	2 (33.3%)
>40%		0.52	43.3%	100%	71.7%	0.61	71 (80.7%)	17 (19.3%)	0 (0.0%)	13 (100.0%)	0.14	20.0%	91.5%	55.8%	0.30	43 (84.3%)	8 (15.7%)	4 (66.7%)	2 (33.3%)
>50%		0.52	43.3%	100%	71.7%	0.61	71 (80.7%)	17 (19.3%)	0 (0.0%)	13 (100.0%)	0.14	20.0%	91.5%	55.8%	0.30	43 (84.3%)	8 (15.7%)	4 (66.7%)	2 (33.3%)

*Based on 1,000 Bootstrap replications.
†Negative predictive value in parentheses.
‡Positive predictive value in parentheses.
SE = sensitivity; SP = specificity.
Bold data indicate probability thresholds.

FIGURE 3. Prediction of M-RNA-B using M-PET/CT-C (receiver-operating-characteristic curve): M-PET/CT-C in training cohort (A) and in testing cohort (B).

external cohort. These data highlighted the strength of radiogenomics and opened the possibility of imputing our model in LR prediction modeling and possibly not using the M-RNA. As expected, results were not significant in the radiogenomics cohort. Response to treatment is known to be independent from $Mut_{KEAP1/NFE2L2}$ in patients who had surgery (*14*).

Certain limitations could not be overcome. Prediction of the $Mut_{KEAP1/NFE2L2}$ rather than a surrogate would probably limit the complexity of our approach. Nevertheless, the AUC of 0.80 for the prediction of $Mut_{KEAP1/NFE2L2}$ using M-PET/CT-C in the testing cohort demonstrates the potential of our approach. The M-PET/CT was trained and validated in patients among several cohorts. The semiautomatic segmentation ensures robustness and low intervariability. The neuroCombat harmonization method (*28*,*29*) limits the heterogeneity associated with multicentric data without compromising interpatient variability. Although the external validity of such a model is probably enhanced, the testing cohort for M-PET/CT-B cannot be seen as an external validation. Having a real external validation remains necessary, especially given the possible instability of wavelet-based features (*30*). Finally, the pathogenicity of $Mut_{KEAP1/NFE2L2}$ was not evaluable, thus limiting the explainability of M-PET/CT. Maximum probability is a radiomics feature extracted on the gray level cooccurrence matrix. It represents the number of occurrences of the most predominant pair of neighboring intensity values. Although a significant correlation was found between the selected radiomics features including the maximum probability and most transcriptomics features, the positive correlation between the maximum probability and M-PET/CT-B indicates that the probability of mutation is associated with the ^{18}F-FDG heterogeneity uptake. Despite these limitations, M-PET/CT-B significantly stratified patients treated with radiotherapy in an external cohort.

FIGURE 4. Prediction of LRFS in NSCLC-Radiogenomics (A) and volumetric modulated arc radiotherapy (B) cohorts using M-PET/CT-B.

CONCLUSION

Using a hybrid approach, a model combining PET/CT-extracted radiomics features was able to predict the $Mut_{KEAP1/NFE2L2}$ as well as the risk of LR after radiotherapy. This model appears to be generalizable without any added costs or sequencing delays and could be used in the selection of patients for genetic testing and LR prediction modeling. It could thus have a significant impact in helping clinicians select thoracic radiotherapy or surgery for their patients. External validation of this model is currently under investigation, opening the field to new treatment strategies.

DISCLOSURE

No potential conflict of interest relevant to this article was reported.

KEY POINTS

QUESTION: Can a PET/CT-based radiomics model predict the $Mut_{KEAP1/NFE2L2}$ and thus LRFS after thoracic radiotherapy?

PERTINENT FINDINGS: In this innovative research article, a transcriptomics signature was developed and internally validated using a cohort of 770 NSCLC patients. A radiomics-based M-PET/CT was able to predict the transcriptomics signature. This radiomics signature was validated on an external cohort of 151 patients treated with radiotherapy, in which patients at high risk of relapse as calculated by the radiomics signature were 2.6 times more likely to present with LR.

IMPLICATIONS FOR PATIENT CARE: This model appears to be generalizable without any added costs or sequencing delay and could be used for the selection of patients for genetic testing and LR prediction modeling. This model is accessible for external use and validation on request.

REFERENCES

1. Ettinger DS, Wood DE, Aisner DL, et al. NCCN guidelines insights: non-small cell lung cancer, version 2.2021. *J Natl Compr Canc Netw.* 2021;19:254–266.
2. Antonia SJ, Villegas A, Daniel D, et al. Durvalumab after chemoradiotherapy in stage III non-small-cell lung cancer. *N Engl J Med.* 2017;377:1919–1929.
3. Antonia SJ, Villegas A, Daniel D, et al. Overall survival with durvalumab after chemoradiotherapy in stage III NSCLC. *N Engl J Med.* 2018;379:2342–2350.
4. Chen H, Laba JM, Boldt RG, et al. Stereotactic ablative radiation therapy versus surgery in early lung cancer: a meta-analysis of propensity score studies. *Int J Radiat Oncol Biol Phys.* 2018;101:186–194.
5. Chang JY, Senan S, Paul MA, et al. Stereotactic ablative radiotherapy versus lobectomy for operable stage I non-small-cell lung cancer: a pooled analysis of two randomised trials. *Lancet Oncol.* 2015;16:630–637.
6. Baine MJ, Sleightholm R, Neilsen BK, et al. Stereotactic body radiation therapy versus nonradiotherapeutic ablative procedures (laser/cryoablation and electrocautery) for early-stage non-small cell lung cancer. *J Natl Compr Canc Netw.* 2019; 17:450–458.
7. Darling GE, Allen MS, Decker PA, et al. Randomized trial of mediastinal lymph node sampling versus complete lymphadenectomy during pulmonary resection in the patient with N0 or N1 (less than hilar) non-small cell carcinoma: results of the American College of Surgery Oncology Group Z0030 trial. *J Thorac Cardiovasc Surg.* 2011;141:662–670.
8. White A, Swanson SJ. Surgery versus stereotactic ablative radiotherapy (SABR) for early-stage non-small cell lung cancer: less is not more. *J Thorac Dis.* 2016; 8(suppl 4):S399–S405.
9. Bellezza I, Giambanco I, Minelli A, Donato R. Nrf2-Keap1 signaling in oxidative and reductive stress. *Biochim Biophys Acta Mol Cell Res.* 2018;1865:721–733.
10. Zimta AA, Cenariu D, Irimie A, et al. The role of Nrf2 activity in cancer development and progression. *Cancers (Basel).* 2019;11:1755.
11. Jeong Y, Hoang NT, Lovejoy A, et al. Role of KEAP1/NRF2 and TP53 mutations in lung squamous cell carcinoma development and radiation resistance. *Cancer Discov.* 2017;7:86–101.
12. Sánchez-Ortega M, Carrera AC, Garrido A. Role of NRF2 in lung cancer. *Cells.* 2021;10:1879.
13. Sitthideatphaiboon P, Galan-Cobo A, Negrao MV, et al. *STK11*/LKB1 mutations in NSCLC are associated with KEAP1/NRF2-dependent radiotherapy resistance targetable by glutaminase inhibition. *Clin Cancer Res.* 2021;27:1720–1733.
14. Binkley MS, Jeon YJ, Nesselbush M, et al. KEAP1/NFE2L2 mutations predict lung cancer radiation resistance that can be targeted by glutaminase inhibition. *Cancer Discov.* 2020;10:1826–1841.
15. Zhu H, Xie D, Yu Y, et al. KEAP1/NFE2L2 mutations of liquid biopsy as prognostic biomarkers in patients with advanced non-small cell lung cancer: results from two multicenter, randomized clinical trials. *Front Oncol.* 2021;11:659200.
16. Xu X, Yang Y, Liu X, et al. NFE2L2/KEAP1 mutations correlate with higher tumor mutational burden value/PD-L1 expression and potentiate improved clinical outcome with immunotherapy. *Oncologist.* 2020;25:e955–e963.
17. Dang Y, Wang R, Qian K, Lu J, Zhang H, Zhang Y. Clinical and radiological predictors of epidermal growth factor receptor mutation in nonsmall cell lung cancer. *J Appl Clin Med Phys.* 2021;22:271–280.
18. Kirk S, Lee Y, Kumar P, et al. The Cancer Genome Atlas lung squamous cell carcinoma collection (TCGA-LUSC) (version 4). Cancer Imaging Archive website. https://doi.org/10.7937/K9/TCIA.2016.TYGKKFMQ. Updated May 29, 2020. Accessed January 26, 2024.
19. Albertina B, Watson M, Holback C, et al. The Cancer Genome Atlas lung adenocarcinoma collection (TCGA-LUAD) (version 4). Cancer Imaging Archive website. https://doi.org/10.7937/K9/TCIA.2016.JGNIHEP5. Updated May 29, 2020. Accessed January 26, 2024.
20. National Cancer Institute Clinical Proteomic Tumor Analysis Consortium (CPTAC). The Clinical Proteomic Tumor Analysis Consortium lung squamous cell carcinoma collection (CPTAC-LSCC) (version 13). The Cancer Imaging Archive website. https://doi.org/10.7937/K9/TCIA.2018.6EMUB5L2. Updated February 24, 2023. Accessed January 26, 2024.
21. National Cancer Institute Clinical Proteomic Tumor Analysis Consortium (CPTAC). The Clinical Proteomic Tumor Analysis Consortium lung adenocarcinoma collection (CPTAC-LUAD) (version 11). The Cancer Imaging Archive website. https://doi.org/10.7937/K9/TCIA.2018.PAT12TBS. Updated February 24, 2023. Accessed January 26, 2024.
22. Bakr S, Gevaert O, Echegaray S, et al. A radiogenomic dataset of non-small cell lung cancer. *Sci Data.* 2018;5:180202.
23. Namani A, Zheng Z, Wang XJ, Tang X. Systematic identification of multi omics-based biomarkers in KEAP1 mutated TCGA lung adenocarcinoma. *J Cancer.* 2019;10:6813–6821.
24. Bourbonne V, Lucia F, Jaouen V, et al. Development and prospective validation of a spatial dose pattern based model predicting acute pulmonary toxicity in patients treated with volumetric arc-therapy for locally advanced lung cancer. *Radiother Oncol.* 2021;164:43–49.
25. Bourbonne V, Delafoy A, Lucia F, Quéré G, Pradier O, Schick U. Toxicity after volumetric modulated arc therapy for lung cancer: a monocentric retrospective study. *Transl Lung Cancer Res.* 2021;10:156–166.
26. Bourbonne V, Jaouen V, Nguyen TA, et al. Development of a radiomic-based model predicting lymph node involvement in prostate cancer patients. *Cancers (Basel).* 2021;13:5672.
27. van Griethuysen JJM, Fedorov A, Parmar C, et al. Computational radiomics system to decode the radiographic phenotype. *Cancer Res.* 2017;77:e104–e107.
28. Fortin JP, Parker D, Tunç B, et al. Harmonization of multi-site diffusion tensor imaging data. *Neuroimage.* 2017;161:149–170.
29. Fortin JP, Cullen N, Sheline YI, et al. Harmonization of cortical thickness measurements across scanners and sites. *Neuroimage.* 2018;167:104–120.
30. Welch ML, McIntosh C, Haibe-Kains B, et al. Vulnerabilities of radiomic signature development: the need for safeguards. *Radiother Oncol.* 2019;130:2–9.

Promising Candidate Prognostic Biomarkers in [^{18}F]FDG PET Images: Evaluation in Independent Cohorts of Non–Small Cell Lung Cancer Patients

Narinée Hovhannisyan-Baghdasarian[1], Marie Luporsi[1,2], Nicolas Captier[1], Christophe Nioche[1], Vesna Cuplov[1], Erwin Woff[1,3], Nadia Hegarat[4], Alain Livartowski[4], Nicolas Girard[4,5], Irène Buvat[1], and Fanny Orlhac[1]

[1]LITO U1288, Institut Curie, PSL University, Inserm, Orsay, France; [2]Department of Nuclear Medicine, Institut Curie, Paris, France; [3]Department of Nuclear Medicine, Institut Jules Bordet, Hôpital Universitaire de Bruxelles, Université Libre de Bruxelles, Brussels, Belgium; [4]Institut du Thorax Curie-Montsouris, Institut Curie, Paris, France; and [5]Paris Saclay Cancer Campus, UVSQ, Versailles, France

The normalized distances from the hot spot of radiotracer uptake (SUV_{max}) to the tumor centroid (NHOC) and to the tumor perimeter (NHOP) have recently been suggested as novel PET features reflecting tumor aggressiveness. These biomarkers characterizing the shift of SUV_{max} toward the lesion edge during tumor progression have been shown to be prognostic factors in breast and non–small cell lung cancer (NSCLC) patients. We assessed the impact of imaging parameters on NHOC and NHOP, their complementarity to conventional PET features, and their prognostic value for advanced-NSCLC patients. **Methods:** This retrospective study investigated baseline [^{18}F]FDG PET scans: cohort 1 included 99 NSCLC patients with no treatment-related inclusion criteria (robustness study); cohort 2 included 244 NSCLC patients (survival analysis) treated with targeted therapy (93), immunotherapy (63), or immunochemotherapy (88). Although 98% of patients had metastases, radiomic features including SUVs were extracted from the primary tumor only. NHOCs and NHOPs were computed using 2 approaches: the normalized distance from the localization of SUV_{max} or SUV_{peak} to the tumor centroid or perimeter. Bland–Altman analyses were performed to investigate the impact of both spatial resolution (comparing PET images with and without gaussian postfiltering) and image sampling (comparing 2 voxel sizes) on feature values. The correlation of NHOCs and NHOPs with other features was studied using Spearman correlation coefficients (r). The ability of NHOCs and NHOPs to predict overall survival (OS) was estimated using the Kaplan–Meier method. **Results:** In cohort 1, NHOC and NHOP features were more robust to image filtering and to resampling than were SUVs. The correlations were weak between NHOCs and NHOPs ($r \leq 0.45$) and between NHOCs or NHOPs and any other radiomic features ($r \leq 0.60$). In cohort 2, the patients with short OS demonstrated higher NHOCs and lower NHOPs than those with long OS. NHOCs significantly distinguished 2 survival profiles in patients treated with immunotherapy (log-rank test, $P < 0.01$), whereas NHOPs stratified patients regarding OS in the targeted therapy ($P = 0.02$) and immunotherapy ($P < 0.01$) subcohorts. **Conclusion:** Our findings suggest that even in advanced NSCLC patients, NHOC and NHOP features pertaining to the primary tumor have prognostic potential. Moreover, these features appeared to be robust with respect to imaging protocol parameters and complementary to other radiomic features and are now available in LIFEx software to be independently tested by others.

Key Words: [^{18}F]FDG PET; lung cancer; oncology; immunotherapy; radiomics

J Nucl Med 2024; 65:635–642
DOI: 10.2967/jnumed.123.266331

Among radiomic features derived from PET images, those reflecting the geometric characteristics of the metabolically active part of a tumor might have some prognostic value for survival. For instance, asymmetric and irregular tumor shapes on PET appear to be associated with high-grade neoplasms and thus with poor survival (*1*,*2*). Moreover, geometry-based features have been shown to be robust to imaging protocol parameters (*3*), which is an asset for translation in clinical settings. Recently, the normalized distance between the hot spot of radiotracer uptake (SUV_{max}) and the tumor centroid (NHOC) has been introduced as a novel PET feature by Jiménez-Sánchez et al. (*4*), based on a mathematic model of solid-tumor growth. This model suggested that the maximum metabolic activity of a tumor (reflected by SUV_{max} in a PET image) is expected to increase and to move toward the lesion edge as the tumor grows. Another feature for evaluating the change in intratumor heterogeneity, called normalized SUV_{max} to perimeter distance (nSPD), has been proposed by Jiménez Londoño et al. (*5*), defined as the normalized closest distance between the maximum metabolic activity location (SUV_{max}) and the tumor perimeter (NHOP). Both NHOC and nSPD were proposed as hallmarks of tumor aggressiveness. They were demonstrated to be associated with worse outcome in breast and advanced non–small cell lung cancer (NSCLC) patients, outperforming the conventional PET features such as SUVs (*5*). Originally, the nSPD was defined on the axial slice of the tumor that included the voxel with maximum activity (*5*). In our study, we computed NHOP considering the tumor in 3 dimensions to make it more comparable to NHOC.

The goal of the present study was thus to evaluate the robustness of NHOC and NHOP to image characteristics such as spatial resolution and voxel size, to determine their correlation with conventional PET features, and to evaluate their prognostic value in predicting survival in NSCLC patients.

Received Jul. 19, 2023; revision accepted Jan. 11, 2024.
For correspondence or reprints, contact Narinée Hovhannisyan-Baghdasarian (narinee.hovhannisyan@curie.fr).
Published online Mar. 7, 2024.

MATERIALS AND METHODS

Patient Cohorts

The study was conducted in accordance with the Declaration of Helsinki and approved by the ethical board of Institut Curie, France (approval DATA200130) with a waiver of informed consent through the no-objection rule.

This retrospective study included 2 cohorts of a total of 343 patients with advanced, metastatic NSCLC treated at our institute between 2009 and 2021, who had undergone baseline [^{18}F]FDG PET/CT before treatment initiation. The first cohort was used to analyze the robustness of NHOC and NHOP with respect to imaging parameters, whereas the second cohort was used to assess the performance of the features in predicting overall patient survival. Cohort 1 consisted of 99 patients, with no selection criteria regarding their subsequent treatment. Cohort 2 consisted of 244 patients and included 3 subcohorts of patients treated with either targeted therapy, namely tyrosine kinase inhibitors for epithelial growth factor receptor–mutated patients (93), or immunotherapy, namely pembrolizumab (alone or in combination with chemotherapy, 63 and 88, respectively). The inclusion criteria were as follows: baseline [^{18}F]FDG PET/CT scan available in the PACS, detectability of primary lesion on the PET scan, and at least 1-y follow-up of the patient. For all patients, survival data were retrieved. Patient characteristics such as age, sex, histologic subtype, and stage are summarized in Table 1.

Image Database and Image Processing

The [^{18}F]FDG PET/CT scans were acquired at different centers using 13 scanners from different vendors (Supplemental Table 1; supplemental materials are available at http://jnm.snmjournals.org). The volume of interest (VOI) encompassing the primary tumor was defined on the axial views of the PET scan by an experienced nuclear medicine physicist (8 y of experience) under the supervision of a nuclear medicine physician (10 y of experience). The metabolically active volume of the lesion was delineated automatically using a threshold set to 40% of SUV_{max}. A morphologic closing operation was applied to include internal necrotic areas in the VOI if necessary. To investigate the impact of tumor delineation on NHOC and NHOP and radiomic feature values, 30 scans randomly chosen from cohort 1 were segmented independently by a second observer (with 10 y of experience). All images were resampled to a fixed $4 \times 4 \times 4$ mm voxel size, and the intensity was discretized with a fixed bin width of 0.31 SUV and 192 gray levels between 0 and 60 SUV (*6*). Thirteen features were then extracted from the VOI, including 6 conventional PET features (SUV_{max}, SUV_{peak} [SUV within a 1 cm^3 sphere with maximum average uptake (*7*)], SUV_{mean}, SUV_{min}, metabolic tumor volume [MTV], and total lesion glycolysis), along with a shape feature (sphericity) and 6 textural features (joint entropy log10, inverse difference moment, short run emphasis, long run emphasis, low gray-level zone emphasis, and high gray-level zone emphasis) (definitions available at https://www.lifexsoft.org/index.php/resources/documentation). These indices were previously identified (*8*) as not strongly correlated features and were found to be the most robust with respect to tumor segmentation method. In addition, NHOCs and NHOPs were computed using 2 approaches: the distance from the localization of SUV_{max} or SUV_{peak} to the tumor centroid (and perimeter, respectively) divided by the radius of a hypothetical sphere having the same volume as the tumor, thus yielding dimensionless quantities: maximum NHOC ($NHOC_{max}$), peak NHOC ($NHOC_{peak}$), maximum NHOP ($NHOP_{max}$), and peak NHOP ($NHOP_{peak}$) (Supplemental Fig. 1).

For the robustness study using cohort 1, 2 other sets of PET images were generated to evaluate the effects of spatial resolution and voxel size on image-derived features. The first set was obtained by postfiltering (gaussian, SD [σ] of 2, 3, and 4 mm; corresponding to a full width at half maximum of approximately 5, 7, and 9 mm, respectively) the original images of cohort 1. The second set was obtained by resampling the original images of cohort 1 to a $2 \times 2 \times 2$ mm fixed voxel size. Cohort 2 was used for survival analyses. If the VOI was too small (diameter $<$ 12 mm), SUV_{peak} and therefore $NHOC_{peak}$ and $NHOP_{peak}$ could not be calculated and were replaced by SUV_{max} and by $NHOC_{max}$ and $NHOP_{max}$, respectively. Additionally, to investigate the impact of necrotic foci on NHOCs and NHOPs and other radiomic feature values, all 244 lesions of cohort 2 were labeled as necrotic or nonnecrotic using visual assessment of PET images by an experienced nuclear medicine physicist under the supervision of a nuclear medicine physician.

Image processing, tumor segmentation, and feature extraction were performed with LIFEx (version 7.4.0, www.lifexsoft.org) (*9*), which is an Image Biomarker Standardisation Initiative–compliant software (*10*).

TABLE 1
Patient Characteristics

Characteristic	Cohort 1	Cohort 2
Number of patients		
Total	99	244
Male	55 (56%)	122 (50%)
Female	44 (44%)	122 (50%)
Age (y)		
Mean ± SD	66.3 ± 10.2	65.4 ± 10.1
Range	35–86	35–87
NSCLC subtype		
Adenocarcinoma	58 (58%)	196 (80%)
Squamous cell carcinoma	28 (28%)	24 (10%)
Other	13 (13%)	24 (10%)
Stage		
III	50 (51%)	5 (2%)
VI	49 (49%)	239 (98%)

Data are number with percentage in parentheses, except for age.

Statistical Analysis

Statistical analyses were conducted using R software (R Core Team 2021).

For the robustness study, before-and-after comparison analyses were performed using the Bland–Altman method with 95% limits of agreement (±1.96 SDs) to investigate the impact of spatial resolution (with vs. without postfiltering) and voxel size ($2 \times 2 \times 2$ mm vs. $4 \times 4 \times 4$ mm) on NHOCs, NHOPs, and SUVs.

To characterize the correlations between features, the Spearman rank correlation coefficient (r) was computed between each pair of features.

The impact of tumor delineation on radiomic feature values was assessed using the 30 lesions segmented by 2 observers, by calculating the intraclass correlation coefficient based on the 1-way model with agreement-type and single-score settings.

The ability of NHOCs, NHOPs, and other radiomic features to predict overall survival (OS) was investigated using Kaplan–Meier analysis, where the duration of follow-up was defined as the time between the pretreatment PET scan and the date of death or last day of follow-up. The significance of differences between survival curves was assessed by log-rank testing, with a P value of less than 0.05 defined as statistically significant. The stratification involved the

maximally selected rank statistics methodology, which assesses 2-sample rank statistics of all possible cutoffs and selects the optimal one. The Harrell C-index was also used to evaluate the ability of each feature to predict survival. The relevant predictors after Kaplan–Meier analysis were further combined in pairs for multivariable analysis, where 3 risk categories were defined on the basis of whether the feature's high or low value was associated with good or poor outcome (e.g., high MTV associated with worse survival). The pairwise comparisons between survivals of the risk groups were calculated using log-rank tests, including the Benjamini–Hochberg method for *P* value adjustment.

The impact of the presence of visible necrosis on PET images on NHOCs and NHOPs and other imaging features was evaluated by Wilcoxon rank testing by comparing feature values between tumors with and without necrotic cores. Moreover, we compared the survival prediction accuracy based on log-rank testing with and without the necrosis included in the tumor region, that is, no morphologic closing operation applied after thresholding.

RESULTS

The statistical distribution of the NHOCs and NHOPs is shown in Table 2 and compared with those of the other 13 features. According to MTV, the tumor size ranged from 0.3 to 1,019.6 cm^3. The mean values were 0.62 (range, 0.09–1.83) for $NHOC_{max}$, 0.54 (range, 0.04–1.83) for $NHOC_{peak}$, 0.26 (range, 0.05–1.26) for $NHOP_{max}$, and 0.27 (range, 0.05–0.63) for $NHOP_{peak}$.

Robustness Study

In cohort 1, Bland–Altman analysis showed that NHOCs were little affected by image postfiltering (mean difference of −0.12 for $NHOC_{max}$ and −0.09 for $NHOC_{peak}$, with the greatest smoothing with a σ of 4 mm [Fig. 1]; similar results with smaller filter sizes [Supplemental Figs. 2 and 3]) and even less by the voxel size (mean difference of 0.02 and 0.003, respectively [Supplemental Fig. 4]). The mean difference was only 0.03 for both $NHOP_{max}$ and $NHOP_{peak}$ when the postfiltering was applied (σ of 4 mm) and was −0.02 and −0.07, respectively, when the voxel size was varied. For both features, the measurements based on SUV_{max} demonstrated greater variability (larger CI) than those based on SUV_{peak}. For comparison purposes, SUV_{peak} and SUV_{max} were more affected by postfiltering and voxel size than the NHOC and NHOP features, with increasing systematic differences observed for greater SUVs (Supplemental Figs. 2–5).

Comparing feature values obtained for VOIs drawn by 2 observers, the reproducibility was excellent (intraclass correlation coefficient ≥ 0.8) for NHOCs and NHOPs and for most features (Supplemental Table 2).

As illustrated in the correlogram (Fig. 2), NHOCs and NHOPs did not correlate strongly with any of the other features, with correlations always less than 0.60 and 0.30 in absolute value for NHOCs and NHOPs, respectively. The correlations between NHOCs and NHOPs did not exceed 0.45.

Survival Analysis

Among the 244 patients included in cohort 2, SUV_{peak} and therefore $NHOC_{peak}$ and $NHOP_{peak}$ could be calculated in 218 (89%) and were replaced by SUV_{max} and by $NHOC_{max}$ and $NHOP_{max}$, respectively, in the remaining 26 patients, who had a primary tumor less than 12 mm in largest diameter.

NHOCs identified 2 survival profiles in patients treated with immunotherapy only (*P* value of log-rank test < 0.01; cutoffs, 0.79 for $NHOC_{max}$ and 0.50 for $NHOC_{peak}$ [Fig. 3; Table 3]). In the other 2 subcohorts, the distinction of patients with low and high OS did not reach significance. NHOPs significantly distinguished long- from short-OS patients in the targeted therapy and immunotherapy groups (Table 3). The highest C-index for NHOCs and NHOPs was 0.58 for $NHOC_{max}$, 0.61 for $NHOC_{peak}$, 0.57 for $NHOP_{max}$, and 0.59 for $NHOP_{peak}$ (Table 3). For other features, the greatest observed C-indexes were for MTV (0.62) and for

TABLE 2
Statistical Distribution of Features for Cohort 2 (*n* = 244 Patients)

Variable	Mean	SD	Range
SUV_{min}	3.8	2.6	0.0–17.0
SUV_{max}	13.3	7.2	1.8–51.8
SUV_{peak}	11.4	6.1	2.6–40.0
SUV_{mean}	7.5	4.1	1.2–30.9
$NHOC_{max}$	0.615	0.290	0.087–1.833
$NHOC_{peak}$	0.538	0.292	0.042–1.833
$NHOP_{max}$	0.255	0.155	0.049–1.264
$NHOP_{peak}$	0.271	0.131	0.053–0.628
MTV (cm3)	57.1	112.0	0.3–1019.6
Total lesion glycolysis	396.9	810.2	0.9–8557.9
Sphericity	0.763	0.110	0.320–0.903
Joint entropy log10	3.586	0.332	2.874–4.189
Inverse difference moment	0.040	0.024	0.014–0.227
Short run emphasis	0.992	0.007	0.935–1.000
Long run emphasis	1.034	0.041	1.000–1.462
Low gray-level zone emphasis	0.010	0.010	0.000–0.049
High gray-level zone emphasis	7,374.3	2,228.4	1,338.7–13,788.2

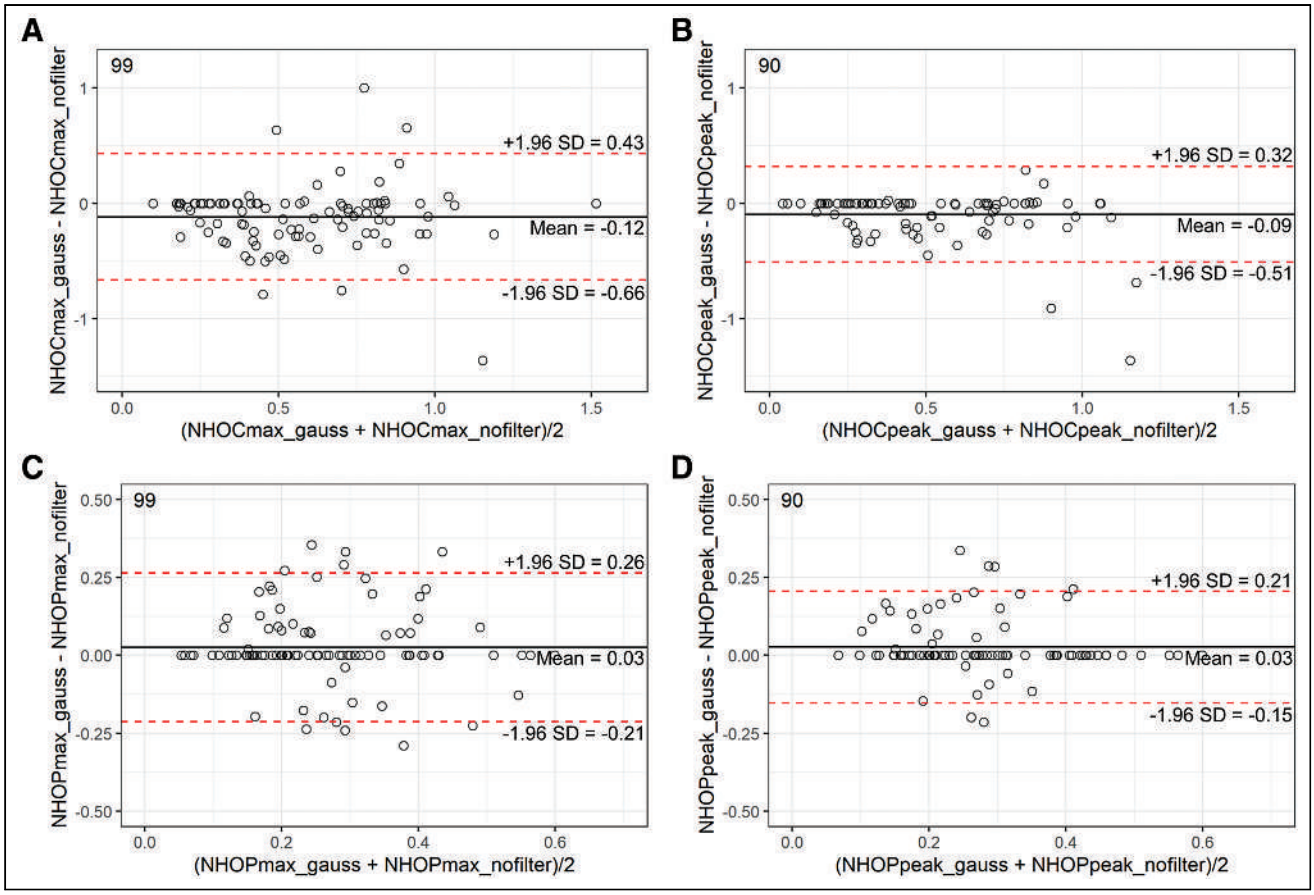

FIGURE 1. Bland–Altman plots for cohort 1, showing concordance between feature values extracted from PET images (4-mm voxel size) before (suffix _nofilter on the graphs) and after gaussian postfiltering (σ = 4 mm, suffix _gauss) for $NHOC_{max}$ (A), $NHOC_{peak}$ (B), $NHOP_{max}$ (C), and $NHOP_{peak}$ (D). Limits of agreement (95%) are shown as dotted red lines, and bias is shown as solid black line. Numbers in top-left corner of each graph correspond to number of measurements available.

sphericity (0.69), both in the immunotherapy group. Supplemental Figure 6 shows the results for $NHOC_{max}$, $NHOP_{max}$, MTV, and sphericity, where for each feature the survival curves of the 3 treatment groups are overlaid on a single graph using the same cutoff (0.80 for $NHOC_{max}$, 0.37 for $NHOP_{max}$, 30.4 cm^3 for MTV, and 0.73 for sphericity). For each feature, the common cut point was determined according to the optimal separation between patients concerning long and short OS when considering all patients of cohort 2 regardless of their treatment. In multivariable analysis, none of the feature combinations significantly distinguished the survival distributions of the patients according to 3 risk categories (Supplemental Table 3). Nevertheless, better intercategory distinction was observed in the immunotherapy group with the combination of $NHOC_{max}$/$NHOP_{max}$ and sphericity, for instance (Supplemental Fig. 7).

As reported in Supplemental Table 4, the lesions labeled as necrotic (68/244, 28%) or nonnecrotic based on visual evaluation of PET images yielded significantly different values (Wilcoxon test) for all features except SUV_{mean}, sphericity, inverse difference moment, short run emphasis, long run emphasis, low gray-level zone emphasis, and high gray-level zone emphasis. The lesions with a necrotic core exhibited higher NHOCs and lower NHOPs than those without necrosis (Supplemental Fig. 8). This is illustrated in Figure 4, which shows representative PET/CT scans of tumors with different NHOCs and NHOPs. However, the accuracy of survival predictions with NHOCs and NHOPs was little affected by exclusion of the necrotic areas in the tumor VOIs (Supplemental Fig. 9; Fig. 3; Supplemental Table 5).

DISCUSSION

Several imaging features, such as SUV and MTV, are widely studied for the management of cancer patients (*11*,*12*). More sophisticated radiomic features are also extensively investigated and considered for inclusion in classification, prognostic, and predictive models. However, none of the advanced imaging features has yet gained wide acceptance, partly because of their challenging intuitive interpretation and lack of easy-to-understand reference values. NHOC and nSPD are recently introduced model-informed PET metrics, characterizing the drift of highly proliferative cells toward the tumor periphery (*4*,*5*), which can thus be related to tumor growth, and are easy to calculate and to interpret. They were defined as the distance from the localization of the [^{18}F]FDG hot spot to the tumor centroid or perimeter. To avoid the size dependence of these metrics, they were divided by the radius of a hypothetical sphere having the same volume as the tumor. Although their prognostic value has been demonstrated in breast cancer and NSCLC (*4*,*5*), to the best of our knowledge, they have not been confirmed yet in any independent study. Therefore, the current study first investigated the sensitivity of NHOC and NHOP (the

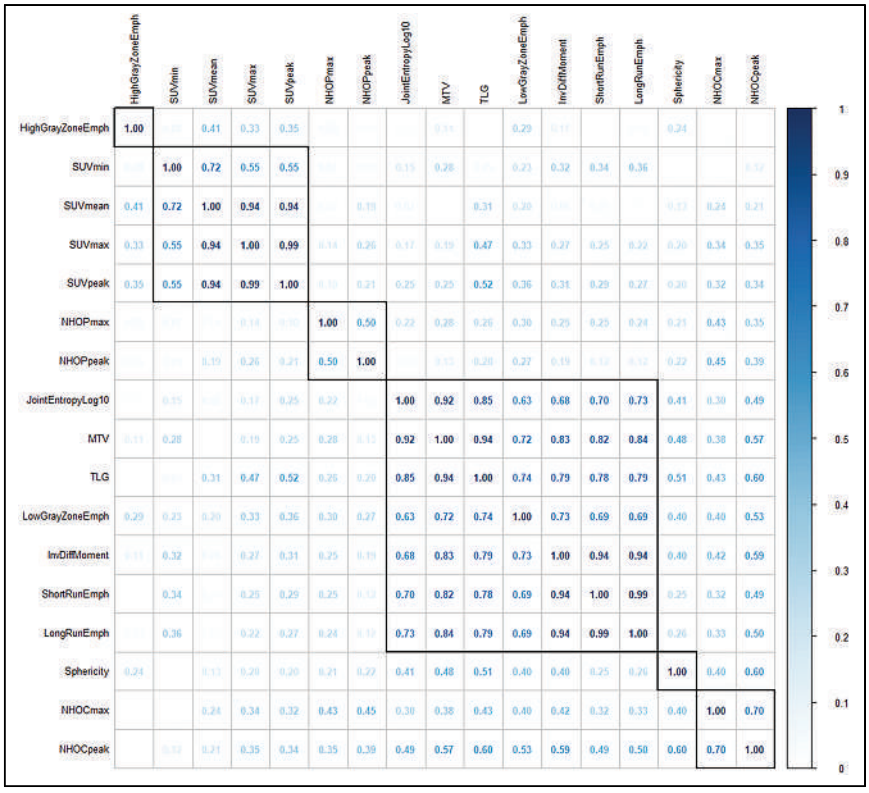

FIGURE 2. Correlogram from cohort 1, showing absolute Spearman correlation coefficient between each pair of radiomic features. Rectangles are generated on graph according to hierarchic clustering. HighGrayZoneEmph = high gray-level zone emphasis; InvDiffMoment = inverse difference moment; JointEntropyLog10 = joint entropy log10; LongRunEmph = long run emphasis; LowGrayZoneEmph = low gray-level zone emphasis; ShortRunEmph = short run emphasis; TLG = total lesion glycolysis.

3-dimensional [3D] version of the nSPD feature) to image spatial resolution, spatial sampling, and tumor delineation and then studied their prognostic value in independent cohorts of NSCLC patients.

For each biomarker, 2 measurement approaches were used: $NHOC_{max}$, as initially modeled and reported by Jiménez-Sánchez et al. (*4*), and $NHOC_{peak}$, as introduced by Jiménez Londoño et al. (*5*). $NHOP_{max}$ is a 3D surrogate of the already reported feature (*5*), and $NHOP_{peak}$ is an alternative of the SUV_{max}-based NHOP measurement. Because $NHOC_{peak}$ and $NHOP_{peak}$ calculations require the tumor to be larger than 1 cm^3 so that SUV_{peak} can be calculated, they were replaced by $NHOC_{max}$ and $NHOP_{max}$ for tumors less than 12 mm in diameter.

Our results showed that NHOCs and NHOPs varied less with spatial resolution and image sampling than did SUV_{max} and SUV_{peak}. Given that both SUV_{max} and SUV_{peak} are widely used although they are known to depend on image properties, our results suggest that NHOCs and NHOPs are usable even in multicenter studies, where the image quality often varies, and will not be strongly affected by imaging conditions. Another limiting issue with novel radiomic features is that they often correlate closely with existing ones, hence not bringing clear complementary information. We thus checked whether NHOCs and NHOPs correlated with existing features, in particular with shape features, as they can be seen as geometric features (Supplemental Fig. 1). The correlation analysis demonstrated that NHOCs and NHOPs correlated strongly with neither sphericity ($r \leq 0.60$) nor with conventional PET features such as SUV ($r \leq 0.35$) and MTV ($r \leq 0.57$) or textural features ($r \leq 0.59$), confirming their potential added value compared with widely investigated radiomic features. The correlations between NHOCs and NHOPs were also weak (Fig. 2), as these variables would be perfectly negatively correlated only if the tumors were perfectly spheric. Last, for a radiomic feature to be potentially useful, its values should not heavily depend on accurate tumor delineation. We therefore compared the feature values obtained when 2 different observers drew the VOI and observed an intraclass correlation coefficient greater than 0.8 for NHOCs and NHOPs, confirming these as suitable PET biomarker candidates. However, the observers used the same semiautomatic isocontouring (40%) approach on the manually delineated VOIs, and intraclass correlation coefficients might have been smaller had the segmentation methods been different.

The orders of magnitude of NHOCs found in our study are quite similar to the ones reported in the literature ($NHOC_{max}$, 0.62 ± 0.29 in our study vs. 0.43 ± 0.20 in the literature (*4*); $NHOC_{peak}$, 0.54 ± 0.29 in our study vs. 0.34 ± 0.20 in the literature (*5*)), facilitating their interpretation. No direct comparison could be made between reported nSPDs and our NHOPs because of differences in the definition of distance to perimeter (2-dimensional vs. 3D). For comparison purposes, the maximum nSPDs were similar in the present and previous (*5*) research, with mean values of 0.26 ± 0.16 and 0.40 ± 0.12, respectively. However, for tumor characterization we recommend the 3D approach (NHOP) to be consistent with the NHOC feature.

The differences in the cohorts in the previous (*4*,*5*) and present studies are major, preventing meaningful comparisons of feature values. Indeed, the 2 published studies included only surgically treated patients with different adjuvant treatment regimens, whereas in our study the patients of cohort 2 were not operable and were treated using various approaches. Moreover, the dataset of Jiménez-Sánchez et al. (*4*) was based on inclusion criteria (e.g., a tumor size of at least 2 cm, absence of distant metastases, and a tumor SUV twice higher than background SUV) different from ours (detectability of the primary tumor on the PET images).

In survival analysis, the patients with higher NHOCs had shorter OS than those with lower NHOCs. Inversely, patients with lower NHOPs were associated with worse survival (except for $NHOP_{peak}$ in the immunochemotherapy subcohort, for which the *P* value was 0.043 [Table 3]). These results are consistent with those of the previous studies. Jiménez-Sánchez et al. (*4*) reported an $NHOC_{max}$ of 0.64 as the best cutoff to identify 2 survival profiles, which led to a C-index of 0.75 for OS. Here, a very similar cutoff (0.61) was obtained in the immunochemotherapy group, which, however, did not reach statistical significance in distinguishing patient survival, with the C-index result substantially lower in the present study (0.54 vs. 0.75). A higher cutoff of $NHOC_{max}$ (0.79) stratified patients regarding OS in the immunotherapy group. Jiménez Londoño et al. (*5*) investigated $NHOC_{peak}$, instead of

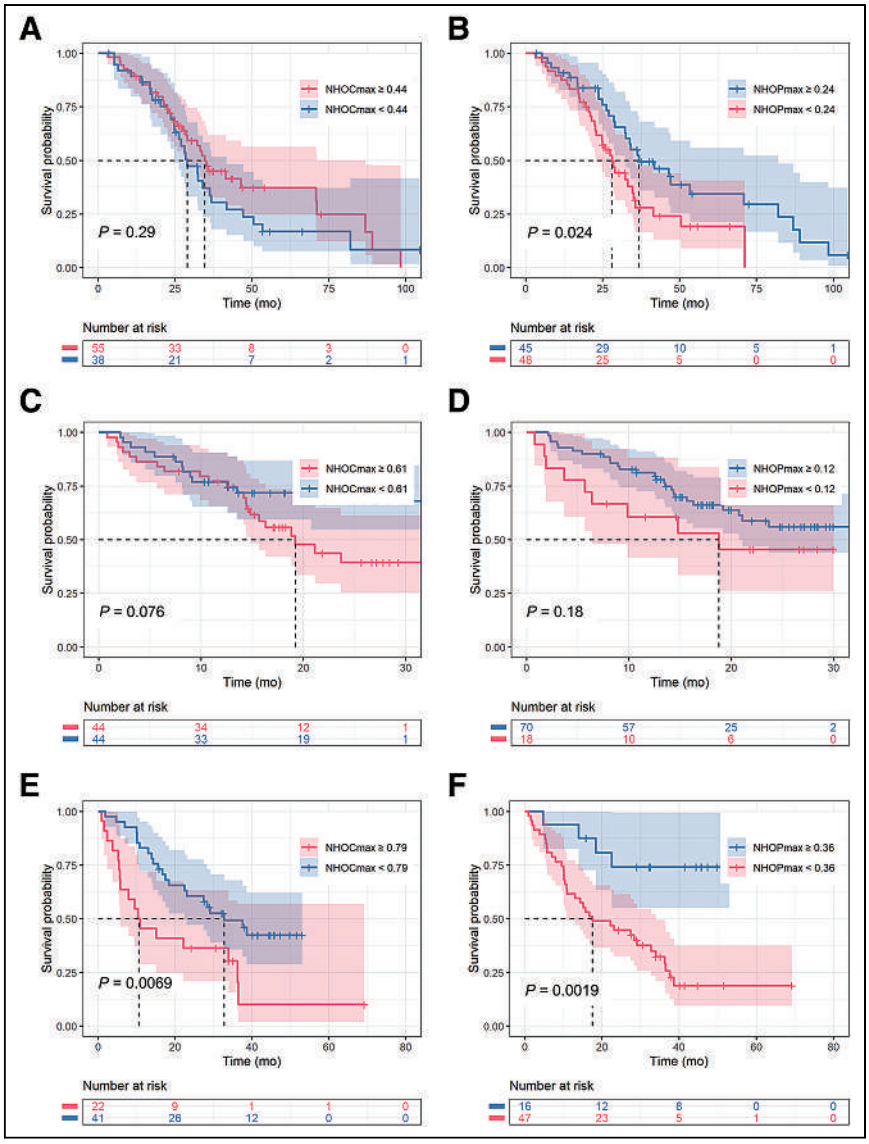

FIGURE 3. Kaplan–Meier OS curves with best cutoffs for $NHOC_{max}$ and $NHOP_{max}$ for patients treated by targeted therapy (A and B), immunochemotherapy (C and D), and immunotherapy only (E and F), based on baseline [^{18}F]FDG PET scans.

$NHOC_{max}$, with higher values of $NHOC_{peak}$ (0.39 ± 0.21) being significantly associated with short-term mortality, defined as OS of less than 36 mo. In our study, an $NHOC_{peak}$ of 0.50 significantly distinguished long- from short-OS patients in the immunotherapy group with a median follow-up of 24.2 mo. Jiménez Londoño et al. have also investigated nSPD as an alternative approach for measuring the displacement of the [^{18}F]FDG hot spot (SUV_{max}) from the center of the tumor to its periphery. This biomarker was reported as a significant prognostic factor for OS (a lower nSPD was significantly associated with short-term mortality) and correlated strongly with tumor histologic type and TNM stage. In the present study, we introduced the 3D surrogate of this biomarker, $NHOP_{max}$, and its other variant, $NHOP_{peak}$. Optimized cutoffs enabled patient stratification as a function of their OS with $NHOP_{max}$ and $NHOP_{peak}$ in the targeted therapy and immunotherapy groups. As a supplement, we considered C-index and OS estimates with the nSPD approach. Even if its prediction performances were similar with NHOP in all therapy groups (C-index, 0.51–0.57 for $NHOP_{max}$ and 0.53–0.58 for maximum nSPD [Supplemental Fig. 10; Supplemental Table 6]), we recommend the 3D approach, which is in line with the other features such as MTV or NHOC calculated in 3 dimensions. According to our results, NHOPs outperformed NHOCs in predicting survival in 2 treatment groups, whereas NHOCs predicted survival only in the immunotherapy group. $NHOC_{max}$ and $NHOP_{max}$ were retained for further multivariate analysis in combination with the basic features such as SUV_{max}, MTV, and sphericity. The best intercategory distinction was observed in the immunotherapy group with $NHOC_{max}$–sphericity and $NHOP_{max}$–sphericity pairs, which, however, could not significantly distinguish the survival distributions of the patients according to 3 risk categories.

Tumors with a necrotic core demonstrated significantly higher NHOCs and lower NHOPs. However, the survival outcomes were little affected by exclusion of the necrotic areas in the tumor VOIs. This is consistent with results published by Noortman et al. (*13*) for other radiomic features.

To our knowledge, this work was the first to compare the robustness and prognostic ability of $NHOC_{max}$, $NHOP_{max}$, $NHOC_{peak}$, and $NHOP_{peak}$. These features appeared equivalent with their maximum and peak approaches; however, $NHOC_{peak}$ and $NHOP_{peak}$ might be preferable to $NHOC_{max}$ and $NHOP_{max}$ for greater robustness to noise in PET images.

Similar to SUV, NHOCs and NHOPs pertain to a single lesion. When multiple lesions are present, the best way to account for NHOCs and NHOPs in all lesions remains to be investigated.

Our study had limitations. We investigated the prognostic value of NHOCs and NHOPs calculated in the primary tumor only, whereas 98% of patients had metastases. However, the results suggest that even in advanced-stage NSCLC patients, NHOC and NHOP features pertaining to the primary tumor have some prognostic value. Combining the NHOCs and NHOPs of the primary tumor with patient-level features such as total whole-body MTV and maximal distance between tumor foci—2 widely investigated whole-body radiomic features (*14*,*15*)—is under way. The minimal tumoral volume needed for meaningful measurement of these features should also be investigated to avoid the partial-volume effect related to spatial resolution and respiratory motion.

Finally, further studies are needed to determine the added value of NHOCs and NHOPs for different types of cancer and clinical questions of interest, as well as for tracers different from [^{18}F]FDG. The dynamic changes in NHOCs and NHOPs could also be worth studying, as such changes may have the potential to predict treatment response. To encourage the PET community to reproduce our findings and to investigate NHOCs and NHOPs under various conditions, both biomarkers are now offered as additional radiomic features in the free LIFEx software (*9*).

TABLE 3
Survival Analyses with Kaplan–Meier Estimate of OS and C-Index

	Targeted therapy				Immunochemotherapy				Immunotherapy			
Feature	Cutoff	*P*	Short-OS	C-index	Cutoff	*P*	Short-OS	C-index	Cutoff	*P*	Short-OS	C-index
SUV_{min}	1.4	0.030*	−	0.499	5.2	0.031*	−	0.468	5.4	0.004*	+	0.488
SUV_{max}	10.5	0.007*	+	0.577	9.1	0.230		0.460	18.2	0.110		0.517
SUV_{peak}	9.1	0.023*	+	0.571	12.9	0.230		0.462	11.9	0.190		0.520
SUV_{mean}	6.0	0.019*	+	0.563	8.4	0.068		0.471	12.4	0.004*	+	0.472
$NHOC_{max}$	0.435	0.290		0.477	0.608	0.076		0.540	0.793	0.007*	+	0.581
$NHOC_{peak}$	0.521	0.220		0.496	0.475	0.150		0.500	0.502	0.005*	+	0.614
$NHOP_{max}$	0.238	0.024*	−	0.572	0.115	0.180		0.510	0.361	0.002*	−	0.541
$NHOP_{peak}$	0.238	0.008*	−	0.540	0.192	0.043*	+	0.449	0.468	0.013*	−	0.586
MTV (cm3)	55.7	0.029*	+	0.529	21.4	0.006*	+	0.592	21.0	0.003*	+	0.624
Total lesion glycolysis	84.5	0.170		0.542	53.9	0.014*	+	0.577	193.6	0.002*	+	0.616
Sphericity	0.784	0.095		0.502	0.721	0.017*	−	0.546	0.830	<0.001*	−	0.690
Joint entropy log10	3.725	0.140		0.532	3.695	0.007*	+	0.607	3.665	0.068		0.538
Inverse difference moment	0.04	0.030*	+	0.488	0.036	0.022*	+	0.455	0.039	0.025*	+	0.421
Short run emphasis	0.99	0.071		0.480	0.993	0.015*	−	0.449	0.991	0.024*	−	0.433
Long run emphasis	1.04	0.035*	+	0.486	1.026	0.015*	+	0.459	1.034	0.024*	+	0.431
Low gray-level zone emphasis	0.003	0.011*	−	0.563	0.004	0.150		0.529	0.004	<0.001*	−	0.594
High gray-level zone emphasis	6183	0.042*	+	0.570	5776	0.034*	−	0.433	6695	0.013*	−	0.406

*$P < 0.05$ (log-rank test).
+ or − = higher or lower than cutoff feature value associated with poor survival.

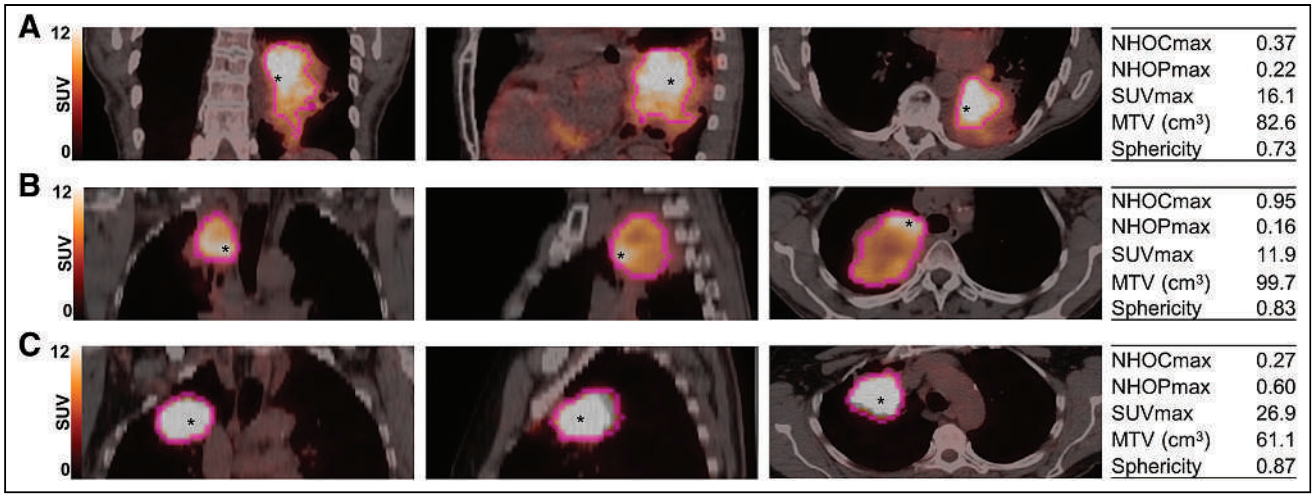

FIGURE 4. Examples of tumor and corresponding feature values on [^{18}F]FDG PET/CT coronal, sagittal, and axial slices from patients with different survivals: 17.6 mo (A), 35.1 mo (B), and alive at 49.8 mo (C). Position of hottest voxel is indicated with asterisk.

CONCLUSION

We validated the prognostic value of NHOC extracted from baseline [^{18}F]FDG PET images of patients with NSCLC, independently of the original work of Jiménez-Sánchez et al. (*4*). We introduced the 3D surrogate of nSPD originally proposed by Jiménez Londoño et al. (*5*). Our findings confirmed the prognostic potential of NHOC and NHOP features when pertaining to the primary tumor in NSCLC patients. The prognostic significance of NHOC was obvious in the immunotherapy-treated patients (high NHOC associated with short OS), whereas low NHOP was associated with poor survival in the targeted therapy and immunotherapy groups. We demonstrated the robustness of NHOCs and NHOPs to postfiltering and voxel size resampling and their complementarity to SUVs, MTV, total lesion glycolysis, sphericity, and other commonly reported texture features. We encourage the PET community to include NHOCs and NHOPs in their PET image analysis to further evaluate their relevance for tumor characterization.

DISCLOSURE

This work was supported by Fondation ARC (TIPIT project SIGNIT202001322) and by Fondation Janssen Horizon (PANACEE project). No other potential conflict of interest relevant to this article was reported.

KEY POINTS

QUESTION: Are NHOC and NHOP robust and prognostic PET biomarkers for lung cancer patients?

PERTINENT FINDINGS: NHOC and NHOP biomarkers are robust to postfiltering of PET images and voxel size. They do not substantially correlate with other radiomic features. Depending on the treatment, they distinguished long- from short-OS lung cancer patients on baseline [^{18}F]FDG PET images.

IMPLICATION FOR PATIENT CARE: NHOC and NHOP are robust and prognostic biomarkers that deserve further evaluation in radiomic studies.

REFERENCES

1. Kirienko M, Gallivanone F, Sollini M, et al. FDG PET/CT as theranostic imaging in diagnosis of non-small cell lung cancer. *Front Biosci (Landmark Ed).* 2017;22:1713–1723.
2. Apostolova I, Ego K, Steffen IG, et al. The asphericity of the metabolic tumour volume in NSCLC: correlation with histopathology and molecular markers. *Eur J Nucl Med Mol Imaging.* 2016;43:2360–2373.
3. Shiri I, Rahmim A, Ghaffarian P, Geramifar P, Abdollahi H, Bitarafan-Rajabi A. The impact of image reconstruction settings on ^{18}F-FDG PET radiomic features: multi-scanner phantom and patient studies. *Eur Radiol.* 2017;27:4498–4509.
4. Jiménez-Sánchez J, Bosque JJ, Jiménez Londoño GA, et al. Evolutionary dynamics at the tumor edge reveal metabolic imaging biomarkers. *Proc Natl Acad Sci USA.* 2021;118:e2018110118.
5. Jiménez Londoño GA, Vicente AMG, Bosque JJ, et al. SUVmax to tumor perimeter distance: a robust radiomics prognostic biomarker in resectable non-small cell lung cancer patients. *Eur Radiol.* 2022;32:3889–3902.
6. Orlhac F, Nioche C, Klyuzhin I, Rahmim A, Buvat I. Radiomics in PET imaging: a practical guide for newcomers. *PET Clin.* 2021;16:597–612.
7. Wahl RL, Jacene H, Kasamon Y, Lodge MA. From RECIST to PERCIST: evolving considerations for PET response criteria in solid tumors. *J Nucl Med.* 2009;50(suppl 1):122S–150S.
8. Orlhac F, Soussan M, Maisonobe JA, Garcia CA, Vanderlinden B, Buvat I. Tumor texture analysis in ^{18}F-FDG PET: relationships between texture parameters, histogram indices, standardized uptake values, metabolic volumes, and total lesion glycolysis. *J Nucl Med.* 2014;55:414–422.
9. Nioche C, Orlhac F, Boughdad S, et al. LIFEx: a freeware for radiomic feature calculation in multimodality imaging to accelerate advances in the characterization of tumor heterogeneity. *Cancer Res.* 2018;78:4786–4789.
10. Zwanenburg A, Vallières M, Abdalah MA, et al. The Image Biomarker Standardization Initiative: standardized quantitative radiomics for high-throughput image-based phenotyping. *Radiology.* 2020;295:328–338.
11. Sharma A, Mohan A, Bhalla A, et al. Role of metabolic tumor volume (MTV) and standardized uptake value (SUV) based parameters derived from whole body (WB) ^{18}F-FDG PET/CT in interim treatment response assessment of NSCLC [abstract]. *J Nucl Med.* 2019;60(suppl 1):1326.
12. Ulaner GA, Eaton A, Morris PG, et al. Prognostic value of quantitative fluorodeoxyglucose measurements in newly diagnosed metastatic breast cancer. *Cancer Med.* 2013;2:725–733.
13. Noortman WA, Vriens D, Mooij CDY, et al. The influence of the exclusion of central necrosis on [^{18}F]FDG PET radiomic analysis. *Diagnostics (Basel).* 2021;11:1296.
14. Dall'Olio FG, Calabrò D, Conci N, et al. Baseline total metabolic tumour volume on 2-deoxy-2-[^{18}F]fluoro-d-glucose positron emission tomography-computed tomography as a promising biomarker in patients with advanced non-small cell lung cancer treated with first-line pembrolizumab. *Eur J Cancer.* 2021;150:99–107.
15. Girum KB, Rebaud L, Cottereau AS, et al. ^{18}F-FDG PET maximum-intensity projections and artificial intelligence: a win-win combination to easily measure prognostic biomarkers in DLBCL patients. *J Nucl Med.* 2022;63:1925–1932.

Deep Semisupervised Transfer Learning for Fully Automated Whole-Body Tumor Quantification and Prognosis of Cancer on PET/CT

Kevin H. Leung[1], Steven P. Rowe[2], Moe S. Sadaghiani[1], Jeffrey P. Leal[1], Esther Mena[3], Peter L. Choyke[3], Yong Du[1], and Martin G. Pomper[1]

[1]*Russell H. Morgan Department of Radiology and Radiological Science, Johns Hopkins University School of Medicine, Baltimore, Maryland;* [2]*Department of Radiology, University of North Carolina at Chapel Hill School of Medicine, Chapel Hill, North Carolina; and* [3]*Center for Cancer Research, National Cancer Institute, Bethesda, Maryland*

Automatic detection and characterization of cancer are important clinical needs to optimize early treatment. We developed a deep, semisupervised transfer learning approach for fully automated, whole-body tumor segmentation and prognosis on PET/CT. **Methods:** This retrospective study consisted of 611 ^{18}F-FDG PET/CT scans of patients with lung cancer, melanoma, lymphoma, head and neck cancer, and breast cancer and 408 prostate-specific membrane antigen (PSMA) PET/CT scans of patients with prostate cancer. The approach had a nnU-net backbone and learned the segmentation task on ^{18}F-FDG and PSMA PET/CT images using limited annotations and radiomics analysis. True-positive rate and Dice similarity coefficient were assessed to evaluate segmentation performance. Prognostic models were developed using imaging measures extracted from predicted segmentations to perform risk stratification of prostate cancer based on follow-up prostate-specific antigen levels, survival estimation of head and neck cancer by the Kaplan–Meier method and Cox regression analysis, and pathologic complete response prediction of breast cancer after neoadjuvant chemotherapy. Overall accuracy and area under the receiver-operating-characteristic (AUC) curve were assessed. **Results:** Our approach yielded median true-positive rates of 0.75, 0.85, 0.87, and 0.75 and median Dice similarity coefficients of 0.81, 0.76, 0.83, and 0.73 for patients with lung cancer, melanoma, lymphoma, and prostate cancer, respectively, on the tumor segmentation task. The risk model for prostate cancer yielded an overall accuracy of 0.83 and an AUC of 0.86. Patients classified as low- to intermediate- and high-risk had mean follow-up prostate-specific antigen levels of 18.61 and 727.46 ng/mL, respectively ($P < 0.05$). The risk score for head and neck cancer was significantly associated with overall survival by univariable and multivariable Cox regression analyses ($P < 0.05$). Predictive models for breast cancer predicted pathologic complete response using only pretherapy imaging measures and both pre- and posttherapy measures with accuracies of 0.72 and 0.84 and AUCs of 0.72 and 0.76, respectively. **Conclusion:** The proposed approach demonstrated accurate tumor segmentation and prognosis in patients across 6 cancer types on ^{18}F-FDG and PSMA PET/CT scans.

Key Words: deep learning; semisupervised transfer learning; PET/CT; tumor segmentation; cancer prognosis

J Nucl Med 2024; 65:643–650
DOI: 10.2967/jnumed.123.267048

Received Nov. 10, 2023; revision accepted Jan. 29, 2024.
For correspondence or reprints, contact Kevin H. Leung (kleung8@jhmi.edu).
Published online Feb. 29, 2024.

Cancer is a worldwide health concern and the second leading cause of death in the United States, with approximately 2 million projected cases in 2023 (*1*). Prostate, breast, lung, melanoma, lymphoma, and oral cavity and pharyngeal cancers were among the leading types of new estimated cases (*1*). Delays in cancer diagnosis and treatment were associated with increased mortality for surgical, chemotherapeutic, and radiotherapeutic modalities and may lead to increased advanced-stage disease (*2*).

Quantitative measures of molecular tumor burden on ^{18}F-FDG and prostate-specific membrane antigen (PSMA) PET/CT are prognostic biomarkers (*3*). However, manual tumor quantification by radiologists is time-consuming, laborious, and subject to inter- and intrareader variability (*4*). Generalizable approaches for automated PET/CT tumor quantification are an important clinical need for early detection and treatment of cancer.

Radiomics performs high-throughput extraction of quantitative engineered features of malignant tumors from radiologic data (*4*). Deep learning methods automatically extract features from input images to model medical endpoints directly and require large training datasets with physician-defined annotations (*4*). Additionally, manual tumor delineation is not easily scalable, especially for patients with a high tumor burden. Manual delineation is further impacted by interobserver variability because of differences in levels of reader experience. Lastly, deep learning models for PET/CT are often developed for specific radiotracers, limiting their general applicability.

We developed a deep, semisupervised transfer learning (DeepSSTL) approach for fully automated whole-body tumor segmentation and prognosis on ^{18}F-FDG and PSMA PET/CT scans using limited annotations. Radiomics features and whole-body imaging measures were extracted from predicted segmentations to build prognostic models for risk stratification, overall survival analysis, and prediction of response to therapy. Our approach demonstrated robust performance across patients with melanoma; lymphoma; and prostate, lung, head and neck, and breast cancers and may help alleviate physician workload for whole-body PET/CT tumor analysis.

MATERIALS AND METHODS

This retrospective study was approved by the Johns Hopkins institutional review board with a waiver for obtaining informed consent. Deidentified data were collected, in part, from The Cancer Imaging Archive (*5*).

Semisupervised Transfer Learning

A semisupervised transfer learning framework was developed to learn the whole-body tumor segmentation task using limited manual tumor annotations. The approach jointly optimized a nnU-net backbone, an automatically self-configuring deep learning framework (*6*), across source and target domains of ^{18}F-FDG and PSMA PET/CT images with complete and incomplete annotations comprising fully and partially labeled manual segmentations, respectively. The DeepSSTL approach performed domain adaptation on ^{18}F-FDG and PSMA PET/CT while iteratively improving segmentation performance.

Data

Data from 1,019 patients with cancer with PET/CT scans across 5 datasets and 6 cancer types were used. Patient demographics are provided in Table 1.

Datasets 1 and 2 included ^{18}F-DCFPyL PSMA PET/CT scans of prostate cancer patients. Dataset 1 had 270 patients with incomplete manual segmentations (Fig. 1), with PSMA reporting and data system (PSMA-RADS) scores of 1–5 being assigned to segmented lesions and overall scans indicating the likelihood of prostate cancer (*7*). Dataset 2 had Gleason scores, initial serum prostate-specific antigen (PSA)

TABLE 1
Patient Characteristics

Characteristic	Data	Characteristic	Data
Dataset 1*		Dataset 3†	
Age (y) (mean ± SD)	65.67 ± 7.97	Age (y) (mean ± SD)	60.11 ± 16.51
Sex		Sex	
Men	270	Men	290
Women	0	Women	211
Overall PSMA-RADS score		Dataset 4‡	
NA	12	Age (y) (mean ± SD)	62.47 ± 7.78
1	3	Sex	
2	24	Men	62
3	63	Women	12
4	48	AJCC stage	
5	120	I	14
Dataset 2*		II	5
Age (y) (mean ± SD)	66.46 ± 7.35	III	13
Sex		IV	42
Men	138	Surgery	
Women	0	No	70
Gleason score		Yes	4
NA	2	Chemotherapy	
≤6	11	No	61
7	43	Yes	13
8	29	Radiotherapy time (d)	37 (31–47)
9	44	Dataset 5§	
10	9	Age (y) (mean ± SD)	48.69 ± 10.33
Initial PSA level (ng/mL)	6.38 (0.02–5,000.00)	Sex	
Follow-up PSA level (ng/mL)	2.24 (0.00–7,270.00)	Men	0
PSA doubling time (mo)	5.20 (0.23–81.70)	Women	36
Post-PSMA PET therapy		Pathologic response	
NA	37	pCR	10
None	7	Non-pCR	26
Local	18		
Systemic androgen-targeted	56		
Systemic and cytotoxic	20		

*Prostate cancer.
†Lung cancer, melanoma, and lymphoma.
‡Head and neck cancer.
§Breast cancer.
NA = not applicable.
Qualitative data are number; continuous data are median and range, except for age.

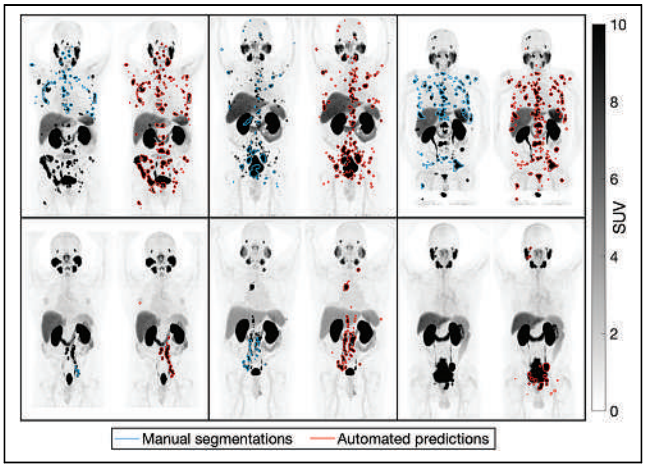

FIGURE 1. Incomplete manual tumor segmentations compared with predicted segmentations on maximum-intensity projections of PSMA PET scans of 6 patients with prostate cancer.

levels, follow-up PSA levels, PSA doubling times, and post-PSMA PET/CT therapies for 138 patients with no tumor annotations.

Datasets 3–5 consisted of ^{18}F-FDG PET/CT scans from The Cancer Imaging Archive. Dataset 3 had complete manual tumor annotations for 168, 188, and 145 patients with lung cancer, melanoma, and lymphoma, respectively (*8*). Dataset 4 had clinical information on overall staging (by the cancer staging manual of the American Joint Committee on Cancer [AJCC], seventh edition), surgery, chemotherapy, radiotherapy duration, and overall survival for 74 head and neck cancer patients with no tumor annotations (*9*). Dataset 5 had longitudinal scans of 36 breast cancer patients undergoing neoadjuvant chemotherapy (*10*). Pre- and posttherapy scans were acquired for 36 and 25 patients, respectively, with no tumor annotations. Pathologic complete response (pCR) was defined as the absence of invasive cancer in the breast or lymph nodes at definitive surgery. Non-pCR was defined as residual invasive cancer or disease progression.

Datasets 1 and 3 were used to cross-validate the segmentation task via 5-fold cross-validation. Datasets 2, 4, and 5 were used for external testing and prognostic model development.

Tumor Quantification

Tumor detection and segmentation were evaluated on a lesionwise and voxelwise basis. True-positive rate, positive predictive value, Dice similarity coefficient, false-discovery rate, true-negative rate, and negative predictive value were assessed. Tumor detection performance was compared with that of models trained only on ^{18}F-FDG or PSMA PET/CT images. Imaging measures, including molecular tumor volume (MTV), total lesion activity (TLA), number of lesions, SUV_{mean}, and SUV_{max}, were quantified from predicted segmentations.

Radiomics Analysis

We used the Standardized Environment for Radiomics Analysis based on the Image Biomarker Standardization Initiative (*11*). First-order statistical and higher-order textural features, including morphology, intensity, intensity histogram, intensity volume histogram, cooccurrence matrix, run length matrix, size zone matrix, distance zone matrix, and neighborhood gray tone difference matrix, were extracted and redundant features were removed. In total, 397 radiomics features were calculated from PET/CT volumes of interest. Radiomics classifiers using random forest detected true-positive volumes of interest via 10-fold cross-validation (*12*). Overall accuracy and receiver-operating-characteristic analysis were assessed.

Risk Stratification

A risk model for prostate cancer was developed using the extracted whole-body imaging measures. Initial PSA levels of less than 10 ng/mL, 10–20 ng/mL, or more than 20 ng/mL were assigned to low-, intermediate-, or high-risk groups, respectively (*13*). The risk model used random forest to classify low- to intermediate- versus high-risk via 10-fold cross-validation. Risk predictions and Gleason scores were combined; patients who were predicted as high-risk, with Gleason scores of at least 8, were considered high-risk. Patients predicted as low-risk, with Gleason scores of 7, and patients with Gleason scores of 6 or lower were considered low-risk. Other cases were intermediate-risk. Overall accuracy, area under the receiver-operating-characteristic (AUC) curve, follow-up PSA levels, and PSA doubling times were assessed.

Survival Analysis

A risk score for head and neck cancer incorporated imaging measures and AJCC staging. Imaging measures in the lower quartile, within the interquartile range, or in the upper quartile were assigned 0, 1, or 2 points, respectively. AJCC stages I, II, or III–IV were assigned 0, 1, or 2 points, respectively. Points were summed to yield a risk score ranging from 0 to 12. Patients with a risk score of 0, 1–9, and 10–12 were considered low-, intermediate-, and high-risk, respectively. Overall survival was estimated by the Kaplan–Meier method, with groups being compared by the log-rank test (*14*). Univariable and multivariable Cox regression models were assessed. The Harrell C-index was evaluated.

Treatment Response Prediction

Imaging measures were extracted and assessed for both pre- and posttherapy scans of breast cancer patients undergoing neoadjuvant chemotherapy. Decision tree classifiers predicted pCR via leave-one-out cross-validation using pre- and posttherapy imaging measures. Overall accuracy, AUC, area under the precision-recall curve, true-positive rate, positive predictive value, true-negative rate, and negative predictive value were assessed.

Statistical Assessment

Normality was assessed by the Shapiro–Wilk test. Statistical significance was assessed using the Wilcoxon signed-rank test, Wilcoxon rank-sum test, and McNemar test when comparing paired, unpaired, and binary observations, respectively. A P value of less than 0.05 was used to infer significant differences. The Benjamini–Hochberg method was used for multiple comparisons. Spearman rank correlation coefficients (ρ) were quantified. Receiver-operating-characteristic curves with 95% CIs were computed with 1,000 bootstrap samples. Optimal thresholds were determined by receiver-operating-characteristic analysis using the Youden index. Analyses were conducted with MATLAB (2023b) and Python (3.10.5). The approach was implemented with PyTorch (1.12.0) using an NVIDIA A6000 GPU.

RESULTS

Tumor Quantification

Illustrative examples of predicted segmentations are shown in Figures 1 and 2. Tumor detection and segmentation performances are quantified in Figure 3. Our approach yielded median true-positive rates of 0.75, 0.85, 0.87, and 0.75; median positive predictive values of 0.92, 0.76, 0.87, and 0.76; median Dice similarity coefficients of 0.81, 0.76, 0.83, and 0.73; and median false-discovery rates of 0.08, 0.24, 0.13, and 0.24 for patients with lung cancer, melanoma, lymphoma, and prostate cancer, respectively, on voxelwise segmentation. The approach yielded median true-negative rates and negative predictive values of 1.00 across all patients.

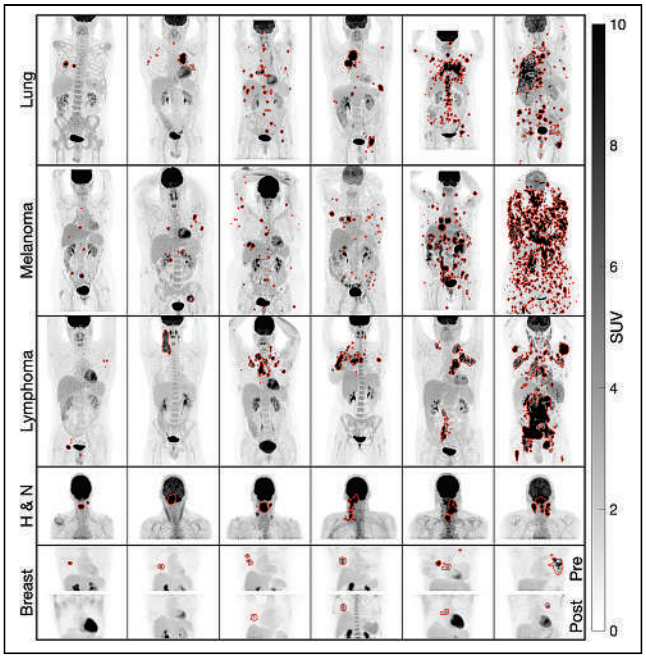

FIGURE 2. Predicted segmentations on maximum-intensity projections of ^{18}F-FDG PET scans of lung cancer, melanoma, lymphoma, head and neck cancer (H & N), and breast cancer. Pre- and posttherapy scans of breast cancer are shown (bottom row), with first 2 patients from left to right having pCR and the others being nonresponders.

The DeepSSTL approach yielded a true-positive rate of 0.77 on PSMA-RADS-4/5 lesions, with improved detection rates throughout training ($P < 0.001$) (Fig. 3C). The approach had a higher true-positive rate of 0.76 on prostate cancer lesions than did baseline models trained on only ^{18}F-FDG or PSMA PET/CT images, with true-positive rates of 0.38 and 0.63, respectively ($P < 0.001$) (Fig. 3D). Although a model trained on ^{18}F-FDG and PSMA PET/CT images had a higher true-positive rate than baseline models, the model trained on both sets of images had a higher false-discovery rate of 0.33 than did the model trained only on PSMA PET/CT images, which had a false-discovery rate of 0.28. Our DeepSSTL approach maintained a high true-positive rate and had the lowest false-discovery rate (0.25) of all models ($P < 0.05$).

The DeepSSTL approach yielded higher detection rates for lesions with higher tumor volumes across all cancer types (Supplemental Fig. 1; supplemental materials are available at http://jnm.snmjournals.org). Radiomics classifiers detected true-positive volumes of interest with overall accuracies of 0.85, 0.81, 0.74, and 0.93 and AUCs of 0.87, 0.83, 0.79, and 0.87 for patients with lung cancer, melanoma, lymphoma, and prostate cancer, respectively (Supplemental Fig. 2; Fig. 4A).

Risk Stratification

A prognostic risk model stratified prostate cancer patients by low- to intermediate- versus high-risk with an overall accuracy of 0.83 and an AUC of 0.86 (Fig. 4B). Risk scores derived from the model had positive correlations with overall PSMA-RADS scores ($\rho = 0.44$, $P < 0.001$) and post-PSMA PET therapies ($\rho = 0.37$, $P < 0.001$) (Figs. 4C and 4D). Risk stratifications by imaging measures, initial PSA levels, Gleason scores, risk model predictions, and the risk model predictions combined with Gleason scores were evaluated (Supplemental Fig. 3). Optimal thresholds for MTV, TLA, lesion number, SUV_{mean}, SUV_{max}, and Gleason score were 22.00 cm^3, 174.56 $SUV \cdot cm^3$, 10, 9.38, 38.87, and 8, respectively.

High-risk patients classified by MTV, TLA, the risk model, and the risk model combined with Gleason scores had higher follow-up PSA levels than low- to intermediate-risk patients ($P < 0.05$).

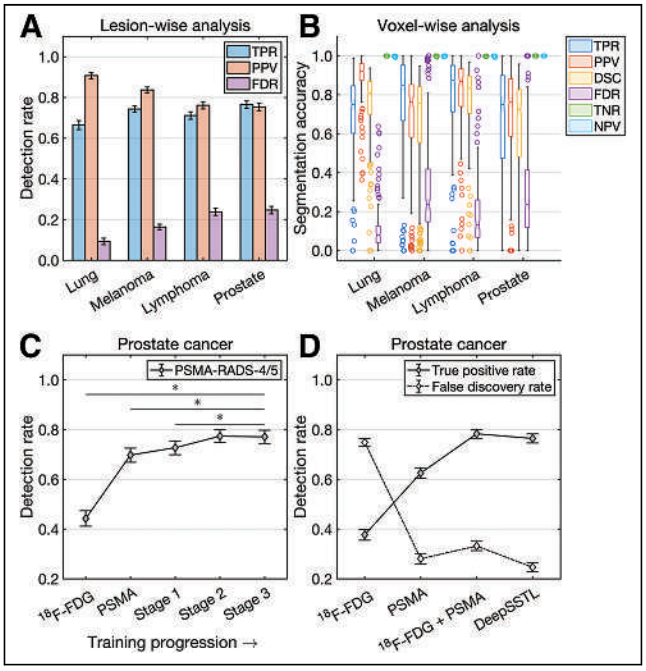

FIGURE 3. (A and B) Lesionwise (A) and voxelwise (B) analysis of tumor detection and segmentation. (C and D) Prostate cancer detection rates by DeepSSTL approach throughout different stages of training progression (C) and compared with baseline models (D). DSC = Dice similarity coefficient; FDR = false-discovery rate; NPV = negative predictive value; PPV = positive predictive value; TNR = true-negative rate; TPR = true-positive rate.

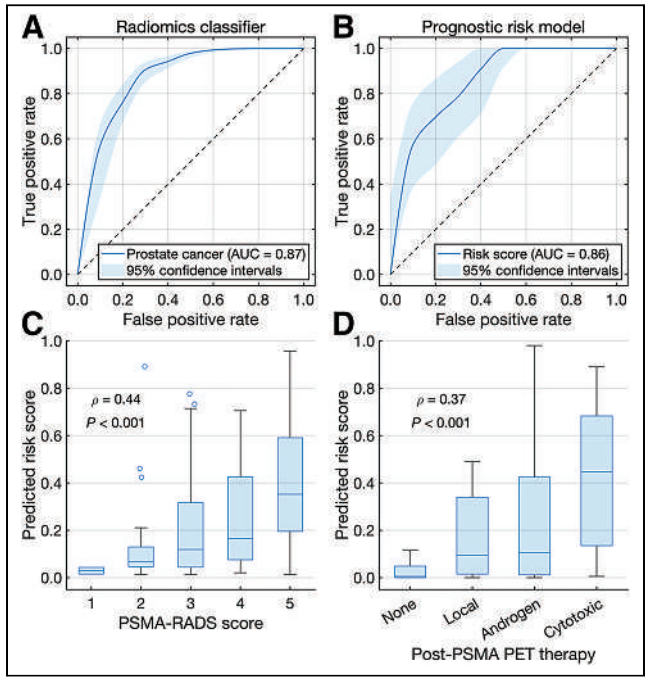

FIGURE 4. (A and B) Receiver-operating-characteristic curves for radiomics classifier (A) and risk model (B) for prostate cancer. (C and D) Box plots of predicted risk scores vs. overall PSMA-RADS scores (C) and post-PSMA PET therapies (D).

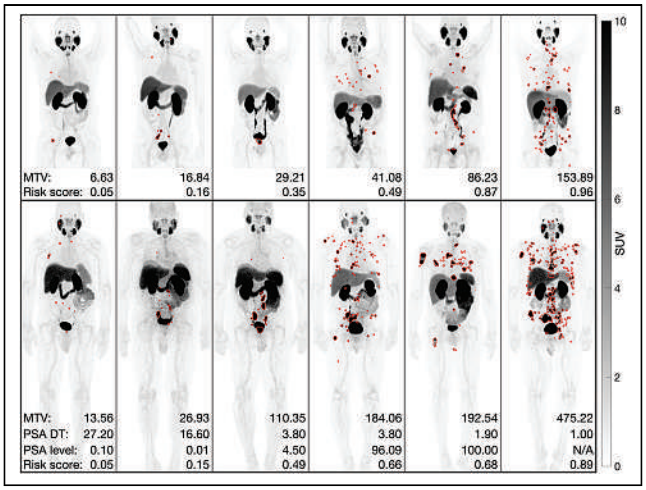

FIGURE 5. Predicted segmentations on maximum-intensity projections of PSMA PET scans of prostate cancer from datasets 1 (top row) and 2 (bottom row). MTV, PSA doubling times (DT), and follow-up PSA levels were measured in cubic centimeters, months, and ng/mL, respectively.

High-risk patients classified by Gleason scores and the risk model with Gleason scores had shorter PSA doubling times than low- to intermediate-risk patients ($P < 0.05$). Low-, intermediate-, and high-risk patients classified by the risk model combined with Gleason scores had mean follow-up PSA levels of 9.18, 26.92, and 727.46 ng/mL and mean PSA doubling times of 8.67, 8.18, and 4.81 mo, respectively. Illustrative examples are shown in Figure 5.

Survival Analysis

Imaging measures were extracted from ^{18}F-FDG PET/CT scans of head and neck cancer patients. MTV (measured in cm^3), TLA, SUV_{mean}, and SUV_{max} were used as continuous variables in the survival analysis. MTV, TLA, lesion number, SUV_{mean}, SUV_{max}, age, AJCC stage, and the risk score were significantly associated with overall survival by univariable Cox regression analysis (Fig. 6A). Age and risk score were independent prognosticators of overall survival by multivariable Cox regression analysis. The risk score yielded a C-index value of 0.71, indicating concordance between overall survival and the predicted risk scores. Hazard ratios with 95% CI and C-index values are reported in Table 2.

Stratification of patients was based on median values for all imaging measures and plotted using Kaplan–Meier estimators (Supplemental Fig. 4). For MTV, TLA, and SUV_{max}, patients in the upper half had a significantly shorter median overall survival ($P < 0.05$). Stratification of patients was based on the risk score and plotted using Kaplan–Meier estimators (Fig. 6B). High-risk patients had a shorter median overall survival than low- or intermediate-risk patients (1.64 y vs. median not reached, $P < 0.001$). Intermediate-risk patients had a shorter median overall survival than low-risk patients ($P < 0.05$).

Treatment Response Prediction

Imaging measures were extracted from pre- and posttherapy ^{18}F-FDG PET/CT scans of breast cancer patients (Fig. 6C). Posttherapy measures were all lower for pCR than for non-pCR, indicating a higher posttherapy tumor burden for nonresponders ($P < 0.05$). Optimal thresholds of pretherapy measures for MTV, TLA, lesion number, SUV_{mean}, and SUV_{max} were 188.96 cm^3, 96.46 $SUV \cdot cm^3$, 2, 1.85, and 7.84, respectively. Accuracy metrics for predicting pCR using pretherapy measures are reported in Table 3. Classifiers trained to predict pCR using only pretherapy measures (decision tree 1) and both pre- and posttherapy measures (decision tree 2) had overall accuracies of 0.72 and 0.84, AUCs of 0.72 and 0.76, and areas under the precision-recall curve of 0.51 and 0.67, respectively.

DISCUSSION

Molecular imaging modalities provide important molecular insights into the pathophysiologic processes underlying disease and are powerful tools for the detection and localization of cancer and metastases (*15*). Deep learning approaches have been developed for research and clinical care in nuclear medicine (*7*,*16*–*21*). Methods developed for narrow applications, such as image classification and segmentation, often require vast training datasets with physician-defined annotations, which are expensive to produce, subject to interreader variability, and unscalable. Accordingly, we developed a DeepSSTL approach and used it to perform fully automated whole-body tumor detection and segmentation on ^{18}F-FDG and PSMA PET/CT images of 1,019 patients with 6 different cancer types using limited annotations. The proposed approach demonstrated accurate quantification of molecular tumor burden and prediction of risk, survivability, and treatment response. Our approach may also play a role in longitudinal tumor quantification to track whole-body tumor volume changes in response to therapy.

The approach performed domain adaptation, with source domain ^{18}F-FDG PET/CT

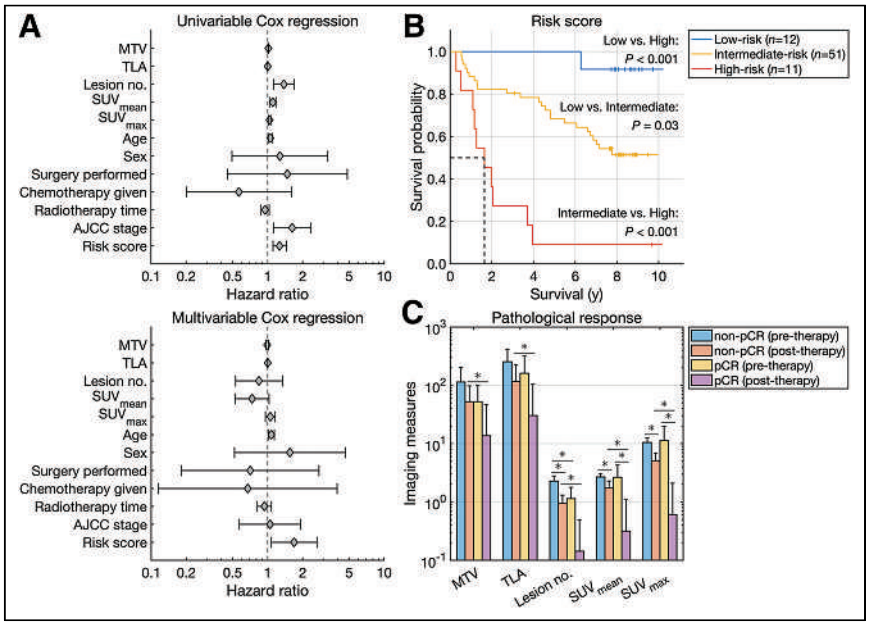

FIGURE 6. (A) Forest plots of univariable and multivariable Cox regression analysis. (B) Kaplan–Meier survival curves for head and neck cancer. (C) Imaging measures quantified from pre- and posttherapy scans of breast cancer.

TABLE 2
Cox Regression Analysis and Respective C-Index Values

	Univariable Cox regression			Multivariable Cox regression			
Parameter	Hazard ratio	95% CI	*P*	Hazard ratio	95% CI	*P*	C index
MTV	1.01	1.01–1.02	<0.001	0.99	0.97–1.02	0.57	0.68
TLA	1.00	1.00–1.00	<0.001	1.00	1.00–1.00	0.27	0.69
Lesion no.	1.38	1.13–1.69	0.002	0.84	0.53–1.34	0.47	0.69
SUV_{mean}	1.11	1.04–1.18	0.002	0.74	0.53–1.03	0.07	0.65
SUV_{max}	1.04	1.02–1.06	<0.001	1.06	0.96–1.17	0.27	0.65
Age	1.06	1.01–1.10	0.02	1.08	1.02–1.14	0.01	0.61
Sex	1.27	0.49–3.28	0.62	1.56	0.52–4.67	0.43	0.47
Surgery	1.48	0.45–4.83	0.52	0.71	0.18–2.76	0.62	0.50
Chemotherapy	0.57	0.20–1.61	0.29	0.67	0.12–3.95	0.66	0.47
Radiotherapy time	0.95	0.88–1.03	0.23	0.94	0.82–1.08	0.38	0.46
AJCC stage	1.62	1.12–2.34	0.01	1.05	0.57–1.92	0.88	0.61
Risk score	1.27	1.11–1.45	<0.001	1.69	1.07–2.66	0.02	0.71

images of patients with lung cancer, melanoma, and lymphoma with complete manual annotations being used for training and cross-validation (Figs. 1 and 2). DeepSSTL was applied and enabled tumor segmentation on target domain PSMA PET/CT images of prostate cancer patients with incomplete annotations. Despite limited annotations, the approach yielded accurate tumor segmentation on PSMA PET/CT and achieved a high detection rate of PSMA-RADS-4/5 lesions, for which prostate cancer was highly likely, while limiting false discoveries by leveraging radiomics analysis (Fig. 3). The approach generalized across ^{18}F-FDG– and PSMA-targeted radiotracers and performed well on external test datasets with out-of-distribution cancers not seen during training or cross-validation, including head and neck and breast cancers.

A risk model for prostate cancer using PSMA PET/CT imaging measures achieved an accuracy of 0.83 in classifying low- to intermediate- versus high-risk. Higher-risk scores were predicted for patients who received higher PSMA-RADS scores and systemic therapies, corroborating the risk model against 2 separate indications (Fig. 4). Although SUV measures and initial PSA levels were individually poor predictors of risk based on follow-up PSA levels and PSA doubling times, respectively, the risk model yielded improved performance by incorporating all molecular imaging measures, including MTV, TLA, number of lesions, SUV_{mean}, and SUV_{max} (Fig. 5). Risk model predictions combined with Gleason scores were validated against follow-up PSA levels and PSA doubling times and yielded significant differences between risk groups.

A risk score for head and neck cancer incorporated ^{18}F-FDG PET/CT imaging measures and overall AJCC staging based on tumor–node–metastasis classification. The risk score and all imaging measures were significant prognosticators of overall survival by univariable Cox regression. The risk score was a negative prognosticator of overall survival with a hazard ratio of 1.69 by multivariable Cox regression, with patients who had higher risk levels having a shorter median overall survival by Kaplan–Meier analysis (Fig. 6). Risk stratification and survival estimation were improved when imaging measures were combined with Gleason scores and AJCC staging for patients with prostate cancer and head and neck cancer, respectively, indicating synergy between molecular imaging measures and clinical, pathologic, and anatomic factors.

A classifier for breast cancer using ^{18}F-FDG PET/CT imaging measures from pre- and posttherapy scans predicted pCR with an accuracy of 0.84. Although the classifier achieved a positive predictive value of 1.00, true-negative rate of 1.00, and negative

TABLE 3
Predicting pCR

Model and parameter	Accuracy	AUC	Area under precision-recall curve	True-positive rate	Positive predictive value	True-negative rate	Negative predictive value
MTV	0.42	0.55	0.28	1.00	0.32	0.19	1.00
TLA	0.67	0.58	0.30	0.50	0.42	0.73	0.79
Lesion no.	0.47	0.67	0.39	0.80	0.32	0.35	0.82
SUV_{mean}	0.72	0.44	0.28	0.30	0.50	0.88	0.77
SUV_{max}	0.64	0.44	0.27	0.40	0.36	0.73	0.76
Decision tree 1	0.72	0.72	0.51	0.50	0.50	0.81	0.81
Decision tree 2	0.84	0.76	0.67	0.43	1.00	1.00	0.82

predictive value of 0.82, the classifier had a true-positive rate of 0.43. Interestingly, predicting pCR with an optimized MTV threshold yielded a perfect true-positive rate and negative predictive value of 1.00 with an accuracy of 0.42, highlighting the trade-off between prediction strategies. A classifier using only pretherapy measures predicted pCR with an accuracy of 0.72, demonstrating the feasibility of predicting pCR to inform treatment management before neoadjuvant therapy and surgery using a small cohort of 36 patients. Larger prospective studies will be required to validate the approach.

^{18}F-FDG PET/CT has broad utility in oncologic imaging by targeting glycolytic metabolism present in most malignancies. Many prostate cancers are not ^{18}F-FDG–avid, and alternative imaging agents have been developed to target metabolic pathways, including ^{18}F-fluciclovine and ^{11}C-choline, and specific cell-surface receptors, such as PSMA (*15*). PSMA-targeted agents, including ^{18}F-DCFPyL and ^{68}Ga-PSMA-11, have demonstrated prostate cancer detection rates superior to those of conventional imaging (*15*).

Given the wide array of available radiotracers, artificial intelligence approaches must generalize across molecular imaging agents to support automated analysis. Indeed, our approach performed whole-body tumor quantification on ^{18}F-FDG and PSMA PET/CT images of multiple cancers despite the differences in biodistribution between ^{18}F-FDG and PSMA-targeted uptake patterns. A prospective study by Buteau et al. found that an SUV_{mean} of 10 or higher on PSMA PET and an MTV lower than 200 cm^3 on ^{18}F-FDG PET were predictive biomarkers for a higher PSA response to ^{177}Lu-PSMA therapy in metastatic castration-resistant prostate cancer (*3*). Interestingly, our retrospective analysis found that an SUV_{mean} of 9.38 on PSMA PET was the optimal cutoff for prostate cancer risk stratification. That agreement, combined with the generalizability of our approach, highlights the potential utility of the proposed approach for selection of patients for PSMA-targeted radioligand therapy.

We and others have developed convolutional neural networks for tasks on PSMA PET, including classification according to the PSMA-RADS and PROMISE (Prostate Cancer Molecular Imaging Standardized Evaluation) frameworks and segmentation of intraprostatic gross tumor volume and metastases (*7*,*22*–*24*). Jemaa et al. proposed cascaded 2- and 3-dimensional convolutional neural networks with a U-net architecture for region-specific tumor segmentation on ^{18}F-FDG PET/CT (*25*). Unlike approaches focusing on specific volumes of interest or cross-sectional slices, our approach provides fully automated whole-body PET/CT tumor quantification and lesionwise radiomics analysis to support more precise staging, disease tracking, and therapeutic monitoring. We used the state-of-the-art nnU-net architecture (*6*) as a backbone for our approach and achieved robust tumor quantification. nnU-net was among the top performers in the autoPET challenge for automated tumor segmentation on ^{18}F-FDG PET/CT, with a common feature of the top algorithms being the use of a U-net backbone (*26*). Comparison of the performance of the proposed DeepSSTL approach to publicly available benchmarks, such as the autoPET challenge, is an important area of investigation. Another approach used nnU-net for normal-organ segmentation on ^{18}F-FDG PET/CT (*27*). Our DeepSSTL approach may also incorporate multiorgan segmentation for systemic analysis and radiation dosimetry applications.

Deep learning models require training data with extensive expert annotations. That limitation is partially ameliorated by our DeepSSTL approach that learns the segmentation task on the target domain using incomplete annotations. However, our approach remains reliant on manual annotations for performance assessment, which may be confounded by inaccurate or inconsistent annotations. Consensus readings or histopathologic validation may be warranted in such scenarios. Alternatively, realistic simulated images with known ground truth may be used to assess task-based performance (*17*). Our approach may incorporate physician-in-the-loop continuous feedback and assist physicians by flagging potential foci of disease as a second reader.

A limitation of this study was that prostate cancer detection was evaluated on advanced PSMA-RADS-4/5 lesions and that testing on lower PSMA-RADS scores was lacking. Evaluation of indeterminant findings, such as PSMA-RADS-3, may provide further insights into the true positivity of such lesions (*28*). Another limitation was that the available retrospective imaging and clinical datasets were heterogeneous, dependent on cancer type. However, such heterogeneity reflects real-world clinical settings where information is often incomplete across patient cohorts. Although evaluation on independent test data is ideal, the performance of the proposed approach was evaluated via cross-validation because of the limited availability of heterogeneous datasets. All aspects of model training and hyperparameter optimization took place only on the training folds, with the hold-out test folds being used only during evaluation to provide accurate estimates of model performance. Additionally, performance estimates of predicting pCR for patients with breast cancer may be impacted by the limited data and the class imbalance between patients with pCR versus non-pCR (Table 3). Precision-recall curve metrics were reported in addition to overall accuracy and AUC to evaluate classifier performance more thoroughly in the context of such class imbalances.

CONCLUSION

The DeepSSTL approach performed fully automated, whole-body tumor segmentation on PET/CT images using limited tumor annotations and generalized across patients with 6 different cancer types imaged with ^{18}F-FDG and PSMA-targeted radiotracers. Molecular imaging measures were automatically quantified and demonstrated prognostic value for risk stratification, survival estimation, and treatment response prediction.

KEY POINTS

QUESTION: How can we develop generalizable approaches for automated whole-body tumor quantification on PET/CT with limited manual annotations?

PERTINENT FINDINGS: Our DeepSSTL approach performed accurate tumor segmentation on the ^{18}F-FDG and PSMA PET/CT images of 1,019 patients with 6 different cancers using incomplete annotations. The approach incorporated radiomics analysis and achieved a high tumor detection rate while minimizing false discoveries. Molecular imaging measures were automatically quantified and were predictive of risk stratification, overall survival, and treatment response.

IMPLICATIONS FOR PATIENT CARE: The developed approach reduces physician workload by providing generalizable tumor segmentation on PET/CT and automatic quantification of prognostic molecular parameters.

DISCLOSURE

Financial support was provided, in part, by National Institutes of Health grants R01CA184228, R01CA134675, P41EB024495,

U01CA140204, and K99CA287045. The content of this work is solely the responsibility of the authors and does not necessarily represent the official views of the National Institutes of Health. No other potential conflict of interest relevant to this article was reported.

ACKNOWLEDGMENT

We thank The Cancer Imaging Archive for providing data access.

REFERENCES

1. Siegel RL, Miller KD, Wagle NS, Jemal A. Cancer statistics, 2023. *CA Cancer J Clin.* 2023;73:17–48.
2. Hanna TP, King WD, Thibodeau S, et al. Mortality due to cancer treatment delay: systematic review and meta-analysis. *BMJ.* 2020;371:m4087.
3. Buteau JP, Martin AJ, Emmett L, et al. PSMA and FDG-PET as predictive and prognostic biomarkers in patients given [^{177}Lu] Lu-PSMA-617 versus cabazitaxel for metastatic castration-resistant prostate cancer (TheraP): a biomarker analysis from a randomised, open-label, phase 2 trial. *Lancet Oncol.* 2022;23:1389–1397.
4. Hatt M, Krizsan AK, Rahmim A, et al. Joint EANM/SNMMI guideline on radiomics in nuclear medicine. *Eur J Nucl Med Mol Imaging.* 2023;50:352–375.
5. Clark K, Vendt B, Smith K, et al. The Cancer Imaging Archive (TCIA): maintaining and operating a public information repository. *J Digit Imaging.* 2013;26:1045–1057.
6. Isensee F, Jaeger PF, Kohl SAA, Petersen J, Maier-Hein KH. nnU-Net: a self-configuring method for deep learning-based biomedical image segmentation. *Nat Methods.* 2021;18:203–211.
7. Leung KH, Rowe SP, Leal JP, et al. Deep learning and radiomics framework for PSMA-RADS classification of prostate cancer on PSMA PET. *EJNMMI Res.* 2022;12:76.
8. Gatidis S, Hepp T, Früh M, et al. A whole-body FDG-PET/CT dataset with manually annotated tumor lesions. *Sci Data.* 2022;9:601.
9. Aerts HJWL, Velazquez ER, Leijenaar RTH, et al. Decoding tumour phenotype by noninvasive imaging using a quantitative radiomics approach. *Nat Commun.* 2014;5:4006.
10. Li X, Abramson RG, Arlinghaus LR, et al. Multiparametric magnetic resonance imaging for predicting pathological response after the first cycle of neoadjuvant chemotherapy in breast cancer. *Invest Radiol.* 2015;50:195–204.
11. Ashrafinia S. *Quantitative Nuclear Medicine Imaging Using Advanced Image Reconstruction and Radiomics*. Dissertation. The Johns Hopkins University; 2019.
12. Breiman L. Random forests. *Mach Learn.* 2001;45:5–32.
13. D'Amico AV, Whittington R, Malkowicz SB, et al. Biochemical outcome after radical prostatectomy, external beam radiation therapy, or interstitial radiation therapy for clinically localized prostate cancer. *JAMA.* 1998;280:969–974.
14. Bland JM, Altman DG. Survival probabilities (the Kaplan-Meier method). *BMJ.* 1998;317:1572–1580.
15. Rowe SP, Pomper MG. Molecular imaging in oncology: current impact and future directions. *CA Cancer J Clin.* 2022;72:333–352.
16. Leung KH, Rowe SP, Pomper MG, Du Y. A three-stage, deep learning, ensemble approach for prognosis in patients with Parkinson's disease. *EJNMMI Res.* 2021;11:52.
17. Leung KH, Marashdeh W, Wray R, et al. A physics-guided modular deep-learning based automated framework for tumor segmentation in PET. *Phys Med Biol.* 2020;65:245032.
18. Leung K, Sadaghiani MS, Dalaie P, et al. A deep learning-based approach for lesion classification in 3D ^{18}F-DCFPyL PSMA PET images of patients with prostate cancer [abstract]. *J Nucl Med.* 2020;61(suppl 1):527.
19. Leung K, Ashrafinia S, Sadaghiani MS, et al. A fully automated deep-learning based method for lesion segmentation in ^{18}F-DCFPyL PSMA PET images of patients with prostate cancer [abstract]. *J Nucl Med.* 2019;60(suppl 1):399.
20. Leung K, Marashdeh W, Wray R, et al. A deep-learning-based fully automated segmentation approach to delineate tumors in FDG-PET images of patients with lung cancer [abstract]. *J Nucl Med.* 2018;59(suppl 1):323.
21. Leung KH, Salmanpour MR, Saberi A, et al. Using deep-learning to predict outcome of patients with Parkinson's disease. In: *2018 IEEE Nuclear Science Symposium and Medical Imaging Conference Proceedings (NSS/MIC)*. IEEE; 2018:1–4.
22. Capobianco N, Sibille L, Chantadisai M, et al. Whole-body uptake classification and prostate cancer staging in ^{68}Ga-PSMA-11 PET/CT using dual-tracer learning. *Eur J Nucl Med Mol Imaging.* 2022;49:517–526.
23. Holzschuh JC, Mix M, Ruf J, et al. Deep learning based automated delineation of the intraprostatic gross tumour volume in PSMA-PET for patients with primary prostate cancer. *Radiother Oncol.* 2023;188:109774.
24. Xu Y, Klyuzhin I, Harsini S, et al. Automatic segmentation of prostate cancer metastases in PSMA PET/CT images using deep neural networks with weighted batch-wise dice loss. *Comput Biol Med.* 2023;158:106882.
25. Jemaa S, Fredrickson J, Carano RAD, Nielsen T, de Crespigny A, Bengtsson T. Tumor segmentation and feature extraction from whole-body FDG-PET/CT using cascaded 2D and 3D convolutional neural networks. *J Digit Imaging.* 2020;33:888–894.
26. Gatidis S, Früh M, Fabritius M, et al. The autoPET challenge: towards fully automated lesion segmentation in oncologic PET/CT imaging. Research Square website. https://www.researchsquare.com/article/rs-2572595/v1. Published June 14, 2023. Accessed February 9, 2024.
27. Shiyam Sundar LK, Yu J, Muzik O, et al. Fully automated, semantic segmentation of whole-body ^{18}F-FDG PET/CT images based on data-centric artificial intelligence. *J Nucl Med.* 2022;63:1941–1948.
28. Werner RA, Hartrampf PE, Fendler WP, et al. Prostate-specific membrane antigen reporting and data system version 2.0. *Eur Urol.* 2023;84:491–502.

Errata

In the article "MRI or 18F-FDG PET for Brain Age Gap Estimation: Links to Cognition, Pathology, and Alzheimer Disease Progression," by Doering et al. (*J Nucl Med*. 2024;65:147–155), the footnote of Table 1 mistakenly reads, "*Significantly different from ADNI CD."; however, the footnote should read, "*Significantly different from ADNI CN." The error has been corrected in the online article. We regret the error.

In the article, "^{177}Lu-Prostate-Specific Membrane Antigen Therapy in Patients with Metastatic Castration-Resistant Prostate Cancer and Prior ^{223}Ra (RALU Study)" by Rahbar et al. (*J Nucl Med.* 2023;64:1925–1931), some errors have been identified in Table 1, the abstract, main body of the article, and the supplemental data. The corrected Table 1 is provided here. The corrected Supplemental Table 4 can be found in the supplemental data online. The errors do not change the message or key findings of the paper. However, the authors regret the errors.

In Table 1 and in the first paragraph of the Results section of the main body of the article, the number (percentage of patients with ECOG PS 1 and 2 was incorrectly stated as being 82 (62) and 51 (38), respectively. The correct ECOG values are as follows: *ECOG 1, 17 (13); ECOG 2, 49 (37); ECOG 3, 13 (10); ECOG 4, 2 (2); missing, 52 (39)*.

In Table 1, the Results section of the abstract, the second paragraph of the Results section in the main body of the article, and the graphical abstract, the number (percentage) of patients who received at least 4 prior life-prolonging therapies was incorrectly stated as being 75 (56). The correct values are *76 (57)*.

In the Results section of the abstract and the second paragraph of the Results section in the main body of the article, the percentage of patients who received 5–6 ^{223}Ra injections was incorrectly stated as being 73%. The correct percentage is *74%*.

In Supplemental Table 4, the number (percentage) of patients with ECOG PS 1 or 2 was incorrectly stated as 37 (65) and 20 (35), respectively, for patients who received the Ra→Tax→Lu treatment sequence and 31 (62) and 19 (38), respectively, for patients who received the Tax→Ra→Lu treatment sequence. The correct ECOG PS values for Ra→Tax→Lu treatment are as follows: *ECOG 1, 6 (11); ECOG 2, 22 (39); ECOG 3, 7 (12); ECOG 4, 1 (2); missing 21 (37)*. The correct ECOG PS values for Tax→Ra→Lu treatment are as follows: *ECOG 1, 7 (14); ECOG 2, 16 (32); ECOG 3, 6 (12); ECOG 4, 1 (2); missing, 20 (40)*.

Table 1. Baseline Demographics and Clinical Characteristics Before or at Start of ^{177}Lu-PSMA

Characteristic	Data
Patients	133
Age (y)	73 (49–90)
ECOG PS	
1	17 (13)
2	49 (37)
3	13 (10)
4	2 (2)
Missing	52 (39)
PSA* (ng/mL) (*n* = 130)	286 (1–12,229)
ALP* (U/L) (*n* = 112)	146 (23–973)
Extent of metastatic disease†	
Bone metastases with lymph node metastases	63 (47)
Bone metastases without lymph node metastases	33 (25)
Visceral metastases	36 (27)
Prior therapies for mCRPC, *n* (%)	
≥4 Life-prolonging therapies‡	76 (57)
^{223}Ra	133 (100)
Number of ^{223}Ra injections	
1–4	35 (26)
5–6	98 (74)
Abiraterone	95 (71)
Enzalutamide	92 (69)
Abiraterone and enzalutamide	71 (53)
Chemotherapy lines§	
0	31 (23)
1	67 (50)
≥2	35 (26)
Docetaxel	99 (74)
Cycles‖	
1–4	27 (24)
≥5	59 (53)
Missing/unknown	26 (23)
Cabazitaxel	30 (23)
Cycles¶	
1–4 cycles	7 (21)
≥5 cycles	14 (42)
Missing/unknown	12 (36)

*In case of multiple measures, value nearest to ^{177}Lu-PSMA start was chosen.
†Prebaseline period, patient may have multiple metastatic diseases.
‡Docetaxel, cabazitaxel, abiraterone, enzalutamide, ^{223}Ra.
§Chemotherapies with same start date ± 15 d were counted as 1 line.
‖*n* = 112; percentages were based on number of docetaxel therapies (i.e., patients who received 2 lines of docetaxel were counted twice).
¶*n* = 33; percentages were based on number of cabazitaxel therapies (i.e., patients who received 2 lines of cabazitaxel were counted twice).
ECOG PS = Eastern Cooperative Oncology Group performance status.
Qualitative data are number and percentage; continuous data are median and range.

Performance Evaluation of the uMI Panorama PET/CT System in Accordance with the National Electrical Manufacturers Association NU 2-2018 Standard

Guiyu Li*, Wenhui Ma*, Xiang Li*, Weidong Yang, Zhiyong Quan, Taoqi Ma, Junling Wang, Yunya Wang, Fei Kang, and Jing Wang

Department of Nuclear Medicine, Xijing Hospital, Fourth Military Medical University, Xi'an, China

The uMI Panorama is a novel PET/CT system using silicon photomultiplier and application-specific integrated circuit technologies and providing exceptional spatial and time-of-flight (TOF) resolutions. The objective of this study was to assess the physical performance of the uMI Panorama in accordance with the National Electrical Manufacturers Association (NEMA) NU 2-2018 standard. **Methods:** Spatial resolution, sensitivity, count rate performance, accuracy, image quality, and TOF resolution were evaluated in accordance with the guidelines outlined in the NEMA NU 2-2018 standard. Energy resolution was determined using the same dataset acquired for the count rate performance evaluation. Images from a Hoffman brain phantom, a mini-Derenzo phantom, and 3 patient studies were evaluated to demonstrate system performance. **Results:** The transaxial spatial resolution at full width at half maximum was measured as 2.88 mm with a 1-cm offset from the center axial field of view. The sensitivity at the center axial field of view was 20.1 kcps/MBq. At an activity concentration of 73.0 kBq/mL, the peak noise-equivalent count rate (NECR) reached 576 kcps with a scatter fraction of approximately 33.2%. For activity concentrations at or below the peak NECR, the maximum relative count rate error among all slices remained consistently below 3%. When assessed using the NEMA image quality phantom, overall image contrast recovery ranged from 63.2% to 88.4%, whereas background variability ranged from 4.2% to 1.1%. TOF resolution was 189 ps at 5.3 kBq/mL and was consistently lower than 200 ps for activity concentrations at or below the peak NECR. The patient studies demonstrated that scans at 2 min/bed produced images characterized by low noise and high contrast. Clear delineation of nuclei, spinal cords, and other substructures of the brain was observed in the brain PET images. **Conclusion:** uMI Panorama, the world's first commercial PET system with sub–200-ps TOF resolution, demonstrated fine spatial and fast TOF resolutions, robust count rate performance, and high quantification accuracy across a wide range of activity levels. This advanced technology offers enhanced diagnostic capability for detecting small and low-contrast lesions while showing promising potential under high-count-rate imaging scenarios.

Key Words: NEMA; performance evaluation; uMI Panorama PET/CT; time of flight

J Nucl Med 2024; 65:652–658
DOI: 10.2967/jnumed.123.265929

The concept of using time-of-flight (TOF) information to better determine the location of positron annihilation in PET was first introduced during the early stages of PET development (*1*). By measuring the difference in arrival time between the detection of 2 coincident photons, it is possible to determine the annihilation position along a line of response (LOR) within a spatial uncertainty of $c\Delta t/2$, where c and Δt represent the speed of light and the timing resolution, respectively. The incorporation of TOF not only expedites PET reconstruction convergence but also reduces image noise and enhances the image signal-to-noise ratio by constraining the LORs within a smaller image volume during the image reconstruction process (*2,3*). In analytic image reconstruction algorithms, compared with non-TOF PET, TOF PET can achieve a relative gain in image signal-to-noise ratio equal to the square root of the object size divided by the product of speed of light and the system's timing resolution (*4–8*).

The first TOF PET scanner was developed in the 1980s by coupling cesium fluoride or barium fluoride scintillators with photomultiplier tubes, achieving a TOF resolution ranging from 400 to 600 ps (*9,10*). However, factors such as poor stopping power and low light yield limited the use of cesium fluoride– or barium fluoride–based TOF PET systems to primarily high-count-rate brain or cardiac studies. The introduction of lutetium-based scintillation materials such as lutetium oxyorthosilicate and lutetium-yttrium oxyorthosilicate (LYSO) significantly improved sensitivity while maintaining TOF resolution ranging from 450 to 600 ps (*11–16*).

In recent years, silicon photomultipliers (SiPMs) have made remarkable progress as novel photodetectors with enhanced photodetection efficiency, reduced detector noise/cross talk, and improved timing performance (*17*). As new photodetectors with linear arrays or matrices of various sizes, SiPMs are progressively preferred as the photodetectors for the next generation of commercial TOF PET scanners. Furthermore, advancements in photodetector technology have led to the development of PET detectors with expanded coverage and reduced signal multiplexing (i.e., the number of crystals per photosensor channel), aiming to improve both timing and spatial resolutions. These detectors require low power consumption and highly integrated readout electronics that allow for the individual acquisition of charge and timing information from tens of thousands of SiPM channels. Consequently, dedicated TOF PET application-specific integrated circuit (ASIC) chips have been developed and implemented in various commercial TOF PET scanners (*18–20*). These new scanners have achieved improved TOF resolution, sensitivity, and spatial resolution compared with photomultiplier tube–based systems, resulting in improved lesion detectability, decreased scan time, and reduced injected radioactivity (*21–24*).

Received Apr. 24, 2023; revision accepted Jan. 11, 2024.
For correspondence or reprints, contact Jing Wang (13909245902@163.com) or Fei Kang (fmmukf@qq.com).
*Contributed equally to this work.
Published online Feb. 22, 2024.

The uMI Panorama (United Imaging Health Care) is a novel digital PET/CT system that uses SiPM-based detectors coupled with LYSO crystals of $2.76 \times 2.76 \times 18.1$ mm^3. The equipped modular uExcel detector platform provides flexibility to vary the axial field of view (FOV). To enhance signal quality and minimize the effects of dead time, an intricately designed multichannel ASIC capable of precise time and amplitude measurements is used.

The aim of this study was to assess the physical performance of the uMI Panorama system in accordance with the National Electrical Manufacturers Association (NEMA) NU 2-2018 standard (*25*). Furthermore, an initial evaluation of its capabilities was conducted by assessing images acquired using a Hoffman brain phantom, a mini-Derenzo phantom, and 3 patient studies.

MATERIALS AND METHODS

PET/CT System

The uMI Panorama PET/CT system consists of an SiPM-based PET scanner with LYSO crystals and a 160-slice clinical CT scanner. The CT scanner is equipped with a liquid metal bearing x-ray tube, capable of rotating at a maximum speed of 0.25 s/360° and achieving a minimum slice thickness of 0.5 mm. The PET system has a transaxial FOV of 76.0 cm and an axial FOV of 35.1 cm. The system comprises 34 detector modules, with each module consisting of 5 axial "cells" with an intercell gap of 2.2 mm. The PET system's extendable design allows for the extension of the axial FOV of the scanner by concatenating different numbers of axial "cells."

Each "cell" comprises a 2×2 matrix of miniblocks, and each miniblock consists of a 4×4 matrix of microblocks. Each microblock has a 3×3 array with a pitch size of 2.85 mm. The total number of crystals is 816×120 (transaxial $\times$ axial). Additionally, each microblock is coupled to a 2×2 SiPM array, achieving an Anger multiplexing ratio of 9:4 for crystal identification. Two multichannel ASIC chips are integrated into each miniblock to obtain the charge and arrival times from SiPMs in each array.

Raw PET coincidence data are stored in list-mode format. The TOF measurement is discretized into 6.1-ps bins, and the energy measurement is discretized into 1-keV bins within an energy window of 430–650 keV. Detectors within the same miniblock share energy information, enabling the recovery of intercrystal scattered events from 1 microblock to another within the same miniblock (*26*).

Measurements

Spatial Resolution. Spatial resolution was assessed by imaging an ^{18}F-FDG point source (0.77 MBq) that had an inner diameter of 0.5 mm and an axial length of less than 1 mm and that was encapsulated at the end of a capillary tube. The source was positioned at 2 axial planes: 1/2 axial FOV and 1/8 axial FOV from the end of the scanner. At each axial plane, resolution measurements were obtained at 3 transaxial positions (x, y): (0, 1 cm), (0, 10 cm), and (0, 20 cm). List-mode data of LORs with oblique angles of less than 3.7° were rebinned into 2-dimensional sinograms using the Fourier rebinning method (*27*). The data were subsequently reconstructed using the 2-dimensional filtered backprojection algorithm without attenuation correction, scatter correction, or postreconstruction smoothing. The voxel size was set to $0.6 \times 0.6 \times 0.8$ mm^3. The axial, radial, and tangential resolutions were evaluated in accordance with the NEMA NU 2-2018 standard. Additionally, PET resolution performance was further assessed using a mini-Derenzo phantom. This phantom consisted of hot rods with various diameters (1.6, 2.0, 2.4, 3.6, 4.0, and 4.8 mm) distributed across 6 sectors. The center-to-center spacing between rods within a given sector was twice the rod diameter. Initially filled with 16.3 MBq of ^{18}F-FDG, the phantom was imaged for 10 min with the hot rods oriented in line with the axial direction. The same phantom, with an initial activity of 8.6 MBq, was then imaged for 20 min with the hot rods oriented perpendicular to the axial direction. Image reconstruction was performed using the TOF ordered-subset expectation maximization (OSEM) algorithm with the point spread function (PSF), 7 iterations, 10 subsets, and a 1-mm gaussian postreconstruction filter. The voxel size of the image was $0.6 \times 0.6 \times 0.8$ mm^3.

Sensitivity. The sensitivity of the system was evaluated using a NEMA NU 2 sensitivity phantom, which consists of 5 concentric aluminum sleeves, each 70 cm long. Polyethylene tubing (70 cm long) filled with 12.8 MBq of ^{18}F-FDG solution was inserted into the aluminum sleeves and positioned at the center of the transaxial FOV. Five 300-s acquisitions were conducted by successively removing the outermost sleeve to extrapolate attenuation-free sensitivity. Then, the entire process was repeated with the line source positioned at 10 cm off-center in the transaxial FOV. List-mode data at both positions were processed using the single-slice rebinning method with a slice thickness of 1.46 mm, and random coincidences were subtracted using the delayed coincidence time window technique.

Scatter Fraction, Count Losses, and Randoms. In accordance with the NEMA NU 2-2018 standard, count rate performance was measured by inserting a 70-cm line source into the NEMA NU 2 scatter phantom, a 20-cm-diameter, 70-cm-long polyethylene cylinder. The phantom was positioned at the center of the FOV and was axially aligned with the scanner axis. The line source contained 1.82 GBq of ^{18}F-FDG solution at the beginning of the acquisition. A total of 34 acquisitions were performed throughout the PET scan protocol described in Supplemental Table 1 (supplemental materials are available at http://jnm.snmjournals.org). Random estimation was obtained using raw data from the delayed coincidence channel. Subsequently, the scatter fraction, count rates for different types of coincident events, and the NECR were determined.

Timing Resolution and Energy Resolution. The data acquired from the count rate performance measurement were used to evaluate the timing resolution and energy resolution (*28*). To determine the source position, data acquired at activity concentrations below the peak NECR were reconstructed using non-TOF OSEM with all corrections applied. Only coincidences within the ±20-mm region of interest centered on the line source were used to obtain the timing histogram. The timing error was calculated for the data for each coincidence by finding the difference between the measured TOF data and the expected TOF offset on the basis of the point closest to the line source on the corresponding LOR. Scatter and random coincidences were subtracted using the tails of the TOF histograms. The timing resolution was obtained by measuring the full width at half maximum (FWHM) of the final time distribution histogram. For all 34 acquisitions, crystal-level energy spectra with a 1-keV energy bin width were combined into a single spectrum by aligning the 511-keV peaks. The maximum value of the 511-keV peak was determined by fitting a parabolic curve based on 3 points: 1 at the peak and 2 at its nearest neighboring points. The FWHM was determined through linear interpolation between adjacent pixels at half of the maximum value of the peak.

Accuracy: Correction for Count Losses and Randoms. The quantitative accuracy was measured using the same dataset acquired during the count rate performance measurement. Images under various activity concentrations were reconstructed with all PET data corrections. Random coincidences were corrected by using data from the delayed coincidence channel. Dead time correction was based on a nonparalyzable model–based adaptive dead time correction method (*29,30*). The standard whole-body image reconstruction protocol used at our institution was applied, that is, a PSF-based TOF OSEM algorithm with 3 iterations, 10 subsets, a voxel size of $1.8 \times 1.8 \times 2.14$ mm^3, and a 2-mm FWHM gaussian postreconstruction filter. For each reconstruction, 12 slices at each end of the axial FOV were excluded from the analysis.

Image Quality and Accuracy of Correction. To conform to the NEMA NU 2-2018 standard, a NEMA NU 2 image quality phantom

was used to evaluate image quality. The NEMA NU 2 scatter phantom, used for the count rate performance measurement, was positioned adjacent to the NEMA image quality phantom. At the start of image acquisition, the background activity concentration of ^{18}F-FDG was 5.3 kBq/mL, and the line source activity in the scatter phantom was 116 MBq. The duration of the phantom scan was set to 6.8 min with a 35% bed overlap, which is the overlap used in our clinical routines. Six spheres with diameters of 10, 13, 17, 22, 28, and 37 mm were filled with an ^{18}F-FDG solution containing an activity concentration ratio of 4.0:1 relative to the background. In accordance with the NEMA NU 2-2018 standard, duplicate scans were performed sequentially 3 times to evaluate the reproducibility of the results. The durations of the second and third scans were adjusted to compensate for the decay of ^{18}F. The resulting image was reconstructed using our institutional standard whole-body protocol with all data corrections applied.

Hoffman Brain Phantom. A Hoffman brain phantom was filled with 48.8 MBq of ^{18}F-FDG and scanned for 10 min. The acquired images were reconstructed using the PSF-based TOF OSEM algorithm, with a voxel size of $0.6 \times 0.6 \times 0.8$ mm^3, 7 iterations, 10 subsets, and a 1-mm gaussian postreconstruction filter—our institutional standard brain protocol. In accordance with the method described by Leemans et al. (*31*), a central slice of the Hoffman brain phantom at the level of the basal ganglia and lateral ventricle was selected to visualize gray matter, white matter, and cerebrospinal fluid. The radioactivity concentration ratios between the gray matter and the white matter, as well as the contrast recovery of gray matter relative to cerebrospinal fluid, were calculated.

Patient Study. The clinical performance of the system was assessed through a study conducted on 3 patients. The study was approved by the Institutional Review Board of Xijing Hospital (KY20212145-F-1), and informed consent was obtained from all patients (informed consent for the publication of related images was obtained from all human research participants). The first patient, a 56-y-old woman (160.3 cm, 58.2 kg), was diagnosed with plantar squamous cell carcinoma and metastases. This patient received an injection of 314 MBq of ^{18}F-FDG. A whole-body PET/CT scan was performed at 69 min after injection, with a scan duration of 2 min/bed, a bed overlap of 40%, and a total of 7 beds. Reconstructions with and without TOF were performed using the PSF-based TOF OSEM algorithm with 3 iterations, 10 subsets, a voxel size of $1.8 \times 1.8 \times 2.14$ mm^3, and a 2-mm FWHM gaussian postreconstruction filter for comparison. Three additional TOF reconstructions were performed using portions of the original 2-min/bed–position list-mode file to evaluate the impact of scan duration. The second patient, a 63-y-old man (180 cm, 59 kg), was diagnosed with cognitive impairment and received an injection of 303 MBq of ^{18}F-FDG. At 52 min after injection, a 10-min brain scan was conducted and reconstructed using our standard brain protocol. Again, the non-TOF and TOF images were compared. The third patient, a 72-y-old man (172 cm, 55 kg), presented with non–small cell lung cancer for staging. This patient received an injection of 203 MBq of ^{18}F-FDG. A whole-body PET/CT scan consisting of 4 beds (2 min/bed with a bed overlap of 45%) was performed at 65 min after injection. The same whole-body PET image reconstruction protocol was used.

The datasets generated during the present study are available from the corresponding authors on reasonable request.

RESULTS

Spatial Resolution

The spatial resolution performance of the system is summarized in Table 1. The transverse resolution, averaged over both tangential and radial directions at a distance of 1 cm off-center, was 2.88 mm. Figure 1 displays image slices of the mini-Derenzo phantom positioned at the center of the axial FOV in 2 orientations. Single-slice images (with slice thicknesses of 0.8 mm for the transaxial orientation and 0.6 mm for the coronal orientation) as well as averaged multiple-slice images (over 30 slices for the transaxial orientation and over 40 slices for the coronal orientation) are shown. In the transaxial orientation, the smallest resolved rod size was 2.0 mm, and the shape of the hot rods remained visually undistorted. In the coronal orientation, most of the 2-mm rods were resolved, but some were slightly distorted along their axial direction.

Sensitivity

The sensitivity profiles are shown in Figure 2. The system sensitivities were 20.1 kcps/MBq at the transaxial center and 20.9 kcps/MBq at 10 cm off-center.

Count Rate Performance, Timing and Energy Resolution, and Accuracy

Figure 3A shows a plot of count rates for different types of coincident events and NECR at various activity concentrations. The peak NECR was 576.0 kcps at 73.0 kBq/mL. Even at the highest activity concentration of 82.9 kBq/mL, the true count rate reached 3.6 Mcps and continued to increase. Figure 3B depicts the scatter fraction, TOF resolution, energy resolution, and accuracy as a function of activity. The scatter fractions were 34.7% at 5.3 kBq/mL and 33.2% at the peak NECR. The TOF resolutions observed were 189 and 197 ps at 5.3 kBq/mL and at the peak NECR, respectively. The energy resolution was 9.6% FWHM at the 511-keV photopeak with 5.3 kBq/mL. The maximum absolute error, at or below the peak NECR, was 2.81%.

TABLE 1
Measured NEMA NU 2-2018 Spatial Resolutions

		FWHM (mm)		
Location	Position (cm)	Tangential	Radial	Axial
Center axial FOV	1	3.02	2.72	2.74
	10	3.21	3.19	2.89
	20	3.57	4.80	3.10
1/8 axial FOV	1	3.03	2.73	2.80
	10	3.06	3.22	2.95
	20	3.53	4.91	3.08
Average of 1/2 and 1/8	1	3.03	2.73	2.77
	10	3.14	3.2	2.92
	20	3.55	4.85	3.09

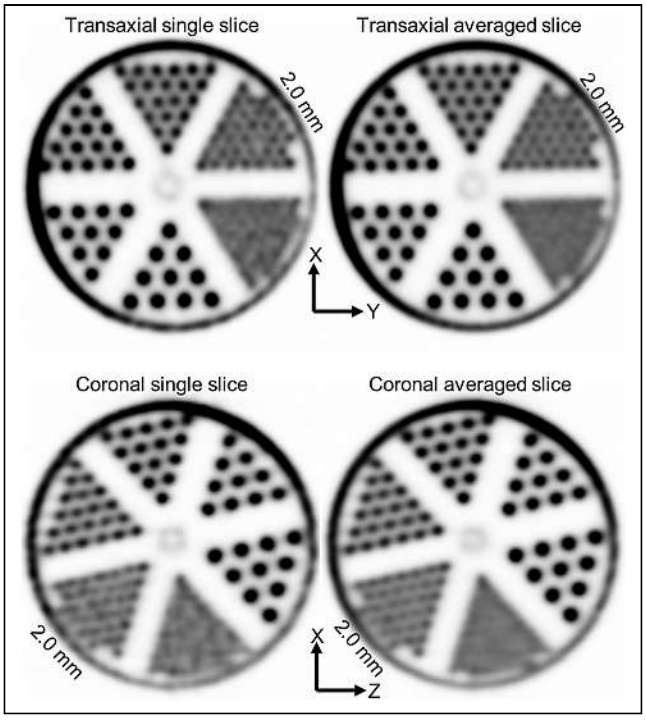

FIGURE 1. Illustrations of single slice (left) and average of multiple slices (right) for mini-Derenzo phantom at center of FOV in 2 orientations: with rod perpendicular to axial plane (initially filled with 16.3 MBq of ^{18}F-FDG and imaged for 10 min) and in coronal plane (same phantom imaged for 20 min with initial activity of 8.6 MBq). Images were reconstructed using PSF-based TOF OSEM algorithm with 7 iterations, 10 subsets, voxel size of $0.6 \times 0.6 \times 0.8$ mm^3, and 1 mm FWHM gaussian postreconstruction filter. Gray scale was adjusted to cover range from minimum value to 40% of maximum value for each respective image.

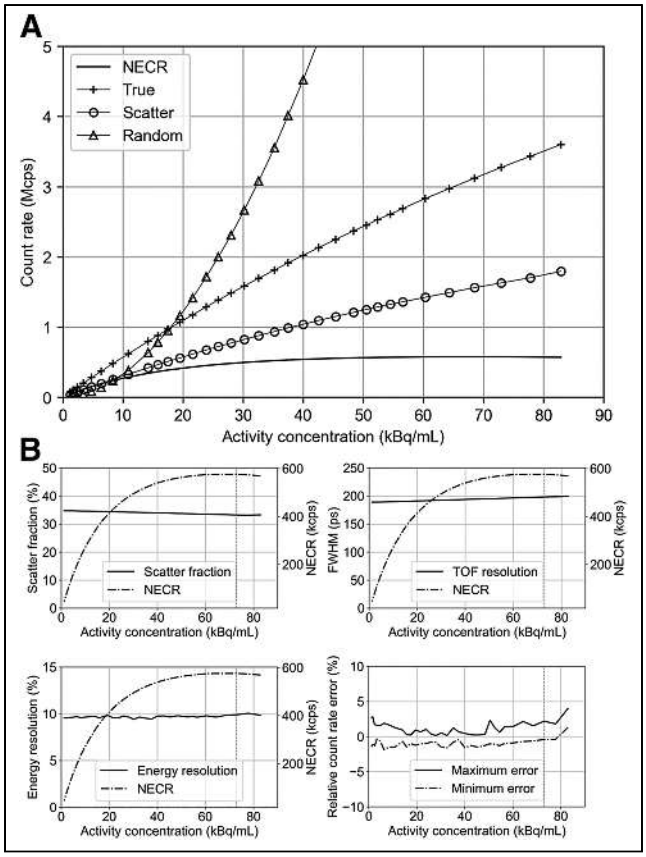

FIGURE 3. (A) Results for true, scatter, and random count rates and NECR as function of activity concentration. (B) Scatter fraction, TOF resolution, energy resolution, and accuracy measured as function of activity concentration. NECR curve was plotted using double *y*-axes. Vertical dashed lines denote peak NECR.

Image Quality

Table 2 summarizes the contrast recovery, background variability, and lung residual error for 3 duplicate scans.

Hoffman Brain Phantom

Four transverse slices of the Hoffman brain phantom are shown in Figure 4. The radioactivity concentration ratio between the gray matter and the white matter was 3.27:1, compared with the ground truth of 4:1; the contrast recovery of gray matter relative to cerebrospinal fluid was 0.95, in comparison to the true value of 1.

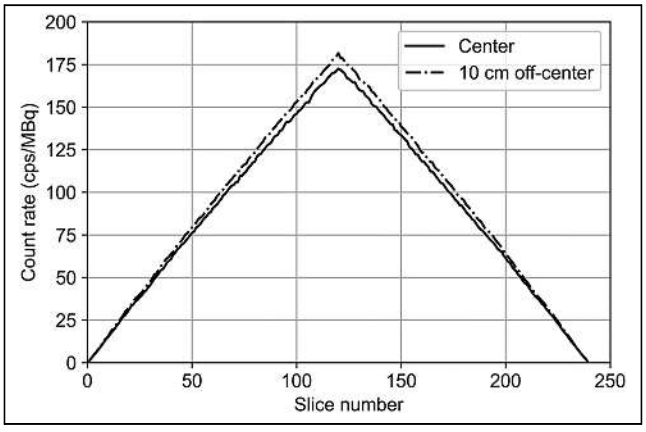

FIGURE 2. Axial sensitivity profiles measured with 70-cm line source positioned at transaxial center and 10 cm off-center. Sinogram slice thickness was 1.46 mm.

Patient Study

Figure 5A shows the maximum-intensity projections and axial slices across the liver of the first patient. There was no obvious increase in false-positive lesions or absence of suspected lesions for all scan durations. Figures 5B and 5C show axial images containing 2 subcentimeter pulmonary nodules. In the TOF image, 2 nodules in very close proximity could be clearly distinguished. The comparison of the brain images of the second patient with and without TOF correction is shown in Figure 6. The TOF images clearly revealed more detailed substructures of the brain, demonstrating significant benefits from the improved TOF resolution of the system. Figure 7 displays the primary lesion and multiple suspected metastatic lesions in the lung, including both hilar and right lower-lobe areas. In both PET and CT images, several nodules with a diameter of approximately 4 mm and a suggestive hypodense cyst with a diameter of approximately 6 mm could be observed. No motion correction was applied to any of the patient studies.

DISCUSSION

In the present study, we assessed the performance of uMI Panorama in accordance with the NEMA NU 2-2018 standard. The aims of this evaluation were to provide a reference for the system's performance characteristics and to facilitate comparisons with other commercial PET/CT scanners.

TABLE 2
Mean, Maximum, and Minimum Percentages of Contrast Recovery, Background Variability, and Lung Residual for 4.0:1 Sphere-to-Background Ratio*

Parameter	Percentage for sphere diameter of:						Percentage for lung residual
	10 mm	13 mm	17 mm	22 mm	28 mm	37 mm	
Contrast recovery							
Mean	63.2	69.6	76.7	80.7	84.3	88.4	1.2
Maximum	64.8	70.4	77.5	81.3	85.2	88.9	1.3
Minimum	61.1	68.9	75.6	79.9	83.7	88.1	1.1
Background variability							
Mean	4.2	3.3	2.4	1.7	1.4	1.1	1.3
Maximum	4.9	3.7	2.6	1.8	1.4	1.2	1.4
Minimum	3.6	2.9	2.1	1.5	1.3	1.0	1.2

*Based on 3 sequential measurements of NEMA image quality phantom.

Spatial Resolution

Compared with most commercially available PET/CT scanners today, uMI Panorama exhibited improved spatial resolution, primarily due to the smaller crystal size and a higher multiplexing ratio between the crystal and SiPM. The radial spatial resolution results were better than the tangential resolution results at a 1-cm offset position; this finding may be attributable to the rebinning method used in the filtered backprojection reconstruction. In the coronal images of the mini-Derenzo phantom, the hot rods exhibited distortion along the axial direction, possibly because of the slower convergence caused by PSF modeling for LORs with larger axial oblique angles.

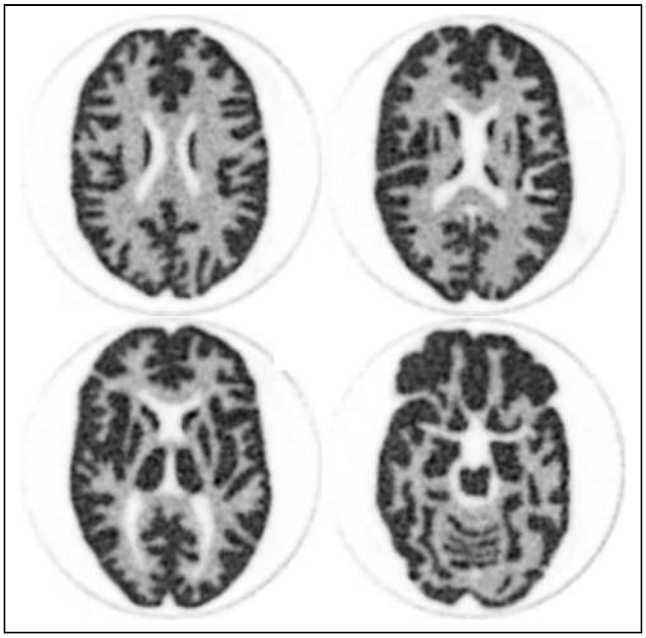

FIGURE 4. Four transverse image slices of Hoffman brain phantom. Phantom was filled with 48.8 MBq of ^{18}F-FDG and scanned for 10 min. Gray scale was scaled to same range from minimum to maximum for each slice. Bottom left slice was used to calculate radioactivity concentration ratio and contrast recovery.

Sensitivity

The sensitivity of uMI Panorama was 20.1 kcps/MBq with an axial FOV of 35.1 cm. Although at first glance it may seem that the system was not as sensitive (in terms of sensitivity per scanner length) as other commercially available systems (*18,20*), this relative difference in sensitivity per scanner length may be attributable to the slightly lower absorption efficiency of annihilation photons because of the use of shorter and smaller transaxial crystals to provide improved tradeoffs among sensitivity, spatial resolution, TOF performance, and axial coverage. Also notable was that the sensitivity at 10 cm off-center was greater than that at the center, a finding that may be explained by the shorter crystal length and longer axial FOV.

Count Rate Performance and Accuracy of Corrections

The combination of high peak NECR and minimal error enabled the system to maintain high efficiency and quantitative accuracy across a wide dynamic range. These characteristics make the system suitable for clinical scenarios involving high count rates as well as for dynamic imaging. Of note was that as the activity concentration increased, the scatter fraction decreased. This phenomenon may be attributable to the energy peak drifting toward the lower end as the count rate rose because of pulse pileup and temperature increase in the detector. The energy drift effect resulted in more scattered events being excluded by the low-level discriminator (430 keV) than by true events.

Timing Resolution

The timing resolution increased to 197 ps at peak NECR because of pileup affecting the detector signal when the count rate increased. The improved timing resolution led to higher image signal-to-noise ratio and contrast compared with the results provided by conventional PET scanners with a slower TOF resolution. Considering that OSEM images converge differently for different TOF resolutions at the same number of iterations and that convergence could be influenced by patient and lesion sizes, a more comprehensive method for comparing the benefits of various TOF resolutions may be used in future studies.

Image Quality

Contrast recovery is highly dependent on reconstruction parameters, such as voxel size, number of iterations/subsets, and

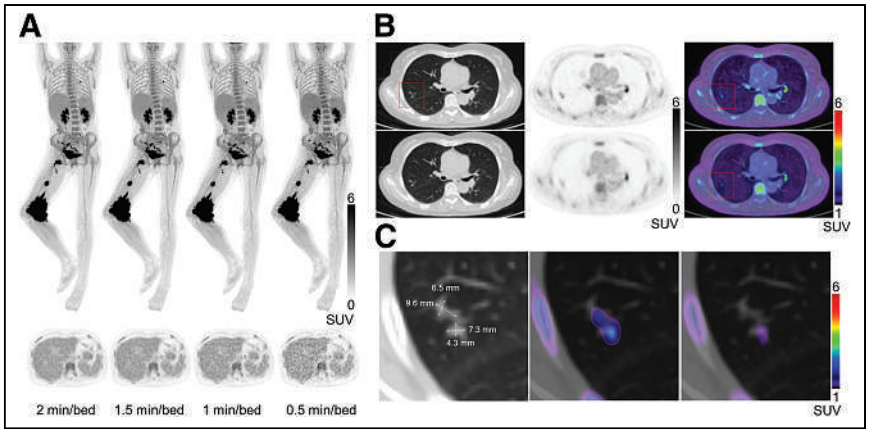

FIGURE 5. Images from 56-y-old female patient (body mass index, 22.6) diagnosed with plantar squamous cell carcinoma; injected activity was 314 MBq, and uptake time was 69 min. Images were reconstructed using PSF-based TOF OSEM algorithm with 3 iterations, 10 subsets, 2 mm FWHM gaussian postreconstruction filter, and voxel dimensions of $1.8 \times 1.8 \times 2.14$ mm^3. (A) Sequential maximum-intensity projections and transaxial image slices with acquisition times of 14, 10.5, 7, and 3.5 min from left to right, corresponding to 2, 1.5, 1, and 0.5 min/bed, respectively. Liver coefficients of variability were 12.8%, 15.3%, 19.7%, and 25.6% from left to right, respectively. (B) Comparison of TOF (upper row) and non-TOF (lower row) images; from left to right, images represent CT, PET, and PET/CT fusion images, respectively. (C) Zoomed-in images from B, highlighting high resolution of closely located pulmonary nodules in TOF images. Images from left to right represent CT, TOF fusion, and non-TOF fusion images, respectively. For fusion images in C, lower window of intensity scale bar was set to SUV of 1.

postreconstruction smoothing methods (*32*). Increasing the number of iterations and decreasing the voxel size can improve contrast recovery but may also amplify noise and increase reconstruction time. Using a protocol similar to that used in clinical scenarios, we did not observe obvious Gibbs artifacts, which may lead to a higher contrast recovery for smaller spheres (*18*). In addition, the low residual of the cold area could be explained by the fine spatial and fast timing resolutions of the scanner.

Hoffman Phantom Study

Brain imaging is often affected by involuntary movement of the patient and variations in individual metabolic characteristics. In contrast, the Hoffman brain phantom offers quantitative and qualitative analyses of a normal brain structure with ground truth. The fine spatial resolution contributes to a high radioactivity concentration ratio between the gray matter and the white matter as well as accurate delineation of anatomic structures. The improved contrast recovery of the ventricle, which lacks radioactivity, is consistent with the low residual observed in the lung region of the NEMA image quality phantom.

Patient Study

The patient study provided initial insights into clinical patient images acquired by the system. The brain and whole-body images presented in this study illustrate the feasibility of fine-resolution imaging with the system using our standard scan duration and injection dose. In addition, there is potential for further reduction in either injection dose or scan time. For example, as illustrated in Figure 5A, clinically acceptable images could still be obtained when the scan time was reduced to 1 min/bed for this case, even when the injection activity was less than the minimum administered ^{18}F-FDG activity according to European Association of Nuclear Medicine guidelines (*33*). The uMI Panorama's high sensitivity and fast TOF performance primarily contributed to the low noise level and high contrast of the reconstructed images, even with a small voxel size.

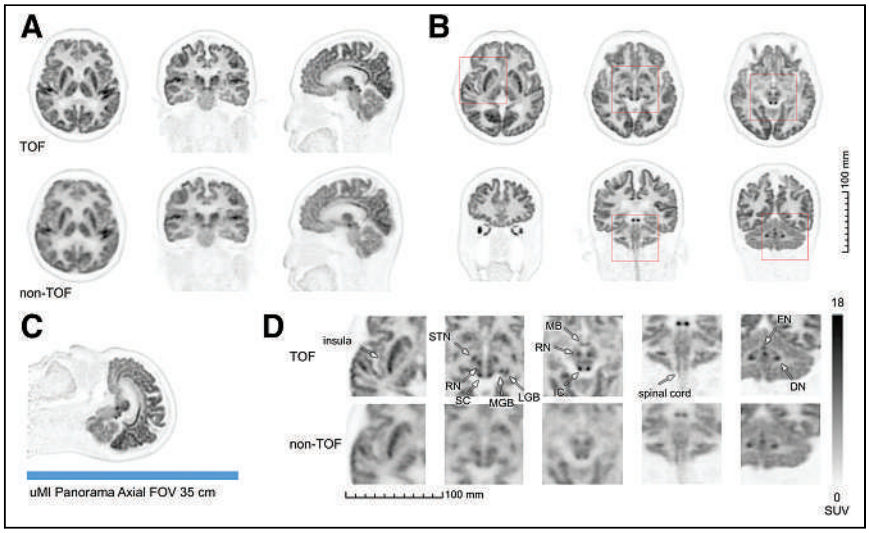

FIGURE 6. Neuroimaging of 63-y-old patient (body mass index, 18.2) who had cognitive impairment with 303 MBq of ^{18}F-FDG PET. Images were acquired at 52 min after injection with single-bed acquisition lasting 10 min. TOF and non-TOF images were reconstructed using PSF-based TOF OSEM algorithm with 7 iterations, 10 subsets, 1 mm FWHM gaussian postreconstruction filter, and voxel size of $0.6 \times 0.6 \times 0.8$ mm^3. (A) TOF images compared with non-TOF images, showing better recovery of cold regions in ventricles, gyri, sulci, and nucleus with TOF. (B) Multiple transaxial planes of TOF images. (C) Sagittal view showcasing single-bed axial FOV (35.1 cm) of uMI Panorama. (D) Zoomed-in comparison of TOF with non-TOF images from B, revealing enhanced clarity of insula gyri, nuclei, and spinal cords in TOF images. Grayscale consistency was maintained across PET images in A–D. DN = dentate nucleus; FN = fastigial nucleus; IC = inferior colliculus; LGB = lateral geniculate body; MB = mammillary body; MGB = medial geniculate body; RN = red nucleus; SC = superior colliculus; STN = subthalamic nucleus.

CONCLUSION

The uMI Panorama system achieved a fine spatial resolution of 2.88 mm at a 1-cm offset from the FOV center. Demonstrating an average sensitivity of 20.1 kcps/MBq and a peak NECR of 576 kcps at 73.0 kBq/mL and maintaining less than 3% quantitative bias with activity concentrations below the peak NECR, the system showed robust performance. The incorporation of LYSO crystals, SiPM-based detectors, and ASIC chips led to the system's fast timing resolution of 189 ps. Results from patient studies underscored the uMI Panorama system's clinical potential in enhancing diagnostic capabilities, particularly for smaller or lower-contrast lesions, leveraging its exceptional spatial resolution.

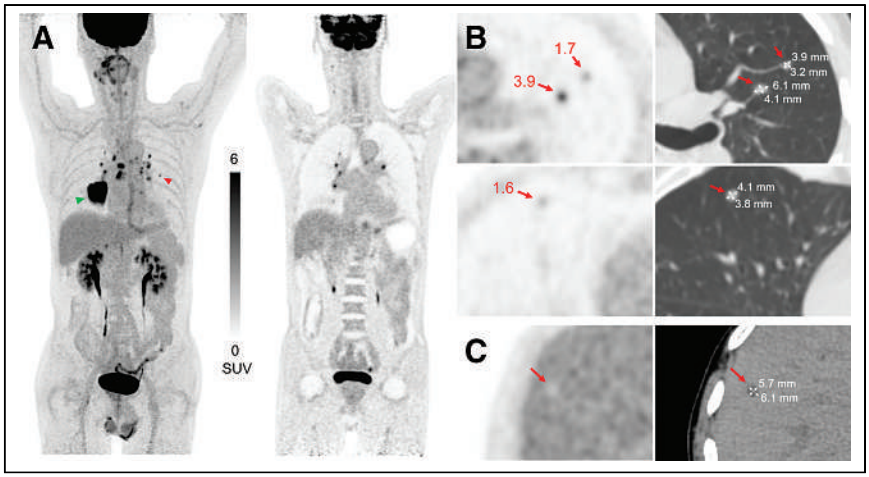

FIGURE 7. 72-y-old male patient (body mass index, 18.6) presenting with non–small cell lung cancer for staging. Patient received injection of 203 MBq of ^{18}F-FDG. Four-bed (2 min/bed, 45% bed overlap) whole-body scan was performed at 65 min after injection. Image was reconstructed using PSF-based TOF OSEM algorithm with 3 iterations, 10 subsets, 2 mm FWHM gaussian postreconstruction filter, and voxel size of $1.8 \times 1.8 \times 2.14$ mm^3. (A) Primary lesion (green arrowhead) and suspected metastatic lesion (red arrowhead). (B) CT transverse image reveals nodules of approximately 4-mm diameter in both lungs, corresponding to abnormal uptake on PET image. Long-axis measurement of 6.1 mm corresponds to suspected lesion highlighted by red arrowhead in A. Numeric values indicate lesion SUV_{mean}. (C) Subcentimeter cold region suggestive of hepatic cyst, consistent with hypodense appearance on CT scan.

DISCLOSURE

This work was supported by the National Natural Science Foundation of China (grant numbers 92259304, 91959208, 82122033, and 81971646) and the Key Science and Technology Program of Shaanxi Province (grant number 2022ZDLSF04-12). No other potential conflict of interest relevant to this article was reported.

KEY POINTS

QUESTION: What are the performance characteristics of the new SiPM- and ASIC-based uMI Panorama PET/CT system according to the NEMA NU 2-2018 standard?

PERTINENT FINDINGS: The uMI Panorama offers fine spatial (2.88 mm) and fast timing (189 ps) resolutions. It also shows improved count rate performance and quantitative accuracy over a wide range of activity levels (up to a peak NECR of 73 kBq/mL).

IMPLICATIONS FOR PATIENT CARE: The uMI Panorama offers improved diagnostic capabilities for small and low-contrast lesions and shows potential in applications involving high-count-rate scenarios.

REFERENCES

1. Brownell GL, Burnham CA, Wilensky S, Aronow S, Kazemi H, Strieder D. New developments in positron scintigraphy and the application of cyclotron-produced positron emitters. In: Ericson A, ed. *Medical Radioisotope Scintigraphy*. Vol 1. Vienna, Austria: IAEA (Proceedings Series); 1968:163–176.
2. Conti M. Why is TOF PET reconstruction a more robust method in the presence of inconsistent data? *Phys Med Biol.* 2011;56:155–168.
3. Conti M. Effect of randoms on signal-to-noise ratio in TOF PET. *IEEE Trans Nucl Sci.* 2006;53:1188–1193.
4. Moses WW. Time of flight in PET revisited. *IEEE Trans Nucl Sci.* 2003;50:1325–1330.
5. Surti S, Karp JS. Advances in time-of-flight PET. *Phys Med.* 2016;32:12–22.
6. Surti S, Karp JS, Muehllehner G, Raby PS. Investigation of lanthanum scintillators for 3-D PET. *IEEE Trans Nucl Sci.* 2003;50:348–354.
7. Conti M. Focus on time-of-flight PET: the benefits of improved time resolution. *Eur J Nucl Med Mol Imaging.* 2011;38:1147–1157.
8. Budinger TF. Time-of-flight PET: status relative to conventional PET. *J Nucl Med.* 1983;24:73–78.
9. Ter-Pogossian MM, Ficke D, Yamamoto M, Hood JT. Super PETT I: a positron emission tomograph utilizing photon time-of-flight information. *IEEE Trans Med Imaging.* 1982;1:179–187.
10. Lewellen TK, Bice AN, Harrison RL, Pencke MD, Link JM. Performance measurements of the SP3000/UW time-of-flight positron emission tomograph. *IEEE Trans Nucl Sci.* 1988;35:665–669.
11. Conti M, Bendriem B, Casey M, et al. First experimental results of time-of-flight reconstruction on an LSO PET scanner. *Phys Med Biol.* 2005;50:4507–4526.
12. Melcher CL, Schweitzer JS. Cerium-doped lutetium oxyorthosilicate: a fast, efficient new scintillator. *IEEE Trans Nucl Sci.* 1992;39:502–505.
13. Moses WW, Derenzo SE. Prospects for time-of-flight PET using LSO scintillator. *IEEE Trans Nucl Sci.* 1999;46:474–478.
14. Jakoby BW, Bercier Y, Conti M, Casey ME, Bendriem B, Townsend DW. Physical and clinical performance of the mCT time-of-flight PET/CT scanner. *Phys Med Biol.* 2011;56:2375–2389.
15. Surti S, Kuhn A, Werner ME, Perkins AE, Kolthammer J, Karp JS. Performance of Philips Gemini TF PET/CT scanner with special consideration for its time-of-flight imaging capabilities. *J Nucl Med.* 2007;48:471–480.
16. Bettinardi V, Presotto L, Rapisarda E, Picchio M, Gianolli L, Gilardi MC. Physical performance of the new hybrid PET/CT Discovery-690. *Med Phys.* 2011;38:5394–5411.
17. Roncali E, Cherry SR. Application of silicon photomultipliers to positron emission tomography. *Ann Biomed Eng.* 2011;39:1358–1377.
18. van Sluis J, de Jong J, Schaar J, et al. Performance characteristics of the digital Biograph Vision PET/CT system. *J Nucl Med.* 2019;60:1031–1036.
19. Zhang J, Maniawski P, Knopp MV. Performance evaluation of the next generation solid-state digital photon counting PET/CT system. *EJNMMI Res.* 2018;8:97.
20. Pan T, Einstein SA, Kappadath SC, et al. Performance evaluation of the 5-Ring GE Discovery MI PET/CT system using the National Electrical Manufacturers Association NU 2-2012 Standard. *Med Phys.* 2019;46:3025–3033.
21. Surti S, Karp JS, Popescu LM, Daube-Witherspoon ME, Werner M. Investigation of time-of-flight benefit for fully 3-D PET. *IEEE Trans Med Imaging.* 2006;25:529–538.
22. Kadrmas DJ, Casey ME, Conti M, Jakoby BW, Lois C, Townsend DW. Impact of time of flight on PET tumor detection. *J Nucl Med.* 2009;50:1315–1323.
23. Surti S, Scheuermann J, El Fakhri G, et al. Impact of time-of-flight PET on whole-body oncologic studies: a human observer lesion detection and localization study. *J Nucl Med.* 2011;52:712–719.
24. Surti S, Viswanath V, Daube-Witherspoon ME, Conti M, Casey ME, Karp JS. Benefit of improved performance with state-of-the art digital PET/CT for lesion detection in oncology. *J Nucl Med.* 2020;61:1684–1690.
25. *NEMA Standards Publication NU 2-2018: Performance Measurements of Positron Emission Tomographs (PETs).* Rosslyn, VA: National Electrical Manufacturers Association; 2018.
26. Wagadarikar AA, Ivan A, Dolinsky S, McDaniel DL. Sensitivity improvement of time-of-flight (ToF)-PET detector through recovery of Compton scattered annihilation photons. *IEEE Trans Nucl Sci.* 2014;61:121–125.
27. Defrise M, Kinahan PE, Townsend DW, Michel C, Sibomana M, Newport DF. Exact and approximate rebinning algorithms for 3-D PET data. *IEEE Trans Med Imaging.* 1997;16:145–158.
28. Bharkhada D, Rothfuss H, Conti M. A new method to calculate energy resolution based upon NEC phantom. *IEEE Nucl Sci Symp Conf Rec.* 2017:1–2.
29. Heemskerk JWT, Defrise M. Gamma detector dead time correction using Lambert W function. *EJNMMI Phys.* 2020;7:27.
30. Liu YL, Tang SS, Wang JX, Dong Y. Dead-time correction method for block detector based ultra-long axial FOV PET scanner. *IEEE Nucl Sci Symp Conf Rec.* 2019:1–4.
31. Leemans EL, Kotasidis F, Wissmeyer M, Garibotto V, Zaidi H. Qualitative and quantitative evaluation of blob-based time-of-flight PET image reconstruction in hybrid brain PET/MR imaging. *Mol Imaging Biol.* 2015;17:704–713.
32. Spencer BA, Berg E, Schmall JP, et al. Performance evaluation of the uEXPLORER total-body PET/CT scanner based on NEMA NU 2-2018 with additional tests to characterize PET scanners with a long axial field of view. *J Nucl Med.* 2021;62:861–870.
33. Boellaard R, Delgado-Bolton R, Oyen WJ, et al. FDG PET/CT: EANM procedure guidelines for tumour imaging—version 2.0. *Eur J Nucl Med Mol Imaging.* 2015;42:328–354.

The Accomplishments and Legacy of Saul Hertz, MD

Bennett S. Greenspan[1], Michael S. Hofman[2,3], and John Buscombe[4]

[1]*Department of Radiology, Augusta VA Medical Center, Augusta, Georgia;* [2]*Prostate Cancer Theranostics and Imaging Centre of Excellence, Department of Molecular Imaging and Therapeutic Nuclear Medicine Cancer Imaging, Peter MacCallum Cancer Centre, Melbourne, Victoria, Australia;* [3]*Sir Peter MacCallum Department of Oncology, University of Melbourne, Melbourne, Victoria, Australia; and* [4]*Department of Nuclear Medicine, Cambridge University Hospitals, Cambridge, United Kingdom*

The early history of the use of radioactive iodine (RAI) is complicated and interesting, and also difficult to discover, especially since several histories have presented inaccurate content. This article is a comprehensive review of the accomplishments of Saul Hertz. Extensive use of primary-source verification has clarified several issues, including the question of whether Hertz alone conceived and asked the pivotal question: "Could iodine be made radioactive artificially?"; on what date RAI was first used to treat hyperthyroidism; and why 2 articles on the first use of RAI for treatment of hyperthyroidism, from 2 different sets of authors from the same department of the same institution, appeared adjacent to each other in the same issue of the *Journal of the American Medical Association* in 1946. Our review also chronicles several major challenges that Hertz overcame to produce his pivotal work. Hertz was clearly the originator and a visionary of RAI therapy in benign and malignant thyroid disease. We believe he can be considered one of the fathers of nuclear medicine. Hertz's paradigm-changing work was a pivotal medical discovery of the 20th century. The legacy of Hertz continues while the application of RAI therapy continues to evolve. RAI therapy remains the preferred treatment in most situations for autonomous nodules and toxic multinodular goiter and remains a safe and effective treatment for Graves disease after more than 80 y of global clinical use. RAI treatment of differentiated thyroid cancer remains a first-line treatment for most patients after surgery, especially for those with intermediate- or high-risk disease.

Key Words: Saul Hertz; radioactive iodine; hyperthyroidism; thyroid cancer; theranostics

J Nucl Med 2024; 65:659–663
DOI: 10.2967/jnumed.124.267524

In the landscape of medical history and innovation, few figures exemplify the blend of groundbreaking scientific achievement and selfless service as well as Saul Hertz does. Born on April 20, 1905, Hertz's journey in medicine began with his graduation from Harvard Medical School in 1929, a time of strict quotas for outsiders. He served as chief of the Thyroid Unit at Massachusetts General Hospital (MGH) from 1931 to 1943. Despite the promise of a burgeoning research and clinical career, Hertz's path took a detour as he answered the call of duty, serving as a commander in the U.S. Navy during the tumultuous years of World War II from 1943 to 1945. Tragically, his life and career were cut short when he passed away on July 28, 1950, at the age of 45 because of a myocardial infarction, as confirmed by autopsy. This review article seeks to explore not just the professional milestones of Hertz but also the personal and historical context that shaped his remarkable, albeit too brief, journey through life and medicine (Table 1).

Four scientific advancements and discoveries provide the basis for the pivotal question and subsequent research and clinical work of Hertz. These include the understanding of the role of iodine in thyroid metabolism and function, the discovery of radioactivity, the development of the tracer principle, and the production of artificial radioactivity (*1*).

On November 12, 1936, Karl Compton, president of the Massachusetts Institute of Technology, presented to the faculty at the Harvard Medical School a guest lecture entitled, "What Physics Can Do for Biology and Medicine" as part of a weekly lecture series and luncheon. At the conclusion of the lecture, Hertz solely conceived and spontaneously asked the pivotal question "Could iodine be made radioactive artificially?" Karl Compton was uncertain and said he would look into it. He wrote back to Hertz on December 15, 1936, apologized for the delayed response, and wrote, "Iodine can be made artificially radioactive." In fact, Enrico Fermi had produced ^{128}I in 1934, and earlier in 1934, Frederic Joliot and Irene Joliot-Curie created artificial radioactivity, for which they received the Nobel Prize for Chemistry in 1935. Letters between Hertz and Compton make it clear that the idea of using radioactive isotopes to study metabolism came solely from Hertz (*1–4*). The fact that Hertz solely asked the question was confirmed by James Means, chief of medical services at MGH, in a letter to the Markle Foundation (Fig. 3 in (*2*)) in which he stated, "when it became apparent that there might be radioactive isotopes of iodine, it at once occurred to Hertz that we might make use of them to solve a problem we were already working on" (*1–5*). Robley Evans, director of the Massachusetts Institute of Technology Radiation Laboratory, also wrote a letter of recommendation to the Navy confirming that Hertz was the one who conceived the idea of using radioactive iodine (RAI) for research and therapy of thyroid disease (*5*).

Hertz collaborated with Arthur Roberts, a medical physicist who was hired at Massachusetts Institute of Technology by Robley Evans. Earle Chapman was an endocrinologist in the MGH Thyroid Clinic. When Hertz was leaving MGH to join the Navy in 1943, Hertz asked Chapman to supervise the clinical trials and follow the established protocols, to which Chapman agreed. However, Chapman changed the protocols. John Stanbury was an endocrinologist in the Thyroid Clinic, who wrote a book on the history of the MGH Thyroid Clinic from 1913 to 1990. Unfortunately, the book contained significant misinformation. Roberts wrote a letter to Stanbury on April 3, 1991, in an attempt to correct

Received Jan. 26, 2024; revision accepted Jan. 30, 2024.
For correspondence or reprints, contact Bennett S. Greenspan (bengreenspan0708@gmail.com).
Published online Mar. 7, 2024.

TABLE 1
Accomplishments of Saul Hertz

Year	Accomplishment
	Scientific
1932	First to combine thyroid metabolism with discovery of radioactivity (first publication on blood picture in exophthalmic goiter) (*10*)
1936	Conceived and asked seminal question: "Could iodine be made radioactive artificially?"
1937	First to publish preclinical study of RAI metabolism in rabbits*
	First to publish tracer use of RAI in studying thyroid physiology (*1–3*)
1937	First to conceive of using RAI for biomedical investigation, and one of first to use radiotracers as tools for biomedical research (*1–3*)
	First to demonstrate linkage between RAI uptake and thyroid function, including effects of thyroid-stimulating hormone and diet
	First to conceive of using uptake measurement for diagnosis and for administered activity calculation
	First to use molecularly targeted therapy
	First to use RAI in patients
	First to use RAI as both therapeutic agent and diagnostic agent (theranostics)
	First to conceive of pharmacologic intervention for research and clinical studies, extending clinical utility of diagnostic tests and enhancing therapy
	First to use RAI as biomarker
1937	First to suggest that RAI may also be used to treat thyroid cancer (*1*,*2*)†
1941	First to use therapeutic RAI in clinic at MGH (*1*,*8*)
	First to demonstrate safety and success of RAI therapy for hyperthyroidism
1942	First to use RAI to treat patient with thyroid cancer
	First to present RAI treatment of hyperthyroidism (along with Arthur Roberts, presented to Markle Foundation results of treatment of first 10 hyperthyroid patients)
1946	Published results of first 29 patients in *Journal of the American Medical Association* (*8*)
	Administrative
1931–1943	Served as director of MGH Thyroid Unit
1937–1946	One of the first physicians to collaborate with a medical physicist (Arthur Roberts)
1946	Founder of Radioactive Isotope Research Institute
	Strong proponent of making RAI widely available by urging Atomic Energy Commission to do so
	Helped promote peaceful uses of atomic energy by developing effective uses of RAI, advocating wide distribution and availability of RAI with reasonable cost, and issuing guidelines for safety
	Developed curriculum (together with Arthur Roberts) in applied nuclear physics for physicians and biologists
1949	Established first nuclear medicine department (at Massachusetts Women's Hospital)

*Hertz demonstrated remarkable discipline in proceeding systematically from exploration of concept in preclinical animal studies, including studies of function and safety, to successful clinical use of RAI in patients for diagnosis and treatment. Hertz's use of dosimetry, RAI uptake testing, and RAI as tracer and biomarker are enduring essentials of precision targeted approach.

†Hertz suggested that RAI therapy of thyroid cancer was a model for radiopharmaceutical therapies for cancer and that therapy of other types of cancer might be addressed in the future. "My new research is in Cancer of the Thyroid which I believe holds the key to the larger problem of Cancer in general." Letter by Hertz to MGH (*4*).

FIGURE 1. Hertz with his assistant and multiscaler probe. (Colorized version made using hotpot.ai deep learning.)

TABLE 2
Awards and Honors Received by Saul Hertz

Year	Award or honor
1931–1933	Dalton Scholar, MGH
1935–1937	Henry Pickering Wolcott Fellow, Harvard Medical School
1940	Key to Science/Sigma Xi Chapter of Massachusetts Institute of Technology
1941	Elected member of American Society for Clinical Investigation ("Young Turks" Society)
1946	Honorable Mention, American Goiter Association Van Meter Award
2021*	Honored by American Chemical Society with National Historical Chemical landmark designation at MGH
	Honored by U.S. Congress for pioneering work in developing medical applications for RAI
2023*	As originator of precision targeted personalized medicine, honored by Northeastern Chapter of American Chemical Society with Saul Hertz Memorial Symposium

*Posthumously honored.

the misinformation. Roberts also stated in the letter, "Evans made it a condition of my employment that his name was to appear on all publications" (*2*). Hertz and Roberts included Evans on the first 2 papers, but not after that, since Evans never participated in any of the studies (*5*). It is to be noted that Hertz and Roberts designed the research, executed the work, analyzed the data, and wrote the papers (*4*). Evans was not involved in any of those activities. Evans directed the laboratory that initially provided the neutron source to produce RAI. The Massachusetts Institute of Technology cyclotron produced greater quantities of RAI that were critically important for RAI therapy.

Although it is often assumed science and scientific endeavor occur in a world isolated from the prejudices and mores of the time, this is sadly hardly ever the case. At the time Hertz was working and publishing his research, he was living and working in a city in which antisemitic opinion and actions had become commonplace. In the 1930s, Boston was the most anti-Jewish city in the United States and the headquarters of an organization called the Christian Front (*6*). Until 1941, this organization, at the very time that Hertz was working in Boston, was financed and led by the national socialist (Nazi) government in Germany. Even after the United States entered the war against Germany, the organization continued to flourish and organize antisemitic protest marches through the streets of Boston. The organization was implicated in physical attacks on Jewish men and boys up to the end of 1943.

Hertz faced and overcame several major challenges during his career: pushback from surgeons, who were concerned that he was taking business from them; interruption of his clinical studies by World War II; questionable ethics in medical publishing (ghost authoring); others trying to steal credit for his work; and confrontation with strict quotas and restrictions—he was a target of personal and systemic antisemitism.

The true story of Hertz includes elements of exploitation, failure to honor those who served in the war, greed, stolen intellectual property, and antisemitism. Evans deliberately muddied the waters as to the truth regarding whether Hertz was the one who asked the pivotal question. The truth was explained in April 2016 by MGH's chairman emeritus of the Department of Radiology, James Thrall, who stated, "… Chapman and Evans had basically stolen Hertz's work … the most flagrant, unethical, academically reprehensible behavior … worst yet …. Chapman and Evans spent a great deal of time and effort rewriting history" (*7*).

In 1946, there were 2 adjacent publications in the same May 11 issue of *Journal*

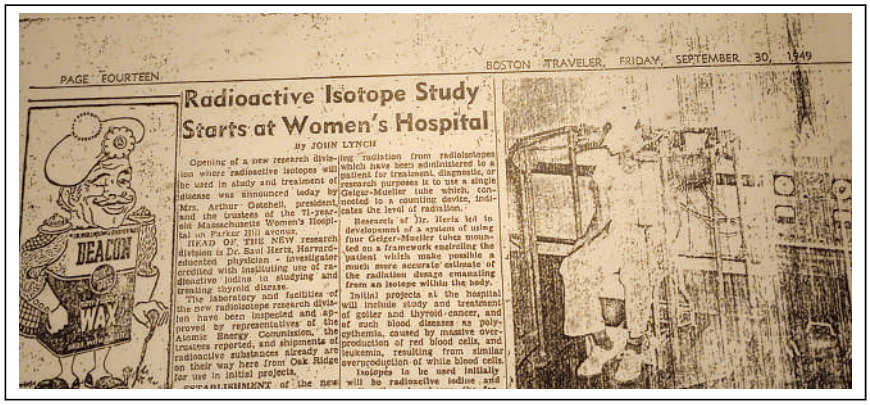
PAGE FOURTEEN BOSTON TRAVELER, FRIDAY, SEPTEMBER 30, 1949

Radioactive Isotope Study Starts at Women's Hospital

By JOHN LYNCH

Opening of a new research division where radioactive isotopes will be used in study and treatment of disease was announced today by Mrs. Arthur Gotchell, president, and the trustees of the 71-year-old Massachusetts Women's Hospital on Parker Hill avenue.

HEAD OF THE NEW research division is Dr. Saul Hertz, Harvard-educated physician - investigator credited with instituting use of radioactive iodine in studying and treating thyroid disease.

The laboratory and facilities of the new radioisotope research division have been inspected and approved by representatives of the Atomic Energy Commission, the trustees reported, and shipments of radioactive substances already are on their way here from Oak Ridge for use in initial projects.

ESTABLISHMENT of the new ing radiation from radioisotopes which have been administered to a patient for treatment, diagnostic, or research purposes is to use a single Geiger-Mueller tube which, connected to a counting device, indicates the level of radiation.

Research of Dr. Hertz led to development of a system of using four Geiger-Mueller tubes mounted on a framework encircling the patient which make possible a much more accurate estimate of the radiation dosage emanating from an isotope within the body.

Initial projects at the hospital will include study and treatment of goiter and thyroid cancer, and of such blood diseases as polycythemia, caused by massive overproduction of red blood cells, and leukemia, resulting from similar overproduction of white blood cells.

Isotopes to be used initially will be radioactive iodine and

FIGURE 2. *Boston Traveler* newspaper of September 30, 1949, announcing new research division where radioactive isotopes were to be used in study and treatment of disease.

TABLE 3
Legacy of Saul Hertz

Category	Legacy
Revolutionizing of …	Thyroid disease management with use of RAI therapy, which has become standard of care for benign thyroid disease (hyperthyroidism) and for differentiated thyroid cancer (papillary and follicular cell)
Establishment of …	Culture of collaboration (between physicians and physicists, between departments, between institutions, and with government agencies)
	Culture of safety (patient safety and proposal of review process to investigate infringement of rights of physicians by hospital boards)
	Theranostic approach for cancer therapy
	Nuclear medicine as medical specialty
Development of …	Detection device (multiscaler uptake probe, which is believed to have influenced development of rectilinear scanner [Bennedict Cassen, 1950] and γ-camera [Hal Anger, 1958])
	Radiotracer for detectability and localization, and subsequent use of many different radiotracers in diagnosis and treatment
Realization of …	Use of dosimetry for effective treatment using personalized targeted therapy
Increasing use of …	Radiopharmaceutical therapy for many different cancers*
Continuing evolution of …	Applications of RAI therapy, which remains preferred in most situations for autonomous nodules and toxic multinodular goiter, remains safe and effective for Graves disease after more than 80 y of clinical use worldwide, and remains first-line treatment for most differentiated thyroid cancer patients after surgery, especially those with intermediate or high-risk disease (use of dosimetry is increasingly recognized as valuable in treatment of thyroid disease; tumor heterogeneity has been identified as key factor limiting response to targeted treatments such as ^{131}I; and imaging with ^{124}I and ^{18}F-FDG PET/CT has role in selecting patients and directing therapy, marking new area of personalized medicine)
Eponym of …	Saul Hertz World Theranostics Day (celebrating ongoing innovation and advancement in field of nuclear theranostics)†
	Saul Hertz Award and Symposium, Society of Nuclear Medicine and Molecule Imaging (lifetime achievement award for outstanding contributions to radionuclide therapy)
	Saul Hertz Young Investigator Award, South African Society of Nuclear Medicine
	Saul Hertz Young Investigator Award, Indian Society of Nuclear Medicine
	Saul Hertz Young Investigator Award, Pakistan Society of Nuclear Medicine
	Saul Hertz Memorial Prize, British Nuclear Medicine Society (best oral paper and best paper concerning science or delivery of radionuclide therapy)
	Saul Hertz Memorial Lecture Preceptorship, Prostate Theranostics and Imaging Centre of Excellence

*Hertz was quoted in *The American Weekly Magazine* on June 2, 1946, as saying " … demand is expected in the fields of cancer and leukaemia for other radioactive medicines."

†On March 31, 1941, using Massachusetts Institute of Technology cyclotron-produced RAI, Hertz initially used mixture of ^{130}I (90%) and ^{131}I (10%) to treat Graves disease patient Elizabeth D. This date is now established as Saul Hertz World Theranostics Day. He presented results of first 10 patients in 1942 to Markle Foundation. Initially, 29 patients were treated, and results were published in 5-y follow-up in *Journal of the American Medical Association* in 1946. Twenty of 29 were considered cured, and 6 others had partial response to RAI therapy (*1*–*3*).

of the American Medical Association, from the same laboratory on the same topic—the first successful use of RAI to treat hyperthyroidism. The editor of that journal from 1924 to 1950 was Morris Fishbein, who was aware of the previous 6 papers by Hertz and Roberts. He first received a paper from Chapman and Evans. Fishbein sent it back for revision, since it was too long. Fishbein was also concerned that the studies on the same topic from the same laboratory did not include Hertz and Roberts and did not even reference them. Fishbein contacted Means, who assured Fishbein that the Chapman and Evans article was legitimate and that their article was based on a series of different patients. Fishbein contacted Hertz and asked him to submit his paper with the results of his first clinical trial, which he did. After negotiation, Fishbein published both papers next to each other and placed the Hertz and Roberts paper first, to acknowledge their pioneer status, since those studies were done first (*8*,*9*). This issue is discussed further in a paper by Obaldo and Hertz (*5*).

History records Hertz, with Roberts, as a pioneer of RAI therapy and as establishing nuclear medicine as a new specialty of medicine (Figs. 1 and 2). Hertz created a dynamic and enduring fundamental change in modern medicine. He influenced the convergence of the sciences and collaborative teams as well as the use of uptake testing and dosimetry to develop precision targeted medicine. His legacy lives on today (Tables 2 and 3).

We also acknowledge John Lawrence for use of ^{32}P for treatment of leukemia in 1936 and polycythemia vera in 1937. At the

Lawrence Berkeley National laboratory, Lawrence's team was also investigating RAI in the late 1930s and early 1940s and began treating hyperthyroid patients in October 1941 (*1*). Also acknowledged is Charles Pecher for treatment of bone sarcoma with ^{89}Sr in 1941. Today, we stand on the shoulders of these giants as we continue our efforts to develop next-generation theranostics.

DISCLOSURE

No potential conflict of interest relevant to this article was reported.

ACKNOWLEDGMENT

We acknowledge Barbara Hertz, who provided the 2 figures and primary source material for this article.

REFERENCES

1. Fahey FH, Grant FD. Celebrating eighty years of radionuclide therapy and the work of Saul Hertz. *J Appl Clin Med Phys.* 2021;22:4–10.
2. Hertz B. Dr. Saul Hertz (1905–1950) discovers the medical uses of radioactive iodine: the first targeted cancer therapy. In: Ahmadzadehfar H, ed. Thyroid Cancer: Advances in Diagnosis and Therapy. IntechOpen; 2016:1–14.
3. Fahey FH, Grant FD, Thrall JH. Saul Hertz, MD, and the birth of radionuclide therapy. *EJNMMI Phys.* 2017;4:15–23.
4. Hertz B. A tribute to Dr. Saul Hertz: the discovery of the medical uses of radioiodine. *World J Nucl Med.* 2019;18:8–12.
5. Obaldo JM, Hertz BE. The early years of nuclear medicine: a retelling. *Asia Ocean J Nucl Med Biol.* 2021;9:207–219.
6. Gallagher CR. *Nazis of Copley Square: The Forgotten Story of the Christian Front.* Harvard University Press; 2021:1–336.
7. Thrall JH. *MGH Russell Museum presentation, Saul Hertz: radioiodine and the origins of nuclear medicine*. https://www.youtube.com/watch?v=34Qhm8CeMuc. Published April 13, 2016. Accessed February 20, 2024.
8. Hertz S, Roberts A. Radioactive iodine in the study of thyroid physiology; the use of radioactive iodine therapy in hyperthyroidism VII. *J Am Med Assoc.* 1946;131:81–86.
9. Chapman EM, Evans ED. The treatment of hyperthyroidism with radioactive iodine. *J Am Med Assoc.* 1946;131:86–91.
10. Hertz S, Lerman J. The blood picture in exophthalmic goitre and its changes resulting from iodine and operation. A study by means of the supravital technique. *J Clin Invest.* 1932;11:1179–1196.

First-in-Human ^{212}Pb-PSMA–Targeted α-Therapy SPECT/CT Imaging in a Patient with Metastatic Castration-Resistant Prostate Cancer

Matthew R. Griffiths[1], David A. Pattison[1], Melissa Latter[1], Kevin Kuan[2], Stephen Taylor[2], William Tieu[2], Thomas Kryza[2], Danielle Meyrick[2], Boon Quan Lee[2], Aaron Hansen[3], Stephen E. Rose[2], and Simon G. Puttick[2]

[1]Department of Nuclear Medicine and Specialist PET Services, Royal Brisbane and Women's Hospital, Brisbane, Queensland, Australia; [2]AdvanCell, Sydney, New South Wales, Australia; and [3]Department of Medical Oncology, Princess Alexandra Hospital, Brisbane, Queensland, Australia

There is significant interest in the development of ^{212}Pb-PSMA–based targeted α-therapy for patients with metastatic castration-resistant prostate cancer. A previous phantom study has shown that ^{212}Pb SPECT is feasible by imaging the 238.6 keV and 75 to 91 keV γ-emissions produced after the β-decay of ^{212}Pb to its α-emitting progeny (*1*).

Here we present—to the best of our knowledge—the first human ^{212}Pb SPECT/CT images published to date. They were acquired after administration of 60 MBq of ^{212}Pb-ADVC001 to a 73-y-old man with metastatic castration-resistant prostate cancer. This study was approved by the local institutional review board. Imaging was at 1.5, 5, 20, and 28 h after infusion. Two simultaneous triple-energy window acquisitions (78 keV ± 20% with 20% scatter [31% abundance] and 239 keV ± 10% with 10% scatter [43% abundance] were obtained using a Siemens Intevo Bold (high-energy collimators at 30 s per view for 120 views per rotation at 2 bed positions with noncircular orbits; total time, 60 min). Each energy window was reconstructed independently, and the resulting images were summed with removal of Compton-based orbit artifacts.

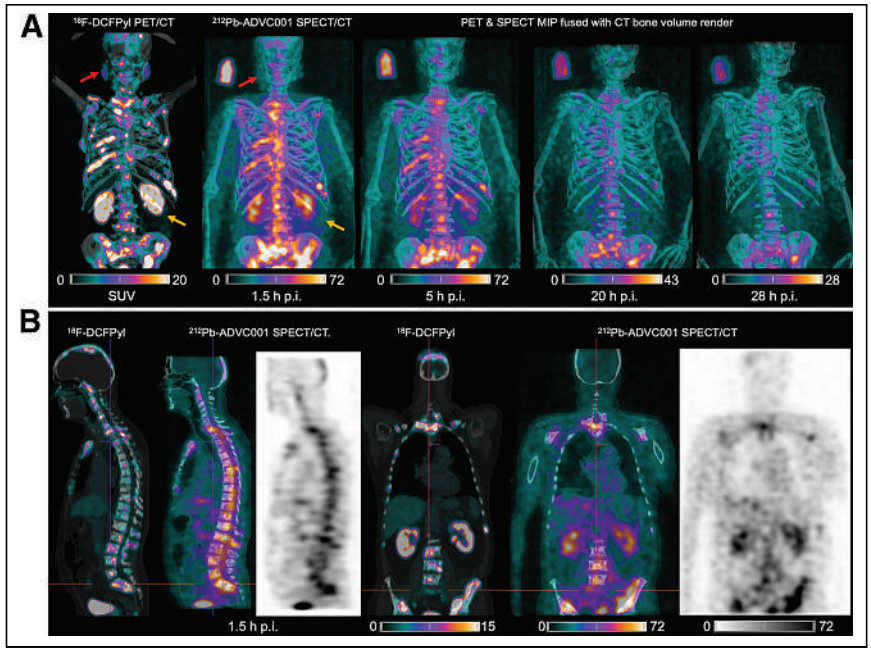

FIGURE 1. (A) ^{18}F-DCFPyl PET/CT and ^{212}Pb SPECT/CT images showing concordant tumor biodistribution with low salivary gland uptake (red arrow) and rapid kidney clearance of 60 MBq of ^{212}Pb-ADVC001 (structure of ^{212}Pb-ADVC001 available as supplemental material at http://jnm.snmjournals.org). A 3-MBq standard solution (100 mL) was included. (B) Sagittal and coronal images at 1.5 h after injection (p.i.). MIP = maximum-intensity projection.

Representative ^{212}Pb SPECT/CT images (Fig. 1) showed rapid tumor uptake of ^{212}Pb-ADVC001 highly concordant with tumor burden delineated on the pretreatment ^{18}F-DCFPyl PET/CT images. Images acquired after 20 h showed persistent tumor uptake despite low counts due to ^{212}Pb decay (10.6 h half-life).

^{212}Pb is a challenging isotope to image because of the high-energy γ-rays from the lead progeny generating Compton scatter from the patient and collimator (*1*). Our approach of summing images reconstructed from both energy windows shows the feasibility and benefit of ^{212}Pb SPECT/CT imaging in providing postinfusion radiopharmaceutical biodistribution and patient-specific dosimetry for clinical development of ^{212}Pb-targeted α-therapy.

DISCLOSURE

This work was financially supported by AdvanCell through the TheraPb clinical trial (NCT05720130). Kevin Kuan, Stephen Taylor, William Tieu, Thomas Kryza, Stephen Rose, and Simon Puttick are AdvanCell employees. Danielle Meyrick and Boon Quan Lee are AdvanCell consultants. No other potential conflict of interest relevant to this article was reported.

ACKNOWLEDGMENT

We acknowledge the clinical staff at the Princess Alexandra Hospital.

REFERENCE

1. Kvassheim M, Revheim MER, Stokke C. Quantitative SPECT/CT imaging of lead-212: a phantom study. *EJNMMI Phys.* 2022;9:52.

Received Dec. 1, 2023; revision accepted Jan. 23, 2024.

For correspondence or reprints, contact Stephen Rose (stephen@advancell.com.au).

Published online Feb. 29, 2024.

DOI: 10.2967/jnumed.123.267189

Imaging PARP Upregulation with [^{123}I]I-PARPi SPECT/CT in Small Cell Neuroendocrine Carcinoma

Honest Ndlovu[1], Ismaheel Lawal[1,2], Kgomotso Mokoala[1], Dineo Disenyane[3], Nonhlahla Nkambule[4], Sheynaz Bassa[4], Yonwaba Mzizi[1], Meshack Bida[3], and Mike Sathekge[1]

[1]Nuclear Medicine Research Infrastructure; Department of Nuclear Medicine, Steve-Biko Academic Hospital, University of Pretoria, Pretoria, South Africa; [2]Department of Radiology and Imaging Sciences, Emory University, Atlanta, Georgia; [3]National Health Laboratory Services and University of Pretoria, Pretoria, South Africa; and [4]Department of Radiation Oncology, University of Pretoria and Steve Biko Academic Hospital, Pretoria, South Africa

A 61-y-old man underwent [^{18}F]FDG PET/CT for staging of right-lung small cell neuroendocrine carcinoma. The images (Fig. 1A) showed a tracer-avid right-lung mass. As part of a feasibility study approved by the University of Pretoria Ethics Committee, the subject gave written informed consent to additionally undergo [^{123}I]I-poly(adenosine diphosphate ribosyl)-polymerase (PARP) inhibitor (PARPi) SPECT/CT. To the best of our knowledge, this study is the first in humans to use [^{123}I]I-PARPi to image PARP upregulation in solid tumors. Images acquired at 4 h after tracer administration demonstrated [^{123}I]I-PARPi avidity in the right-lung mass. Subsequent [^{18}F]FDG PET/CT imaging obtained for response assessment after 2 cycles (Fig. 1B) and 6 cycles (Fig. 1C) of chemotherapy with carboplatin and etoposide continued to show the lung mass, along with new metastases in the mediastinal nodes, right adrenal gland, liver, and bone, consistent with disease progression. Immunohistochemistry was done using rabbit antibody against PARP, with splenic sinusoids and tonsillar tissue as negative and positive controls, respectively. On the baseline right-lung biopsy sample, immunohistochemistry was strongly positive for PARP upregulation.

PARP enzymes are upregulated after single-strand DNA breaks as part of the DNA damage response. Their upregulation confers resistance to conventional therapies but makes treatment with PARPi feasible. PARPi therapy is a novel option with survival benefits in tumors exhibiting homologous recombination DNA repair deficiencies (*1*). Without appropriate patient selection, the benefits of PARPi therapy are limited. These can be improved by selecting patients through use of immunohistochemistry and whole-body imaging for PARP upregulation (*2*,*3*). The synthesis and preclinical characterization of [^{123}I]I-PARPi have been previously reported (*4*). Here, we report the feasibility of [^{123}I]I-PARPi SPECT/CT as a noninvasive tool for whole-body assessment of PARP upregulation in lung small cell neuroendocrine carcinoma. A potential application is patient selection and response prediction for PARPi therapy. [^{123}I]I-PARPi may have therapeutic use by harnessing the cytotoxic effect of the emitted Auger electron.

DISCLOSURE

Theragnostic Inc. supplied the PARPi cold kit, iThemba Labs supplied [^{123}I]iodine, and AXIM Nuclear & Oncology perfomed the radiolabeling. No other potential conflict of interest relevant to this article was reported.

REFERENCES

1. Cortesi L, Rugo HS, Jackisch C. An overview of PARP inhibitors for the treatment of breast cancer. *Target Oncol.* 2021;16:255–282.
2. Pietanza MC, Waqar SN, Krug LM, et al. Randomized, double-blind, phase II study of temozolomide in combination with either veliparib or placebo in patients with relapsed-sensitive or refractory small-cell lung cancer. *J Clin Oncol.* 2018;36:2386–2394.
3. Schöder H, de Souza França PD, Nakajima R, et al. Safety and feasibility of PARP1/2 imaging with ^{18}F-PARPi in patients with head and neck cancer. *Clin Cancer Res.* 2020;26:3110–3116.
4. Wilson TC, Jannetti SA, Guru N, Pillarsetty N, Reiner T, Pirovano G. Improved radiosynthesis of ^{123}I-MAPi, an auger theranostic agent. *Int J Radiat Biol.* 2023;99:70–76.

Received Jul. 13, 2023; revision accepted Nov. 9, 2023.
For correspondence or reprints, contact Mike Sathekge (mike.sathekge@up.ac.za).
Published online Nov. 30, 2023.

DOI: 10.2967/jnumed.123.266348

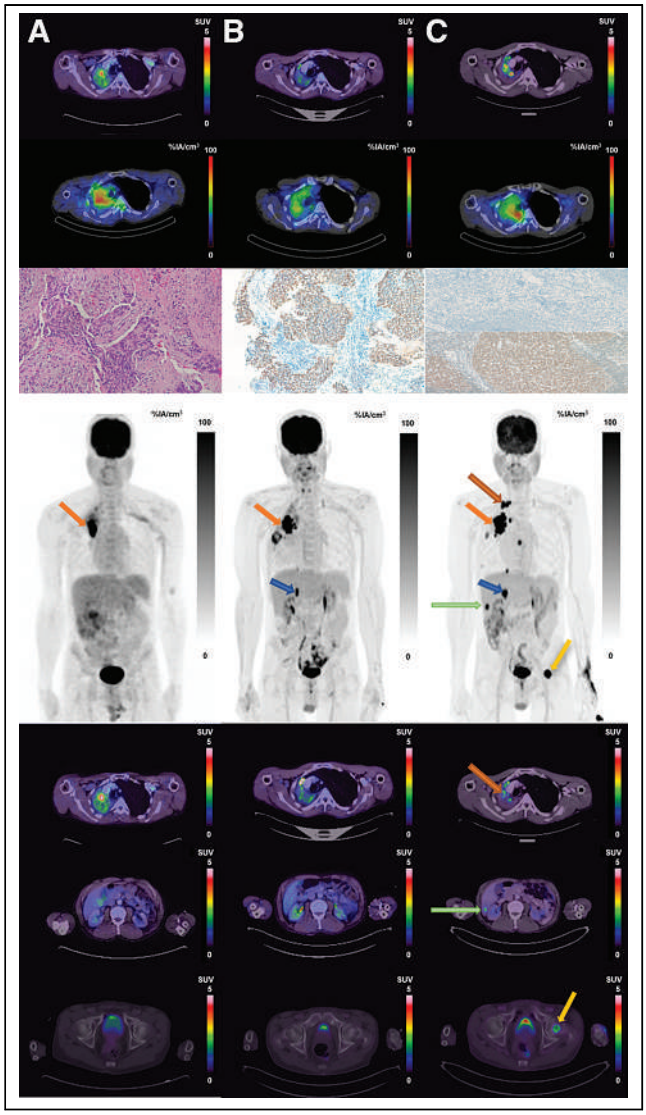

FIGURE 1. Imaging at baseline (A), early response assessment (B), and end of therapy (C). Shown from top to bottom are transaxial PET/CT, transaxial 4-h SPECT/CT, immunohistochemistry (×20 hematoxylin and eosin staining at left, ×10 PARP staining at middle and right), maximum-intensity-projection PET, and PET/CT. Hypermetabolic lung mass is seen on PET/CT (SUV_{max}, 3.8) and SPECT/CT at baseline. Uptake on both modalities persists at early response assessment and at end of therapy (SUV_{max}, 4.5 and 4.9, respectively). Immunohistochemistry was strongly positive for PARP upregulation. Disease progression was noted on maximum-intensity projections and on PET/CT, with new lymph node metastases indicated by amber arrow above orange arrow seen on both maximum-intensity projection and PET/CT imaging (SUV_{max}, 4.5), adrenal gland metastases indicated by blue arrow on maximum-intensity projection images, liver metastases indicated by green arrow on both maximum-intensity projection and PET/CT images, bone metastases indicated by yellow arrow in the maximum-intensity projection images and PET/CT images (last row, third column). %IA = percentage injected activity.

2024 ACNM/SNMMI **HOT TOPICS** Webinar Series

SNMMI and ACNM are excited to announce the lineup for the 2024 Hot Topics Webinar Series. **These informative webinars will take place at 12:00 pm ET on the second Tuesday of each month and are complimentary for ACNM and SNMMI members.**

- **History of Nuclear Medicine Technology**
  On Demand | *Fred Fahey*
- **AI in Nuclear Medicine: State of the Union**
  On Demand | *Katherine Zukotynski*
- **Prostate Radioligand Therapy Prior to Chemotherapy**
  On Demand | *Oliver Sartor*
- **PET/MR for Pediatrics**
  April 9 | *Helen Nadel*
- **Evolving Landscape of Prostate Cancer Imaging**
  May 14 | *François Bénard*
- **The Evolution of PRRT for NET–Y90, Lu177, Ac225**
  June-SNMMI AM | *Lisa Bodei*
- **Advancing Precision Therapeutics in Dementia–How Does Imaging Fit In?**
  July 9 | *Sandra Black*
- **Contemporary Approach to PET Myocardial Perfusion Imaging**
  August 13 | *Panithaya Chareonthaitawee*
- **ER/PR/HER2-Targeted Imaging for Breast Cancer**
  September 10 | *Farrokh Dehdashti*
- **PET for Histiocytosis/ Erdheim Chester Disease**
  October 8 | *Sonia Mahajan*
- **What is New in Infection Imaging?**
  November 12 | *Ora Israel*
- **Prostate Cancer Imaging Agents–Is There a Difference?**
  December 10 | *Wolfgang Weber*

SNMMI SOCIETY OF NUCLEAR MEDICINE & MOLECULAR IMAGING

ACNM American College of Nuclear Medicine

Register today!

www.acnmonline.org/webinars

03204241

SPECTRUM
DYNAMICS MEDICAL

VERITON-CT®
SERIES

QUANTITATION
Tumor burden | Dosimetry

ACCURACY
Across all energies

SPEED
Highest sensitivity

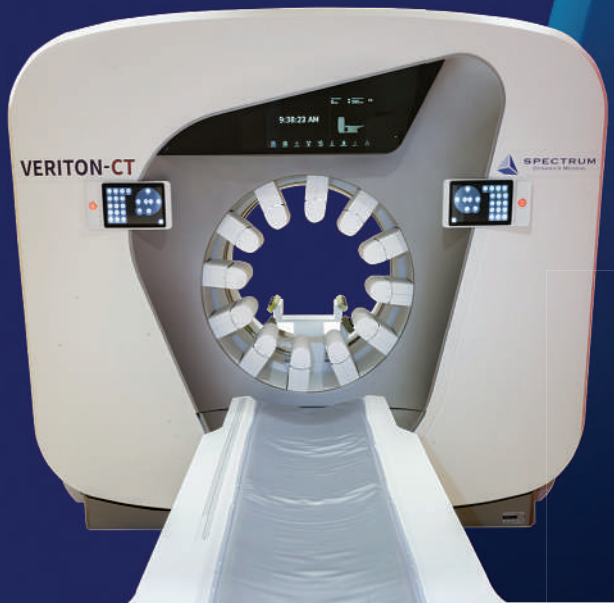

Breaking Barriers in SPECT Theranostics

VERITON-CT digital SPECT/CT, the system with the best sensitivity and energy resolution, enables you to image Lu177 PSMA and Lu177 Dotatate with speed and accuracy, and prepares you for future Theranostic agents.

BroadView Technology
High sensitivity swiveling digital detectors

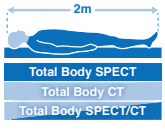

Total Body 3D Imaging
200cm hybrid scan range, real-time body contour

Wide Bore SPECT/CT
80cm SPECT and CT

16/64 High Resolution CT
Choice of 16sl or 64sl, low dose CTAC

TruView Console
Acquisition, reconstruction and advanced quantitative analysis in one location

Performance
Reaching new peaks in digital SPECT imaging 400+keV isotopes.*

www.spectrum-dynamics.com

*VERITON-CT 300 up to 300 keV, VERITON-CT 400+ keV

Scan to Learn More

4/24

The Journal of Nuclear Medicine

April 2024 ■ Vol. 65 ■ Pages 499–666